

WRDC-TR-90-4096
VOLUME 2

AD-A242 871



DTIC
ELECTS
NOV 20 1991
S C D



**DETERMINATION OF THE TRIBOLOGICAL
FUNDAMENTALS OF SOLID LUBRICATED CERAMICS
VOLUME 2: APPENDICES A THROUGH O**

M.N. Gardos
Hughes Aircraft Company
El Segundo, CA 90245

September 1991

Final Report for Period 09 September 1985 to 16 September 1989

Approved for public release, distribution is unlimited

91-15963



**MATERIALS DIRECTORATE
WRIGHT RESEARCH AND DEVELOPMENT CENTER
AIR FORCE SYSTEMS COMMAND
WRIGHT-PATTERSON AIR FORCE BASE, OHIO 45433-6533**

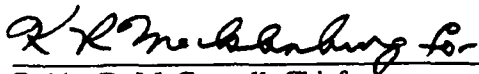
91 1119 000

NOTICE

When Government drawings, specifications, or other data are used for any purpose other than in connection with a definitely Government-related procurement, the United States Government incurs no responsibility or any obligation whatsoever. The fact that the government may have formulated or in any way supplied the said drawings, specifications, or other data, is not to be regarded by implication, or otherwise in any manner construed, as licensing the holder, or any other person or corporation; or as conveying any rights or permission to manufacture, use, or sell any patented invention that may in any way be related thereto.

This report is releasable to the National Technical Information Service (NTIS). At NTIS, it will be available to the general public, including foreign nations.

This technical report has been reviewed and is approved for publication.



Bobby D. McConnell, Chief
Nonstructural Materials Branch
Nonmetallic Materials Division

FOR THE COMMANDER

Merrill L. Minges, Director
Nonmetallic Materials Division

If your address has changed, if you wish to be removed from our mailing list, or if the addressee is no longer employed by your organization please notify WL/MLBT, WPAFB, OH 45433-6533 to help us maintain a current mailing list.

Copies of this report should not be returned unless return is required by security considerations, contractual obligations, or notice on a specific document.

UNCLASSIFIED

SECURITY CLASSIFICATION OF THIS PAGE

REPORT DOCUMENT PAGE				Form Approved OMB No. 0704-0188		
1a. REPORT SECURITY CLASSIFICATION UNCLASSIFIED			1b. RESTRICTIVE MARKINGS			
2a. SECURITY CLASSIFICATION AUTHORITY EDSG Document			3. DISTRIBUTION / AVAILABILITY OF REPORT Approved for public release; distribution is unlimited			
2b. DECLASSIFICATION / DOWNGRADING SCHEDULE						
4. PERFORMING ORGANIZATION REPORT NUMBER(S)			5. MONITORING ORGANIZATION REPORT NUMBER(S) WRDC-TR-90-4096, Vol. 2			
6a. NAME OF PERFORMING ORGANIZATION Hughes Aircraft Company Electro-Optical & Data Systems Group		6b. OFFICE SYMBOL (If applicable) EDSG	7a. NAME OF MONITORING ORGANIZATION Materials Directorate (WL/MLBT) Wright Research and Development Center, AFSC			
6c. ADDRESS (City, State, and ZIP Code) P.O. Box 902 El Segundo, CA 90245			7b. ADDRESS (City, State, and ZIP Code) Wright-Patterson AFB OH 45433-6533			
8a. NAME OF FUNDING / SPONSORING ORGANIZATION		8b. OFFICE SYMBOL (If applicable)	9. PROCUREMENT INSTRUMENT IDENTIFICATION NUMBER F33615-85-C-5087			
8c. ADDRESS (City, State, and ZIP Code)			10. SOURCE OF FUNDING NUMBERS			
			PROGRAM ELEMENT NO. 61101E	PROJECT NO. 5177	TASK NO. 00	WORK UNIT ACCESSION NO. 01
11. TITLE (Include Security Classification) Determination of the Tribological Fundamentals of Solid Lubricated Ceramics Volume 2: Appendices A through O						
12. PERSONAL AUTHOR(S) Michael N. Gardos						
13a. TYPE OF REPORT Final Report		13b. TIME COVERED FROM 09-85 TO 09-89		14. DATE OF REPORT (Year, Month, Day) September 1991		15. PAGE COUNT 572
16. SUPPLEMENTARY NOTATION						
17. COSATI CODES			18. SUBJECT TERMS (Continue on reverse if necessary and identify by block number)			
FIELD	GROUP	SUB-GROUP	Ceramics Ab-initio Solid Lubricants			
			Diamond Molecular Dynamics Extreme Environments			
			Tribology Analytical Tribometry Friction/Wear Testing			
19. ABSTRACT (Continue on reverse if necessary and identify by block number)						
<p>The goals, structure and highlights of a recently completed multiyear/multinational research program are described. The main driving force behind this effort was the aim to advance the technology base so engineers can successfully and confidentially design, build and operate solid lubricated ceramic tribocomponents in extreme environments. Specially designed friction and wear testers were employed to perform well-defined model experiments on single crystal and polycrystalline ceramics and solid lubricants. The research led to discoveries such as (1) a lubricious oxide with the shear strength of MoS₂ in vacuum, (2) CVD diamond films with low friction and extraordinarily low wear, (3) intercalated graphites with high tribothermal resistance in vacuum and in air, and (4) a wear equation for Si₃N₄ ceramics. The fundamental nature of the research was exemplified by ab-initio predictions of the friction coefficient of single crystal (111) diamond sliding against its mating (111) diamond plane, and molecular dynamics calculations on single crystal CaF₂ and BaF₂ (111) [110] interface shear forces. The test equipment developed for completing the model experiments included an Anger/ESCA tribometer capable of unidirectional and oscillatory sliding at room temperature, a SEM tribometer designed for oscillatory sliding to 1000°C in vacuum and in partial pressures of reactive gases, an 850°C + dual-rubeshoe friction and wear tester employing a rolling contact fatigue rod as one of the sliding specimens, and 850°C + friction/traction apparatus capable of operating to extraordinarily high PV limits.</p> <p>The fundamental nature of the research notwithstanding, the main goals were directed towards finding potential solutions and applications useful to practicing tribologists and lubrication engineers.</p>						
20. DISTRIBUTION / AVAILABILITY OF ABSTRACT <input checked="" type="checkbox"/> UNCLASSIFIED/UNLIMITED <input type="checkbox"/> SAME AS RPT. <input type="checkbox"/> DTIC USERS			21. ABSTRACT SECURITY CLASSIFICATION UNCLASSIFIED			
22a. NAME OF RESPONSIBLE INDIVIDUAL KARL R. MECKLENBURG			22b. TELEPHONE (Include Area Code) (513) 255-2465		22c. OFFICE SYMBOL WL /MLBT	

FOREWORD

The overall objective of this 48-month interdisciplinary program was to investigate fundamental microscopic, macroscopic and continuum phenomena which occur between bare and solid lubricated ceramic surfaces exposed to a variety of extreme, triboenvironmental conditions. The title of the program is "Determination of Tribological Fundamentals", DARPA Order No. 5177, WRDC Contract No. F33615-85-C-5087.

Key government personnel monitoring the program included: Lt. Col. Steven G. Wax, Dr. Kay Rhyne and Dr. Benjamin A. Wilcox as the DARPA Program Managers and Bobby D. McConnell as the WRDC/MLBT Project Engineer. Dr. Larry L. Fehrenbacher (TA&T, Inc., Annapolis, MD) was a consultant to DARPA, assisting in the programmatic oversight and guidance of the technical efforts.

Various aspects of research were performed within the Technology Support Division of the Electro-Optical and Data Systems Group (EDSG) of Hughes Aircraft Company, under the direction of Dr. Michael N. Gardos as the Principal Investigator. The Hughes Program Managers were Dr. Gardos, Robert W. Seibold, Dr. Arthur B. Naselow and Earl B. Holst in chronological order of service. The research activities were conducted by personnel at EDSG and other Hughes groups, ably assisted by expert subcontractors from academia and industry located in this country and Western Europe.

Hughes personnel performing various technical tasks included Bonnie L. Soriano, Bruce W. Buller, Patrick S. Davis, Gerald L. Meldrum and Phil M. Magallanes (tribotesting and data reduction), Leo Fiderer, Dr. Stuart S. Gassel, Larry Czichola, Hans D. Metzler and Jim J. Erickson (tribotester design), Crawford R. Meeks, Ahn A. Tran, John P. Harrell and Rick Williams (mechanical and thermal analyses by computer methods), Dr. Norman H. Harris, Dr. Daniel A. Demeo and Phyllis J. Kelleghan (ceramic science and chemical analysis), as well as Dr. Mort Robinson, Mr. Kevin W. Kirby and Dr. John A. Roth (CaF₂/BaF₂ single crystal growth, polishing and analysis). Special recognition is given to Dora A. Monteiro (technical publications).

The Hughes subcontractors and the DoD scientists which closely cooperated within the confines of the program are properly recognized in the INTRODUCTION AND EXECUTIVE SUMMARY section.



Accession For	
NTIS GRA&I	<input checked="" type="checkbox"/>
DTIC TAB	<input type="checkbox"/>
Unannounced	<input type="checkbox"/>
Justification	
By	
Distribution/	
Availability Codes	
Dist	Avail and/or Special
A-1	

CONTENTS

	Page
VOLUME 2	
APPENDIX A – W.A. Goddard III, "Atomic Level Modeling of the Chemical and Tribological Properties of Ceramic Surfaces," Final Report, California Institute of Technology, Pasadena, CA, 17 February 1988; Hughes P.O. S9-225147-237, Rev. A.....	A1-A33
APPENDIX B – U. Landman, "Microscopic Modeling of Tribological Phenomena," Final Report, Georgia Institute of Technology, Atlanta, GA, Hughes P.O. S9-512917-SKG.....	B1-B35
APPENDIX C – S. Granick, "Assessment of the Usefulness of Direct Force Methods to Elucidate the Adhesion and Tribology of Solid Lubricated Ceramics," Final Report, U. of Illinois, Urbana-Champaign, IL, October 23, 1989; Hughes P.O. M9-515286-Z6L.....	C1-C25
APPENDIX D – J.-M. Martin, and Th. Le Mogne, "Friction of Hexagonal Boron Nitride in Various Environments," Final Report, Ecole Centrale de Lyon/SORETRIB, Lyon, France, Feb. 1990; Hughes P.O. S9-317657-SKD.....	D1-D154
APPENDIX E – J.-M. Martin, Th. Le Mogne, H. Montes, and M.N. Gardos, "Tribiochemistry of Alpha Silicon Carbide Under Oxygen Partial Pressure," Proc. 5th Int. Congress on Tribology, EUROTRIB '89, Paper S2. 5/5, June 12-15, 1989, Helsinki, Finland.....	E1-E6
APPENDIX F – J.J. Erickson, "Meeting at MRL Re: SEM Cryogenic Tribotester" Hughes Interdepartmental Correspondence No. 7641.20/1076, 30 November 1987.....	F1-F4
APPENDIX G – L. Fiderer, "Unique Friction and Wear Tester for Fundamental Tribology Research," Hughes Technical Internal Correspondence No. 867282.00/920, 22 September 1986.....	G1-G44
APPENDIX H – J.P. Harrel, "Tribotester Structural Analysis," Hughes Interdepartmental Correspondence No. 867282.20/930, 29 October 1986.....	H1-H15
APPENDIX I – R. Williams, "Thermal Analysis of the Tribotester Test Fixture," Hughes Interdepartmental Correspondence No. 7735.10/234, 09 September 1986.....	I1-I12
APPENDIX J – B.L. Soriano, "Room Temperature Friction and Wear Testing for Bare Ceramic Contacts," Hughes Interdepartmental Correspondence No. 7621.12/121.87, 02 November 1987.....	J1-J35
APPENDIX K – H. Kaplan, "Summary Report on Infrared Pyrometer Selection," Honeyhill Technical Co., Norwalk, CT, 01 August 1986, Hughes P.O. S9-245763-Z6X.....	K1-K5
APPENDIX L – PYROLASER Description and Specifications, Pyrometer Instrument Co., Inc., Northvale, NJ, Tech. Bulletin.....	L1-L3

CONTENTS (Concluded)

	<u>Page</u>
 VOLUME 2	
APPENDIX M – W.O. Winer, "Tester 2A," technical letter to M.N. Gardos (Hughes) from the Georgia Institute of Technology, 13 April 1987.....	M1-M5
APPENDIX N – H. Heshmat, "Rotor and Structural Dynamic Analysis and Assess- ment of Hughes Tribotester 2A," Technical Report, Mechanical Technology, Inc., Latham, NY, Hughes P.O. S9-266415-S7H.....	N1-N87
APPENDIX O – H. Heshmat, P. Albrecht, and J.F. Dill, "Friction and Wear Testing of Ceramic Materials," Final Report, MTI Report No. 90TR1, Mechanical Technology, Inc., Latham, NY, Hughes P.O. S9-316055-SAC.....	01-087

APPENDIX A

W.A. Goddard III, "Atomic Level Modeling of the Chemical and Tribological Properties of Ceramic Surfaces," Final Report California Institute of Technology, Pasadena, CA, 17 February 1988; Hughes P.O. S9-225147-237, Rev. A

**Atomic-Level Modeling of the Chemical and
Tribological Properties of Ceramic Surfaces**

Final Technical Progress Report

Prepared by: Professor William A. Goddard III

California Institute of Technology

17 February 1988

for

Hughes Aircraft Company

Purchase Order No. S9-225147-Z37

Revision "A", Dated 29 May 1987

I. INTRODUCTION

There were several goals to this research. The major one was to develop a strategy for establishing a microscopic atomic-level understanding of the fundamental surface processes ultimately responsible for friction, adhesion at surfaces, and abrasion. The major focus was on ceramics because of their promise both at high temperature (high performance turbines) and at low temperatures (space). A secondary focus was on the solid lubricants likely to be important in these severe temperature regimes.

The strategy developed here for obtaining a microscopic atomic-level understanding of friction involves a cooperative, two-pronged attack using both theory and experiment. The theoretical approaches use the techniques of quantum chemistry, molecular mechanics, and Monte Carlo sampling to simulate at the atomic level the dynamical processes involved in tribology. The new experimental approaches use the techniques of surface science to characterize the surface species and to measure the fundamental forces relevant to tribology.

Critical to this strategy is the development of a sequence of tribologically relevant systems suitable both for theoretical study and amenable to development of procedures for achieving particular surface configurations. This is necessary so that experimentalists in different laboratories using different techniques will obtain reproducible results about the same surface system. It is also essential for developing theoretical models.

2.0 SUMMARY OF THE KEY ISSUES

2.1 Fundamentals of Tribology

At the heart of such technological challenges as designing the next generation of high performance gas turbines is the critical need to solve extremely difficult tribological problems, particularly for ceramic components. In order to progress substantially in this endeavor, it is essential to establish a microscopic atomic-level understanding of the fundamental surface processes ultimately responsible for friction, adhesion, abrasion, and wear. Both theory (quantum chemistry, simulation) and experiment (surface chemistry, surface physics) are essential in establishing this fundamental microscopic atomic-level understanding (see Figure 1). At the most basic level, all of tribology is chemistry, i.e., making and breaking of chemical bonds (adhesion, oxidation, chemical dissolution, movement of atoms, dislocations, slip planes). Elucidation of the chemistry controlling tribology should lead to completely new strategies in designing tribological systems for extreme environments.

2.2 Hierarchy of Modeling

The overall plan is to establish a hierarchy of modeling (see Figure 2), starting at the most fundamental with quantum theory (electrons and nuclei), proceeding then to atomic-level molecular dynamics/Monte Carlo simulations and progressing through more approximate lumped parameter models involving grains instead of atoms and then with more approximate descriptions, involving a continuum instead of grains. This progression allows consideration of larger systems with longer time scales, albeit with a loss of detailed atomic-scale information. At each level, the precise parameters (including chemistry and thermochemistry) of the deeper level get lumped into those of the next. The overlap between each level is used to establish these connections. This hierarchy allows motion up and down as new experiments and theory lead to new understanding of the higher levels, and new problems demand new information from the lower levels.

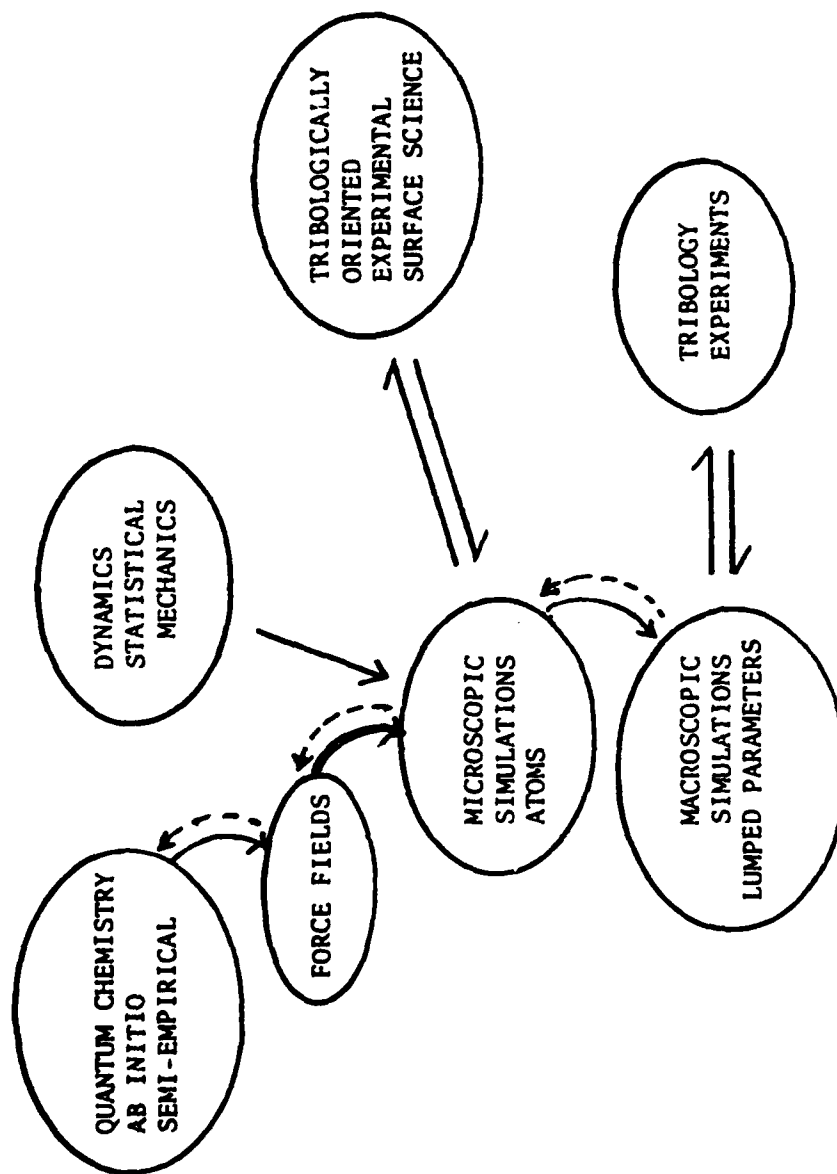


FIGURE 1.

HIERARCHY OF MODELS TRIBOLOGY

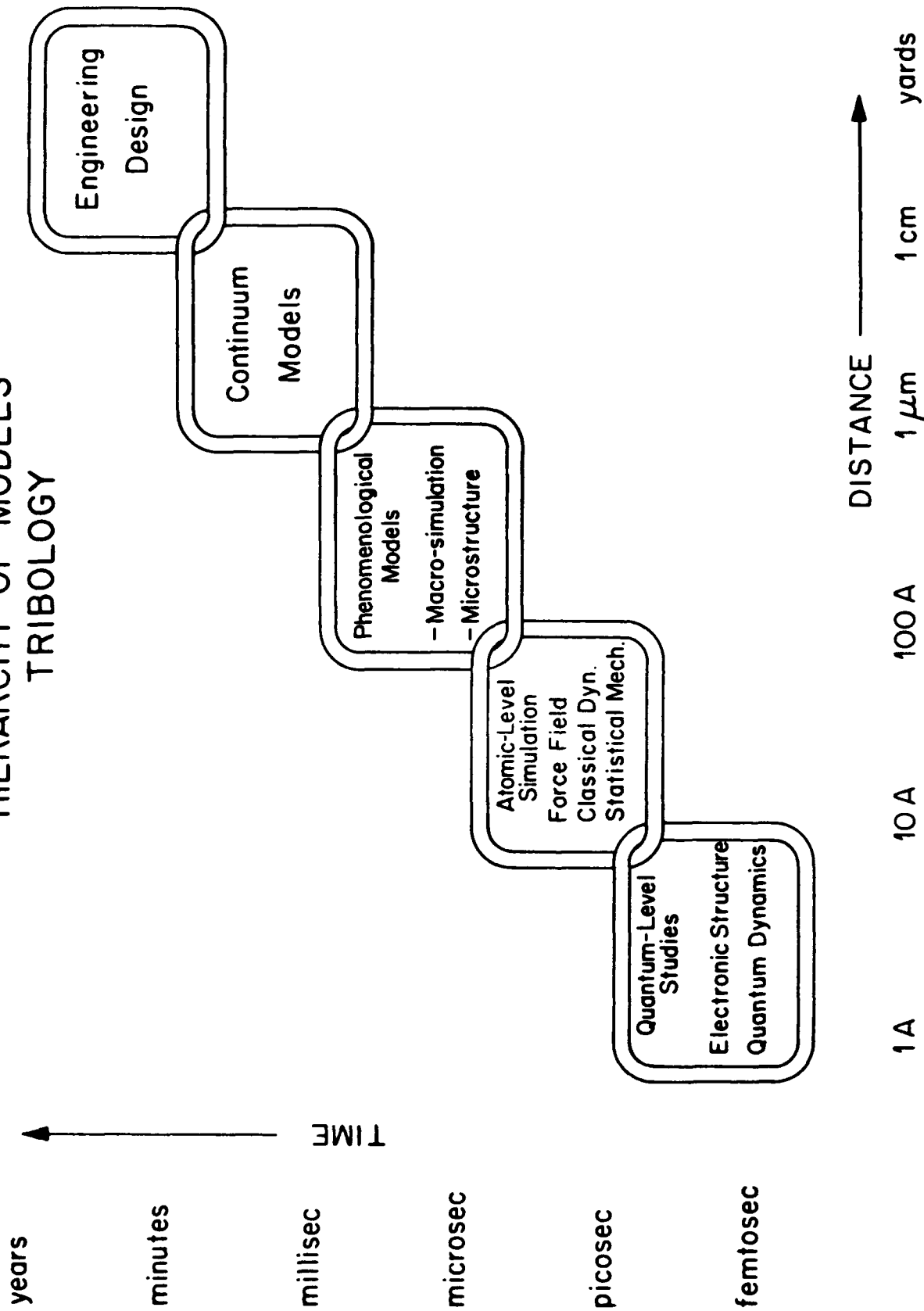


Figure 2. Sketch indicating the relationships and connections between atomic-level descriptions of materials and the microscopic, macroscopic, and engineering models used in rationalizing experiments and designing new materials.

2.3 Standard Systems for Model Experiments and Theory

Critical to development of these fundamentals is a set of systems that can be prepared and studied reproducibly in *different* laboratories by techniques capable of atomic-level resolution and suitable to test the results of theoretical modeling.

3.0 OUTLINE OF THEORETICAL MODELING

Although there have been rapid advances in the experimental techniques for examining composition at surfaces and interfaces relevant for catalysis, tribology, corrosion, and materials synthesis, there is yet very little in the way of a microscopic theoretical model suitable for understanding the chemical, physical, and mechanical properties in terms of atomic-level structure and bonding concepts. We recommend a broad-based theoretical program aimed at providing the fundamentals for constructing such an atomic-level microscopic model of the chemical, tribological, physical, and mechanical properties of ceramic surfaces and interfaces. The approach would be

1. to carry out a series of quantum chemical studies to establish the dominant surface species for clusters of atoms modeling various ceramics and to elucidate the thermochemistry and detailed mechanistic steps involved in surface reactions of such systems;
2. to use the energy surfaces for clusters from (1.) to develop theoretical force fields that allow predictions of the energies and geometries for infinite surfaces and interfaces;
3. to develop procedures for molecular dynamics and Monte Carlo simulations that in conjunction with the force fields from (2.) could be used to predict the rates for various diffusive and chemical processes relevant for tribology and for materials synthesis processes; and
4. to interface the results of these simulations onto appropriate graphics systems, allowing the designer to follow a three-dimensional image of the evolving system while interactively changing conditions and characteristics of the systems.

Through simultaneous examination of all properties of the surface (chemical, tribological, physical, and mechanical) with the same theory, there is the possibility for strong tests on different aspects of the theory. In addition, such a central theory would provide new connections between these properties that would serve to relate what are now discon-

nected experiments. These theoretical developments of experimentally relevant systems should provide a level of understanding useful in designing new materials with useful tribological properties, and such computer-aided materials simulations should provide tools allowing many of the design concepts to be tested on the computer in advance of attempting difficult syntheses and characterizations in the laboratory.

3.1 Simulations of Ionic Solids

Over the last decade, there has been a great deal of progress in simulating ionic solids such as halides and oxides.¹ Thus, in a variety of systems, it has been possible to provide rather accurate predictions of the energy of formation of such point defects as vacancies,^{2,3} vacancy-interstitial pairs,² and substitutional impurities.² In addition, it has been possible to obtain useful estimates of band gaps and of donor and acceptor energies for various defects.²

These approaches have been used to predict rather complicated defect equilibria (e.g., vacancy clustering⁴) and have been used to predict diffusion in ternary oxides⁵ and the detailed transport properties of fast ion conductors (e.g., CaF_2 ,^{6,7} AgI ,^{7,8} and $-\text{Al}_2\text{O}_3$). Even heavily doped systems have been treated.⁹ For alkali halides, surface reconstruction,^{10,11} surface energies,¹⁰ and point defects on surfaces¹² have also been calculated,^{10,11} and indeed even grain boundary properties have been predicted.¹³ Critical to such calculations are the potentials. The most successful seem to be those of Catlow¹¹ in which empirical two-body potentials are fitted to experimental structure and elastic constants, and a simple shell model of the atomic polarizabilities is fitted to the dielectric properties. However, use of approximate theoretical ion-ion potentials (in conjunction with a shell model for polarizability) has also been reasonably successful.¹⁴

Despite the above successes, it appears that a totally new approach will be necessary in order to attack the problems relevant to tribology of ceramics. The use of empirical two-body potentials implicitly includes the effect of three-body and higher interactions, which makes these potentials dependent upon the structure being considered (thus, the

F^-F^- potential in alkali halides^{11a} is significantly different from that in CaF_2 .^{11b} This leaves completely open the question of what to use at surfaces, grain boundaries, disordered regions, etc. In addition, for many systems of interest, there will be insufficient empirical data to determine the potentials. Worse yet, many of the systems of interest are quite covalent (e.g., Si_3N_4 , WC) and hence outside the province of the above methods. However, it appears that purely theoretical methods can be used to determine all potential parameters.

3.2 Simulation of Covalent Systems

Quantum chemistry approaches have, over the last decade, led to a number of advances in our understanding of surface science and catalysis.¹⁵ These studies typically involve calculating the electronic wavefunctions for a molecule as a function of nuclear geometry to obtain energy surfaces for ground and excited states and then examining the role of these energy surfaces for various reactions. Such quantum chemical studies will be important as the first step in examining surface configurations for various ceramic surfaces; however, to contribute a new understanding of tribology of ceramics, it will be necessary to develop methods for simulating the reaction dynamics on realistic models of these ceramic surfaces.

For the important materials questions relevant for ceramics, one must necessarily consider many thousands of atoms, and one must examine the dynamics over time scales appropriate both for chemical reactions and for diffusion. That is, we need to simulate on the computer the microscopic chemical and diffusion processes in the real system. Such simulations involve the following aspects:

1. The computer uses a general force field (describing the interactions of all particles in terms of two-, three-, and four-body forces) to evaluate the forces on all atoms at a given instant, takes the appropriate stochastic limits for nonessential degrees of freedom (describing, for example, the bulk atoms comprising the energy sink or source), and calculates the locations and velocities of the various atoms at the next

time step using classical (e.g., generalized Langevin) equations of motion.

2. At appropriate time steps, a corrected set of coordinates is passed from the computer to the graphics system (*vide infra*). The screen of the graphics system is continually refreshed with the current coordinates so that the user "sees" the reaction as it proceeds and can interactively examine the reactive system and follow the dynamics of the reaction.
3. The graphics system (with its own microprocessor and local memory so that it can rotate, translate, zoom, and window in real time) displays the whole reactive system (say, 10,000 atoms), rotates and translates the view to find the critical regions, and zooms in on a selected portion of this system. This graphics system automatically cuts away extraneous atoms of the reactive system and automatically lets more distant atoms fade away in intensity (depth cueing). It shows the system in three dimensions (using stereo glasses) so that the user can see the reactive system as a real three-dimensional image. It automatically color codes the atoms so that one can recognize instantly the composition and identity of the various species.
4. From the perspective of the user, he is watching the reaction as it proceeds. He can then interactively modify various parts of the system [surface structure (e.g., steps), vapor composition, atom identity, velocity (temperature of incoming particles), bulk defects, temperature on the surface, etc.] and follow the subsequent dynamics to determine the impact of these changes upon various processes.

This overall procedure is referred to as Computer-Assisted Materials Simulation (CAMS). CAMS involves two major theoretical components:

1. theoretical force fields (obtained from both theory and experiment) that accurately describe the forces on various atoms and molecules interacting at surfaces and with each other, and
2. theoretical methods to handle the dynamics of chemical processes within solids and on solid surfaces, including making and breaking of bonds and a description of energy

dissipation.

For systems with covalent bonds, a proper description of reactions requires the explicit treatment of how bonding changes from reactant to product with the proper resonance between the forms in the transition stage region. This requires a generalization of usual force fields where spin-pairing is optimized for the electrons involved in the reacting bonds. We have nearly completed¹⁶ an approach treating this problem. More serious difficulties arise in metallic systems where the multitude of low-lying electronic states and delocalization of electrons conspire to make reliable force fields a very difficult problem indeed. Progress on this problem has been made¹⁷ and these potentials should soon be suitable for simulations. However, for ceramics such delocalization is not a serious issue.

This theoretical approach to force fields allows one to consider any possible combination of atoms (even when no experimental data are available) and to examine regions of the potential surface (e.g., saddle points for reactions) not readily available to experiment. It also avoids a serious problem, the interdependence of potential parameters, endemic to fully empirical force fields due to the fact that there are little empirical data on highly excited states and on radicals and diradicals that would be needed to disentangle various interaction terms.

An additional issue concerns the dynamics. Various groups have developed efficient classical dynamics programs^{18,19} that can rapidly calculate all the forces and update all coordinates and velocities. Thus, the simulation of a small enzyme DHFR (dihydrofolate reductase), complete with cofactor (NADPH) and the cancer therapy agent methotrexate, all bathed in a thousand molecules of water (a total of 4500 atoms), takes 45 sec/time step on a VAX minicomputer.²⁰ With a good starting point (properly folded configurations), a well-optimized structure for a protein can be obtained in 600 steps (five hours on a VAX). Although such calculations are practical on the molecular time scale (picoseconds), many solid state processes require consideration of long time scales (microseconds, milliseconds, or longer). In solving this problem, the active atoms (the ones undergoing reaction) are

followed explicitly, but the more remote atoms are transformed away while retaining their role as a heat sink.²¹⁻²⁶ We have been handling this problem by a combination of stochastic approaches (Monte Carlo²⁷ or Brownian torsional dynamics²⁸) and modified dynamics (particularly the canonical dynamics of Nose²⁹).

As should be apparent, there are enormous theoretical difficulties in developing the force fields and dynamics methodology suitable for the critical materials problems. However, there are also enormous payoffs in terms of the potential for a new level of microscopic understanding of materials processes—an understanding that should promote the development of new materials designed to achieve a desired microscopic structure pretested by computer simulation.¹⁵

4.0 Methodologies

In theoretical studies of friction and wear, one can simulate moving contacts between surfaces by

- (1) modeling each surface (and any lubricant, wear particles, etc.) using the above techniques,
- (2) applying perpendicular forces of various magnitudes, and
- (3) displacing the surfaces with various velocities.

Such simulations would allow one to relate such useful macroscopic concepts as friction coefficients and hardness to the atomic structures and forces underlying these phenomena. In addition, the simulations would allow us to examine at the atomic level such phenomena as gouging and crack initiation and to determine the nature and role of atomistic defects induced under various conditions. These developments should provide a level of understanding useful in designing new materials and should provide tools allowing materials scientists to test many of the design concepts using computer graphics and the theoretical models to simulate the properties of the newly designed systems. In this way the designer would be able to refine many of the ideas in advance of attempting difficult syntheses and characterizations in the laboratory.

4.1 Theory

A variety of theoretical methods must be brought to bear in order to provide detailed predictions for comparison with experiment.

The methods of quantum chemistry can be used to predict the equilibrium geometries and vibrational frequencies for the various surfaces. In order to describe breaking and formation of chemical bonds (as involved in crack initiation and wear), it is necessary to carry out high-level calculations including electron correlation or many-body effects [e.g., generalized valence bond (GVB) theory].^{15,30} Such high-level treatments are also required in describing surface active species containing broken bonds or radical sites. For geometries and vibrational frequencies of passivated surfaces (where radical centers are not present),

less sophisticated methods [Hartree-Fock (HF) theory, local density approximations (LDF, LDA)] should be useful.

The methods suitable for accurately describing local phenomena are limited to a small number of atoms (with 20 atoms being a large system). However, for tribologically relevant studies, it is necessary to describe semi-infinite surfaces. This is achieved by developing a force field with which the dependence of the energy upon geometric configuration of the cluster (obtained from the accurate quantum chemistry calculations) is fitted to energy terms that depend on the distances and angles between various atoms,

$$E_{\text{cluster}}(x_1 y_1 z_1 \cdots x_{20} y_{20} z_{20}) = \sum_{i,j=1}^{20} E_{ij}(R_{ij}) + \sum_{ijk} E_{ijk}(R_{ij}, R_{jk}, \theta_{ijk}) + \sum_{ijk\ell} E_{ijk\ell}$$

If this fitting is carried out so that the components E_{ij} , E_{ijk} , etc., have physical significance, then these same terms can be superimposed to describe the energetics of the semi-infinite surface.

$$E_{\text{surface}}(x_1 y_1 z_1 \cdots x_{10000}, y_{10000}, z_{10000}) = \sum_{i,j=1}^{10000} E_{ij} + \sum_{ijk} E_{ijk} + \sum_{ijk\ell} E_{ijk\ell}$$

The forces on each atom are obtained by taking the derivative of the energy

$$F_{Ix} = -\frac{\partial E}{\partial x_I} \quad I = 1, 10000$$

which can be used in Newton's equations

$$\frac{\partial^2 X_I}{\partial t^2} = \frac{1}{M_I} F_{IX} \quad I = 1, 10000$$

to calculate the dynamics of motion (position and velocities of all atoms as a function of time).

This simulation of the dynamics of motion can include a description of two surfaces and the associated lubricant to examine an atomic-level representation of tribological systems. Combining these approaches of quantum chemistry, force fields, and dynamics, one can study adhesion of various adsorbates and lubricants to surfaces. However, to simulate wear processes requires a description of bond breaking that has not yet been implemented.

In principle, the methods for atomic-level simulations provide the information needed to establish the fundamentals of tribology. However, there remain a number of difficulties in implementation. The fundamental quantum chemistry calculations are difficult and time-consuming. Only a few systems have been studied. The extraction of force fields from such calculations is still in its infancy. Force fields for a few systems have been extracted; however, the adequacy of these force fields for describing bond breaking processes (important for wear) has not been adequately tested.

The methods of solving Newton's equations of motion are adequate for systems with 5000 particles and can be used with periodic boundary conditions to describe semi-infinite systems. However, only fragmentary progress has been demonstrated for describing the bond disruption processes involved, for example, in wear. Thus, for theory to play its necessary role in providing a foundation for the fundamental principles of tribology, a major effort is required to push forward the techniques required to solve these problems. These developments will be greatly aided by development of detailed experimental data on well-characterized systems that can be used to test the adequacy of various theoretical techniques.

4.2 Experiment

Absolutely critical here is the development of experimental protocols so that the surface characteristics can be reproduced reliably in different laboratories. In addition, it is important that the materials used be such that the theorist can hope to simulate the same surface that the experimentalist is studying. Because of these requirements, there will be a focus upon single crystals prepared under well-defined conditions. However, useful surfaces for tribology will be chemically inactive, and it is important to passify the above surfaces under well-controlled conditions. In many cases it will be useful to have surface hydrides, fluorides, oxides, or nitrides, and we suggest that a useful protocol might involve (1) cleaving the single crystal in vacuum and then exposing it to an appropriate plasma (H_2 , O_2 , F_2 , N_2), or (2) cutting and polishing the sample outside the vacuum system,

cleaving it in the vacuum system (using appropriate ions), and then exposing it to the appropriate deposition conditions for preapring a surface layer.

These systems would then be characterized by standard surface science techinques. For example, (1) high resolution electronic energy loss spectroscopy (HREELS) will be used to obtain vibrational frequencies of the various bonds at the surface; (2) surface geometries can be obtained using electron-stimulated desorption with ion angular distribution (ESDIAD) and with near-edge extended fine structure spectroscopy (NEXAFS); and (3) various photoelectron spectroscopies (XPS, UPS) can be used to characterize the electronic states for the surface species.

Use of scanning tunneling microscopy (STM) and the atomic force microscope have the potential for direct observation of the geometry and forces for comparison with theory. However, experimental conditions (interaction of tip and associated electric fields with the surface) may modify the surface.

With such well-characterized surfaces, it is important to develop experimental procedures for measuring quantitative relationships to friction coefficients, hardness, and wear under well-defined conditions.

5.0 Standard Systems

In order to make progress on the fundamentals, it is important to choose several standard systems on which all available experimental and theoretical methods will be applied.

A list of suggested standard materials has been compiled using the criteria that they be suitable for precise experimental and theoretical study.

(i) Diamond (a model for the pyrolytically formed diamond that might be used in high performance systems).

α . hydrogen-saturated surface (use cut and polish diamond or to cleave in vacuum and expose to H_2 plasma).

β . fluorine-saturated surface (clean in vacuum and expose to F_2 plasma).

(ii) Si(111) (allows very pure, very large single crystals).

α . freshly cleaved.

β . saturated with hydrogen.

γ . Controlled dry oxidation (O_2 , N_2O) and wet oxidation (H_2O).

(iii) Graphite

α . examine without H_2O or absorbed gases.

β . examine with carefully controlled amounts of rare gases (Ar, Xe).

γ . examine with carefully controlled amounts of H_2O .

(iv) MoS_2

α . determine orientation upon binding to various clean metal surfaces (\perp versus \parallel to surface).

β . determine effect of adsorbed overlayers on surface (H, O, S).

(v) Ag(111), (110), (100) (easy to clean, reconstruction not a major problem).

(vi) Au (resistant to oxidation; easy to clean).

- (vii) LiF (experiments easier because do not need UHV conditions).
- (viii) CaF_2 and BaF_2 (useful high temperature lubricants for ceramics).
- (ix) BN (oxidatively stable).
- (x) Amorphous Si and diamond (no grains)
 - α . saturation with H.
 - β . saturation with F.
 - γ . Controlled dry oxidation (O_2 , N_2O) and wet oxidation (H_2O).
- (xi) Al_2O_3 (advantage - transparent to infrared for real friction experiments).
- (xii) SiC
 - α . Single crystals
 - β . CVD prepared
 - γ . Controlled dry oxidation (O_2 , N_2O) and wet oxidation (H_2O).
- (xiii) CVD Si_3N_4
 - α . as grown (oxide surface layer)
 - β . oxide removed and replaced with H or F
 - γ . wet- and dry-oxidized
- (xiv) MoO_3 (basal plane).
- (xv) CoO.
- (xvi) Ni (100) (well studied both by experiment and theory)
 - α . clean.
 - β . sulfur covered.
 - γ . oxygen covered.
- (xvii) Effects of Doping

Particularly relevant for ceramics is the effect of doping of ceramic (or of lubricant)

upon adhesion of lubricant to surface.

(xviii) High Temperature Lubricants

Worthy of study would be high temperature oxide glasses that would be good lubricants at high temperatures (e.g., based on B_2O_3 , Al_2O_3 , SiO_2).

Based on these considerations, we recommend that the initial studies focus on single crystals of diamond prepared so as to saturate the surface with hydrogen or fluorine. These materials have potential for application in extreme conditions and should be most amenable to qualitative study.

Because of their relevance as model solid lubricants, we recommend graphite and MoS_2 as secondary systems.

6.0 Calculations of Friction

In order to gain some insight into some of the issues in extracting qualities describing macroscopic quantities for microscopic calculations, we carried out a series of simulations of diamond surfaces being displaced with respect to each other. We examined the (111) surface of diamond with each surface atom terminated by a C-H bond. In order to eliminate edge effects, we treated a finite thickness slab with periodic boundary conditions, as in Figure 3.

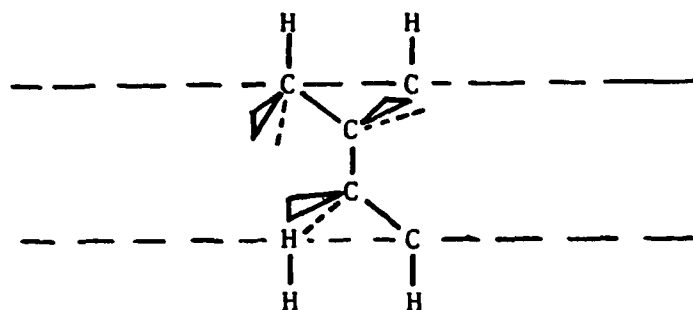


Figure 3.

The lattice constants parallel to the slab were restricted to remain those of the infinite system; however, each atom was allowed to move an equilibrium position. These slabs were then stacked, as in Figure 4a, to form a three-dimensional infinite system.

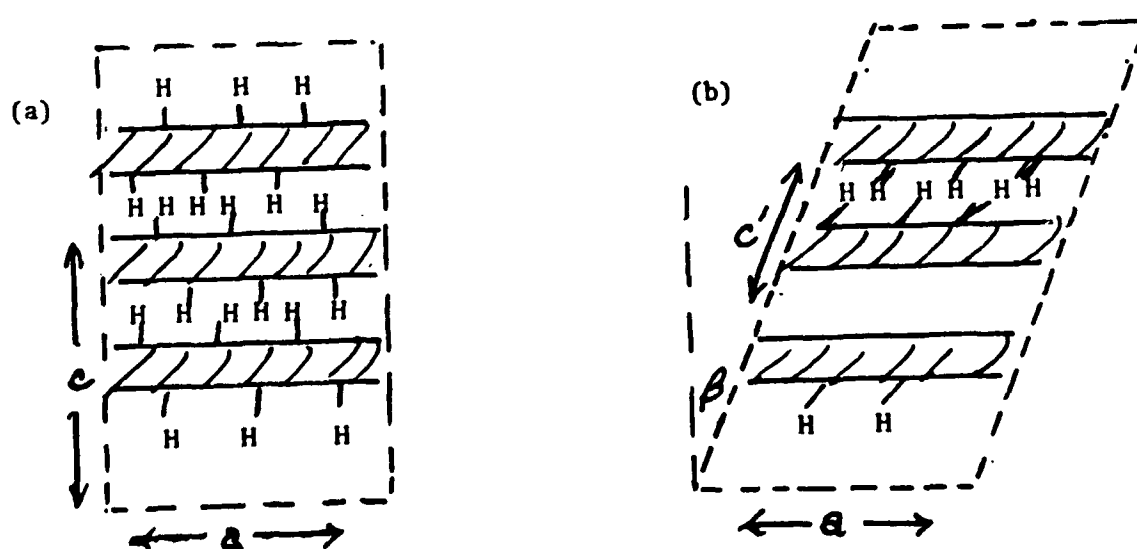


Figure 4.

The spaces between the slabs and the relative location of one slab with respect to the next were optimized to obtain the overall equilibrium system. This system represents two perfect diamond (iii) surfaces in equilibrium. We then calculated the equilibrium structures as each surface is displaced with respect to the next, while simultaneously imposing an external load on the system. This was carried out by treating the lateral displacement as a shear in the fundamental unit cell of the three-dimensional system, as indicated in Figure 4b. Thus, for each value of shear (β), we reoptimized all atomic positions, allowing the surface hydrogens to bend out of the wave as the surfaces were displaced, and we allowed the distance between the layers to reoptimize. This was done as a function of external stress. The results are presented in Figures 5 and 6. Figure 5 shows the energy surface (with no imposed load) superimposed on the atom position of the lower surface. The minimum position has the C-H bond of the upper surface symmetrically between the three C-H bonds of the lower surface. The minimum energy path for displacement has the C-H of the upper surface move over an energy barrier of 0.14 kcal/mol to a new equilibrium position with the C-H of the upper surface above a second layer C of the lower system. In this position, the energy is but 0.01 kcal higher than the original equilibrium position. In the minimum energy pathway, the CH bond of the upper state must next move northeast toward the center of the next hexagon and then east to the next second-layer carbon etc. If the surfaces are constrained to move exactly along a line, the lowest energy pathway would be one that crosses over the sides of each hexagon, leading to a barrier of 0.47 kcal/mol. The highest energy point occurs when the surfaces are displaced so that the lower CH bond points at the CH bond of the upper surface, leading to an energy 1.0 kcal higher than the minimum position.

But how do we go from this optimum energy surface to, say, a coefficient of friction? As one approach, consider the vertical displacements between the slabs necessary for the system to move along the minimum energy pathway (see Figure 6). The slabs are closest for the minimum energy position where the CH bond of the top slab points in the middle of the hexagon of the lower slab. As the slabs are displaced to the right over the 0.14 kcal/mol

ENERGY SURFACE

MOVING IN DIAMOND-H TERM
OVER IN DIAMOND H-TERM

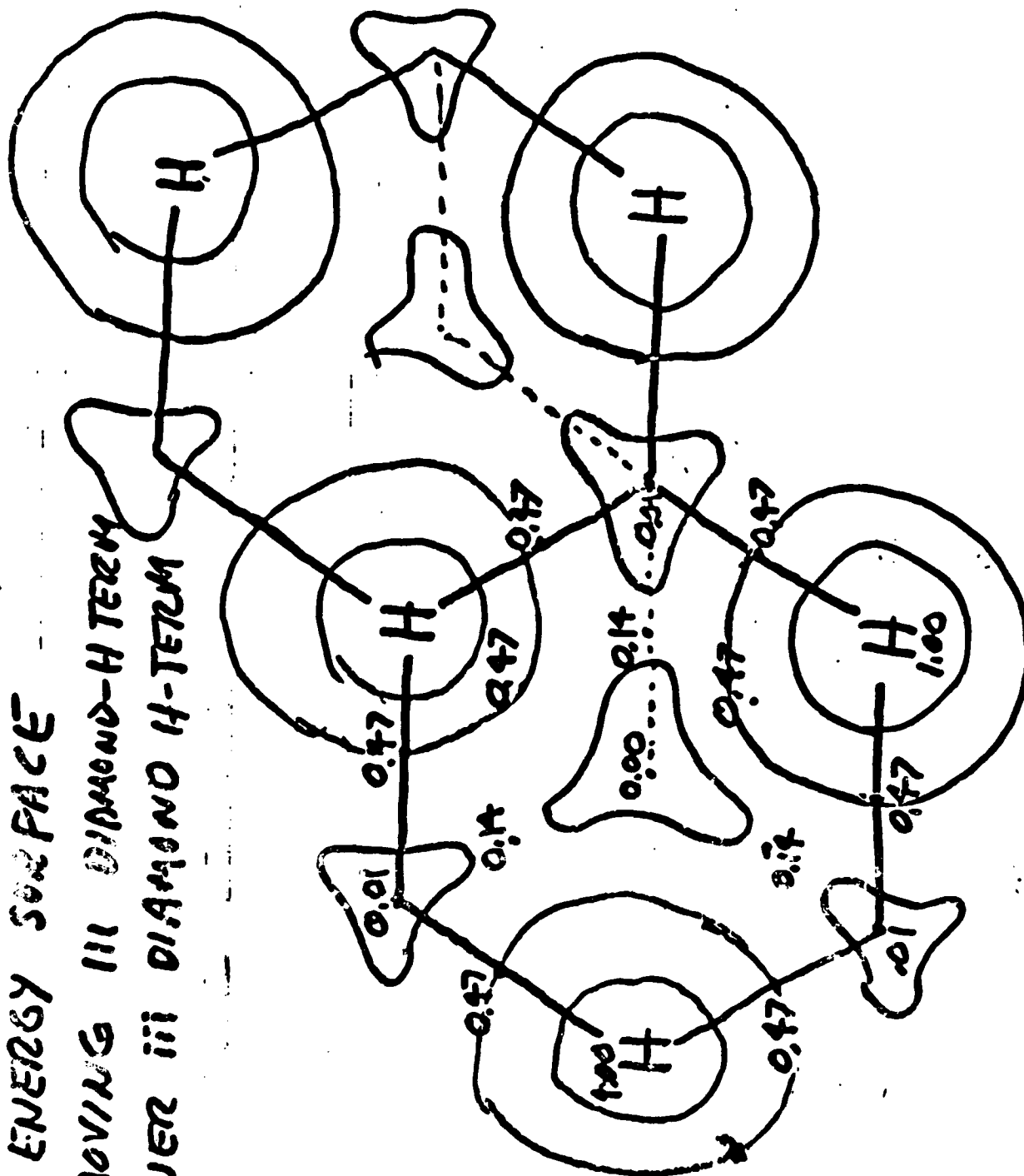


Figure 5.

VERTICAL DISPLACEMENTS

MOVE (111) DIAMOND-H
OVER DIAMOND (111)-H

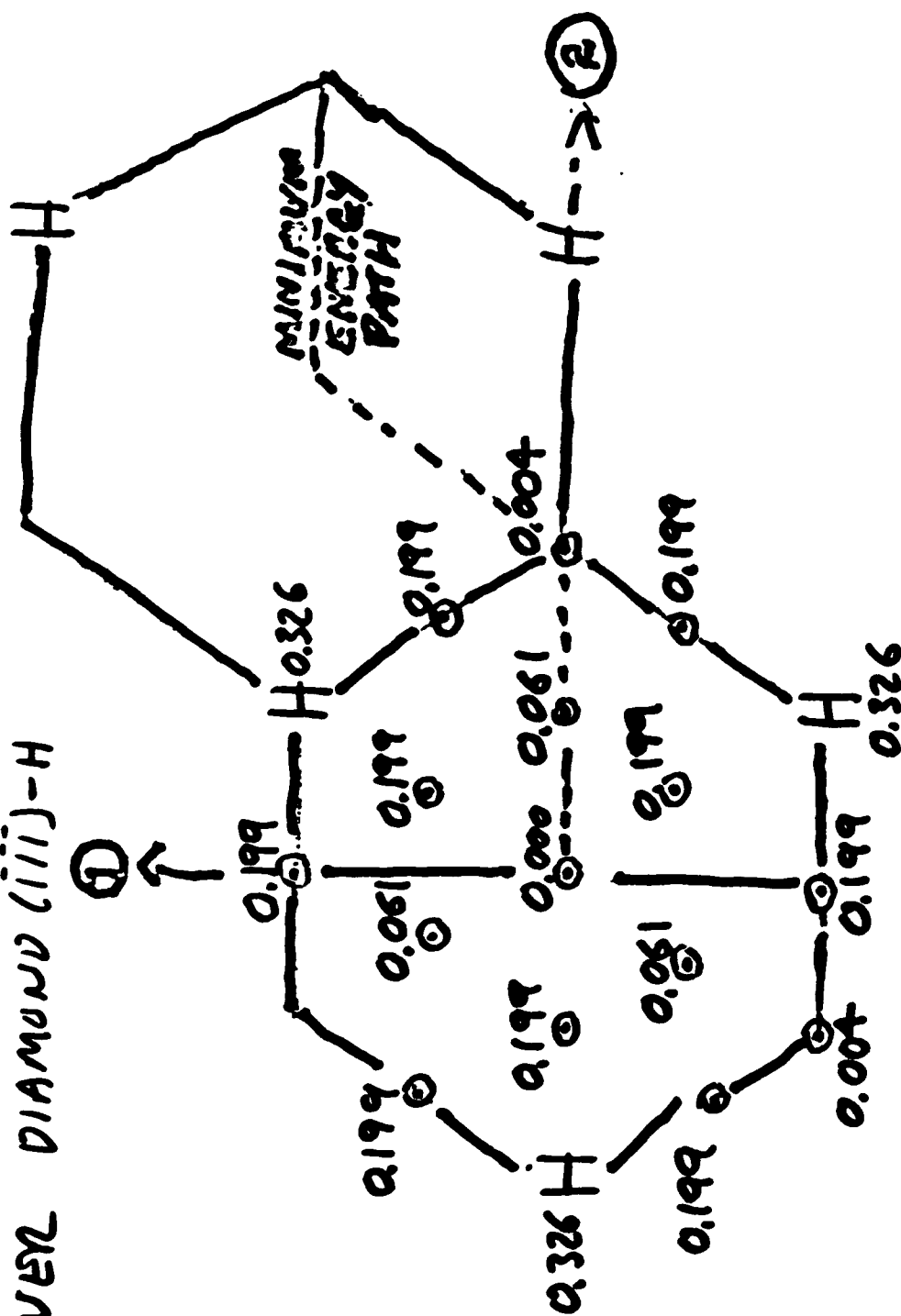


Figure 6.

barrier, the top slab must move away by 0.061 Å and then it comes back to the secondary minimum (above the second layer C) where it is only 0.004 Å above the optimum vertical displacement. Thus, as the system is displaced along the minimum energy pathway, the vertical displacements are as in Figure 7.

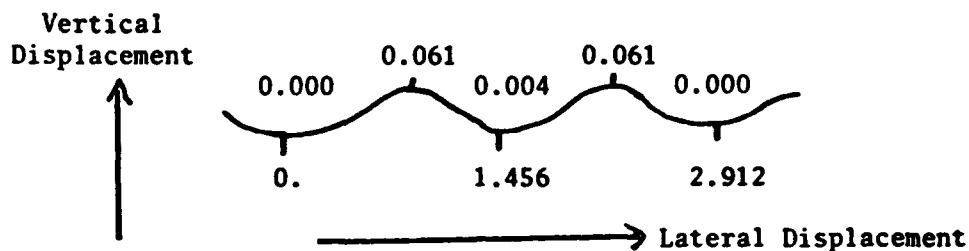


Figure 7.

If there is an external load on the system, we must do work against this bond to displace it back 0.06 Å to go over the first hill, but the bond can do work on the system as we go down the hill again. If this process were carried out with no energy transfer, there would be no friction. That is, the energy cost in going up one hill is returned upon going down and is then available to go up the next hill. However, if the energy is dissipated from the surface as it goes down one hill, it cannot be returned to climb the next and there is friction. To get an idea whether there is time for such dissipation, consider that a velocity of 2 meters/sec converts to 0.02 Å per picosec. Thus, at this velocity, it takes 35 picosec for the system to go back down hill. On the other hand, the characteristic time for energy transfer from the C-C-H bending modes at the surface is likely to be ~1 psec. Thus the energy should be dissipated.

Given the description in Figure 7, we can estimate the maximum coefficient of friction as the maximum slope of the displacement curve or

$$f = \pi \frac{0.061}{1.456} = 0.132.$$

It is interesting that this value is in the ballpark of experimental measurements of the coefficient of friction in diamond by Tabor³¹ who reports $f = 0.1$ for diamond (111). This does not prove our simple model. The experiments on diamond were carried out with

a metal probe in a normal atmosphere. We now know that a well polished diamond surface is covered with C-H bonds. Hence these experiments should be repeated in an inert atmosphere with a diamond probe so that one does not have to worry about the surface H on the diamond being transferred to the metal.

It is also not clear that the coefficient of friction for a completely flat surface is relevant for friction studies where even for a single crystal there will be steps and other imperfections that may keep parts of the surface from interacting (Figure 8).

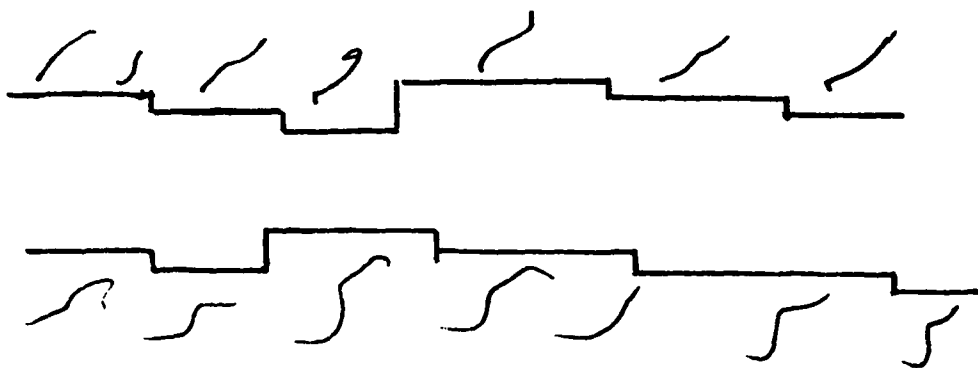


Figure 8.

That is, the experiments on the best quality single surface may be dominated by what happens when two steps come together rather than by the sliding of two surfaces with respect to each other. Of course, similar theoretical calculations can be carried out at the steps; however, there are new questions. Are the step atoms also completely saturated with C-H bonds? We could assume this in the calculations, but this should be tested with appropriate surface science experiments. Using these theoretical approaches, one should be able to examine systems modeling the system in Figure 8 and provide simulations of friction and wear for these systems.

7.0 Scanning Tunneling Microscopy

A new tool of significant potential for characterizing the surface topography of tribologically relevant systems is scanning tunneling microscopy. In this system, a small voltage, say, 100 mV, is applied between a probe [prepared so as to obtain extremely small (atomic dimensions) points] and the surface and the tunneling current is measured and used with various electronics and piezoelectric elements to maintain atomic-level resolution. The probe is maintained at distances of 5 to 10 Å and the tunneling current [which is assumed to vary exponentially with distance (s)]

$$I_T(s) = e^{-\sqrt{\phi}s}$$

is measured. In one mode of operation, the current is kept constant as the tip is displaced along the surface, and the voltage applied to the piezoelectric element is monitored to obtain the effective displacement of the tip. Assuming that the work function of the surface ϕ is independent of position, one then gets the topography of the surface. The problem here is that at the atomic level the effective work function and rate of electron transfer *does* depend upon the nature of the orbitals describing the electrons.

Thus, to extract topographically useful information from this problem, we need to develop theoretical techniques that can describe how the current would change for various surface topographies of atoms.

To do this we have used small clusters of atoms to represent both the surface and the tip.³² Our first calculation used two Ni_{13} clusters (having the bond distances of bulk Ni), as indicated in Figure 9.

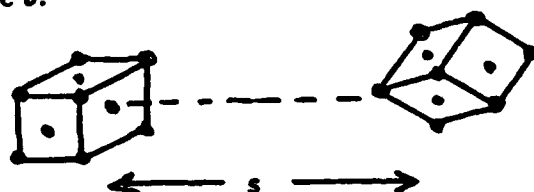


Figure 9.

The current is calculated as follows. We start, say, with a neutral Ni_{13} cluster on the left and a positively charged Ni_{13} cluster on the right and solve self-consistently for the

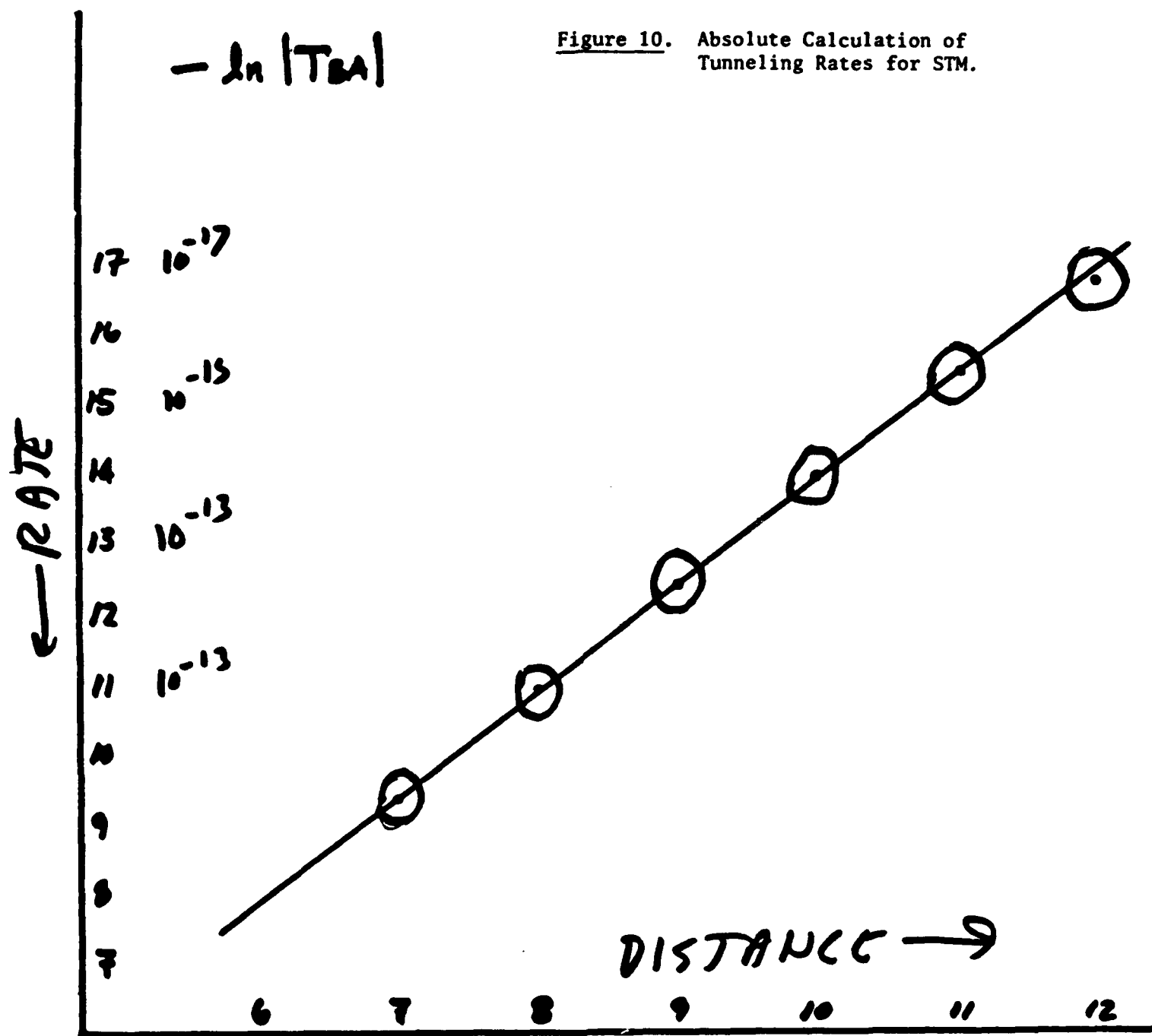
full (GVB) wavefunction of the 26 atom positions as a function of distance to yield the wavefunction $\Psi_R(s)$. We then redo the calculations but starting with the positive charge on the left and again solve self-consistently for the full wavefunction of the system, $\Psi_L(s)$. Then, for each distance s , we calculate the rigorous electron transfer matrix elements

$$H_{LR}(s) = \langle \Psi_L(s) | H | \Psi_R(s) \rangle$$

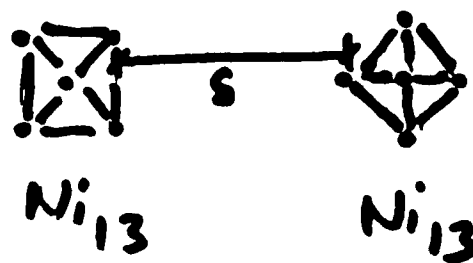
where H is the full hamiltonian for the 26-atom system. The rate of electron transfer T_{LR} is proportional to the square of H_{LR} . [To do this, we modified the RGVB procedures of Voter and Goddard,³³ allowing evaluation of H_{LR} even though every orbital of Ψ_L overlaps every orbital of Ψ_R .] We find that, in agreement with simple analysis, it has an approximately exponential dependence upon distance, see Figure 10. However, we find that the maximum electron transfer from L to R occurs when the probe is over a bond midpoint, not above the atom! This occurs because the orbitals involving the bonding electrons in metals tend to be in interstitial positions in between the atoms.

Our conclusion from these studies is that STM has a great deal of promise for characterizing tribological systems; however, theory will be critical in extracting the physics from the data.

Figure 10. Absolute Calculation of Tunneling Rates for STM.

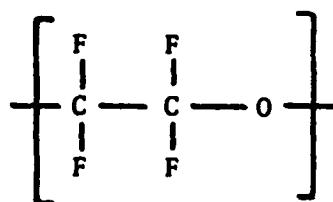


SEPARATION BETWEEN Ni(100) FACE AND TIP ATOM.

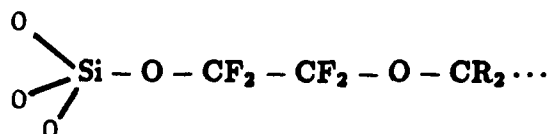


8.0 Silicon Nitride

Preliminary calculations were carried out on both the α and β phases of silicon nitride. However, we expect that in a normal operating environment the surfaces of these systems are probably oxidized so that the proper model of the surface is amorphous SiO_2 . Such surfaces will have a variety of chemically active sites that for low friction and weak should be kept passivated. Thus, there will be surface Si-OH , $\text{Si-O}\cdot$, and SiO^- units that can promote undesired adhesion to another surface or to the lubricant. Considering the thermochemistry of these systems, an effective strategy for lubrication might include providing an appropriate reservoir of F atoms that could bond to the surface silicons to form strong passive Si-F bonds. For systems operating at temperatures consistent with liquid lubricants, an ideal system might be perfluorinated ethers



They could provide a reservoir of F to react with exposed surface Si to form the Si-F bonds. In addition, the surface site could react with the oxygen to form a brush of surface



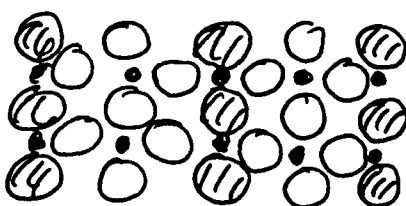
groups that would help provide a boundary layer region protecting the surface.

For operation at higher temperatures where liquid lubricants are no longer suitable, one can imagine a system (perhaps with a slightly porous bearing element) where a small continuous stream, say, of SiF_4 gas is allowed to react with the surface and to passivate any active sites being formed by oxidation or wear processes.

These reflections suggest a series of experimental and theoretical studies on silicon-oxides and silicon-fluorides that could be useful in formulating new structures for lubrication of silicon-nitride and other ceramics.

9.0 Surface Modification

As an example of how simple theoretical considerations can be useful in suggesting strategies for surface modification to aid surface properties, consider TiO_2 . In bulk TiO_2 , each Ti has six oxygen neighbors. Since Ti has a valence of +4, this means that each Ti-O bond involves an electron transfer of $2/3$ electron. Since O needs two electrons, it must have three Ti neighbors to obtain its full charge. But at a surface the number of neighbors is necessarily different. Thus, for a perfect (110) surface, the environment would be



where the \bullet represents Ti and \bigcirc represents the oxygen (shading indicating the outer layer of oxygens). Thus the shaded oxygens have only two of the three Ti neighbors, requiring an extra $2/3$ electron, while the Ti in the middle of the unshaded oxygens have five of the six O neighbors, so that the Ti has $2/3$ of an electron left. This would lead to an active five-coordinate Ti with nearly an extra electron. Such misbalance in the charges leads to reconstruction of the surfaces to more effectively neutralize the surface atoms, leading to steps, vacancies, and other features that make the surfaces chemically active. If we replace this surface Ti with surface Fe, which prefers to be Fe^{3+} , then the five-coordinate surface site of the flat surface is locally electrically neutral. This allows a stable flat surface with good tribological properties. Experimental studies by M. Gardos on surface-modified TiO_2 can be interpreted in terms of such ideas.

REFERENCES

1. *Computer Simulation of Solids*, C. R. A. Catlow and W. C. Mackrodt, Eds. (Springer, Berlin, 1982).
2. W. C. Mackrodt, *Solid State Ionics*, **12**, 175 (1984).
3. C. R. A. Catlow, J. Corish, K. M. Diller, P. W. M. Jacobs, and M. J. Norgett, *J. Phys. C*, **12**, 451 (1979).
4. C. R. A. Catlow and A. M. Stoneham, *J. Am. Ceram. Soc.*, **64**, 234 (1981).
5. R. Dieckmann, *Solid State Ionics*, **12**, 67 (1984).
6. A. Rahman, *J. Chem. Phys.*, **65**, 4845 (1976).
7. M. J. Gillan, *Solid State Ionics*, **9**, 755 (1983).
8. P. Vashishta and A. Rahman, *Phys. Rev. Lett.*, **40**, 1337 (1978).
9. C. R. A. Catlow, *Solid State Ionics*, **12**, 67 (1984).
10. P. W. Tasker, *Phil. Mag.*, **39**, 119 (1979).
11. (a) C. R. A. Catlow, K. M. Diller, and M. J. Norgett, *J. Phys. C*, **10**, 1395 (1977);
(b) C. R. A. Catlow, M. J. Norgett, and T. A. Ross, *ibid.*, **10**, 1627 (1977).
12. W. C. Mackrodt and R. F. Stewart, *J. Phys. C*, **10**, 1431 (1977).
13. D. Wolf, *Phil. Mag.*, **49**, 823 (1984).
14. W. C. Mackrodt and R. F. Stewart *J. Phys. C*, **12**, 431 (1979).
15. W. A. Goddard III, *Science*, **227**, 917 (1985).
16. R. E. Donnelly and W. A. Goddard III, to be published.
17. M. H. McAdon and W. A. Goddard III, *J. Non-Cryst. Solids*, **75**, 149 (1985); *Phys. Rev. Lett.*, **55**, 2563 (1985); *J. Phys. Chem.*, **91**, 2607 (1987); *ibid.*, in press (1988); *J. Chem. Phys.*, **88**, 277 (1988); *ibid.*, submitted (1988); *Phys. Rev. B*, submitted (1988).
18. B. R. Brooks, R. E. Brucoleri, B. D. Olafson, D. J. States, S. Swaminathan, and M.

- Karplus. *J. Comp. Chem.*, **4**, 187 (1983).
19. Behrendson (1984).
 20. A. M. Naylor and W. A. Goddard III, "Theoretical Studies of Methotrexate and Dihydrofolate Bound to Natural and Mutated DHFR", *Proc. Nat. Acad. Sci. U.S.*, manuscript in preparation.
 21. J. D. Doll, *J. Chem. Phys.*, **68**, 3158 (1978).
 22. E. K. GrimmeImann, J. C. Tully, and E. Helfand, *J. Chem. Phys.*, **74**, 5300 (1981).
 23. B. J. Garrison, D. J. Diestler, and S. A. Adelman, *J. Chem. Phys.*, **67**, 4317 (1977).
 24. J. C. Tully, *Surf. Sci.*, **111**, 461 (1981); *J. Chem. Phys.*, **73**, 1975 (1980).
 25. A. Redondo, Y. Zeiri, and W. A. Goddard III, *Phys. Rev. Lett.*, **49**, 1847 (1982). A. Redondo, Y. Zeiri, and W. A. Goddard III, *J. Vac. Sci. Technol. B*, **2**, 1639 (1984).
 26. Y. Zeiri, A. Redondo, and W. A. Goddard III, *J. Electrochem. Soc.*, **131**, 1639 (1984).
 27. N. Karasawa and W. A. Goddard III, *J. Phys. Chem.*, submitted for publication.
 28. A. M. Mathiowetz and W. A. Goddard III, to be submitted.
 29. S. Nose, *J. Chem. Phys.*, **81**, 511 (1984).
 30. F. W. Bobrowicz and W. A. Goddard III, in *Modern Theoretical Chemistry: Methods of Electronic Structure Theory*, H. F. Schaefer III, Ed. (Plenum Press, New York, 1977), Vol. 3, Chap. 4, pp. 79-127; W. A. Goddard III and L. B. Harding, *Ann. Rev. Phys. Chem.*, **29**, 363 (1978).
 31. Tabor - coefficient of friction of diamond.
 32. T. R. Coley and W. A. Goddard III, to be submitted.
 33. A. F. Voter and W. A. Goddard III, *J. Chem. Phys.*, **75**, 3638 (1981).

Presentations and Conferences Related to Tribology

1. "The Chemical Character of Surfaces from Theoretical Studies", Workshop on Tribology Fundamentals - Needs and Future Directions, Institute for Defense Analyses, Alexandria, Virginia, 13 December 1984.
2. "New Concepts for Understanding Electronic and Chemical Processes at Surfaces", Science and Technology Division, Institute of Defense Analyses, Alexandria, Virginia, 14 February 1985.
3. "Hughes/DARPA Meeting", Institute for Defense Analyses, Alexandria, Virginia, 20 February 1986.
4. "Presentation for the DARPA/AF Hughes Aircraft Solid Lubrication for Ceramics Fundamentals Program", Hughes Aircraft Company, El Segundo, California, 13 March 1986.
5. "Simulation of Fundamental Aspects of Tribology", Gordon Research Conference on Tribology, Colby-Sawyer College, New London, New Hampshire, 9 June 1986.
6. "Theoretical Studies and Simulations of Biological or Materials Systems", Physics Research Conference, California Institute of Technology, Pasadena, 9 October 1986.
7. "Theoretical Studies of Structure and Chemistry at Surfaces", Meeting of the Southern California Section of The Electrochemical Society, California Institute of Technology, Pasadena, 3 December 1986.
8. "Application of Electronic Structure Theory to Tribology", Workshop on Fundamentals of Tribology", Air Force Office of Scientific Research, Air Force Wright Aeronautical Laboratories (AFSC), Wright-Patterson Air Force Base, DC, 10 February 1987.
9. "Atomic Simulations", Program Review: Determination of Tribological Fundamentals of Solid Lubricated Ceramics, Hughes Aircraft Company, El Segundo, California, 31 March 1987.
10. "Atomic Level Modeling of Chemical and Tribological Properties". Symposium on Ceramics Tribology III, Status and Future Research Needs in Tribology of Ceramics, 1987 Annual Meeting of the American Society of Lubrication Engineers, Anaheim, California, 13 May 1987.
11. "Materials Simulation with Application to Ceramics and Tribology", 1987 AFOSR Contractor's Meeting on Surface Chemistry, Air Force Academy, Colorado Spring, Colorado, 18 September 1987.

APPENDIX B

**U. Landman," Microscopic Modeling of Tribological Phenomena,"Final
Report, Georgia Institute of Technology, Atlanta, GA, Hughes P.O. S9-
512917-SKG**

1. Introduction

The primary objectives of our investigations were the development and implementation of theoretical methods for studies of atomic-scale mechanisms of deformation and yield processes in materials, and application of such methods to ionic solids (CaF_2 in particular, in order to complement the experimental investigations under this project, of the tribological properties of this class of materials).

In accord with the above stated objectives we have formulated and implemented new approaches to studies of the micromechanics and microdynamics of materials based on molecular-dynamics (MD) simulations [1,2]. In these simulations the properties of a multi-particle system are investigated by direct integration of the equations of motion of the atoms, interacting via tested interatomic potentials and, if desired, subject to external influences (such as imposed stresses). The phase-space trajectories which are obtained in these simulations allow analysis of the atomistic mechanisms of materials processes with refined spatial and temporal resolution, thus allowing to gain insights into the fundamental microscopic nature of complex materials phenomena.

The interaction potentials which we have used are those developed previously in the context of studies of the properties of bulk CaF_2 crystals and they contain contributions from Coulomb, Born-Meyer and dispersion terms [3]. These parametrized potentials have been shown to reproduce rather faithfully many known properties of bulk perfect crystals of CaF_2 , such as elastic moduli, cohesive energy, Frenkel defect formation energy and vacancy and interstitial migration energies. In addition they have been employed in extensive studies of thermally activated bulk superionic conductivity in CaF_2 [3,4].

In the first stage of our studies we have investigated the surface

properties of CaF_2 crystals, as well as properties of the bulk under zero strain, over a range of temperatures (see Section 2). In the second stage we have investigated the response of bulk CaF_2 crystals to externally imposed strains or stresses (see Section 3a), and the atomistic mechanisms of deformation and tribological processes induced by the interaction of large faceted CaF_2 tips with CaF_2 surfaces (see Section 3b).

2. Studies of Unstressed Bulk and Surface Systems

In these simulations the computational cell was periodically replicated (in two directions parallel to the surface plane for surface simulations, and in three directions for bulk simulations) and the Ewald summation technique was used to account for the long-range Coulomb interactions [5]. In the bulk simulations we employed the constant pressure MD method of Parrinello and Rahman [6], which treats the vectors defining the computational cell as auxiliary dynamical variables (both magnitudes and directions) thus allowing for volume and structural changes induced thermally or by phase transformations. In constant temperature simulations (canonical ensemble) the kinetic temperature of the system was controlled via scaling of particle velocities to the desired temperature (past the equilibration stage, the temperature remained stable fluctuating about the desired one, thus at the data collecting stage temperature control was applied infrequently so as to not interfere with the natural dynamical evolution of the system).

Selected results, taken from simulations of bulk crystals (504 particles, i.e., 168 CaF_2 units) are shown in Figs. (1 and 2), where we exhibit versus temperature the variations in the lattice constant, and fluorine anion diffusion constant, respectively. The diffusion constant was determined from the relation

$$R_{\alpha}^2(t) = \frac{1}{N} \left\langle \sum_{i=1}^N (\vec{R}_i^{\alpha}(t) - \vec{R}_i^{\alpha}(0))^2 \right\rangle = 2n_d D_{\alpha} t \quad , \quad (1)$$

where, $\vec{R}_i^{\alpha}(t)$ is the position vector of the i th particle of species α ($\alpha = \text{Ca}^{+2}$ or F^{-}) at time t , n_d is the dimensionality of the system ($n_d = 3$ for bulk), D_{α} is the diffusion constant of species α , and the angular brackets indicate average over particles' trajectories generated in the simulations.

It is evident from Fig. 2 that the mobility of the fluorine anions is greatly enhanced as the temperature increases (onset at $T \sim 1400\text{K}$), correlating both in magnitude and temperature dependence with experimental data [7]. We have also verified that the anion diffusion mechanism involves the octahedral sites through the generation of vacancy-interstitial Frenkel defect pairs [3,4,8].

We turn next to simulations of the (110) and (111) surfaces of CaF_2 . In these simulations the system is setup as a crystalline slab, with the atoms in the slab treated dynamically, and situated on top of a static substrate. The material in the calculational cell contains N_L^d dynamic atomic layers (with n atoms per layer) exposing either the (110) or (111) surface, interacting with N_L^s static layers of the same crystallographic orientation. Thus the total number of crystalline layers is $N_L = N_L^d + N_L^s$. To facilitate the application of the Ewald summation method the calculational cell is extended in the direction normal to the surface plane such that the material system is surrounded by empty space of sufficient extent to assure negligible interactions between the system in the cell and its periodic replicas in the z direction. Finally, the whole system is periodically replicated in three dimensions.

For simulations at different temperatures, the dimensions of the calculational cell in the directions parallel to the surface plane and the layer spacings in the static substrate are adjusted according to the temperature variation of lattice constant given in Fig. 1. The number of dynamic layers, N_L^d is taken large enough to minimize effects due to the underlying static substrate (see details for the two surface systems in reference 9).

The structure of the two surface systems which we investigated are qualitatively different, which as will be discussed below, correlates with

their different properties. While the (111) surface system exposes a polar surface layer, (i.e., all atoms in the topmost layer are fluorine anions) and stacks as $\text{FCaFOFCaFO}\dots\dots$ (where O denotes a layer containing octahedral vacant sites in the ideal lattice, and F and Ca denote the chemical species in a given layer) the atomic layers in the system exposing the (110) surface are charge neutral (containing each a stoichiometric ratio (z11) of Ca^{+2} and F^- ions), and are arranged in an ABAB..... stacking.

The main result of these simulations is that while the mobility of the F^- ions is greatly enhanced in the surface region of the (110) surface (see Fig. 3), starting at a lower temperature than the onset of superionic conductivity in bulk crystalline FaF_2 , the effect observed for the (111) surface system is much smaller.

The onset of surface superionic conductivity at the (110) surface occurs at a temperature of ~ 1100 K, and is most pronounced for the two topmost surface layers of the material. In this context we note that the Ca^{+2} ion mobility remains negligibly small throughout the whole temperature range, up to melting, and that no noticable changes in lattice structure are observed.

The enhanced mobility of the fluorine anions at the surface region (1-3 top layers of the (110) surface) correlates with smaller formation energies for vacancy-interstitial and vacancy-adlayer (i.e., when the F^- anion is displaced from its crystalline position and placed on top of the topmost surface layer) for the (110) surface system in comparison with the vacancy-interstitial formation energy in the bulk crystal. On the other hand these formation energies for the (111) surface do not favor generation of such defects at the surface as compared to the bulk (see Table I).

3. Studies of Bulk Crystal and Surface Systems Under Stress and Strain

3a. Bulk Crystal Simulations

To investigate the response of CaF_2 perfect bulk crystals to externally imposed mechanical perturbations, and in order to determine the temperature dependence of the mechanical properties of this system, we have explored the dynamical evolution of the system under external strains or stresses which, in accord with the experimental configuration chosen in the tribotesting experiments at the Hughes laboratories, were applied in the (111) plane along the $\langle \bar{1}10 \rangle$ direction.

In the constant strain simulations the computational cell is distorted to produce the required strain and then equilibrated at the desired temperature to allow for full relaxation of the atomic configuration under the specified strain. We note that in this series of simulations the shape of the computational cell (except for the strain imposed distortion) is not allowed to vary. The results of such simulations for $T = 300\text{K}$, 1073K , 1300K and 1450K , are given in Figs. 4 and 5. Variations versus strain (γ) of the σ_{xz} component of the internal stress in the system (i.e., in the (111) plane, with the $\langle 111 \rangle$ direction along the z axis, along the $\langle \bar{1}10 \rangle$ (i.e., x) direction), and of the potential energy (per CaF_2 unit) obtained at various temperatures are shown in Fig. 4 (in this figure the stress values are given for strain values up to the yield point). As may be seen the stress versus strain relationship is linear over an extended range of strains, exhibiting only small deviations from linearity for strains approaching the critical yield-strain value. This behavior which is also reflected in the parabolic variation of the potential energy versus strain indicates that the system responds elastically up to the yield point.

In Figure 5(a) variation of the σ_{xz} versus time is shown for the bulk system at 1300K starting from an unstrained equilibrated system at $t = 0$, the external strain is incremented in several stages (signified by the marked stepwise variations in the recorded internal stress at approximately 10 ps intervals). As seen, following the increase in strain at ~ 30 ps the system yields after a short period. The yield process is accompanied by relief of internal stress.

It is of interest to note that the application of strain to the bulk system is accompanied by enhancement of the mobility of the fluorine anions, while the mobility in the calcium-cation sublattice remains negligible up to the yield point. This behavior is portrayed in Figs. 5(b-f), where $R_{\alpha}^2(t)$, see Eq. (1), for the Ca^{+2} and F^{-} species, and its components parallel (x-direction) and perpendicular to the applied strain direction are shown. (In plotting these results $R_{\alpha}^2(t)$ was rezeroed after each incremental increase in the strain). It is particularly noteworthy that for the unstrained system ($t \leq 10$ ps) the F^{-} mobility is very small at this temperature (which is below the onset of the bulk superionic conductivity temperature at $T_{\text{sic}} \sim 1450\text{K}$), markedly increasing upon the application of strain. No such effect was observed by us in simulations at a temperature of 1073K and below. This phenomenon may be regarded as strain-induced superionic conductivity in CaF_2 occurring at a temperature below T_{sic} of the unperturbed bulk system. We suggest that the enhanced mobility of the F^{-} ions in the strained crystal correlates with the reduced resistance of the material to yield, which ultimately occurs following an increase in strain (at $t > 30$ ps). As seen from inspection of Figs. 5(c-e) the crystal slips in the (111) plane along the x ($\langle \bar{1}10 \rangle$) direction. A similar behavior, with larger mobility of the F^{-} ions, was observed by us also in simulations at $T = 1450\text{K}$ (see Fig. 6).

Values for the critical strain γ_c and internal stress σ_{xz}^c obtained from our constant-strain simulations are given in Table II. As seen the values which we obtained for the yield stress are higher than those estimated from analysis of experimental data [10]. This is not surprising, in view of the structural and chemical perfection of the simulated systems as compared to those used in the laboratory experiments. Nevertheless to further investigate the predicted values we have performed a set of constant-stress simulations [1] at $T = 300K$, $1073K$ and $1450K$. In these simulations both the shape and volume of the computational cell are allowed to vary in response to an externally imposed stress (in the (111) plane along the $\langle \bar{1}10 \rangle$ direction). The results of these simulations are summarized in Table III. Comparison of these results with those of the constant-strain simulations given in Table II, shows that the critical yield stresses (and associated strains) obtained by the two simulation methods are of similar magnitude, with the values obtained via the constant stress simulations somewhat lower. Furthermore, in both cases we observed that yield occurs via (111) interplanar slip (glide) in the direction of the applied external perturbation ($\langle \bar{1}10 \rangle$). In this context we note that while CaF_2 is known to cleave at room temperature in the (111) plane, the primary and secondary glide systems are reported to be the (001) plane in the $\langle \bar{1}10 \rangle$ direction and the (110) plane in the $\langle 1\bar{1}0 \rangle$ direction [11]. Since our simulated systems slipped in the (111) plane we have performed an additional constant-stress simulation (at 300K) with the external stress applied in the (100) plane along the $\langle 1\bar{1}0 \rangle$ direction. As seen from Table III, the critical yield stress obtained in this simulation is lower than in our previous simulations. Finally constant-stress simulations for systems in which defects (such as a single CaF_2 vacancy or a stacking fault) were deliberately introduced yielded similar results to those shown in Table III

indicating that the mechanical properties of the system are not greatly influenced by such defects. Rather, we suspect that the presence of dislocation is the main cause for lowering of the material resistance to slip.

3b. Simulations of Tip-Substrate Interactions

Having discussed the response of crystalline bulk CaF_2 to external mechanical perturbations, we turn next to studies of the interaction of CaF_2 crystalline tips with CaF_2 surfaces. In these simulations the substrate exposes the (111) surface and contains N_L^d layers of dynamic particles ($N_L^d = 12$, with 242 Ca^{+2} ions in a calcium layer and 242 F^- ions in a fluorine layer), positioned on top of a static substrate containing N_L^s layers ($N_L^s = 3$).

The temperature of the system is controlled to $T = 300\text{K}$ via scaling the velocities of only the particles in the 3 layers closest to the static substrate. In this way, heat which may be generated in the surface region as a consequence of the interaction with the tip, propagates toward the interior of the substrate and is dissipated.

The tip, which approaches the substrate along the normal (z) direction from above, is prepared as a tapered faceted micro crystal containing 9 (111) layers of dynamic particles. The bottom layer of the tip (i.e., closest to the substrate) contains 18 F^- ions, the one above it contains 18 Ca^{+2} ions with a layer containing 18 F^- ions on top of it. The next region of the tip contains 3 atomic layers consisting of 50 F^- , Ca^{+2} and 50 F^- ions, respectively. The topmost dynamic region of the tip contains 3 layers with 98 F^- , 98 Ca^{+2} and 98 F^- ions respectively. In addition the dynamic tip particles interact with a static holder composed of 3 CaF_2 (111) layers. Thus the total number of dynamic CaF_2 units in the tip is 166, and 242 in the static holder. The system is periodically replicated in two directions parallel to the surface plane, and no periodic boundary condition is imposed in the normal, z , direction.

Tip Approach and Lift-Off

We start by equilibrating the substrate and tip-holder assembly at $T = 300\text{K}$. Afterwards, they are brought to a distance $d_{hs} = 34 \text{ \AA}$. (In describing

results two distance scales will be used. d_{hs} denotes the distance between the top layer of the static holder and the bottom layer of the static substrate. The actual separation between the proximal layer of the tip, closest to the substrate, and the top-most layer of the dynamic substrate is denoted by d_{ts} . Subsequently, the distance between the tip-holder assembly and the substrate is changed in 0.5 \AA increments (using an integration time-step of $1.0 \times 10^{-15} \text{ s}$, this change occurs in 10^{-12} s). After each such change in the tip-to-substrate separation the system is allowed to evolve dynamically till no discernable variations in energy and structure are detected (i.e., the system is allowed to relax throughout the tip-to-substrate approach and subsequent separation processes).

The average force in the z direction on the tip atoms, recorded for the fully relaxed configurations, versus distance, d_{hs} , is shown in Fig. 7a, and the corresponding variation of the potential energy of the tip atoms is shown in Fig. 7b. In these figures the squares denote values recorded during tip-to-substrate approach and the circles correspond to values calculated upon subsequent detracton (lift-off) of the tip from the substrate. As seen from Fig. 7a, following a gradual slow increase in the interaction between the tip and the substrate atoms, the attractive interaction markedly increases, starting at $d_{hs} \sim 29 \text{ \AA}$, when the bottom layer of the tip is separated by $d_{ts} \sim 3.75 \text{ \AA}$ from the topmost layer of the surface. This stage is accompanied by an increase in the interlayer spacing in the tip material, i.e., elongation of the tip, and is reminiscent of the jump-to-contact phenomena which we have discovered in simulations of the interaction between a gold tip brought to contact with a nickel substrate, although the elongation found in the present case ($\sim 0.35 \text{ \AA}$) is much smaller than that obtained for the intermetallic contact [2]. Decreasing the distance between the tip-holder assembly and the substrate past the distance corresponding to maximum adhesive interaction

(which occurs at $d_{ts} \sim 2.3 \text{ \AA}$) results in a decrease in the attractive interaction, which eventually turns slightly repulsive (positive value of F_z), accompanied by a slight compression of the tip material. Starting from that point ($d_{hs} = 26.5 \text{ \AA}$, $d_{ts} \sim 1.4 \text{ \AA}$) and reversing the direction of motion of the tip-holder assembly (i.e., detracting it from the surface) results in the force curve denoted by circles.

As clearly observed from Fig. 7a, the force versus distance relationship upon tip-to-substrate approach and subsequent separation exhibits a pronounced hysteresis. The origin of this behavior, which is also reflected in the tip potential-energy versus distance curve shown in Fig. 7b, is a plastic deformation of the crystalline tip, leading to eventual fracture. At the end of the lifting processes part of the tip remains bonded to the substrate.

Tip Sliding

Starting from the tip-substrate configuration under a slight attractive load (see point marked by an arrow in Fig. 7a ($h_{ts} = 1.7 \text{ \AA}$, $F_z = -3.0 \text{ nN}$)) lateral motion of the tip parallel to the surface plane is initiated by translating the tip-holder assembly in the $\langle \bar{1}, 1, 0 \rangle$ direction in increments of 0.5 \AA , followed by a period of relaxation, while maintaining the vertical distance between the tip-holder and the substrate at a constant value. This then corresponds to a constant-height scan in the language of atomic-force microscopy. We have also performed constant-load simulations which will not be discussed here.

The recorded component of the force on the tip atoms in the direction of the lateral motion, as a function of the displacement of the tip-holder assembly, is shown in Fig. 8a and the corresponding potential energy of the tip atoms is given in Fig. 8b. As seen, the force on the tip exhibits an oscillatory variation as a function of lateral displacement which is a

characteristic of atomic-scale stick-slip behavior. Inspection of the atomic configurations along the trajectory of the system reveals that the lateral displacement results in shear-cleavage of the tip. The sequence of atomic configurations shown in Fig. 9 reveals that the bottom part of the tip remains bonded to the substrate, and sliding occurs between that portion of the tip material and the adjacent layers. This result indicates that under the conditions of the simulation (i.e., small load), atomic layers of the tip may be transferred to the substrate upon sliding. From the average value of the recorded variation in the tangential force on the tip (see Fig. 9a), and the contact area we estimate that the critical yield stress associated with the initiation of slip in the system is ~ 9 GPa, in good correspondence with our previous results (see Tables II and III).

Table I

Calculated formation energies of vacancy-interstitial pairs for the (110) and (111) surfaces of crystalline CaF_2 . E_F is the formation energy when the displaced F^- anion originates in the topmost surface layer and then placed in the adlayer (i.e., the vacant layer above the surface), away from the original site. E'_F is the formation energy when the displaced anion is moved to an octahedral site away from the original lattice site (that octahedral site is in the top layer for the (110) surface and is subsurface for the (111) surface system).

	E_F	E'_F
(110)	1.95 eV	1.75 eV
(111)	2.70 eV	2.36 eV
Bulk	2.44 eV	
Bulk (exp)	2.71 eV	

Table II

Critical stress, σ_{xz}^c (in GPa), and strains, γ^c , obtained via constant-strain molecular dynamics simulations of bulk crystalline CaF_2 strained in the (111) plane along the $\langle \bar{1}10 \rangle$ (x) direction, at several temperatures. The values of γ^c marked "before" and "after" corresponds to strain values bracketing the critical values of γ^c (i.e., the system did not fail for the values marked "before", and failed for those marked "after"). The corresponding values of σ_{xz}^c are denoted similarly. We note that the stress values, σ_{xz}^c , marked "after" are obtained from a short time interval, since afterwards failure of the system (slip in the (111) plane in the $\langle \bar{1}10 \rangle$ direction) is accompanied by relief of stress).

T (K)	σ_{xz}^c (GPa)		γ_{xz}^c	
	before	after	before	after
300	9.2	9.7	0.20	0.22
1073	5.1	6.1	0.14	0.16
1300	3.5	4.1	0.11	0.14
1450	1.7	3.5	0.06	0.11

Table III

Critical stress, σ_{xz}^C (in GPa), and strains, γ^C , obtained via constant-stress molecular dynamics simulations of bulk crystalline CaF_2 stressed in the (111) plane along the $\langle \bar{1}10 \rangle$ (x) direction, at several temperatures. The values of σ_{xz}^C marked "before" and "after" correspond to strain values bracketing the critical values of σ_{xz}^C (i.e., the system did not fail for the values marked "before", and failed for those marked "after"). The corresponding values of γ_{xz}^C are denoted similarly. We note that the stress values, σ_{xz}^C , marked "after" are obtained from a short time interval, since afterwards failure of the system (slip in the (111) plane in the $\langle \bar{1}10 \rangle$ direction) is accompanied by relief of stress. In addition, results obtained in simulations (at 300 K) where a single defect, or a stacking fault were present, are given.

T (K)	σ_{xz}^C (GPa)		γ_{xz}^C	
	before	after	before	after
300	8.4	8.7	0.20	0.21
1073	4.6	5.6	0.11	0.13
1450	0.26	2.6	0.009	0.01
300 (single defect)	6.6	7.9	0.15	0.15
300 (stacking fault)	8.5	9.2	0.20	0.20

Figures

- Figure 1:** Variation of lattice constant versus temperature in bulk CaF_2 obtained via molecular dynamics simulations.
- Figure 2:** Diffusion constants in bulk CaF_2 versus temperature. Values obtained via MD simulations are denoted by X and those obtained experimentally [7] by o.
- Figure 3:** F^- anion jump rate (proportional to the diffusion constant) determined via MD simulations for the (110) surface of CaF_2 . Jump rates for F^- anions in the topmost surface layer are denoted by diamonds (), those for the second layer down by X, and those for the 5-th layer deep by filled circles (o). Values for the bulk are denoted by filled squares ([]). Note the onset of F^- diffusion in the surface region at a temperature below that for the bulk, and the enhanced mobility in the surface region.
- Figure 4:** Stress component (σ_{xy}) in GPa and potential energy (in eV) versus strain γ applied in the (111) plane along the $\langle 1\bar{1}0 \rangle$ direction, at 300 K, 1073 K and 1450 K, (in (a-d) respectively). Results obtained via constant-strain MD simulations. Yield, via slip, occurs past the maximum value of σ_{xy} .
- Figure 5:** Stress component σ_{xy} (in GPa) and $R_\alpha^2(t)$ (see Eq. 1), versus time (in ps). The strain is incremented at 10ps, 20ps and 30ps, in constant strain simulations of bulk CaF_2 at 1300 K. Note that in the absence of strain ($0 \leq t < 10\text{ps}$) the mobility of the anions is rather small (see Fig. 5b). Strain-induced enhanced mobility of the F^- anions is evident for larger strain rates (signified by the slopes of the curves in (b-e)). Upon reaching the critical strain value the system yields via slip (accompanied by relief of internal stress (see σ_{xz} for $t > 30\text{ps}$, in (a)) achieved a new, strained,

equilibrium configuration. As seen from comparing the displacement of the ions shown in (c-e), the slip (past $t > 30$ ps) occurs along the x ($\langle 1\bar{1}0 \rangle$) direction (see in particular the motion of the C_a^{+2} ions which is negligible up to that stage).

Figure 6: Same as Fig. 5, for simulations at 1450K. Note that at this temperature F^- mobility is significant even for the unstrained.

Figure 7: Component of the force on the tip in the z direction (in a), and potential energy of the tip (in b), obtained via MD simulations of a CaF_2 tip lowered and subsequently retracted from a CaF_2 crystalline (111) surface. Squares denote data obtained during the tip-lowering process and circles for tip lift-off. The distance scale (in Å) correspond to d_{ns} (see text). Note the pronounced hysteresis portrayed in both the force and potential energy curves. Force in nN and potential energy in eV.

Figure 8: Component of the force in the x ($\langle 1\bar{1}0 \rangle$) direction and potential energy of the tip, versus lateral displacement, for a CaF_2 sliding on a (111) surface in the $\langle 1\bar{1}0 \rangle$ direction. Note the oscillatory variations in the force reflecting stick-slip upon sliding.

Figure 9: Selected atomic configurations obtained from MD simulations of a CaF_2 tip interacting with a (111) CaF_2 surface. For the substrate green and red balls correspond to F^- and Ca^{+2} , respectively. For the tip the F^- anions are represented by the yellow balls and the blue balls denote Ca^{+2} . (a) initial configuration (outside the range of interaction between the tip and the substrate); (b) Tip and substrate at contact (point marked by an arrow in Fig. 8(a); (c) A slice through the system at the configuration shown in (b); (d) Configuration corresponding to lateral displacement of $\Delta x = 2.1$ Å, exhibiting slip between tip layers; (e) Configuration

corresponding to $\Delta = 5.8 \text{ \AA}$. Note that the proximal region (i.e., the bottom-most layers) of the tip is bonded to the substrate, and sliding occurs between that bonded region and the rest of the tip assembly.

References

1. M. W. Ribarsky and U. Landman, Phys. Rev. B 38, 9522 (1988); U. Landman, W. D. Luedtke and M. W. Ribarsky, J. Vac. Sci. Technol. A7, 2829 (1989); U. Landman, W. D. Luedtke and M. W. Ribarsky in New Materials Approaches to Tribology, eds. L. E. Pope et al. (MRS, Pittsburgh, 1989), Vol. 140, p. 101.
2. U. Landman, W. D. Luedtke, N. A. Burnham and R. J. Colton, Science 248, 454 (1990); U. Landman, W. D. Luedtke and R. N. Barnett, in Many-Atom Interactions in Solids, eds. R. M. Nieminen et al. (Springer, Berlin, 1990).
3. M. J. Gillan, J. Phys. C 19, 3391 (1986).
4. M. J. Gillan, Physica 131B, 157 (1985) and references therein.
5. M. J. L. Sangster and M. Dixon, Adv. in Phys. 25, 247 (1976).
6. M. Parrinello and A. Rahman, J. Appl. Sci. 52, 7182 (1981).
7. C. E. Derrington, A. Linler and M. O'Keeffe, J. Solid State Chem. 15, 171 (1975).
8. G. Jacucci and A. Rahman, J. Chem. Phys. 69, 417 (1978).
9. For the (110) surface the simulation system consisted of 4 static and 16 dynamic layers, with 36 atoms per layer (12 Ca^{+2} and 24 F^-). For the (111) surface the system contained 6 static and 24 dynamic layers, with 24 atoms per layer (i.e., 24 F^- in a fluorine layer and 24 Ca^{+2} in a calcium layer stacked in an $\text{F}^- \text{Ca}^{+2} \text{F}^- \text{F}^- \text{Ca}^{+2} \text{F}^-$ ----- manner).
10. See report by Dr. M. Gardos et al.
11. M. T. Sprackling, The Plastic Deformation of Simple Ionic Crystals, (Academic Press, London, 1976), p. 168.

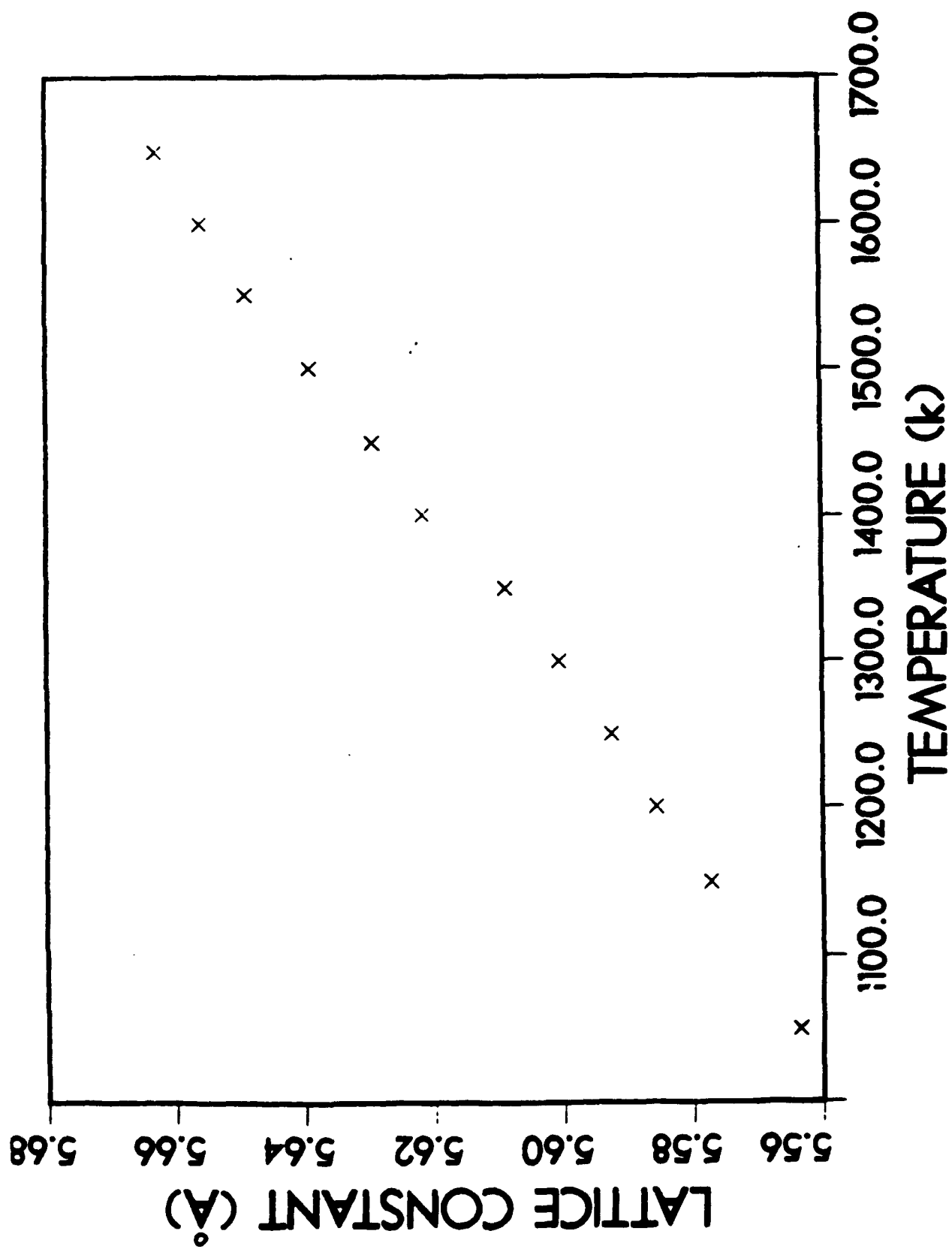


Figure 1

BULK

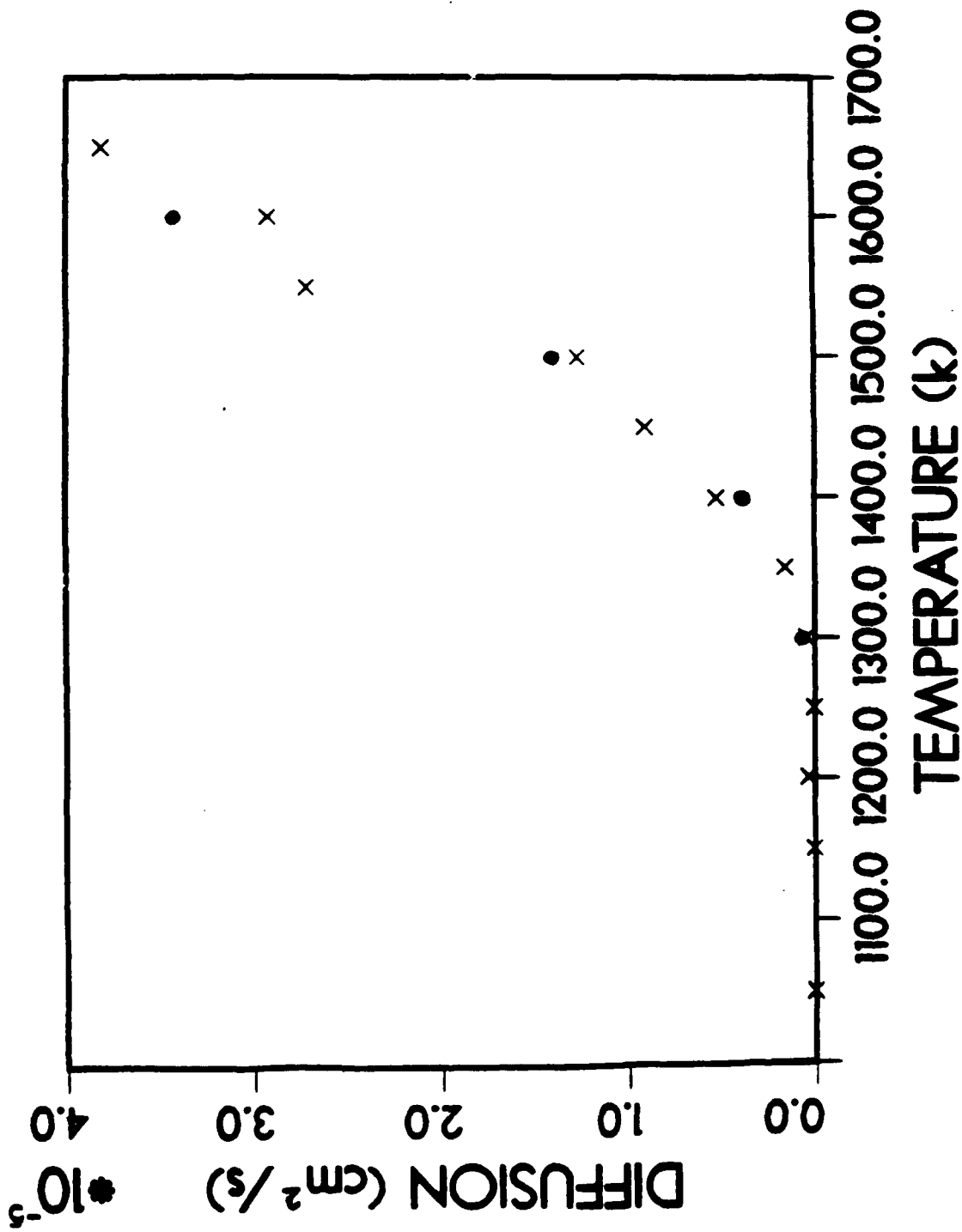


Figure 2

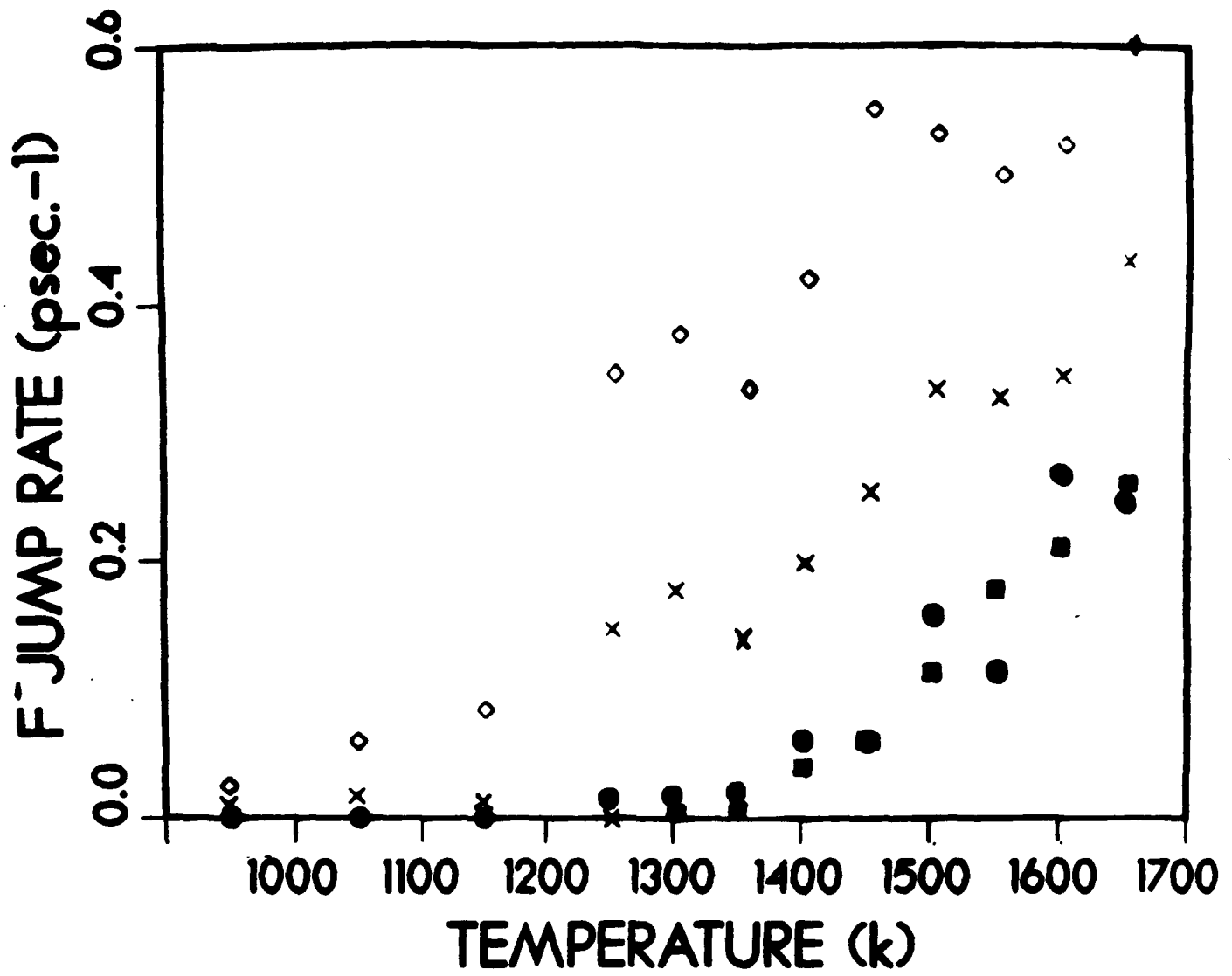
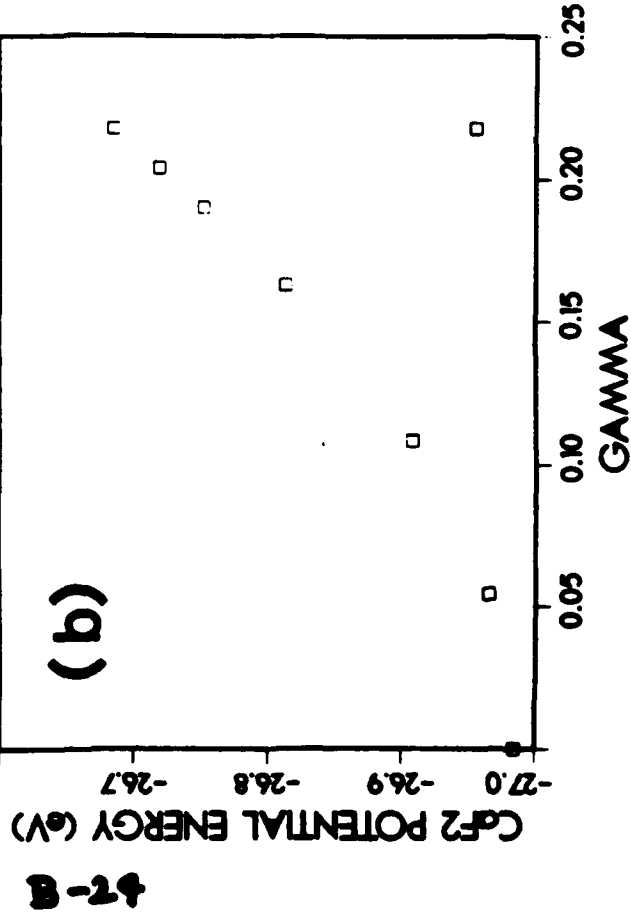
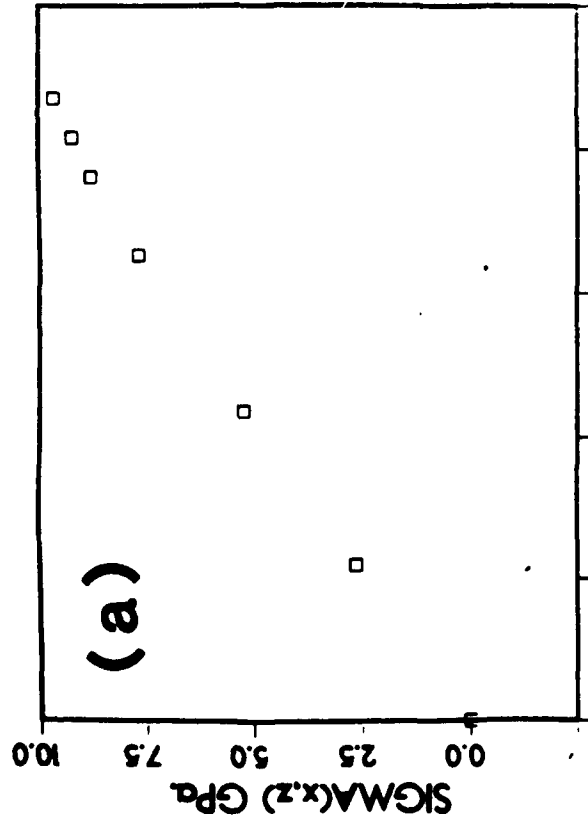


Figure 3

CONSTANT STRAIN $T=300\text{k}$



CONSTANT STRAIN $T=1073\text{k}$

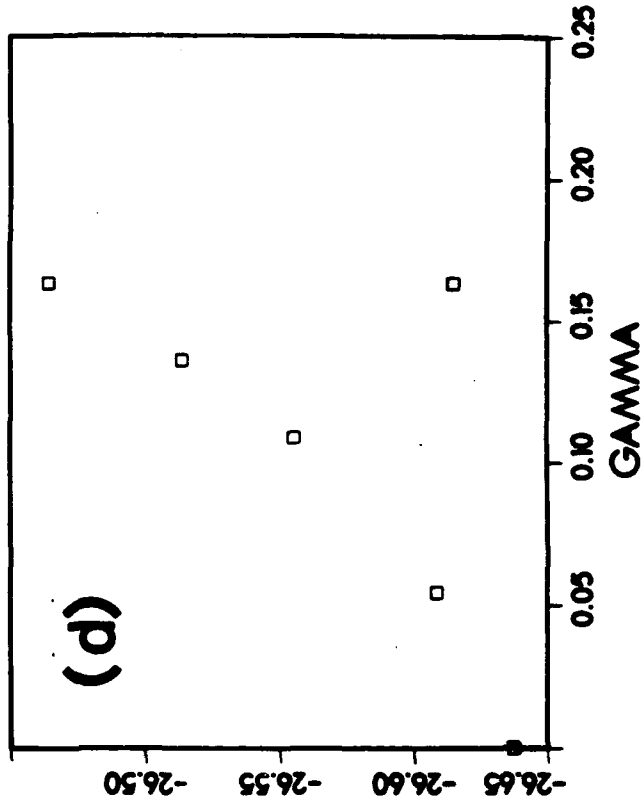
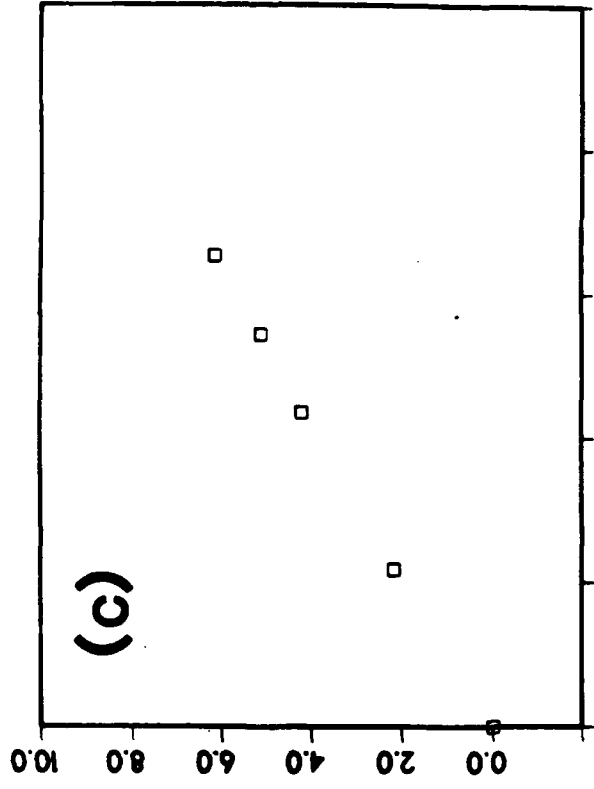
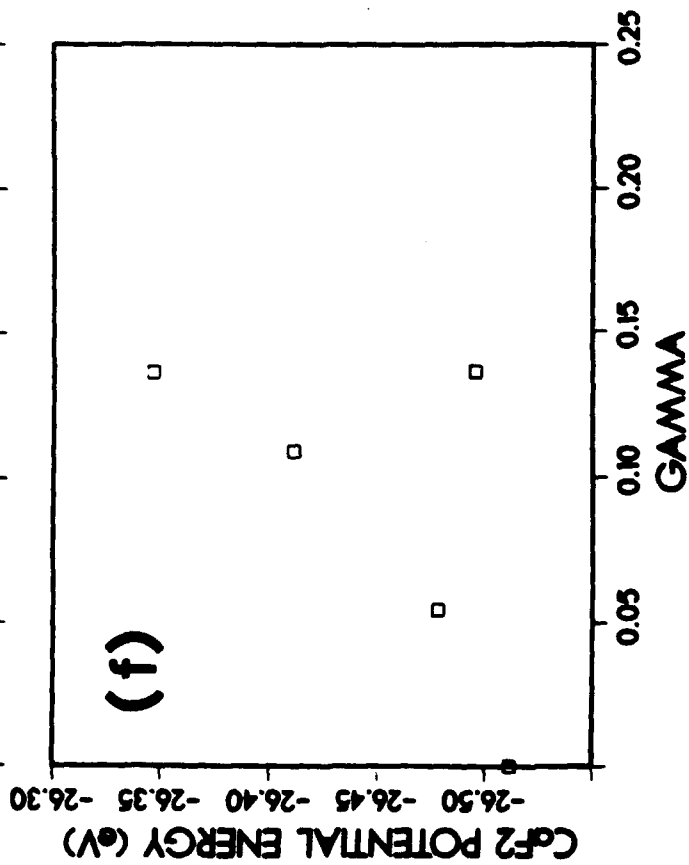
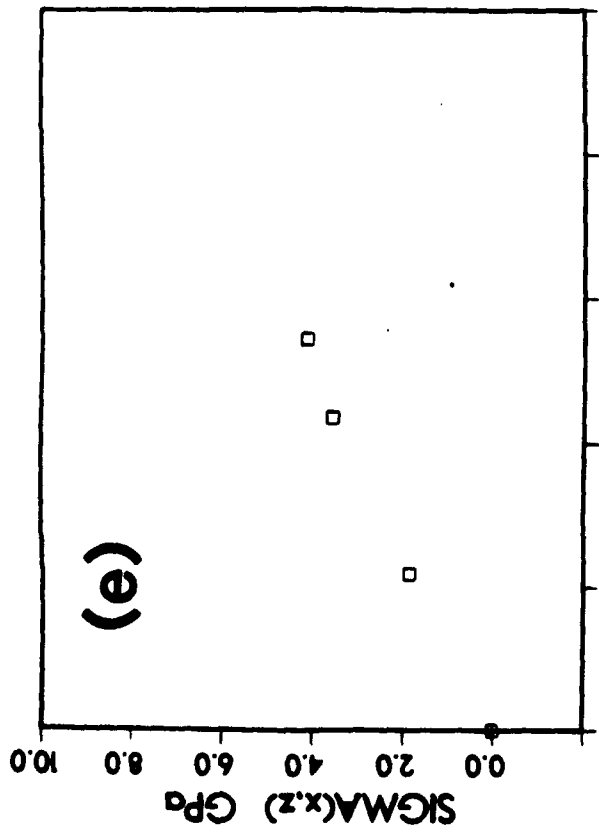


Figure 4

CONSTANT STRAIN T=1300K



CONSTANT STRAIN T=1450

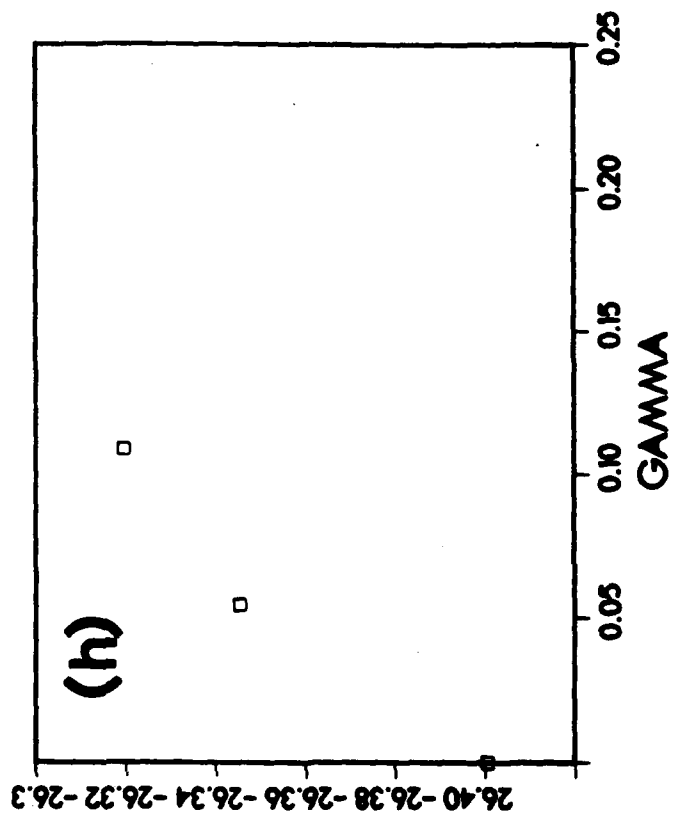
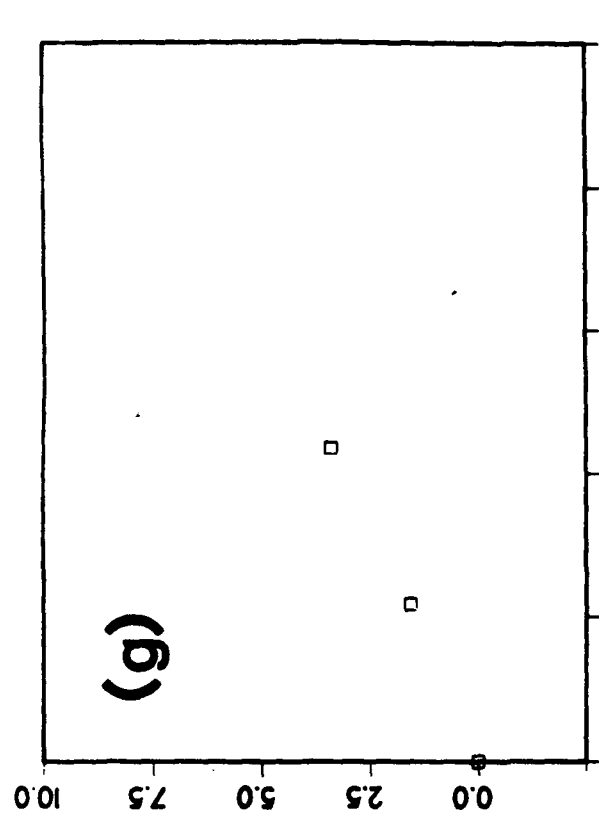


Figure 4

CONSTANT STRAIN $T=1300\text{k}$

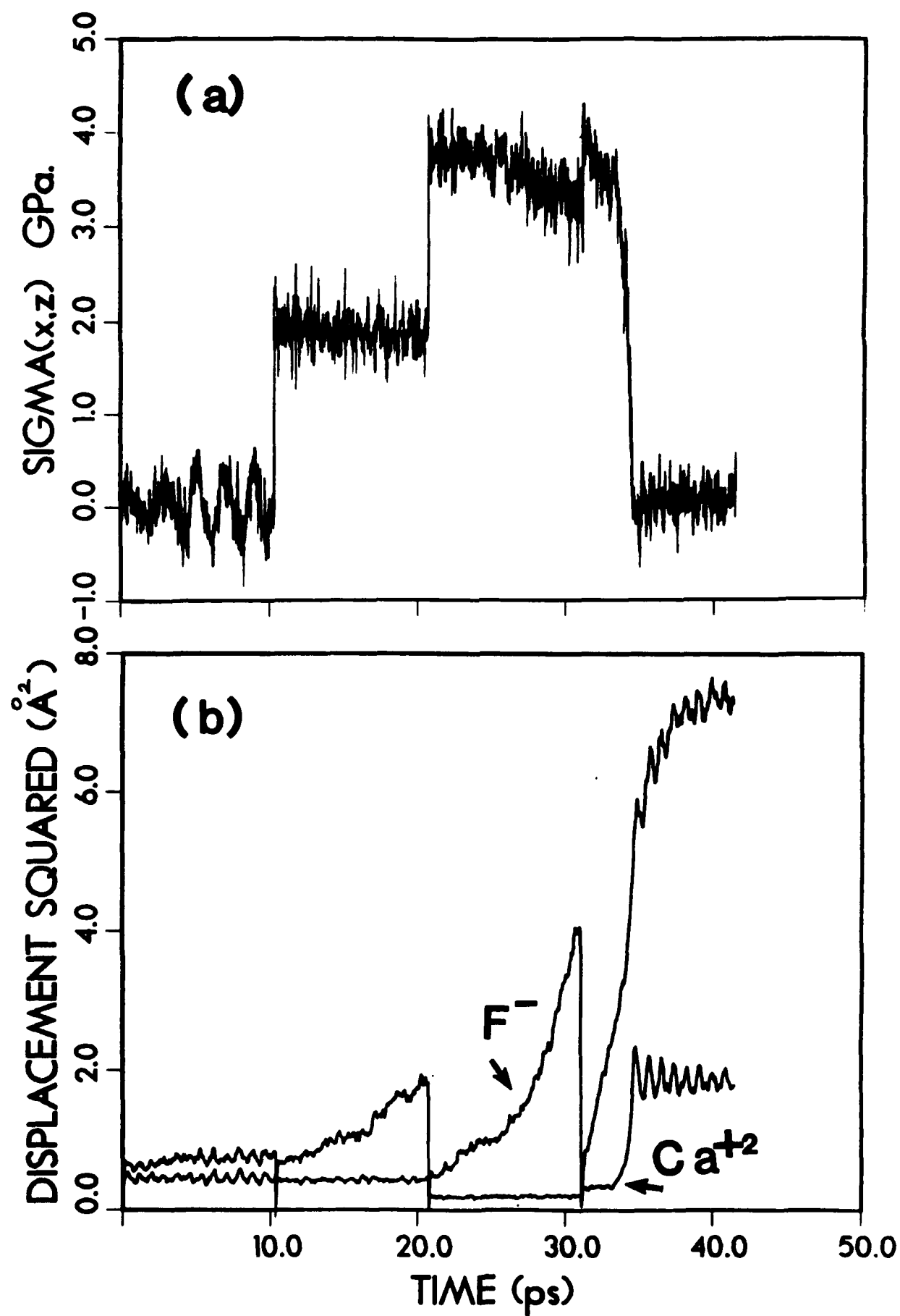
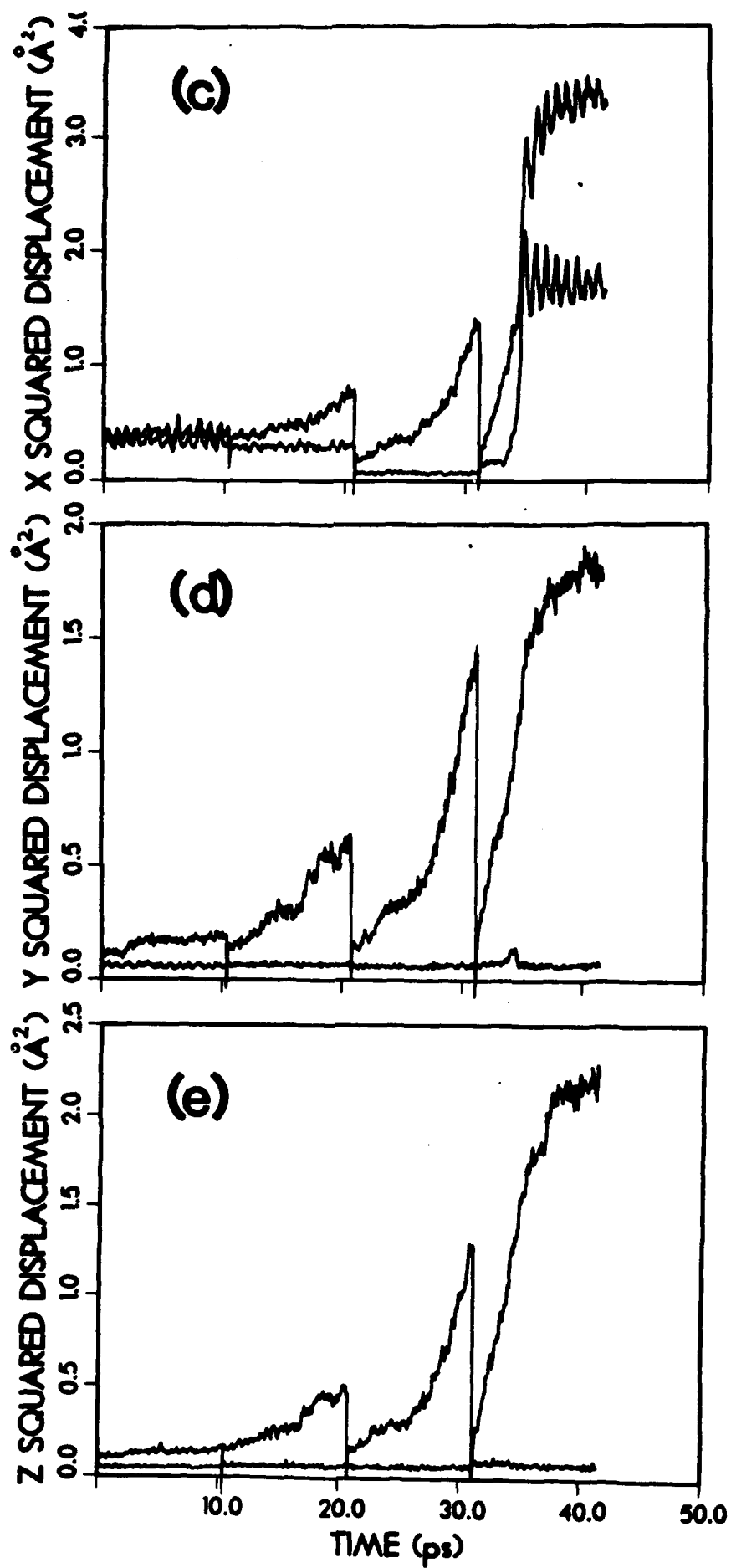


Figure 5



CONSTANT STRAIN $T=1450k$

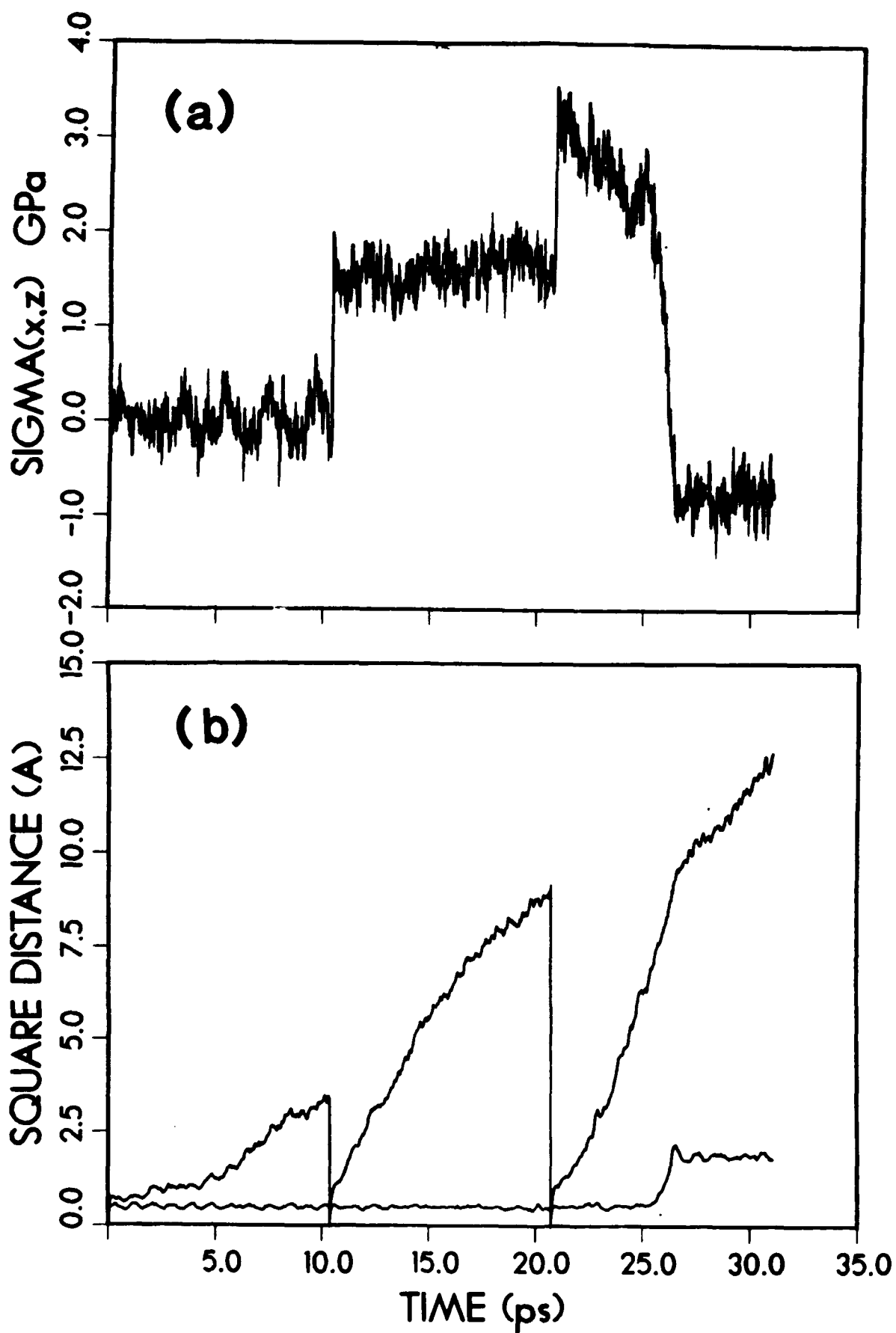
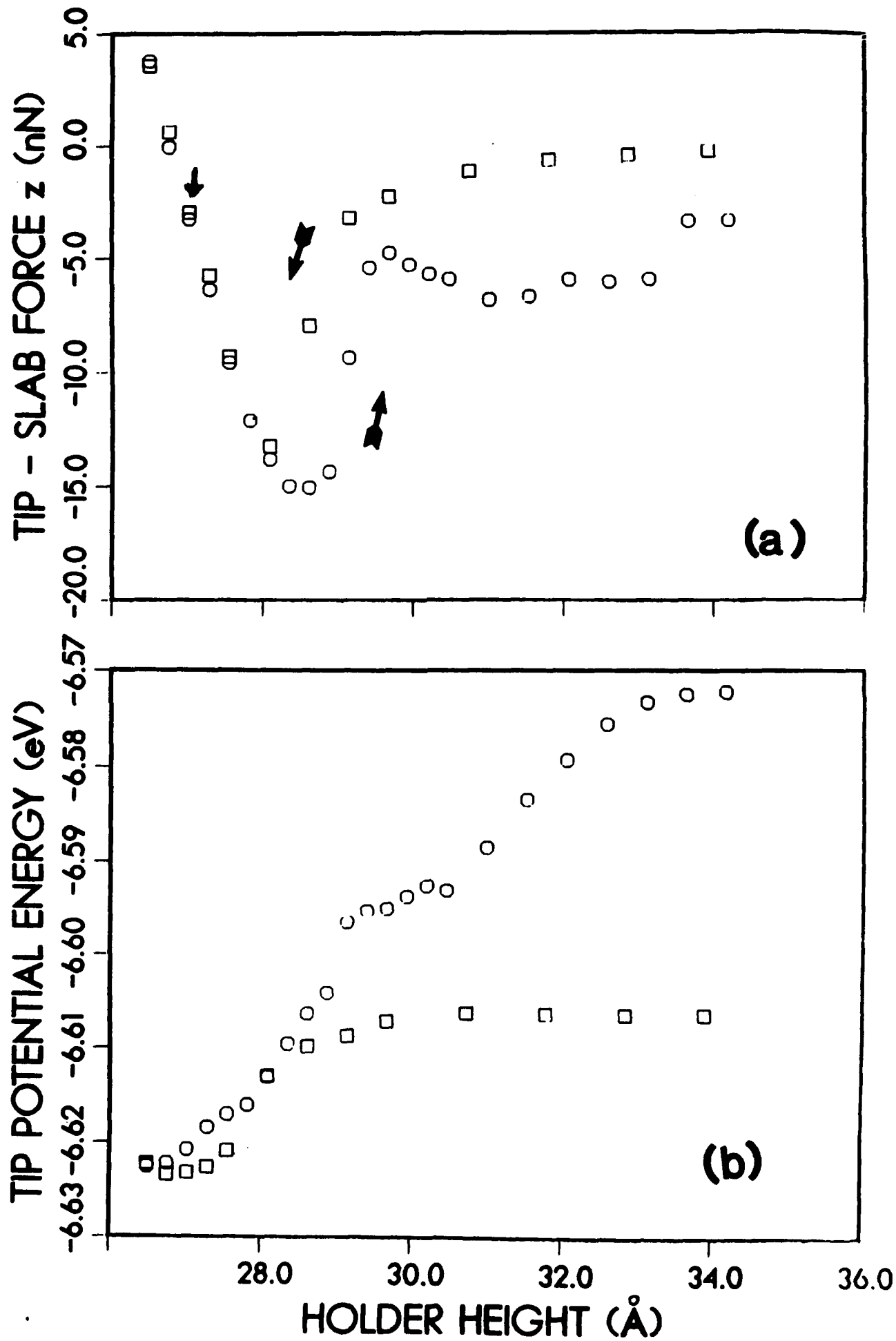
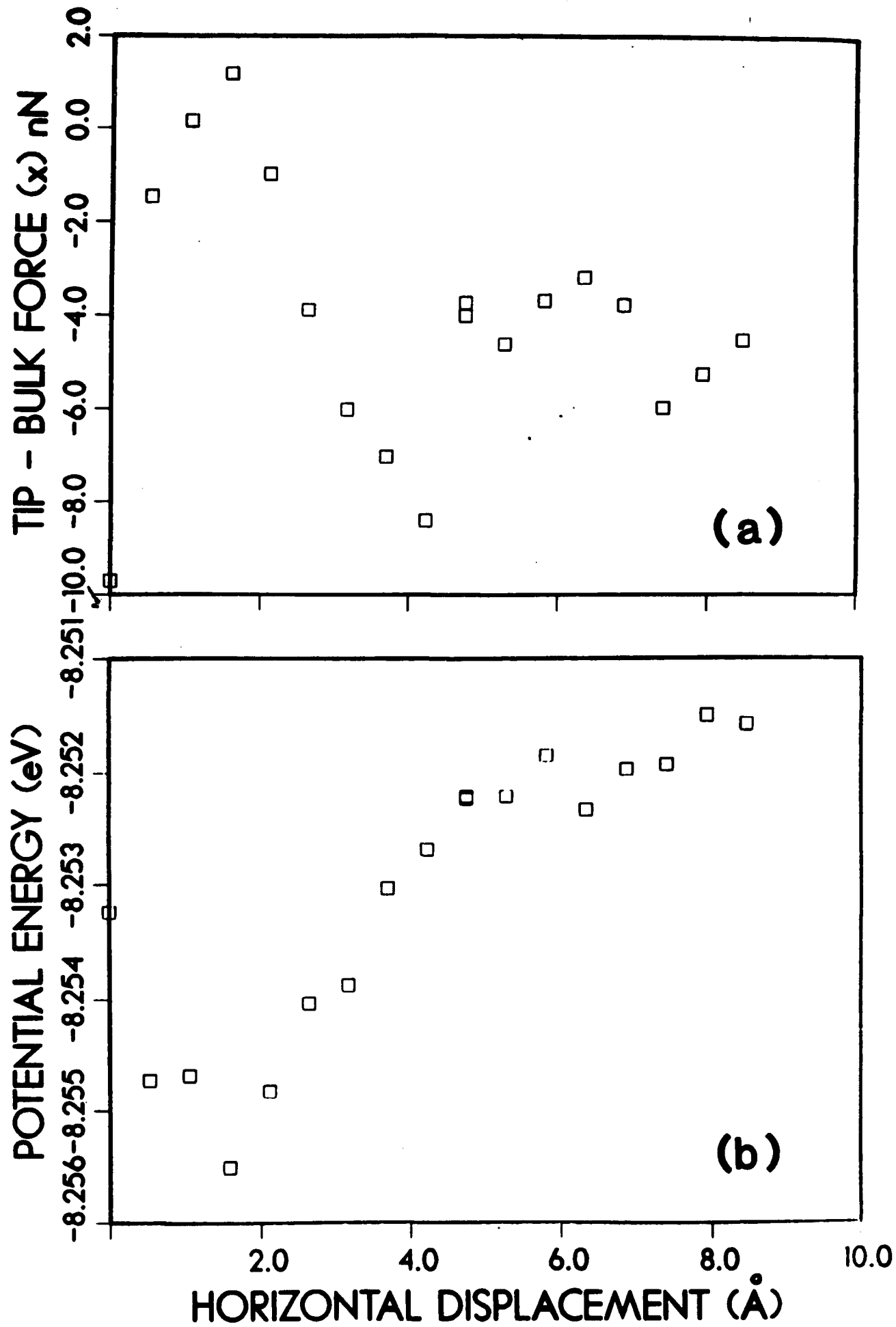


Figure 6





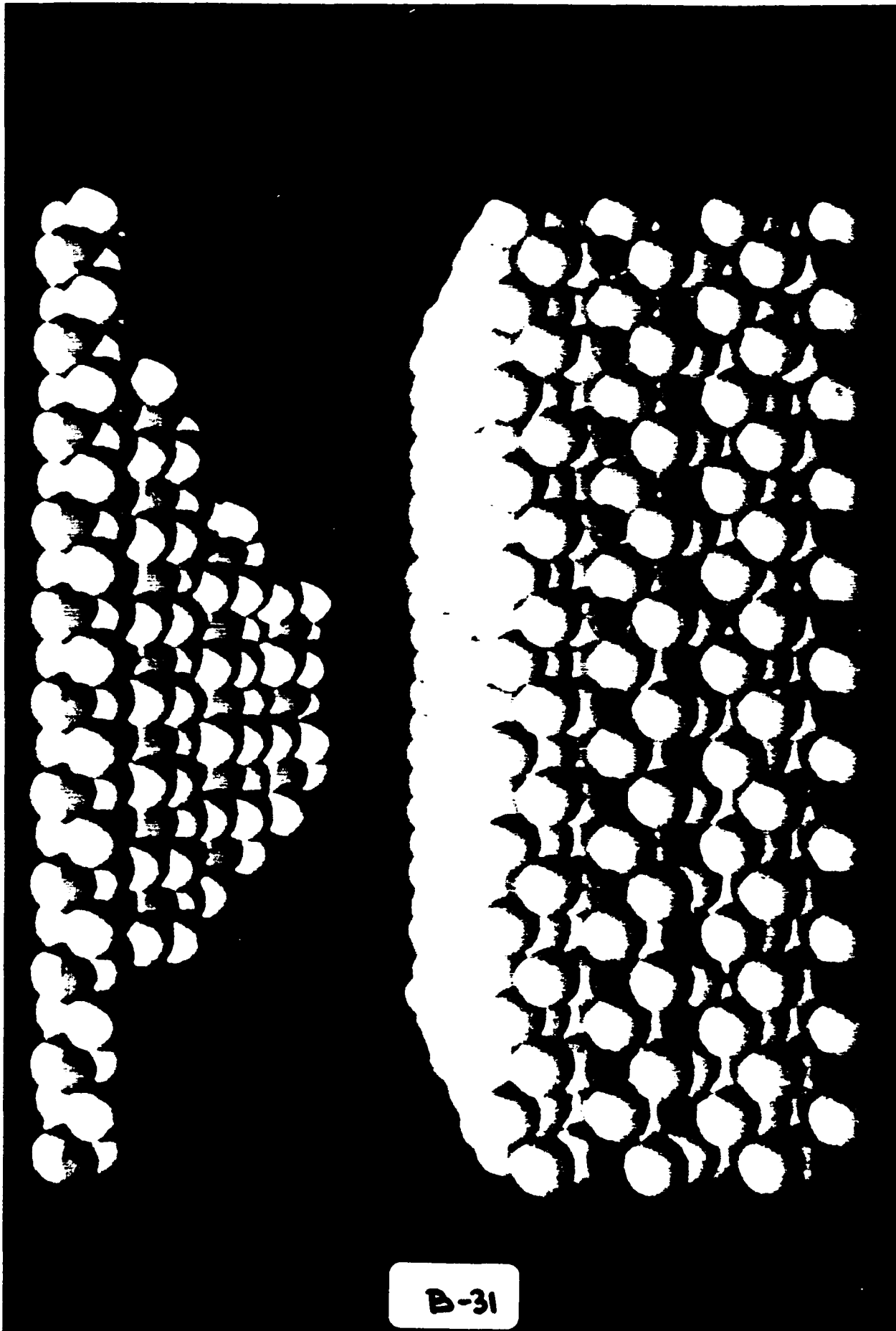
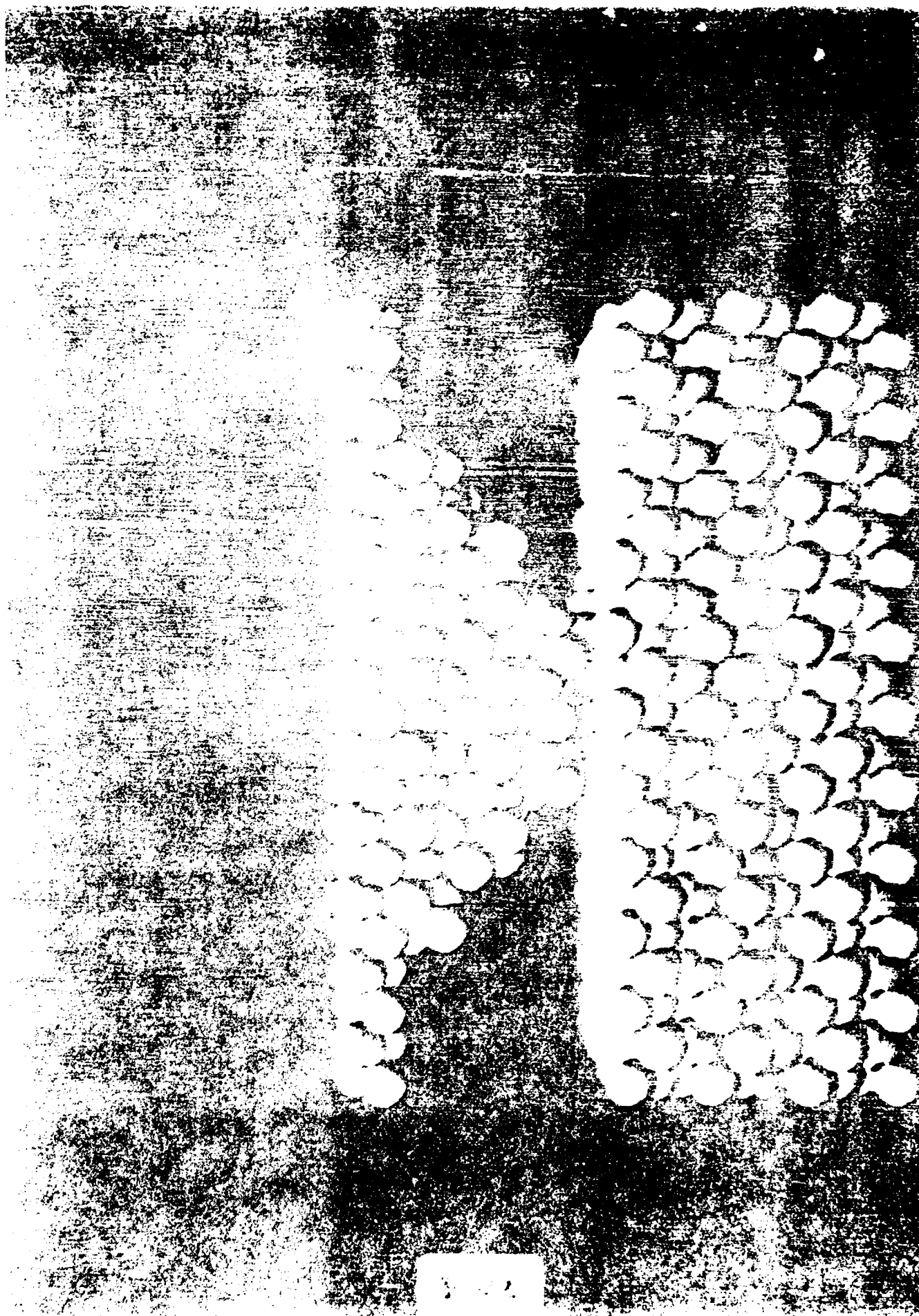


Figure 9a



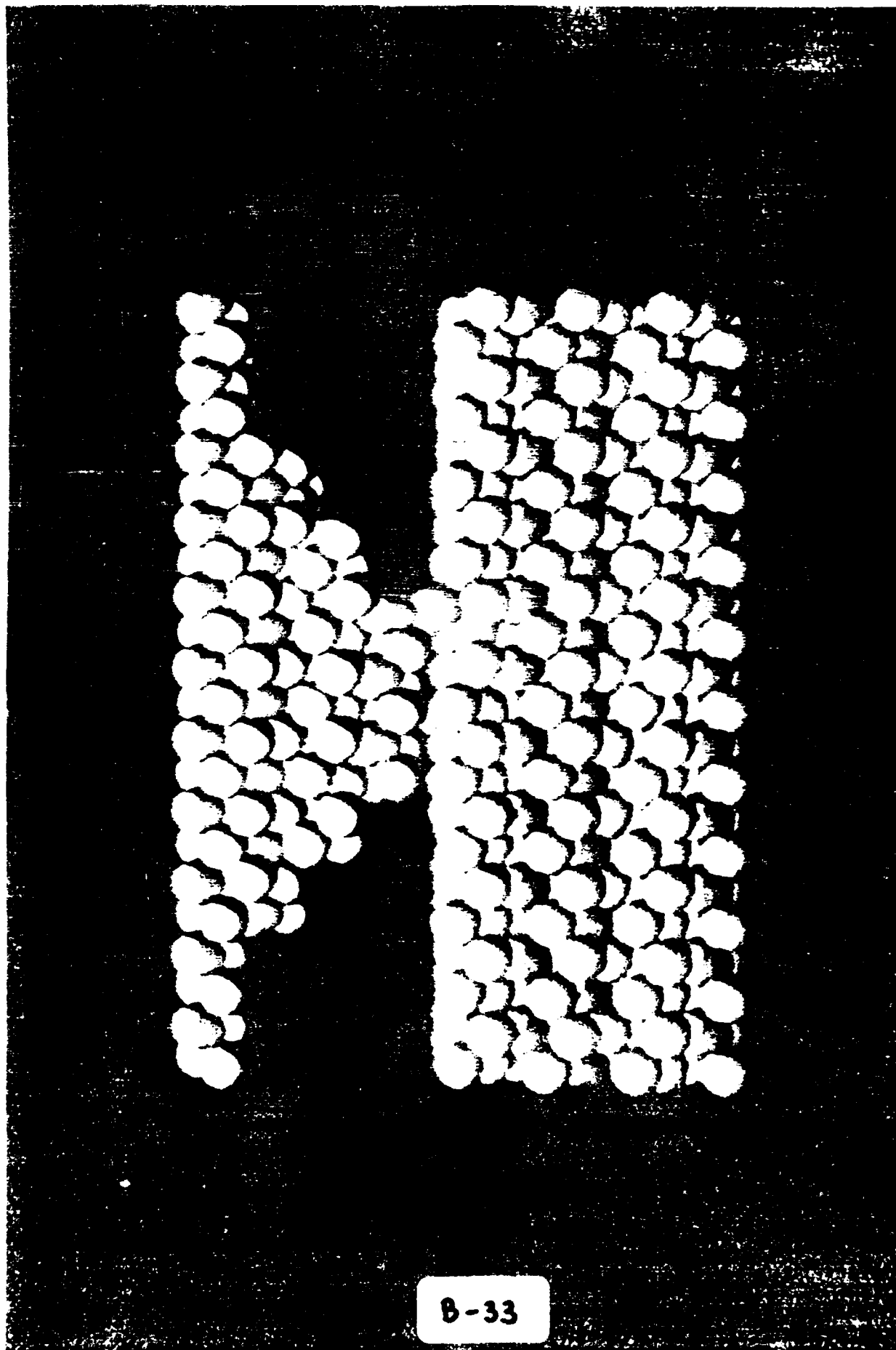
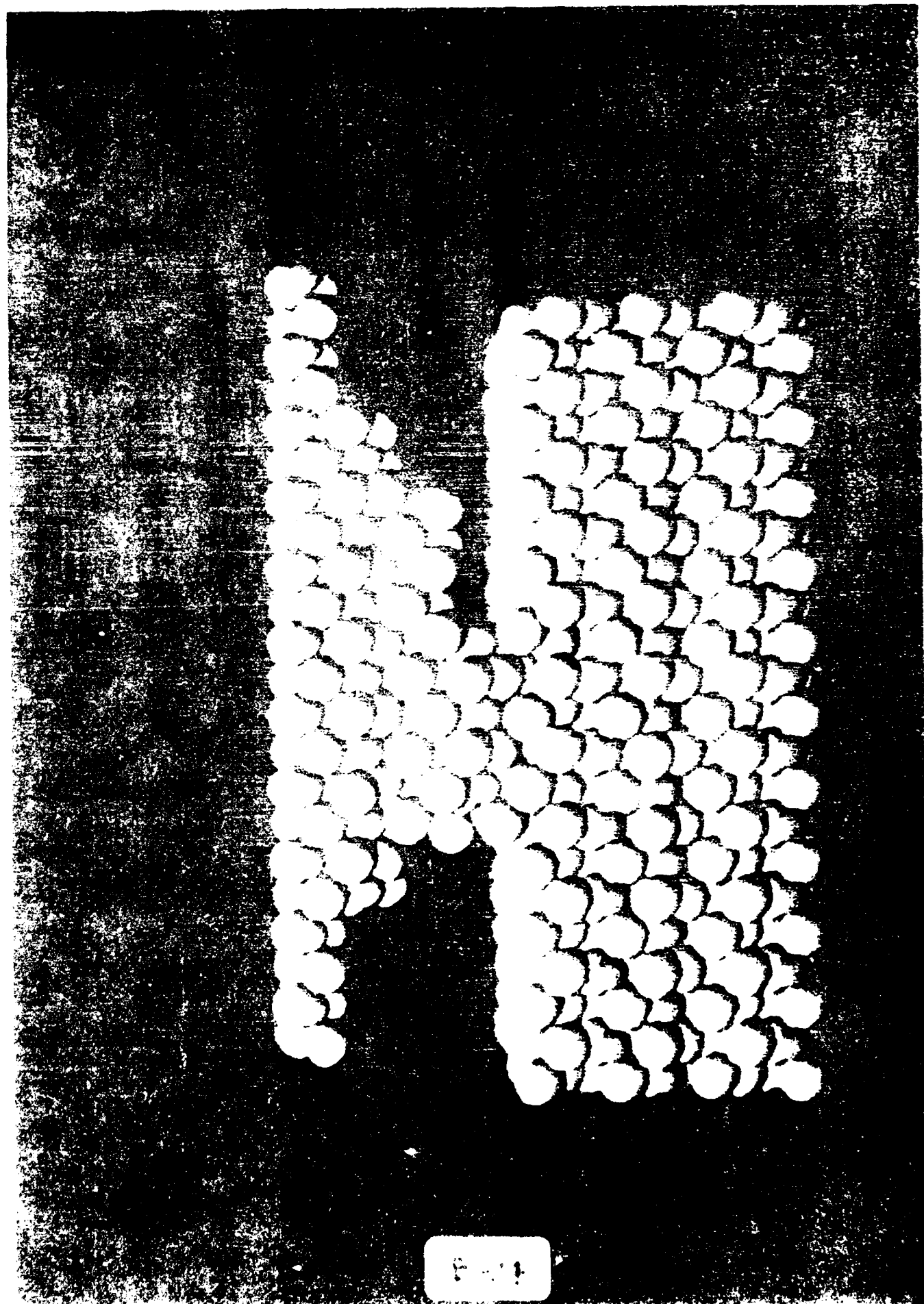
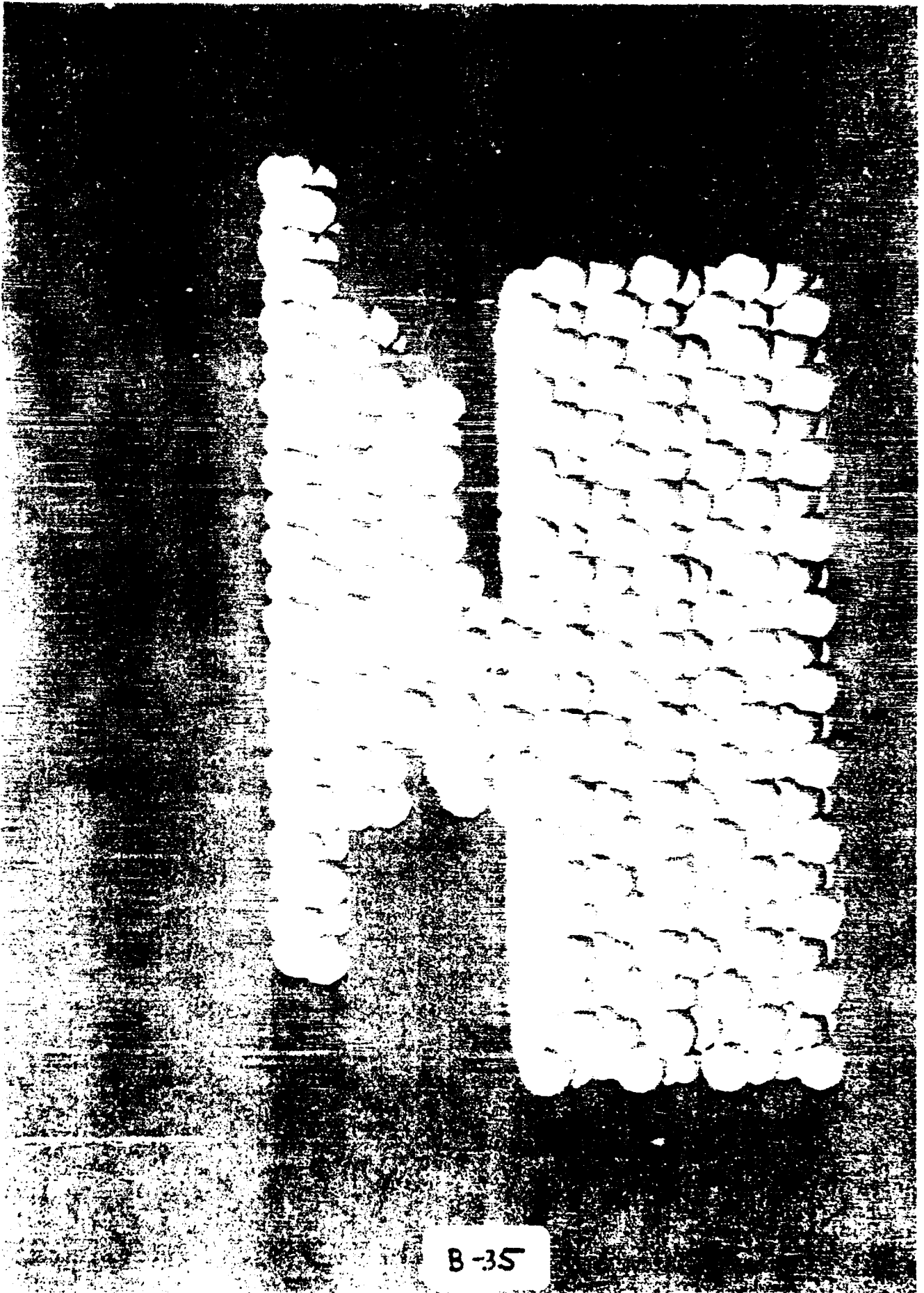


Figure 6





APPENDIX C

S. Granick, "Assessment of the Usefulness of Direct Force Methods to Elucidate the Adhesion and Tribology of Solid Lubricated Ceramics," Final Report, U. of Illinois, Urbana-Champaign, IL, October 23, 1989; Hughes P.O. M9-515286-6L

ASSESSMENT OF THE USEFULNESS OF DIRECT FORCE METHODS

TO ELUCIDATE THE ADHESION AND TRIBOLOGY OF

SOLID LUBRICATED CERAMICS

Prepared for the Hughes Tribology Program

Submitted by Professor Steve Granick

October 23, 1988

OUTLINE

~~~~~

|                                              | page |
|----------------------------------------------|------|
| Scope.....                                   | 2    |
| Description of methods.....                  | 4    |
| a) AFM.....                                  | 4    |
| b) Molecular tribometry.....                 | 5    |
| Results to date                              |      |
| (including unpublished results).....         | 8    |
| a) Atomic periodicity.....                   | 8    |
| b) Quantized friction.....                   | 9    |
| c) Solid lubrication by liquids.....         | 10   |
| d) Microviscosity.....                       | 11   |
| e) Shear strength proportional to pressure.. | 13   |
| Materials requirements.....                  | 15   |
| a) AFM.....                                  | 15   |
| b) Molecular tribometry.....                 | 17   |
| Perspectives and future possibilities.....   | 20   |
| a) Strengths.....                            | 20   |
| b) Limitations.....                          | 22   |
| c) Prospects.....                            | 23   |
| References.....                              | 24   |

## Scope

The design and operation of solid lubricated ceramic machine components in extreme environments is of growing concern in defence projects and other areas. In order to best advance these technologies, there is general recognition that advances in fundamental understanding of friction and wear mechanisms will be required. To this end, on the experimental side it is desirable to seek model systems, i.e. systems of sufficient simplicity that the influences of various variables of interest can be cleanly separated. By contrast, in usual engineering systems, so many variables operate at once that separating the roles of these influences is usually not possible. Inasmuch as interactions between surfaces are mediated by forces, recent approaches to experimental study have concentrated on the measurement of forces. A consensus has emerged that forces should be measured between asperity-free surfaces, or (equivalently) between single model asperities.

This report is an assessment of the usefulness of two methods developed very recently: atomic force microscopy (AFM), and molecular tribometry. The report is organized into four sections. The first summarizes the methods involved and the principles upon which they are based. The second section summarizes results obtained to date (including unpublished results not available in the open literature). The third section consists of technical comments related to particular materials of possible

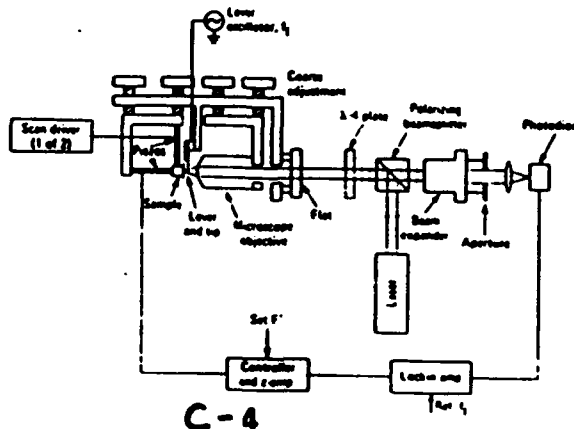
interest. The fourth section provides perspectives, based upon the previous sections, upon the strengths and limitations of these new methods, and concludes with discussion of opportunities for exploiting these methods in developing advanced technologies.

## Description of methods.

a. The atomic force microscope (AFM) evolved from scanning tunnelling microscopy (STM). In distinction to STM, it does not require a conducting substrate. A sharp needle-like tip is held perpendicular to a surface, separated from that surface by less than  $10^{-9}$  meter. The force on the tip, arising from surface-tip energetic interactions, is measured by the deflection of a spring to which the tip is mounted. The extension of AFM to measurement of interesting tribology at the atomic level emerged from the pioneering work of McClelland, Mate, Erlandsson, and Chiang (IBM Almaden Research Laboratories) in a paper published in October 1987 [1].

A schematic diagram of the most recent version of this apparatus [2] is shown in Figure 1. The tip is positioned close to the surface and then is rastered across it by applying voltage to piezoelectric elements. Motion of the tip is detected by optical interferometry. Currently this tip is made of tungsten wire (although, as discussed below, there are many other possibilities), and measurements are made in the ambient air.

Figure 1  
(from reference 2)



An ultra-high-vacuum (UHV) installation in which to make these tribology measurements is near completion in the IBM laboratories [3]. In principle, the friction force on a single atom could be measured by this method.

b. Two molecular tribometry instruments of different design have been developed to date: by Israelachvili [4] and by Van Alsten and Granick [5,6]. Both derive from the surface forces apparatus, an instrument developed originally in the laboratory of David Tabor [7] for the purpose of measuring van der Waals forces as a function of surface separation, and applied to many surface problems during the past 10 years through the trailblazing work of Israelachvili and coworkers [8].

The method involves interactions between two surfaces of macroscopic size (rather than a single surface in contact with the tip of an AFM). In the surface forces apparatus these surfaces are positioned as crossed cylinders as a means to sidestep the otherwise serious problem of aligning two planes to be absolutely parallel. However, the molecular tribometry instruments [4-6] are designed to operate under such large normal pressures (either adhesive or compressive) that the crossed cylinders actually flatten at the point of contact to form two parallel plates separated by boundary layers. In effect, this constitutes a model asperity. When atomically smooth surfaces are

employed in a molecular tribometer, the apparent area of contact is also the true area of contact. This true contact area is measured directly by multiple beam interferometry.

A schematic diagram of the Israelachvili tribometry apparatus is shown in Figure 2. Differential double cantilever springs are used to apply pressure and also to apply shearing force. Strain gauges detect the friction force. Sliding is over macroscopic distances, distances from hundreds of micrometers up to millimeters.

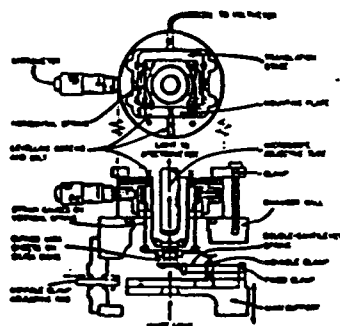


Figure 2  
(from reference 4)

Instrumental improvements to increase the distance and force resolution are underway [9].

A schematic diagram of the Van Alsten-Granick tribometry apparatus is shown in Figure 3. As in the Israelachvili instrument, normal pressures are applied using springs. Unlike that instrument, piezoelectric bimorph elements apply a shearing force and detect the resulting

displacement. The phase lag between stress and strain is measured, so that the viscosity of boundary layers can be calculated. Sliding distances can be varied from 1 nm to 10  $\mu\text{m}$ , making possible direct measurements of the transition from microdisplacements to macrodisplacements.

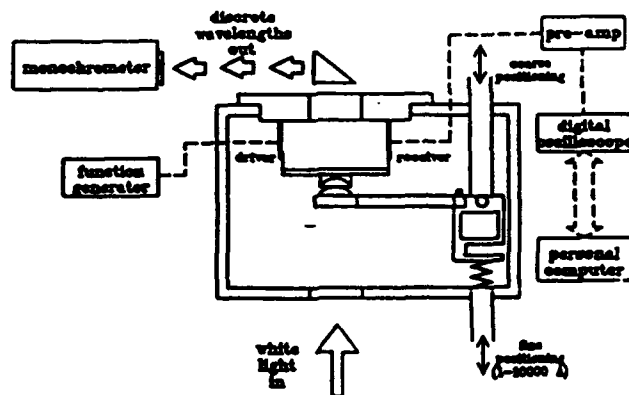


Figure 3  
(from reference 6)



## Results to date (including unpublished results)

Progress to date has been of considerable interest. Even though AFM and molecular tribometry studies have begun to appear in print only within the past 12 months, the accumulation of new results has been rapid. The state of development at the time of this writing (October, 1988) is listed and discussed below.

### a) Atomic periodicity.

McClelland and coworkers [1] found that when the tip of a sharp tungsten wire was slid on the basal plane of graphite, stick-slip was observed with the periodicity of the graphite lattice, approximately 2.5 Å. Later experiments, still unpublished [2], found the analogous result for tungsten wire slid on the basal plane of mica, the period of stick-slip now being that of the mica lattice, approximately 5.2 Å. The general result appears to emerge that the friction of a tip against a crystal surface is modulated with the atomic periodicity of the crystal surface.

Under active investigation by these experimenters is the question of what was sliding on what. Chemistry at the tip was probably tungsten oxide since the experiments were conducted in ambient air. Although the normal forces were exceedingly low by usual standards (as low as  $10^{-8}$  N), this

represents a crushing force if concentrated at a single atom. It follows that the needle-like tips were blunted to diameters of perhaps 2,000-3,000 Å and were probably not smooth over the encompassed area. Finally, the possibility is still open that in these experiments the tip actually dislodged from the easily cleaved graphite and mica substrates thin flakes of these substrates, which stuck to the tip, so that in fact the measurements entailed graphite sliding on graphite and mica sliding on mica. These and other uncertainties have been carefully discussed [1,2]. They have motivated these researchers to undertake the ambitious, time-consuming task of placing their apparatus inside a UHV chamber [3].

b) Quantized friction.

Israelachvili and coworkers [4] found, studying the sliding of parallel sheets of mica past one another when separated by thin films of cyclohexane and octamethyltetrasiloxane (OMCTS) liquid lubricants, that the dynamic friction increased stepwise with decreasing film thickness. In addition the dynamic friction was preceded by a static friction, implying that the liquid films were solid-like. The range of thickness measurements was the extraordinarily thin range of 4 to 1 molecular thicknesses. This finding of "quantized friction" between parallel surfaces separated by

a liquid boundary layer has excited considerable attention in the news media.

More recent work by this group has concentrated on stick-slip phenomena encountered during sliding. Stick-slip was observed in boundary layer systems where the surface-surface interactions are attractive (adhesive), but it was not observed in cases where the surface-surface interactions were repulsive [10].

c) Solid lubrication by liquids.

As noted above, a sufficiently thin boundary layer of liquid appears to solidify when confined under pressure between parallel surfaces. Van Alsten and Granick [6,11] have studied this phenomenon extensively. Boundary layer widths have ranged from 6 to 1 molecular thicknesses. Using the nonpolar liquids hexadecane and OMCTS, these researchers observed [6,11] that when the normal pressure reached levels near those required to cause an additional layer of liquid molecules to drain from between the solid surfaces, the systems became unstable between drainage and solidification. In other words, either liquid-like or solid-like response could be exhibited at the same layer number. The transition from liquid-like response (zero shear stress required to initiate macroscopic sliding) to solid-like response (finite shear stress required to initiate macroscopic sliding) was rapid and reversible, suggesting a phase transition. Such a

phase transition might eventually be of engineering significance in solid lubrication technology.

The shear stress of such solidified liquids has been found to evolve with time after the film was formed. An example is shown in Figure 4. The experiment concerned hexadecane (thickness 2 molecular widths) at a mean normal pressure of 6 MPa. Over a period of 600 seconds, the critical shear stress required to initiate macroscopic slip increased by a factor of over 15%.

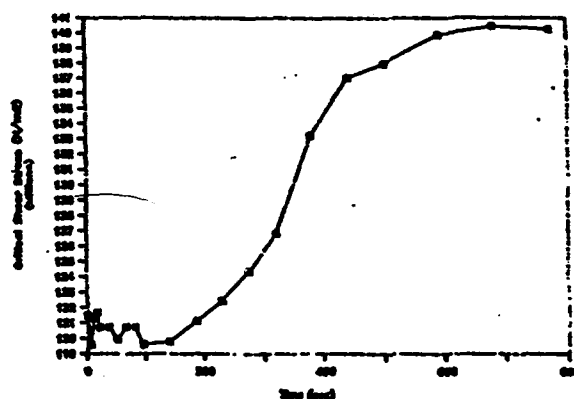


Figure 4  
(from reference 11)

#### d) Microviscosity.

Quantized friction was reported [4] for the dynamic friction which succeeds static friction. Ultrathin liquid films do not, however, always solidify; under certain conditions vastly enhanced microviscosity is observed instead [6,11]. The dissipative drag, characterized as an apparent viscosity ( $\mu_{app}$ ), is illustrated in Figure 5 below

for experiments involving hexadecane. In Figure 5, the arrows indicate the direction of increasing pressure.

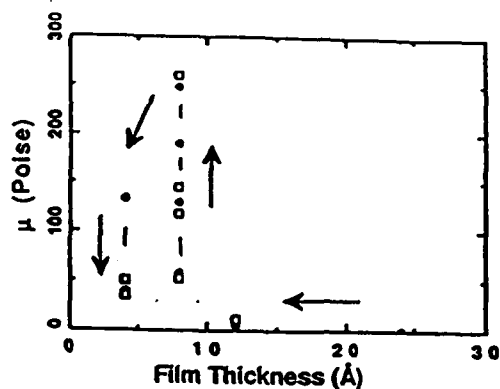


Figure 5  
(from reference 6)

These experiments involved sinusoidal oscillation at 1 Hz with small amplitudes, 200 nm (○) and 1000 nm (●). The lack of dependence of the apparent viscosity on the amplitude of oscillation shows that the quantity which was determined experimentally, the dissipative wall shear stress, was directly proportional to the velocity of motion, which is characteristic of liquid behavior. Clearly, the apparent viscosity was not well-defined as a function of film thickness (D) only, but depended also on the pressure (P):

$$\mu_{\text{app}} = \mu(D, P) \quad .$$

e) Shear strength proportional to pressure.

Molecular tribometry was used [11] to measure the critical shear force required to cause slip between solidified hexadecane films. The static shear strength was calculated after normalizing for the measured areas of contact. This increased rapidly with the mean normal pressure, as illustrated in Figure 6 for hexadecane:

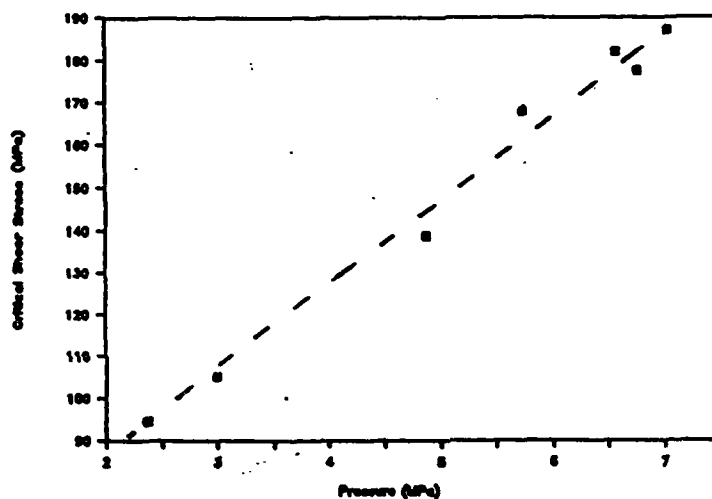


Figure 6  
(from reference 11)

This result and results of extensive other experiments [11] show that the shear strength ( $\tau$ ) in these experiments cannot be described by a single number, but increases in direct proportion to the mean normal pressure ( $P$ ):

$$\tau = \tau_0 + \alpha P \quad .$$

The coefficient of proportionality ( $\alpha$ ) was substantial. For the data shown in Figure 6,  $\alpha \approx 20$ .

### Materials requirements

The practicing engineer who designs advanced solid lubricated ceramic systems is concerned with the use and preparation of specific ceramic materials and solid lubricants. To apply the direct force methods to a wider variety of solid substrates than has been studied yet is clearly desirable. Among ceramic substrates, both single crystal and polycrystalline engineering material versions of  $\alpha$ -SiC,  $\beta$ -SiC,  $\alpha$ -Si<sub>3</sub>N<sub>4</sub>, and of  $\beta$ -Si<sub>3</sub>N<sub>4</sub>, are of evident interest. Among solid lubricants, single crystals, pure CVD and sputtered or ion-plated films of 2H-MoS<sub>2</sub>, graphite, rutile, and hexagonal (pyrolitic) boron nitride are also of evident interest.

Clearly, the feasibility of such endeavors depends on the questions one wishes to answer. This aspect of these experiments is discussed further in the section IV of this report. Central technical considerations are the following.

#### a) Materials requirements for AFM

AFM experiments to date have dealt with single crystal surfaces. What the experiment might tell about an amorphous material is not yet clear. To avoid an influence upon tribological response by mechanical interlocking, the substrate should be free of steps over the area of contact. The expanse of smooth contact area required for AFM with present measurement techniques is approximately 0.1  $\mu$ m in



diameter (to allow for blunting of the tip). This is not difficult to achieve for many materials using straightforward existing methods. For example, even polycrystalline samples have many smooth regions of this expanse.

In AFM, a tip slides on a substrate. Uncertainties regarding chemistry and topography at the tip appear to limit interpretation of AFM experiments at present. The discussion above has mentioned uncertainties regarding the influence of common airborne contaminants. Other uncertainties concern mechanical deformation of the tip in response to the normal and shear forces. These latter issues have been simulated theoretically by Landman [14]. In principle, the AFM method would be capable of probing the friction of a single atom sliding against a ceramic substrate. In practice, considerable development of technique must precede that development.

Many varieties of tip chemistry appear to be feasible. The chief requirement appears to be a stiff tip. Thus Pt,  $\text{CaF}_2$ , W, and the like are candidate tip materials; polyethylene, graphite, and  $\text{MoS}_2$  are not because they are too compliant.

The applicability of AFM to studying lubrication has not yet been investigated directly. As discussed above, however, the experiments which show periodic friction with the repeat spacing of the substrate's crystal lattice do not show any evident influence of the common adsorbed airborne

contaminants which surely coated these substrates. It is not yet clear whether the AFM method could be sensitive at the same time to a solid substrate and to a lubricant layer which coated it.

b) Materials requirements for molecular tribometry

Molecular tribometry concerns the sliding of one atomically smooth surface past another atomically smooth surface. The contact area is vastly larger (presently ca. 100  $\mu\text{m}$  in diameter) than molecular dimensions. This is desirable for two reasons. In the first place it affords a simple means to achieve low (i.e. not a crushing) normal force per molecule. In the second place, it is closer to actual engineering practice. As in AFM, the surface separation is comparable to molecular dimensions.

The requirements for the solid substrate surfaces presently are essentially three: atomic smoothness over large area, translucency to white light, and crossed cylinder (not planar) geometry. Muscovite mica substrates, smooth over ca. 1  $\text{cm}^2$ , are presently used, but the actual smooth area required is less than this. Atomic smoothness over an area of ca. 1 mm in diameter is required for experiments using the Israelachvili apparatus, and over an area of ca. 100  $\mu\text{m}$  in diameter for experiments using the Van Alsten-Granick apparatus. Translucency is required in order to do optical interferometry; light must pass through the substrates at the actual contact spot. Crossed cylinder

geometry is required to alleviate problems of alignment, as discussed above. However, note that the actual sliding is between substrates which have been flattened at the place of physical contact. The substrate does not need to be flat at this point of contact.

There is little experience yet in altering the chemistry of muscovite mica. However, it is clear that polycrystalline samples with crystals smaller than the contact area would be undesirable, because this would inevitably introduce elements of wear and mechanical deformation into an experiment a large part of whose appeal is that presently those elements are absent. On the other hand, even polycrystalline samples are of course comprised of many single crystals. A polycrystalline sample is suitable providing that the contact area is sufficiently small. As noted in the preceeding paragraph, there is no requirement that the crystals be curved (although, to be sure, a curved geometry simplifies considerably the logistics of the experiment).

Fairly straightforward extension of the Van Alsten-Granick tribometer would permit measurements using contact areas 10 to 100 times smaller than at present. Use of surfaces with smaller radius of curvature (currently, 2 cm radius of curvature is customary), along with improved optical detection schemes, would make this possible.

More extensive instrumental extension of the Van Alsten-Granick tribometer would permit measurements using

films too thick to allow optical translucency. Many materials become opaque when they are thicker than approximately 100 Å. Thicker films (0.2  $\mu\text{m}$  or thicker) would be desirable because atomic smoothness is more difficult to achieve with thin films than with thick films. However, a price would be paid because with opaque films one would no longer be able to directly image the zone of contact. Detection by capacitance or by interferometry between points close to, but not quite at, the position of physical contact, should be possible, although the necessary methods development would require time, effort, and expense.

The requirements with respect to solid lubricants are more flexible. As described above, the experiments conducted to date in fact have focused on lubricated sliding. It is clear from the outset that the method is extremely sensitive to the presence of lubricants -- this researcher knows well from bitter experience that the mica-mica friction measured in a humid nitrogen atmosphere (moisture condensed on the substrates) is completely different from that measured in dry nitrogen atmosphere.

Three examples of solid lubricant studies exist. First is the curious case of solidified ultrathin liquid films, discussed above in the Results section. Second is  $\text{MoS}_2$ . Dr. Paul Fleischauer (Aerospace Corp.) is investigating [13] the feasibility of vacuum deposition of  $\text{MoS}_2$  onto muscovite mica, in collaboration with Granick and coworkers who will characterize these films with their tribometer. Since the

experiments began 2 months ago, promising results have already been obtained. The third example is the case of organic solid lubricants. The feasibility of covalent binding of octamethyltrichlorosilane (OTS) films to mica has been demonstrated [12]. This indicates the feasibility of studying by this method the performance of bonded lubricants.

The statement of work for the present report requested discussion of up-down hysteresis and of scan rates. The former does not appear to be a problematical issue for the tribometers described in this report. However, different scan rates between the Israelachvili and the Van Alsten-Granick tribometers (and correspondingly different equilibration times allowed to the boundary layer lubricant molecules within the zone of contact) may underlie some quantitative differences between the findings obtained with the respective instruments. The strong influence of scan rate on results is illustrated by the data shown in Figure 6 (page 13).

### Perspectives and future possibilities

The strengths of the AFM and molecular tribometry methods can be summarized as follows. Above all, with these tools friction is probed at the molecular level on well-defined systems. Tribologists are well aware of the many respects in which tribology is poorly understood at present; this is inevitable because of the complexity of usual engineering systems. The understanding which may be gained from studies at the molecular level is essential in order to achieve qualitatively new -- as opposed to incrementally perfected -- advances in technology.

Second, experiments using these tools can generate firm answers regarding the role of parameters long known to influence boundary layer friction, but which have been difficult to measure or separate in many past studies: true area of contact, adhesion, and thickness of and chemical species within the boundary layer. The surface chemical components of friction can be separated from the mechanical ones.

Third, it is important to note that the conclusions that are emerging so far concern very general physical properties: role of periodicity of substrate lattice, unusual packing of lubricant molecules in constricted geometries, and so forth. These conclusions go beyond the characterization of any particular material. They are generic, and in time they may actually change our

understanding of friction as a physical phenomenon. They may allow the eventual design of qualitatively new tribology materials which do not exist yet.

The limitations of AFM and molecular tribometry can be summarized to be the following (which researchers are working to deal with). First, the experiments have so far focused on friction and have ignored wear. Second, all the experiments have been performed, at some stage, in the ambient laboratory air. Thus the tungsten tips used in the AFM approach were surely oxidized; the mica surfaces used in the molecular tribometry approach surely bore condensed vapors. Third, the materials studied have been limited to a small number of instances, chosen for experimental convenience rather than their technological interest. The conclusions from these experiments, although curious and exciting, have not yet been material-specific.

AFM and molecular tribometry are complementary, not competing approaches. AFM studies substrate-tip tribology; molecular tribometry studies substrate-substrate-lubricant tribology.

The ultimate well-defined system -- a single sliding atom! -- which is obtainable in principle using atomic force microscopy is its shining advantage. However, the variety of tip surfaces one might work with is apt to be limited even in principle to stiff materials, and the possibilities of studying lubricated sliding are not yet known.

The chief virtues of molecular tribometry are the well-defined area of contact, the ease of studying boundary layer lubrication, and the chemical control over both sliding surfaces which is obtainable in principle. However, the requirements of substrate smoothness are stringent. Because the measurements average over an area of contact vastly larger than that from a single atom, these measurements always concern an assembly of atoms, although the surface-surface separation is well-defined to 0.1 nm or less.

Both AFM and molecular tribometry are extremely recent, their lifetimes being measured in months rather than years. Development is proceeding rapidly. The findings obtained to date could not have been predicted based on prior accumulated knowledge in the discipline. As experimental work continues on tribology studies with carefully prepared surfaces, and as theoreticians continue to analyze these novel experiments [14], one may confidently expect further unsuspected findings and understandings to emerge.



## References

1. Mate, C. M., McClelland, G. M., Erlandsson, R., and Chiang, S., "Atomic-Scale Friction of a Tungsten Tip on a Graphite Surface," Physical Review Letters, 59, 1942 (1987).
2. Erlandsson, R., Hadziioannou, G., Mate, C. M., McClelland, G. M., and Chiang, S., "Atomic Scale Friction between the Muscovite Mica Cleavage Plane and a Tungsten Tip," Journal of Chemical Physics, in press.
3. McClelland, G. M., private communication.
4. Israelachvili, J. N., McGuiggan, P. M. and Homola, A. M., "Dynamic Properties of Molecularly Thin Liquid Films," Science, 240, 189 (1988).
5. Van Alsten, J. and Granick, S., "Friction Measured with a Surface Forces Apparatus," STLE Preprint 88-AM-1E-3; also Journal of Tribology, in press.
6. Van Alsten, J. and Granick, S., "Molecular Tribometry of Ultrathin Liquid Films," submitted for publication to Physical Review Letters.
7. Tabor, D. and Winterton, R. H., "The Direct Measurement of Normal and Retarded van der Waals Forces," Proc. R. Soc. (London), A312, 435 (1969).
8. Israelachvili, J. N. and Adams, G. E., "Measurement of Forces between Two Mica Surfaces in Aqueous Electrolyte Solutions in the Range 0-100 nm," J. Chem. Soc. Faraday Trans. I, 74, 975 (1978).

9. Israelachvili, J. N., private communication.
10. Israelachvili, J. N., presented at A.C.S. Symposium on Tribology, Los Angeles, CA, September 30, 1988.
11. Van Alsten, J. and Granick, S., manuscript in preparation.
12. Carson, G. and Granick, S., presented at A.C.S. Symposium on Tribology, Los Angeles, CA, September 30, 1988.
13. Fleischauer, P., private communication.
14. Landman, U., private communication.

## **APPENDIX D**

**J.-M. Martin, and Th. Le Mogne, "Friction of Hexagonal Boron Nitride in Various Environments," Final Report, Ecole Centrale de Lyon/SORETRIB, Lyon, France, Feb. 1990; Hughes P.O. S9-317657-SKD**

SORETRIB  
36 avenue Guy de Collongue  
69131 ECULLY Cedex

Ecole Centrale de Lyon  
Laboratoire de Technologie des  
Surfaces  
URA CNRS 855  
36 avenue Guy de Collongue  
B.P. 163 - 69131 ECULLY Cedex

DETERMINATION OF TRIBOLOGICAL FUNDAMENTALS OF SOLID LUBRICATED CERAMICS

Contract F 33615-85-C-5087

Final report

FRICTION OF HEXAGONAL BORON NITRIDE IN VARIOUS ENVIRONMENTS

RFG 520765

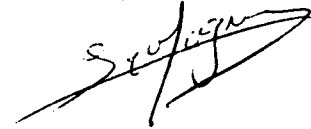
Prepared for :

HUGHES AIRCRAFT COMPANY  
Electro-Optical & Data Systems Group  
Mike Gardos, Chief Scientist

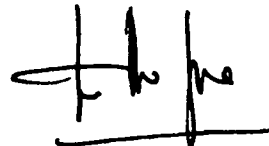
Prepared by : - J.M. MARTIN



- Th. LE MOGNE



Adm. Div. :



Etude Soretrib n° D50

Tél : 78.33.81.27

Fax : 78.43.39.62

Télex : ECE LY 310856F

**UHV TRIBOMETRY AND HIGH  
RESOLUTION ANALYSIS OF WEAR  
FRAGMENTS**

## TABLE OF CONTENTS

|                                                                         |      |
|-------------------------------------------------------------------------|------|
| <u>INTRODUCTION</u> .....                                               | P 1  |
| <u>AES/XPS TRIBOMETER</u> .....                                         | P 2  |
| <u>A BRIEF OVERVIEW OF THE STRUCTURE OF HEXAGONAL BORON NITRIDE</u> ... | P 3  |
| <u>CHARACTERIZATION OF h-BN SURFACES</u> .....                          | P 5  |
| - X-ray Photoelectron Spectroscopy (XPS).....                           | P 5  |
| - XPS analysis of standards.....                                        | P 5  |
| - XPS analysis of as-received h-BN.....                                 | P 6  |
| - XPS analysis of ion-etched h-BN.....                                  | P 7  |
| - XPS analysis of head treated h-BN to 450°C.....                       | P 8  |
| - Conclusion.....                                                       | P 9  |
| <u>TRIBOLOGICAL BEHAVIOR OF h-BN IN VARIOUS ENVIRONMENTS</u> .....      | P 10 |
| - Friction under vacuum.....                                            | P 10 |
| - Friction under ambient air.....                                       | P 11 |
| - Wear measurements.....                                                | P 12 |
| - Effect of environmental gases.....                                    | P 12 |
| - Conclusion.....                                                       | P 14 |
| <u>WEAR DEBRIS ANALYSIS</u> .....                                       | P 16 |
| - Analytical electron microscopy.....                                   | P 16 |
| - Results.....                                                          | P 16 |
| <u>DISCUSSION - MECHANISMS OF h-BN FRICTION</u> .....                   | P 18 |
| - Introduction.....                                                     | P 18 |
| - Friction under vacuum.....                                            | P 19 |
| - Vapor effect.....                                                     | P 20 |
| <u>CONCLUSION</u> .....                                                 | P 22 |
| <u>REFERENCES</u> .....                                                 | P 24 |
| <u>LIST OF FIGURES</u> .....                                            | P 27 |
| <u>ANNEXES</u> : Monthly reports                                        |      |

## INTRODUCTION

Layered hexagonal lubricants (such as graphite and molybdenum disulphide  $\text{MoS}_2$ ) have been extensively studied in the literature, because of their unique anisotropic shear strength properties.

For these two materials however, the presence of defects in the crystal structure and of intercalants determines the magnitude of the shear strength [1].

For the graphite, the superficial orientation is obtained only in the presence of moisture and oxygen and friction is high in vacuum. On the other hand,  $\text{MoS}_2$ , which is oriented in vacuum, lose its lubricating property in the presence of water vapor.

Hexagonal boron nitride (h-BN) belongs to the same family, but surprisingly, little is known about the friction properties of this material of considerable interest. Nevertheless a survey of the literature indicates that it should resemble graphite and indeed there is some evidence for this [2].

The good thermal and oxidation resistance of h-BN means that it may be a good candidate for high temperature lubrication. The friction study of h-BN in vacuum at room temperature represents a good basic approach, since the role of environmental gases (a first parameter to take into account with lamellar solids) can be emphasized and this determines the basis for other experiments in more practical situations.

From the fundamental point of view, friction under vacuum presents several advantages in the field of the study of tribochemistry :

- surface chemistry can be accurately controlled by well established surface analysis techniques (ESCA, AES...),
- surfaces can be cleaned by ion etching or by annealing in non reactive environments,
- the effects of environment gas pressures can be carefully studied,
- the friction experiment in vacuum can be easily followed by low magnification scanning electron microscopy and video recorded (if specimens are not insulators).

## AES/XPS TRIBOMETER

We have developed a U.H.V. friction machine coupled with surface analysis and thin films deposition instrumentation. The diagram of this apparatus is shown in figure 1 .

In this tester a flat disc is rotated or a flat plate is oscillated against a hemispherical pin, in an ultrahigh vacuum (UHV) chamber. A vacuum environment of 10 nPa can be achieved. The test chamber can be filled (4) with different partial pressures of reactive gases for the tribo-tests and pumped down for surface analysis. The purity of the gas can be accurately controlled with a residual gas analyzer (11). XPS data acquisition and analysis are controlled by a microcomputer. An electron gun (16) with a probe of 200 nm diameter at 10 KV and 0.5 nA current permits both low magnification SEM, with the electron detector (15) during or after the friction test, (with video recording for image processing) and Auger Electron Spectroscopy (AES) with the use of the electron spectrometer (17). An important feature is that both the flat and the pin can be imaged and analyzed, because the pin can be lifted off and turned around for periodic analysis of its wear scar.

The entire system (pin and disc) can be first transferred into a preparatory chamber for vacuum evaporated layers (13), (14), ion etching, annealing or heating with a reactive gas. Before analysis and tribotesting, the specimen can be cleaned by ion etching (10) or annealed at a given temperature (12) and then transferred-back into the test chamber, analyzed by X-ray Photoelectron Spectroscopy (XPS) (19), tribo-tested and the wear scars periodically analyzed with the Scanning Auger Microscope (SAM). The chamber is equipped with a fast entry lock (9) and a transfer mechanism, so that specimens can be changed without breaking UHV conditions in the main test chamber. Both pin and plate can be changed with this system. Another feature is the computerized data logging system, which permits the recording of the friction coefficient under different tribological conditions.



A BRIEF OVERVIEW OF THE  
STRUCTURE OF HEXAGONAL  
BORON NITRIDE

Boron nitride (BN), is a material of considerable interest. Stoichiometric BN can exist in both hexagonal (h-BN) and cubic (C-BN) crystalline modification. The molecular structure of the hexagonal phase (h-BN) is very similar to graphite except that layers are aligned vertically. All the atoms are aligned in the b direction in boron nitride (c-axis), figure 2a, in particular, boron and nitrogen atoms are positioned on top of each other in adjacent layers.

Small flakes of h-BN can be deposited on a TEM grid, and electron transparent material is found to be oriented with the c-axis parallel to the primary incident beam ; the selected area diffraction (SAD) pattern from a single crystal flake shows the hexagonal symmetry, the intense hkl reflections corresponding to hexagonal boron nitride according to Wyckoff [3].

When the electron beam is directed in direction 2 (parallel to the BN layers), by tilting the preparation, the SAD pattern presents higher order 00l reflections. By using a suitable objective aperture in the TEM, 002 lattice fringes can be imaged (figure 2b) showing the periodicity of adjacent BN layers (interlayer distance :  $3.33 \text{ \AA}$ ). It is evident that defects are common.

It is also observed that small flakes of h-BN which consist of single crystals are surprisingly ductile and that dislocation movements are relatively easy.

It is not easy to obtain large single crystals of lamellar boron nitride ; the bulk material generally consists of small crystallites which are sintered or bonded together with a binder.

It is the electronic structure of a material which determines the crystal structure. Regarding the crystal structure of h-BN, it is seen that it resembles graphite and this is consistent with simple  $sp_2$  hybridization of the boron and nitrogen orbitals within the planes, resulting in trigonal  $\sigma$  bonding. This would require all the boron valence electrons (except those donated ionically to nitrogen) to be involved in  $\sigma$  bonding ; this is very well demonstrated by the Electron Energy Loss (EEL) spectrum obtained on a thin h-BN flake (figure 3). As the core edge fine structure can be related

to density of states, a resemblance is expected between peaks in the EEL spectrum and the density of unoccupied conduction states in the solid.

Theoretically, boron and nitrogen have the same band structure, discrepancies observed in the fine structure of the two K-edges in the EEL spectrum are attributed to a charge transfer from boron to nitrogen. Actually, the XPS core level binding energies [4] indicate prove that h-BN is partially ionic (as would be expected on the basis of electronegativities). The existence of a dipole moment can explain the fact that the planar layers of fused hexagons are aligned vertically (compared to graphite which is fully covalent).

The band structure of h-BN is composed of narrow bands which are quite flat [5] ; this band structure is similar to that of graphite, but one striking difference between the two electronic structures is that graphite, unlike h-BN, does not have a band gap (consistent with its semimetallic nature).

The interplanar forces are of special interest for the frictional properties of lamellar solids. It is seen that the atoms arranged in layers are relatively far apart (3.33 Å in h-BN) whilst the B and N atoms "in plane" are 1.45 Å apart. Thus the interlayer bonding between "sheets" is very weak and is generally attributed to Van der Waals forces in the case of graphite. The situation is quite different for h-BN where the layers consist of a mosaic of positive and negative charges ; it is speculated that bonding between BN layers is of an electrostatic nature, according to Joyner [3] there is unlikely to be significant  $\pi$  bonding normal to the layers because of the large interplanar distance. In the case of FeCl<sub>3</sub> intercalated graphite it has been shown [6] that the  $\pi$  band structure is not significantly different from pure graphite. Actually, intercalation of h-BN is not reported in the literature.

Anyway, the cleavage face of h-BN cannot be a particularly low-energy surface although it will be less reactive than the edges of the crystal. On the other hand, organic compounds are known to form complexes with the filled N<sub>2</sub>p<sub>x</sub> orbitals.

Oxygen does not easily react with h-BN ; it is known that h-BN begins to oxidize in air at 800°C, leading to boron trioxide B<sub>2</sub>O<sub>3</sub> [7].

In conclusion, in spite of small differences in the valence band structures, friction properties of h-BN and graphite are speculated to be very similar (at least under vacuum), because of anisotropic properties due to their crystallographic structure.

## CHARACTERIZATION OF h-BN SURFACES

### I - X-RAY PHOTOELECTRON SPECTROSCOPY (XPS)

The X-ray source ( $AlK_{\alpha}$  at 1486.6 eV or  $Mg K_{\alpha}$  at 1253.6 eV) has a probe size of approximately  $1 \text{ cm}^2$ . The electron spectrometer is the CLAM 100 (from VG Scientific) coupled with a channeltron detection system. The data acquisition and processing are controlled by a microcomputer.

The spectra processing involves the different steps :

- smoothing using a polynomial law,
- subtracting a non-linear background (Shirley method),
- resolution of the photopeaks in different components (the peak shape can be varied, from gaussian, assymetric or not, to lorentzian). In the case of boron nitride, we used a mixture (45 % gaussian in a lorentzian). The final procedure involves a fitting of the experimental curve with calculated components. The result is the position (binding energy) of the different contributions and peaks areas. For quantification, we used empirical atomic sensitivity factors given by BRIGGS and SEAH [8].

### II - ANALYSIS OF STANDARDS

Pure h-BN, pure boron trioxide ( $B_2O_3$ ) (FLUKA AG) and boron carbide (as  $B_4C$ ) were used to obtain standard values for the binding energies of B1s, C1s, N1s and O1s photopeaks (see table 1). Due to charge effects, the standard energy differences  $\delta$  (B-N),  $\delta$  (B-O) and  $\delta$  (B-C) are also reported and are characteristic of the chemical bonding involved. By using the ionization cross-sections reported in the literature and measuring the intensities of the photopeaks, semi-quantitative results were obtained for h-BN and  $B_2O_3$ . As a whole, our results are in very good agreement with previously published data [9] [10] [11] and give a basis for the characterization of h-BN COMBAT specimens.

|                               | B1s   | C1s   | N1s   | O1s | $\delta( )$           | Atomic %<br>ratio |
|-------------------------------|-------|-------|-------|-----|-----------------------|-------------------|
| h-BN                          | 190.3 | /     | 397.9 | /   | $\delta(B-N) = 207.6$ | B/N = 0.9         |
| B <sub>2</sub> O <sub>3</sub> | 193.4 | /     | /     | 533 | $\delta(B-O) = 339.6$ | O/B = 1.7         |
| B <sub>4</sub> C              | 186.3 | 283   | /     | /   | $\delta(B-C) = 96.7$  | /                 |
| BeI                           | 187.7 | /     | /     | /   | /                     | /                 |
| Cg                            | /     | 284.2 | /     | /   | /                     | /                 |

Table 1 : XPS analysis of standards (all energies in eV).

### III - SURFACE ANALYSIS OF AS-RECEIVED COMBAT H-BN

COMBAT h-BN, grade A, is a polycrystalline material containing boron trioxide (B<sub>2</sub>O<sub>3</sub>) as a sintering aid (6 % by weight). Since COMBAT h-BN is anisotropic due to hot-pressing, specimens were directionally machined to obtain pins and flats presenting either edge sites or BN flat layers on the surface. Such specimens are hereafter named "*edge*" or "*flat*" configuration.

Before XPS characterization, h-BN specimens were cleaned with propanol-2. XPS results are presented in figure (4) and table 2 and are practically the same whatever the crystallographic orientation may be (*edge* or *flat* configuration).

|     | E(eV)     | atomic % | $\delta(eV)$          |
|-----|-----------|----------|-----------------------|
| B1s | B-N 190.3 | 35.3     | $\delta(B-N) = 207.6$ |
|     | B-O 192.5 | 1.6      | $\delta(B-O) = 339.6$ |
| N1s | 397.9     | 39.2     | /                     |
| C1s | 284.5     | 16.2     | /                     |
| O1s | 532.2     | 7.7      | /                     |

|                      |     |
|----------------------|-----|
| $\frac{B-N}{N-B}$    | 0.9 |
| $\frac{O_{ox}}{B-O}$ | 4.8 |

Table 2 : XPS analysis of propanol-cleaned h-BN (all energies in eV).

A comparison of tables 1 and 2 indicates that the specimens are mainly composed of h-BN, boron oxide and carbon from contamination. The only problem is the surstoichiometry of boron oxide in oxygen, the O/B ratio being 4.8 in our specimen, compared to 1.5 in  $B_2O_3$ .

Some specimens were also analyzed by SIMS (figure 5). Results also indicate the presence of contamination on the surface (thickness probed approximately 10 nm) ; when profiling, it is not quite the same but carbon is also present in the SIMS spectrum. Water ( $OH^-$  negative ion) was always practically absent in the SIMS spectra.

#### IV - XPS ANALYSIS OF ION-ETCHED H-BN

Propanol-2 cleaned h-BN samples underwent ion etching with argon ions of 3 KeV energy, for 15 minutes. The XPS analysis of this treated surface is shown in table 3.

|                 | E(eV)     | atomic % | $\delta$ (eV)    |
|-----------------|-----------|----------|------------------|
| B <sub>1s</sub> | B-N 190.3 | 29.1     | $\delta = 207.5$ |
|                 | B-O 192.7 | 6.3      | $\delta = 339.8$ |
| N <sub>1s</sub> | 397.8     | 19.5     | /                |
| C <sub>1s</sub> | 283.7     | 13.5     | /                |
| O <sub>1s</sub> | 532.5     | 25       | /                |

|     |     |
|-----|-----|
| B/N | 1.5 |
| O/B | 4   |

Table 3 : XPS analysis of ion etched h-BN (all energies in eV).

This shows :

- a BN stoichiometric deviation, the B/N ratio being 1.5 after etching ; surprisingly, the selective sputtering of nitrogen does not shift the B<sub>1s</sub> binding energy (or it was not detectable with the equipment at hand),
- a residual content of carbon (13.5 atomic per cent) in a modified chemical form different from hydrocarbons and not very different from the graphitic and/or carbidic chemical bonding,

- a change in the colour of the h-BN surface, turning from opalescent white to grey or even black.

The result can be compared with the dynamic SIMS analysis, where the h-BN is sputtered with 10 KeV Gallium ions ; in the negative spectrum-figure (5)- the strong contribution of  $CN^-$  and  $C_2^{--}$  can be seen.

The overall data strongly suggest that graphitic carbon is formed or revealed by selective sputtering. However the presence of boron carbonitride is not excluded.

#### V - XPS ANALYSIS OF HEAT-TREATED H-BN TO 450°C

Table 4 shows the XPS analysis of a propanol cleaned specimen heated to 450°C (12 cycles of one minute each) under vacuum. The residual gas analyzer indicated the presence of CO, CO<sub>2</sub>, CH<sub>2</sub> and H<sub>2</sub>O during the annealing process.

|     |     | E(eV) | atomic % | $\delta$ (eV)    |
|-----|-----|-------|----------|------------------|
| B1s | B-N | 190.3 | 41.4     | $\delta = 207.6$ |
|     | B-O | 192.8 | 3.0      | $\delta = 339.8$ |
| N1s |     | 397.9 | 44.5     | /                |
| C1s |     | 284.2 | 2        | /                |
| O1s |     | 532.6 | 10.1     | /                |

|     |      |
|-----|------|
| B/N | 0.93 |
| O/B | 3    |

Table 4 : XPS analysis of 450°C annealed h-BN (all energies in eV).

It is clear that the "C-H" contribution has completely disappeared from the surface ; only a residual content of 2 atomic per cent graphitic carbon is present after annealing. The BN stoichiometry is preserved and again, the boron oxide is surstoichiometric in oxygen.

## VI - CONCLUSION

In low-Z elements, such as boron nitride, the thickness probed by the XPS technique is about 10 nm ; therefore it is difficult to know if hydrocarbons are only adsorbed on the very top surface or if they enter the BN material, say over the 10 nm thickness range. Anyway, it is unlikely that hydrocarbons are present after hot-pressing of the h-BN powder. Concerning this point, our opinion is that hydrocarbons are not only adsorbed but can penetrate the h-BN surface.

Concerning the "boron oxide" surstoichiometry, we have three possible explanations of this deviation :

- the presence of true surstoichiometric boron oxide (as  $\text{BO}_4$  for example),
- the presence of  $\text{O}_2$  or  $\text{H}_2\text{O}$  intercalated in h-BN,
- the presence of other oxides.

Looking at our complete XPS/SIMS data, the best compromise is the existence of mixed oxide glasses such as borosilicate, boroaluminate etc... which were formed during hot-pressing in presence of  $\text{B}_2\text{O}_3$  and other impurities ( $\text{SiO}_2$ ,  $\text{Al}_2\text{O}_3$ ,  $\text{CaO}$  etc...). This is confirmed by the fact that impurities are present in the positive ions SIMS spectrum. As a matter of fact, in these conditions, only a slight enlargement of the  $\text{O}1s$  photopeak is expected in the XPS spectrum.

Water was practically not detected on the h-BN surface under vacuum. On the other hand, a RAMAN study [12] indicated that surface fluorescence due to adsorbed OH or organic species in the air was readily removed by laser excitation after 3s illumination. It seems that water (if any) is not strongly adsorbed on boron nitride, and is quickly out-gassed under vacuum or by heating.

In any case, annealing at  $450^\circ\text{C}$  under vacuum gives clean h-BN, free from water and contamination and boron oxide is not affected at this temperature.

Consequently, two surface preparations were used for h-BN friction tests, namely :

- cleaning with propanol-2,
- annealing to  $450^\circ\text{C}$  under vacuum.

TRIBOLOGICAL BEHAVIOR OF h-BN vs.  
ITSELF IN VARIOUS ENVIRONMENTS

Friction experiments were conducted with machined COMBAT h-BN pins and flats. The tribological conditions were the same for all the test, i.e.:

|                        |                                        |
|------------------------|----------------------------------------|
| - normal load          | : 2 N                                  |
| - sliding speed        | : $0.6 \cdot 10^{-3} \text{ m.s}^{-1}$ |
| - length of the stroke | : $3 \cdot 10^{-3} \text{ m}$          |
| - number of cycles     | : 75                                   |
| - temperature          | : room temperature = 300 K             |

The calculated mean Hertz pressure was 0.3 GPa and the contact surtemperature was calculated as negligible..

#### I - FRICTION UNDER VACUUM

For these tests, two specimen preparations were used :

- cleaning with propanol-2,
- annealing at  $450^{\circ}\text{C}$  under vacuum (the vacuum state was  $10^{-10}$  mbar or 10 nPa).

Before the friction test, the surface chemistry of h-BN was checked by XPS. Note that annealing at  $450^{\circ}\text{C}$  removes carbon contamination from the surface, but does not modify the "boron oxide" binder, and that the analysis is the same for both configurations ("*flat*" and "*edge*").

Two crystallographic orientation combinations were tested :

- pin "*flat*" vs flat "*flat*"
- pin "*edge*" vs flat "*edge*", (the edge basal planes being, in principle, parallel to the sliding direction).

Among the nine possible *edge/flat* combinations, the two cases that we chose here correspond to extreme ones. The others are thought to give intermediate results.

First, we show (figures 6 and 7) the good reproductibility of the friction tests for each configuration, and the surface preparation, which was duplicated on different specimens.



Friction data vs the number of cycles are summarized (figure 8) for the two combinations and for the two preparation procedures. The main observations are :

- propanol-cleaned h-BN specimens give a lower stabilized friction coefficient than heat-treated h-BN (0.3/0.5 vs 0.6/0.7). By referring to previously described XPS data, the reduction in friction can be attributed to the presence of hydrocarbons in the h-BN surface,
- the crystallographic orientation of h-BN is not a first order parameter. Nevertheless, in the case of propanol-cleaned specimens, friction begins at a lower value (0.1) for the *flat/flat* configuration ; after 10 cycles, the effect disappears, but the stabilized friction coefficient is always smaller for the "flat/flat" configuration.
- clean h-BN, under vacuum, gives high friction whatever the crystallographic orientation may be. As a matter of fact, it seems that there is no lubrication effect of the 6% boron oxide sintering aid present in the material, at room temperature.

## II - FRICTION IN AMBIENT AIR

First h-BN specimens are cleaned with propanol friction curves are shown in figure 9a.

It is readily seen that friction of h-BN in ambient air (50 % moisture) gives very low friction coefficients (below 0.1) which are very well stabilized. At the same time, we observe that the effect of the crystallographic orientation is negligible in air. It already seems that the tribological behavior of h-BN is very similar to graphite [13] as was predicted by the structure similarities of the two materials.

Second, h-BN specimens are annealed under vacuum. When ambient air is introduced into the chamber at atmospheric pressure ( $10^5$  Pa) (figure 9b) in static conditions, the friction coefficient stabilizes at 0.25. Note that this value is higher than that obtained in air with non-annealed h-BN specimens ( $f = 0.1$ ).

### III - WEAR MEASUREMENTS

Wear of h-BN specimens was studied by examination of worn surfaces after the friction test (optical and electron micrographs) and by profilometric measurements in the wear scars. Results are summarized in table 5.

| preparation environment | crystal configuration | f (average) | pin wear scar diameter | flat wear damage |
|-------------------------|-----------------------|-------------|------------------------|------------------|
| propanol air            | <i>flat/flat</i>      | 0.09        | not visible            | not visible      |
| propanol air            | <i>edge/edge</i>      | 0.08        | not visible            | not visible      |
| propanol UHV            | <i>flat/flat</i>      | 0.40        | ≈ 1 mm                 | + +              |
| propanol UHV            | <i>edge/edge</i>      | 0.50        | ≈ 1.3 mm               | not visible      |
| heat treated UHV        | <i>flat/flat</i>      | 0.65        | ≈ 0.8 mm               | + + + +          |
| heat treated UHV        | <i>edge/edge</i>      | 0.65        | 1.4 mm                 | +                |

Table 5

Results indicate :

- that, in air, wear of h-BN is not detected by our measurements,
- that under UHV, and in the presence of contaminants, wear mainly occurs on the h-BN,
- that under UHV, with clean h-BN, wear is detrimental.

### IV FRICTION OF PYROLITIC h-BN. EFFECT OF ENVIRONMENTAL GASES

As it appears that friction of h-BN on itself is more sensitive to environmental factors (gas, contamination, cleaning...) than to the initial crystallographic orientation, we decided to carry out a set of friction experiments at room temperature and in different gases, in order to know if it is possible to lubricate h-BN in these conditions. Friction tests were conducted under static low partial pressures of different gases, namely water vapor (H<sub>2</sub>O) carbon monoxide (CO), propane (C<sub>3</sub>H<sub>8</sub>) and ambient air. The complete results are shown (figures 10, 11, 12, 13, 14, 15) and summarized in table 6.

1) Friction of h-BN on itself under low partial pressures of gases

For these different gases, the pressure in the main chamber of the AES/XPS tribometer was controlled at  $10^{-3}$  Pa before the friction test.

The h-BN materials were COMBAT h-BN specimens used in the "flat/flat" configuration ; before the friction test, they were annealed at  $450^{\circ}\text{C}$  under UHV to eliminate hydrocarbons from the surface.

As can be seen, under these low partial pressures, and by comparison with UHV conditions, the friction of h-BN on itself is not affected by the presence of environmental gases, even with water vapor (figure 10), the value of the average friction coefficient lying in the range 0.65-0.7 (note that the computer averages the friction coefficient for each pass, so local fluctuations are not reproduced, but generally they are weak for h-BN in our conditions).

As a rule-of-thumb, remember that at  $10^{-4}$  Pa, the contamination is approximately one monolayer per second (depending on the gas and temperature).

|                                     | 0.2   | 0.4   | 0.6   | 0.8   | 1.0   |
|-------------------------------------|-------|-------|-------|-------|-------|
| UHV $10^{-8}$ Pa                    | ..... | ..... | ..... | ..... | ..... |
| CO } $10^{-3}$ Pa                   | ..... | ..... | ..... | ..... | ..... |
| C <sub>3</sub> H <sub>8</sub> }     | ..... | ..... | ..... | ..... | ..... |
| H <sub>2</sub> O }                  | ..... | ..... | ..... | ..... | ..... |
| air $10^{-3}$ Pa                    | ..... | ..... | ..... | ..... | ..... |
| CO } 10 Pa                          | ..... | ..... | ..... | ..... | ..... |
| N <sub>2</sub> }                    | ..... | ..... | ..... | ..... | ..... |
| O <sub>2</sub> }                    | ..... | ..... | ..... | ..... | ..... |
| air 10 Pa                           | ..... | ..... | ..... | ..... | ..... |
| C <sub>3</sub> H <sub>8</sub> 10 Pa | ..... | ..... | ..... | ..... | ..... |
| air $10^5$ Pa                       | ..... | ..... | ..... | ..... | ..... |

Table 6

## 2) Friction of h-BN on itself under higher partial pressures of gases

Friction tests were conducted in the same conditions, on the same h-BN flat for each gas.

Several experiments are presented here :

- nitrogen 10 Pa (static) (figure 11),
- oxygen 10 Pa (static) (figure 12),
- air  $10^{-3}$  Pa  $\rightarrow$  10 Pa (figure 13),
- carbon monoxide  $10^{-3}$  Pa  $\rightarrow$  10 Pa (figure 14),
- propane  $10^{-3}$  Pa  $\rightarrow$  10 Pa  $\rightarrow$   $10^{-3}$  Pa (figure 15).

In our conditions, it was not possible to obtain 10 Pa of water vapour in the chamber ; (note that this represents high pressure and some problems for the UHV instrumentation).

As can be seen, propane ( $C_3H_8$ ) and air at 10 Pa lubricate h-BN on itself, the friction coefficient immediately dropping down to 0.4 (approximately one half of the UHV value). Note that in the case of propane, the friction increases again to 0.6-0.7 when the pressure is decreased to  $10^{-3}$  Pa at the end of the test.

Surprisingly pure oxygen had no effect on friction at 10 Pa.

### CONCLUSION

h-BN friction, at room temperature, is extremely dependent on the presence of environmental gases and on the surface preparation.

#### \* With as-received h-BN specimens (propanol-cleaned)

##### - Under UHV

. Under high vacuum ( $10^{-8}$  Pa), friction is moderately high (0.3/0.5) and stabilized,

. The "flat configuration" gives a lower friction (0.3) than the "edge configuration" (0.5).

##### - In ambient air

. The presence of air (50 % humidity) gives a very low friction (inferior to 0.1) and negligible wear, whatever the crystallographic orientation may be.

\* With UHV-annealed h-BN specimens (contamination-free)

- Under UHV

. Under high vacuum ( $10^{-8}$  Pa), friction is high (0.7) and wear is detrimental.

. There is no effect of the crystallographic orientation.

- Under a low partial pressure ( $10^{-3}$  Pa) of air,  $H_2O$ ,  $C_3H_8$  and CO

. Compared with UHV conditions, no significant change is observed in these conditions.

- Under a partial pressure of 10 Pa of  $N_2$ ,  $O_2$  and CO

. Compared with UHV conditions, no effect is observed.

- under a partial pressure of 10 Pa of air,  $C_3H_8$

Friction of h-BN versus itself is reduced to 0.3/0.4 (one half of the UHV value)

- under ambient air at atmospheric pressure ( $10^5$  Pa)

. The friction coefficient is reduced to 0.25.

Considering our friction results, it is shown that h-BN friction is reduced by the presence of moisture, hydrocarbon gases, and surface contamination.

With regard to the specific effect of moisture, the tribological behavior of h-BN is very similar to that of graphite.

There is a synergic effect of moisture and hydrocarbons from surface contamination.

# WEAR DEBRIS ANALYSIS

## I - ANALYTICAL ELECTRON MICROSCOPY

High resolution analysis of wear fragments (originating from the friction experiments with h-BN) was carried out in the analytical transmission electron microscope (TEM). The electron microscope (Philips EM 420) can operate either in the TEM or in the STEM mode, for high resolution scanning electron microscopy (secondary electron detection). The accelerating voltage was 120 KV for all examinations.

For boron nitride specimens, the analysis was performed with an Electron Energy Loss Spectrometer (EELS) coupled to the microscope. The electron spectrometer (GATAN 666) has a parallel detection system consisting of a 1024 photodiodes array. The dwell time necessary to record an EELS spectrum of h-BN is generally inferior to one second in our conditions.

Wear fragments are collected in the wear scars on a 3 mm diameter copper grid covered with a holey carbon film (an optical microscope is necessary for this operation)

## II - RESULTS

Five types of h-BN wear particles were generally detected, they were classified as follows, depending on how they were produced in the wear process :

- basal-plane slip flakes (a)            see figures 16, 17
- small bent flakes (b)
- crumpled flakes (c)
- rolled flakes (d)
- amorphized spheroidal grains (e)

Generally, these wear fragments were all present in all the situations, but the proportion of each type depends on the tribological

test. In table 7, we have reported the presence or not of each type of wear fragment in the various friction tests.

| Preparation environment | crystal configuration | f average | pin wear scar value | flat wear scar diameter | wear particle types |     |     |     |     |
|-------------------------|-----------------------|-----------|---------------------|-------------------------|---------------------|-----|-----|-----|-----|
|                         |                       |           |                     |                         | a                   | b   | c   | d   | e   |
| propanol air            | <i>flat/flat</i>      | 0.09      | not visible         | not visible             | +++                 | +   | +   |     |     |
| propanol air            | <i>edge/edge</i>      | 0.08      | not visible         | not visible             | +++                 | +   | +   |     |     |
| propanol UHV            | <i>flat/flat</i>      | 0.40      | ≈ 1 mm              | + +                     | +                   | +++ | +++ | +++ | +++ |
| propanol UHV            | <i>edge/edge</i>      | 0.50      | ≈ 1.3 mm            | not visible             |                     | +++ | +++ | +++ | +++ |
| heat treated UHV        | <i>flat/flat</i>      | 0.65      | ≈ 0.8 mm            | + + + +                 | +                   | +++ | +++ | +++ | +++ |
| heat treated UHV        | <i>edge/edge</i>      | 0.65      | 1.4 mm              | +                       |                     | +++ | +++ | +++ | +++ |

Table 7

The under UHV results indicate that :

- in the *edge/edge* configuration, only a few type (a) particles are present along with a lot of other ones,
- in the *flat/flat* configuration, type (a) particles are more numerous, but there are still more of the other types.

(Note that no quantitative analysis was attempted to distinguish (b), (c), (d), (e) particles accurately ).

In air, surprisingly, only type (a) particles (basal plane slip) are observed (even in the *edge/edge* configuration).

Indoubtedly, the roles of moisture and contaminants are of prime importance in generating wear debris morphologies (and therefore wear mechanisms).

|                                           |
|-------------------------------------------|
| DISCUSSION<br>MECHANISMS OF h-BN FRICTION |
|-------------------------------------------|

## INTRODUCTION

The friction mechanisms of hexagonal boron nitride (h-BN) are explained in terms of the deformation modes of individual BN grains in the contact area.

The survey of the literature [2] [14] [15] [16] [17] shows up three major (and non exclusive) mechanisms to explain the low friction of h-BN :

1) Friction-induced preferential orientation of the lamellar material. When their cleaved planes can be oriented parallel to the sliding direction, the tangential shear acts between the solid layers which are weakly bonded. Basal plane slip in h-BN grains can occur and give a low value of interface shear strength.

2) When the orientation is lost, the defects, dislocation edges, h-BN cleavage fragments... predominate in the response to the exterior strain. Rotation of "rolling pins" in the interface can, however, produce a low friction.

3) The tribo-oxidation of h-BN in the presence of oxygen may lead to the formation of boron oxide. This can be added to the 6 per cent  $B_2O_3$  present as a sintering aid. Low friction and wear can be explained by the low shear strength and low melting point of the lubricious amorphous boron oxide.

The high resolution analysis of wear fragments indicated to us two major points which are summarized in table 8. It indicates that h-BN basal-plane slip is the only mechanism which is found associated with low friction and wear in our conditions. Fracture, shear and amorphization of h-BN lead to high friction.



| enrironmental<br>conditions<br>(room temperature) | crystal<br>orientation<br>(pin/flat  | average<br>friction<br>coefficient | wear debris<br>characteristic                         |
|---------------------------------------------------|--------------------------------------|------------------------------------|-------------------------------------------------------|
| air<br>(50% moisture)                             | <i>flat/flat</i><br><i>edge/edge</i> | 0.1<br>0.1                         | basal plane slip<br>(no oxidation<br>takes place)     |
| UHV                                               | <i>flat/flat</i><br><i>edge/edge</i> | 0.4/0.7                            | fracture-shear<br>towards<br>amorphization<br>of h-BN |

Table 8

#### I - FRICTION UNDER UHV

Clean h-BN is not a good material for friction under high vacuum, at room temperature. In the absence of gases and contaminants, h-BN is amorphized and superficially disoriented whatever the initial crystallographic orientation may be.

Consequently, friction is high and remarkable wear and surface damage is observed.

Bearing these data in mind, it is obvious that increasing the temperature is not in favor of h-BN friction, unleast that the melting of the boron oxide sintering aid may provide an effective lubrication up to 500°C.

Nevertheless, two perspectives open out to use h-BN under vacuum as a friction material :

- friction of h-BN at low temperature under vacuum (the preferential adsorption and/or condensation of selected condensable gases may be an advantage in these conditions),
- friction of hybrid compositions of boron nitride and carbon.

## II - VAPOR EFFECT ON h-BN FRICTION

### 1) Moisture effect

In air, surprisingly, only type (a) particles (basal plane slip) are observed (even in the *edge/edge* configuration (see table 7)).

Undoubtedly, the roles of moisture and contaminants are of prime importance in generating wear debris morphologies (and therefore wear mechanisms). The evidence is that superficial friction-induced orientation of h-BN is only obtained in the presence of moisture. So, under the rubbing action, the BN layers tend to take up a position of minimum energy. Actually, this result is very similar to the case of graphite [13].

Three mechanisms can explain how h-BN basal plane slip is favored in presence of water vapor :

1) weakening of interplanar forces due to the intercalation of water molecules between BN layers, or to adsorption of water on cleaved faces, leading to a decrease of the magnitude of the shear strength,

2) tribochemical reaction of h-BN with water leading to a lubricious borate hydrate (ammonium borate hydrates have recently been observed [18]),

3) condensation of liquid water into h-BN crystal defects, such as wedge-shaped cavities, pores or holes between incomplete separated planes, or even on cleaved faces. A decrease of the surface tension may explain the effect on the critical shear strength. This effect was recently recognized on the friction coefficient of graphite [13] and MoS<sub>2</sub> [19].

In the case of h-BN friction, although that the mechanism is certainly not unique, the third explanation has also our favor for the following reasons :

- a relative high partial pressure of water vapor is necessary to obtain the decrease of the friction coefficient ( $> 10$  Pa at room temperature). This shows that adsorbed layers have no significant effect on h-BN friction.
- a high resolution TEM image of the slip interface zone (002 lattice fringes) between two h-BN stacks (figure 18) shows that, although that sliding is found limited in certain zones of the crystal without generating turbostratic BN within the stacks, it is not really concentrated between two hexagon-fused BN layers only. On the other hand, it seems that crystal defects are involved in the deformation process (dislocation movement along the (001) direction,

ondulation of basal planes, wedge shaped cavities between separate BN sheets etc...),

- water was never detected by "in vacuum" analysis of h-BN wear debris, but in some cases, we found that the slip surface of h-BN crystals was not atomically smooth. This shows that no chemical reaction occurred and that water is outgassed under vacuum.

## 2) Hydrocarbon effect

Hydrocarbons can also lubricate h-BN, but to a lesser extent. Compared with moisture, it seems that the mechanism is different ; for example propane, which is a non-condensable gas at room temperature gives h-BN wear debris whose the EELS spectrum (figure 19) shows that carbon can be incorporated in the h-BN layers. We can also say that carbon has the  $sp_2$  hybridization and that the electronic structure of boron nitride is preserved. At this time, the exact location of carbon is not known, but it seems that h-BN is partially amorphized in these conditions. The existence of hybrid compositions is not excluded. Consequently, a tribochemical reaction may be involved, leading to the decomposition of hydrocarbons into lubricating carbon [19]

Surprisingly, we have also shown a synergic effect of hydrocarbons and water to obtain very low friction and wear and the explanation for this may be that friction-induced graphitic carbon is also lubricated by water vapor.

## CONCLUSION

Hexagonal boron nitride (h-BN) is a well known lamellar solid. The structure of h-BN has been studied by Transmission Electron Microscopy (TEM) and Electron Energy Loss Spectroscopy (EELS). The crystallographic structure of h-BN is deduced from the  $sp_2$  hybridization of both boron and nitrogen atoms ; it is very similar to that of graphite and defects are found to be common in both structures. Striking differences are to be noted, however, with regard to the electronic structure of outer-shell electrons (valence and conduction bands). Consequently h-BN, unlike graphite, has a band gap consistent with its electrical properties. On the other hand, the chemical reactivity of h-BN with environment is different (of special interest for tribological applications). Particularly, the structure of hybrid compositions of carbon and h-BN are not well established.

The h-BN surface chemistry can be accurately determined by X-ray Photoelectron Spectroscopic (XPS) and the effect of surface preparation methods can be studied.

COMBAT h-BN is a polycrystalline material containing 6 % by weight of boron oxide as a sintering aid. Actually, our XPS results indicate that the presence of mixed oxide glasses is more likely to occur in this material.

The surface of as-received h-BN contains contamination from hydrocarbons ; cleaning with propanol-2 does not remove this contamination ; ion-etching also does not remove the contamination, moreover h-BN is deeply modified by argon ions bombardment, and becomes sub-stoichiometric in nitrogen.

Annealing at  $450^{\circ}\text{C}$  under vacuum gives clean and stoichiometric h-BN surfaces, moreover, boron oxide is not modified at this temperature.

Friction of h-BN versus itself has been studied respectively under high vacuum ( $10^{-8}$  Pa), under a low partial pressure ( $10^{-3}$  Pa) of different gases (air, CO,  $\text{C}_3\text{H}_8$  and  $\text{H}_2\text{O}$ ), under a higher partial pressure (10 Pa) of  $\text{N}_2$ ,  $\text{O}_2$  air and  $\text{C}_3\text{H}_8$  and finally in ambient air (50 % humidity) at atmospheric pressure ( $10^5$  Pa).

Two crystallographic orientation combinations were used, namely the *flat/flat* configuration and the *edge/edge* configuration.

In the case of annealed h-BN specimens (contamination-free surfaces) main results are :

- friction under high vacuum ( $10^{-8}$  Pa) is high ( $f \approx 0.7$ ) and wear is detrimental whatever the crystallographic orientation may be.
- there is no effect of a low partial pressure ( $10^{-3}$  Pa) of air, CO,  $C_3H_8$  and  $H_2O$ , compared with UHV conditions,
- when humid air is introduced to a pressure up to 10 Pa, friction is reduced to 0.2/0.4 (one half of the UHV value). However neither oxygen (10 Pa) nor nitrogen (10 Pa) are efficient. Consequently, friction is certainly reduced by water vapor to pressures up to 10 Pa,
- when propane is introduced to a pressure up to 10 Pa, h-BN friction is also reduced to values of about 0.4.

In the case of carbon-contaminated h-BN surfaces, results are :

- friction under vacuum ( $10^{-8}$  Pa) is moderately high and stabilized (0.3/0.5), the *flat/flat* configuration giving the lowest value,
- in ambient air (50 % moisture), h-BN friction is very low ( $< 0.1$ ), whatever the configuration may be.

High resolution analysis of wear debris was performed in an analytical TEM. The major point is that h-BN basal plane slip is the only deformation mode which is associated with very low friction and wear in our conditions. Generally, fracture, shear and amorphization give higher friction values.

The mechanism of friction-induced basal plane slip in h-BN is thought to be mainly related to the presence of condensed liquid water in crystal defects, leading to a decrease of the surface tension and therefore of the critical shear strength.

The mechanism of action of hydrocarbons is different, it seems that lubricating carbon is formed by a tribochemical reaction.

## REFERENCES

- [1] M.N. GARDOS  
"On the elastic constants of thin solid lubricant films ", 16th  
Leeds-Lyon Symposium on Tribology, (Mechanics of Coatings) Sept. 5-8  
1989, Lyon.
- [2] F.B. BOWDEN and D. TABOR  
"The friction of lamellar solids", Part 2, Chapter 11, Ed oxford 1964.
- [3] R.W.G. WYCKOFF  
"Crystal structures", p. 186, R. Krieger Publishing Company, (1982).
- [4] D.J. JOYNER and D.M. HERCULES  
"Chemical bonding and electronic structure of  $B_2O_3$ ,  $H_3BO_3$  and BN. An  
ESCA, Auger, SIMS and SXS study, J. Chem. Phys., Vol 72, n° 2,  
pp. 1095-1107, (1980).
- [5] A. CASTELLANI and al.  
"Electronic interlayer states in hexagonal boron nitride", Physical  
Review B, Vol 32, n° 10, pp. 6997-6999, (1985).
- [6] J.J. RITSKO and E.J. MELE  
"Experimental determination of the momentum dependent dielectric  
response of stage 1  $FeCl_3$ -intercalated graphite", Physical Review B,  
Vol 21, n° 2, pp. 730-737 (1980).
- [7] A.K. TSAPUK, L.G. PODOBEDA  
"Oxidation of materials based on boron nitride", Porosh Kovaga  
Metytalurgiga n° 3, (183), pp. 51-54, (1978).
- [8] D. BRIGGS and M.P. SEAH  
"Practical surface analysis" by Auger and X-Ray Photoelectron  
Spectroscopy, J. Wiley et Sons (1983).
- [9] S. KOHIKI, T. OHMURA and K. KUSAO  
J. Electron Spectroscopy Relat. Phenom, 31, 85-90, (1983).

- [10] K. HAMRIN, G. JOHANSSON, U. GELIUS, C. NORDLING and K. SIEGBAHN  
Phys. Scr., 1 pp 277 (1970).
- [11] J. KISS, K. REVESZ and F. SOLYMOSI  
Applied Surface Science, 37, pp. 95-110, (1989).
- [12] G.J. EXARHOS and M.S. DONLEY  
"Real-time Raman detection of molecular changes in ceramic undergoing sliding friction", Microbeam Analysis, San Francisco, Press Inc., (1987).
- [13] H. ZAIDI and D. PAULMIER  
"Protective coating with strongly enhanced mechanical properties on the surface of polycrystalline graphite", 16th Leeds-Lyon Symposium on Tribology, Sept. 5-8th, Lyon, (1989).
- [14] G. ROWE  
"Some observations of the frictional behaviour of boron nitride and of graphite", Wear, 3, pp. 274-285, (1960).
- [15] E. RABINOWICZ and M. IMAI  
"Frictional properties of pyrolytic boron nitride and graphite", Wear, 7, pp. 298-300, (1964).
- [16] D.H. BUCKLEY  
"Friction and transfer behavior of pyrolytic boron nitride in contact with various metals", ASLE paper at the ASLE/ASME lubrication conference in Boston, Massachusetts, oct. 5-7, 1976.
- [17] M. MIYOSHI, D.H. BUCKLEY and T. SPALVINS,  
"Tribological properties of boron nitride synthesized by ion beam deposition", J. Vac. Sci. Techn. A3(6), Nov/Dec. 1985.
- [18] T. MATSUDA  
"Stability to moisture for chemically vapour-deposited boron nitride", Journal of Materials Science, 24, pp. 2353-2358, (1989).

[19] M. UEMURA, K. SAITO, K. NAKAO

"A mechanism of vapor effect on friction coefficient of molybdenum disulfide", 35th STLE/ASME Tribology Conference, Fort Lauderdale, Preprint n° 89.TC.5D.4, Oct. 26-29 1989.



## LIST OF FIGURES

Figure 1 : Diagram of the AES/XPS tribotester. Optical micrograph showing the pin on disk friction machine surrounded by analytical tools.

Figure 2 : a) Crystal structure of hexagonal boron nitride.  
b) (002) lattice fringes image of h-BN (interlayer distance = 3.33 Å). Note that crystal defects are common.

Figure 3 : Electron Energy Loss Spectrum (EELS) of h-BN. The boron and nitrogen K-edges show evidence for the  $sp_2$  hybridization.

Figure 4 : Processed XPS spectra of as received COMBAT h-BN.

Figure 5 : Static SIMS spectra of COMBAT h-BN (thickness probed inferior to 10 nm).  
a) negative ions  
b) positive ions

Figure 6 : Influence of the surface preparation on the friction of h-BN (flat/flat configuration) (duplicated runs).

Figure 7 : Influence of the surface preparation on the friction of h-BN (edge/edge configuration) (duplicated runs).

Figure 8 : Friction on h-BN under vacuum (summary). Influence of the crystallographic orientation and of the surface preparation.

Figure 9 : Friction of h-BN in ambient air (50 % humidity) (propanol-cleaned species).  
a) Influence of the crystallographic orientation, comparison with UHV conditions.  
b) Annealed specimens (flat/flat configuration) comparison with UHV conditions.

Figure 10 : Friction on h-BN under low partial pressure of water vapor ( $P = 10^{-5}$  mBar) (flat/flat configuration with two surface preparations, comparison with vacuum).

Figure 11 : Friction of h-BN under nitrogen ( $10^{-1}$  mBar) (flat/flat configuration, comparison with vacuum).

Figure 12 : Friction of annealed h-BN under oxygen ( $10^{-1}$  mBar) (flat/flat configuration, comparison with vacuum).

Figure 13 : Friction of h-BN under air (50 % humidity). Flat/Flat configuration, effect of partial pressure.

Figure 14 : Friction of h-BN under carbon monoxide. Flat/flat configuration. Effect of partial pressure.

Figure 15 : Friction of h-BN under propane. Flat/flat configuration. Effect of partial pressure.

Figure 16 : TEM micrographs of h-BN wear debris (basal-plane slip).

Figure 17 : High resolution S(T)EM image of h-BN wear debris (basal plane slip with two tilting conditions).

Figure 18 : High resolution TEM image (002 lattice fringes) of a basal plane slip in h-BN wear debris.

Figure 19 : EELS spectrum of h-BN wear debris showing evidence for the presence of graphitic carbon.

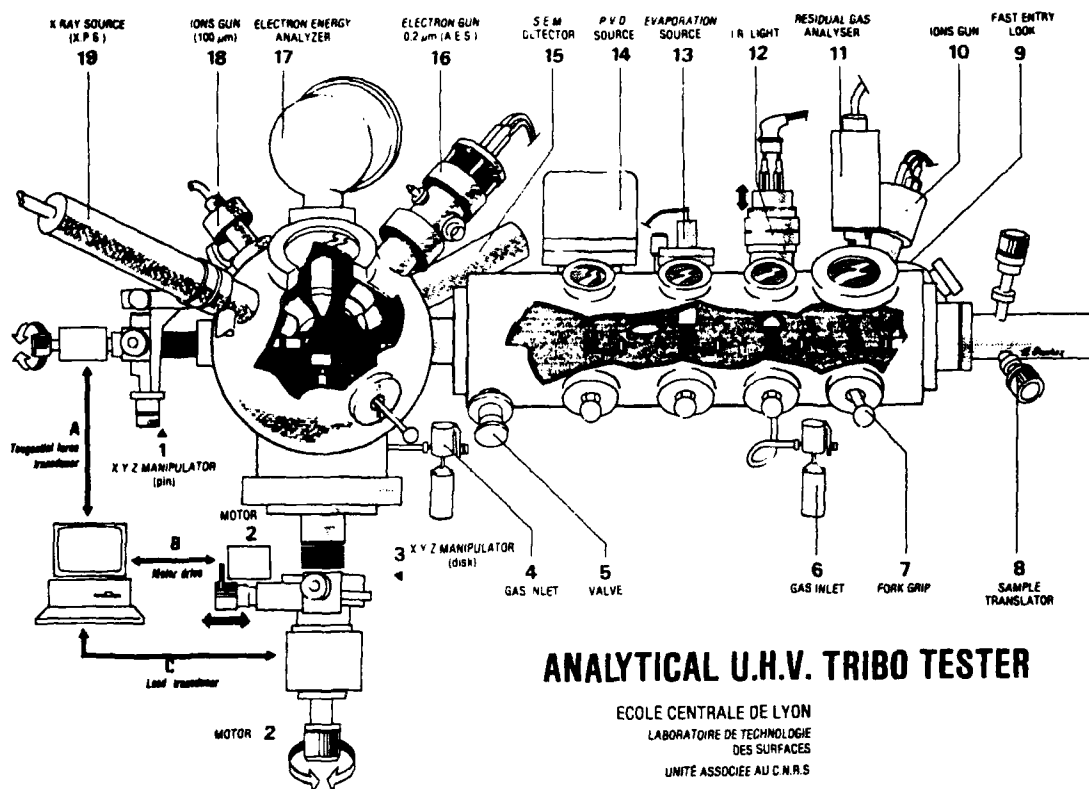
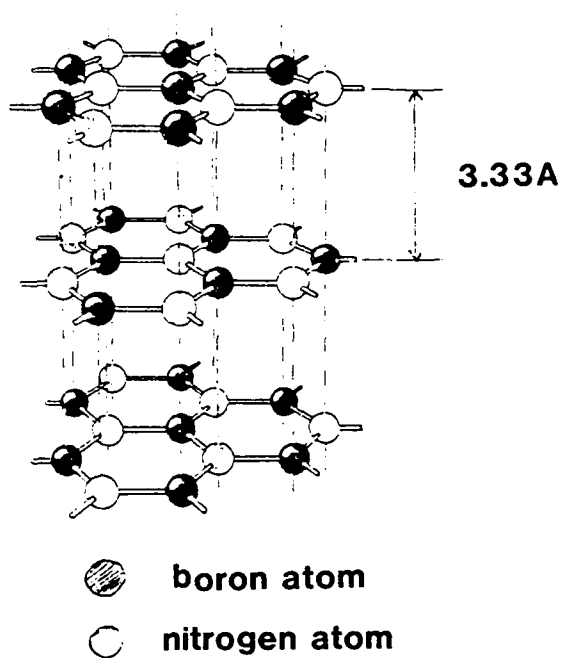


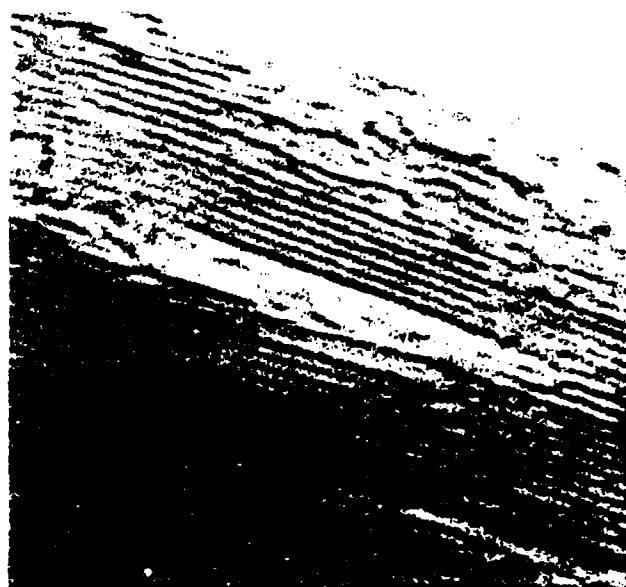
FIGURE 1

D-32

a)



b)



10A

FIGURE 2

# BORON NITRIDE

hotodiode Counts

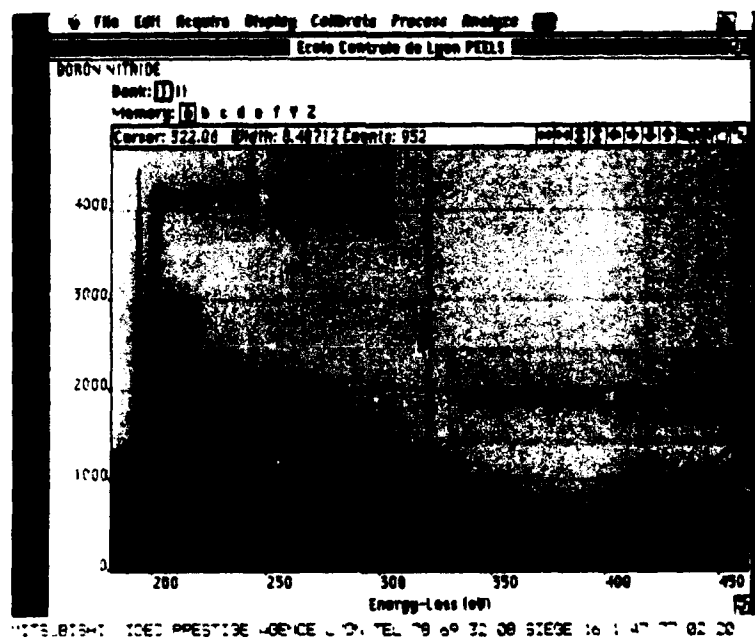
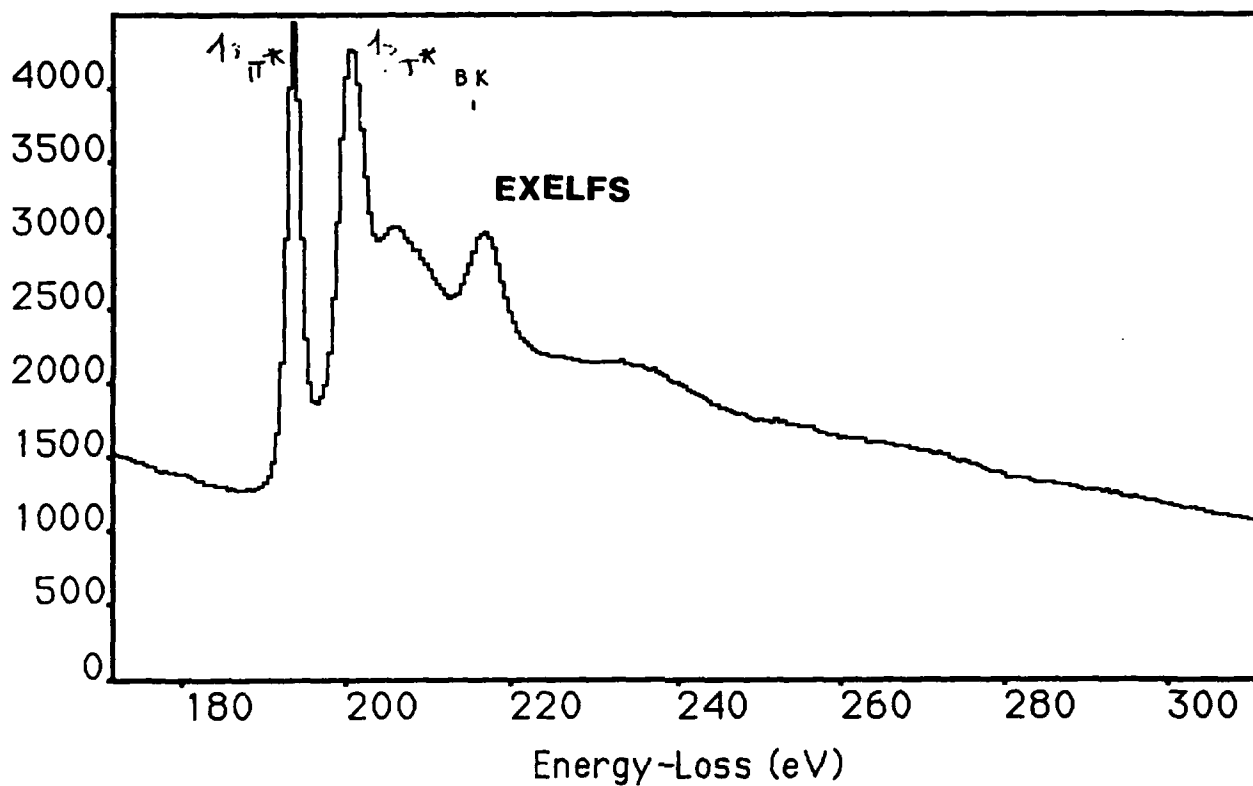
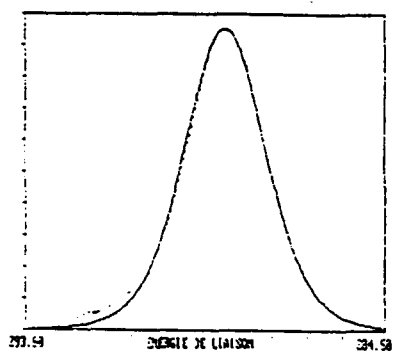
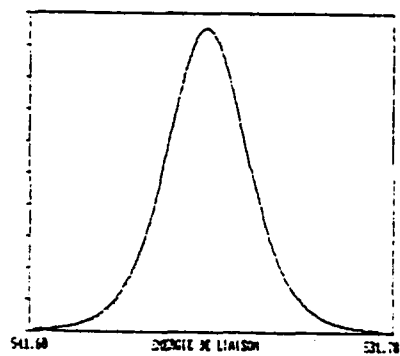


FIGURE 3

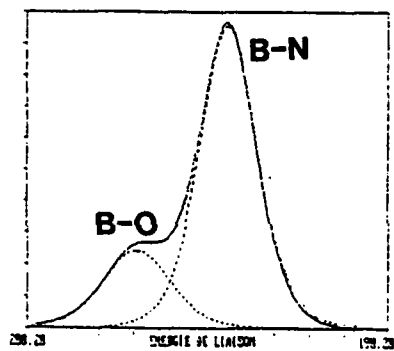
**C 1s**



**O 1s**



**B 1s**



**N 1s**

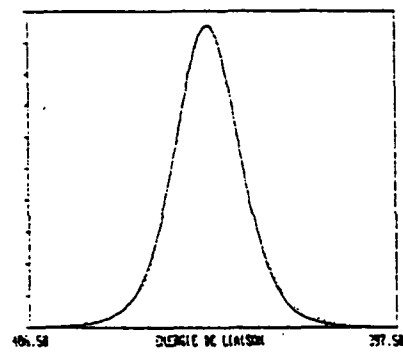
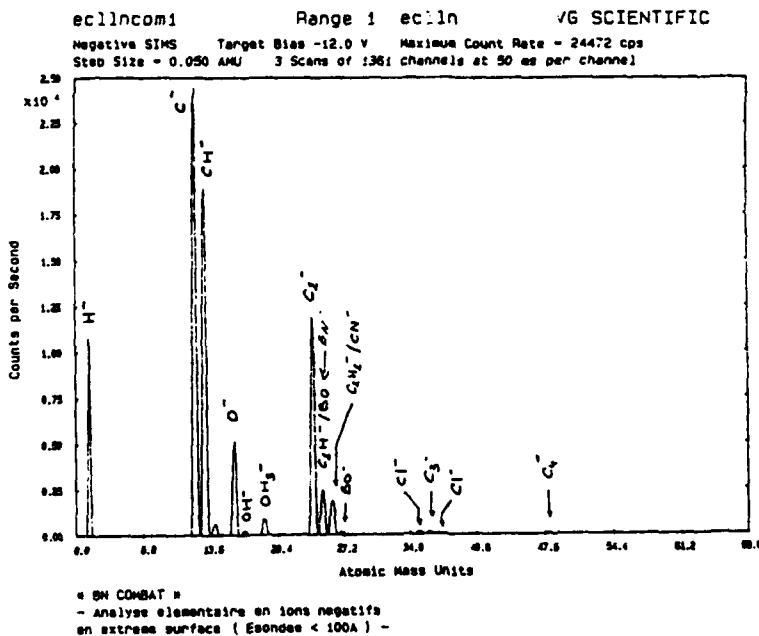


FIGURE 4

**D-35**

a )



b )

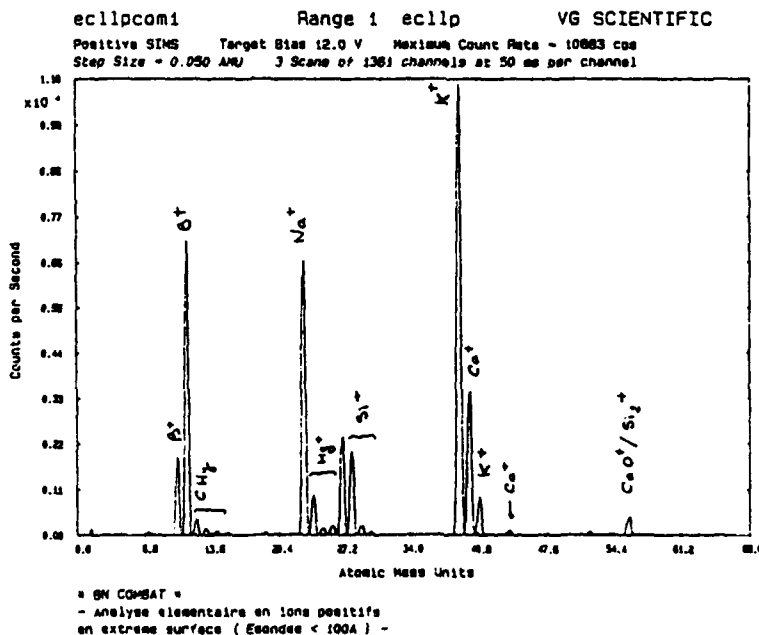
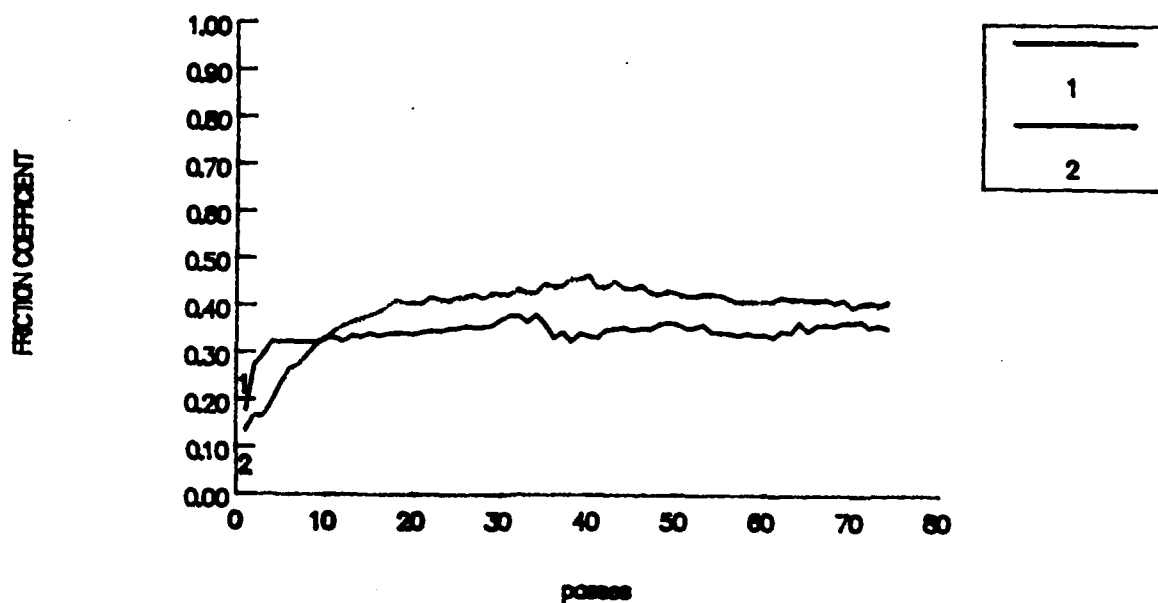


FIGURE 5

D-36

# h BN Combat Flat \ Flat

## Ultra High Vacuum (Propanol)



# h BN Combat Flat \ Flat

## Ultra High Vacuum (Annealing)

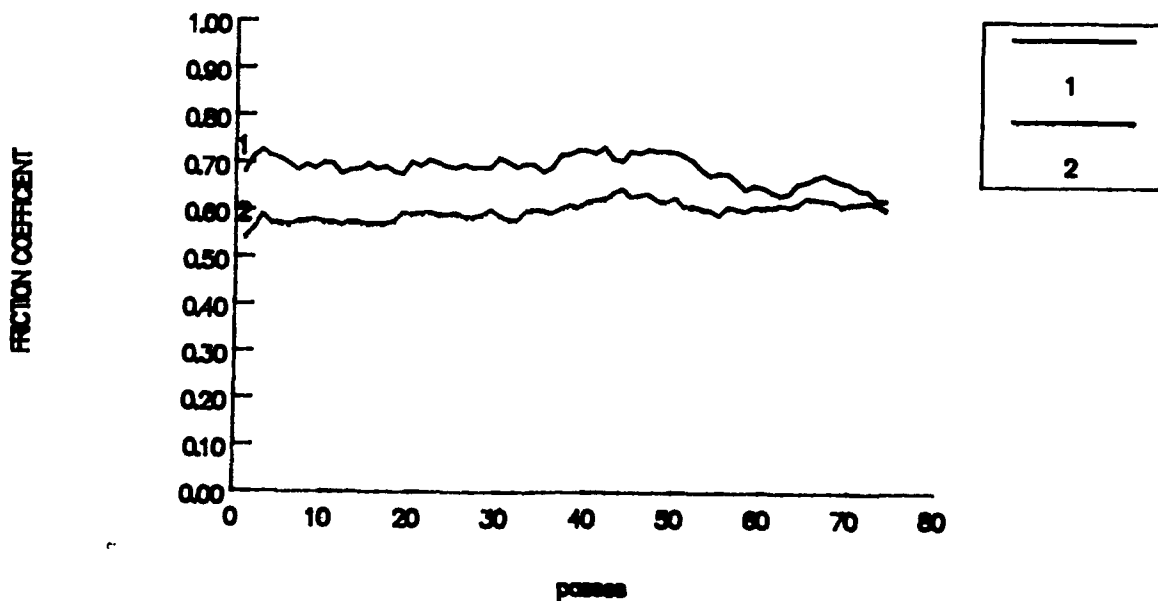
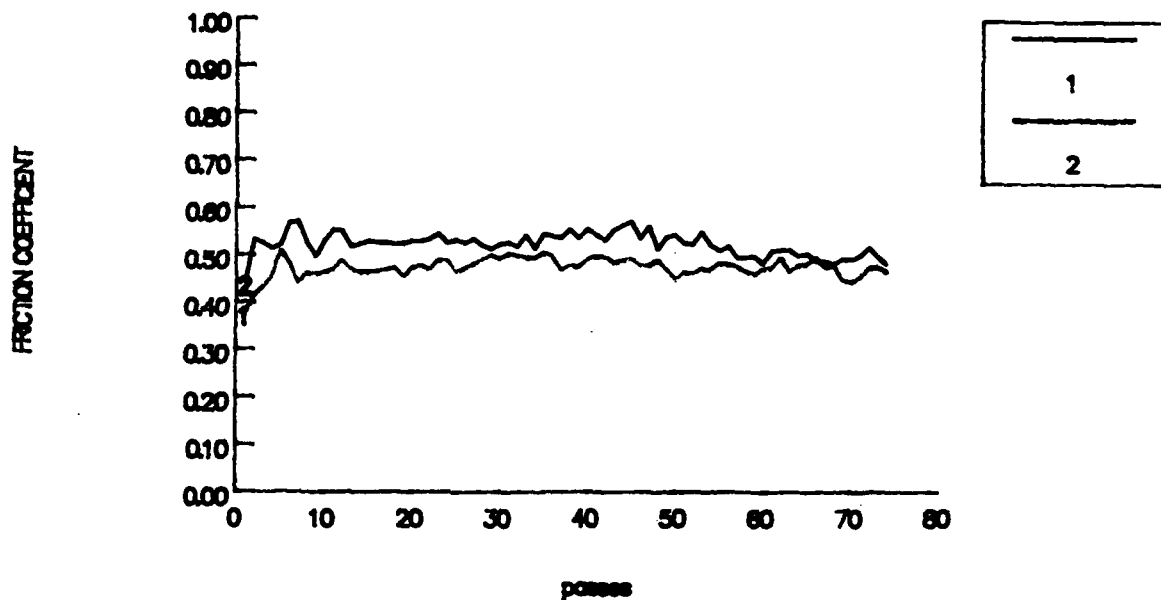


FIGURE 6



# h BN Combat Edge \ Edge

## Ultra High Vacuum (Propanol)



# h BN Combat Edge \ Edge

## Ultra High Vacuum (Annealing)

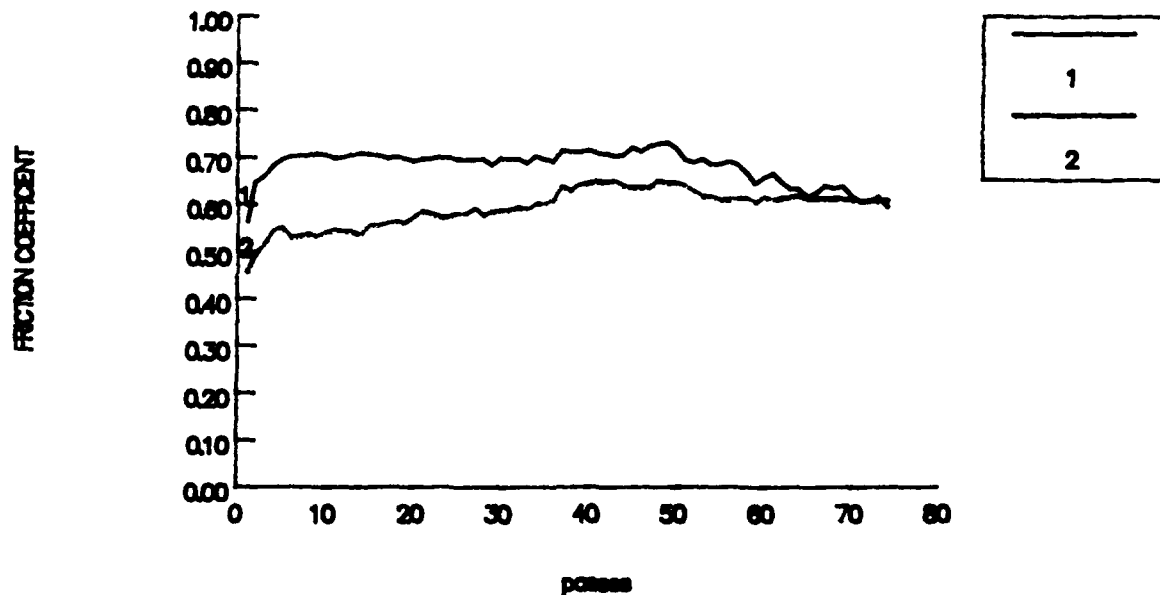


FIGURE 7

# h BN Combat \ h BN Combat

## Ultra High Vacuum

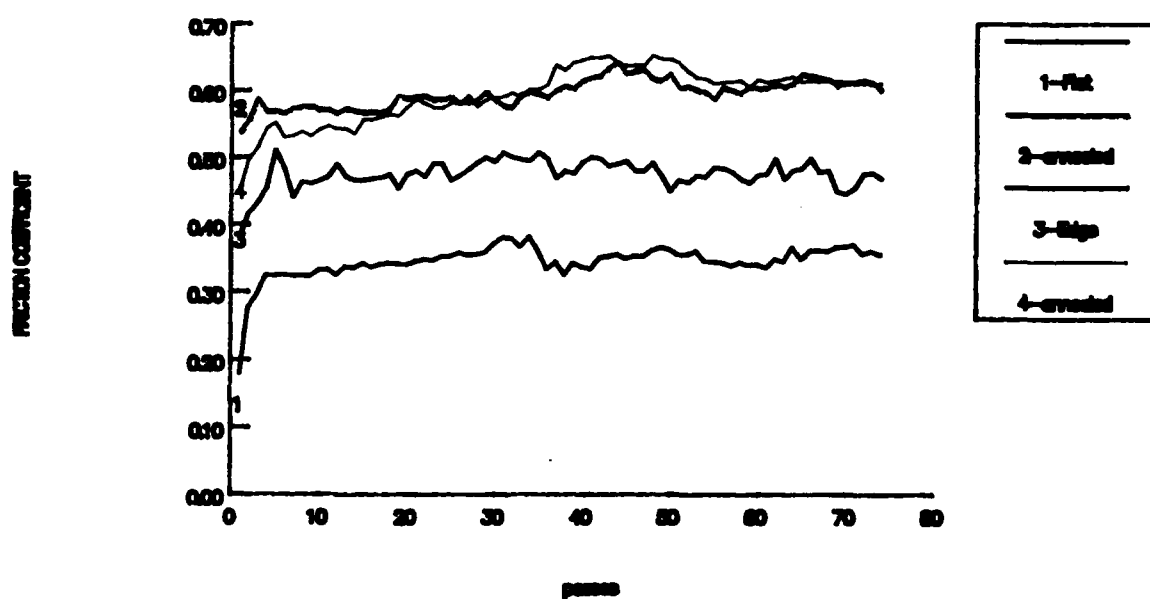
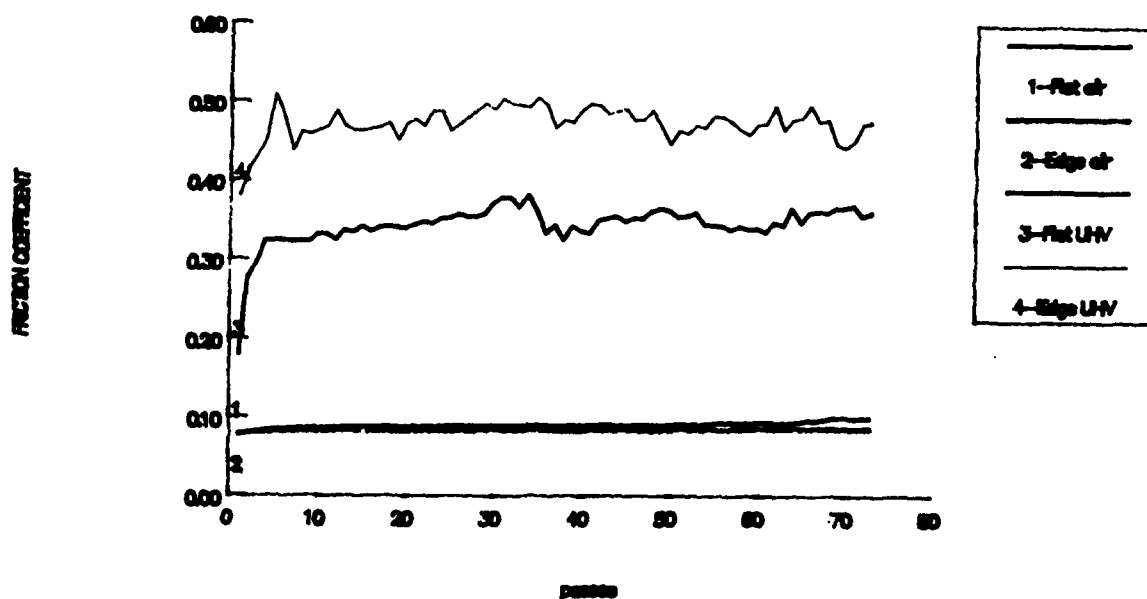


FIGURE 8

D-39

# h BN Combat \ h BN Combat

a) Ultra High Vacuum / Air



# h BN Combat Flat \ Flat UHV and air

b)

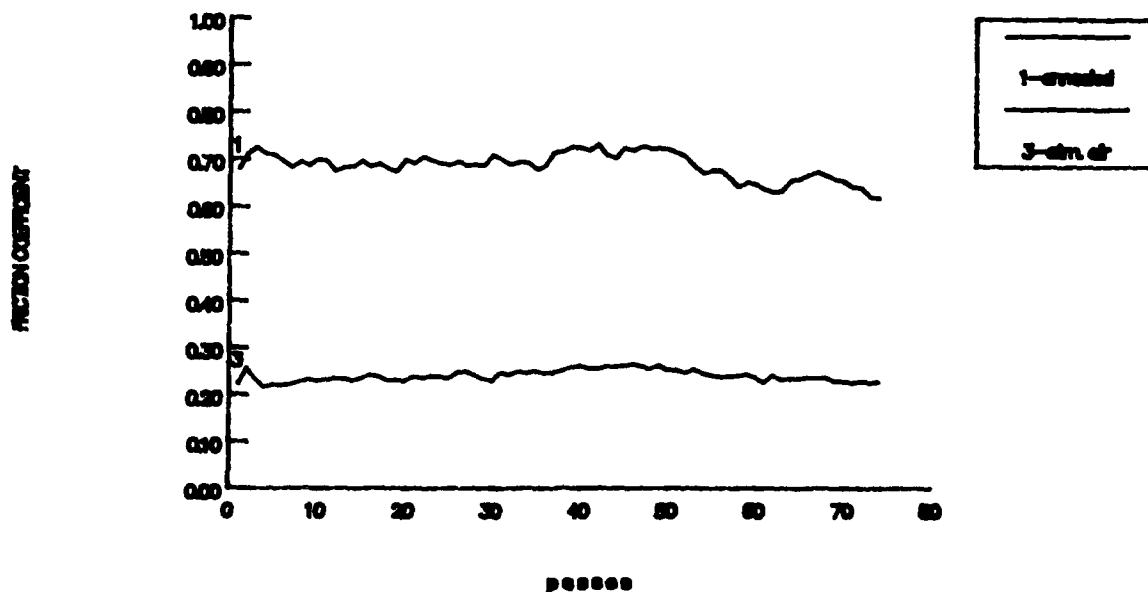


FIGURE 9

D-40

# h BN Combat \ h BN Combat

## Flat \ Flat UHV and H2O

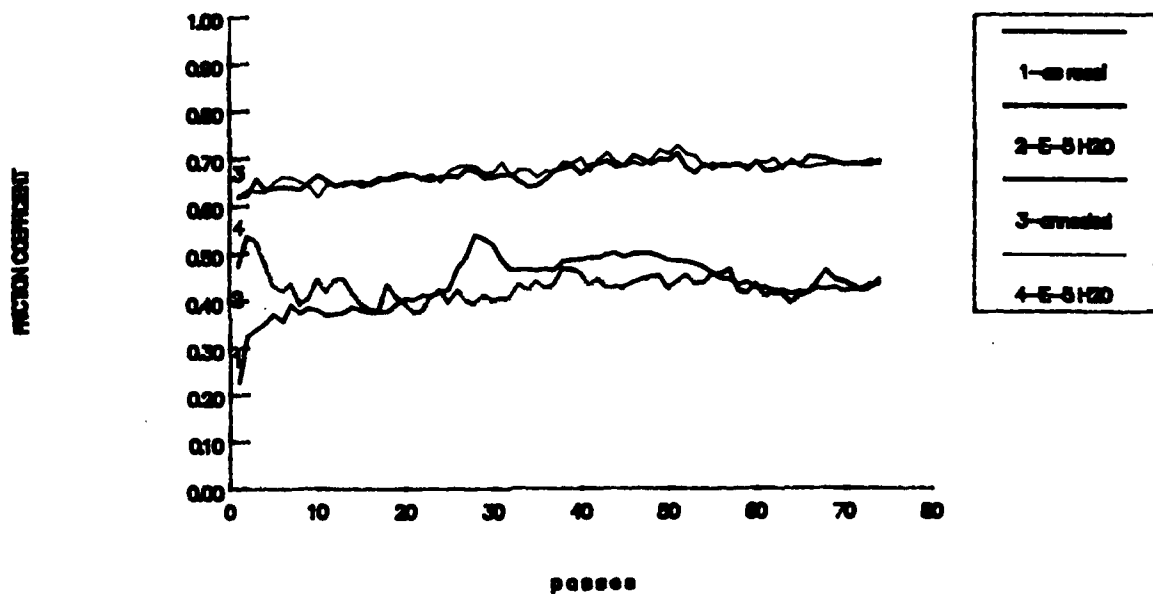


FIGURE 10

# h BN Combat \ h BN Combat

## Flat \ Flat UHV and N2

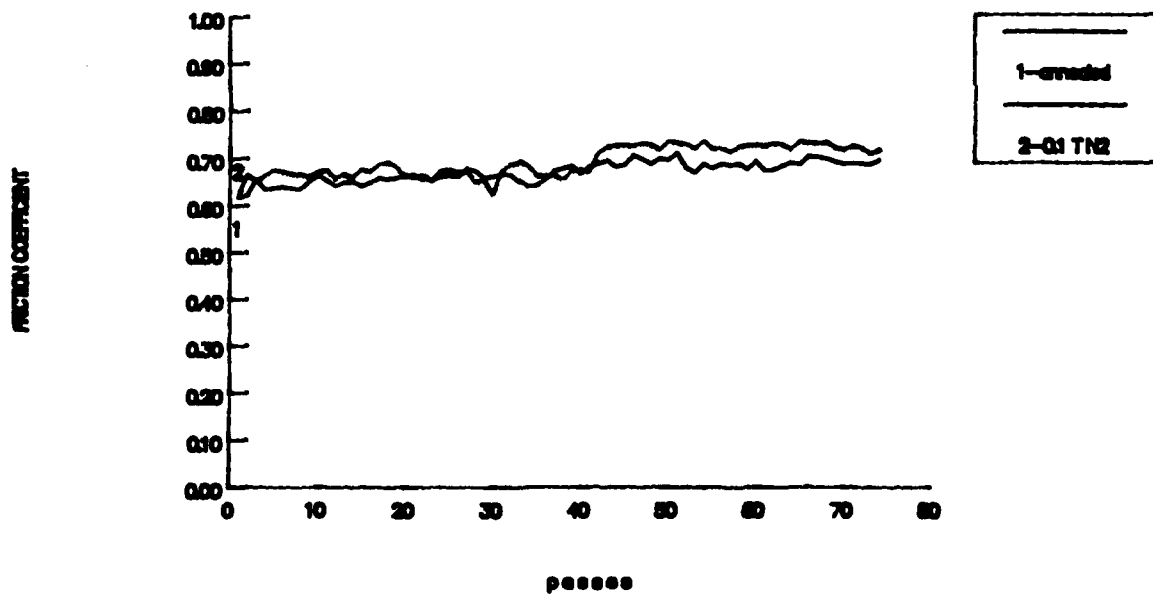


FIGURE 11

# h BN Combat Flat \ Flat

## Oxygen effect

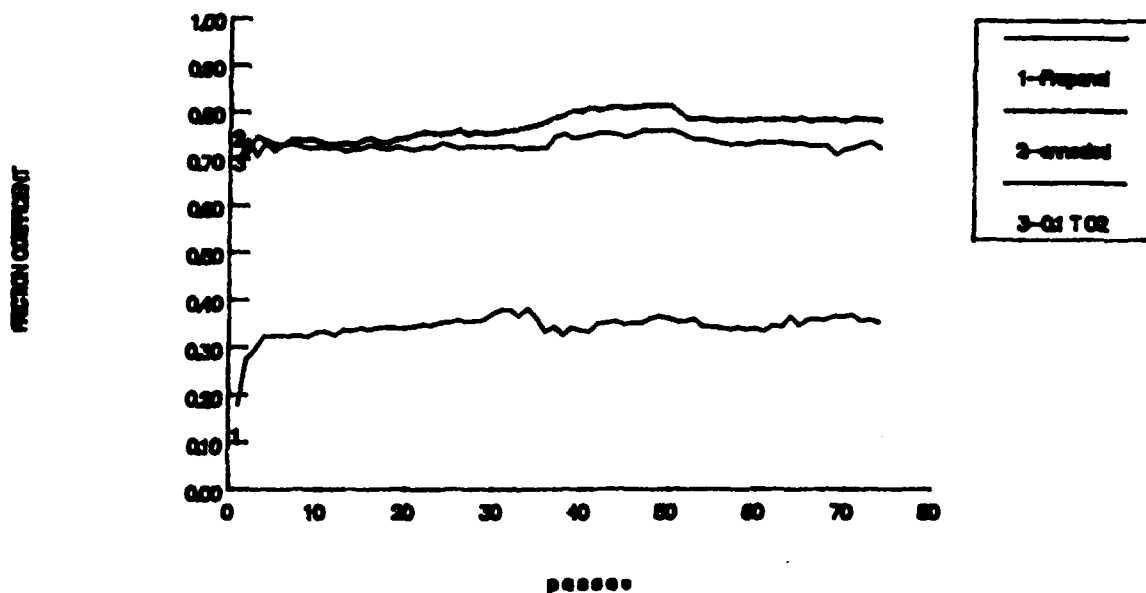


FIGURE 12

# h BN Combat Flat \ Flat

## UHV and air

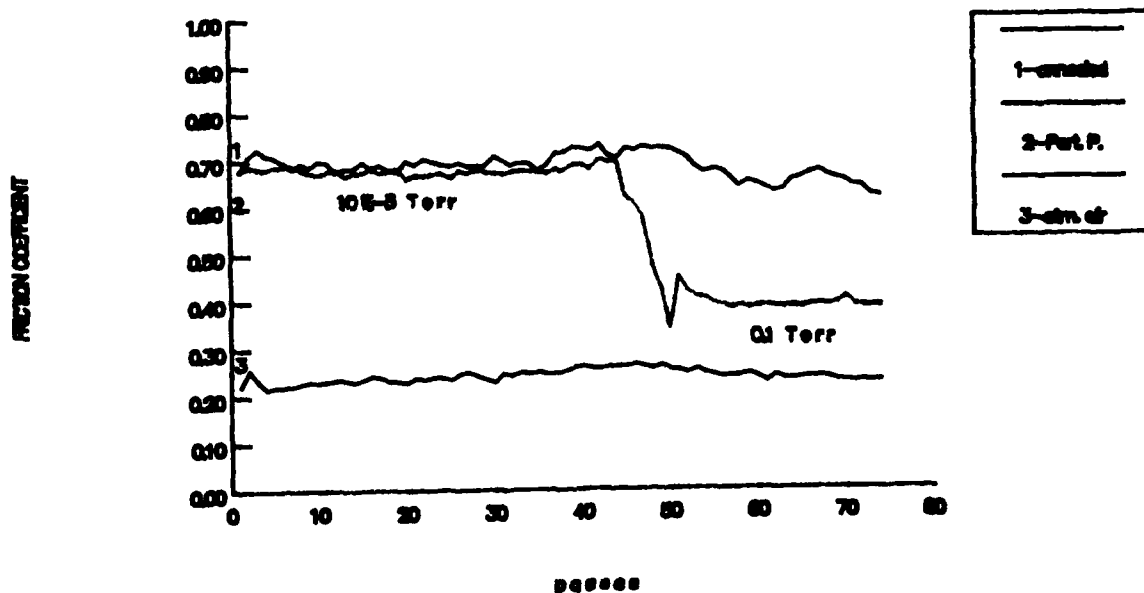


FIGURE 13

D-42

# h BN Combat \ h BN Combat

## Flat \ Flat UHV and CO

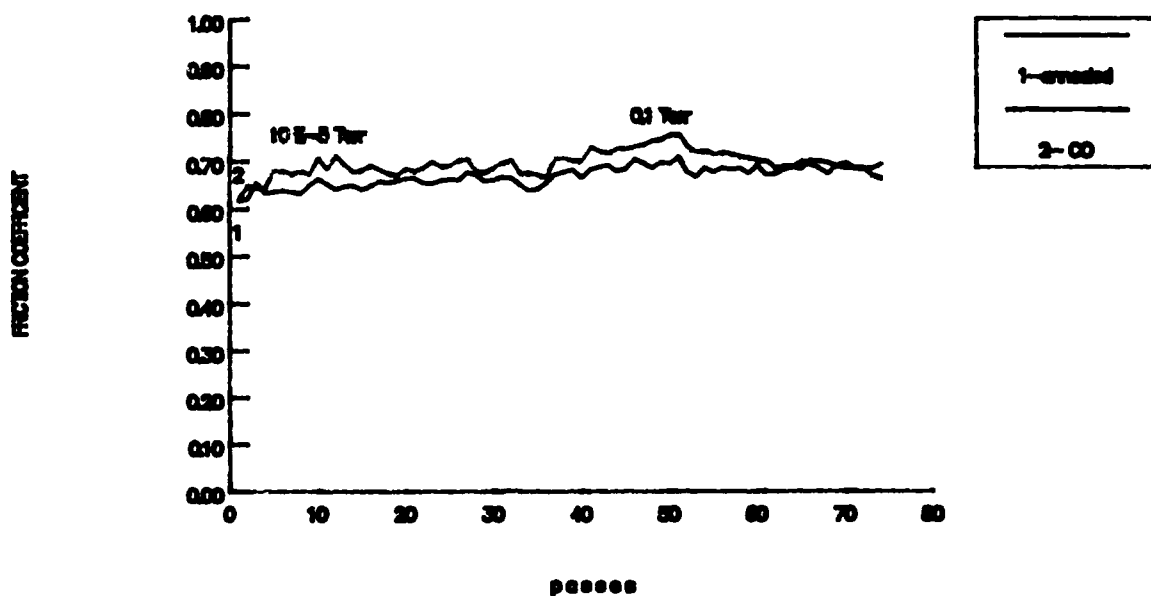


FIGURE 14

# h BN Combat \ h BN Combat

## Flat \ Flat UHV and C3H8

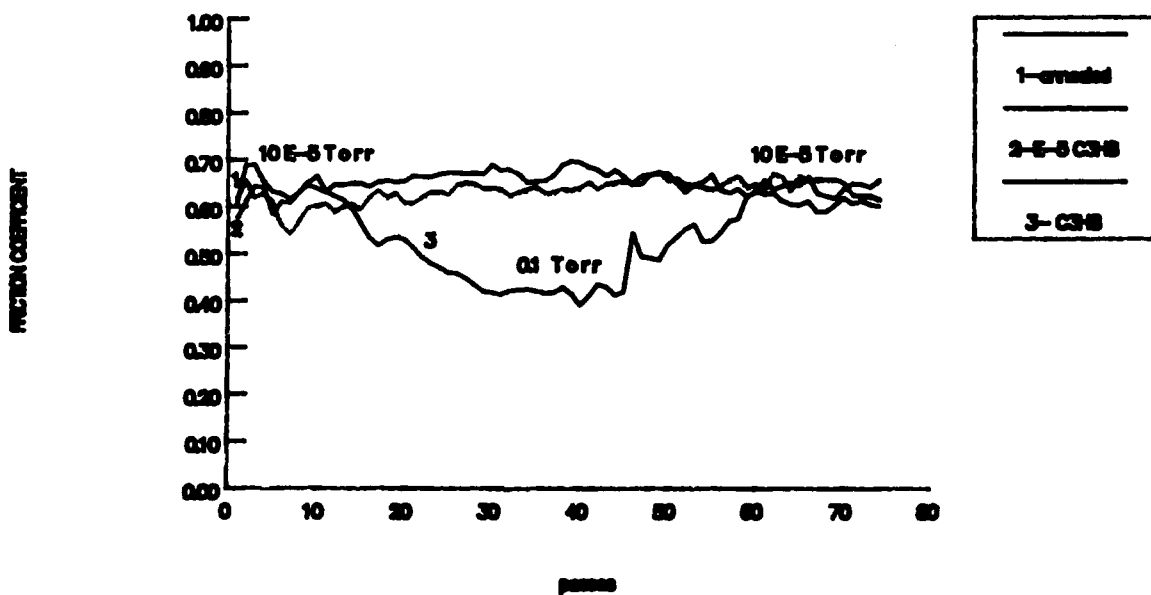
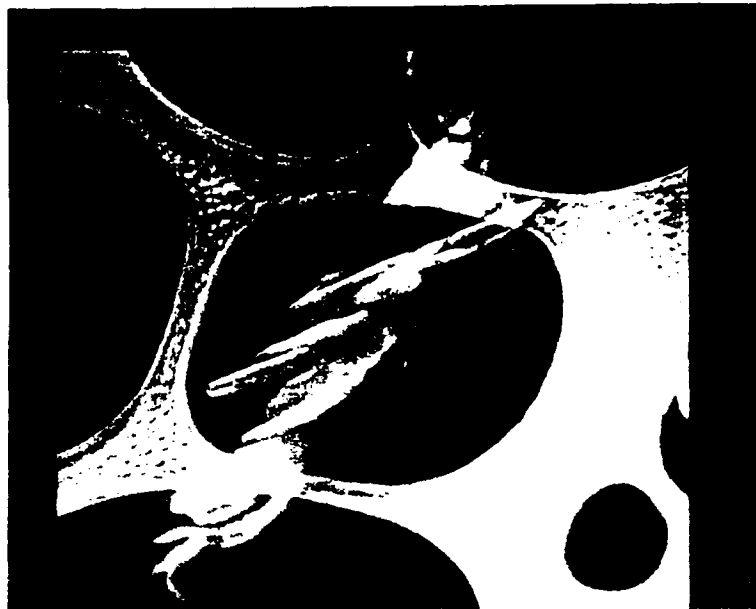


FIGURE 15



FIGURE 16

D-44



1076081-1 ELECTRON

11

0.1  $\mu$ m



1076081-1 ELECTRON

FIGURE 17

D-45





12A

FIGURE 18

D-46

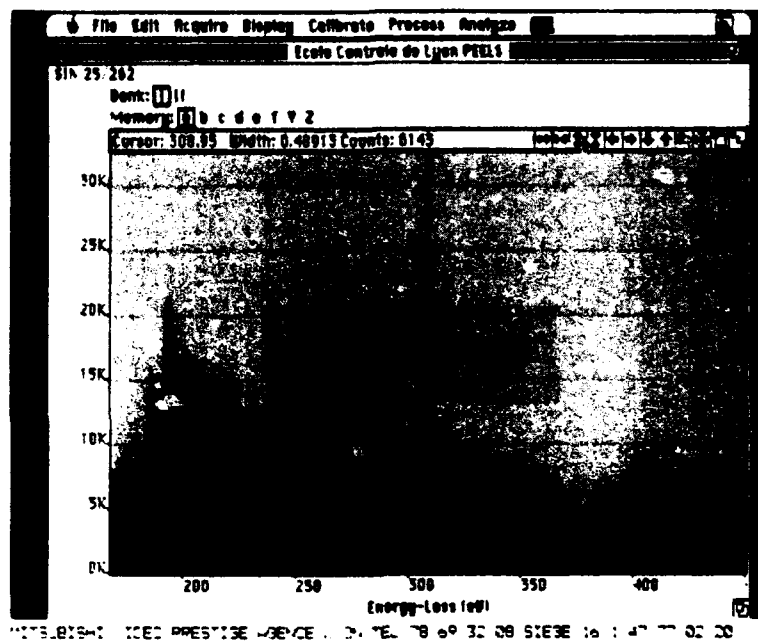


FIGURE 19

## **ANNEXES**

**D-48**

SORETRIB  
36 avenue Guy de Collongue  
B.P. 163  
69131 ECULLY Cedex

Ecole Centrale de Lyon  
Laboratoire de Technologie des  
Surfaces  
26 avenue Guy de Collongue  
B.P. 163 - 69131 ECULLY Cedex  
fax : 78.43.39.62

DETERMINATION OF TRIBOLOGICAL FUNDAMENTALS OF SOLID LUBRICATED CERAMICS

Contract F 33615-85-C-5087

Monthly report from December 1<sup>st</sup> to December 31<sup>th</sup> 1988

Report n° 3

CHARACTERIZATION OF hBN SPECIMENS PRIOR TO UHV FRICTION

RFQ 520765

Prepared for :

HUGUES AIRCRAFT COMPANY  
Electro-Optical & Data Systems Group  
Mike GARDOS, Senior Scientist

Prepared by : - J.M. MARTIN

Adm. Div. :

  
- Th. LE MOGNE

  
Etude SORETRIB n° D50

D-49

## I - Survey of h BN friction

Classically, h-BN friction is associated and compared with graphite friction, because there are some basic similarities in the crystallographic structure. Both compounds contain low energy shear planes in the {002} direction (van der Waals interactions). Nevertheless, their electronic structures are quite different as far as valence and conduction bands are concerned. The mechanisms of h-BN friction are reviewed by TABOR [1], and are closely related to those of graphite. The main features are the following :

- friction depends on the orientation of basal planes of the crystallites in the sliding direction,
- friction depends on the chemical state of the edges of individual crystallites (dangling bonds, oxides etc...),
- friction depends on the energy of the surface of crystallites (adsorption of gases...),
- friction depends on the presence of intercalated compounds in the graphite structure (presence of water, mineral species...).

But the respective role of each phenomenon is not clearly understood when testing a manufactured specimen.

## II - Caracterization of h-BN specimens

h-BN specimens were previously analyzed by XPS and EELS (see reports Dec. 1987 and Jan. 1988). The results showed that carbon was present in great quantities in both specimens. Before the friction test, and taking into account the role of impurities and the microstructure in the mechanisms of h-BN friction, we decided to explore in more detail the two specimens that we have at the moment, namely :

- the CVD h-BN plate
- the COMBAT sintered h-BN.

The detection of water was carried out by SIMS and the microstructure of the CVD sample was investigated by high resolution TEM.

The results are the following :

### - Concerning the CVD h-BN sample

BN is not really oriented with the c axis perpendicular to the external face, the high resolution image (figure 1) shows that {002} lattice fringes can be easily imaged (c axis parallel to the surface) (when sampling a flake inside the 2 mm plate). On the other hand, carbon is a main constituent of the CVD h-BN, and EELS and XPS agree that the atomic concentration is 20% (see table below).

|       | XPS(1) | XPS(2) | EELS         |
|-------|--------|--------|--------------|
| B     | 36*    | 38*    | 50           |
| N     | 28     | 33     | 35           |
| C     | 26**   | 22**   | 15**         |
| O     | 10     | 7      | not analyzed |
| Total | 100    | 100    | 100          |

(1) XPS (VG CLAM 100) after etching Ar<sup>+</sup> 3KeV

(2) XPS (SSL) after etching Ar<sup>+</sup> 0,5 KeV

\* Boron is not found in the oxide chemical state

\*\* Carbon is predominantly graphitic

Moreover, EELS spectra (figure 2) show that carbon is in an amorphous form with the sp<sub>2</sub> hybridation.

SIMS spectra are presented in figures 3-4.

The presence of carbon is confirmed by peaks C<sup>-</sup> and C<sup>-</sup><sub>2</sub>, and the ratio C<sup>-</sup>/C<sup>-</sup><sub>2</sub> indicates that carbon is graphitic. Oxygen is also detected (O<sup>-</sup>) and also hydrogen (H<sup>+</sup>) but the OH<sup>-</sup> peak representing water is very weak, so that the quantity of water can be neglected in our experiment. From these analytical data, it can be concluded that oxygen (= 10% atomic) is neither water, nor boron oxide, nor carbon oxide, nor nitrogen oxide. Therefore, we suggest that gas (oxygen) may be intercalated in the graphitic structure. When analyzing thin flakes in the TEM, oxygen can escape into the vacuum and is not detected. Moreover, as the excess of boron is not oxide, it is also possible that some carbon lies in the graphitic planes close to boron and nitrogen [2].

SIMS is a very sensitive technique to study impurities and traces. The main elements that are found are :

- Ca (Mg and Si are also present) (< 1%)
- Na, K, Li, Cl as traces (< 0.1 %).

- Concerning the COMBAT hBN specimens

BN is oriented with the c-axis perpendicular to the external face. Carbon is present in the chemical composition (22 % atomic in XPS, 1 cm<sup>2</sup> probed) but it is segregated, because EELS on individual flakes does not indicate the presence of carbon, but stoichiometric BN. SIMS spectra (figures 5-6) do not show the presence of water, but show oxygen and carbon (confirming XPS data) and impurities with Mg and Si are more important than in CVD hBN.

|   | XPS | EELS |
|---|-----|------|
| B | 37  | 51   |
| N | 31  | 49   |
| C | 22  | /    |
| O | 9   | /    |

Note : Due to argon or gallium bombardment, the surface of hBN specimens turns to a black colour (figure 7) which is more accentuated for the COMBAT hBN. At the moment, we have no explanation of this.

### III - Conclusion

The h-BN specimen that we have at the moment is of an extremely complex nature. Nevertheless, the situation can be summarized as follows :

#### - CVD - hBN

- \* no preferential orientation of crystallites,
- \* carbon in the graphitic structure (\* 20 % atomic),
- \* oxygen may be intercalated in the structure,
- \* some impurities at a low level (< 1 %).

#### - COMBAT hBN

- \* BN crystallites are oriented parallel to the surface,
- \* carbon is segregated in the microstructure (\* 20 % atomic),
- \* oxygen as borate (?),
- \* impurities at a low level (< 1 %).

The next report will concern friction of BN/BN under vacuum.

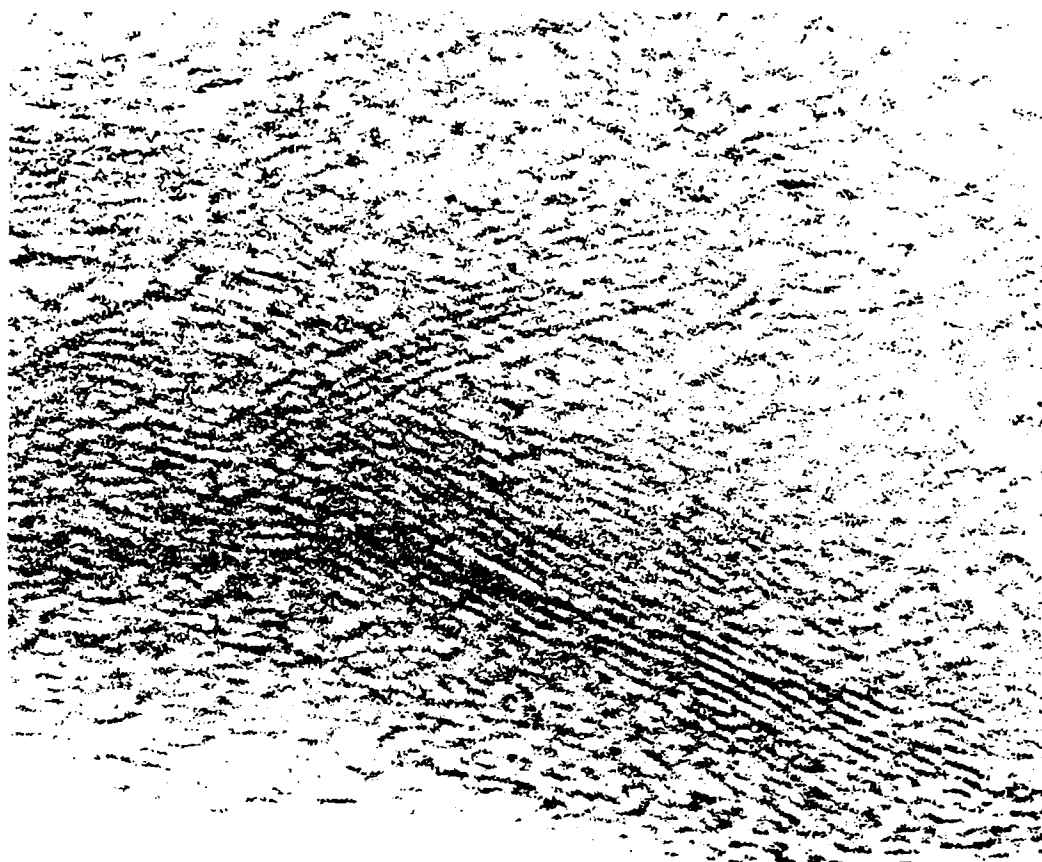
### References

- [1] F.P. BOWDEN and D. TABOR, "The friction of lamellar solids" Part II, Oxford at the Clarendon Press, (1964).
- [2] Amy Y. LIU and al, "Atomic arrangement and electronic structure of BC<sub>2</sub>N", Applications of intercalation compounds, pp. 136-144, (1983).

## LIST OF FIGURES

- Figure 1 : High resolution TEM micrograph of a CVD hBN flake showing (002) lattice fringes lying perpendicular to the external face.
- Figure 2 : EELS spectrum of a CVD hBN flake showing boron and carbon K edges. Note that carbon is  $sp_2$  hybridized in an amorphous form.
- Figure 3 : SIMS spectra of CVD hBN (positive ions).
- Figure 4 : SIMS spectra of CVD hBN (negative ions).
- Figure 5 : SIMS spectra of COMBAT hBN (positive ions).
- Figure 6 : SIMS spectra of COMBAT hBN (negative ions).
- Figure 7 : Optical micrographs of the hBN specimens after ion etching (SIMS).  
a) CVD hBN  
b) COMBAT hBN





20A

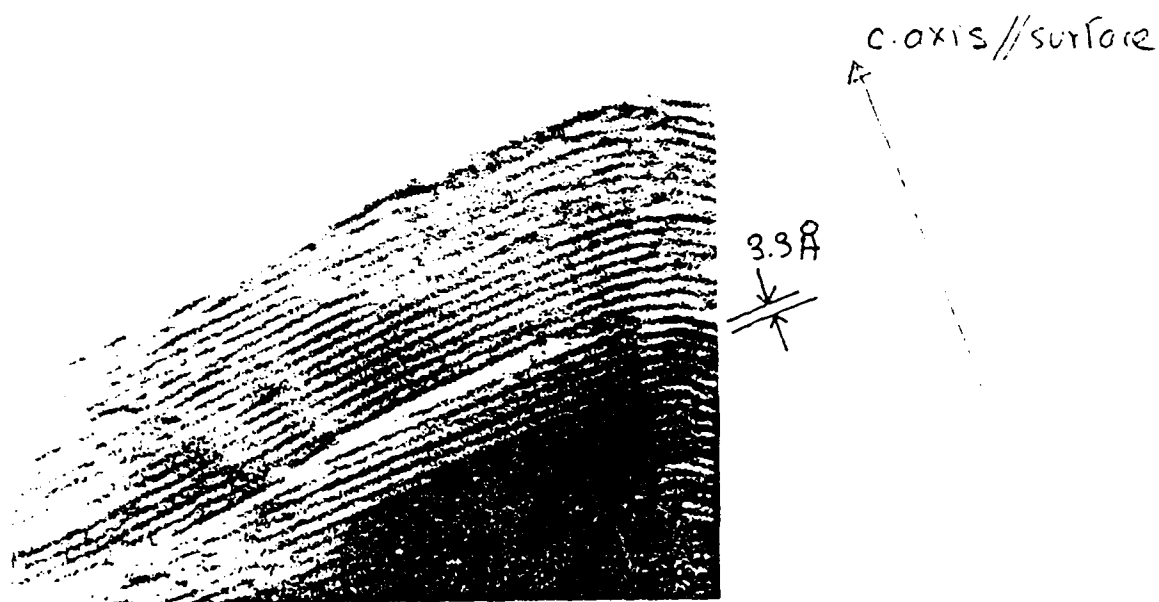


Figure 1

D-54

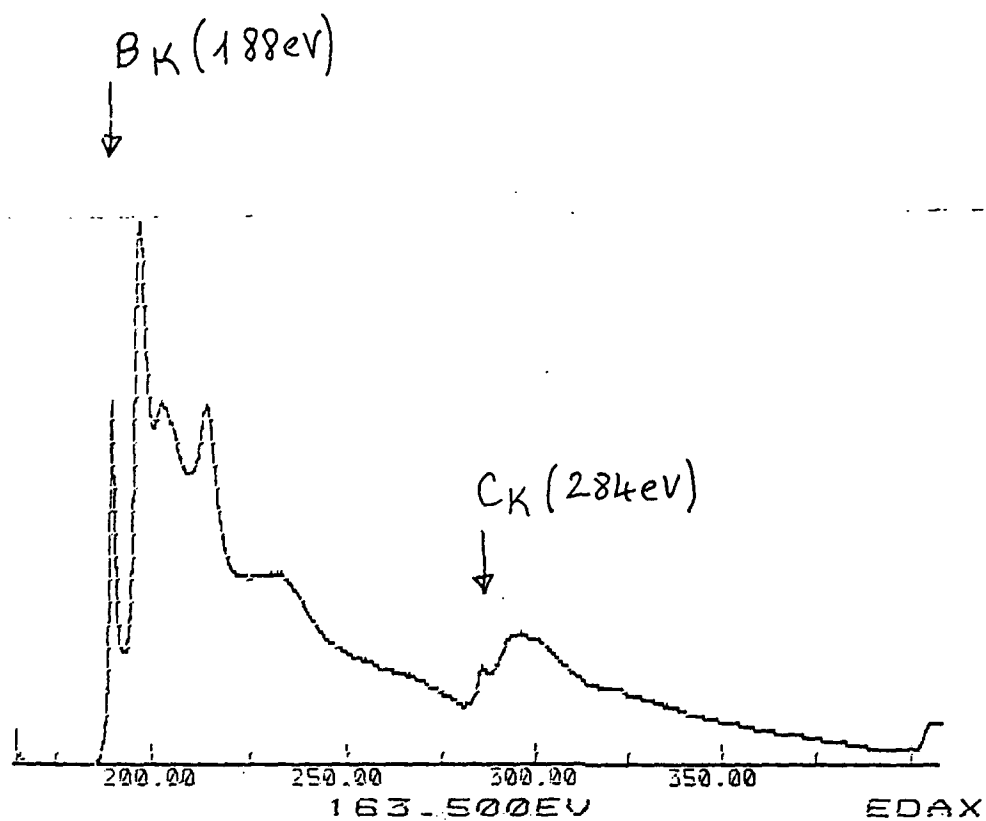


Figure 2

ec1lppyr3

Range 1 ec1lp

VG SCIENTIFIC

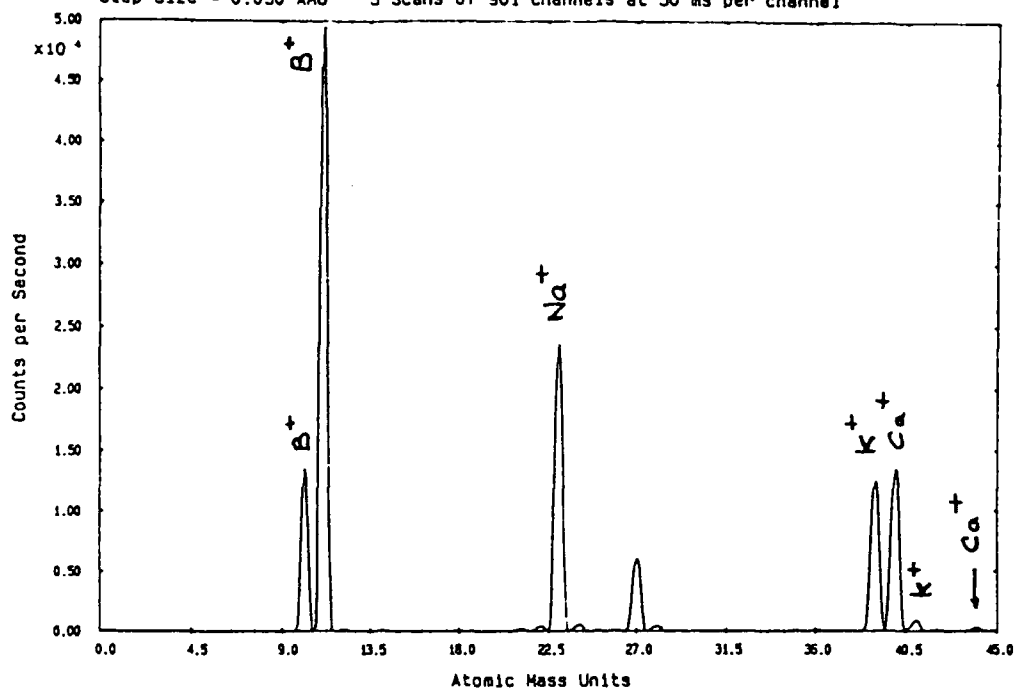
Positive SIMS

Target Bias 12.0 V

Maximum Count Rate = 49546 cps

Step Size = 0.050 AMU

5 Scans of 901 channels at 50 ms per channel



\* BN PYROLYTIQUE \*

- Analyse elementaire en ions positifs

\* a coeur \* -

ec1lppyr3

Range 1 ec1lp

VG SCIENTIFIC

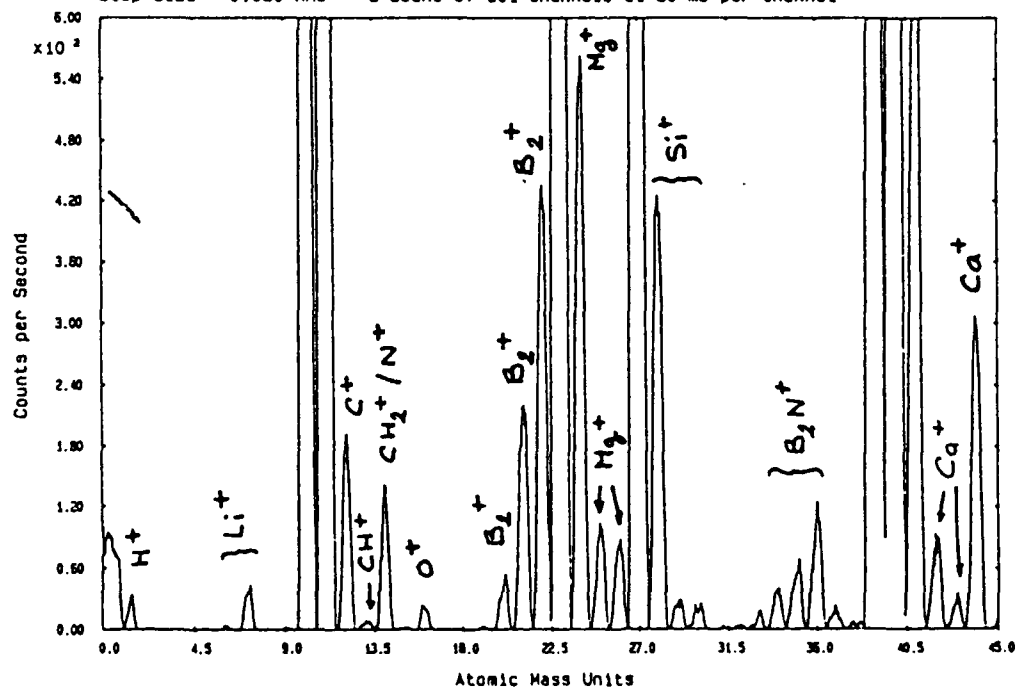
Positive SIMS

Target Bias 12.0 V

Maximum Count Rate = 49546 cps

Step Size = 0.050 AMU

5 Scans of 901 channels at 50 ms per channel



\* BN PYROLYTIQUE \*

- Analyse elementaire en ions positifs

\* a coeur \* -

Figure 3

D-56

ec11npyr3

Range 1 ec11n

VG SCIENTIFIC

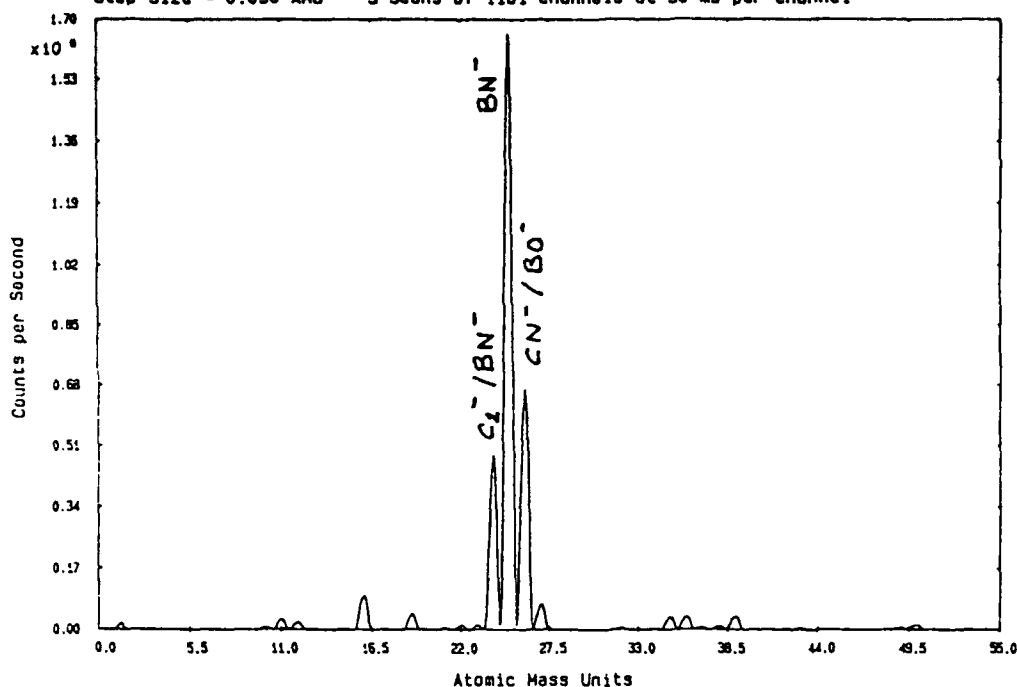
Negative SIMS

Target Bias -12.0 V

Maximum Count Rate = 165882 cps

Step Size = 0.050 AMU

5 Scans of 1101 channels at 50 ms per channel



\* BN PYROLYTIQUE \*

- Analyse elementaire en ions negatifs

\* a coeur \*

ec11npyr3

Range 1 ec11n

VG SCIENTIFIC

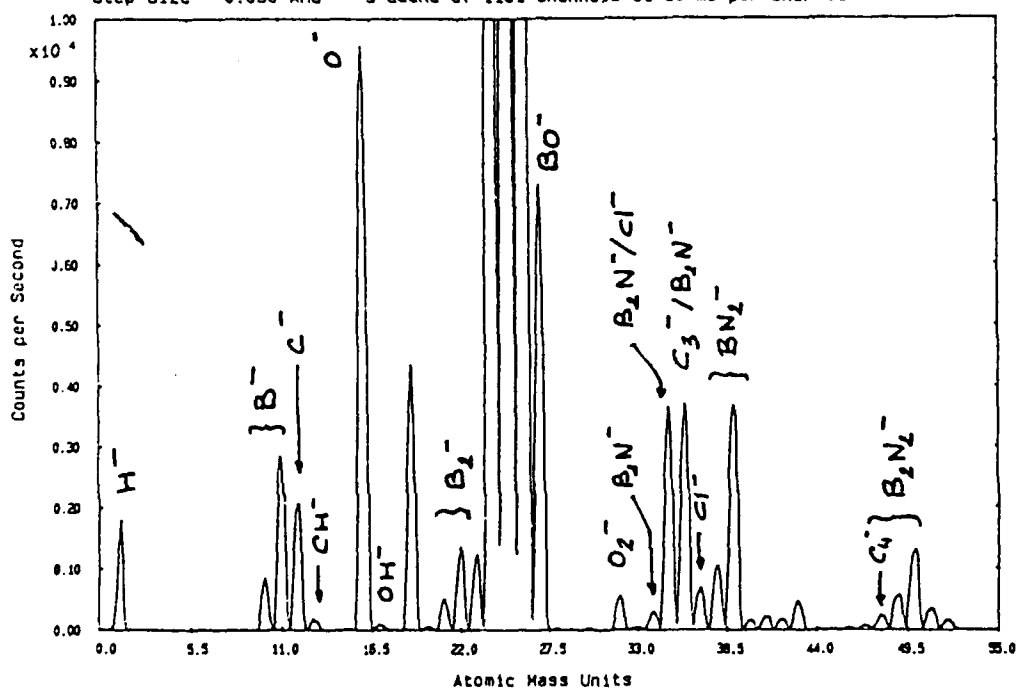
Negative SIMS

Target Bias -12.0 V

Maximum Count Rate = 165882 cps

Step Size = 0.050 AMU

5 Scans of 1101 channels at 50 ms per channel



\* BN PYROLYTIQUE \*

- Analyse elementaire en ions negatifs

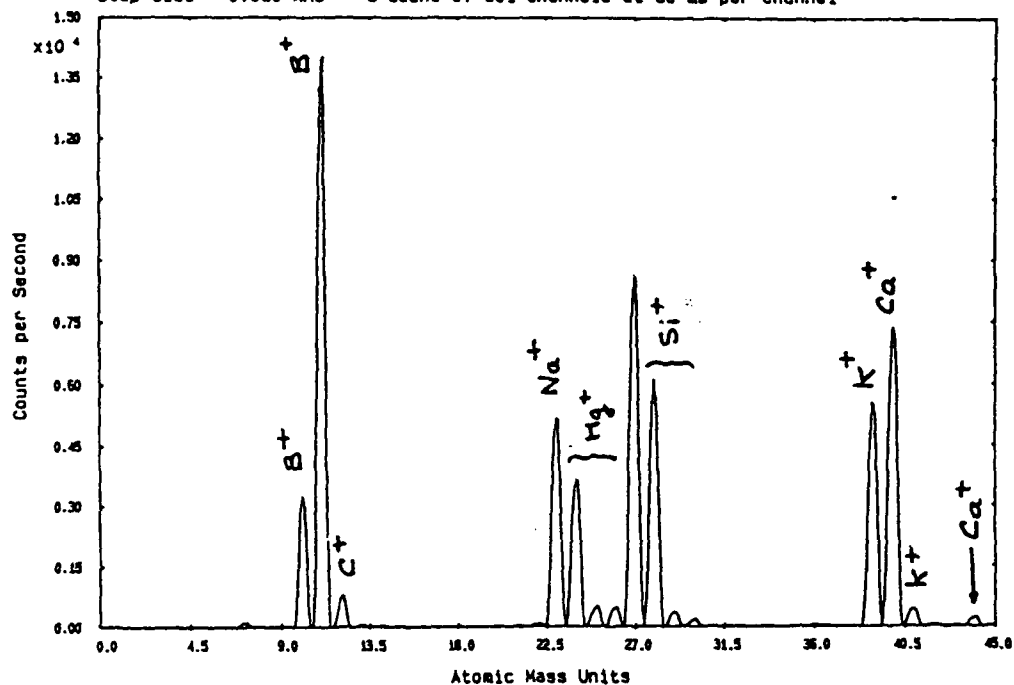
\* a coeur \*

Figure 4

D-57

ec11pcom3 Range 1 ec11p VG SCIENTIFIC

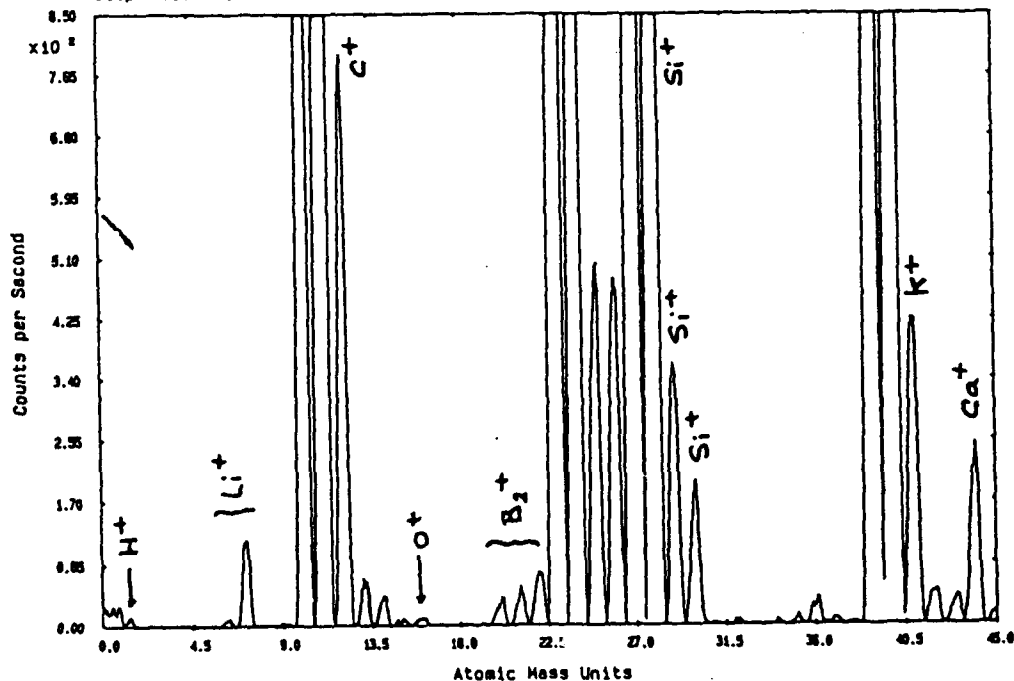
Positive SIMS Target Bias 12.0 V Maximum Count Rate = 14023 cps  
Step Size = 0.050 AMU 5 Scans of 901 channels at 50 ms per channel



\* BN COMBAT \*  
- Analyse elementaire en ions positifs  
" a coeur " -

ec11pcom3 Range 1 ec11p VG SCIENTIFIC

Positive SIMS Target Bias 12.0 V Maximum Count Rate = 14023 cps  
Step Size = 0.050 AMU 5 Scans of 901 channels at 50 ms per channel



\* BN COMBAT \*  
- Analyse elementaire en ions positifs  
" a coeur " -

D-58

Figure 5

ec11ncom3

Range 1 ec11n

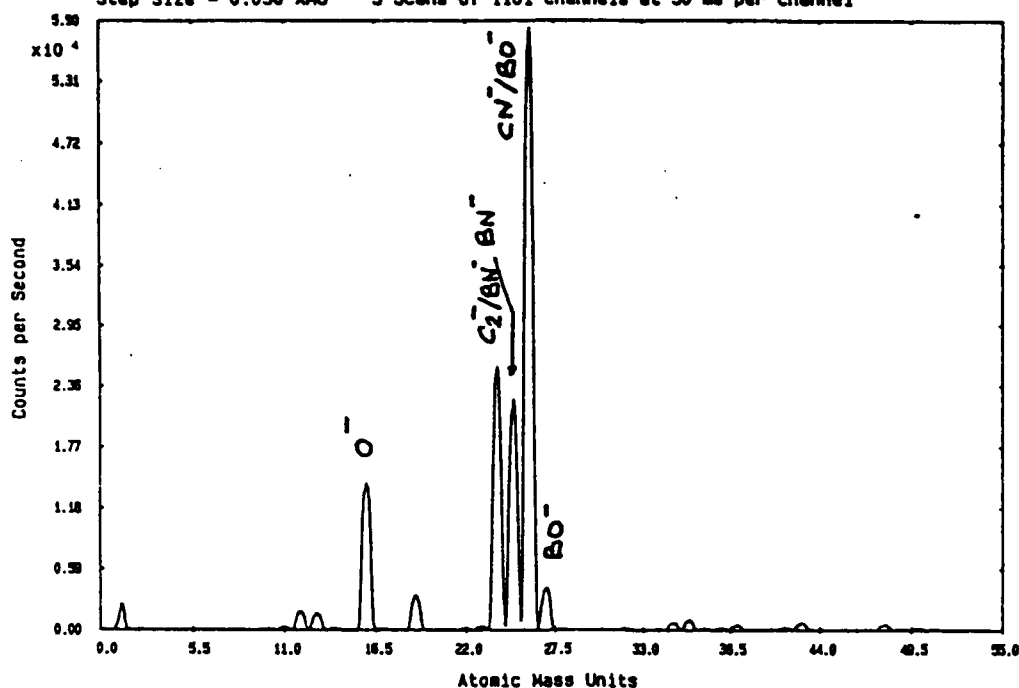
VG SCIENTIFIC

Negative SIMS

Target Bias -12.0 V

Maximum Count Rate = 58296 cps

Step Size = 0.050 AMU 5 Scans of 1101 channels at 50 ms per channel



\* BN COMBAT \*

- Analyse elementaire en ions negatifs

" a coeur " -

ec11ncom3

Range 1 ec11n

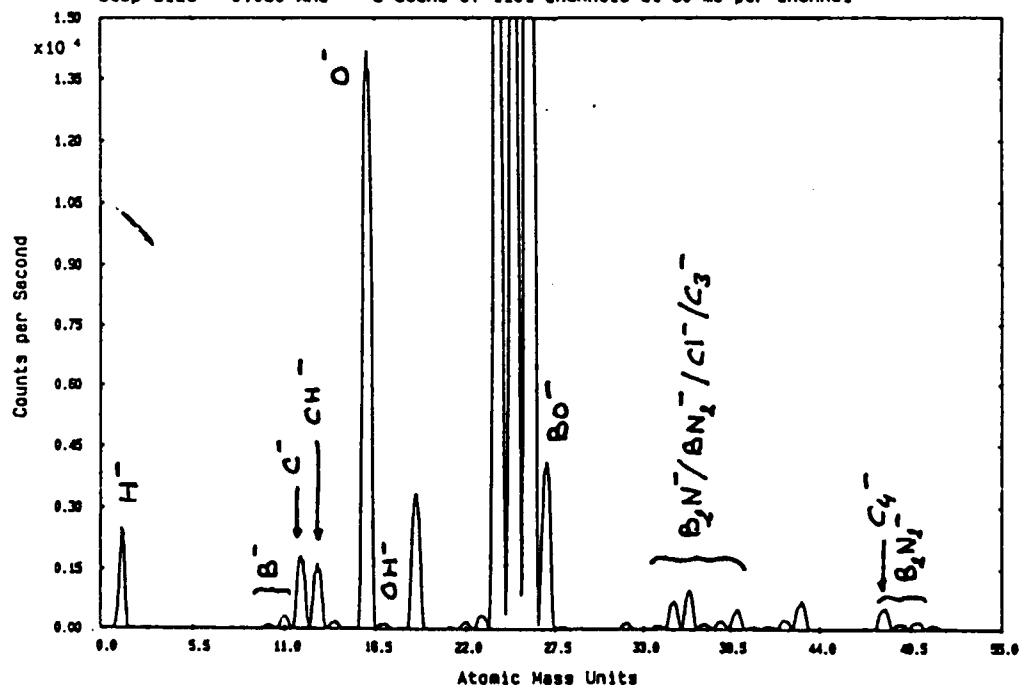
VG SCIENTIFIC

Negative SIMS

Target Bias -12.0 V

Maximum Count Rate = 58296 cps

Step Size = 0.050 AMU 5 Scans of 1101 channels at 50 ms per channel



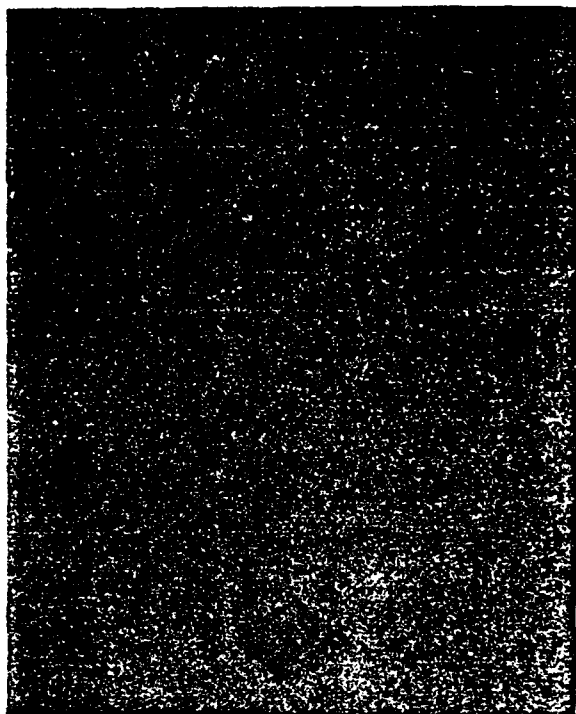
\* BN COMBAT \*

- Analyse elementaire en ions negatifs

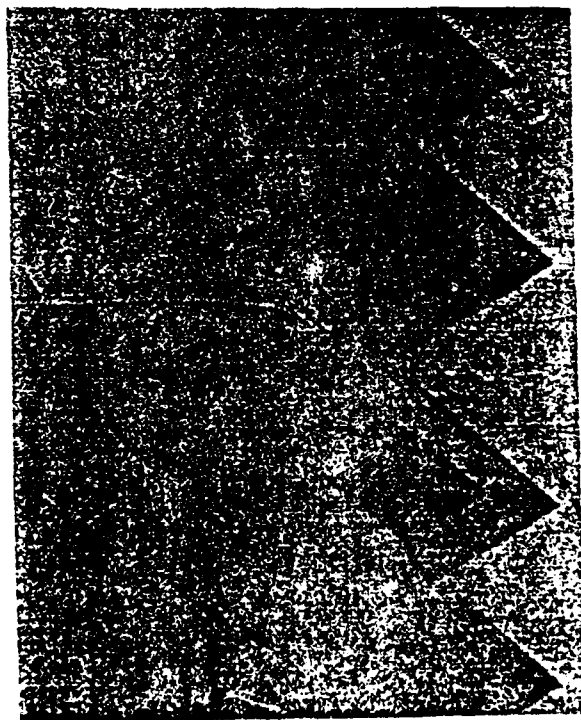
" a coeur " -

Figure 6

D-59



a) CVD hBN



b) Combat hBN

SORETRIB  
36 avenue Guy de Collongue  
B.P. 163  
69131 ECULLY Cedex

Ecole Centrale de Lyon  
Laboratoire de Technologie des  
Surfaces  
36 avenue Guy de Collongue  
B.P. 163 - 69131 ECULLY Cedex  
fax : 78.43.39.62

DETERMINATION OF TRIBOLOGICAL FUNDAMENTALS OF SOLID LUBRICATED CERAMICS

Contract F 33615-85-C-5087

Monthly report from January 1<sup>st</sup> to January 31<sup>th</sup> 1989

Report n° 4

FRICTION OF HEXAGONAL BORON NITRIDE

("FLAT CONFIGURATION")

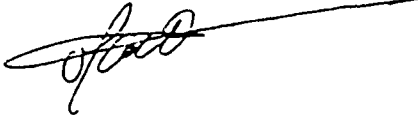
RFG 520765

Prepared for :

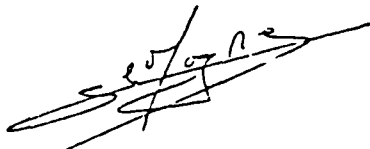
HUGHES AIRCRAFT COMPANY  
Electro-Optical & Data Systems Group  
Mike GARDOS, Senior Scientist

Prepared by : - J.M. MARTIN

Adm. Div. :



- Th. LE MOGNE



Etude SORETRIB n° D50.

D-61



## FRICTION OF HEXAGONAL BORON NITRIDE

### (FLAT CONFIGURATION)

#### I - PREPARATION OF hBN (COMBAT) SPECIMEN

The COMBAT BN, grade A specimen is sintered and hot pressed at high temperature with 6 % molten  $B_2O_3$  as a sintering aid, the hexagonal (flat) BN crystallites align preferentially perpendicular to the direction of the hot pressing, and therefore parallel to the direction of sliding ("flat configuration") see figure (1).

As there is no azimuthal order of the BN crystallites, no special attention was paid to the alignment in terms of sliding direction. As we already mentioned in the previous report, 20 % atomic of carbon is present in the chemical composition of the surface of COMBAT BN.

The preparation of hBN surfaces presents some difficulties. For example, after ionic etching CVD h-BN becomes not stoichiometric (Figure 2) ; annealing at 800 K do not permit to recover the BN composition. Consequently, for this first set of experiments, COMBAT h-BN specimen were ultrasonically cleaned in propanol and dried, without any ionic etching.

The tribological conditions were the following :

- W (normal load) = 2N
- sliding speed : 0.6 mm/s
- length of the stroke : 3 mm
- ambient temperature (20°C).

#### II - RESULTS

##### 1) Friction of hBN under vacuum

The vacuum in the chamber was  $10^{-7}$  Pa. Two similar experiments were conducted in order to check the reproducibility of the results. The evolution of the friction coefficient against the number of passages is shown in figure (3). The friction coefficient has a moderately high value ranging between 0.3 and 0.4.

## 2) Friction of hBN in air

In air, and in the same tribological conditions, the friction coefficient has a lower value (average value 0.1) (figure 4). In order to check the validity of this results, the same experiment was carried out on another pin on flat tribotester operating under atmospheric conditions. Results (presented in figure 4) show that the friction coefficient stabilizes at a similar value (0.1), in good agreement with the previous value found with the UHV tribotester operating in air.

### CONCLUSION

- Friction of h-BN (flat configuration) in UHV is moderately high (0.3 - 0.4),
- Friction of h-BN (flat configuration) in air has a low value (0.1).

As shown in the literature [1], typical values for h-BN friction in air range from 0.2 to 0.4 (at ambient temperature ; as the bulk material used consisted of small sintered crystallites without any preferential orientation with respect to the sliding direction, the lower value (0.1) in our case may be attributed to the alignment of BN hexagons in the "flat configuration". This must be confirmed in the near future when testing the "edge" BN configuration.

Under vacuum, the "higher" value of the friction coefficient is attributed to the absence of environmental gas (oxygen, water) perhaps as in the case of graphite [2].

Next investigation will concern high resolution analysis of wear debris in order to elucidate the mechanisms responsible of h-BN friction.

### References

- [1] F.P. BOWDEN and D. TABOR, "The friction of lamellar solids", Part II, Oxford at the Clarendon Press, (1964).
- [2] H. ZAIMI, D. PAULMIER, "Influence of oxygen on the friction behaviour of graphite", To be published in J. of Chimie Physique.

## LIST OF FIGURES

Figure 1 : Directionally machined pins and flats from anisotropic Combat (R) BN. (Flat configuration).

Figure 2 : XPS analysis of CVD h-BN with different surface treatments (all concentrations in atomic per cent).

Figure 3 : Friction of h-BN Combat in UHV. Evolution of the friction coefficient against the number of passes (two successive experiments).

Figure 4 : Friction of h-BN Combat in air. Evolution of the friction coefficient.

- a) UHV tribotester under atmospheric conditions,
- b) pin on flat tribometer.

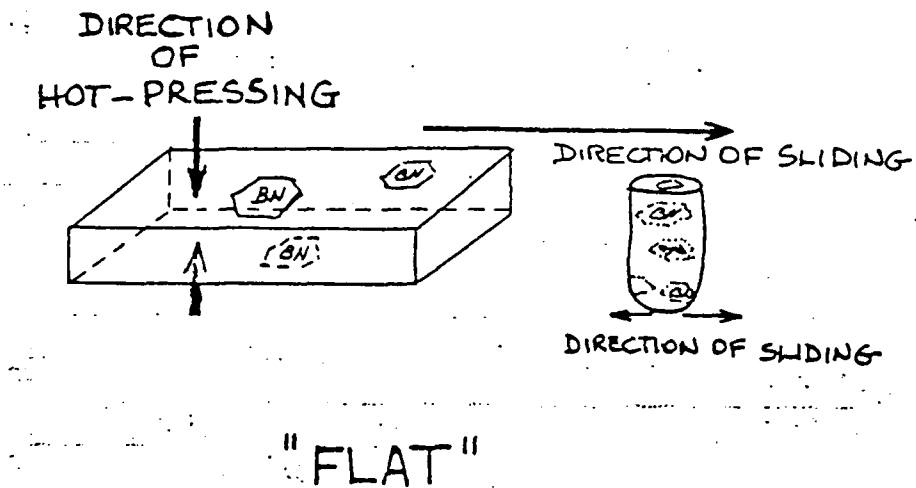


Figure 1

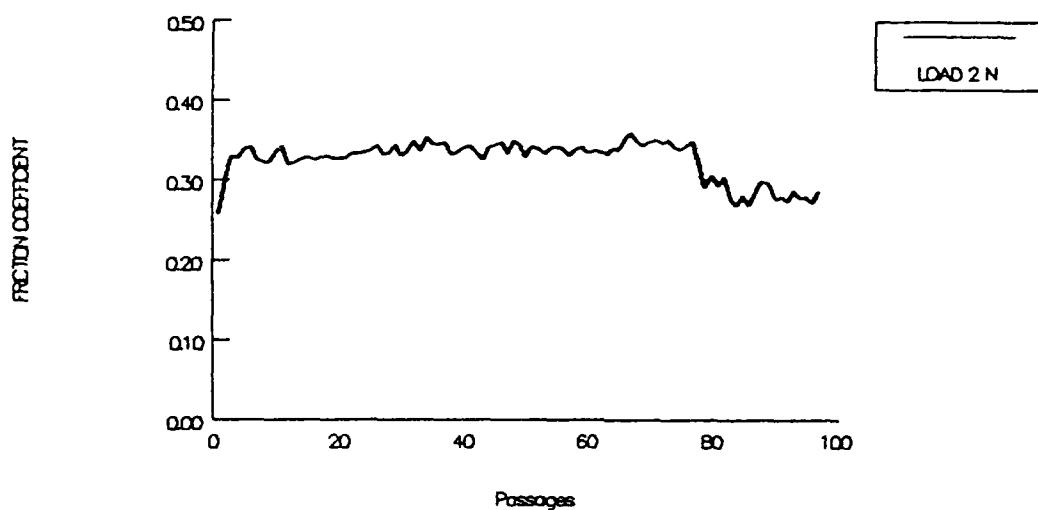
|     | as received | annealing<br>( $\approx 700^{\circ}\text{C}$ ) | ionic etching | annealing<br>( $\approx 700^{\circ}\text{C}$ ) |
|-----|-------------|------------------------------------------------|---------------|------------------------------------------------|
| B   | 26,5        | 46                                             | 46            | 48                                             |
| N   | 23,5        | 42,5                                           | 33            | 34,5                                           |
| C   | 37          | 5                                              | 13            | 10                                             |
| O   | 12          | 6,5                                            | 8             | 7,5                                            |
| B/N | 1,13        | 1,08                                           | 1,4           | 1,4                                            |

all concentrations in atomic per cent

Figure 2

D-65

h.BN Combat/h.BN Combat  
Ultra High Vacuum



h.BN Combat/h.BN Combat  
Ultra High Vacuum

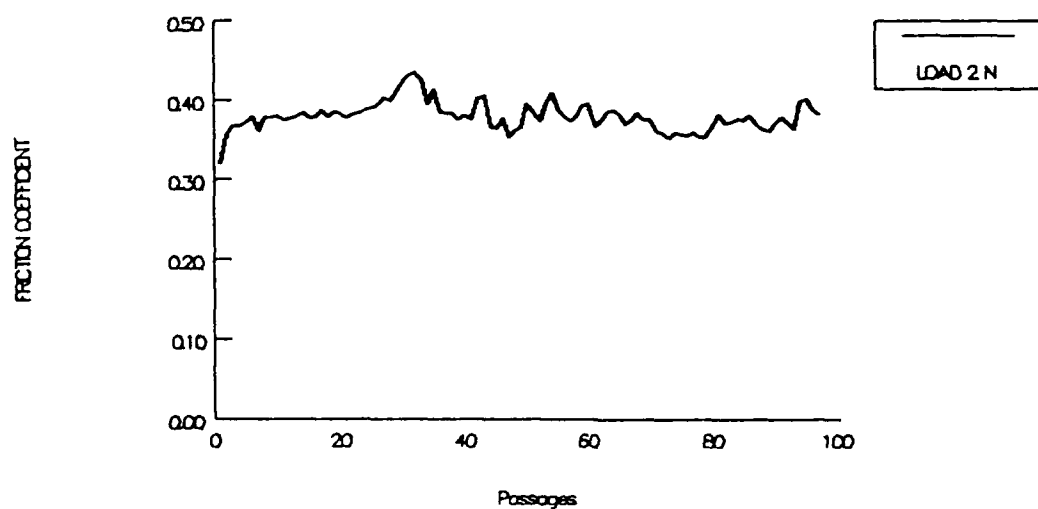


Figure 3

D-66

# h.BN Combat/h.BN Combat in Air

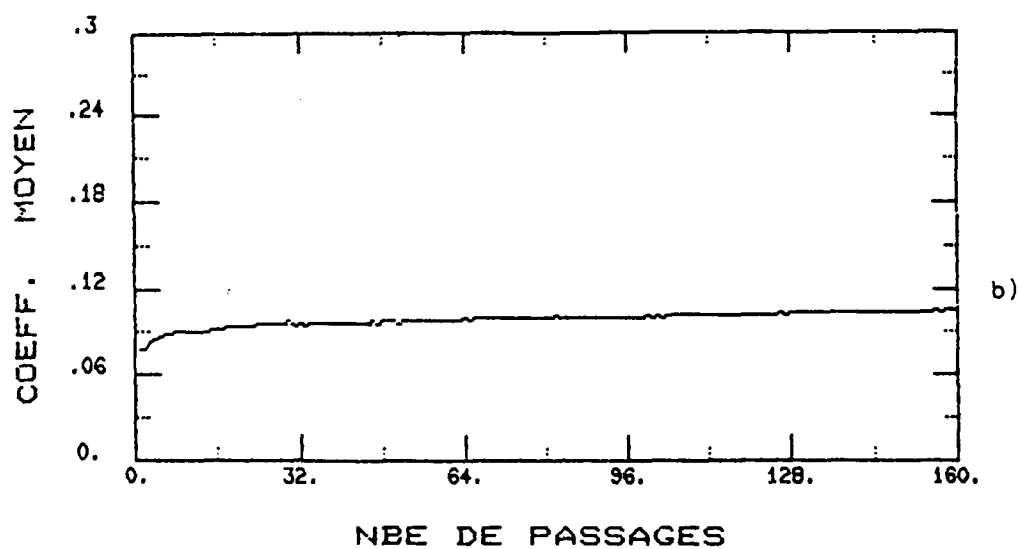
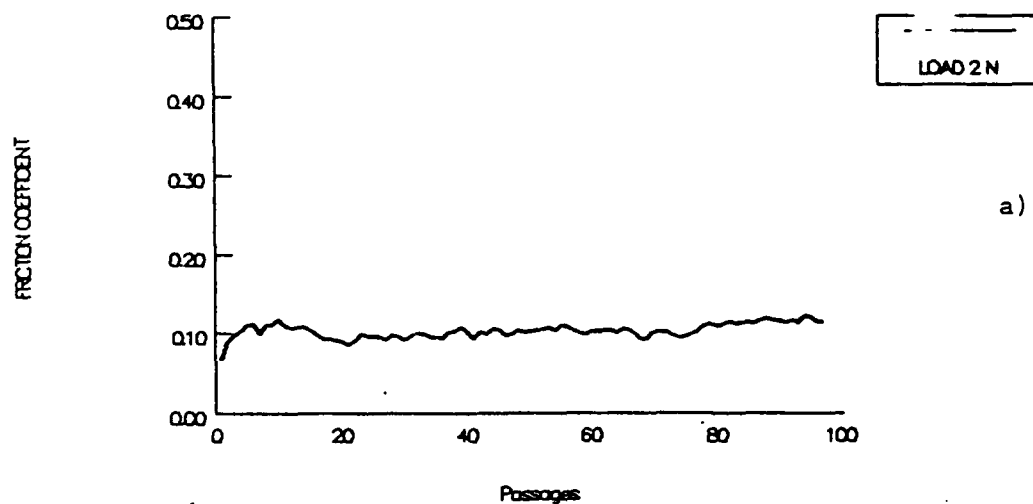


Figure 4

D-67

SORETRIB  
36 avenue Guy de Collongue  
B.P. 163  
69131 ECULLY Cedex

Ecole Centrale de Lyon  
Laboratoire de Technologie des  
Surfaces  
36 avenue Guy de Collongue  
B.P. 163 - 69131 ECULLY Cedex  
fax : 78.43.39.62

DETERMINATION OF TRIBOLOGICAL FUNDAMENTALS OF SOLID LUBRICATED CERAMICS

Contract F 33615-85-C-5087

Monthly report from February 1<sup>st</sup> to February 28<sup>th</sup> 1989

Report n° 5

THE MECHANISM OF THE FRICTION OF HEXAGONAL BORON NITRIDE

IN THE "FLAT CONFIGURATION"

RFG 520765

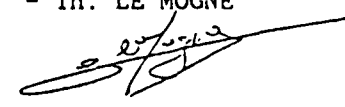
Prepared for :

HUGHES AIRCRAFT COMPANY  
Electro-Optical & Data Systems Group  
Mike GARDOS, Senior Scientist

Prepared by : - J.M. MARTIN

Adm. Div. :

  
- Th. LE MOGNE

  
Etude SORETRIB n° D50.

D-68

THE MECHANISM OF THE FRICTION OF HEXAGONAL BORON NITRIDE  
IN THE "FLAT CONFIGURATION"

I - THE MECHANISM OF THE FRICTION OF HEXAGONAL BORON NITRIDE

The survey of the literature brings out three major (non exclusive) points to explain the friction of hBN, on the tribochemical point of view :

- basal-plane slip of individual boron nitride grain,
- attrition of boron nitride cleavage fragments into minute scrolls,
- shearing of amorphous boron trioxide.

The occurrence of low friction values can be respectively attributed to :

- low value of interplane shear strength,
- rolling of minute scrolls in the interface zone,
- low shear strength of low melting point lubricious boron trioxide.

II - FRICTION OF HBN "FLAT CONFIGURATION" WEAR DEBRIS ANALYSIS

Examining wear debris in the TEM, for our first HBN friction experiments (in air and under vacuum), it immediately appears that the predominant feature observed is small boron nitride flakes originating from slip of individual BN grains (see figures 1, 2, 3).

Nevertheless, attrition and amorphization of BN are sometimes visible, at the same time boron oxide is also analyzed, but as it is present in the Combat BN, it is difficult to decide whether it was formed under friction or originating from the sintering aid. Perhaps, these latter aspects will be more important when testing the "edge configuration" h-BN

The next section is entirely devoted to a high resolution TEM analysis of the mechanisms involved in the "BN small flakes" formation.



### III - HIGH RESOLUTION TRANSMISSION ELECTRON MICROSCOPY OF h-BN WEAR DEBRIS

Wear debris are mainly composed of small BN thin flakes (typically 100 nm thick and 0.5  $\mu$ m large). Very often, sandwiches of BN flakes seem to have been oriented by friction (figure 1). In some cases, it appears that

stacked BN flats have the same morphology and are therefore originating from shearing of the same BN grain (figure 2).

Using the eucentric goniometer stage in the TEM, the structural features of such debris can be studied by electron diffraction, by directing the electron beam either parallel to the flake surface or perpendicular to the flake surface.

First when the BN flake particles are in the observation plane (perpendicular to the electron beam), the selected area electron diffraction pattern (SAD pattern) shows intense hkl reflections corresponding to hexagonal boron nitride, but no 00l reflections, clearly indicating that BN hexagonal atomic layers lie parallel to the flake surface (and therefore to the sliding direction). Moreover, a very weak mutual azimuthal misorientation of the BN atomic layers is evidenced in the diffraction, this suggests that the interface between BN flakes is concentrated in a few shear planes only and that turbostratic BN is not present. Sometimes the rotation between individual BN flats produces Moiré fringes as in figure (3).

Second, when the electron beam is directed along direction 2 (parallel to the BN layers) by tilting the preparation, the SAD pattern presents higher order 00l reflections whose arcs are very little open (namely 002, 004, 006) figure 4. This indicates the perfection of the parallelism between individual layers, which has been conserved after friction.

The electron diffraction study strongly suggests that, under friction, some BN crystallites from the specimen have been sheared or slid along the (00.1) crystallographic direction (sliding direction in this case) and that sliding between BN crystal only occurs in a few BN atomic layers (without generating turbostratic boron nitride within the BN stacks).

In principle, the electron diffraction (figure 4) with the BN planes "edge on" compared to the observation plane, permits 002 lattice fringes imaging by using a suitable objective aperture ; but in our case there are some difficulties to do this principally due to the fact that h-boron nitride (at the opposite of graphite) is not a good conductor of heat. So, the crystallites "edge on" are quite unstable under the electron beam and vibrates, and this is not suitable for high magnification in the TEM. Nevertheless, we succeeded to obtain some micrographs of 002 lattice fringes in the interface zone between two stacks of h-BN crystallites in very thin areas (figure 5). It represents the orthogonal projection of BN layers which have been sheared in the interface zone. Looking at this picture it immediately appears that the BN planes orientation is roughly preserved and that crystals have been slipped but not separated from one another by cleavage. Although some dislocations are visible and may participate to the deformation by their movement along the (001) direction, they cannot

explain sliding along large distance when concentrated in a few planes only.

#### IV - CONCLUSION

Therefore, it is believed that sliding of low energy BN shear planes allows large bi-dimensionnal displacements in the crystal and may explain the friction process (although that it involves a considerable amount of work). But more work is necessary to confirm this fundamental point and to precise the role of oxygen in this configuration.

The next investigation will concern the role of oxygen in hBN friction.

## LIST OF FIGURES

Figures 1, 2 : TEM micrographs of hBN friction "flat configuration" wear fragments (typical feature). Note the aspect of slip of individual BN grains.

Figure 3 : Friction-modified BN grain by rotation of basal plane stacks (presence of rotation Moiré fringes).

Figure 4 : SAD pattern of a slip BN grain showing (001) reflections of the BN basal planes.

Figure 5 : High resolution TEM micrograph of the slip interface between two BN stacks (002 lattice fringes -  $d = 3.33 \text{ \AA}$ ).

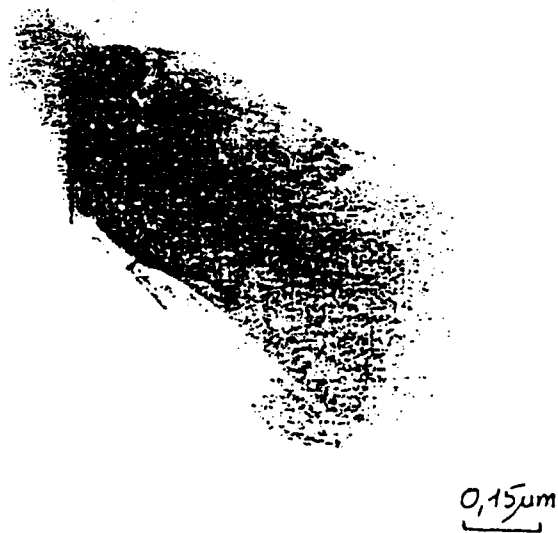
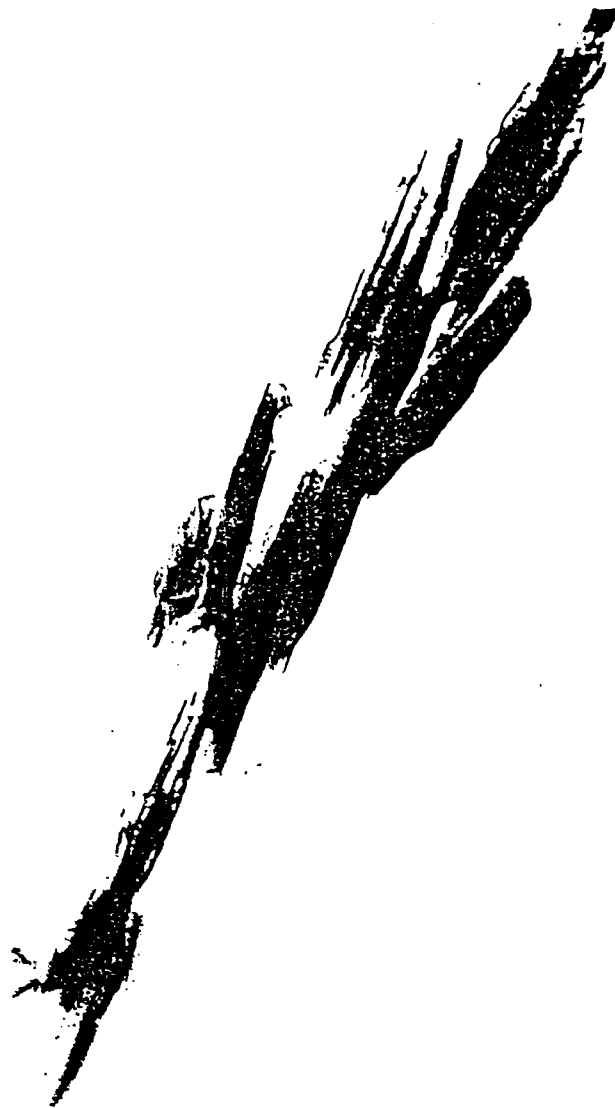


Figure 1

D-73

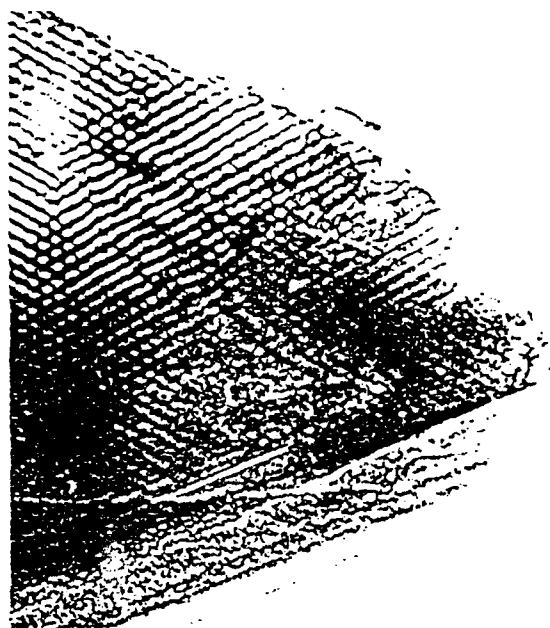


0.1 $\mu$ m



Figure 2

D-74



200Å

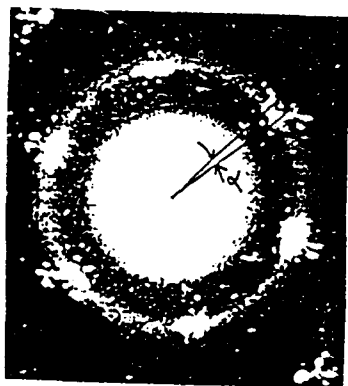
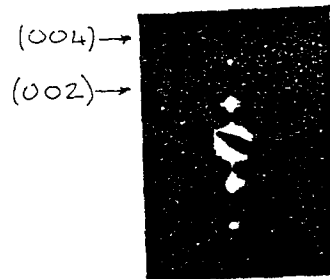


Figure 3

D-75



500Å

Figure 4

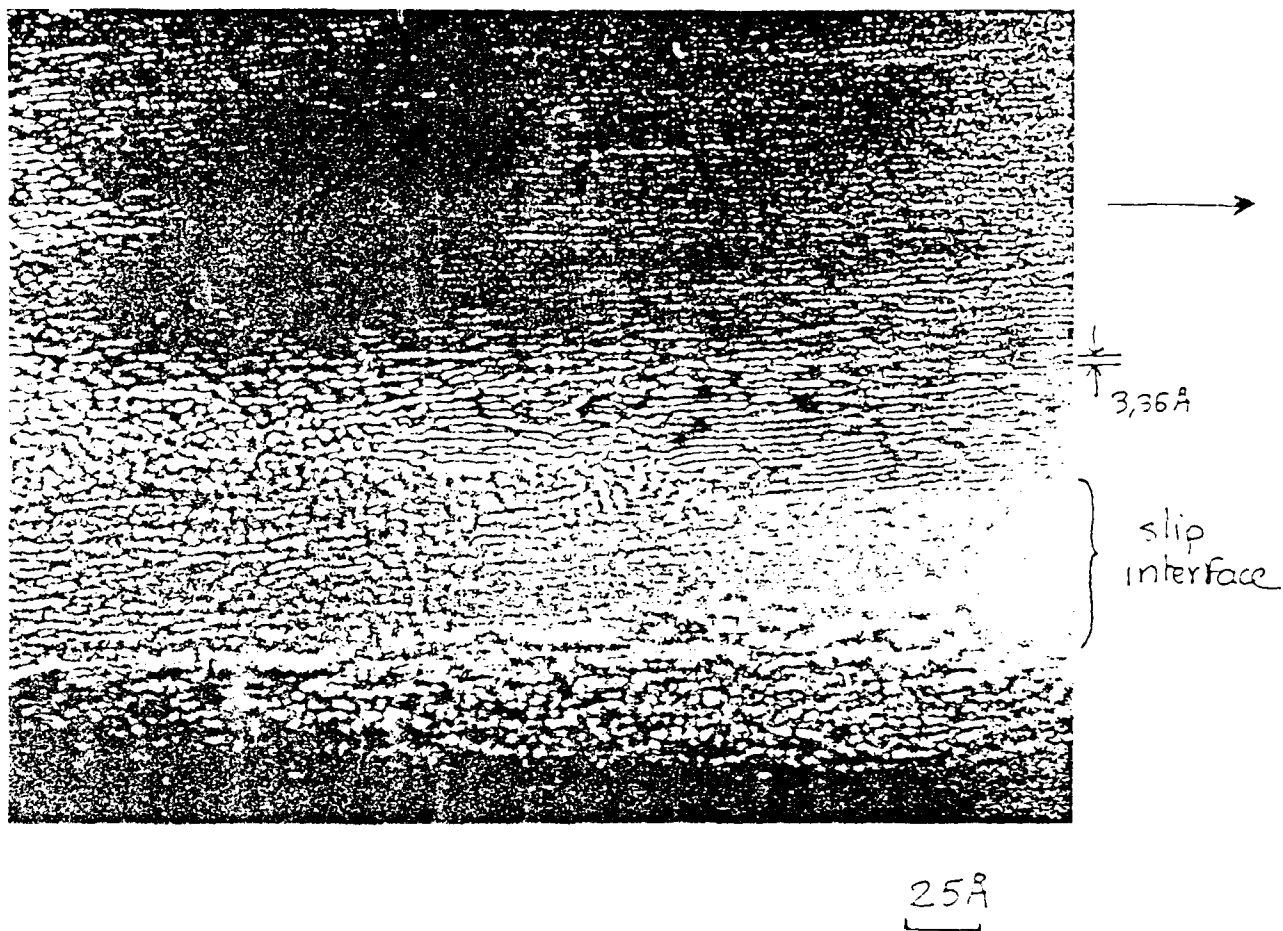


Figure 5

D-77



SORETRIB  
36 avenue Guy de Collongue  
B.P. 163  
69131 ECULLY Cedex  
FRANCE

Ecole Centrale de Lyon  
Laboratoire de Technologie des  
Surfaces  
36 avenue Guy de Collongue  
B.P. 163 - 69131 ECULLY Cedex  
FRANCE

DETERMINATION OF TRIBOLOGICAL FUNDAMENTALS OF SOLID LUBRICATED CERAMICS

Contract F 33615-85-C-5087

Monthly report from March 1<sup>st</sup> to March 31<sup>th</sup> 1989

Report n° 6

THE OBTENTION OF CONTAMINATION FREE AND STOECHEIOMETRIC BN SURFACES  
FROM COMBAT SPECIMEN

RFG 520765

Prepared for :

HUGUES AIRCRAFT COMPANY  
Electro-Optical & Data systems Group  
Mike GARDOS, Senior Scientist

Prepared by : - J.M. MARTIN

Adm. Div.

- Th. LE MOGNE

Etude Soretrib n° D50

Tel : 78.33.81.27

Fax : 78.43.39.62

Télex : ECE LY 310356F

**D-78**

## CONTENTS

INTRODUCTION..... p 1

I - ANALYZING STANDARDS BY XPS..... p 1

II - OPTIMIZING THE COMBAT h-BN SURFACE CHEMISTRY..... p 3

CONCLUSION..... p 6

BIBLIOGRAPHIE..... p 7

INTRODUCTION

Now, we have received the COMBAT h-BN specimens from SAPHIRWERK (namely "flat and edge" configurations). To continue our work, we decided to carry out some preliminary friction tests under UHV, with these new specimens, and with the same procedure that previously described for the h-BN/h-BN combination (see report III). Surprisingly, we found lower friction values, for both configurations, generally inferior to 0.15. Although very interesting, this result is in disagreement with the friction value previously obtained under UHV in the same conditions (0.3-0.4) (see report III). Moreover, we already reported some difficulties to prepare and characterize COMBAT h-BN surfaces, as far as carbon contamination, presence of oxygen and boron/nitrogen stoichiometry are concerned. Consequently, we decided to study in more details the surface of h-BN specimens, depending on the cleaning procedure. The reason is that the initial friction value of the prepared surface is thought to play a key role in the wear process of the h-BN system and that basically it is necessary to know what is beginning to slide on what, to have a good interpretation of the data obtained.

I - ANALYZING STANDARDS BY XPS

Pure h-BN powder, pure boron trioxids ( $B_2O_3$ ) and boron carbide ( $B_4C$ ) (from Fluka AG) were analyzed by XPS, with the purpose to obtain standard values for quantitative analysis of boron, nitrogen and oxygen and to measure chemical shifts of B1s, N1s, C1s, and O1s in their respective chemical bonding. Our results are given in table 1, where available literature data are also shown. Generally it appears that standards are of good quality because XPS peaks (B1s, N1s and O1s) have only one contribution. At the same time, our data are in excellent agreement with values already published. Concerning B1s, the binding energy shifts from 186.3 eV for boron carbide to 187.8 eV for elemental boron to 190.3 eV for boron nitride and to 193.4 eV for boron oxide, so that these different contributions can be easily distinguished in the XPS spectra. Concerning C1s, the binding energy shifts from 284.2 eV for graphitic carbon [1] to 283 eV for boron carbide and to 284.8 eV for environment contamination (hydrocarbon) ; here it is more difficult to separate the different contributions with the equipment at hand.

| BN              | [1]   | [2]   | [3]   | [6]   | [4]   | our results |
|-----------------|-------|-------|-------|-------|-------|-------------|
| B1s             | 190.3 | 190.3 | 190.6 | 190.2 | 190.6 | 190.3       |
| N1s             | 397.9 | 398.0 | 398.3 | 397.6 | 398.3 | 397.9       |
| $\delta(N - B)$ | 207.6 | 207.5 | 207.7 | 207.4 | 207.7 | 207.6       |

| B <sub>2</sub> O <sub>3</sub> | [5]   | [4]   | [1]   | our results |
|-------------------------------|-------|-------|-------|-------------|
| B1s                           | 192.4 | 193.4 | 193.1 | 193.4       |
| O1s                           | 532.6 | 533   | /     | 533         |
| $\delta(O - B)$               | 340.2 | 339.6 | /     | 339.6       |

| B metal | [5]   | [6]   |
|---------|-------|-------|
| B1s     | 187,8 | 187,7 |

| H <sub>3</sub> BO <sub>3</sub> | [5]   |
|--------------------------------|-------|
| B1s                            | 192,8 |

| B <sub>4</sub> C | [6]   | our results |
|------------------|-------|-------------|
| B1s              | 186,3 | 186,3       |
| C1s              | 283,0 | 283,0       |
| $\delta(O - B)$  | 96,7  | 96,7        |

Table 1 : B1s, N1s and O1s binding energy (eV) obtained by XPS for different standards (available data from the literature are also shown).

## II - OPTIMIZING THE COMBAT h-BN SURFACE CHEMISTRY

### II.a) The effect of ion etching

COMBAT h-BN, grade A, is a polycrystalline material containing boron trioxide ( $B_2O_3$ ) as a sintering aid (6 % by weight). Table 2 shows the effect of argon etching at 3 KeV, on the composition of the h-BN surface of as received specimens (the first supply of COMBAT specimens). It is shown :

- a BN stoichiometry deviation, the B/N ration being of 1.5 after etching, surprisingly, the selective sputtering of nitrogen does not shift the binding energy of B1s,

- Argon implantation, as shown by the X-ray analysis of the surface fragments,

- a change in the colour of the h-BN surface, from white opalescent to tarnished and brown,

- a modification in the carbon chemical form. Sputtering cleaning does not eliminate carbon from the h-BN surface (13 % atomic), moreover a change in the C1s binding energy indicates that carbon is graphitized and/or carbide,

- the oxygen content is roughly preserved, under a boron oxide chemical bonding, but the stoichiometry deviates from  $B_2O_3$ .

|     | as received              |                    | after etching  |             |
|-----|--------------------------|--------------------|----------------|-------------|
|     | B.E.                     | % atomic           | B.E.           | % atomic    |
| B1s | 190.3<br>191.9           | 24.7<br>6.2        | 190.3<br>192.7 | 29.1<br>6.3 |
| N1s | 398.1                    | 25.7               | 397.8          | 19.5        |
| C1s | 284.65<br>286.4<br>288.1 | 17.6<br>5.4<br>1.2 | 283.7          | 13.5        |
| O1s | 532.1<br>534.6           | 16.8<br>1.5        | 532.5          | 25.1        |
| B/N | /                        | 1                  | /              | 1.49        |

Table 2 : Etching effect on the COMBAT BN surface : binding energy (B.E.) and atomic concentration.

## II.b) The effect of annealing

We decided to modify our specimen preparation procedure before tribotesting the whole set of new COMBAT specimens, with three purposes in mind :

- eliminate carbon from h-BN surfaces,
- preserve the BN stoichiometry,
- characterize the residual boron oxide from the sintering aid.

The table 3 illustrates the effect of three cleaning sequences on the characterization of h-BN flat surfaces by XPS :

- annealing at 450°C under UHV,
- sputter cleaning with Argon (3 KeV),
- annealing at 450°C under UHV.

After annealing at 450°C, it appears that the carbon content has disappeared, that the BN stoichiometry is preserved ( $B/N \approx 0.9$ ) and that, in these conditions, the h-BN surface is easily cleaned. When the heat treated BN surface is sputter cleaned, the carbon appears again, but under carbide and/or graphitic organization, it seems that boron carbide is also detected with the B1s XPS peak. Annealing of these sputter cleaned BN surface does not remove carbon. It is wondering what is the effect of this treatment on friction ?

The same procedure can be applied to the h-BN pin (flat or edge configuration) see table 4. The conclusions are the same as far as B, N and C are concerned.

The characterization of oxygen is another problem.

|     | Annealed at 450°C<br>in UHV |          |
|-----|-----------------------------|----------|
|     | B.E.                        | % atomic |
| B1s | 190.3                       | 42.4     |
| N1s | 397.9                       | 44.2     |
| C1s | /                           | /        |
| O1s | 532.8                       | 13.4     |
| B/N | /                           | 0.86     |

Table 4 : Analyze of h-BN pin after annealed at 450°C

|           | Step 1 : cleaned with propanol 2     |                  | Step 2 : annealed at 450°C in UHV    |                  | Step 3 : argon etching              |                  | Step 4 : Annealed at 450°C in UHV                       |                    |
|-----------|--------------------------------------|------------------|--------------------------------------|------------------|-------------------------------------|------------------|---------------------------------------------------------|--------------------|
|           | B.E.                                 | % atomic         | B.E.                                 | % atomic         | B.E.                                | % atomic         | B.E.                                                    | % atomic           |
| B1s       | /<br>190.3<br>192.5                  | /<br>35.3<br>1.6 | /<br>190.3<br>192.8                  | /<br>41.9<br>3.0 | 188.3<br>190.3<br>/                 | 3.3<br>45.6<br>/ | 188.4<br>190.3<br>193.5                                 | 1.5<br>41.9<br>1.5 |
| N1s       | 397.9                                | 39.2             | 397.9                                | 45               | 397.8                               | 36.2             | 397.8                                                   | 35.1               |
| C1s       | /<br>284.5                           | /<br>16.2        | /<br>/                               | /<br>/           | 282.4<br>284.2                      | 4.1<br>3         | 282.4<br>283.9                                          | 5.5<br>4.4         |
| O1s       | 532.2                                | 7.7              | 532.6                                | 10.1             | 532.4                               | 7.7              | 532.7                                                   | 8.9                |
| $\delta$  | N - B : 207.6 eV<br>O - B : 339.7 eV |                  | N - B : 207.6 eV<br>O - B : 339.8 eV |                  | N - B : 207.5 eV<br>B - C : 94.1 eV |                  | N - B : 207.5 eV<br>O - B : 339.2 eV<br>B - C : 94.0 eV |                    |
| B/N ratio | /                                    | 0.90             | /                                    | 0.93             | /                                   | 1.26             | /                                                       | 1.19               |

Table 3 : Annealed and etching effect on the h-BN surface : binding energy and atomic concentration.

## II.c) XPS analysis of oxygen on the h-BN surface

As we earlier mentioned the O1s XPS signal peaks at 532.3 eV, is very near from the binding energy of oxygen in pure boron trioxide and shows only one contribution. Surprisingly, the B1s peak corresponding to B-O ( $E_B = 192.4$  eV) is practically absent in the XPS spectra, so that the  $B_2O_3$  stoichiometry is never obtained. In the propanol cleaned specimens O/B ratio is 5.7 and O/B is even more after annealing (the O/B ratio is 1.5 in  $B_2O_3$ ). At the same time, the literature indicates that annealing at 450°C has no chemical effect on boron trioxide composition [5].

As we checked by SIMS that water was not present in the h-BN structure (see report IV), the excess of oxygen was attributed to gas entrapped in the BN microstructure, but this is in disagreement with the O1s XPS peak, the binding energy of which corresponding to O-B bonding. We can observe twice more oxygen with the old specimens than with the new ones (see table 5).

|                    | as received   |          |            |          |
|--------------------|---------------|----------|------------|----------|
|                    | November 1987 |          | April 1989 |          |
|                    | B.E.          | % atomic | B.E.       | % atomic |
| B1s (B-N)<br>(B-O) | 190.3         | 24.7     | 190.3      | 35.3     |
|                    | 191.9         | 6.2      | 192.5      | 1.6      |
| O1s                | 532.1         | 16.8     | 532.2      | 7.7      |
| B oxidized/O       | /             | 0.37     | /          | 0.2      |

Table 5 : Oxygen quantities analyzed in the old and new h-BN COMBAT.

## CONCLUSION

The COMBAT h-BN specimen have a complex nature due to the presence of boron oxide from the sintering aid. It has been observed :

- that the first supply of specimens contain twice more oxygen than the second one,
- that the boron oxide species do not have the  $B_2O_3$  stoichiometry (oxygen is largely surstoichiometric),
- that the cleaning procedure does not remove oxygen from the surface.

It is thought that oxidized species play a key role in the friction process of BN under vacuum.

Analyzing several cleaning procedure, it has been shown :

- that ion etching modifies the BN stoichiometry and changes the chemical form of carbon contaminant,
- that annealing at 450°C preserves the BN stoichiometry and eliminates carbon from the surface,
- that etching a heat treated BN surfaces makes carbon to appear as a bulk contaminant.



## BIBLIOGRAPHY

- [1] C.D. Wagner, W.M. Riggs, L.E. Davis, J.F. Moulder and G.E. Merilenberg (Eds) Handbook of X-Ray Photoelectron Spectroscopy, Perkin Elmer Corp., Minesota, 1979.
- [2] Shigeni Kohiki, Takuhi Ohmura and Kenji Kusao, J. Electron Spectroscopy Relat. Phenom, 31 (1983) 85-90.
- [3] K. Hamrin, G. Johansson, U. Gelius, C. Nordling and K. Siegbahn, Phys. Scr, 1 (1970) 277.
- [4] D.J. Joyner and D.M. Hercules, J. Chem. Phys. 72 (1980) 1095.
- [5] J. Kiss, K. Revesz and F. Solymosi, Applied Surface Science 37 (1989) 95-110.
- [6] Results obtained by Science and Surface Company with an SSX 100 apparatus. Ecully, FRANCE.

SORETRIB  
36 avenue Guy de Collongue  
69131 Ecully Cedex  
FRANCE

Ecole Centrale de Lyon  
Laboratoire de Technologie des  
Surfaces  
URA CNRS 855  
36 avenue Guy de Collongue  
B.P. 163 - 69131 ECULLY Cedex  
FRANCE

DETERMINATION OF TRIBOLOGICAL FUNDAMENTALS OF SOLID LUBRICATED CERAMICS

Contract F 33615-85-C-5087

Monthly report from April 1<sup>st</sup> to April 29<sup>th</sup>

Report n° 7

FRICTION OF PYROLYTIC h-BN UHV. ROLE OF SURFACE CHEMISTRY AND  
OF THE CRYSTALLOGRAPHIC ORIENTATION

RFG 520765

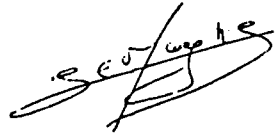
Prepared for :

HUGUES AIRCRAFT COMPANY  
Electro-Optical & Data Systems Group  
Mike GARDOS, Senior Scientist

Prepared by : - J.M. MARTIN

Adm. Div. :

  
- Th. LE MOGNE

  
Etude Soretrib n° D50

Tél : 78.33.81.27

Fax : 78.43.39.62

Télex : ECE LY 310856F

D-87

FRICTION OF PYROLYTIC h-BN UNDER UHV. ROLE OF SURFACE CHEMISTRY AND OF THE  
CRYSTALLOGRAPHIC ORIENTATION

Friction experiments are conducted under UHV (10 nPa) with COMBAT h-BN pins and flats. The tribological conditions are :

- normal load : 2 N,
- sliding speed :  $0,6 \cdot 10^{-3}$  m/s,
- length of the stroke :  $3 \cdot 10^{-3}$  m,
- number of passes : 75,
- temperature : 300 K.

These conditions were the same that for the study of  $\alpha$ -SiC friction. The calculated mean Hertz pressure is 0.3 GPa.

Two specimen preparations were used :

- cleaning with propanol-2,
- annealing at 450°C.

The surface chemistry obtained with these procedures was studied by XPS, and were already detailed (see report 6). We mention here that annealing at 450°C removes carbon contamination from the top surface, but does not remove oxygen and boron oxide.

For each configuration, we found the same surface chemistry after annealing (see table 1).

|   | FLAT     |           | EDGE     |           |
|---|----------|-----------|----------|-----------|
|   | propanol | annealing | propanol | annealing |
| B | 37%      | 43%       | 39%      | 42%       |
| N | 39%      | 47%       | 41%      | 47%       |
| O | 8%       | 8%        | 8%       | 10%       |
| C | 16%      | 2%        | 12%      | 1%        |

Table 1

Two crystallographic orientation systems were studied :

- pin (*flat configuration*) against flat (*flat configuration*),
- pin (*edge configuration*) against flat (*edge configuration*), the edge BN basal planes being parallel to the sliding direction.

It is worthy to note that, among the nine possible *edge/flat* combinations, the two situations that we chose here are the two extremes ones, the others are thought to give intermediate results.

To compare, some similar friction tests were performed in ambient air, but with another tribotester. In this case, the h-BN specimens were cleaned with propanol-2.

## RESULTS

### - Friction under UHV

For each configuration (flat/flat and edge/edge), friction tests were carried out on different specimens and duplicated to show the reproductibility. (see figure 1 for as received BN specimens and figure 2 for annealed specimens).

Friction results are summarized in figure 3 for the two specimen combinations and for the two preparation procedures (four tests). The main observations are :

- friction coefficients range from  $\mu=0.35$  to  $\mu=0.7$  and are quickly stabilized. The results obtained with propanol cleaning samples are in agreement with data of ROWE and BUCKLEY who showed that the friction coefficient of boron nitride under vacuum and not annealed was about 0.4-0.5 [1],

- that friction values are quite reproducible (see figures 1 and 2),
- that, without annealing, friction coefficients are lower than those after annealing (carbon has been removed in these conditions),

- that, without annealing, the trend is that the *flat configuration* gives lower friction values than the *edge configuration* ; this effect is not very important as far as friction is concerned (the effect on wear is also pronounced and will be discussed later).

- that after annealing the friction values increase to 0.65-0.7 for both configurations.

- Friction in air. Comparison with vacuum

Friction curves are shown in figures 4, 5, 6 with different presentations. It can be concluded :

- that friction of COMBAT h-BN in air gives very low friction values ( $< 0.1$ ) which are very well stabilized,
- that the effect of the crystallographic orientation is practically negligible in air.

It can be thought that, in these conditions, the influence of surface contaminant (carbon,...) is decisive ; this is in agreement with the prediction of TABOR [1].

- Conclusion

To conclude on this set of friction experiments with h-BN COMBAT specimen, it can be stated :

- that h-BN friction drastically depends on the environmental conditions (a decrease of a factor 4 from UHV conditions compared to ambient air)
- that friction of h-BN is highly dependent on the presence of contamination on the surface, whatever the crystallographic orientation may be,
- that annealed h-BN surfaces give higher friction values,
- that generally friction is only slightly influenced by the crystallographic orientation of h-BN surfaces. However it seems the *flat* configuration gives lower values than the edge configuration under UHV.

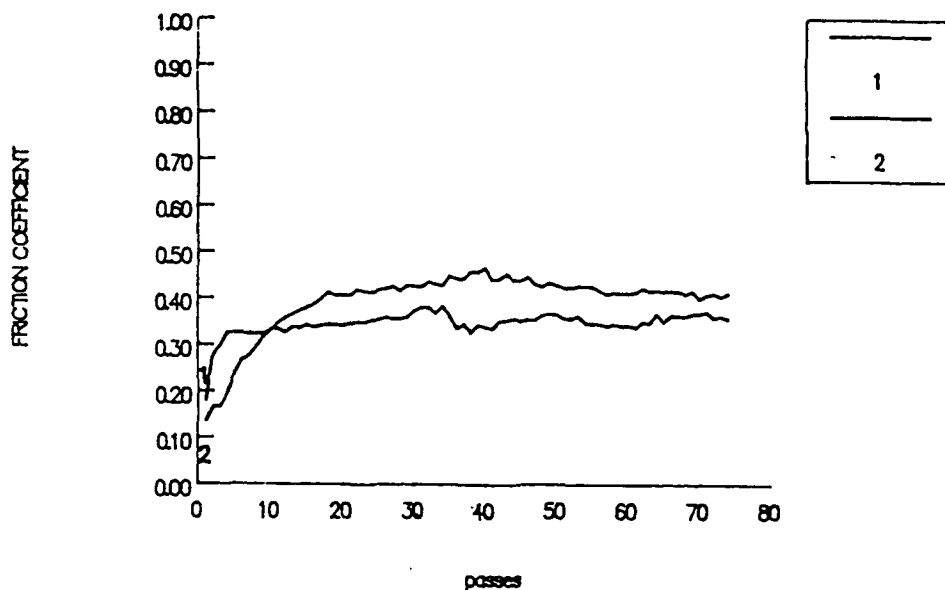
The next report will be concerned with the study of wear of these specimens.

REFERENCES

- [1] F.P. BOWDEN, D. TABOR, "The friction of lamellar solids", Oxford, Clarendon Press, (1964).

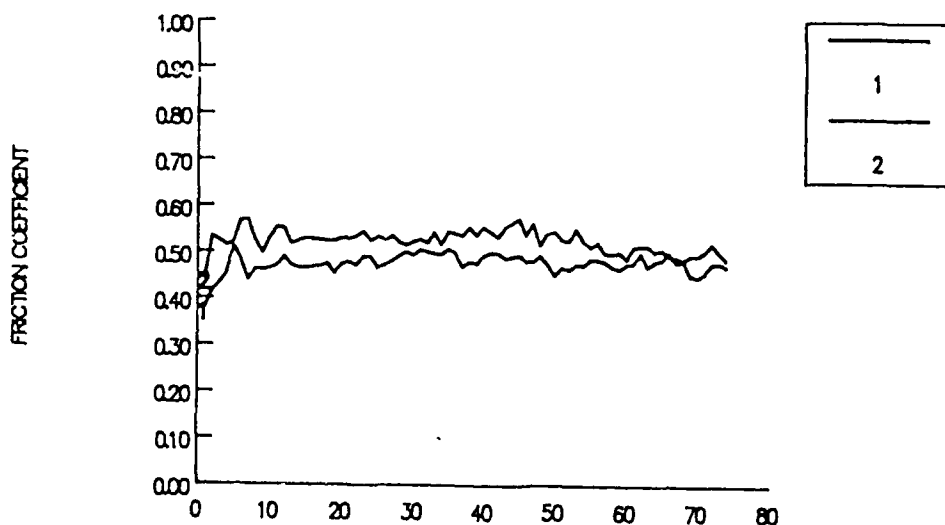
# h BN Combat Flat \ Flat

Ultra High Vacuum (Propanol)



# h BN Combat Edge \ Edge

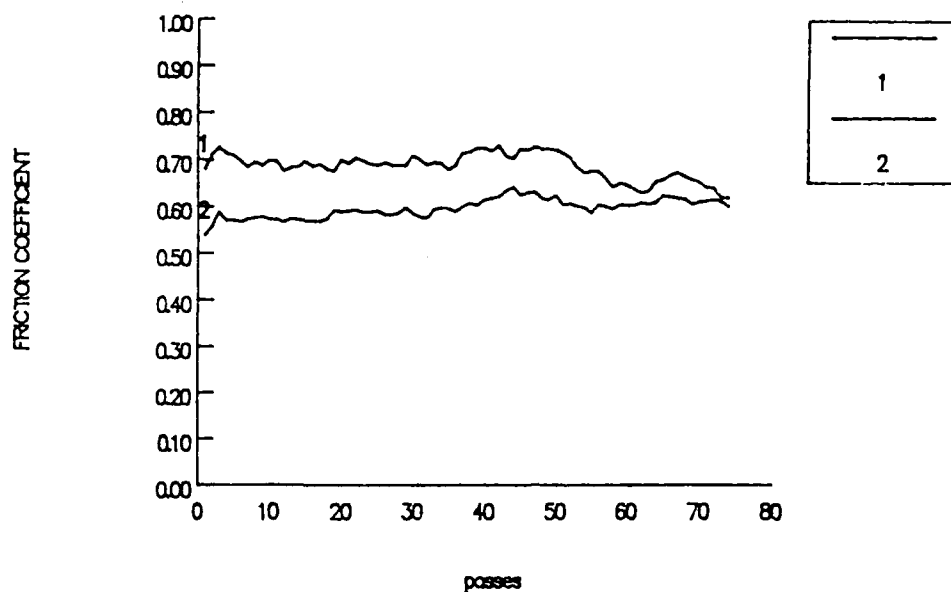
Ultra High Vacuum (Propanol)



D-91

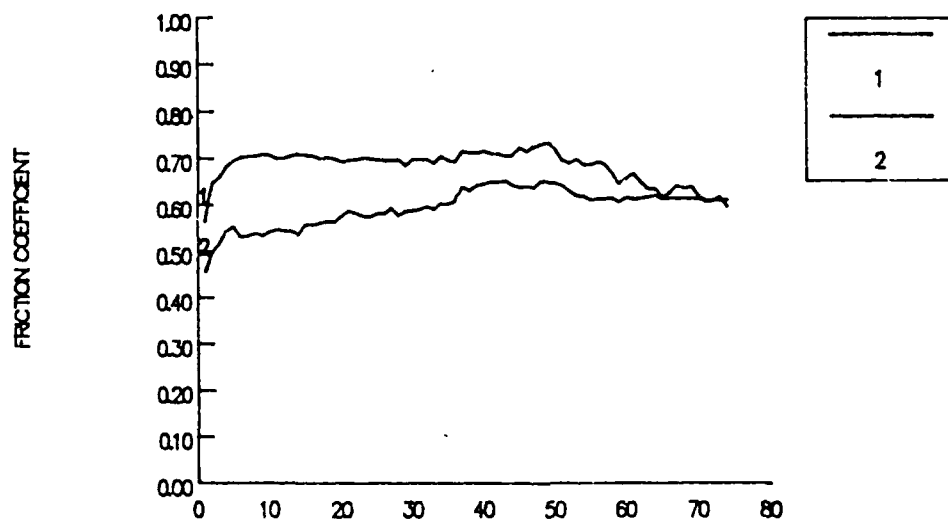
# h BN Combat Flat \ Flat

## Ultra High Vacuum (Annealing)



# h BN Combat Edge \ Edge

## Ultra High Vacuum (Annealing)



# h BN Combat \ h BN Combat

## Ultra High Vacuum

FRICTION COEFFICIENT

D-93

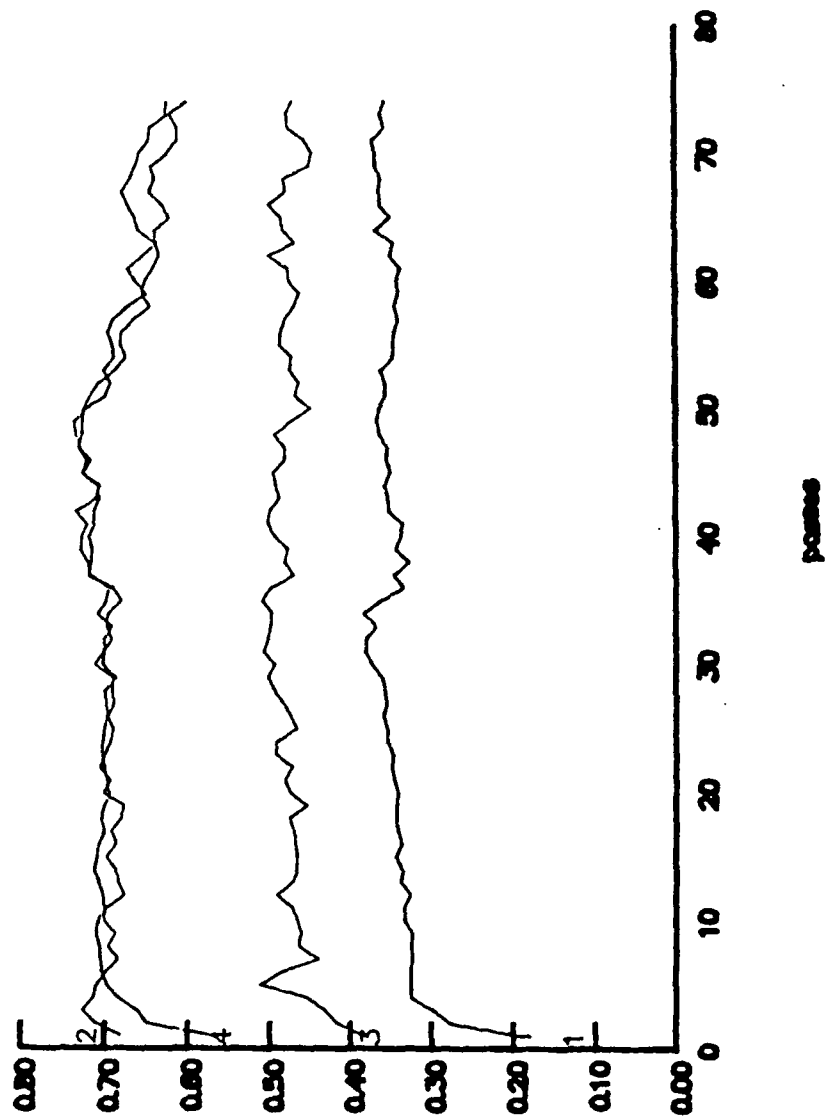


Figure 3



# h BN Combat \ h BN Combat

## Ultra High Vacuum / Air

FRICITION COEFFICIENT

D-94

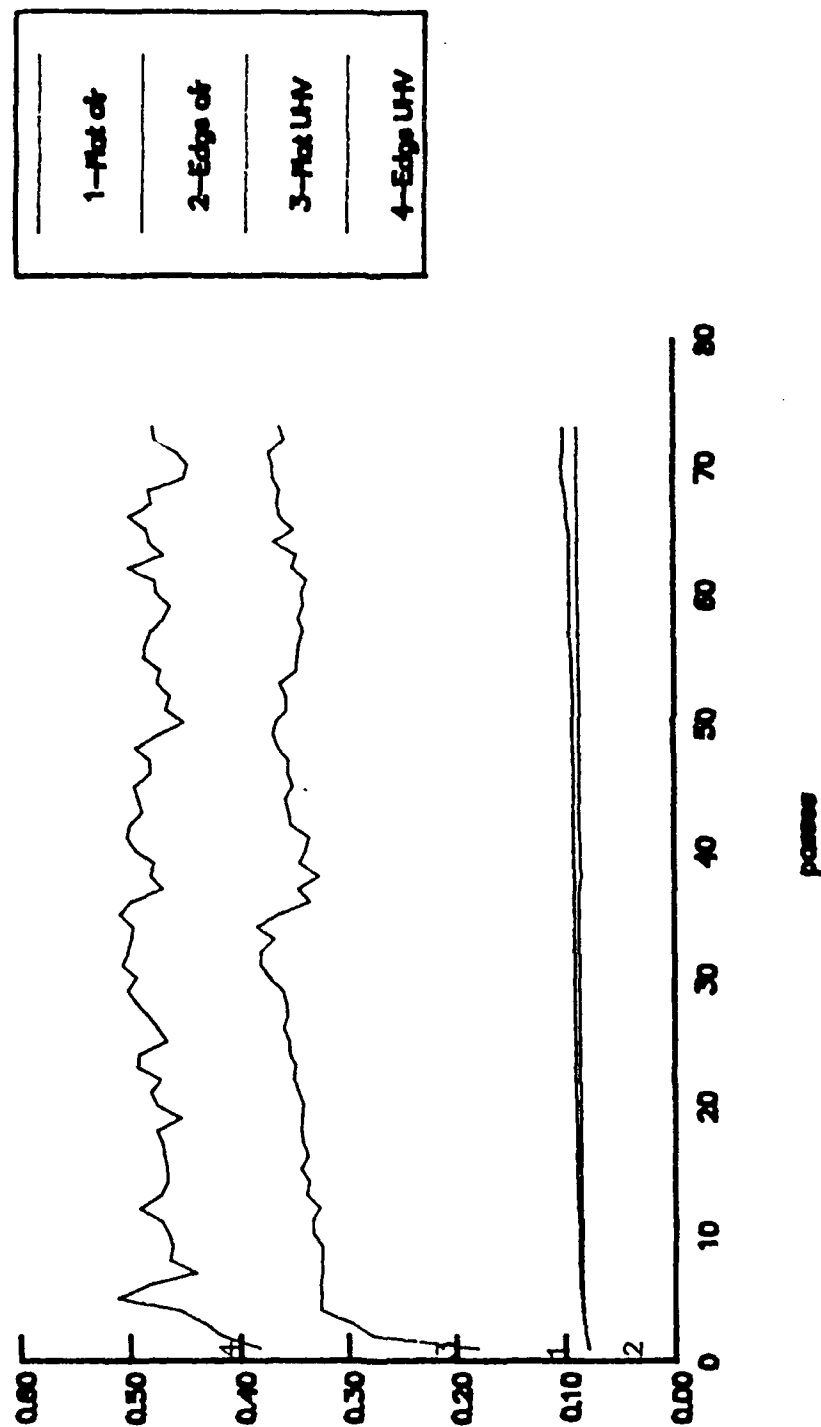
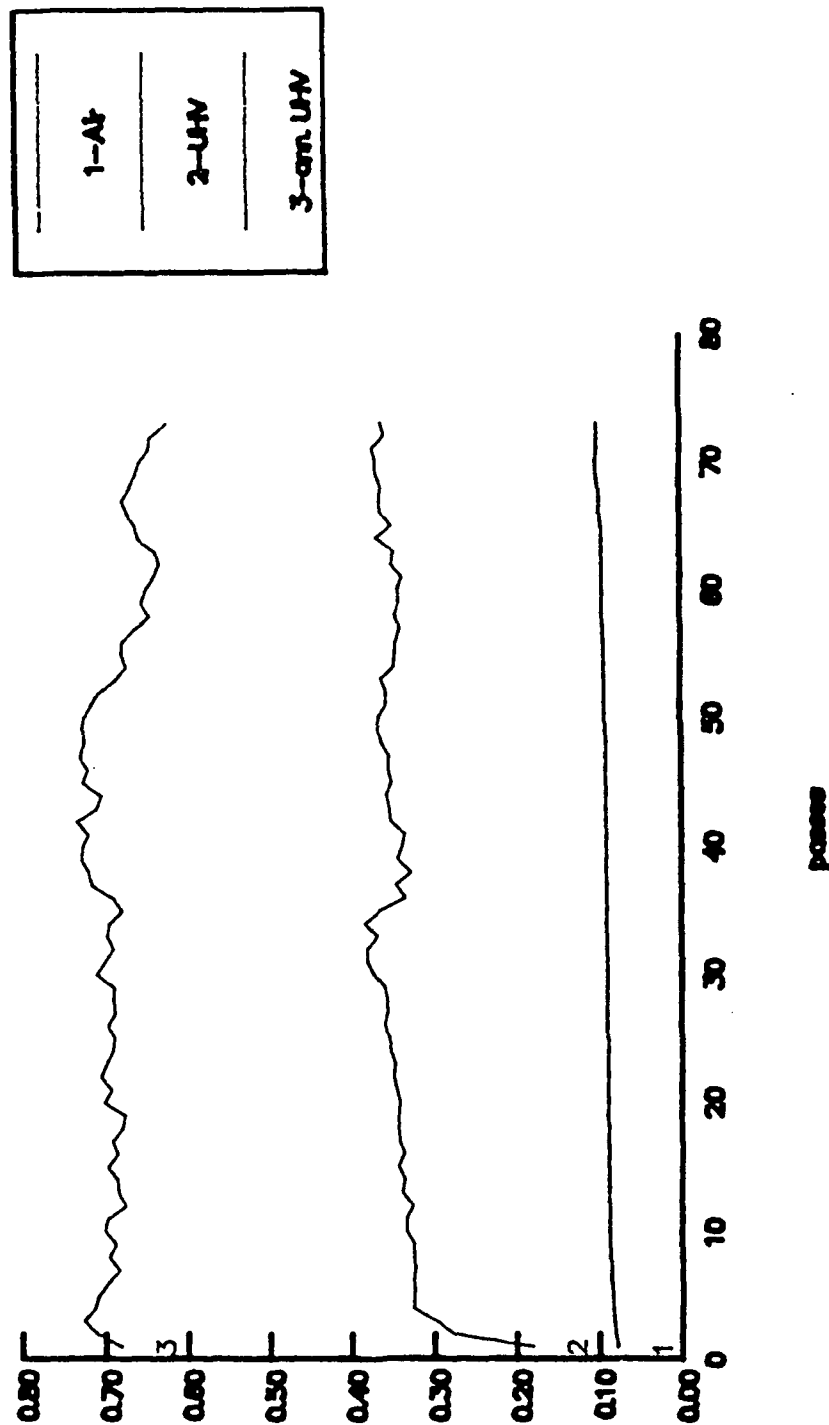


Figure 4

# h BN Combat \ h BN Combat

## Flat \ Flat Air and UHV



FRICTION COEFFICIENT

D-95

Figure 5

# h BN Combat \ h BN Combat Edge \ Edge Air and UHV

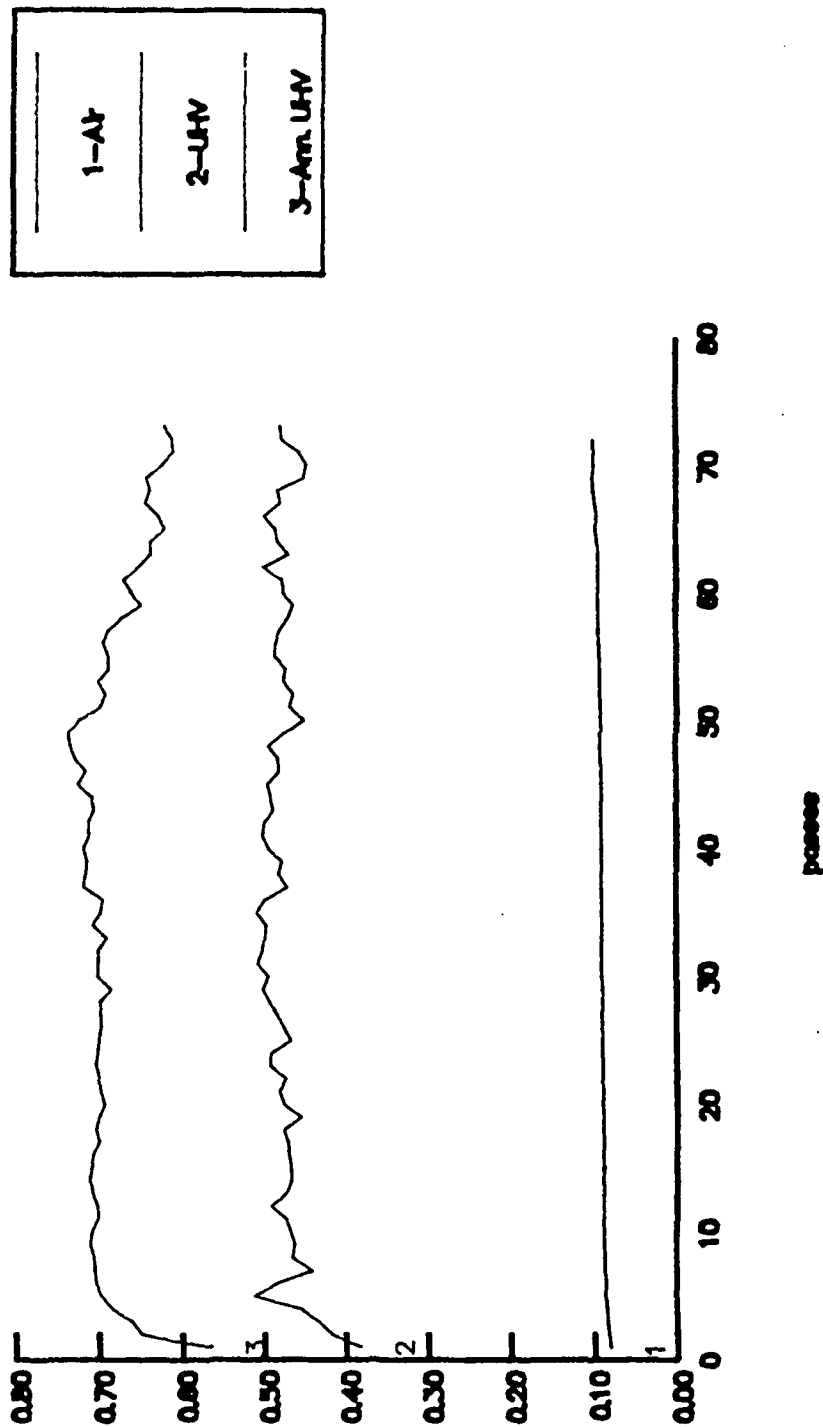


Figure 6

96-4

SORETRIB  
36 avenue Guy de Collongue  
69131 ECULLY cedex  
FRANCE

Ecole Centrale de Lyon  
Laboratoire de Technologie des  
Surfaces  
URA CNRS 855  
36 avenue Guy de Collongue  
B.P. 163 - 69131 ECULLY Cedex  
FRANCE

DETERMINATION OF TRIBOLOGICAL FUNDAMENTALS OF SOLID LUBRICATED CERAMICS

Contract F 33615-85-C-5087

Montly report from May 1<sup>st</sup> to May 31<sup>th</sup>

Report n° 8

WEAR OF h-BN

RFG 520765


Prepared for :

HUGUES AIRCRAFT COMPANY  
Electro-Optical & Data Systems Group  
Mike Gardos, Senior Scientist

Prepared by : - J.M. MARTIN

Adm. Div. :

  
- Th. LE MOGNE

  
Etude Soretrib n° D50

Tél : 78.33.81.27

Fax : 78.43.39.62

Télex : ECE LY 310856F

D-97

## WEAR OF h-BN

### INTRODUCTION

Friction experiments were conducted under UHV (10 nPa) with h-BN pins and flats (see report n° 7).

Wear of h-BN specimens were studied by examination of surfaces after the friction test (optical and electron micrographs) and profilometric measurements in the wear scars. For comparison, the same analysis was performed in the case of friction in ambient air.

### RESULTS

Results can be summarized as followed (see table 1 and selected micrographs) :

- in air, wear of h-BN is found negligible, and this corresponds to low friction values,

- under UHV, and in the presence of contamination (cleaning with n-propanol), wear mainly occurs on the h-BN pin, the diameter of the wear scar is clearly visible. Concerning the h-BN flats, results indicate a better wear resistance for the edge configuration,

- under UHV, after heat-treatment at 450°C (elimination of hydrocarbons), wear is more important. Here again we notice a better behavior of the edge configuration.

| preparation environment | crystal configuration | f average value | pin wear scar diameter | flat wear scar | photos            |
|-------------------------|-----------------------|-----------------|------------------------|----------------|-------------------|
| propanol air            | flat/flat             | 0.09            | not visible            | not visible    |                   |
| propanol air            | edge/edge             | 0.08            | not visible            | not visible    |                   |
| propanol UHV            | flat/flat             | 0.40            | ≈ 1 mm                 | +              | 1 - 2             |
| propanol UHV            | edge/edge             | 0.50            | ≈ 1,3 mm               | not visible    | 7 - 8             |
| heat treated UHV        | flat/flat             | 0.65            | ≈ 0,8 mm               | +              | 3 - 4<br>5 - 6    |
| heat treated UHV        | edge/edge             | 0.65            | 1,4 mm                 | +              | 9 - 10<br>11 - 12 |

Table 1

## DISCUSSION

When analyzing the effects of both the environmental conditions and the crystallographic orientation on the friction and wear of COMBAT h-BN against itself, it appears that the effect of environmental species is of first importance, and particularly :

- air (oxygen and water ?),
- hydrocarbons from contaminants.

The main difficulty is in deciding whether the adsorbed gases are only effective as surface films or they enter the lattice and weaken the bonding between the BN planes, so reducing the shear strength of h-BN itself.

In the absence of these species, the crystallographic orientation of COMBAT h-BN influences the wear results, but the interpretation is rather complex . For example there is an inversion in the wear of the pin and of the flat when using the flat/flat or the edge/edge configuration. Nevertheless, as a whole, it appears that the edge/edge configuration gives better results. Perhaps that the case flat pin/edge flat should be a better compromise.

Of course all these experiments have been conducted at room temperature ; the effect of the temperature during the test is still unknown and should complicate the interpretation.

To conclude on this set of experiments, it appears that the study of friction of h-BN is a very exciting field and results obtained indicate that it should be encouraging to continue the research to optimize the working conditions for COMBAT h-BN. Unfortunately our time is limited.

The next report will be concerned with the mechanisms of friction of h-BN. At the same time, we begin to work with silicon nitride specimens.

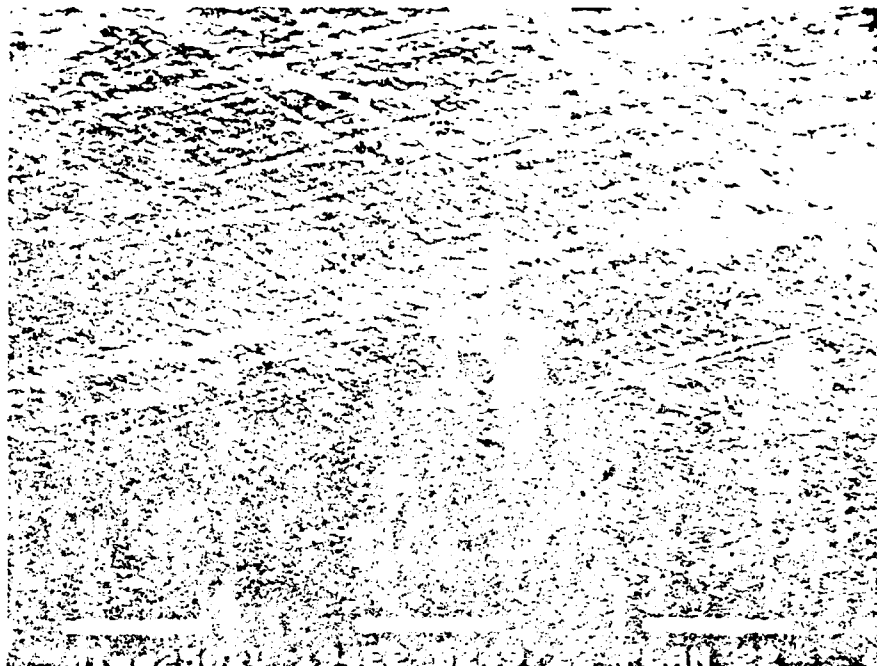
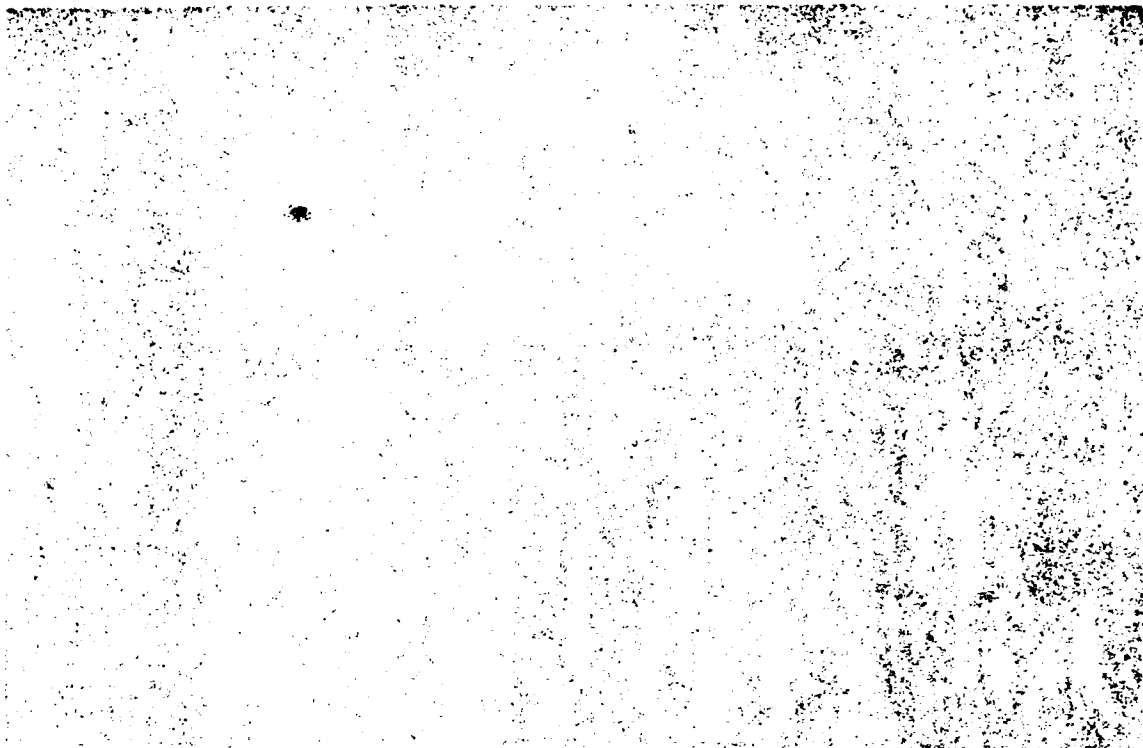
[illegible]

PHOTO 1

 $\langle \text{---} | \text{---} \rangle$ 

PHOTO 2

D-100



<----- 2' 00" ----->

PHOTO 3



PHOTO 4

D-101





PHOTO 5

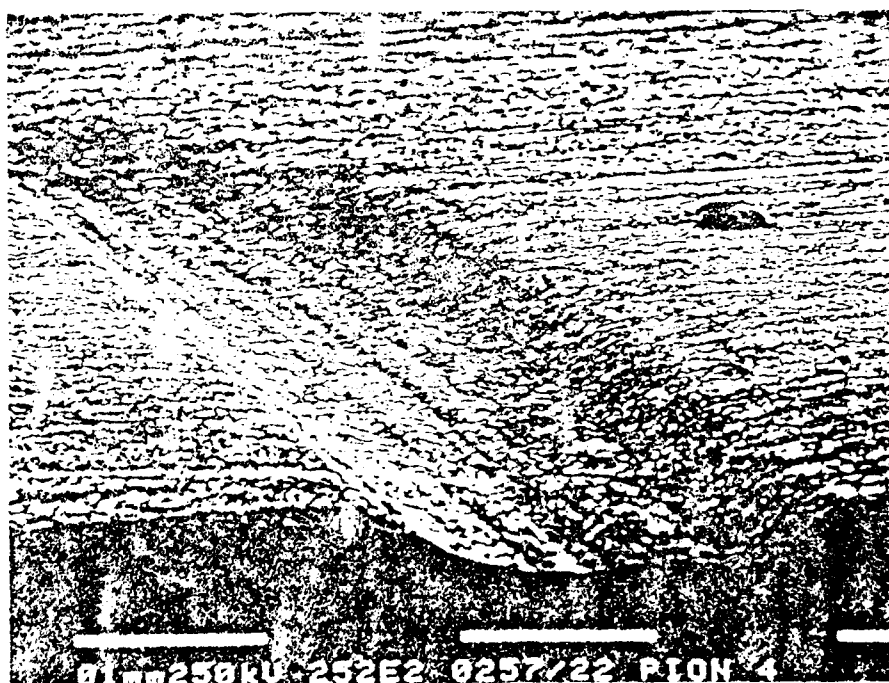
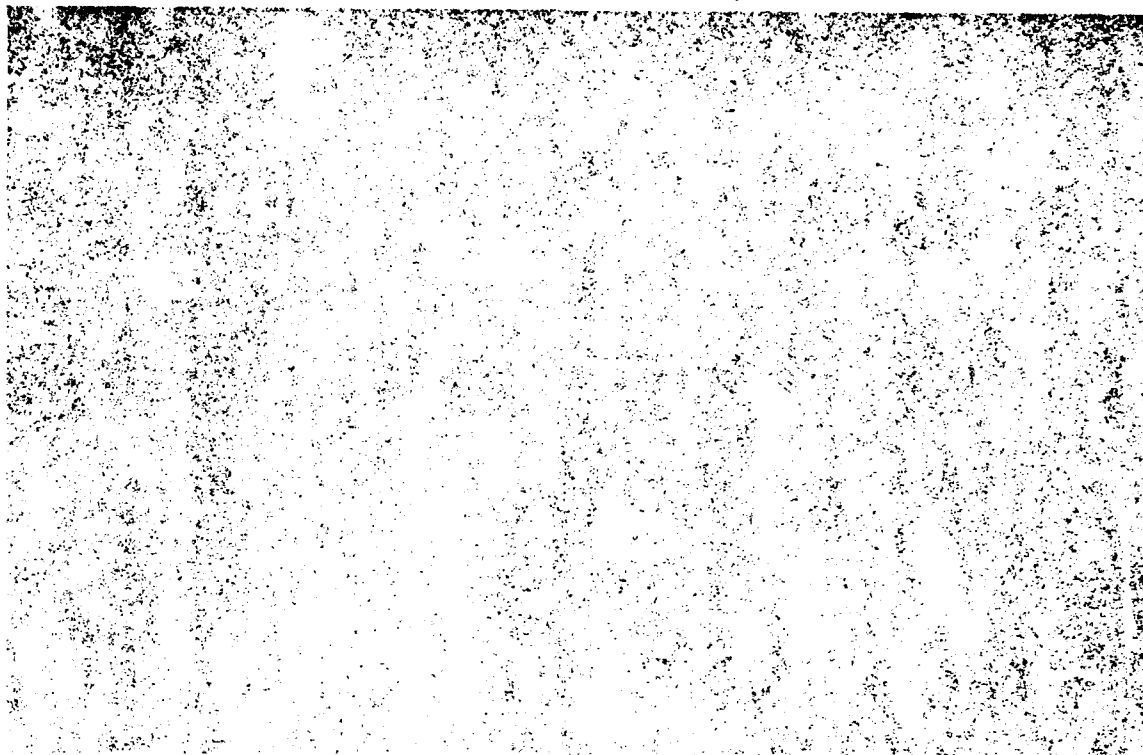


PHOTO 6

D-102



Sliding direction



<----- 3 mm ----->

PHOTO 7



Sliding  
direction

PHOTO 8

D-103

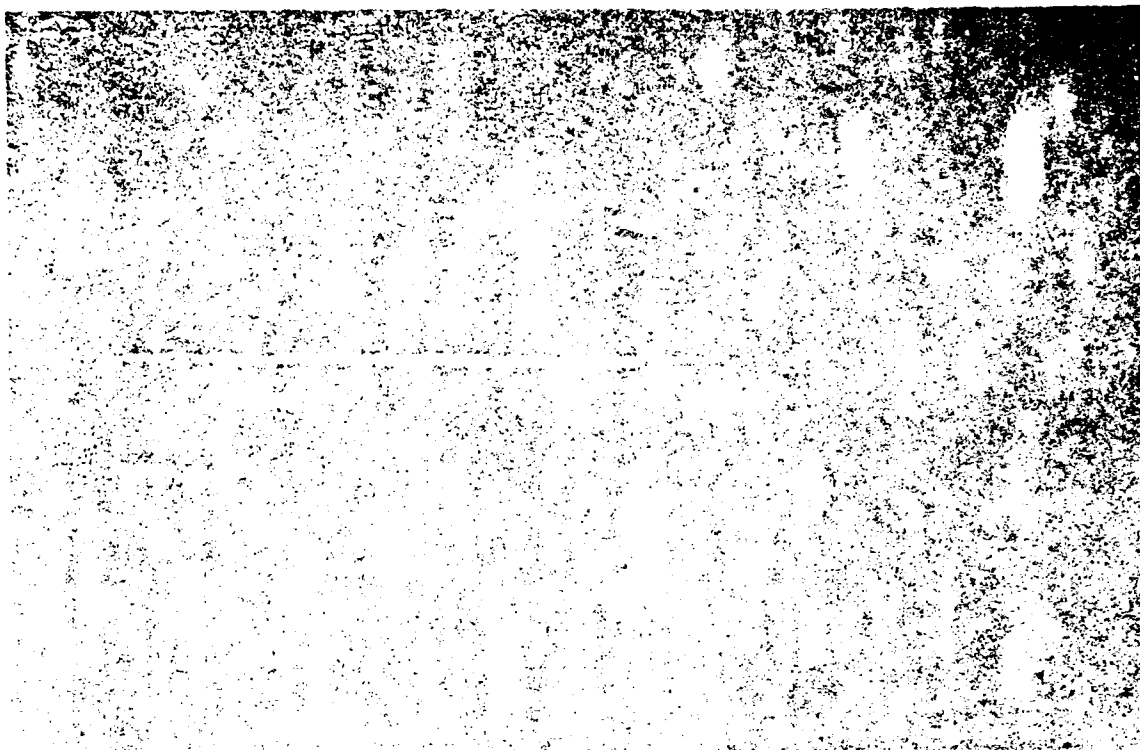


PHOTO 9



PHOTO 10

D-104



Sliding  
direction



Profilemetric  
scar

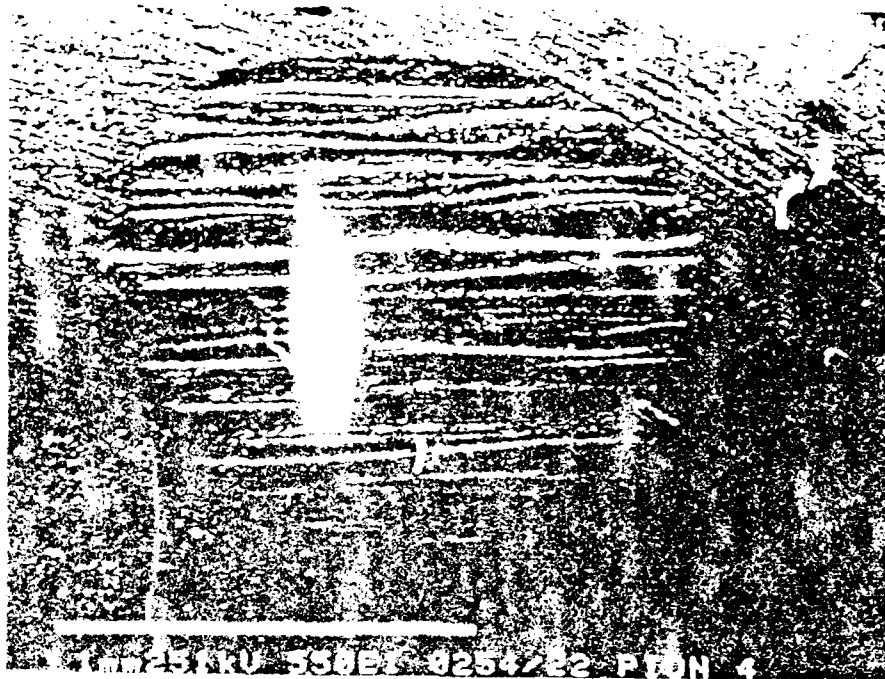


PHOTO 11

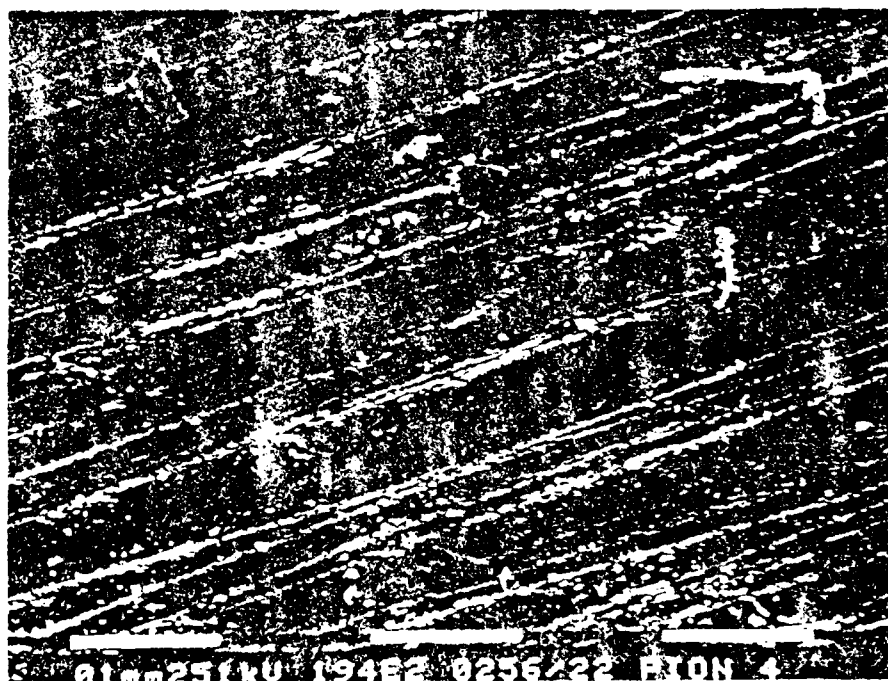


PHOTO 12

D-105

SORETRIB  
36 avenue Guy de Collongue  
69131 ECULLY cedex  
FRANCE

Ecole Centrale de Lyon  
Laboratoire de Technologie des  
Surfaces  
URA CNRS 855  
36 avenue Guy de Collongue  
B.P. 163 - 69131 ECULLY Cedex  
FRANCE

DETERMINATION OF TRIBOLOGICAL FUNDAMENTALS OF SOLID LUBRICATED CERAMICS

Contract F 33615-85-C-5087

Monthly report from June 1<sup>st</sup> to June 30<sup>th</sup>

Report n° 9

MECHANISMS OF h-BN FRICTION

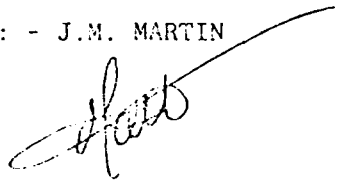
RFG 520765

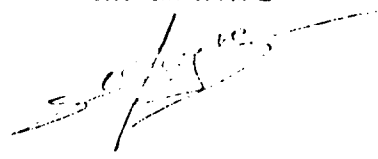
Prepared for :

HUGUES AIRCRAFT COMPANY  
Electro-Optical & Data Systems Group  
Mike Gardos, Senior Scientist

Prepared by : - J.M. MARTIN

Adm. Div. :

  
- TH. LE MOGNE

  
Etude Sorettrib n° D50

Tel : 78.33.81.27

Fax : 78.43.39.62

Télex : ECL LY 310356F

## MECHANISMS OF h-BN FRICTION

### INTRODUCTION

The mechanisms of friction of hexagonal boron nitride (h-BN) are explained here in terms of deformation modes of individual BN grains in the contact area. The study involves the detailed analysis of wear fragments in the same way that it was done for  $\alpha$ -SiC.

### RESULTS

High resolution analysis of wear fragments (originating from all the friction experiments with h-BN) was carried out in the analytical transmission electron microscope (TEM).

But the situation here is much more complex ; five types of h-BN wear particles were generally detected, they were classified as follows, depending on how they were produced in the wear process (see selected TEM micrographs) :

- |                                    |                   |
|------------------------------------|-------------------|
| - basal-plane slip flakes (a)      | photos 1, 2       |
| - bended small flakes (b)          | photo 3           |
| - crumpled flakes (c)              | photos 4, 5       |
| - rolled flakes (d)                | photos 6, 7, 8, 9 |
| - amorphized spheroidal grains (e) | photos 10, 11     |

Generally, these wear fragments are all present in all the situations, but the proportion of each type depends on the tribological test. In table 1, (see report 8) we have reported presence or not of each type of wear fragments in the different friction tests.

| preparation environment | crystal configuration | f average | pin wear scar value | flat wear scar diameter | wear particle types |     |     |     |     |
|-------------------------|-----------------------|-----------|---------------------|-------------------------|---------------------|-----|-----|-----|-----|
|                         |                       |           |                     |                         | a                   | b   | c   | d   | e   |
| propanol air            | flat/flat             | 0.09      | not visible         | not visible             | +++                 | +   | +   |     |     |
| propanol air            | edge/edge             | 0.08      | not visible         | not visible             | +++                 | +   | +   |     |     |
| propanol UHV            | flat/flat             | 0.40      | ≈ 1 mm              | + +                     | +                   | +++ | +++ | +++ | +++ |
| propanol UHV            | edge/edge             | 0.50      | ≈ 1,3 mm            | not visible             |                     | +++ | +++ | +++ | +++ |
| heat treated UHV        | flat/flat             | 0.65      | ≈ 0,8 mm            | + + + +                 | +                   | +++ | +++ | +++ | +++ |
| heat treated UHV        | edge/edge             | 0.65      | 1,4 mm              | +                       |                     | +++ | +++ | +++ | +++ |

Table 1

Under UHV results indicates that :

- in the edge/edge configuration, only a few type (a) particle are present and a lot of other ones,
- in the flat/flat configuration, type (a) particle are more numerous, but the other ones are always in majority.

(Note that no quantitative analysis was attempted to distinguish accurately between (b), (c), (d), (e) particles).

In air, and surprisingly, only type (a) particles (basal plane slip) are observed (even in the edge/edge configuration !).

It is important to note that in a first experiment with h-BN friction under UHV (see report 5), only type (a) particle wear detected. But this first COMBAT specimen contained twice more oxygen than the second supply. Indoubtly, the roles of oxides, gas and contaminants are of first importance in generating wear debris morphologies (and therefore wear mechanisms).

## DISCUSSION

### Friction under UHV

Actually, it appears that during friction and in the absence of gases and contaminants, it is easier to bend and cleave a h-BN grain than to slip basal planes in it, whatever the initial crystallographic orientation. Therefore, wear debris of type (b) are expected to occur in all the situations. When type (b) particles are submitted in to reenter the contact, they can be transformed in type (c), (d) and (e), and this can explained the results obtained under UHV. This can be illustrated by several schemes (see figures 1, 2, 3, 4, 5).

Figure 1 : Formation of type (a) particle (flat and edge configuration).

Figure 2 : Formation of type (b) particle (flat and edge configuration).

Figure 3 : Formation of type (c) particle (flat and edge configuration).

Figure 4 : Formation of rolls (d) (flat and edge configuration).

Figure 5 : Formation of amorphized grains (e) (flat and edge configuration)

### Friction in air

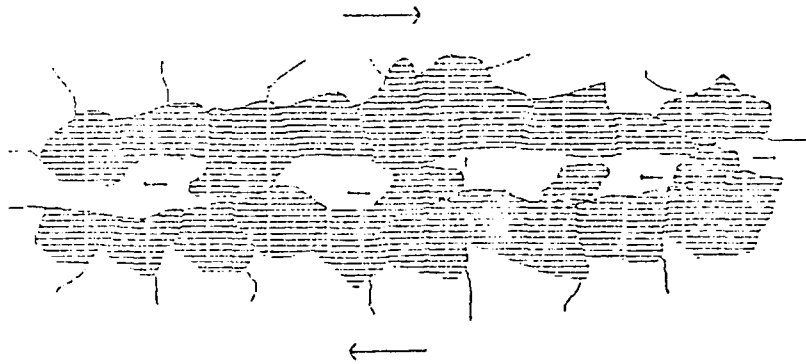
In the presence of reactive gases (oxygen, water ?) it appears that basal plane slip occurs more easily and this deformation mode is conserved even when debris reenter the contact zone. An interpretation is that there is a weakening of Van der Waals forces between BN planes due to the presence of gases and a decrease of the surface energy due the effect of chemisorption. But the situation is not very clear at the moment, friction of h-BN under oxygen or water should be very interesting to investigate this point.

Finally, in figure 6, we present several sequences to illustrate the different ways in which h-BN accomodates during friction and produces wear fragments from basal plane slip to amorphization.

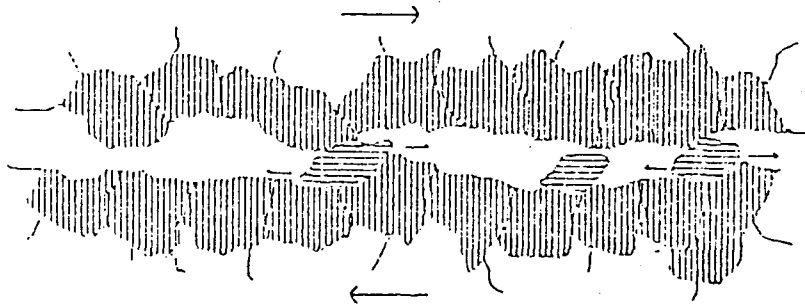


WEAR MECHANISMS

PARTICLES (a)



"flat configuration"

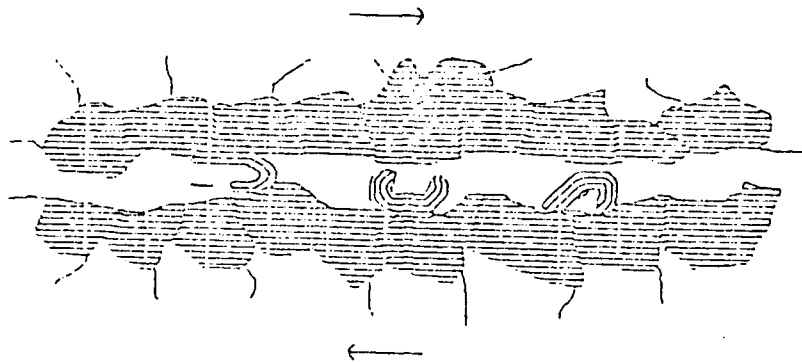


"edge configuration"

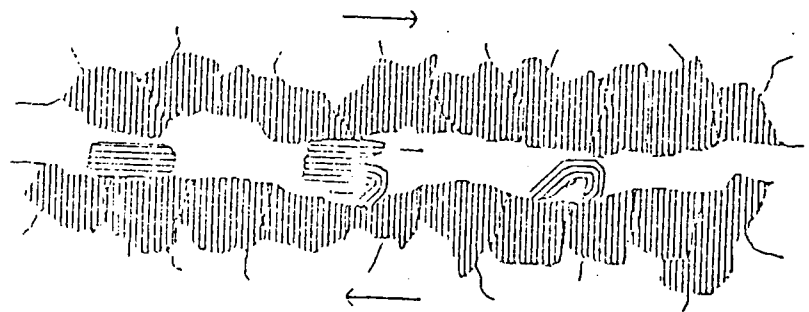
Figure 1

D-110

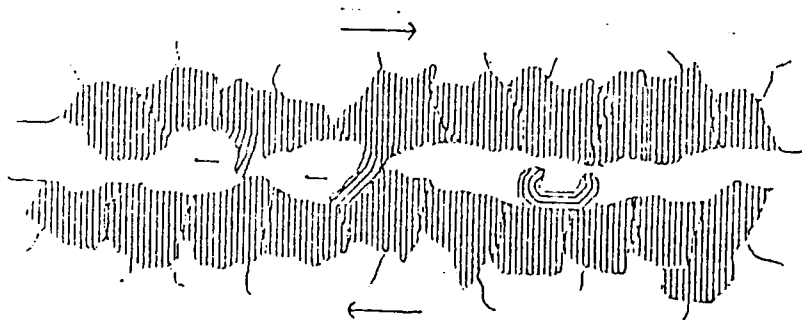
PARTICLES (b)



"flat configuration"



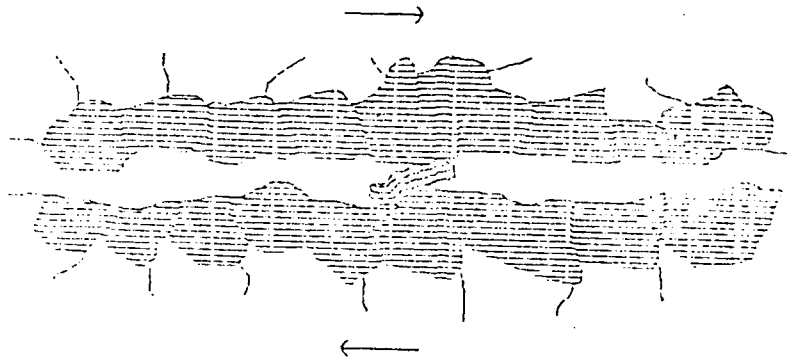
"edge configuration"



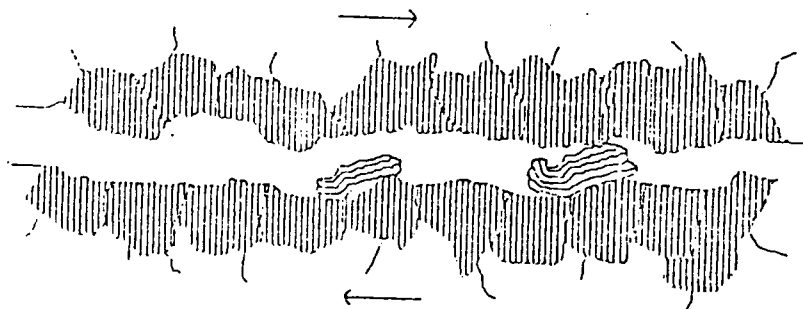
"edge configuration"

Figure 2

PARTICLES (c)



"flat configuration"

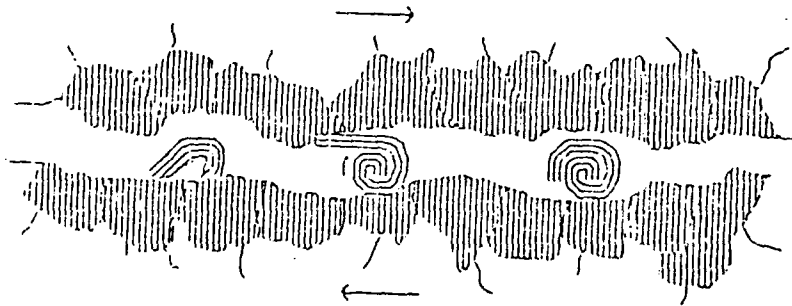


"edge configuration"

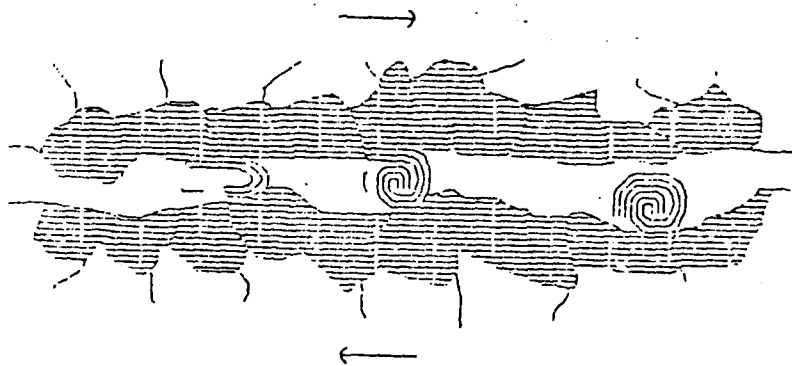
Figure 3

D-112

PARTICLES (d)



"edge configuration"

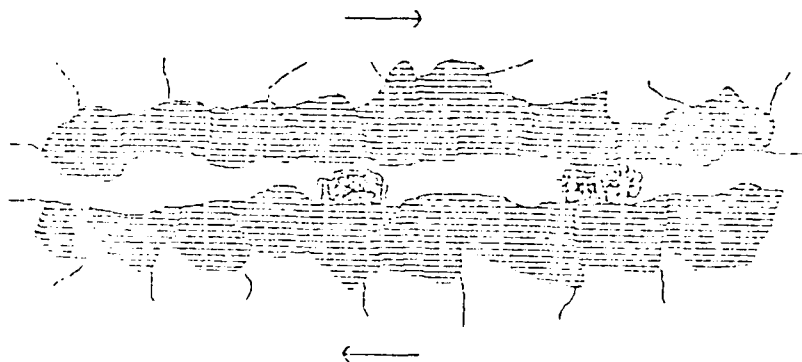


"flat configuration"

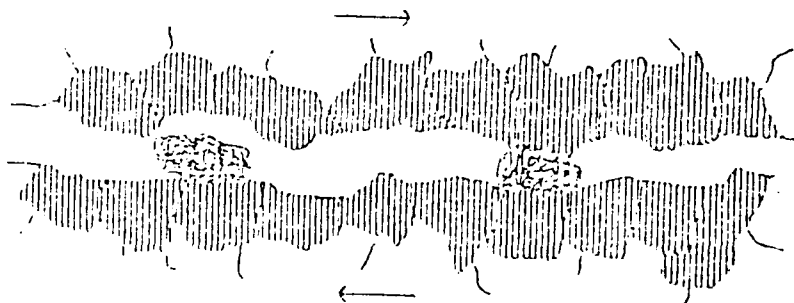
Figure 4

D-113

PARTICLES (c)



"flat configuration"



"edge configuration"

Figure 5

D-114

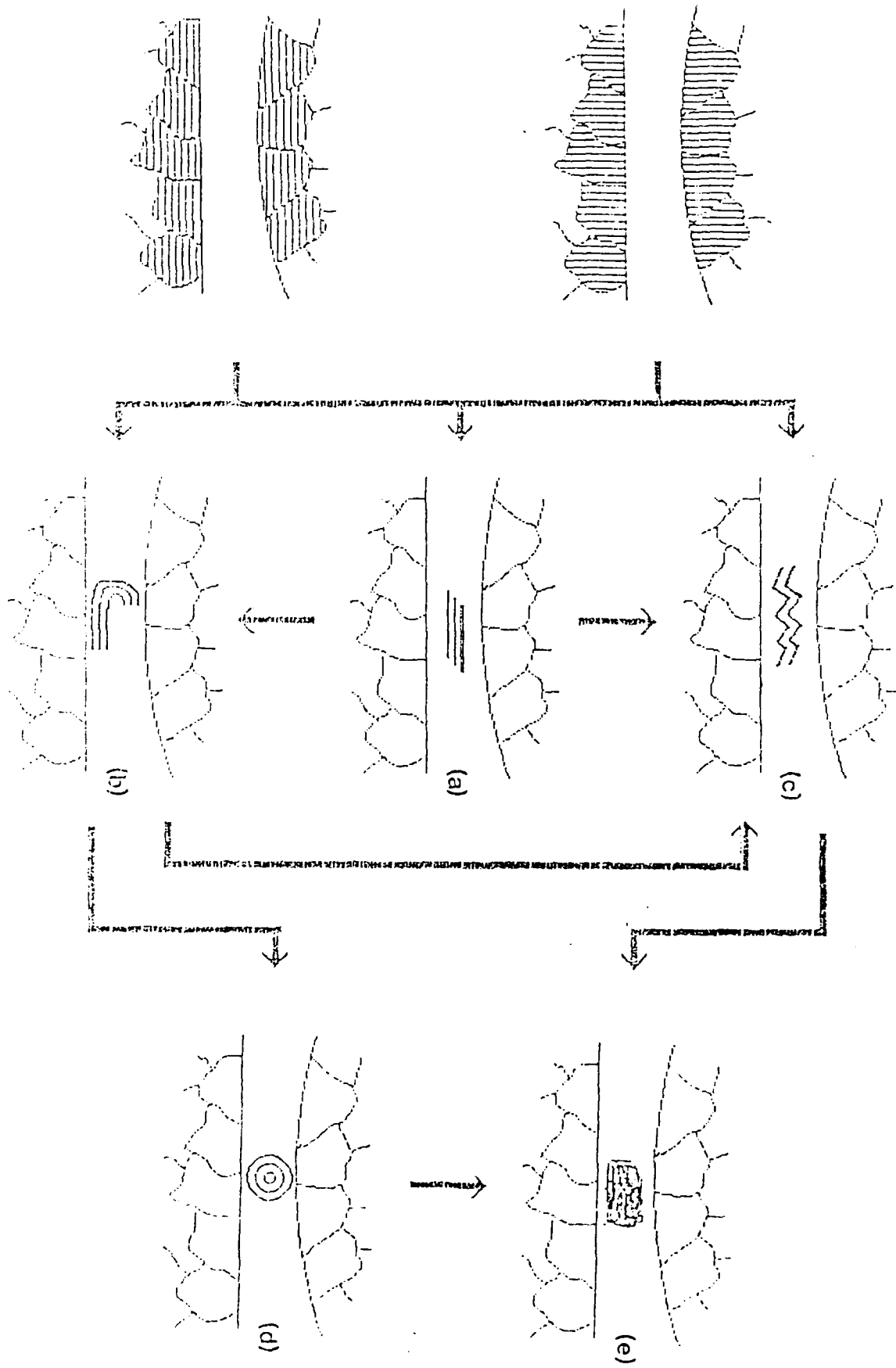


Figure 6

D-115



<----- 1  $\mu$ m ----->

Photo 1

D-116



<----- 1  $\mu$ m ----->

Photo 2

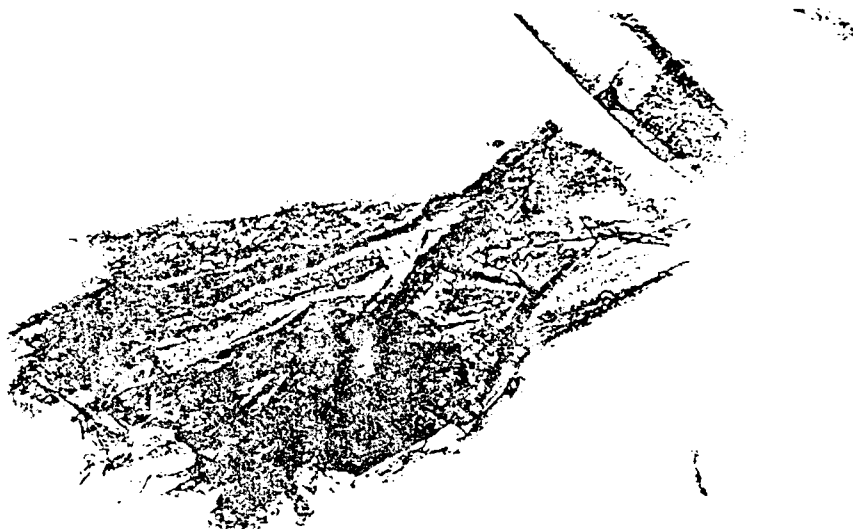


<----- 1  $\mu$ m ----->

Photo 3

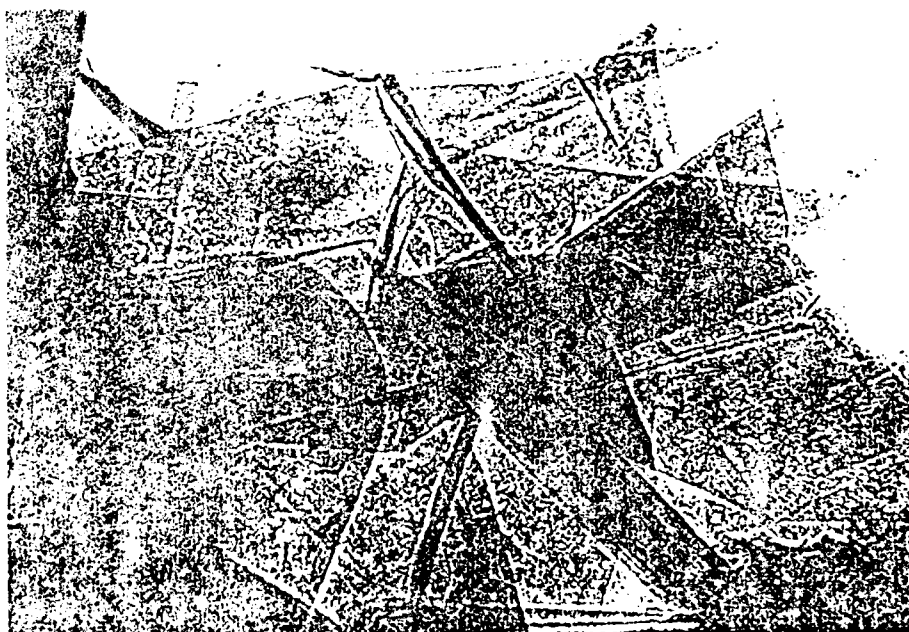
D-117





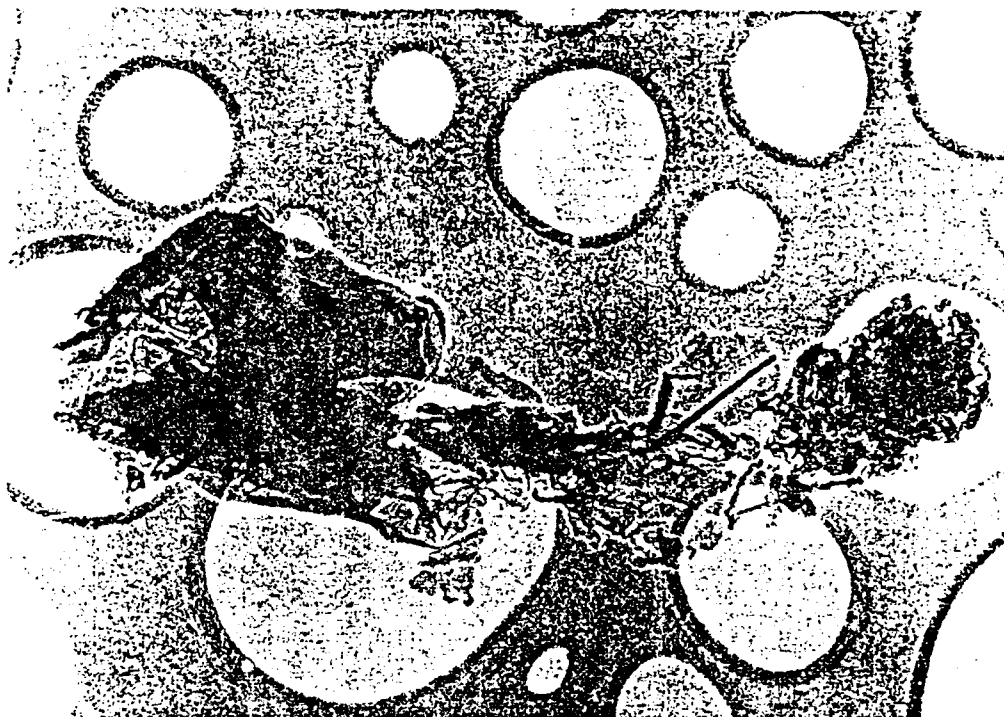
<----- 1  $\mu$ m ----->

Photo 4



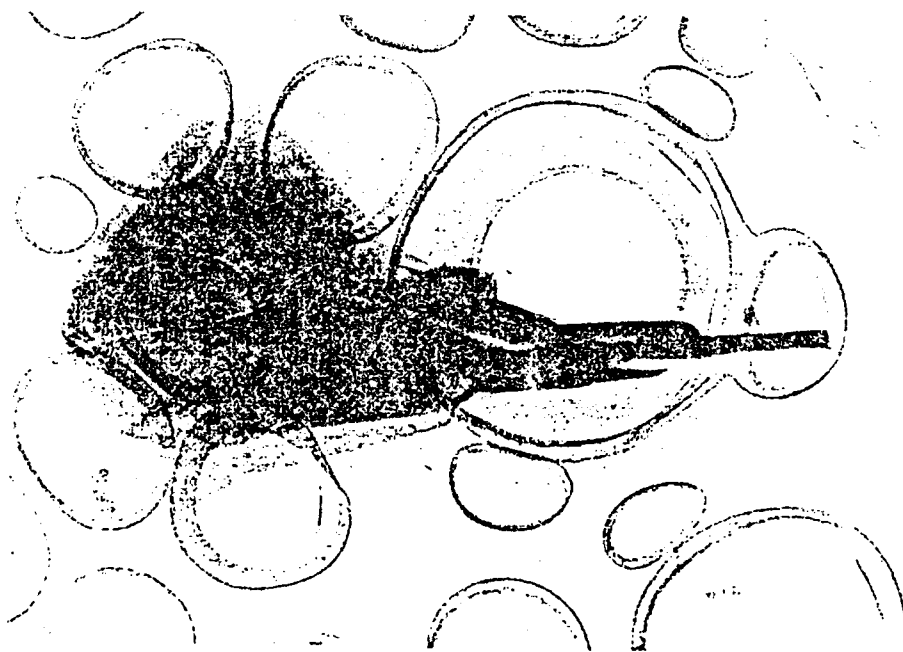
<----- 1  $\mu$ m ----->

Photo 5



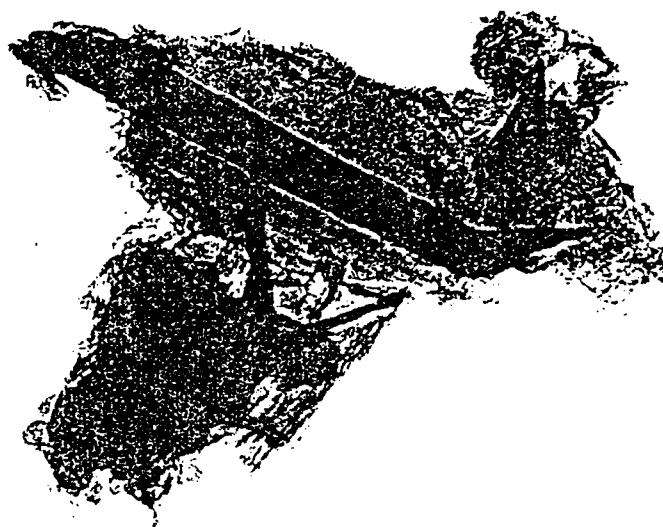
<----- 1  $\mu$ m ----->

Photo 6



<----- 1  $\mu$ m ----->

Photo 7



<----- 1  $\mu$ m ----->

Photo 8



<----- 1  $\mu$ m ----->

Photo 9

D-120



<----- 1  $\mu$ m ----->

Photo 10



<----- 0.5  $\mu$ m ----->

Photo 11

(black field)

D-121

SORETRIB  
36 avenue Guy de Collongue  
69131 ECULLY cedex  
FRANCE

Ecole Centrale de Lyon  
Laboratoire de Technologie des  
Surfaces  
URA CNRS 855  
36 avenue Guy de Collongue  
B.P. 163 - 69131 ECULLY Cedex  
FRANCE

DETERMINATION OF TRIBOLOGICAL FUNDAMENTALS OF SOLID LUBRICATED CERAMICS

Contract F 33615-85-C-5087

Monthly report from July 1<sup>st</sup> to July 30<sup>th</sup>

Report n° 10

HEAT-TREATMENT OF COMBAT h-BN

RFG 520765

Prepared for :

HUGUES AIRCRAFT COMPANY  
Electro-Optical & Data Systems Group  
Mike Gardos, Chief Scientist

Prepared by : - J.M. MARTIN

Adm. Div. :

- Th. LE MOGNE

Etude Soretrib n° D50

Tél : 78.33.81.27

Fax : 78.43.39.62

Télex : ECE LY 310856F

D-122

## I - SURFACE ANALYSIS OF h-BN BY XPS

We have made some progress concerning the XPS analysis of h-BN and especially the origin of the sur-stoichiometric boron oxide that we found in report 6. Also we refined the process of XPS spectra to have a better identification of the different chemical bonding at the boron nitride surface.

For the annealed h-BN surface, we have the following results :

- BN stoichiometry ( $B/N = 0.93$ ),
- boron nitride chemical bonding (estimated at 86 % by weight),
- low content of carbon in the graphitic form only (estimated at 2 % by weight),
- boron oxide :

Remember that the B1s binding energy has the same value that for the standard oxide  $B_2O_3$ , but oxygen is largely surtoichiometric. We have four possible explanations for this :

- 1) surtoichiometric boron oxide,
- 2) oxygen intercalated,
- 3) water intercalated
- 4) contribution of other oxides.

Hypothesis 2) and 3) are refuted by XPS and SIMS results (see reports 3 and 6).

The presence of other cationic oxides is also possible as  $SiO_2$ ,  $CaO$ ,  $MgO$ ,  $AlO$ ,  $Al_2O_3$  etc... The O1s binding energy is close to that of boron trioxide (the sintering aid). A good compromise is the existence of mixed glasses, such as borosilicate or boroaluminate in which the binding energies of B1s and O1s are only slightly shifted compared with  $B_2O_3$ , not enough to be detected by our equipment. This can explain the XPS results and the sur-stoichiometry in oxygen.

## II - ANNEALING OF h-BN at 750°C UNDER UHV

The effect of annealing h-BN at 450°C under vacuum has been studied in part I of this report. As boron trioxide has a melting point of 500°C, and chemically decomposes at 900°C (under UHV  $10^{-9}$  mbar), it seemed to us

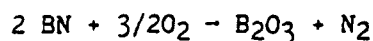
interesting to study the effect of annealing at 750°C for 1 hour under UHV and to XPS-analyze the h-BN surface that is formed. Results (figure 1 and table below) show a relative increase of the "boron oxide" content concomitant with a decrease of the BN concentration. This is attributed to intergranular migration and diffusion of molten B<sub>2</sub>O<sub>3</sub> to the surface.

|      | step 1<br>Annealing<br>at 450°C<br>15 mn | step 2<br>Annealing<br>at 750°C<br>15 mn | step 3<br>Annealing<br>at 750°C<br>15 mn | step 4<br>Annealing<br>at 750°C<br>15 mn | step 5<br>Annealing<br>at 750°C<br>15 mn | step 6<br>Annealing<br>at 750°C<br>15 mn |
|------|------------------------------------------|------------------------------------------|------------------------------------------|------------------------------------------|------------------------------------------|------------------------------------------|
| B-N  | 42.2 %                                   | 38.7 %                                   | 36.8 %                                   | 36.6 %                                   | 37.7 %                                   | 37.8 %                                   |
| B-O  | 2.2 %                                    | 5.5 %                                    | 7.5 %                                    | 8.1 %                                    | 7.2 %                                    | 7.5 %                                    |
| O-ox | 7.4 %                                    | 14.6 %                                   | 15.4 %                                   | 16.0 %                                   | 14.1 %                                   | 14.6 %                                   |
| N-B  | 46.4 %                                   | 41.1 %                                   | 40.02                                    | 39.4                                     | 41.1 %                                   | 40.1 %                                   |

### III - OXIDATION OF h-BN IN AIR AND UHV

It is known that h-BN begins to oxidizes in air at 800°C, and that the presence of SiO<sub>2</sub> can modify this temperature (specimens containing 5 % SiO<sub>2</sub> oxidize at 900°C).

The reaction is :



Five heat treatments were made :

- |                   |               |
|-------------------|---------------|
| - 450°C : 1 hour  | } UHV         |
| - 750°C : 1 hour  |               |
| - 950°C : 1 hour  |               |
|                   |               |
| - 1000°C : 1 hour | } ambient air |

XPS results are presented in figure 2.

It is interesting to see that annealing at 950°C under UHV leads to a decrease of the oxide content, due to the dissociation of B<sub>2</sub>O<sub>3</sub> under vacuum.

Annealing at 1000°C in air leads to oxidation of h-BN, and diffusion of silicon oxide at the surface.

# BORON OXIDE DIFFUSIVITY

## IN h-BN Combat AT 1000 K UHV

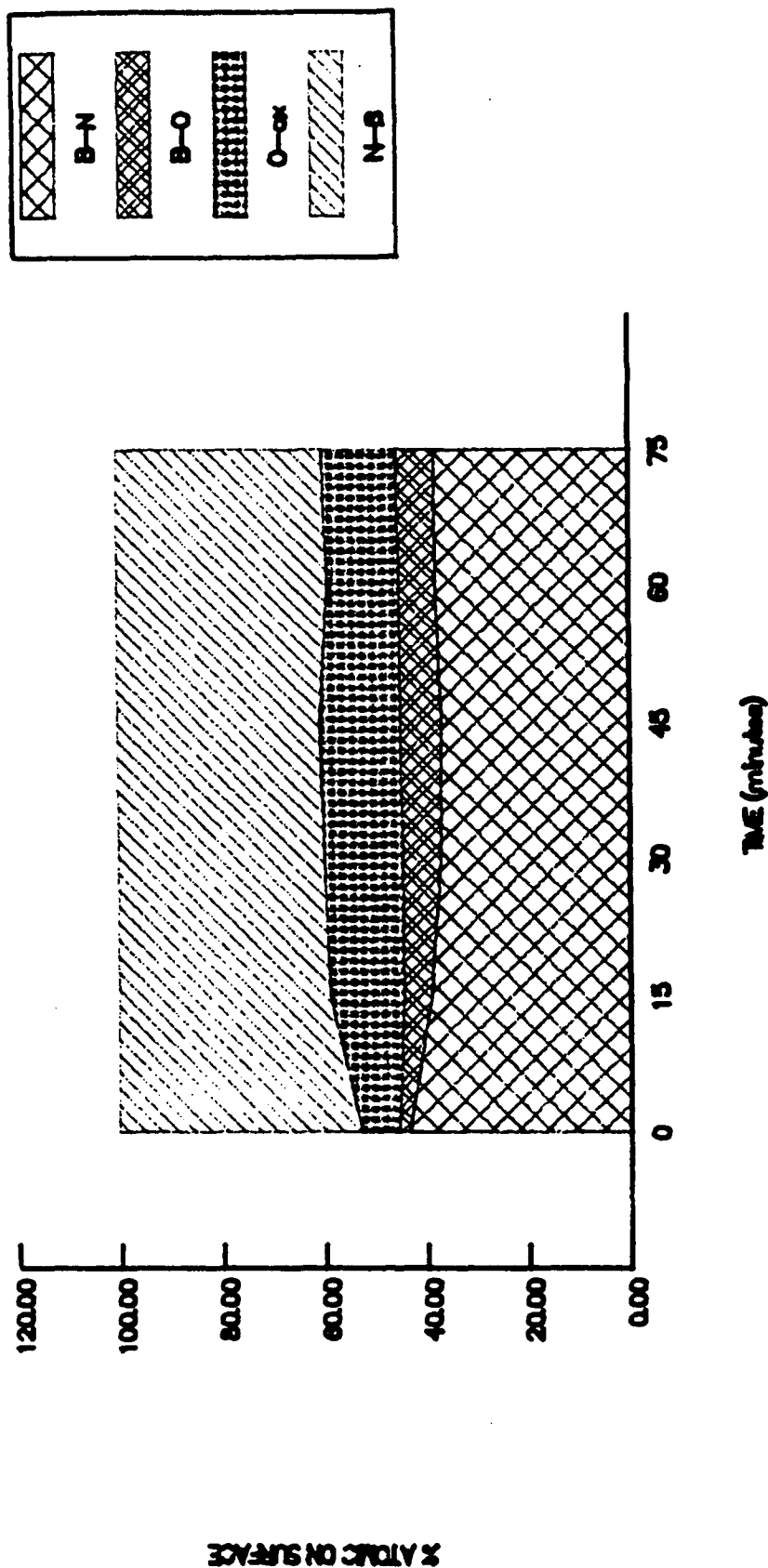


Figure 1



# ANNEALING EFFECT ON h-BN

## at different temperatures during 1 hour

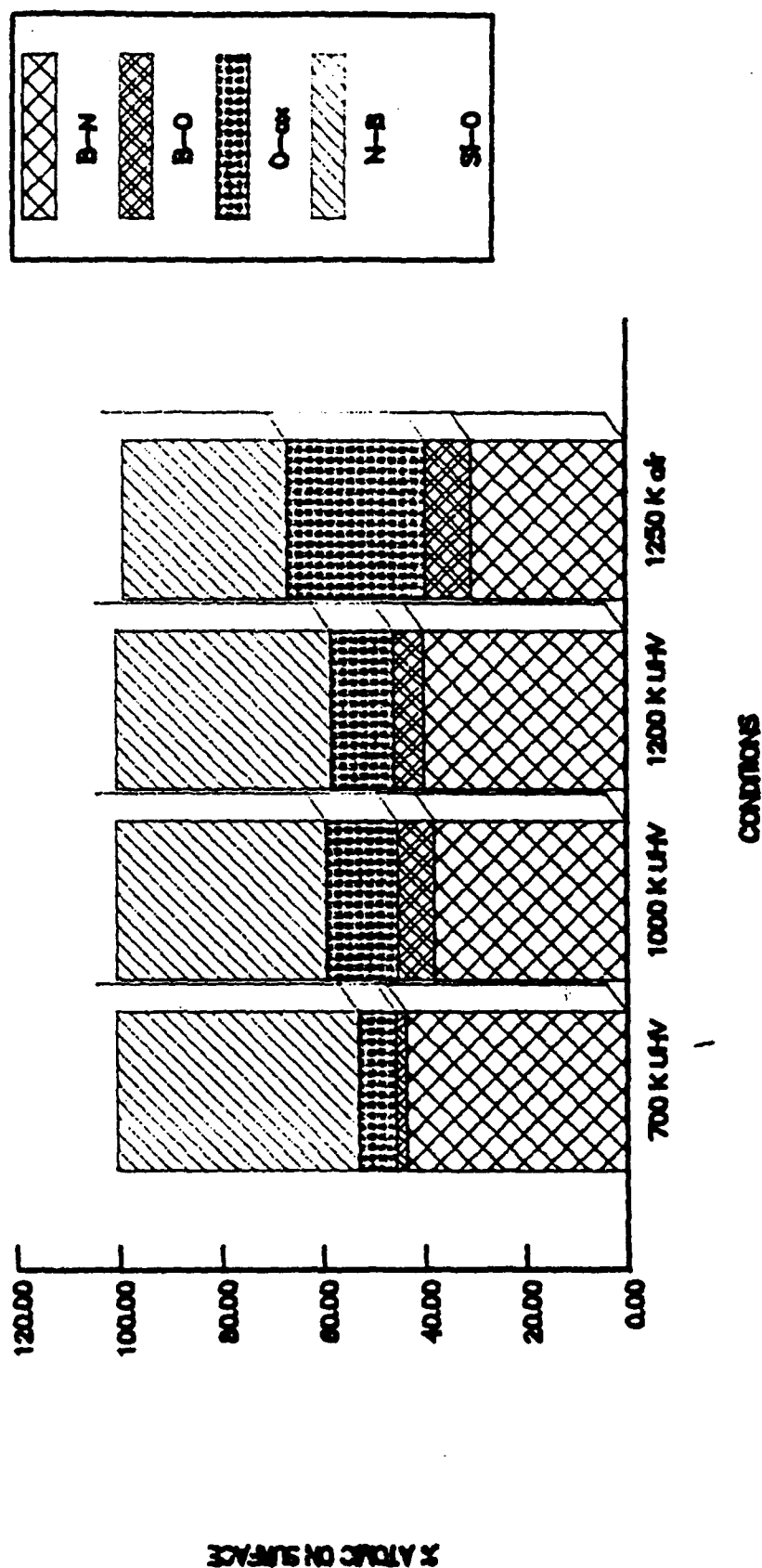


Figure 2

SORETRIB  
36 avenue Guy de Collongue  
69131 ECULLY cedex  
FRANCE

Ecole Centrale de Lyon  
Laboratoire de Technologie des  
Surfaces  
URA CNRS 855  
36 avenue Guy de Collongue  
B.P. 163 - 69131 ECULLY Cedex  
FRANCE

DETERMINATION OF TRIBOLOGICAL FUNDAMENTALS OF SOLID LUBRICATED CERAMICS

Contract F 33615-85-C-5087

Monthly report from August 1<sup>st</sup> to August 31<sup>th</sup>

Report n° 11

FRICTION OF PYROLYTIC h-BN. EFFECT OF ENVIRONMENTAL GASES

RFG 520765

Prepared for :

HUGUES AIRCRAFT COMPANY  
Electro-Optical & Data Systems Group  
Mike Gardos, Chief Scientist

Prepared by : - J.M. MARTIN

Adm. Div. :

- Th. LE MOGNE

Etude Soretrib n° D50

Tél : 78.33.81.27

Fax : 78.43.39.62

Télex : ECE LY 310856F

D-127

## FRICTION OF PYROLYTIC h-BN. EFFECT OF ENVIRONMENTAL GASES

As it appears that friction of h-BN on itself is more sensitive to environmental factors (gas, contamination cleaning...) than to the initial crystallographic orientation, we decided to carry out a set of friction experiments at room temperature and in different gases, in order to know if it is possible to lubricate h-BN in these conditions.

### I - FRICTION OF h-BN ON ITSELF UNDER LOW PARTIAL PRESSURE OF GAS

Friction tests were conducted under static low partial pressures of different gases, namely water ( $H_2O$ ) carbon monoxide ( $CO$ ), propane ( $C_3H_8$ ) and ambient air. For these different gases, the pressure in the main chamber of the AES/XPS tribometer was controlled at  $10^{-5}$  mBar ( $\approx 10^{-5}$  Torr) before the friction test.

The h-BN materials were COMBAT h-BN specimens used in the "flat/flat" configuration ; before the friction test, they were annealed at  $450^\circ C$  under UHV to eliminate hydrocarbons from the surface. The tribological parameters were the followings :

- normal load : 2 N,
- sliding speed :  $0,6 \cdot 10^{-3}$  m/s,
- length of the stroke :  $3 \cdot 10^{-3}$  m,
- number of passes : 75,
- temperature : 300 K.

The results are shown in figures 1, 2, 3, 4.

As can be seen, under these low partial pressures, and in comparison with UHV conditions, the friction of h-BN on itself is not affected by the presence of environmental gases, the value of the average friction coefficient lying in the range 0.65-0.7 (note that the computer averages the friction coefficient for each pass, so the local fluctuations are not reproduced, but generally they are weak in our conditions).

As a rule-of-thumb, remember that at  $10^{-6}$  mBar, the contamination is approximately one monolayer per second (depending on the gas and temperature).

## II - FRICTION OF h-BN ON ITSELF UNDER HIGH PARTIAL PRESSURES OF GAS

Friction tests were conducted in the same conditions on the same h-BN flat for each gas.

Three experiments are presented here :

- oxygen  $10^{-1}$  mBar (static),
- air  $10^{-5}$  mBar  $\rightarrow$   $10^{-1}$  mBar,
- propane  $10^{-5}$  mBar  $\rightarrow$   $10^{-1}$  mBar  $\rightarrow$   $10^{-5}$  mBar.

In our conditions, it was not possible to obtain  $10^{-1}$  mBar of water in the chamber (see the saturation curve). Note also that this represents high pressures and some problems for the UHV instrumentation.

Results are shown in figure 4, 5, 6.

As can be shown, propane ( $C_3H_8$ ) and air at  $10^{-1}$  mBar lubricate h-BN on itself, the friction coefficient immediately dropping down to 0.4 (approximately one half of the UHV value). Note that in the case of propane, the friction increases again to 0.6-0.7 when the pressure is decreased at  $10^{-5}$  mBar at the end of the test.

Surprisingly pure oxygen has no effect on friction at  $10^{-1}$  mBar.

## III - FRICTION OF h-BN ON ITSELF IN AIR

When ambient air is introduced in the chamber at the atmospheric pressure ( $\approx 1$  Bar) in static conditions, the friction coefficient is stabilized at 0.25. Note that this value is higher than the value obtained in air with non-annealed h-BN specimens ( $f \approx 0.1$ ).

## CONCLUSION

We have studied the effect of different gases on the friction of annealed h-BN on itself, at room temperature, and at different partial pressures.

The gases used were water ( $H_2O$ ), carbon monoxide ( $CO$ ), propane ( $C_3H_8$ ), oxygen ( $O_2$ ) and ambient air.

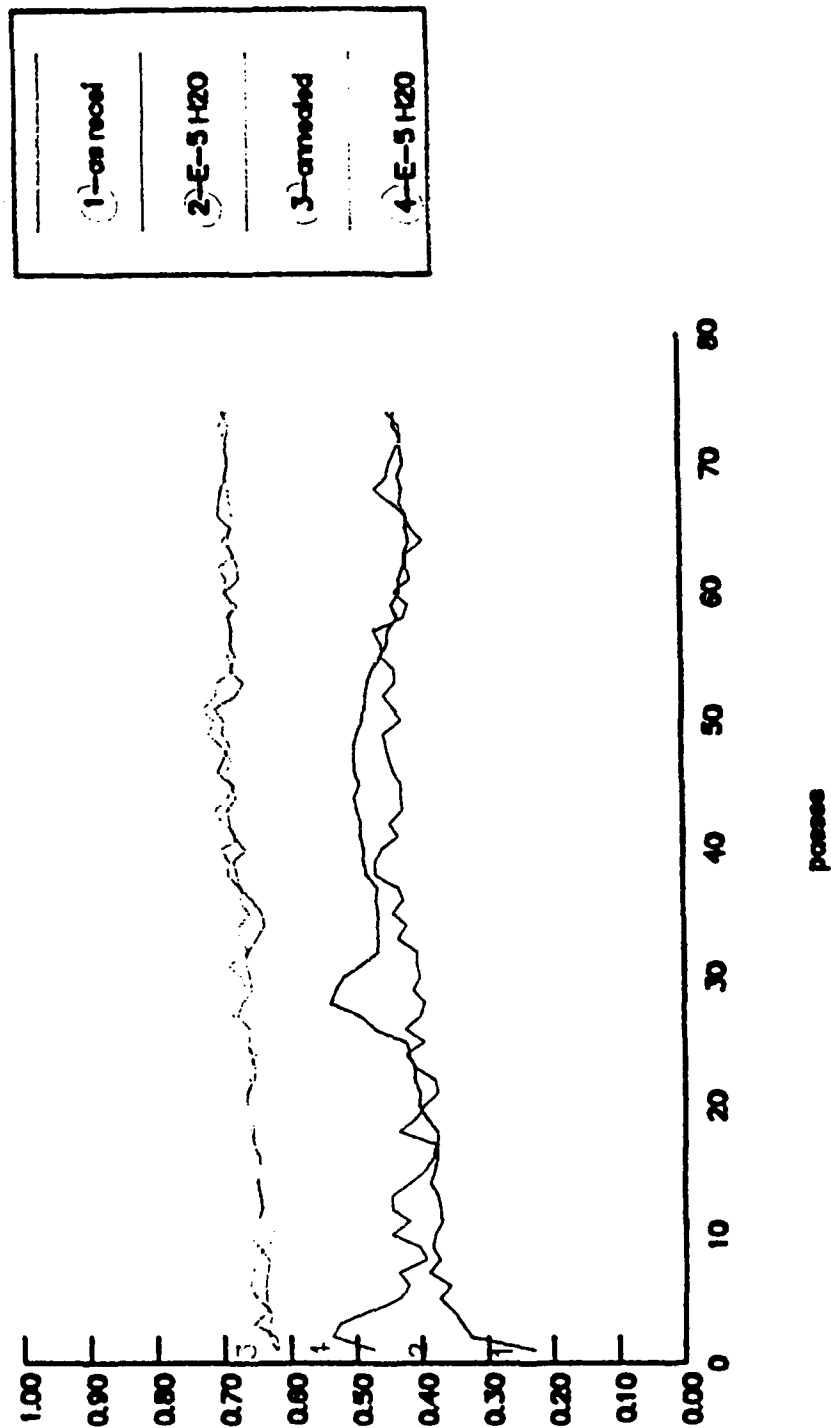
1) At low partial pressure ( $10^{-5}$  mBar), these gases have no effect on friction, the value obtained ( $f = 0.6-0.7$ ) being the same that under UHV ( $10^{-10}$  mBar).

2) At higher partial pressure ( $10^{-1}$  mBar), air and propane make the friction coefficient to be decreased by a factor 2 ( $f = 0.4$ ) the phenomenon being reversible in the case of propane. Surprisingly, in these conditions we found no effect of oxygen.

3) At atmospheric pressure (1 Bar) of air, the friction coefficient is reduced to 0.25 with previously annealed surfaces.

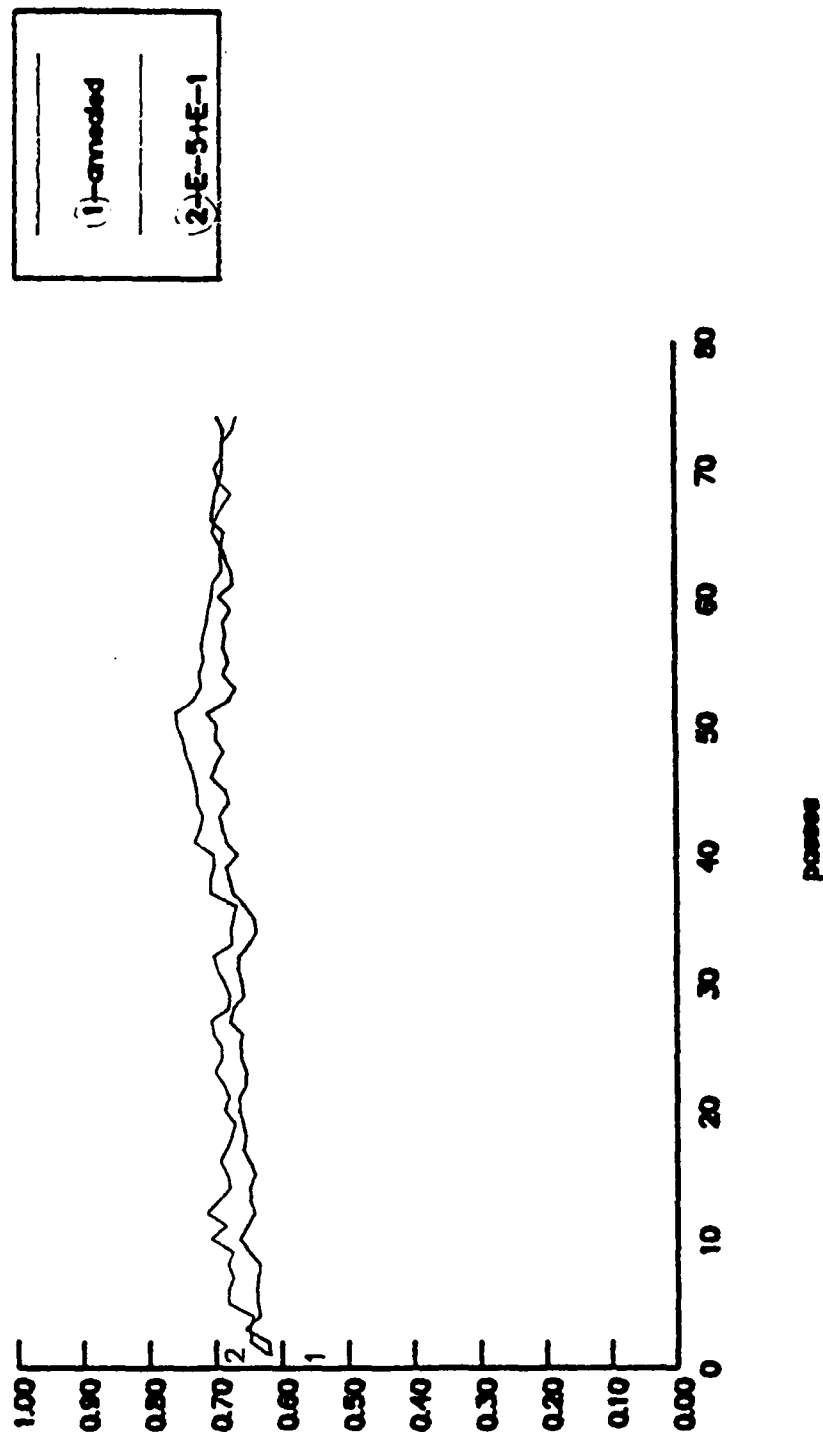
# h BN Combat \ h BN Combat

## Flat \ Flat UHV and H2O



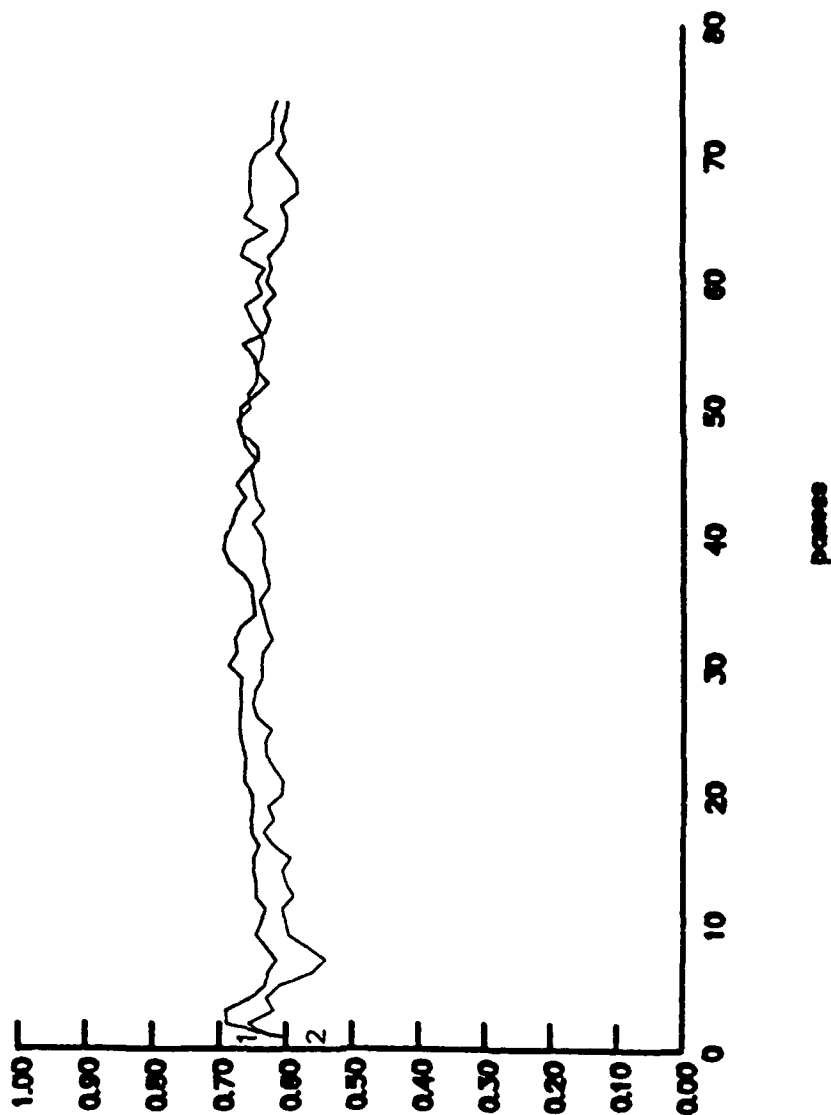
# h BN Combat \ h BN Combat

## Flat \ Flat UHV and CO



# h BN Combat \ h BN Combat

## Flat \ Flat UHV and C3H8



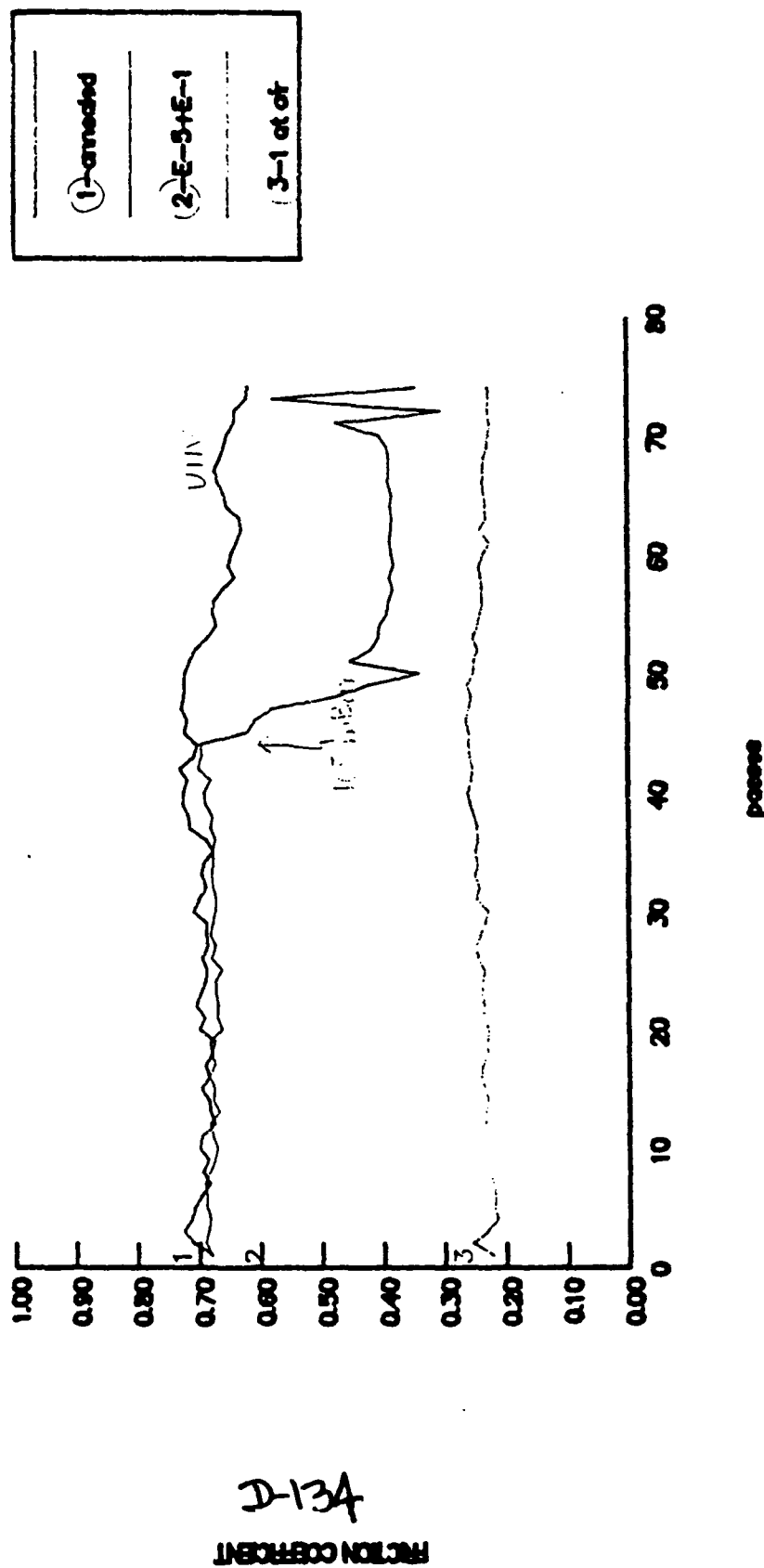
Friction Coefficient

D-133



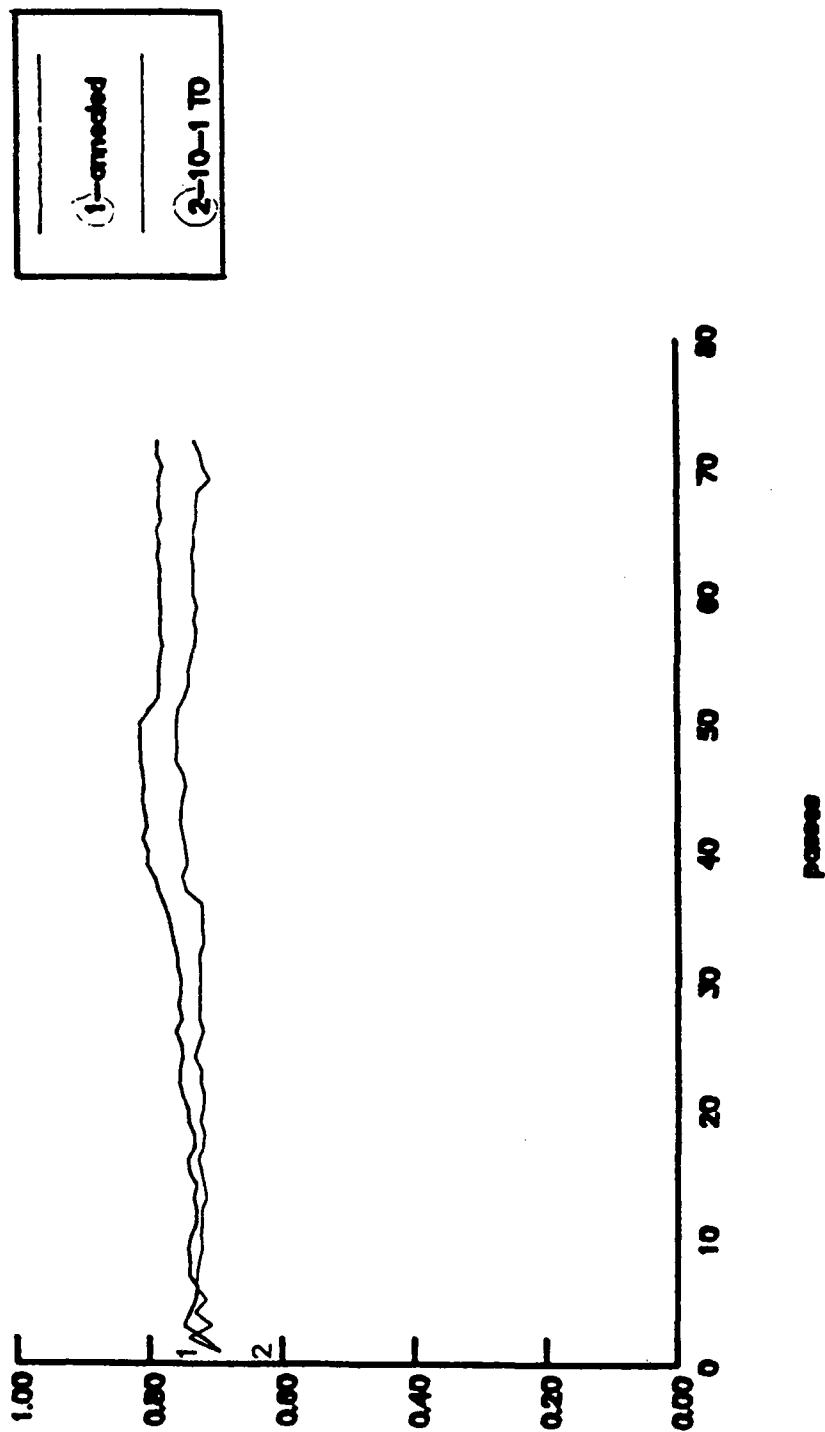
# h BN Combat \ h BN Combat

## Flat \ Flat UHV and air



# 1 BN Combat \ h BN Combat

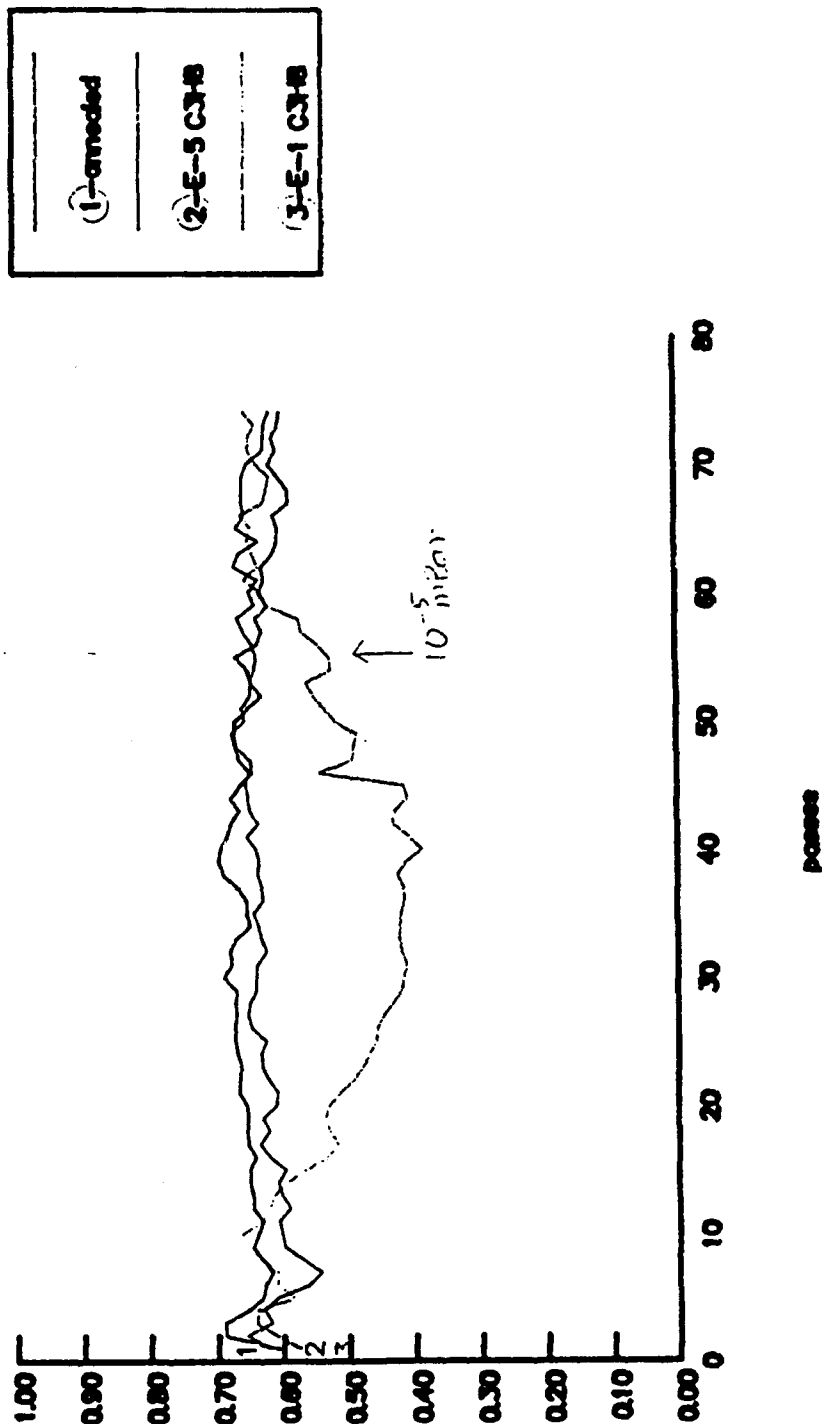
## Flat \ Flat UHV and 02



D-135

# h BN Combat \ h BN Combat

## Flat \ Flat UHV and C3H8



D-136

FRACTION COEFFICIENT

SORETRIB  
36 avenue Guy de Collongue  
69131 ECULLY cedex  
FRANCE

Ecole Centrale de Lyon  
Laboratoire de Technologie des  
Surfaces  
URA CNRS 855  
36 avenue Guy de Collongue  
B.P. 163 - 69131 ECULLY Cedex  
FRANCE

DETERMINATION OF TRIBOLOGICAL FUNDAMENTALS OF SOLID LUBRICATED CERAMICS

Contract F 33615-85-C-5087

Monthly report from September 1<sup>st</sup> to September 30<sup>th</sup>

Report n° 12

FRICTION OF h-BN ON Si<sub>3</sub>N<sub>4</sub>

RFG 520765

Prepared for :

HUGUES AIRCRAFT COMPANY  
Electro-Optical & Data Systems Group  
Mike Gardos, Chief Scientist

Prepared by : - J.M. MARTIN

Adm. Div. :

- Th. LE MOGNE

Etude Sorettrib n° D50

Tél : 78.33.81.27

Fax : 78.43.39.62

Télex : ECE LY 310856F

**D-137**

## FRICTION OF h-BN ON $\text{Si}_3\text{N}_4$

### I - FRICTION OF SILICON NITRIDE ( $\text{Si}_3\text{N}_4$ ) ON ITSELF UNDER UHV. COMPARISON WITH BORON NITRIDE (FLAT CONFIGURATION)

The annealing procedure that we chose was the same that for boron nitride (30 minutes at  $400^\circ\text{C}$ ).

The cleaning solution was 1-propanol.

The tribological conditions were previously described (see report 11).

In this set of UHV friction experiments, we compare the behavior of silicon nitride and boron nitride, depending on the cleaning procedure.

Results are presented in figures 1, 2, 3 and 4.

Friction of annealed  $\text{Si}_3\text{N}_4$  under vacuum is high and reproducible (figure 1)  $f = 0.8$ . The propanol-cleaned specimens give a low friction ( $f < 0.2$ ) at the very beginning of the test, but quickly, after a few passes, the friction drops up to the same high value ( $f = 0.8$ ). Compared to h-BN, we can say that surface contamination does not play the same role, in the case of h-BN friction it lubricates with durability, in the case of  $\text{Si}_3\text{N}_4$  friction, the effect is very limited (see figures 3 and 4). At the same time,  $\text{Si}_3\text{N}_4$  friction is more fluctuating than h-BN friction.

### II - FRICTION OF MIXED COUPLES BN/ $\text{Si}_3\text{N}_4$ and $\text{Si}_3\text{N}_4$ /BN under UHV. COMPARISON WITH THE SAME ANTACONISTS

It was very interesting here to study the friction of h-BN against  $\text{Si}_3\text{N}_4$  when using the two situations of pin on flat.

Results are shown in figures 5 and 6 for UHV conditions, propanol cleaned and annealed surfaces. It is very amazing to note that BN/ $\text{Si}_3\text{N}_4$  under UHV gives lower friction values than the opposite  $\text{Si}_3\text{N}_4$ /BN : (0.4/0.7

for annealed surfaces and 0.2/0.3 for propanol cleaned surfaces) see table below. It is also interesting to see that friction of BN/Si<sub>3</sub>N<sub>4</sub> (0.4) is lower than BN/BN (0.6/0.7) and Si<sub>3</sub>N<sub>4</sub>/Si<sub>3</sub>N<sub>4</sub> (0.8) ! (see figures 7 and 8).

|              | BN/BN | BN/Si <sub>3</sub> N <sub>4</sub> | Si <sub>3</sub> N <sub>4</sub> /BN | Si <sub>3</sub> N <sub>4</sub> /Si <sub>3</sub> N <sub>4</sub> |
|--------------|-------|-----------------------------------|------------------------------------|----------------------------------------------------------------|
| UHV annealed | 0.7   | 0.4                               | 0.7                                | 0.8                                                            |
| UHV          | 0.35  | 0.2                               | 0.3                                | 0.8                                                            |

When examining the friction curves for BN/Si<sub>3</sub>N<sub>4</sub> under vacuum, the reproducible shape suggests that a tribochemical reaction is involved between BN and Si<sub>3</sub>N<sub>4</sub>. At the opposite, the friction curves for Si<sub>3</sub>N<sub>4</sub>/BN are much more monotonous. At the moment we have no clear explanation for this phenomenon, perhaps a hardness effect is also possible, undoubtedly wear debris analysis should help us to interpretate this behavior difference.

### List of figures

Figures 1-2 : Friction of  $\text{Si}_3\text{N}_4$  and BN/BN under UHV. Reproducibility tests.

Figures 3-4 : Comparison of  $\text{Si}_3\text{N}_4/\text{Si}_3\text{N}_4$  and BN/BN friction.

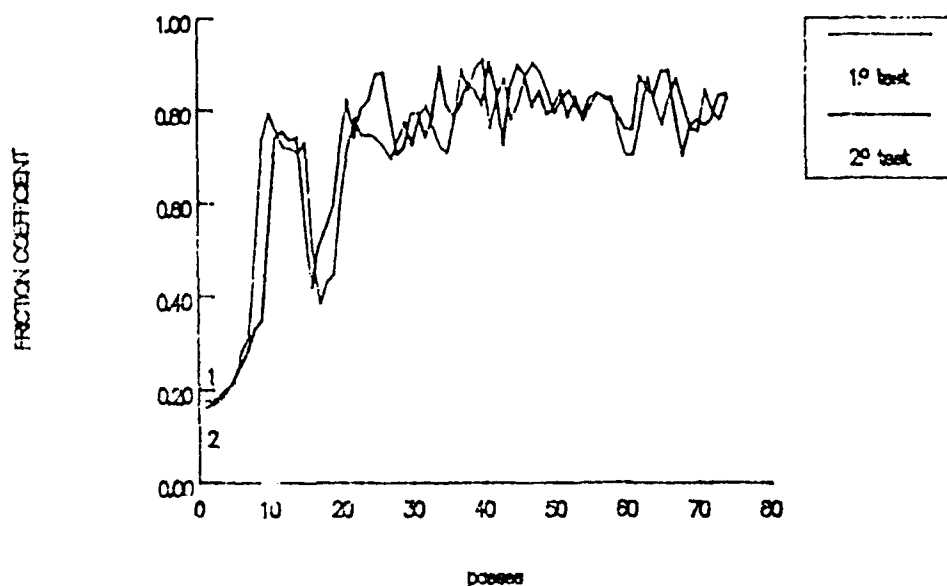
Figures 5-6 : Friction of BN/ $\text{Si}_3\text{N}_4$  and  $\text{Si}_3\text{N}_4$ /BN under UHV. Reproducibility tests.

Figures 7-8-9-10 : Comparison between the different possibilities :

|                                                                             |                              |
|-----------------------------------------------------------------------------|------------------------------|
| BN/BN - BN/ $\text{Si}_3\text{N}_4$                                         | } annealed<br>and<br>cleaned |
| $\text{Si}_3\text{N}_4$ /BN - BN/ $\text{Si}_3\text{N}_4$                   |                              |
| $\text{Si}_3\text{N}_4$ /BN - $\text{Si}_3\text{N}_4/\text{Si}_3\text{N}_4$ |                              |

Si<sub>3</sub>N<sub>4</sub> / Si<sub>3</sub>N<sub>4</sub>

Ultra High Vacuum (Propanol)



Si<sub>3</sub>N<sub>4</sub> / Si<sub>3</sub>N<sub>4</sub>

Ultra High Vacuum (Annealed)

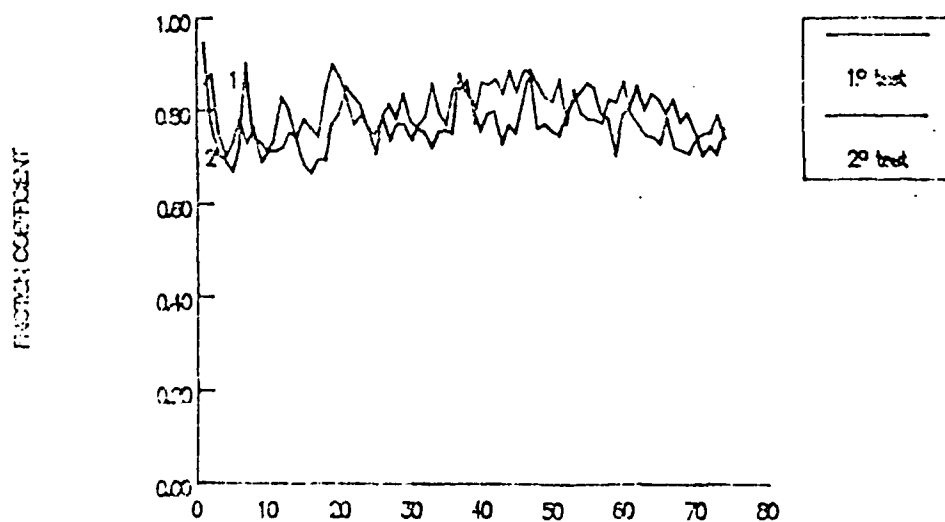
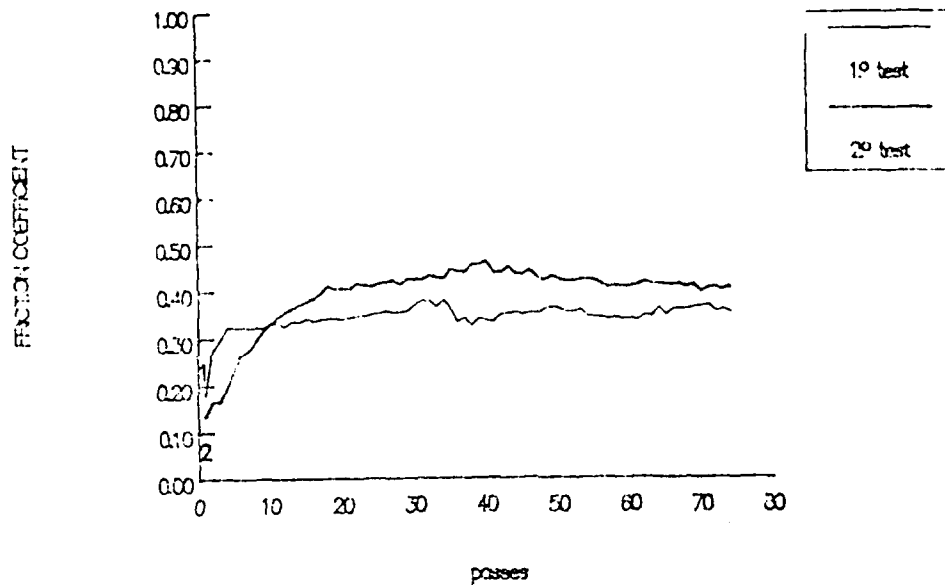


Fig 1 D-141



BN \ BN

Ultra High Vacuum (Propanol)



BN \ BN

Ultra High Vacuum (Annealing)

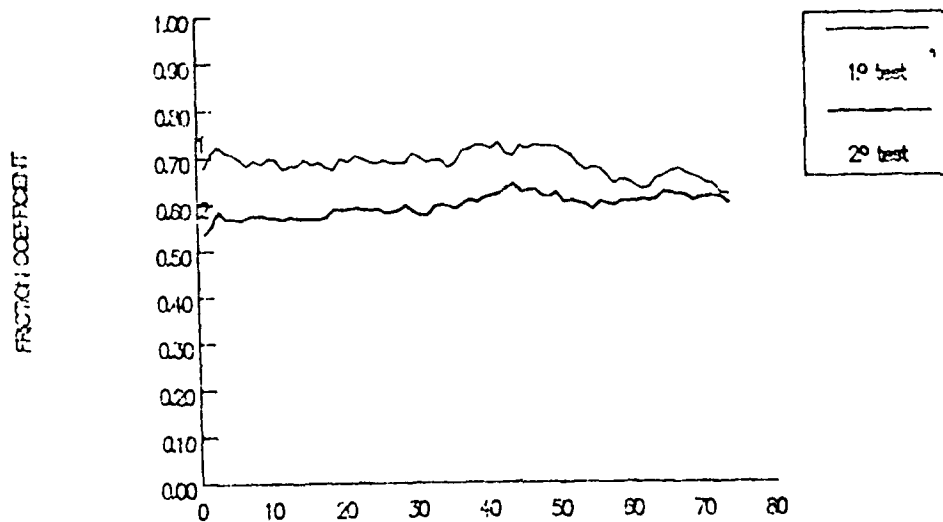


Fig 2 D-142

# Si3N4 / Si3N4

## Ultra High Vacuum

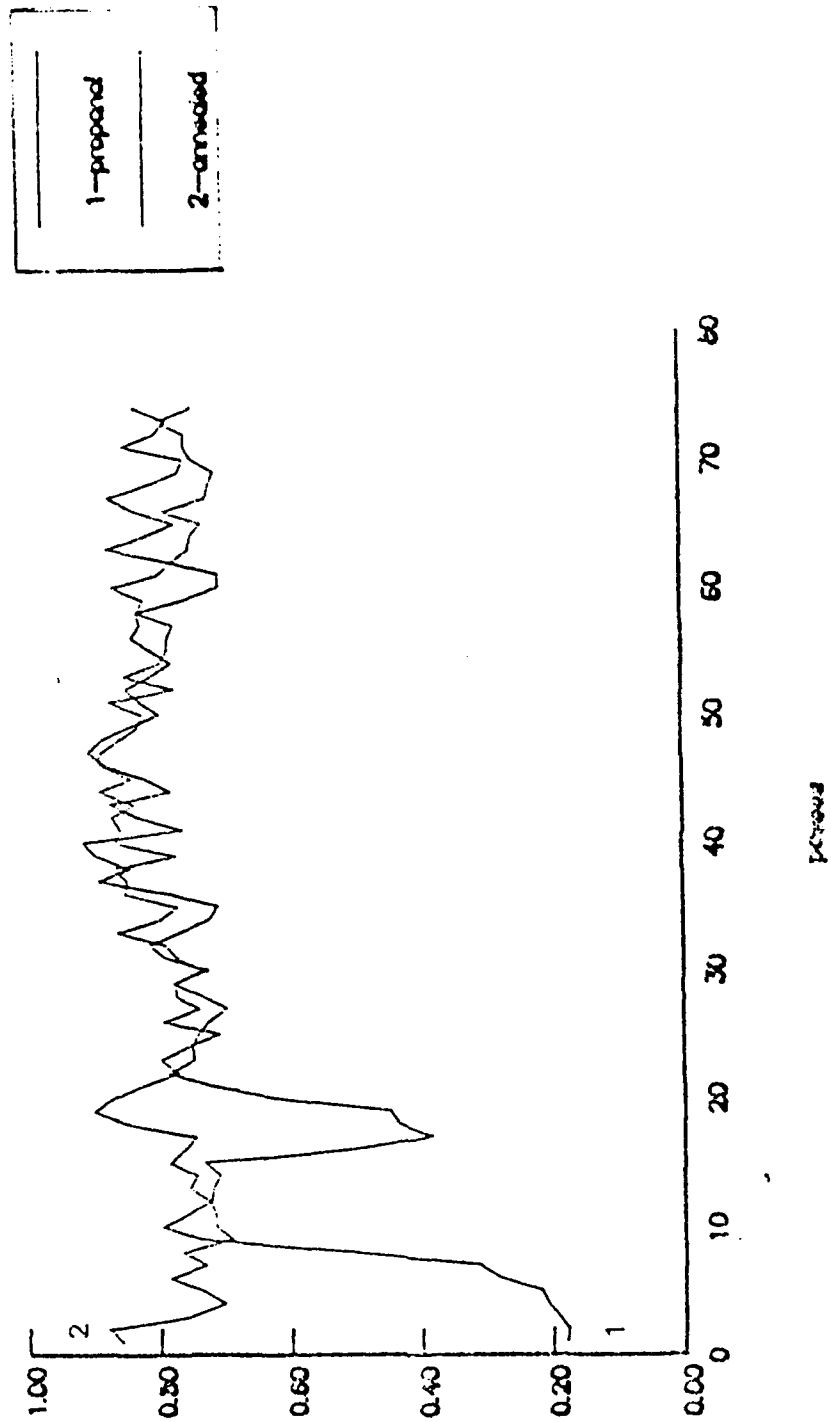


Fig 3

Friction Coefficient

D-143

# BN \ BN

## Ultra High Vacuum

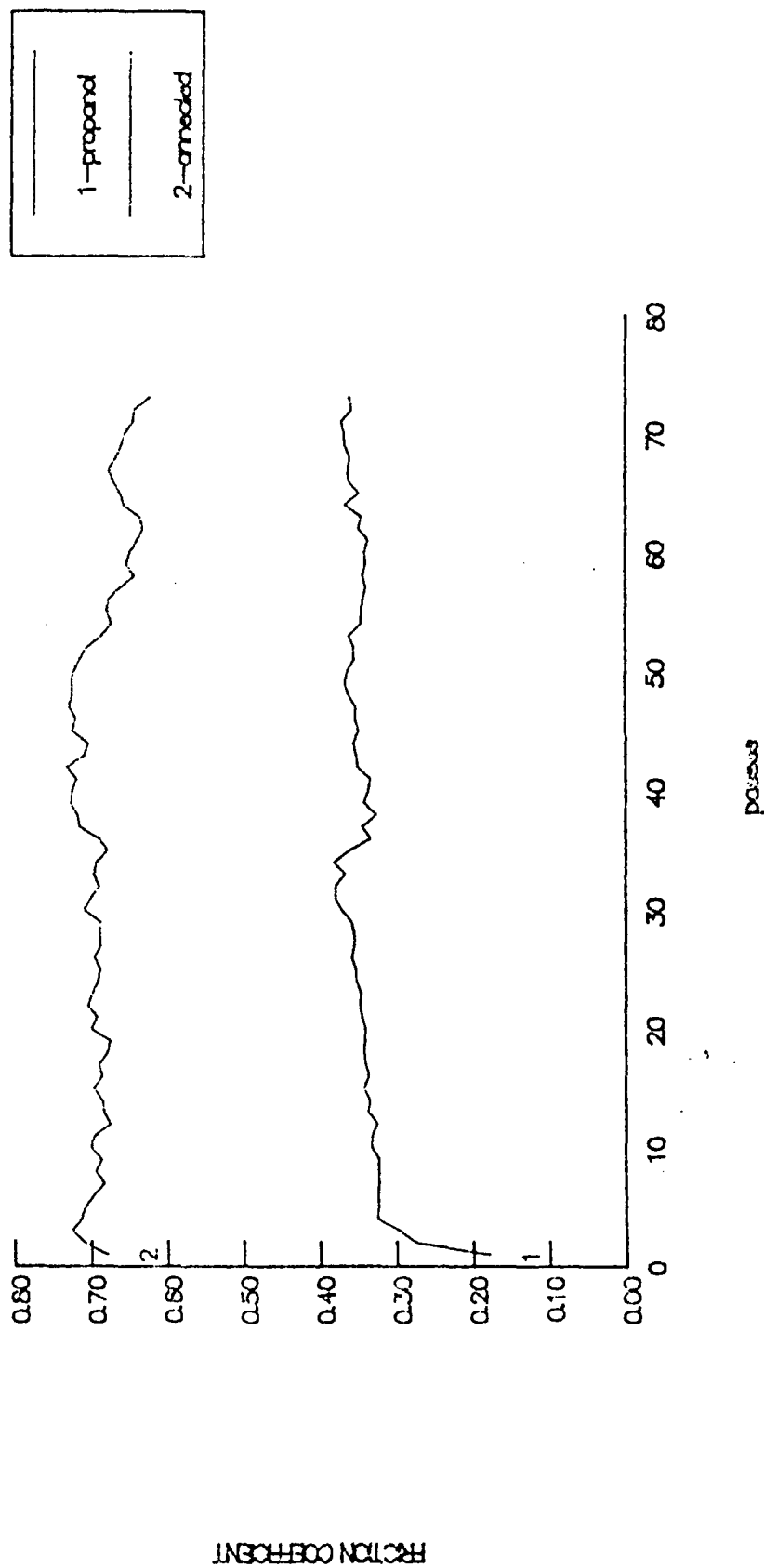
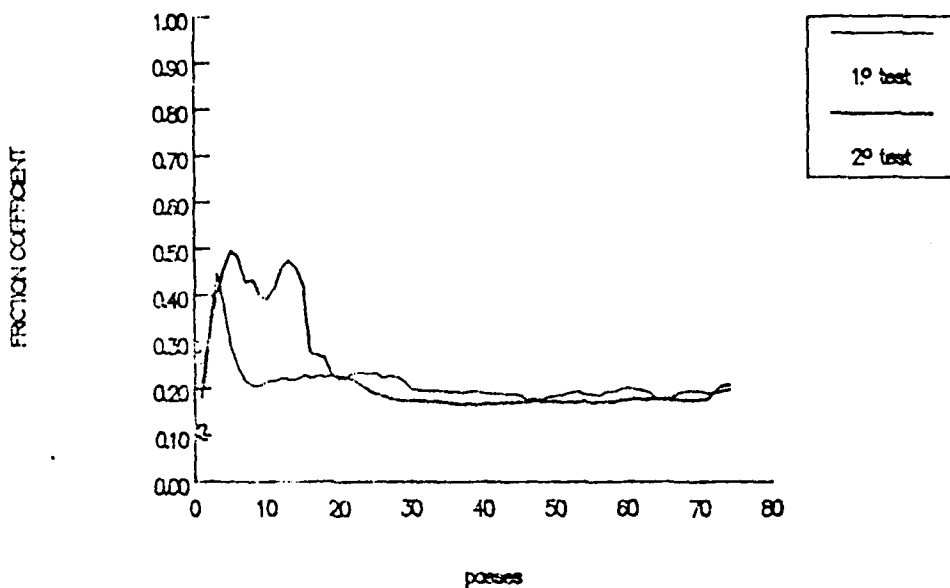


Fig 4

BN \ Si<sub>3</sub>N<sub>4</sub>

Ultra High Vacuum (Propanol)



BN \ Si<sub>3</sub>N<sub>4</sub>

Ultra High Vacuum (Annealed)

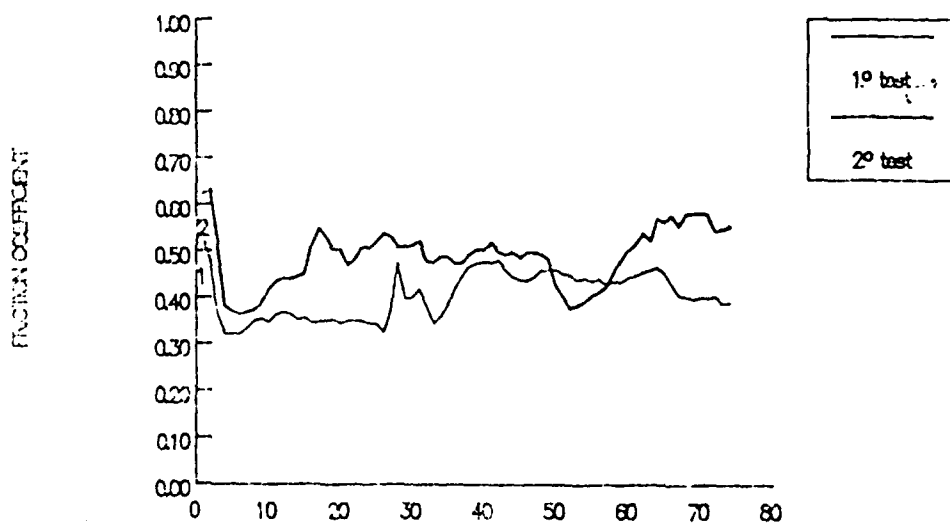
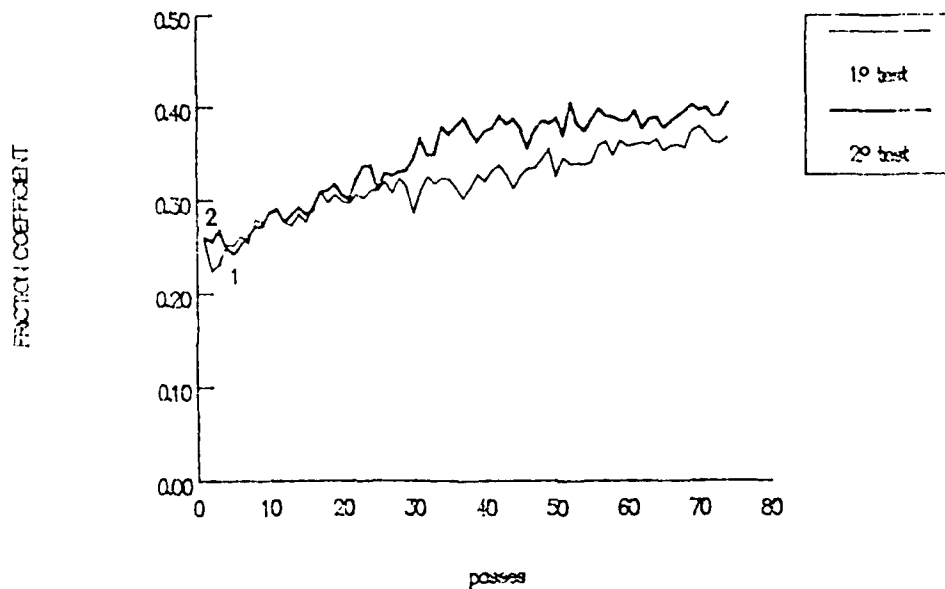


Fig 5 D-145

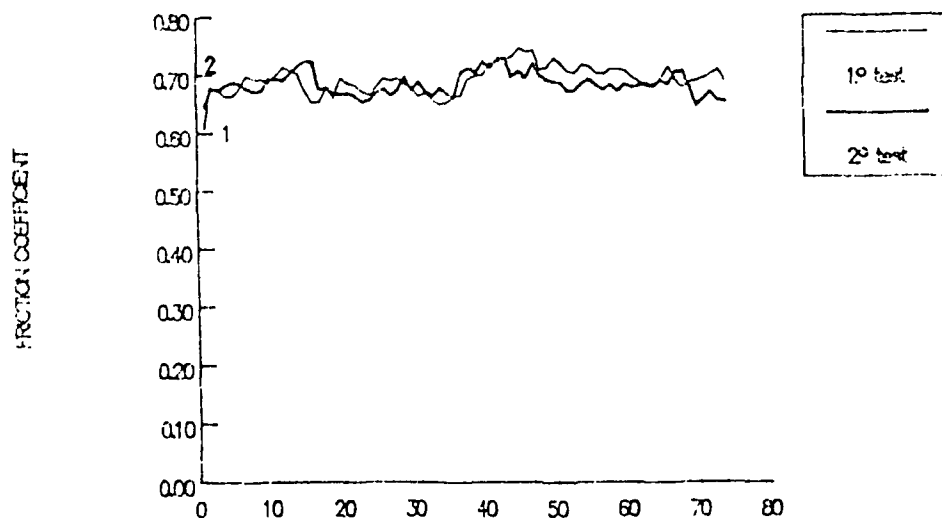
Si<sub>3</sub>N<sub>4</sub> / BN

Ultra High Vacuum (Propanol)



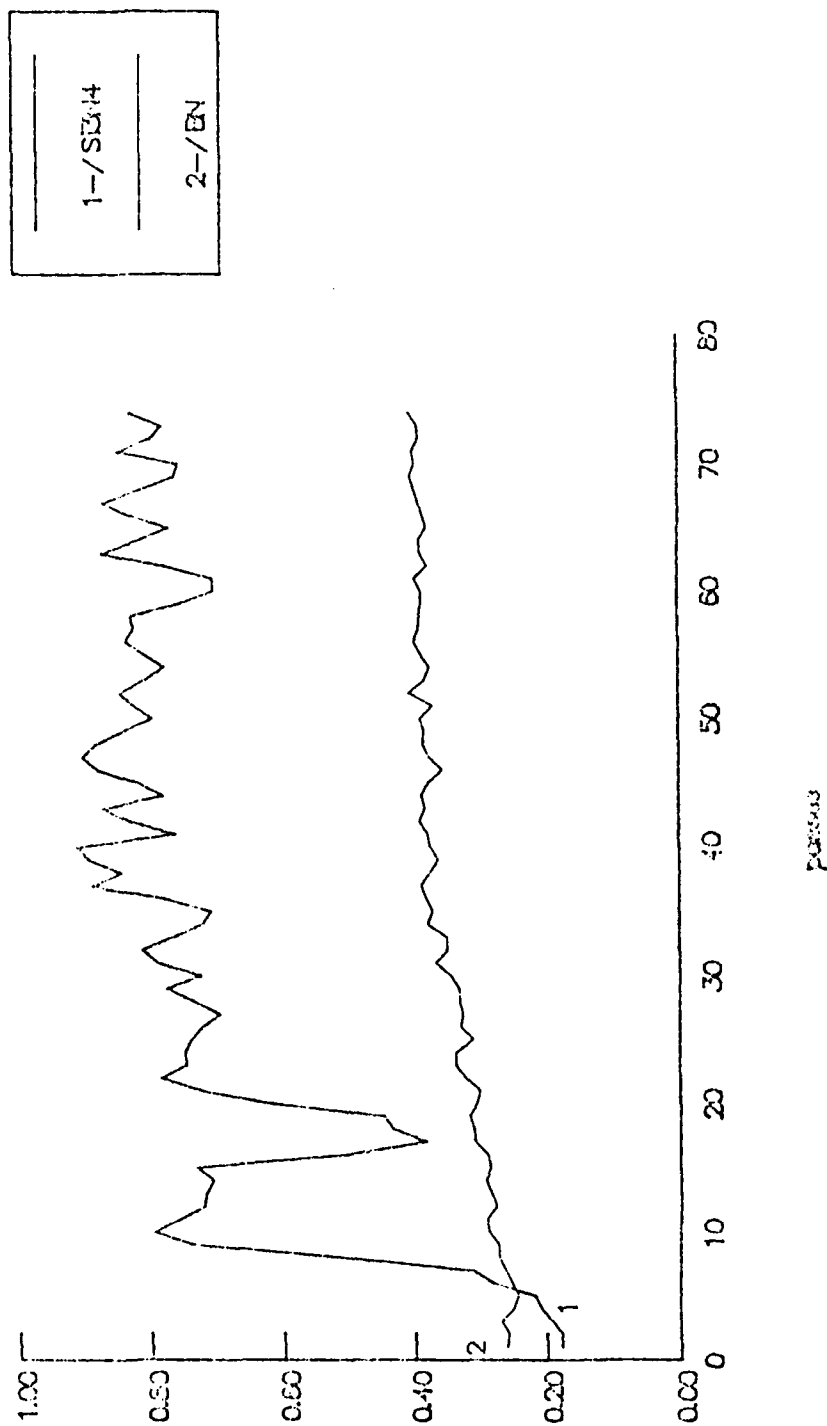
Si<sub>3</sub>N<sub>4</sub> / BN

Ultra High Vacuum (Annealed)



Si3N4 / BN and Si3N4

Ultra High Vacuum (Propenol)

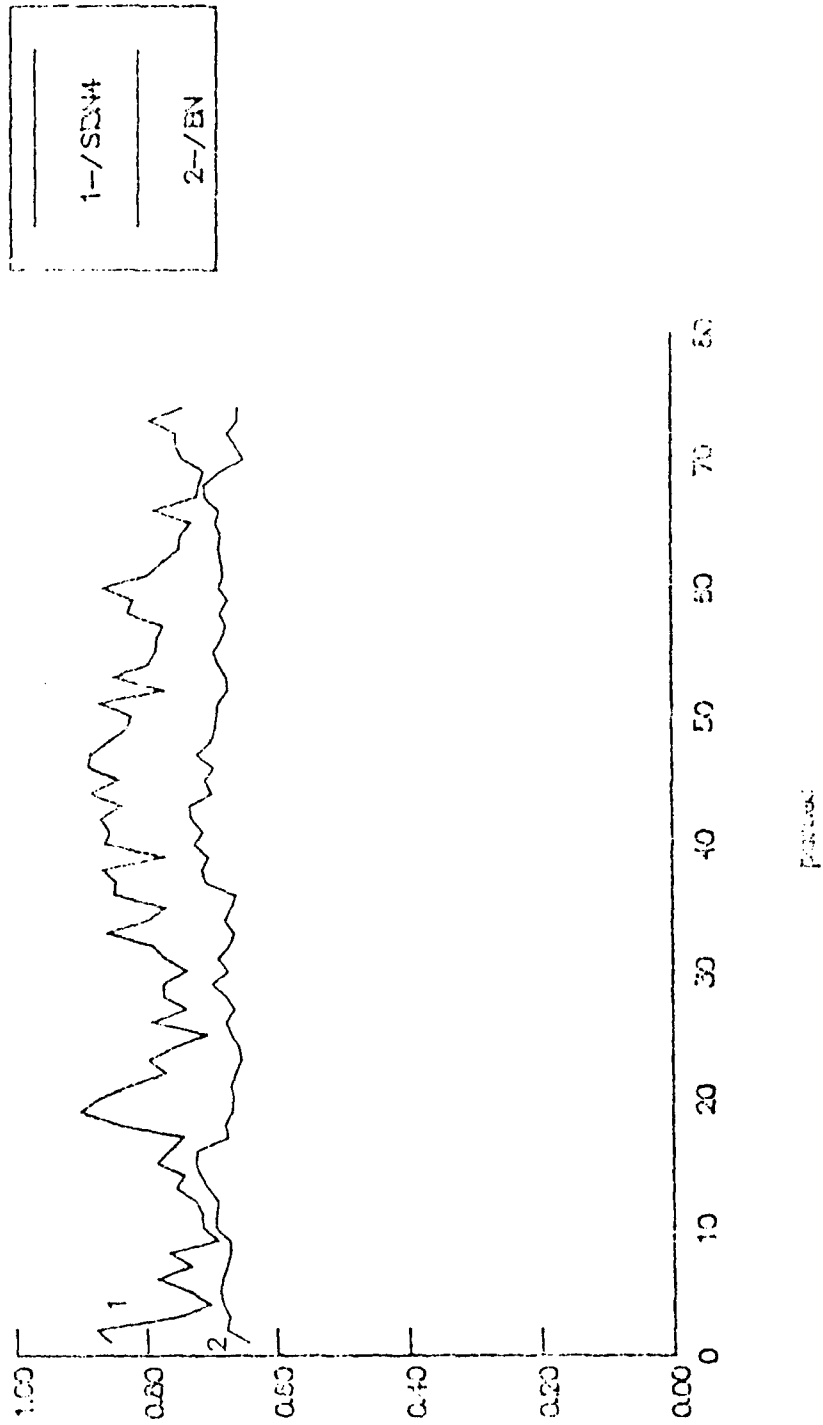


INSTRUMENTATION

D-147

Figure 7

# Si3N4 / EN and Si3N4 Ultra High Vacuum (Annealed)



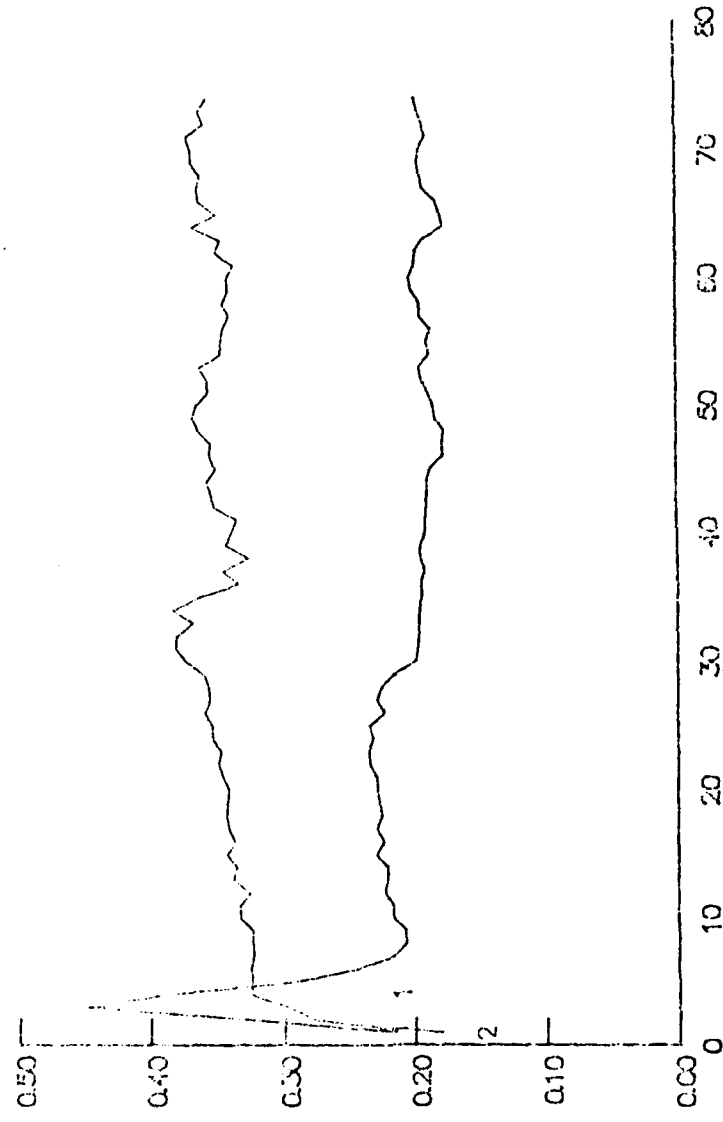
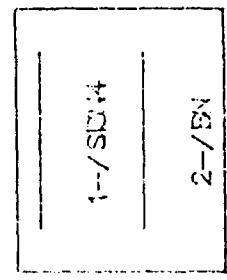
FRICTION COEFFICIENT

D-148

Figure 3

BN / BN and Si3N4

Ultra High Vacuum (Propanol)

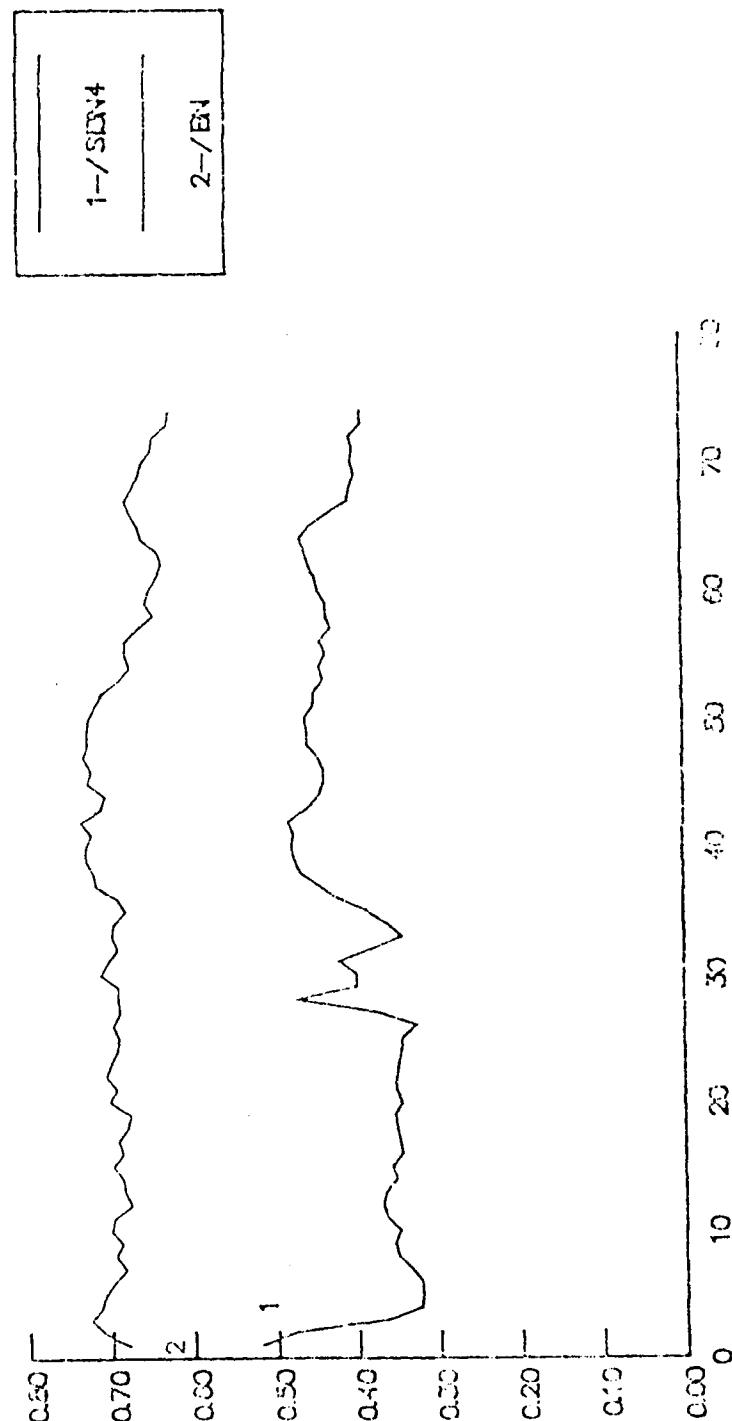


Percent

Fig. 2



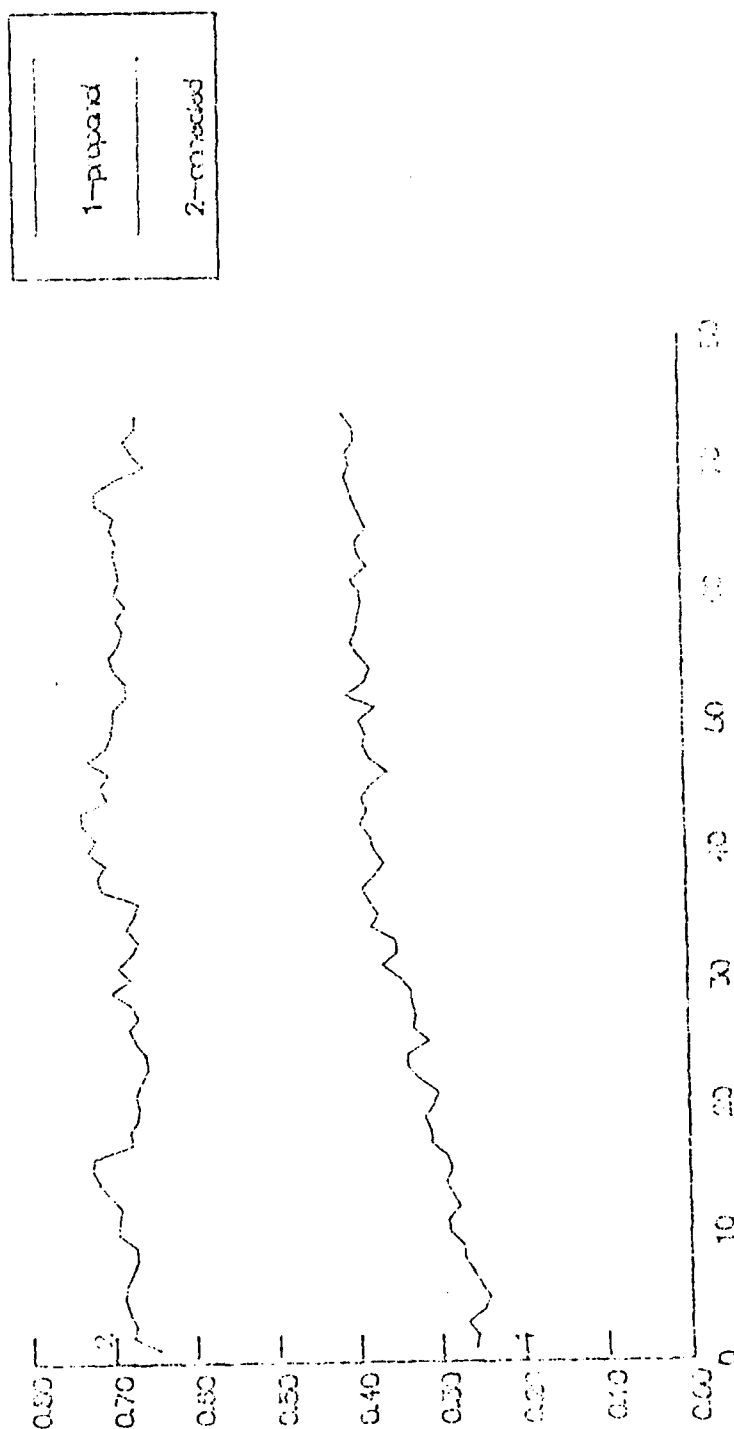
# BN / BN and Si<sub>3</sub>N<sub>4</sub> Ultra High Vacuum (Annealed)



D-650



# Si3N4 / BN Ultra High Vacuum

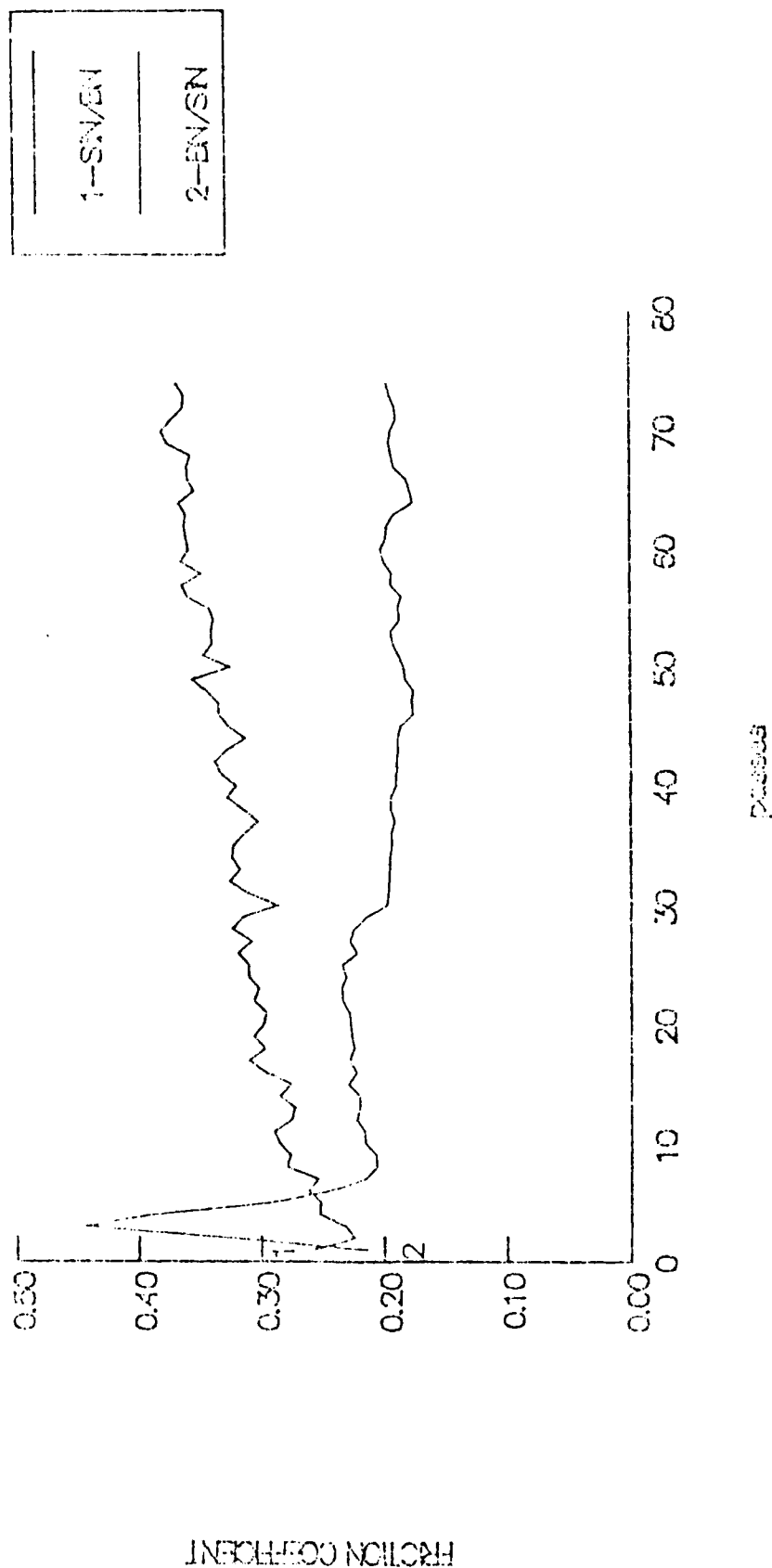


RESEARCH NATIONAL

D-152

Si3N4 / BN and BN / Si3N4

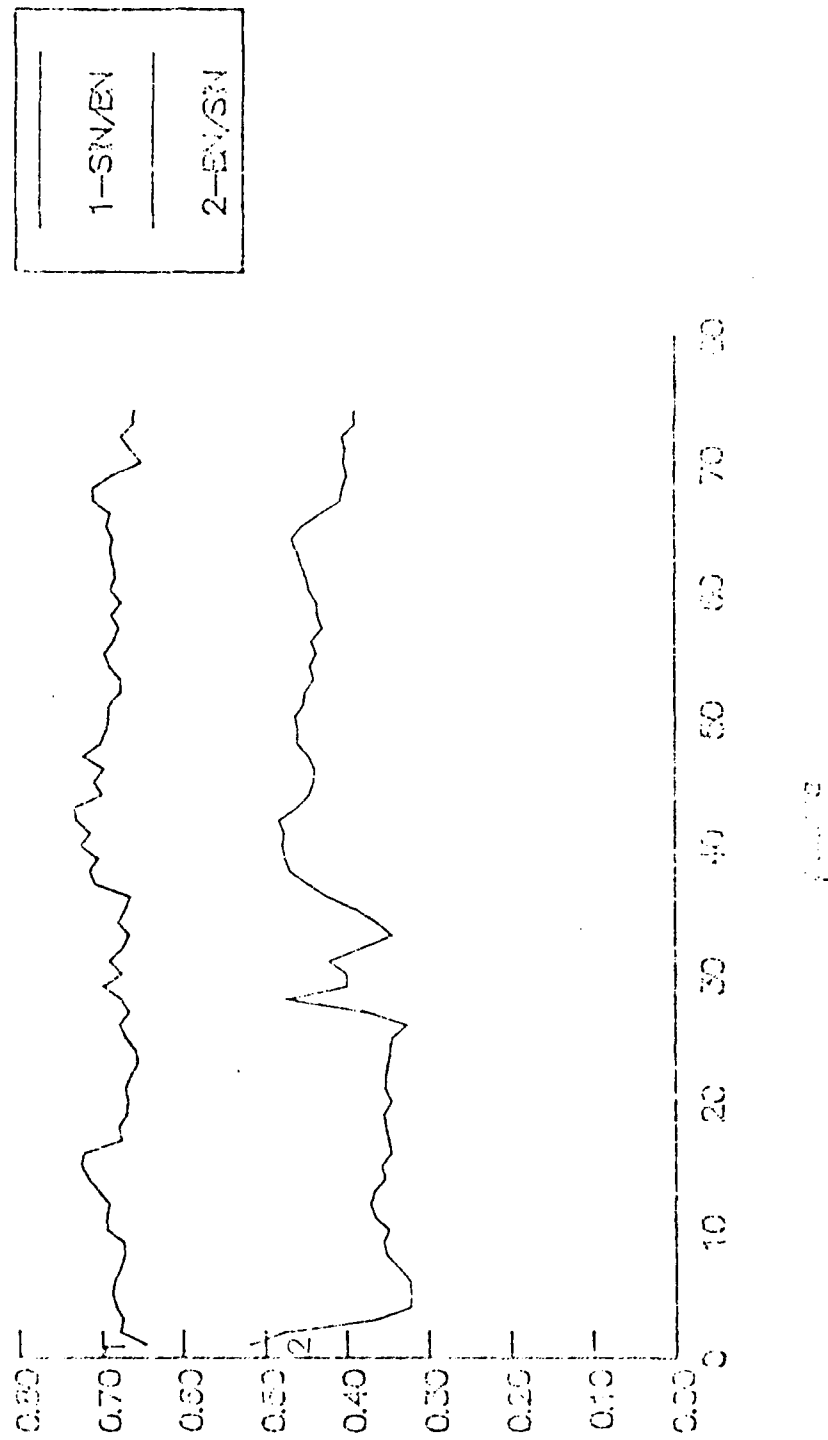
Ultra High Vacuum (Propanol)



D-153

# Si3N4 / BN and EN / Si3N4

## Ultra High Vacuum (Annealed)



Friction Coefficient

D-154

## **APPENDIX E**

**J.-M Martin, Th. Le Mogne, H. Montes, and M.N. Gardos, "Tribochemistry of Alpha Silicon Carbide Under Oxygen Partial Pressure," Proc. 5th Int. Congress on Tribology, EUROTRIB '89, Paper S2, 5/5, June 12-15, 1989, Helsinki, Finland**

# TRIBOCHEMISTRY OF ALPHA SILICON CARBIDE UNDER OXYGEN PARTIAL PRESSURE

J.M. Martin\*, Th. Le Mogne\*, H. Montes\*, M.N. Gardos\*\*

Friction and wear of alpha silicon carbide against itself was experimentally investigated with a pin-on-flat machine installed in an ultra high vacuum (UHV) chamber. The influence of oxygen partial pressure was highlighted. Characterization of interface materials was carried out by surface analysis (AES) and Energy Filtered Electron Microscopy (EFEM). Friction under vacuum is dominated by grain attrition and silicon carbide amorphization, producing high friction values ( $\mu = 0.8$ ). Friction under oxygen is controlled by silicon oxide formation and some graphitization of wear products, which is mainly responsible for a low friction value ( $\mu < 0.1$ ). The data suggest that friction of silicon carbide is tribochemically controlled and extremely dependent on environmental reactive gases.

## 1 INTRODUCTION

The fundamentals of the surface chemistry involved and the tribological properties of alpha silicon carbide ( $\alpha$ -SiC) are not clearly understood. The friction properties depend strongly on the surface chemistry of silicon carbide and also on the crystallographic orientation [1] [2]. The preferred crystallographic slip direction is the  $\langle 1120 \rangle$  direction. The plastic deformation can occur by translational slip in that direction that is along the atoms which are closely packed. The surface of  $\alpha$ -SiC is also affected by temperature [3], because an increase in temperature under vacuum causes graphitization of the surface and yields low friction values. The role of oxygen in  $\alpha$ -SiC friction has also been studied [4], but as far as tribochemistry is concerned, there has been no detailed analysis of the processes involved.

We have developed an UHV tribometer coupled to surface analysis techniques. The diagram of this apparatus is shown in figure 1. We have conducted experimental work at room temperature in order to emphasize the role of tribochemistry and therefore to minimize the role of the static interaction of the  $\alpha$  SiC surface with oxygen prior to sliding.

\* Ecole Centrale de Lyon Ecully, France

\*\* Hughes Aircraft Company, El Segundo, CA 90245, USA

Surface tribochemistry of  $\alpha$ -SiC was analyzed by scanning Auger Electron Spectroscopy (AES) ; high resolution analysis of third bodies was carried out in the Transmission Electron Microscope (TEM).

In this tester one can rotate a flat disc or oscillate a flat plate against a hemispherical pin, in an ultrahigh vacuum (UHV) chamber. A vacuum environment of  $10^{-8}$  Pa can be achieved. The test consisted of alternately sliding the hemispherical pin ( $R = 4$  mm) for 160 passes (length of the stroke = 3 mm) at a sliding speed of 0.2 mm/s with a normal load of 2 N (corresponding to a maximum Hertzian contact pressure of 1 GPa). Two friction tests are presented and discussed here in detail. The first experiment was carried out under UHV ( $10^{-8}$  Pa). AES analyses were performed at the end of this test, inside and outside the wear scar. The second experiment was carried out with an oxygen partial pressure of 50 Pa in the chamber with the same specimens (by slightly turning the pin and displacing the flat to generate a fresh wear scar). The results can thus be compared.

## 2 MATERIAL AND SPECIMEN PREPARATION

The flat was a single crystal of  $\alpha$ -SiC (SOHIO) and the pin was polycrystalline sintered  $\alpha$ -SiC (HEXOLLOY SA) containing mainly BN as a sintering aid. The aim of the preparation was mainly to eliminate oxygen and free carbon species from the surfaces. After polishing with diamond paste, the specimens were placed in the UHV chamber and both pin and flat were submitted to alternate ionic etching and annealing to obtain the silicon-carbon elemental composition before the friction test [6]. Annealing at a temperature over 900 K is known to graphitize the very top of the surface [5] so the annealing temperature was 700 K.

## 3 RESULTS

The evolution of friction coefficients is presented in figure 2. The SEM micrograph of the wear scar on the pin is shown in figure 4. The main results show :

- that friction under UHV is high ( $f \approx 0.8$ ),
- that the presence of 50 Pa oxygen in the chamber rapidly leads to a drastic decrease of the friction coefficient to values below 0.1,
- that the wear volume on the SiC pin is higher in oxygen than in vacuum,
- that the worn surface is smoother under oxygen partial pressure than in vacuum,
- that under UHV, the SiC flat is severely damaged and fractured with possible transfers from the pin.

From this first set of data, it already appears that the wear regime under oxygen is tribochemically controlled.

Some AES spectra obtained inside and outside the wear scar at the end of the tests are presented in figure 3. It can be stated :

- that under 50 Pa oxygen, silicon is preferentially bound to oxygen in the wear scar but the carbon signal has disappeared ; outside the track, the argon peak is always visible and only slight oxidation takes place, in agreement with the literature [7].

The examination of third bodies (as wear debris) were carried out by analytical electron microscopy (EFEM) at the end of the test after breaking vacuum. Typical features are presented in figure 5.



It shows :

- that under UHV, wear debris is composed of collapsed, spheroidal grains whose size lies in the 10 nm-100 nm range without any preferential orientation. Each grain is composed of a crystalline core surrounded by a complex shell and interface between grains. The fully amorphous character of silicon carbide in this shell is demonstrated by electron diffraction and high resolution transmission electron imaging,
- that under 50 Pa oxygen, bulk silicon oxide is formed, no more carbide is detected but pregraphitic organization takes place inside and at the periphery of amorphous silicon oxide. The fine structure of the 1s level excitation of carbon in EELS shows the existence of a short range order in carbon planes and the high resolution image (figure 5) confirms this fact. Surprisingly, carbon was never detected by AES analysis of the wear scar and this is not explained.

#### 4 DISCUSSION

##### 4.1. SiC/SiC friction under UHV

The high average value of the friction coefficient (0.8) is in good agreement with previous works reported in the literature. As is well known in the case of ceramics such as silicon carbide, high adhesion is the cause of fracturing in a Hertzian contact ; moreover, the debris produced can develop an abrasive regime with plastic deformation.

From the tribochemical point of view, the phenomenon extends far beyond simple fracturing. The third bodies formed are sheared, compacted in the interface and reduced to very small, sub-micronic grains. Because there are no preferential, low energy shear planes in the SiC crystal structure, friction-induced attrition is accompanied by amorphization and also by some decomposition of silicon carbide into free carbon species ; a great deal of energy is needed to break the strong covalent Si-C bond ( $sp^3$  hybridization). Our data show that friction-modified silicon carbide is fully amorphous, on the atomic scale ; at the same time, free carbon itself does not exhibit long range order. So the interface material may be described as an arrangement of distorted  $[SiC_4]$  tetrahedra bound to each other in a disordered structure, and intercalated by carbon in a pre-graphitic organization. It is believed that friction energy is mainly dissipated in this amorphous structure, and that the absence of a low energy shear plane can explain the high value of the friction coefficient.

##### 4.2. SiC/SiC friction under oxygen

Under these conditions (50 Pa  $O_2$ ), the friction coefficient rapidly falls to a very low value ( $f = 0.08$ ). The high wear loss of the pin indicates that corrosive wear has occurred, and that carbon in the carbide form has disappeared. The analyses showed that the interface material consisted of a mixture of silicon oxide and graphitic carbon ( $sp^2$  hybridization). When heated to 1500 K under vacuum, the SiC surface graphitizes by the collapse of the carbon planes lying perpendicular to the c axis of the crystallographic unit cell [5]. Friction on this heat-treated surface gives a low friction coefficient [3] due to low van der Waals energy interaction between carbon planes. It is suggested that friction induced oxidation of silicon carbide at low temperature also leads to a graphitic organization by a similar process, because carbon cannot escape as

carbon oxide in the chamber. Although the presence of silicon oxide "rolling pins" may influence the friction process, the graphitic structure is thought to be mainly responsible for the very low friction value.

## 6 CONCLUSION

The tribochemistry of alpha silicon carbide was investigated with a pin-on-flat friction machine in an UHV chamber equipped with surface analysis techniques. Special attention was paid to the role of oxygen partial pressure on the generation of interface products and their role in friction and wear.

The main results are :

- under vacuum,  $\alpha$ -SiC friction is dominated by the fracture, compaction and attrition of spheroidal grains in the interface region. No preferential shear planes appear to form, but the amorphization of silicon carbide takes place mainly at the edge of grains. Consequently, friction is high ( $f = 0.8$ ),
- under 50 Pa  $O_2$  partial pressure, silicon carbide quickly oxidizes at the interface, producing silicon oxide and some graphitization of residual carbon from the carbide. Graphite having low energy shear planes is thought to be responsible for low friction coefficient ( $f < 0.1$ ).

## ACKNOWLEDGEMENT

This work was performed under a subcontract from Hughes Aircraft Company, P.O. n° S9-507874-SRW as a part of the "Determination of Tribological Fundamentals of Solid Lubricated Ceramics" program DARPA order n° 5177, AFWAL contract n° F33615-85-C-5087 with B.D. Mc Connell acting as the AFWAL Project Manager.

## REFERENCES

- [1] MIYOSHI, K. and BUCKLEY, D. "Friction, deformation and fracture of single-crystal silicon carbide", ASLE/ASME Lubrication Conference, Kansas City, October 3-5, (1977).
- [2] MIYOSHI, K. and BUCKLEY D. "Friction and wear behavior of single-crystal carbide in sliding contact with various metals", ASLE Transaction 22, 3, (1979), pp. 245-256.
- [3] MIYOSHI, K. and BUCKLEY D. "Tribological properties and surface chemistry of silicon carbide at temperature to 1500°C", ASLE/ASME Lubrication Conference, New Orleans Louisiana, October 5-7, (1981).
- [4] MIYOSHI, K. and BUCKLEY D. "Effect of oxygen and nitrogen interactions on friction of single-crystal silicon carbide", NASA TP.1265 (1978).
- [5] ADACHI, S., MOHRI, M. and YAMASHINA, T. "Surface graphitization process of SiC (0001) single-crystal at elevated temperatures", Surface Science 161, (1985), pp. 479-490.
- [6] VAN BOMMEL, A.J. CROMBEEN, J.E. VAN TOOREN, A. "Leed and auger electron observations of the SiC(0001) surface", Surface Science 48, (1975), pp. 463-472.
- [7] MUEHLHOFF, L., and al., "Comparative electron spectroscopy studies of surface segregation on SiC(0001)", J. Appl. Phys. 60, (8), 10 October 1986.

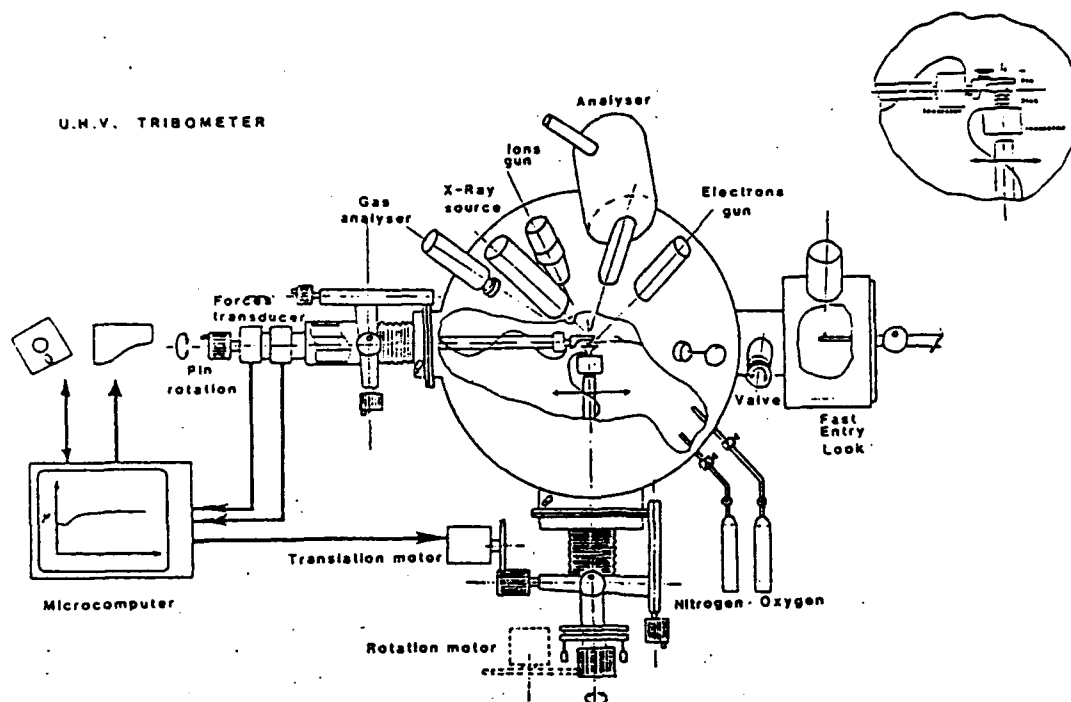


Fig.1 Schematic representation of the UHV tribometer with AES/XPS analysis.

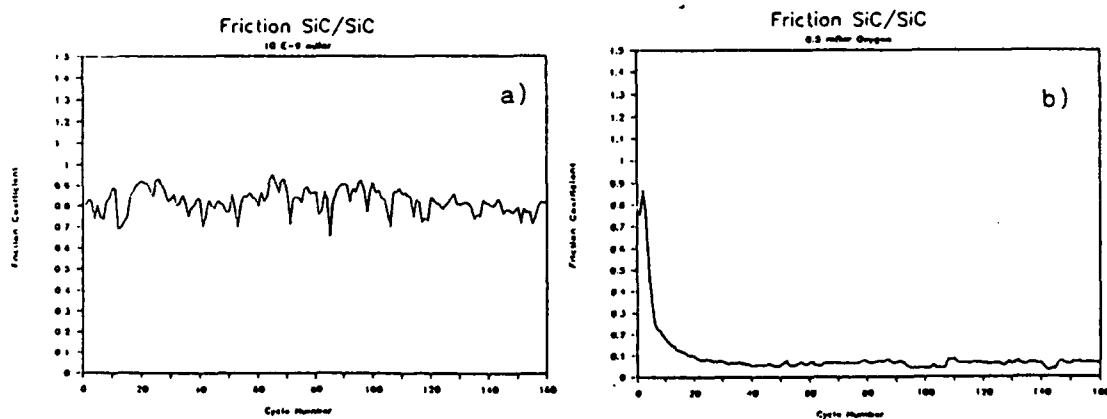


Fig. 2 Evolution of the friction coefficient against number of passages.

- a) SiC/SiC under vacuum ( $10^{-8}$  Pa),
- b) SiC/SiC under 50 Pa oxygen partial pressure

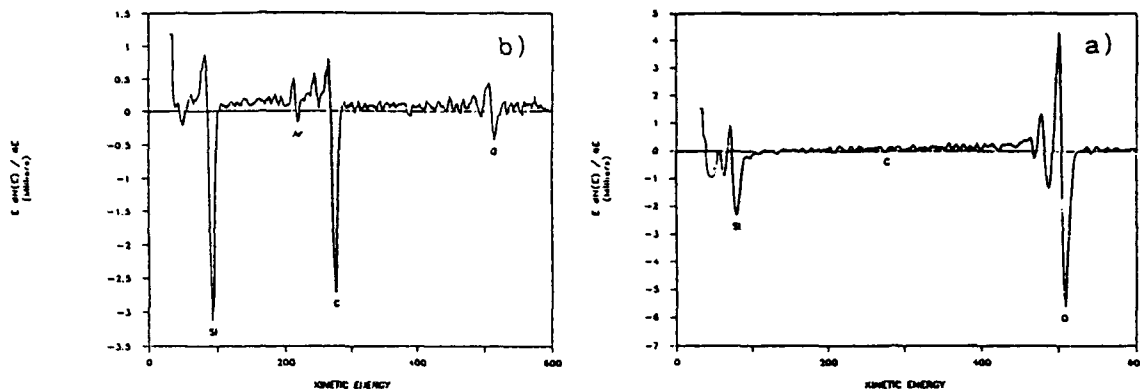


Fig. 3 AES spectra obtained on the  $\alpha$ -SiC surface, at the end of the test under oxygen partial pressure :  
a) inside the wear scar,  
b) outside the wear scar.

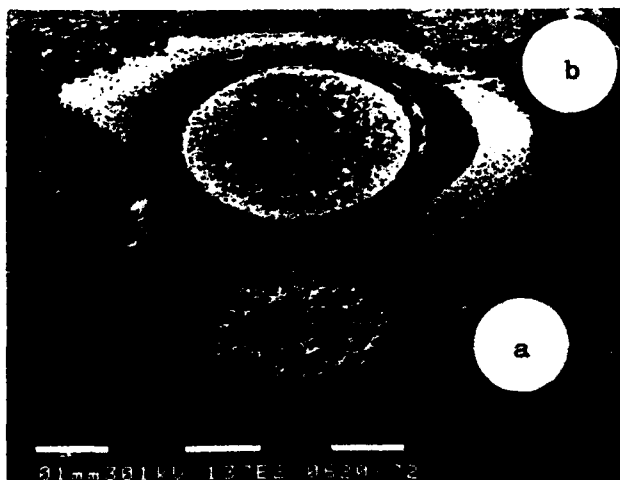


Fig. 4 SEM micrograph of the wear scar on the SiC pin :  
a) under UHV,  
b) under 50 Pa oxygen.



Fig. 5 High resolution TEM micrograph of wear debris from the test under oxygen.

80 Å

## **APPENDIX F**

**J.J. Erickson, "Meeting at MRL Re: SEM Cryogenic Tribotester,; Hughes  
Interdepartmental Correspondence No. 7642.20/1076, 30 November 1987**

# HUGHES

BLDG. **E1** MAIL STA. **C132**  
LOC. **EO** PHONE **66579**

connects the dewar to the specimen holder. The temperature of the holder is monitored by temperature sensors in the holder. Information from the sensors is connected to a rack mountable temperature controller which controls both the flow of nitrogen and a heater in the sample folder.

#### STYLUS HOLDER

The previously discussed specimen holder will hold the flat specimen in the tribotester. A spherically-tipped stylus is rubbed against the flat specimen during the use of the tribotester. This stylus should also be cooled in the cryogenic tribotester. During this meeting it was concluded that this is extremely difficult to accomplish since the stylus is held by a loaded pivoting beam similar to the way a phonograph needle is held against a record. The load and friction forces are measured by orthogonal transducers which are part of the beam. Attempts to cool the stylus through the use of cooled gaseous nitrogen conducted through plastic tubing would introduce forces into the beam that would anomalously alter the load and friction forces.

An alternate method of using a Peltier cooler to cool the stylus was discussed. This also was found to be not feasible due to the amount of heat that a Peltier cooler generates. Since the whole apparatus is in a vacuum the Peltier cooler would best be cooled by conduction through its mounting plate. This would be too close to the force transducers, however, and would cause a large error in the load and friction force readouts due to thermal drift. (A similar problem was encountered in the high temperature SEM tribotester due to the stylus heater.)

The solution that was agreed on was to use a stylus holder that has good thermal capacity (a block of copper, for example) and allow this stylus holder to contact a separate cold block for a period of time. During this period of time, the stylus holder and stylus would be cooled to the temperature of the cold block. Also, during this period of time the stylus would not be in contact with the flat. After the stylus holder was sufficiently cooled, the block would be moved away, allowing the stylus to again come in contact with the flat. Wear experiments would then continue until the stylus temperature got too high and again the cold block would contact the stylus holder and lift it from the flat while it is cooled. The cold block could be cooled by the gaseous nitrogen lines or a Peltier cooler.

#### VARIABLE LOAD CAPABILITY

One of the shortcomings of the high temperature SEM tribotester was the lack of the capability to vary the load force between the stylus and flat while the specimens were being observed in the SEM. The load could be manually varied by adjusting weights prior to placing the tribotester into the SEM, but could only be changed by terminating the

experiment in progress and removing the tester from the SEM to manually readjust the load.

During the meeting it was decided that the load force could be made variable by placing the weight on a jack screw and then driving the screw with a motor controlled external to the SEM. By moving the weight back and forth on the shaft, its distance from the fulcrum of the beam would be varied, thereby varying the effective load force.

A second approach to providing a variable load force will also be investigated. It may be possible to exert a force on the beam by attaching an iron rod to the beam. This rod would then be suspended downward partially into a magnetic coil. By varying the current through the coil it would be possible to vary the attractive force on the rod and therefore vary the load force on the beam. It will be necessary to determine whether small displacements of the iron rod will affect the attractive force of the magnetic field on the rod. In other words, for a constant current through the coil small displacements of the iron rod should result in no changes on the load force.

#### POTENTIAL PROBLEMS

While many of the potential problems for the cryogenic SEM tribotester have already been encountered and resolved in the high temperature SEM tribotester, two potential problems unique to the cryogenic tester were recognized and discussed. The first potential problem is the possibility of any contaminants in the SEM chamber tending to condense on the cryogenically cooled sample. The contaminants could result either from outgassing of the SEM or tribotester materials or more likely from contaminants present in the gases introduced into the SEM tribotester.

Several possible solutions to this problem were proposed. An additional cold block could be installed in the tribotester which would be cooled prior to cooling the sample under test. In addition, the gases introduced into the tester could be passed through a cold trap to condense any contaminants prior to introduction into the tester. Finally, it was decided to simply observe the initial samples during testing to see if there is any indication of condensation on the surface and implement corrective actions as necessary.

The second potential problem is the reduced conductivity of the sample surfaces at cryogenic temperatures. This may result in the surfaces charging excessively under the SEM electron beam resulting in the inability to image the surfaces. The samples in question are at best semiconductors at room temperature and become insulators at cryogenic temperatures. Some problems were encountered when trying to image similar samples in the high temperature tester but the combination of high temperatures and partial pressures dissipated the surface charge sufficiently so that images could be obtained.



Several solutions to this problem were discussed which would either neutralize or dissipate the accumulated surface charge. Two of the more exotic and difficult to effect solutions were the use of a "proton gun" or a positive ion beam to neutralize the charge. Another possible solution might be to use metal "brushes" outside of the area being examined to "sweep" the charges from the surface that was previously bombarded by the electron beam. Again, initial experiments will be performed to determine the severity of the charging problem and corrective actions will be taken as necessary.

#### STATEMENT OF WORK

The final action of the meeting was to prepare a draft of the SOW for MRL that was agreeable to both MRL and the program, as represented by Mike Gardos.



G.J. Erickson  
Senior Scientist

JJE:ik

#### Distribution

R.W. Seibold  
M.N. Gardos  
L. Fiderer  
B.L. Soriano  
E.B. Holst  
A.B. Naselow  
R.Y. Scapple  
L.C. Lipp  
G.L. Meldrum  
P.S. Davis  
D.H. Van Westerhuyzen  
D.H. Buettner  
J.A. Zelik  
D.A. Demeo  
W.G. Brammer

## **APPENDIX G**

**L. Fiderer, "Unique Friction and Wear Tester for Fundamental Tribology Research," Hughes Technical Internal Correspondence No. 867282.00/920, 22 September 1986**

**HUGHES****TECHNICAL INTERNAL CORRESPONDENCE****ELECTRO-OPTICAL & DATA SYSTEMS GROUP**

TO: M. N. Gardos      CC: Distribution  
ORG: 76-21-10

DATE: Sept. 22, 1986  
REF: 86-7282.00/920

SUBJECT:  
Unique Friction and Wear Tester  
for Fundamental Tribology Research

FROM: L. Fiderer  
ORG: 72-82-22

BLDG: E1      M/S: D 145  
LOC: EO      PHONE: 61-64826

---

**ABSTRACT**

A novel apparatus has been developed to test the sliding friction and wear characteristics of various ceramic and other high-temperature material combinations subjected to a wide spectrum of environmental conditions. It is designed mainly for use in conjunction with ceramic-on-ceramic contact configurations in the bare and solid lubricated modes.

In the friction tester, a cylindrical rod specimen is rotated while two stationary material samples (rubshoes) are forced against the rotating surface from opposite sides under a wide range of loads, loading frequencies, speeds and temperatures.

The friction contact surfaces can be heated to temperatures ranging from 25 deg. C (77 deg. F) up to 871 deg. C (1600 deg. F). Sliding contact speeds can be varied from 0.5 to 5 m/sec (20 to 200 inch/sec). The normal contact forces can be adjusted up to 200 Newtons (45 lbs.). The applied load can be either a constant steady-state force or a time-varying, repetitive function (sinusoidal or other), with frequencies up to 50 Hz, thus simulating the actual loading conditions found in many types of machinery. Each stationary specimen can be readily changed to permit tests with flat, concave or convex cylindrical and with spherical contact surfaces. The atmosphere surrounding the contact area can be purged either with standard air or an inert gas, such as dry nitrogen, helium or argon.

The apparatus has instrumentation to monitor the temperature near the contact points, tangential and normal loads, rotational speeds and combined wear depth on the stationary and rotating surfaces. Despite its versatility and many capabilities, the tester is relatively simple, constructed with readily available state-of-the-art components, and is easily operated. Unlike other high temperature testers, it does not require a large furnace, but uses a compact infra-red quartz lamp heater. To the best of our knowledge, there is no friction tester with similar capabilities available anywhere else.

The following report describes the background leading to the development of the tester, its principles of operation, design details, and the results of mechanical and thermal breadboard tests validating the concept.

UNIQUE FRICTION AND WEAR TESTER  
FOR FUNDAMENTAL TRIBOLOGY RESEARCH

CONTENTS:

1. Introduction.
  - 1.1 Theoretical Basis.
  - 1.2 Historical Background.
2. Basic Design Concept.
3. Friction Tester Description.
  - 3.1 Loading Mechanism.
  - 3.2 Heater Assembly.
  - 3.3 Drive Spindle Assembly.
  - 3.4 Mounting Platform.
  - 3.5 Portable Stand.
4. Instrumentation.
  - 4.1 Force Measurements.
  - 4.2 Wear Measurements.
  - 4.3 Speed Measurements.
  - 4.4 Temperature Measurements.
5. Summary and Conclusion.
6. References.
7. Acknowledgements.

## 1. INTRODUCTION .

### 1.1 Theoretical Basis.

The development of the friction and wear tester described in this report is part of a long range interdisciplinary program to investigate the phenomena which occur between bare and solid lubricated ceramic surfaces under a wide variety of environmental conditions. The title of this program is "Determination of Tribological Fundamentals".

Among the main program objectives are determination of the fundamental principles of friction and wear mechanisms of bare and solid lubricated ceramics under environmental stresses and the advancement of the technology base to successfully design, build and operate solid lubricated ceramic machine components for extreme environments.

The research, conducted as part of this program, includes a careful investigation of the effects of shear as well as normal forces during both rolling contact, sliding friction contact and combinations of both. Past studies have indicated (1,2)\* that the subsurface shear stresses predominate under oil-lubricated rolling contact conditions. Under pure sliding friction conditions, the peak stresses occur primarily on the surface (3,4).

In addition, extensive investigations have been conducted and are still in progress about the physical-chemical behavior of ceramic surfaces subjected to rolling contact fatigue stresses, sliding friction, liquid lubricated contacts, solid lubricants and bare contacts. They examine changes in the crystalline structure and the elastic-plastic properties, the initiation of fatigue cracks and their propagation into fatigue spalls. These investigations have been already extensively documented in (5,6,7) and will not be repeated here.

The above mentioned advanced theoretical analyses and scientific investigations require supplementary practical tests with appropriate machinery. Unfortunately, there are not many devices available for such purposes, and none of them is designed to simulate environmental conditions and surface geometries anticipated in actual machine components, such as ball bearings, cams, gears, etc. Therefore, a program was started to develop a series of "Tribo-Testers" to fill this gap.

---

\*The numbers in parentheses designate the references listed at the end of this report.

## 1.2 Historical Background.

The first of these testers, designated "Tribotester No.1", is designed to use a cylindrical rolling contact fatigue (RCF) rod to evaluate the fatigue life of base materials and coatings under pure rolling contact stress conditions, simulating ball bearings. This tester is already commercially available (8). It is routinely used for the RCF resistance measurement of ceramics, testing the subsurface integrity of ceramics as high load carrying tribo-materials.

This Rolling Contact Fatigue Tester was developed by MTN Bower Corp. (formerly Federal Mogul). Originally, it was designed for the testing of steel balls on a steel rod. However, it can also be used in conjunction with ceramic specimens of the same dimensions and geometries as the ones of the original steel specimens.

Its principles and method of operation are illustrated in Figure 1.1. The RCF rod specimen is clamped in the collet of a vertically mounted drive spindle, with a portion of the rod protruding above the spindle nose. Three balls are forced against the protruding segment via two axially loaded cones as shown in the illustration.

The next in the series, "Tribotester No. 2A", has the task of using the same RCF rod in conjunction with sliding pads to evaluate friction and wear of various ceramics under sliding friction conditions simulating phenomena such as ball/race and ball/separator slip of high speed ball bearings, seals, cams, gears, etc. It is intended to test the physical-chemical integrity of tribo-ceramics on the surface.

As it is in the RCF tester, the rod specimen is clamped in a vertically mounted spindle with a portion protruding above the spindle nose and the other material samples are forced against it radially. But this is the point where the similarity ends.

While the RCF tester is designed to operate only at room temperature in standard air and with a constant steady-state load, the friction contact point in the Tribotester 2A can be heated to temperatures of up to 871 deg. C or higher. It can have either a constant steady-state or pulsating load, operate under a wide range of sliding speeds and also has provisions for purging the atmosphere surrounding the contact points with a variety of inert gases. These and many other unique features will be described in more detail in the following sections.

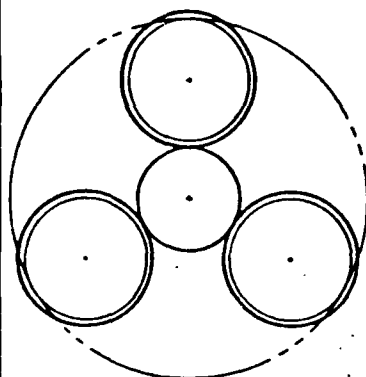
The Tribotester 2A is designed to simulate the actual operating conditions found in many machinery components under a wide range of slip speeds and contact stresses. Figure 1.2 illustrates typical combinations of surface slip speeds and contact stresses found in many systems for present and future needs.

Although the range covered in the initial Tribotester test program does not yet cover the entire spectrum shown, the program calls for an expansion of the velocity and contact pressure ranges after the results of the first tests have been reviewed and evaluated. The design of the tribotester is sufficiently flexible to permit future expansions.

# DESCRIPTION OF TESTER NO. 1 ROLLING CONTACT FATIGUE TESTING OF OIL-LUBRICATED CERAMICS

**HUGHES**

9-5



|                                    |                                            |
|------------------------------------|--------------------------------------------|
| TECHNICAL DESCRIPTION              | RCF ROD                                    |
| MODE OF OPERATION                  | ROLLING                                    |
| TEMPERATURE RANGE OF OPERATION     | ROOM TEMPERATURE                           |
| TEST ATMOSPHERE                    | AIR                                        |
| SPECIMEN LUBRICATION               | OIL                                        |
| COMMERCIAL AVAILABILITY AND SOURCE | YES (COMMERCIAL PURCHASE:) (FEDERAL MOGUL) |

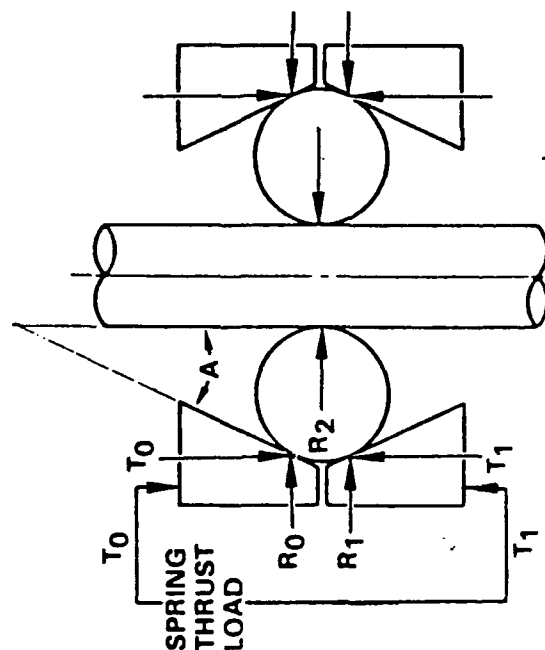


FIGURE 1.1

# TRIBOLOGICAL FUNDAMENTALS OF SOLID LUBRICATED CERAMICS OPERATING REGIMES OF TRIBO-TESTERS BEARING LOADING AND SPEED REGIME DIAGRAM

**HUGHES**

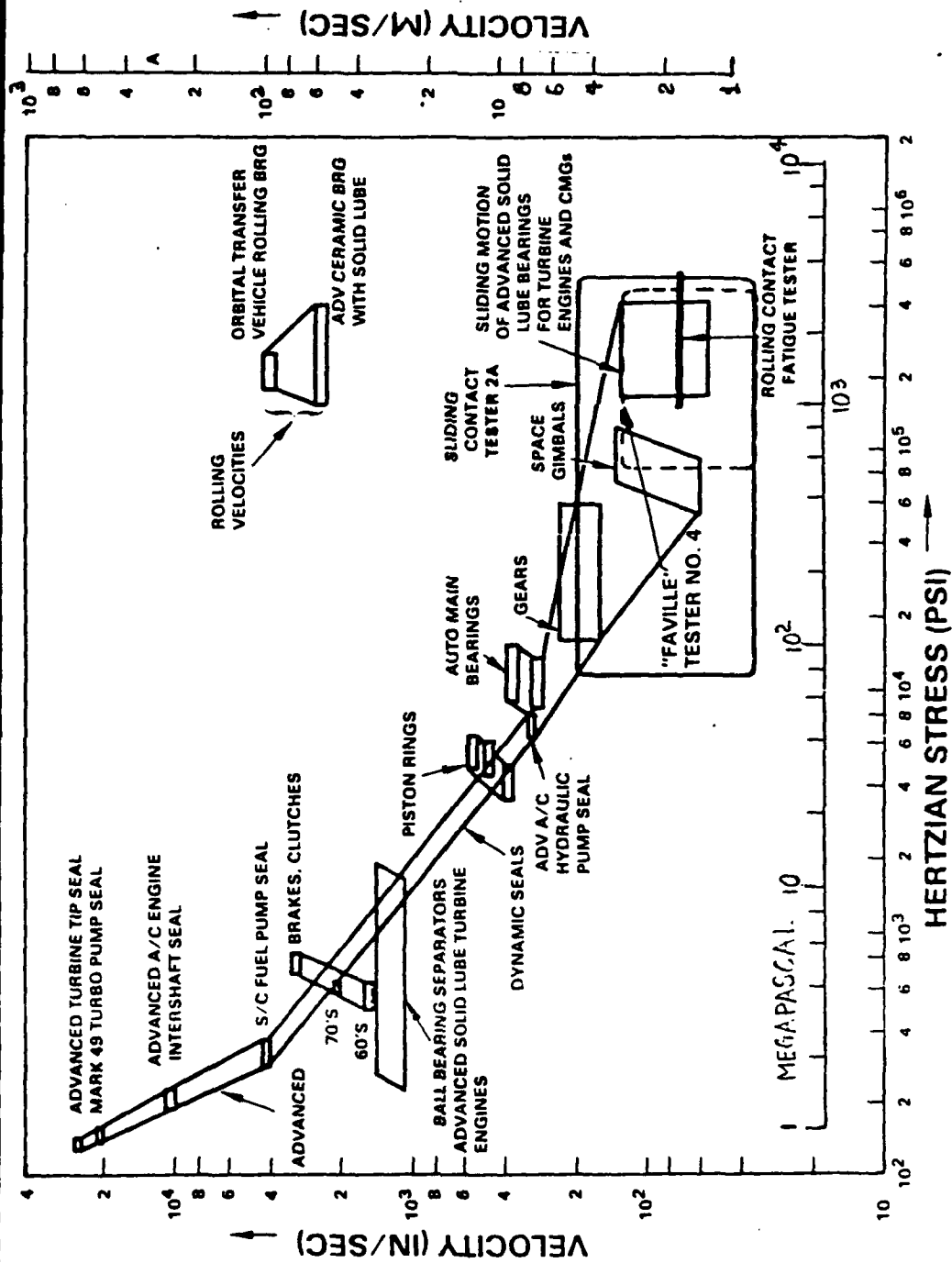


FIGURE 1.2



Dimensions of the specimen clamping fixture in the tester are selected to conform to the ones of the RCF tester, Tribotester No. 1, so that the same RCF rod specimen can be tested in both testers to evaluate both subsurface and surface stress behavior in an identical material specimen.

The third in the series, "Tribotester No. 2B", has the same function as Tribotester 2A, with the added provision of supplying powdered solid lubricants to the friction contacts during the tests and of evaluating their effects.

Other tribotesters are planned for the more distant future for other extreme conditions such as cryogenic temperatures, extreme high rolling speeds and examination of traction coefficients and slip/roll ratios.

This report specifically describes the development program of the model designated as "Tribotester 2A". In addition to being able to readily accept the RCF rod used in the already existing Tribotester No. 1, it can be converted to the next model "Tribotester 2B" with a minimum of redesign effort.

The development program of the Tribotester 2A was started at the end of November 1985. It progressed through a careful process of investigations, analyses and several design reviews, accompanied by breadboard tests of the critical design concepts. During this process, the basic conceptual design evolved through changes, with increasing confidence in the soundness of the design from both the reliability and cost effectiveness points of view.

## 2. BASIC DESIGN CONCEPT.

The operating principle of the Tribotester is illustrated in Figure 2.1. A cylindrical ceramic rod specimen is rotated, while two stationary specimen pads, also called rub shoe pads, are forced against the rod from opposite sides. The rub shoe pads may have either flat, convex cylindrical, concave cylindrical or spherical contact surfaces. Axes of convex cylindrical surfaces may be either parallel or perpendicular to the rotating specimen axis.

The basic requirements for the capabilities of the apparatus have been established as follows:

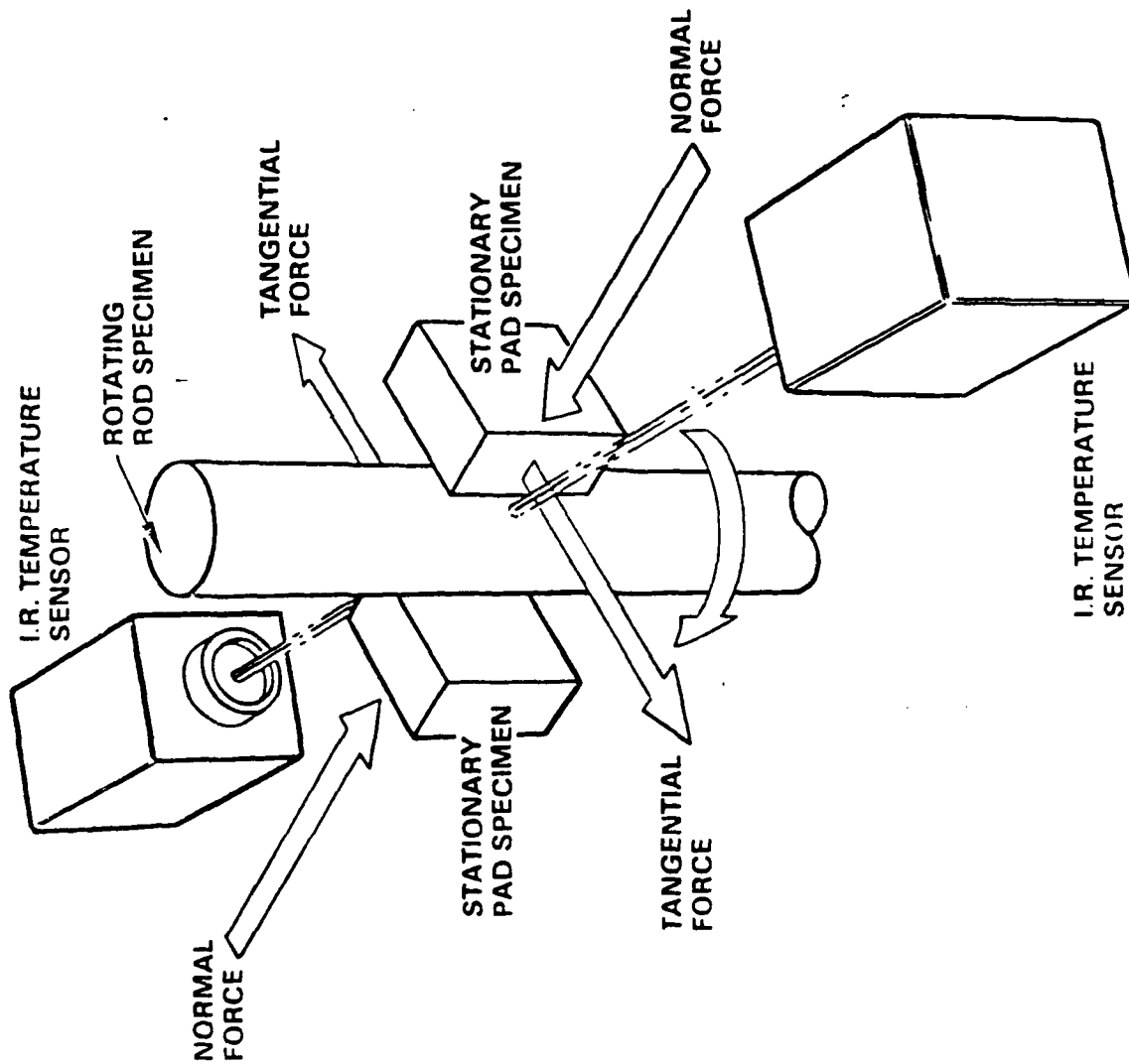
|                                      |                                           |
|--------------------------------------|-------------------------------------------|
| Rotating Specimen Temperature Range: | 25 to 870 deg. C<br>(77 to 1600 deg. F)   |
| Sliding Contact Speeds:              | 0.5 to 5 meter/sec<br>(2 to 200 inch/sec) |
| Normal Contact Forces:               | 200 Newtons max.<br>(45 lbs.)             |

Contact forces may be either steady state or repetitive pulses (sinusoidal or other), with frequencies up to 50 Hz.

**HUGHES**

**TRIBOLOGICAL  
FUNDAMENTALS OF SOLID  
LUBRICATED CERAMICS  
TRIBOTESTER 2A  
OPERATING  
PRINCIPLE**

**FIGURE 2.1**



Provisions have to be made to measure the normal and tangential forces applied to each rub shoe pad. The ratios between the measured tangential forces and the normal forces yield the coefficients of friction for each material and solid lubricant combination.

Temperatures are measured by aiming the beam of an I.R. pyrometer (temperature sensor) at the rotating specimen surface near the point of sliding contact and by thermocouple probes embedded in the rub shoe pads in cavities near the points of contact.

From the above description of requirements, it is apparent that the loading mechanism selected for the Tribotester has to perform several complex functions. Among them are:

- 1) Application of forces normal to the tangent line at the point of sliding contact, synchronized for both rub shoe pads.
- 2) Measurement of the loading forces.
- 3) Measurement of the tangential forces.
- 4) Heating of the rotating rod specimen.
- 5) Provision of sufficient clearance from the optical path from the lens of the I.R. temperature sensor to the target spot on the surface of the rotating rod near the contact point.
- 6) Measurement of the depth of wear scar.

During the preliminary planning phase, many types of mechanisms were considered for the above tasks. Eventually, the choice was narrowed down to three basic concepts, each using moment arms that are pivoted about fulcrums. Measurement of the normal and tangential forces is accomplished by measuring the orthogonal force components exerted on each pivot point.

The three mechanism types which were thoroughly investigated, illustrated in Figure 2.2, are the following:

- 1) Overhead Moment Arm Mechanism, whereby the actuating force is applied simultaneously to the two moment arms by a wedge-and-roller mechanism. One or two I.R. temperature sensors are positioned on the sides.
- 2) In-Line Moment Arm Mechanism, where the fulcrums are located in the lines of tangency of the contact points and I.R. sensors are positioned at an angle off the normal force vectors.
- 3) Offset Moment Arm Mechanism, where the I.R. sensors are positioned in a line close to the line of tangency and the fulcrums are offset with respect to that line.

After careful consideration of the advantages and disadvantages of each of the three basic mechanisms, the in-line moment arm concept has been selected for implementation.

TRIBOLOGICAL FUNDAMENTALS OF SOLID LUBRICATED CERAMICS

# TRIBOTESTER 2A BASIC LOADING MECHANISM CONCEPTS

**HUGHES**

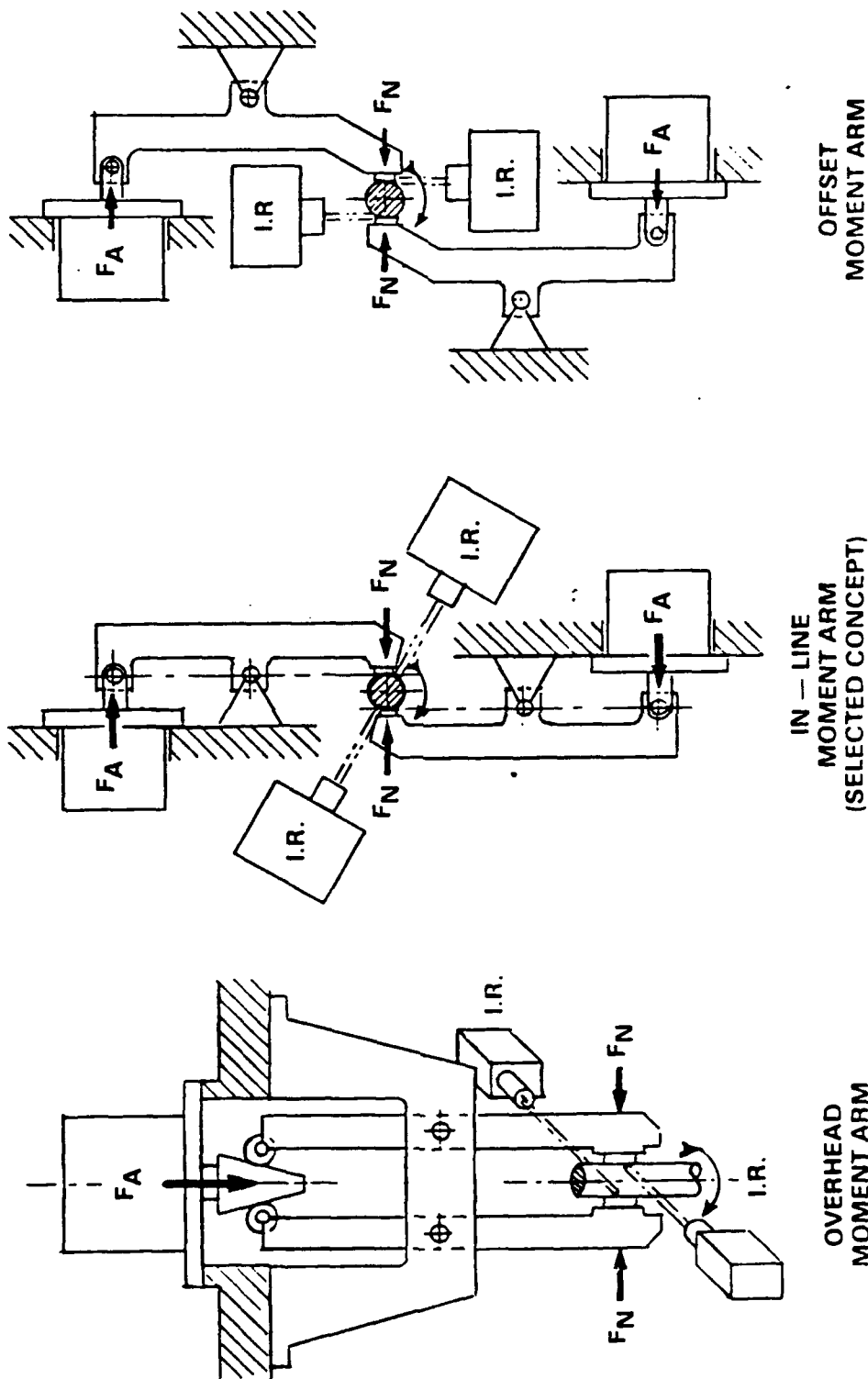


FIGURE 2.2

The illustration in Fig. 2.3 shows a diagram of this concept with the essential input and output transducers. There are two sets of instruments, one set for each of the two rub shoe pads. However, each transducer is labeled only once, because of the space limitations in the sketch.

The following glossary is used in the mechanism analysis:

$F(n)$  = Normal Force  
 $F(t)$  = Tangential Force  
 $F(a)$  = Actuator Force  
 $F(x)$  = X-Axis Force Vector  
 $F(y)$  = Y-Axis Force Vector  
 $S$  = Steady-State Force Component  
 $A$  = Alternating Force Component  
 $f$  = Frequency of Force Pulses  
 $a, b$  = Moment Arm Segment Length

In this concept, the friction forces are measured with two pairs of load cells at right angles to each other. Considering the pivot point (fulcrum) as the origin of a coordinate system, the tangential force load cell is aligned along the x-axis and the normal force load cell along the y-axis.

Since the x-axis is also the line of tangency of the rub shoe pad, the tangential force can be read directly from the load cell:

$$F(t) = F(x)$$

The normal force on the rub shoe pad is proportional to the force in the y-axis load cell, as is the actuating force:

$$F(n) = F(y) * (a / (a+b))$$

$$F(a) = F(y) * (b / (a+b))$$

$$F(n) = F(a) * a/b$$

The coefficient of friction is then simply:  $F(t)/F(n)$

For the initial tests, the normal force on each rub shoe pad will be selected as a dynamic function having the general form:

$$F(n) = S + A \sin(2 \pi f)$$

The values of  $S$  will be selected at least 1.5 times the value of  $A$ , so that a positive contact pressure between the rub shoe pads and the rotating rod is present at all times. The dynamic force components are generated by linear actuators, where the force is a function of the applied current. The inputs to the two actuators are controlled so that the applied normal forces are always in phase, at the same peak value, and in opposite direction.

The actuating force  $F(a)$ , being proportional to the normal force  $F(n)$ , also consists of a steady-state component and a super-imposed dynamic (sinusoidal) component.

TRIBOLOGICAL FUNDAMENTALS OF SOLID LUBRICATED CERAMICS

# TRIBOTESTER 2A INSTRUMENTATION DIAGRAM

**HUGHES**

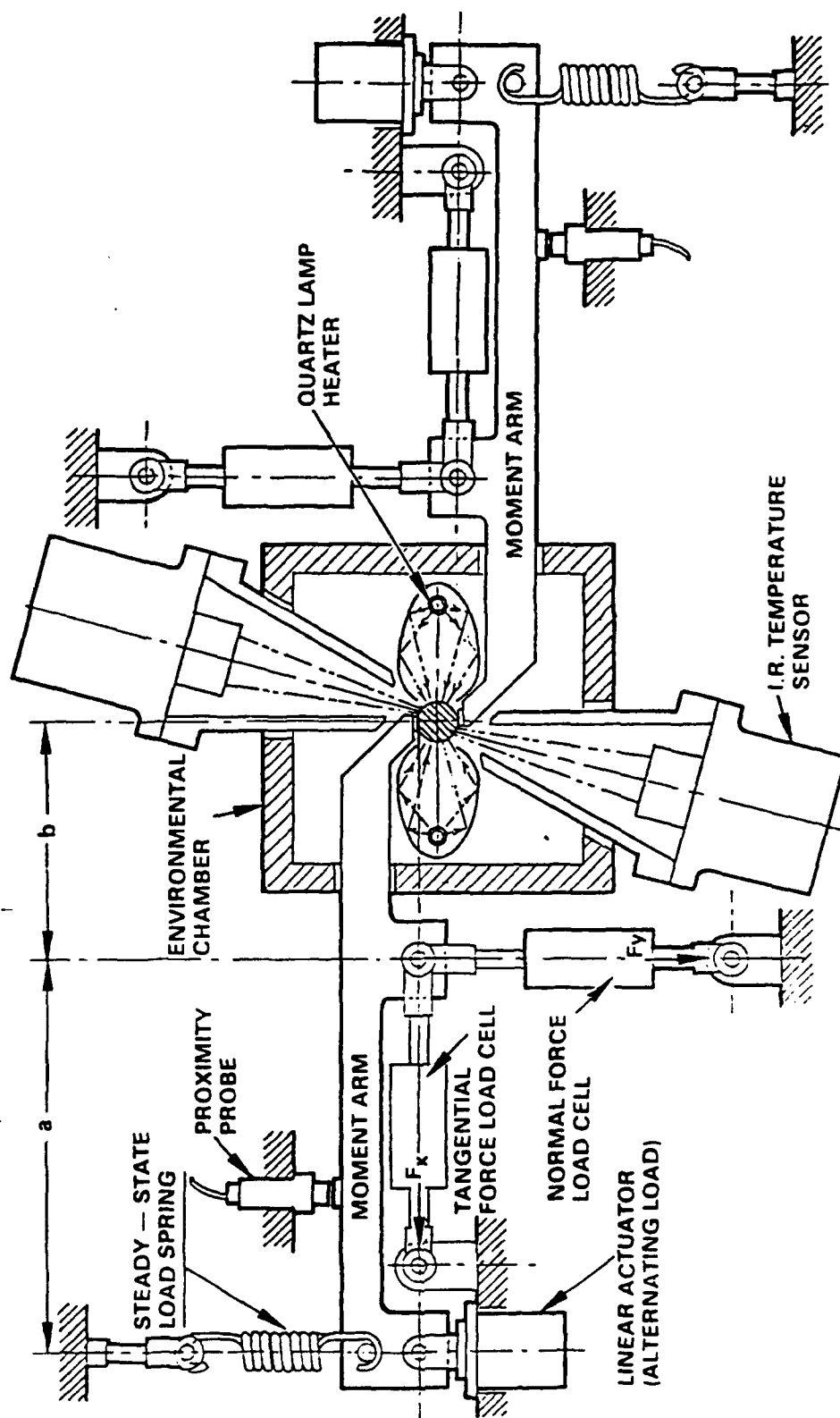


FIGURE 2.3

It is more economical to have the steady-state force component supplied by a spring with a screw type tension adjustment, with the sinusoidal force component supplied by the moving coil actuator in superposition, than to have the entire actuating force supplied by a moving coil actuator alone.

The latter would require a much larger and more expensive model for the actuator with considerably higher power consumption for a given load level, than the spring-actuator combination.

Measurement of the combined depth of the wear scars on the rub shoe pad and the rotating rod as a function of time can be obtained with a proximity probe. This probe generates an electrical signal as a function of the width of the gap between two parallel polished metal surfaces by means of eddy currents. One of these test surfaces is mounted on the moment arm, while the probe is fixed to the mounting platform.

At the beginning of each wear test, after thermal expansion equilibrium has been achieved, the probe gap is set to a controlled width with the aid of a feeler gage. As the test progresses with time, the rub shoe pad contact surface will wear and the moment arm at that end will move closer toward the rod. This movement will cause a change in the gap of the proximity probe, giving a changed signal reading, which in turn can be translated into the combined depth of the wear scars.

As already mentioned in the introduction, the dimensions of the rotating rod specimen are selected to make it compatible with the already existing Tribotester No. 1, the rolling contact fatigue tester. The dimensions of the rotating rod are 9.525 mm diameter x 89 mm length (0.3750 inch x 3.504 inch). On each specimen, separate test tracks are allocated for rolling and sliding contact tests. The spacing of the test track allocations is illustrated in Figure 2.4.

A variety of tests can be performed on the same rod by inserting it into the clamping collet, located at the nose of the drive spindle, to a different depth for each test (see illustration in Fig. 2.5). After one half of the rod has been used up for sliding and rolling contact tests, the rod is inverted and the used portion is inserted into the collet. Thus the other half of the rod is free for further tests.

The stationary pad specimen samples are designed so that they can be cut as slabs from a previously fabricated cylindrical rod specimen. The only exception is the rub shoe pad with the spherical contact surface, which is cut from a 12.7 mm (0.5000 inch) diameter ball used in the Tribotester No.1, the RCF tester.

Various shapes of the rub shoe pads are illustrated in Figure 2.6. They all can be mounted into the same 9.525 mm (0.3750 inch) diameter recess of the specimen holding device and are thus readily interchangeable.

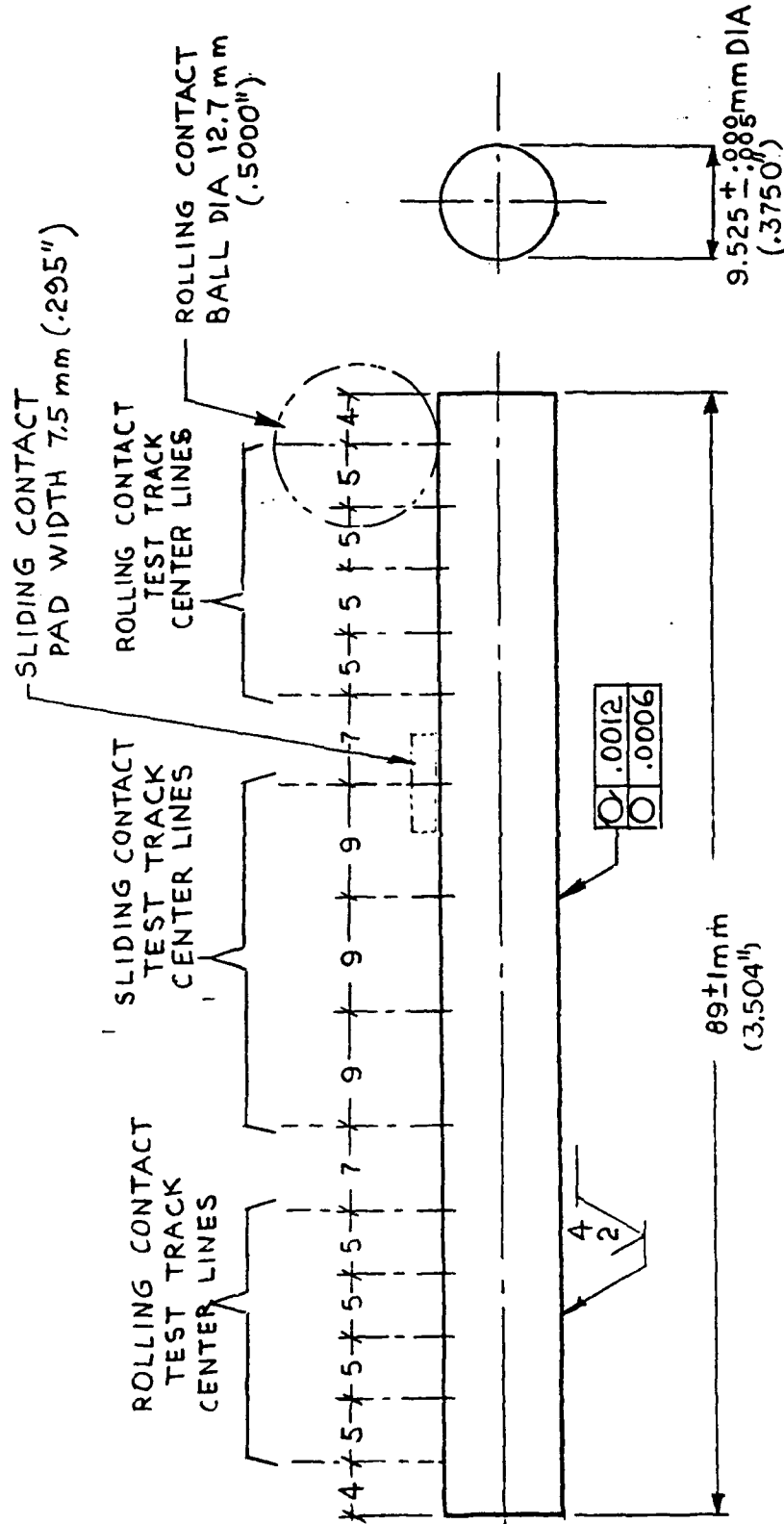


FIGURE 2.4

# ROTATING ROD TEST SPECIMEN DIMENSIONS, TRIBOTESTER 2A

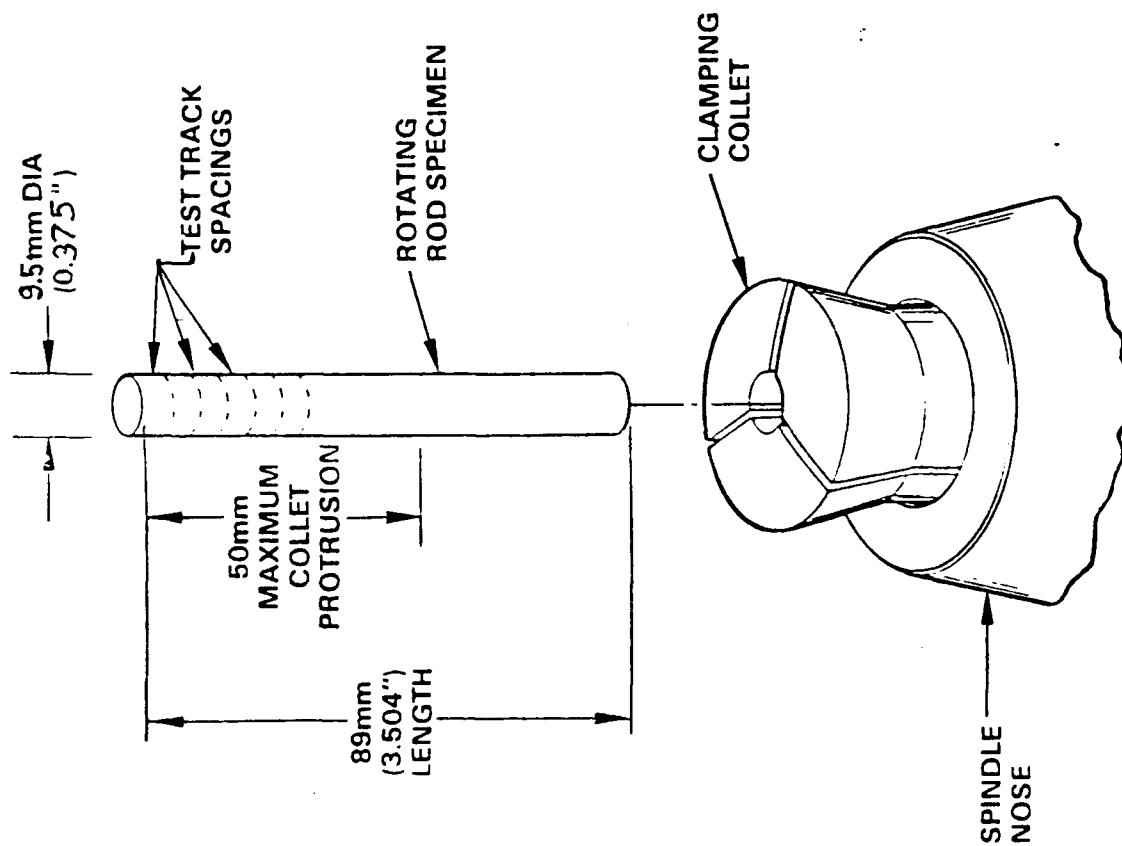
|                                                   |           |                                     |                     |
|---------------------------------------------------|-----------|-------------------------------------|---------------------|
| HUGHES AIRCRAFT COMPANY<br>EL SEGUNDO, CALIFORNIA |           | CONTRACT: TRIBOLOGICAL FUNDAMENTALS |                     |
| DR LEO FIDERER                                    | 11-MAR-86 | SIZE<br>A                           | FSCM NO<br>82577    |
| TEL. (213) 616-4826                               |           | SCALE<br>2/1                        | DWG NO<br>SP 503493 |
|                                                   |           |                                     | SHEET               |



**HUGHES**

TRIBOLOGICAL  
FUNDAMENTALS OF SOLID  
LUBRICATED CERAMICS  
**TRIBOTESTER 2A**  
**STANDARD**  
**ROTATING ROD**  
**SPECIMEN**

FIGURE 2.5



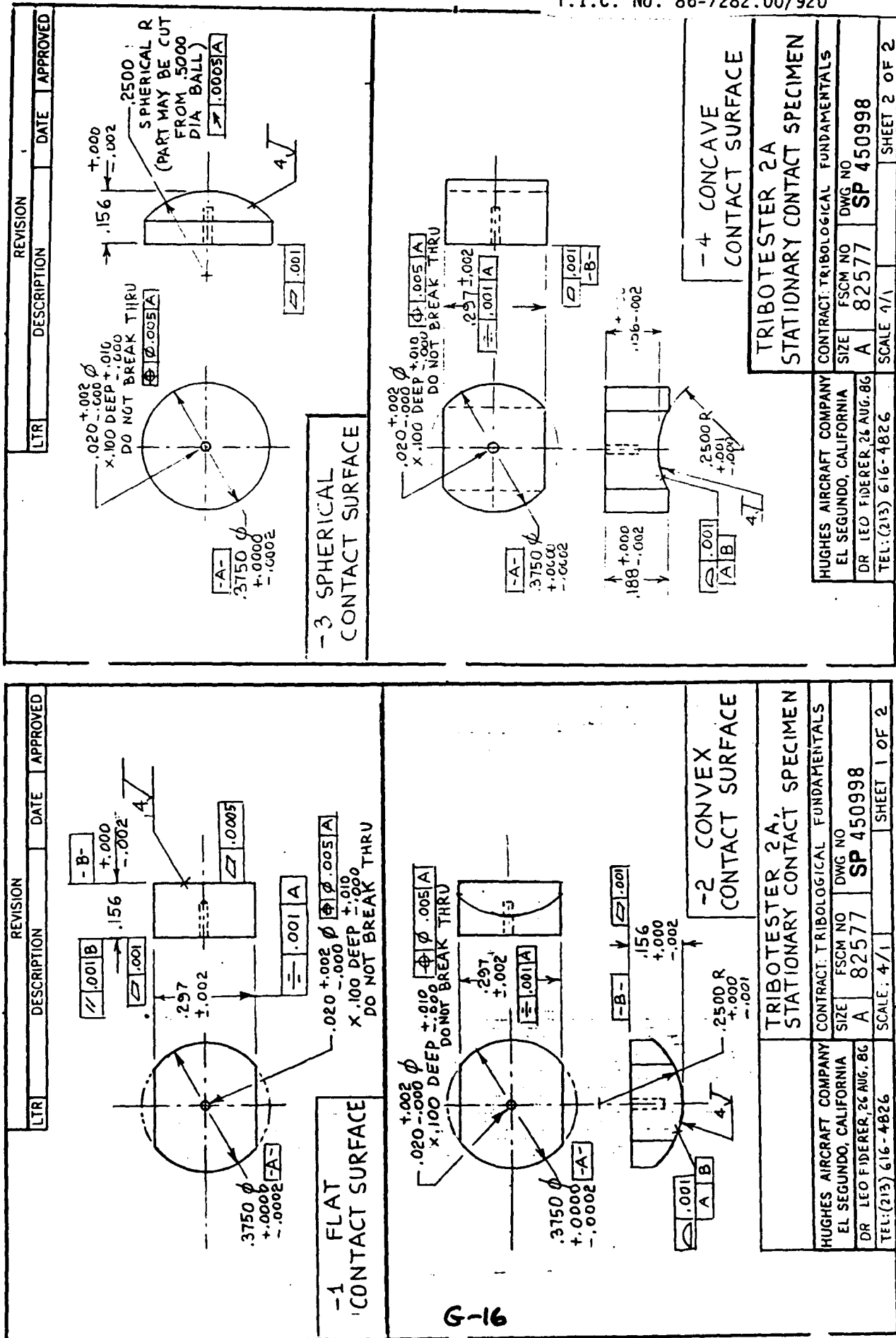


FIGURE 2.6

The principal ceramic material categories considered for investigation are the following:

Hot Pressed Silicon Nitride

Sintered Silicon Carbide

Partially Stabilized Zirconia

Aluminum Nitride

Transparent and Non-Transparent Aluminum Oxide (Sapphire).

After the basic design concept had been established at the preliminary and intermediate design reviews, the actual hardware design of the Tribotester was started. This phase was accompanied by theoretical analysis and breadboard testing of critical design items.

As a result of the analysis and the tests conducted during the hardware design phase, the initial concept which is illustrated in Figure 2.3 was simplified.

A multi-axis load cell was substituted for the two individual orthogonally mounted load cells at each pivot point. Although the basic principle of monitoring the tangential and normal force vectors acting on the pivot is still the same, the fact that both can be obtained from a single instrument permits substantial simplification of the linkage and hardware design.

Furthermore, our thermal breadboard tests established conclusively that a single quartz lamp heater is adequate to heat the rotating rod specimen to the desired temperature, instead of the two originally contemplated.

The theoretical thermal analysis showed that during rotation of the rod the thermal gradient around the periphery of the contact path on the rotating rod surface will be negligible, and that it would be impossible to detect any temperature differences. Therefore, a single I.R. temperature sensor is being used instead of two.

Thus, the cautious approach of preliminary analysis and breadboard testing has paid its way, resulting in the design described on the following pages.

### 3. FRICTION TESTER DESCRIPTION.

The principal elements of the friction tester are the loading mechanism, the heater assembly, the drive spindle assembly, the mounting platform and the portable stand. Each is being described in more detail as follows. Figure 3.1 shows the overall arrangement of the major components in simplified form, with the protective hood over the heater removed for clarity.

#### 3.1 Loading Mechanism.

The loading mechanism consists essentially of the moment arm which is mounted on the pivot bearing, the linear force actuator, the tangential position adjustment with its clamping mechanism, and the rub shoe specimen holding device. The design of these items can be seen in Figure 3.2 and 3.3.

The moment arm is a 19 mm thick aluminum alloy plate with suitable cut-outs for clearance of the adjacent components. A section through the pivot bearing is shown in the left hand portion of Figure 3.3. The portion of the moment arm on the side of the specimen holding device has a multitude of holes to facilitate cooling of the arm by natural convection in order to keep the pivot bearings at a reasonably cool temperature.

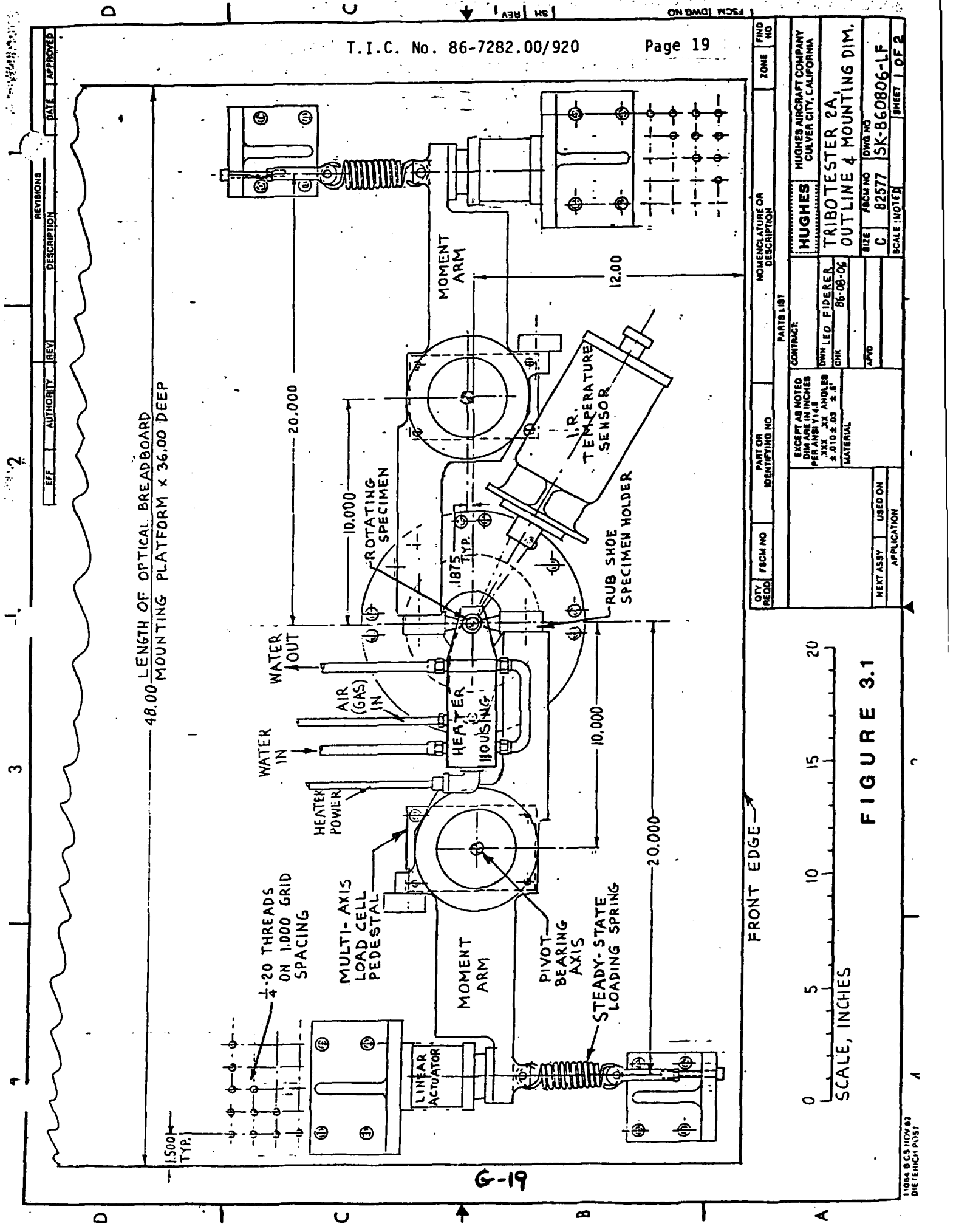
The end of the moment arm near the rub shoe specimen has a tangential position adjusting mechanism that permits the alignment of the specimen pad with respect to the rotating rod. This adjustment is especially important for rub shoe pads with spherical or parallel cylindrical contact surfaces, to compensate for thermal expansion of the moment arm during the heating cycle.

When adjusting the tangential position, the clamping screws are first loosened. The head of the adjusting screw is then rotated in either direction to the desired position and the clamping screws are then tightened again (see Section View B-B in Figure 3.2).

The rub shoe specimen holding device is best seen in Figure 3.4. The specimen holder is made of "Macor" (TM), a machinable ceramic material with excellent heat insulating properties. This specimen holder fits into the jaws of the specimen clamp made of heat resistant stainless steel.

The rub shoe specimen shown in the illustration has a flat contact surface; however, any of the variety of pads with other types of contact surfaces can be accommodated in the recess of the specimen holder. As can be seen from the view, removal and replacement of the specimen holding device and interchange of rub shoe pads are very easily accomplished.

The linear moving coil actuator at the other end of the moment arm is shown in Figure 3.5. It can provide force pulses within its specified limits at shapes and frequencies generated by any function generator.



T.I.C. No. 86-7282.00/920

Page 19

| REV | DESCRIPTION | DATE | APPROVED |
|-----|-------------|------|----------|
|     |             |      |          |

| QTY | FRGM NO | PART OR IDENTIFYING NO | NOMENCLATURE OR DESCRIPTION | ZONE | FIND NO |
|-----|---------|------------------------|-----------------------------|------|---------|
|     |         |                        |                             |      |         |

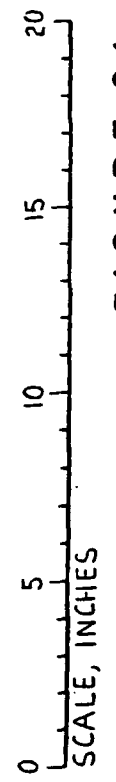
  

|                                                                                             |                                                                           |
|---------------------------------------------------------------------------------------------|---------------------------------------------------------------------------|
| EXCEPT AS NOTED<br>DIM ARE IN INCHES<br>PER ANSI Y14.1<br>.XXX XX ANCHORS<br>±.010 ±.03 ±.1 | CONTRACT:<br>HUGHES<br>HUGHES AIRCRAFT COMPANY<br>CULVER CITY, CALIFORNIA |
| MATERIAL:<br>DWN LEO FIDERER<br>CHK 86-08-06                                                | TRIBOTESTER 2A,<br>OUTLINE & MOUNTING DIM.                                |

|           |                  |                        |
|-----------|------------------|------------------------|
| SIZE<br>C | FRGM NO<br>82577 | DWG NO<br>5K-860806-LF |
| NEXT ASSY | USED ON          | SCALE: 1 OF 2          |

FIGURE 3.1



11084 BCS NOV 82  
DIE TECHNOT

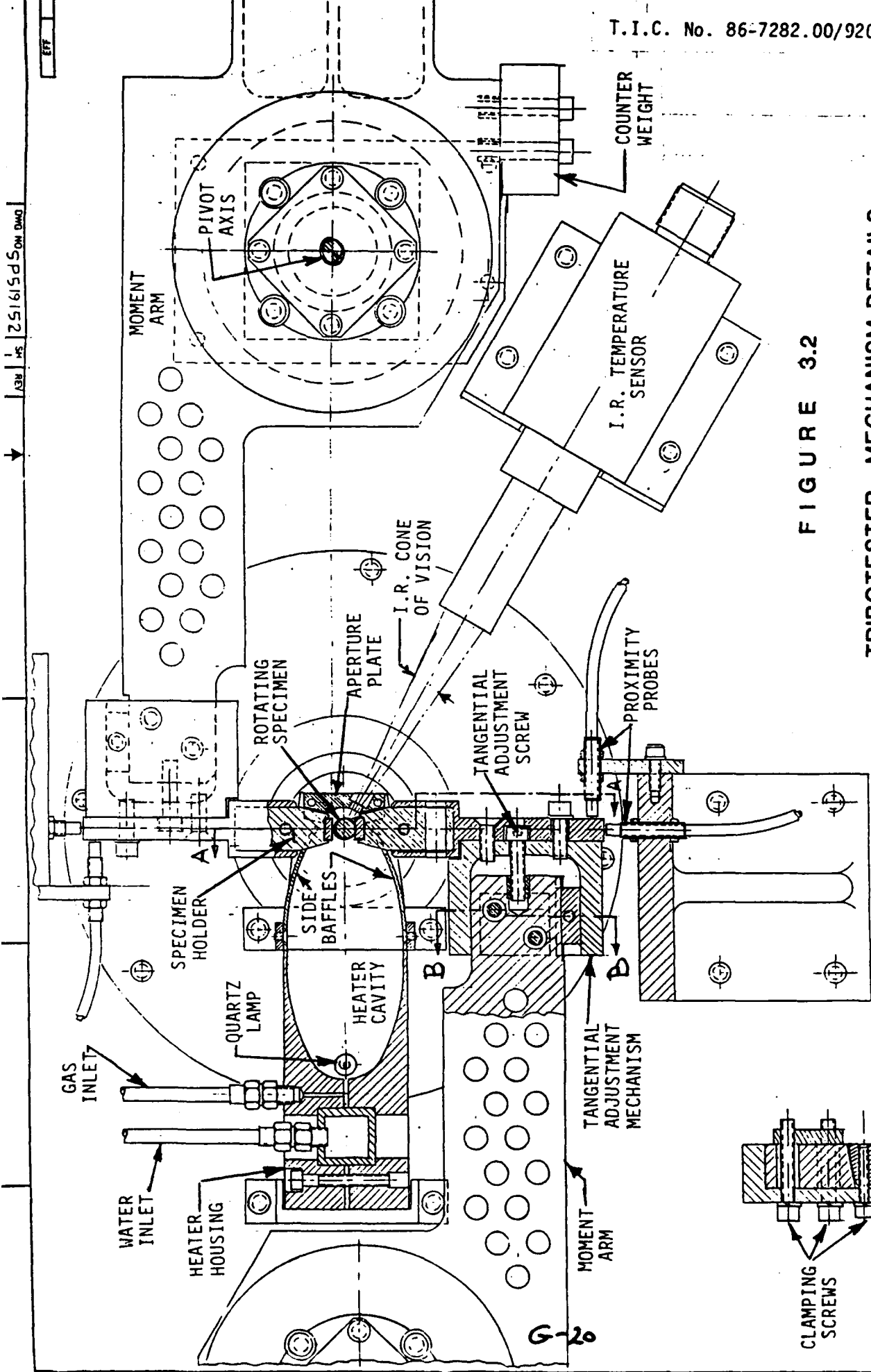
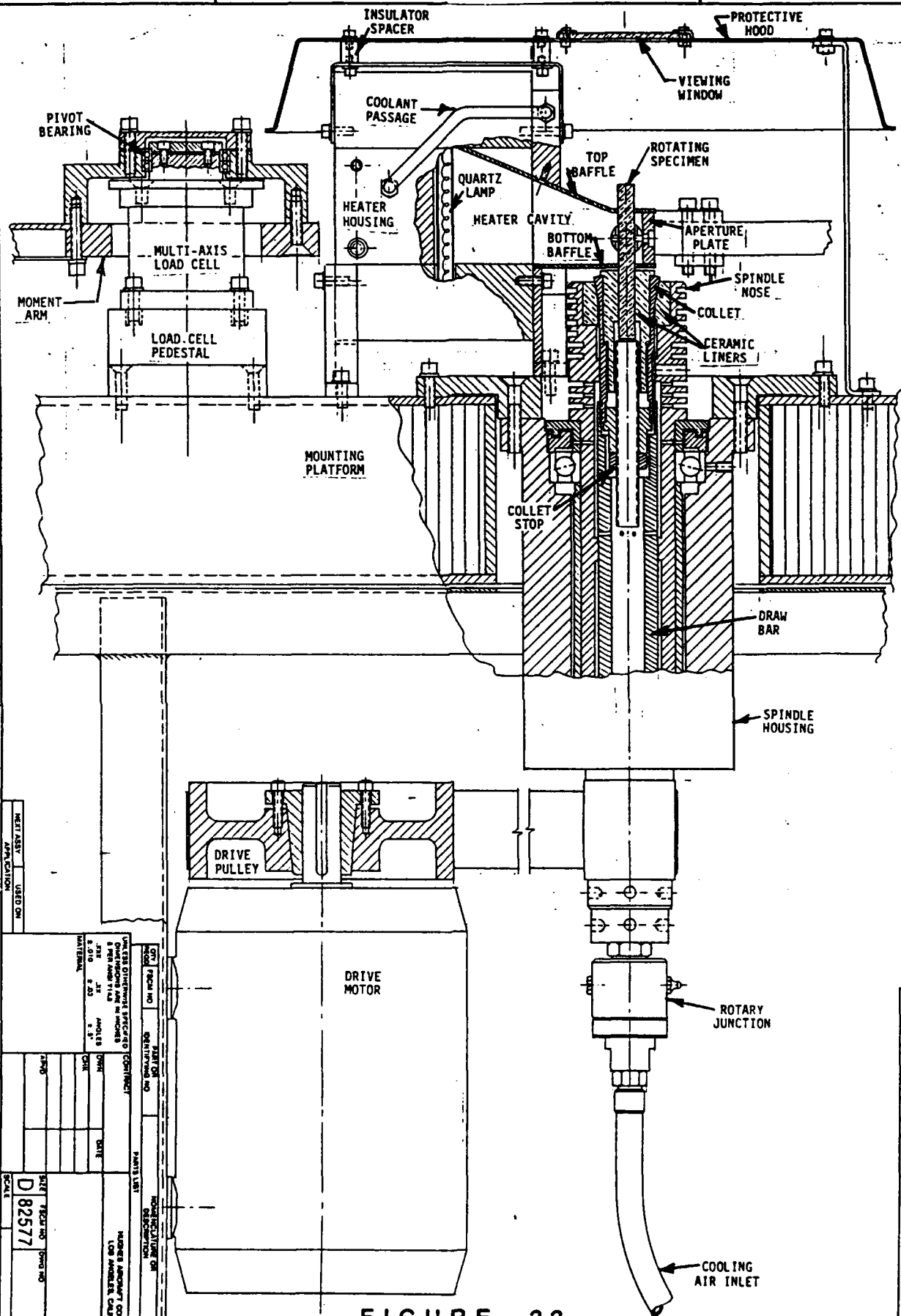


FIGURE 3.2  
TRIBOTESTER, MECHANISM DETAILS

SECTION  
B-B

G-20



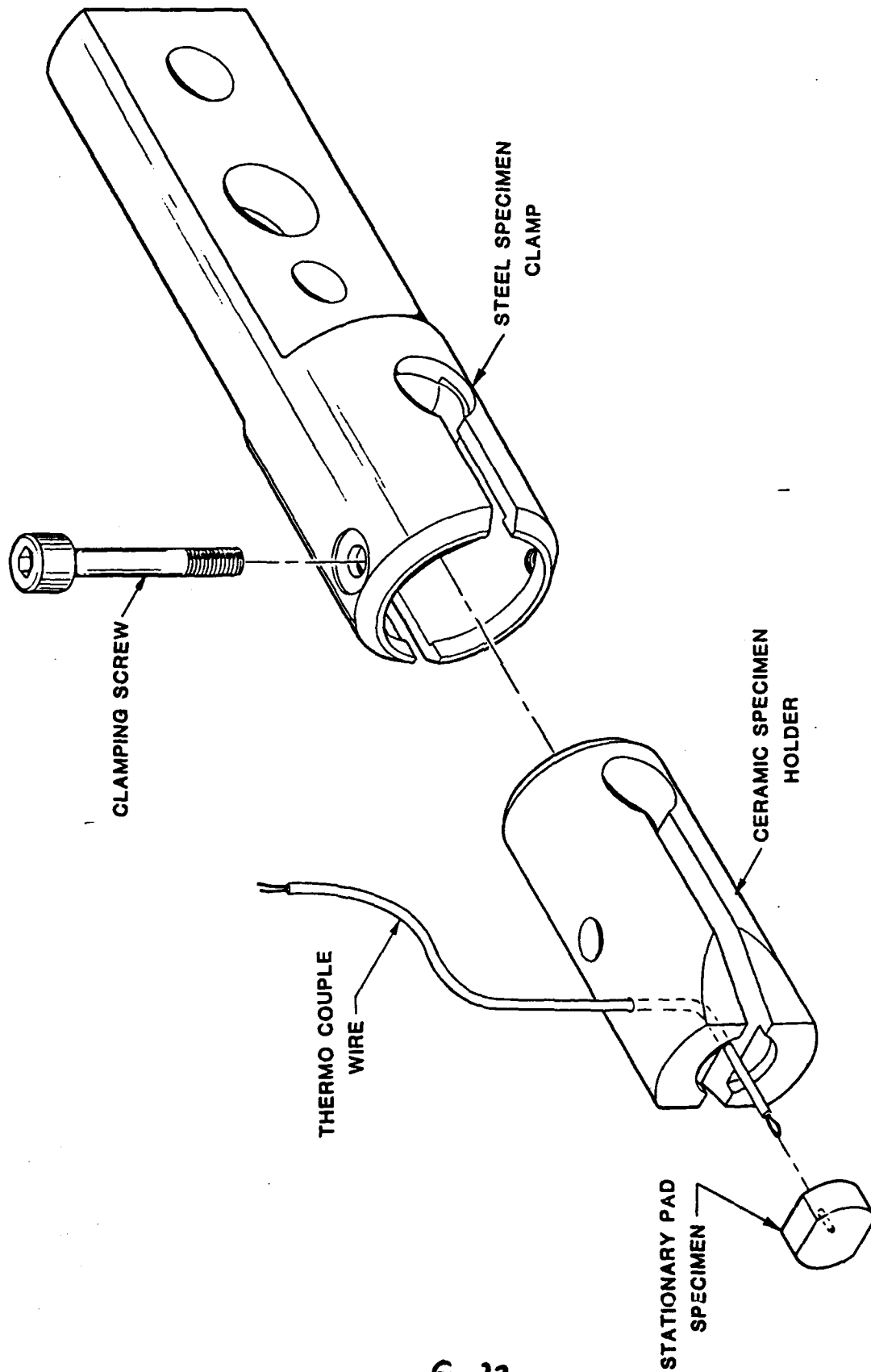


FIGURE 3.4  
SPECIMEN HOLDING DEVICE

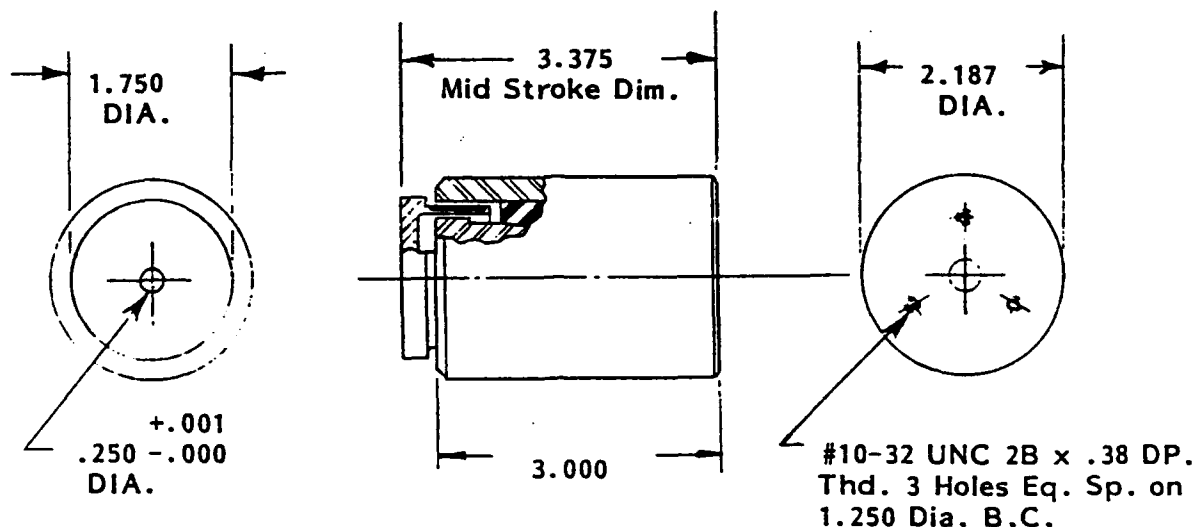


# LINEAR ACTUATOR

LA22-34

-MOVING COIL-  
-SmCo Magnet-

## MECHANICAL DATA



## PERFORMANCE DATA

- PEAK FORCE ( $F_p$ ) (INTERMITTENT)
- FORCE CONSTANT ( $K_F$ )
- BACK EMF CONSTANT ( $K_B$ )
- MOTOR CONSTANT ( $K_M$ ) (25°C)
- CURRENT @ PEAK FORCE ( $I_p$ )
- POWER AT PEAK FORCE ( $P_p$ ) (25°C)
- RESISTANCE (25°C)
- ELECT. TIME CONSTANT
- THERMAL RESISTANCE OF COIL
- STROKE
- CLEARANCE EACH SIDE OF COIL
- MAX. ALLOWABLE COIL TEMP.
- WEIGHT OF MOVING COIL
- TOTAL WEIGHT

LBS  
LBS/AMP  
VOLTS/FT/SEC  
LBS/ $\sqrt{\text{WATTS}}$   
AMP  
WATTS  
OHMS  
MICRO. SEC  
°C/WATT  
INCH±  
INCH  
°C  
LBS  
LBS

| WINDING |      |   |   |
|---------|------|---|---|
| A       | B    | C | D |
| 15      | 15   |   |   |
| .75     | 3.0  |   |   |
| 0.10    | 4.06 |   |   |
| 1.09    | 1.09 |   |   |
| 20.0    | 5.0  |   |   |
| 188     | 188  |   |   |
| .47     | 7.52 |   |   |
|         |      |   |   |
| 2.2     | 2.2  |   |   |
| .06     | .06  |   |   |
| .030    | .030 |   |   |
| 155     | 155  |   |   |
| .07     | .07  |   |   |
| 3.0     | 3.0  |   |   |

G-23

FIGURE 3.5

Although the actuator is capable of responding to inputs of frequencies up to 500 Hz, the initial test plan calls for actuation of up to 50 Hz only. A structural analysis of the moment arm indicated resonances at 130 Hz, and we will attempt to remain below half of that value.

After evaluation of initial test results, low amplitude frequency sweeps will be conducted to ascertain actual resonances and safe maximum pulse frequencies. Moreover, experiments with square wave and saw tooth pulses will be considered, too, after completion of sinusoidal pulse dynamic tests.

### 3.2 Heater Assembly.

The heater assembly is constructed around an infra-red quartz lamp heater, manufactured by Research, Inc. of Minneapolis, Minn. A copy of the catalog information about this heater, Model No. 5193-2, is shown in Figure 3.6. It is designed to concentrate high radiant flux energy along a target line. A tungsten-filament tubular quartz lamp is utilized as the emitter, producing a very high temperature (2200 to 3000 deg. C) heat flux.

The heater housing contains built-in reflecting surfaces in the shape of an elliptical cylinder. The axis of the heating lamp is located at one of the focal lines of that elliptical cylinder, thus directing all the reflected rays to the other focal line of that ellipse.

With the heater as delivered by the manufacturer, the reflecting surfaces extend only to a portion of a complete elliptical cylinder, so that about 65% of the available radiant energy is captured by the reflectors. The flux density along the focal line thus obtained is 100 watts per centimeter (254 watts per inch).

The tribotester design provides for additional reflector surfaces on the sides, extending the contour of the ellipse and directing an added portion of the radiant energy to the focal line. These added reflectors are labeled "side baffles" in the illustration Figure 3.2.

In addition, flat reflector surfaces are extended from the heater housing to the rod specimen, thus gathering additional rays and concentrating them along the center portion of the rod. These reflectors are labeled "top baffle" and "bottom baffle" in Fig. 3.3. In addition, the curved reflecting surface of the aperture plate behind the rod specimen bounces heating rays back onto the specimen.

With this arrangement, most of the radiant energy from the lamp is captured, with a flux density in the heated region much higher than the 100 watts per centimeter obtained without the reflector extensions.

The reflecting aluminum alloy surfaces are highly polished to a mirror like finish, resulting in a reflectivity of nearly 95%, and also acting as effective heat shields for the adjacent components. With the reflector extensions, the length of the heated region is compacted from the initial 6.6 cm to approximately 3.0 cm along the focal line.

# MODEL 5193 ELLIPTICAL-INFRARED LINE HEATER



# RESEARCH INC

BOX 24064 MINNEAPOLIS, MINNESOTA USA 55424

**HEAT FLUX DENSITY:** Heat density radiant heat flux up to 406 Watts per linear inch (based on calorimeter tests) on a narrow (.08-.18") focal line can be generated.

**POWER RATINGS:** See table. Units may be operated at up to double rated voltage for short duty cycles, provided the lamp envelope and reflector are not permitted to overheat. When operating Model 5532-2-25 and -38 at twice rated voltage, special electrical insulator considerations must be made.

**EMITTER CHARACTERISTICS:** Emitter is a tungsten filament in argon atmosphere enclosed in a 3/8" (O.D.) clear quartz tube. Operates at approximately 4,000°F at rated and 5,400°F at 2x rated voltage with 1.1 and .85 micron spectral energy peak, respectively.

**REFLECTOR:** The reflector used to focus the energy radi-

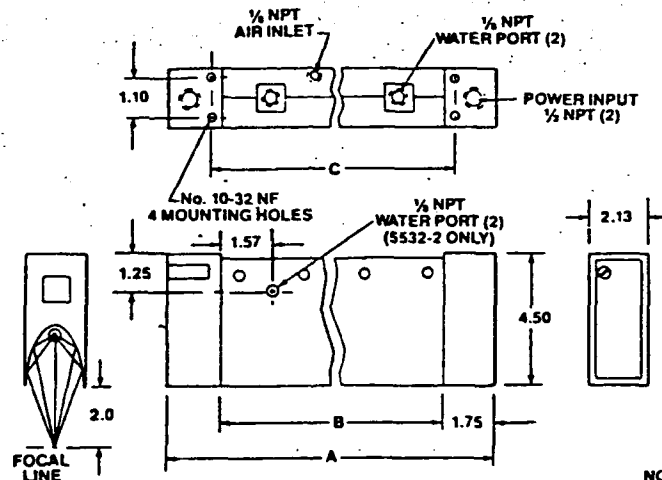
ated from the linear emitter filament is a two-dimensional ellipse of specular aluminum with provisions for water cooling and lamp envelope cooling.

**MODULAR CONSTRUCTION:** Line heater construction consists of a water cooled aluminum backbone to which aluminum end covers and reflector are attached.

**MOUNTING PROVISION:** Four No. 10-24 N.C. threaded holes are provided on the main frame for mounting and for attaching various accessories.

**SERVICES:** Power is applied to lamp through 1/2" NPT holes at each end of main frame. Clean water at 70°F or less for reflector cooling should be supplied to the reflector through two 1/8" NPT ports provided. Gas or air for purging the reflector cavity or for cooling lamp envelope can be introduced through the 1/8" port centered on the main frame.

## Dimensions



## Specifications

|                            | Model Number                                            | 5193 - 2                        | 5193 - 5                     | 5193 - 6                        | 5193 - 10                            | 5193 - 16      | 5193 - 25                         | 5193 - 38       |
|----------------------------|---------------------------------------------------------|---------------------------------|------------------------------|---------------------------------|--------------------------------------|----------------|-----------------------------------|-----------------|
| DIM                        | A Overall Length, in. (cm)                              | 6.08 (15.4)                     | 9.5 (24.1)                   | 11.0 (27.9)                     | 14.5 (36.8)                          | 20.5 (52.1)    | 29.5 (75.0)                       | 42.5 (108.0)    |
|                            | B Chamber Length, in. (cm)                              | 2.58 (6.6)                      | 6.0 (15.2)                   | 7.5 (19.1)                      | 11.0 (27.9)                          | 17.0 (22.2)    | 26.0 (66.0)                       | 39.0 (98.8)     |
|                            | C Mounting Hole Spacing in. (cm)                        | 3.33 (8.5)                      | 6.75 (17.2)                  | 8.25 (21.0)                     | 11.75 (29.9)                         | 17.75 (24.1)   | 26.75 (67.9)                      | 39.75 (100.7)   |
|                            | Weight, lb. (kg)                                        | 3.0 (1.4)                       | 5.2 (2.3)                    | 6.0 (2.7)                       | 7.9 (3.6)                            | 11.2 (5.1)     | 16.1 (7.3)                        | 23.0 (10.4)     |
| LAMP (one req., not incl.) | Type                                                    | Q500 Q1000<br>T3/ T3/<br>CL 4CL | 500 1200<br>T3/ T3/<br>CL CL | Q1250 Q1500<br>T3/ T3/<br>CL CL | 1000 2000<br>T3/ T3/<br>2CL/HT CL/HT | 1600<br>T3/CL  | 2500 5000<br>T3/ T3/<br>CL 1CL/HT | 3800<br>T3/CL   |
|                            | Lighted Length, in. (cm)                                | 2.4 2.6<br>(6.1) (6.6)          | 5.0 6.0<br>(12.7) (15.2)     | 6.0 6.75<br>(15.2) (17.2)       | 10.0 10.0<br>(25.4) (25.4)           | 16.0<br>(20.3) | 25.0 25.0<br>(63.5) (63.5)        | 38.8<br>(118.7) |
|                            | Rated Voltage                                           | 120 120                         | 120 144                      | 208 240                         | 240 240                              | 240            | 480 600                           | 570             |
|                            | Current, Amps                                           | 4.17 8.34                       | 4.17 8.34                    | 6.0 6.25                        | 4.35 8.70                            | 6.96           | 5.32 8.33                         | 6.67            |
|                            | Rated Power, KW                                         | .50 1.00                        | .50 1.20                     | 1.25 1.50                       | 1.00 2.00                            | 1.60           | 2.50 5.00                         | 3.80            |
|                            | Power at 2x Rated Volts, KW                             | NA** NA**                       | 1.4 3.4**                    | NA** NA**                       | 2.9 5.8                              | 4.7            | 7.3 14.5                          | 11.0            |
|                            | Cooling Water Flow,*2 GPM                               | .05 .10                         | .05 .12                      | .13 .15                         | .10 .20                              | .16            | .25 .50                           | .29             |
|                            | Heat Flux at Focus, Watts/Linear Inch, At Rated Voltage | 133 254                         | 59 128                       | 133 144                         | 65 130                               | 67             | 68 138                            | 69              |
|                            | at 2x Rated Voltage                                     | NA** NA**                       | 167 406                      | NA** NA**                       | 183 373                              | 190            | 114 394                           | 191             |

NOTES: \*\* Do not exceed rated voltage on quartzline lamps. \*\* At 240 volts, the 1200T3/CL dissipates 2.6 KW, produces 312 watts/linear inch.  
\*2 Flow at long term steady state conditions.

G-25  
FIGURE 3.6

The rotating rod specimen is mounted close to the focal line of the ellipse, extending through clearance holes in the top and bottom baffles, so that only its center portion is subjected to the incident and reflected radiation from the quartz lamp.

The two stationary specimen pads are mounted in the specimen holders that protrude into the heated cavity through cut-outs in the side baffles. They make contact with the rotating rod in the region of maximum heat concentration and are also exposed to a portion of the incident and reflected rays.

This arrangement is highly efficient to produce extremely high temperatures in a concentrated small space, without excessively heating the surrounding area, as has been confirmed by successful breadboard tests.

The walls of the heater housing are cooled by a flow of clean water as recommended by the heater manufacturer. In addition, a flow of air or gas for purging the reflector cavity and for cooling the lamp envelope is introduced through a port in the housing frame.

This flow of gas is funneled to the specimen contact region via the reflector extensions, to be exhausted through the narrow clearance spaces around the rotating specimen and the specimen holders. A positive gas pressure is thereby constantly maintained inside the heated cavity. Thus, it is possible to examine the behavior of the ceramic materials subjected to friction under a variety of purging gas atmospheres.

The opening in the aperture plate permits the examination of the surface temperature on the rotating specimen in the band of the contact region. The cone of vision of the I.R. temperature sensor is focused to a target spot of 1.2 to 1.5 mm at the surface of the specimen. The aperture diameter in the plate has a diameter of 4.5 mm, thus allowing sufficient clearance for possible alignment errors.

Experience from the breadboard tests has shown that the air surrounding the heater housing remains at relatively comfortable temperatures. The wall of the housing itself was measured at a temperature of about 100 deg. C. The two heater support brackets contain built-in cooling fins for added heat dissipation.

A protective sheet metal hood is mounted on top of the heated region during operation, to cover the region above the heater, the specimen holders and portions of the moment arms. This hood is designed to prevent accidental touch contact of the hot components by the operator.

A viewing window, made of the same material as the one used for protective welders' goggles, is placed in the center above the rotating rod specimen to permit visual observation.

### 3.3 Drive Spindle Assembly.

The drive spindle is made by one of the leading manufacturers of precision spindles in the United States, Whitton Spindle Division of Farmington, Conn. It is especially designed to handle objects subjected to extremely high temperatures.

This capability is achieved by two special features:

- 1) Introduction of cooling air to the spindle interior to be exhausted near the spindle nose and directed to a set of circular fins.
- 2) Utilization of ceramic inserts to impede the heat transfer path from the heated specimen to the spindle bearings.

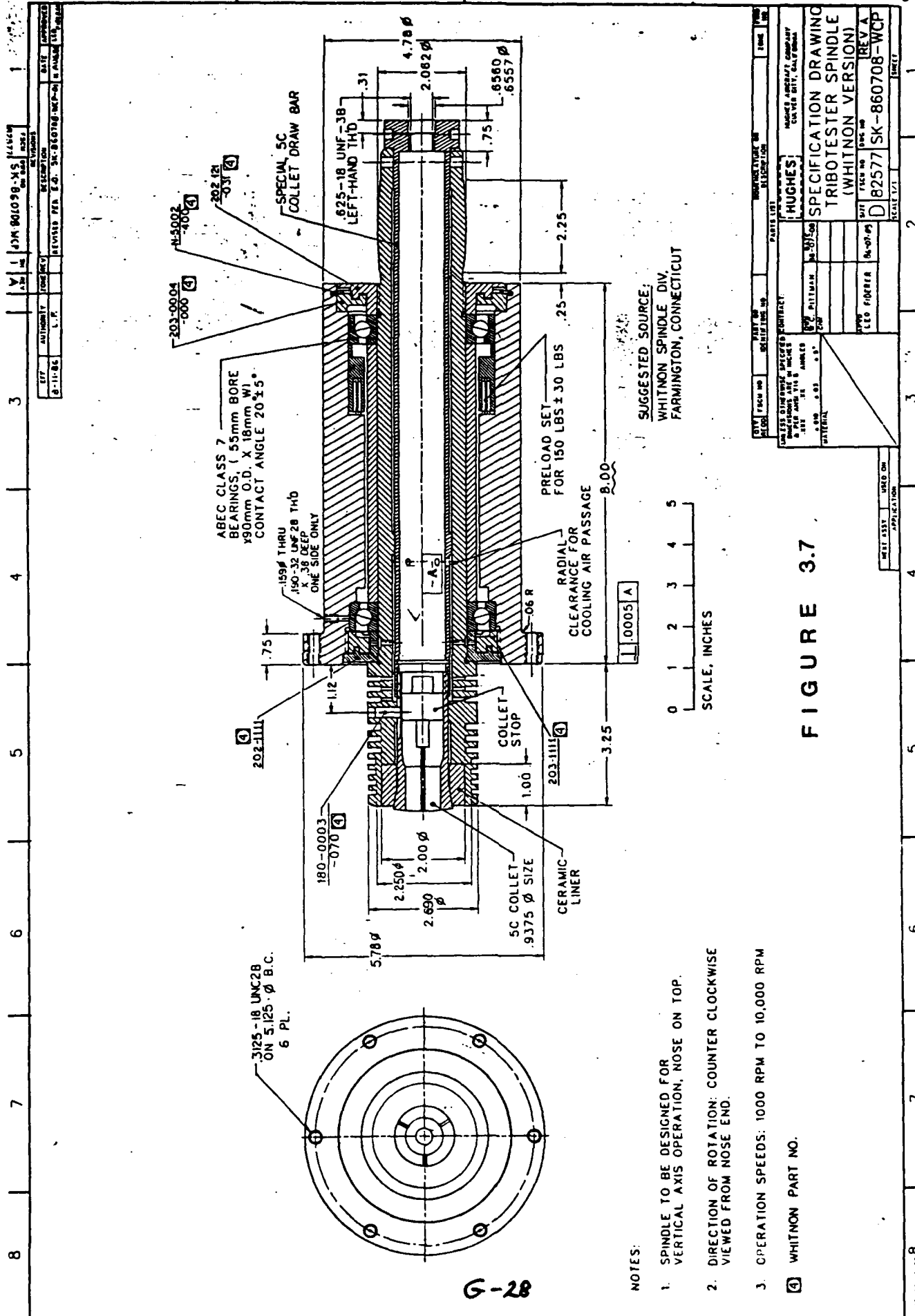
The design of the spindle is illustrated in Fig. 3.3 and Fig. 3.7. Cooling air is introduced to the spindle at the bottom through a high speed rotary junction, illustrated in Fig. 3.8. This rotary junction is attached to the specially designed collet draw bar at the bottom.

As can be seen in the illustration Fig. 3.3, the cooling air is directed through a set of passage holes in the draw bar into the annular clearance space between the draw bar and the interior of the spindle shaft. From there the air is directed to the exit holes interspersed between the set of circular fins near the spindle nose. The turbulence created by the air exiting through the orifices provides an effective heat transfer through forced convection.

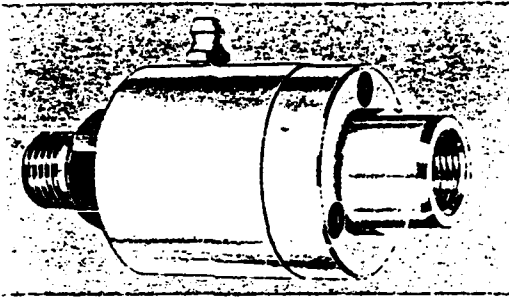
The section view in Fig. 3.3 also illustrates the use of the ceramic inserts, fabricated of "Macor", a material already mentioned in connection with the stationary pad specimen holders. The outer sleeve is permanently attached to the spindle nose via shrink fitting. This sleeve has the collet seat accurately ground in place after being assembled to the spindle.

The inner sleeve is actually a ceramic "collet inside a collet", that has its bore finish machined while being held in the spindle inside a standard precision collet, Type 5C. Thus the clamping surface which holds the rotating specimen has a run-out tolerance held to the minimum possible. The clamping force is provided by the precision steel collet. Thus, the ceramic liners are stressed only in compression, in which they are strongest, and not in tension or bending.

With this arrangement, a double layer of heat insulation is provided between the heated specimen and the spindle nose. It permits the upper spindle bearings to be operated at reasonably safe temperatures and at the same time prevents drainage of the heat from the specimen. The effectiveness of this method of heat insulation has been confirmed by actual breadboard tests.



## DEUBLIN *Super Hi-Speed Rotating Coolant Union*



### OPERATING DATA

|                          |            |            |
|--------------------------|------------|------------|
| Max. Hydraulic Pressure* | 1500 PSI   | 102 bar    |
| Max. Temperature         | 250°F      | 121°C      |
| Max. Speed*              | 15,000 RPM | 15,000 RPM |

Recommended coolant filtration—5 microns.

\*Operation at maximum pressure combined with maximum speed should be avoided. If operating conditions are marginal, please consult our engineering department.

### FOR SINGLE PASSAGE APPLICATIONS

This efficient union is specifically designed for installation on super high-speed machine tool spindles which have been tooled for gun-drilling small holes. Virtually no friction is generated since the seal-face rubbing speed is very low. Heat build-up is also prevented by the precision mounting of the ball bearings in accordance with high-speed spindle practices. This permits higher operating speeds with a minimum of heat.

Seal face contact with its rotating member is improved by accomplishing the initial loading of the seal through the use of three springs located *outside* of the coolant flow. Thus, coolant turbulence is greatly reduced.

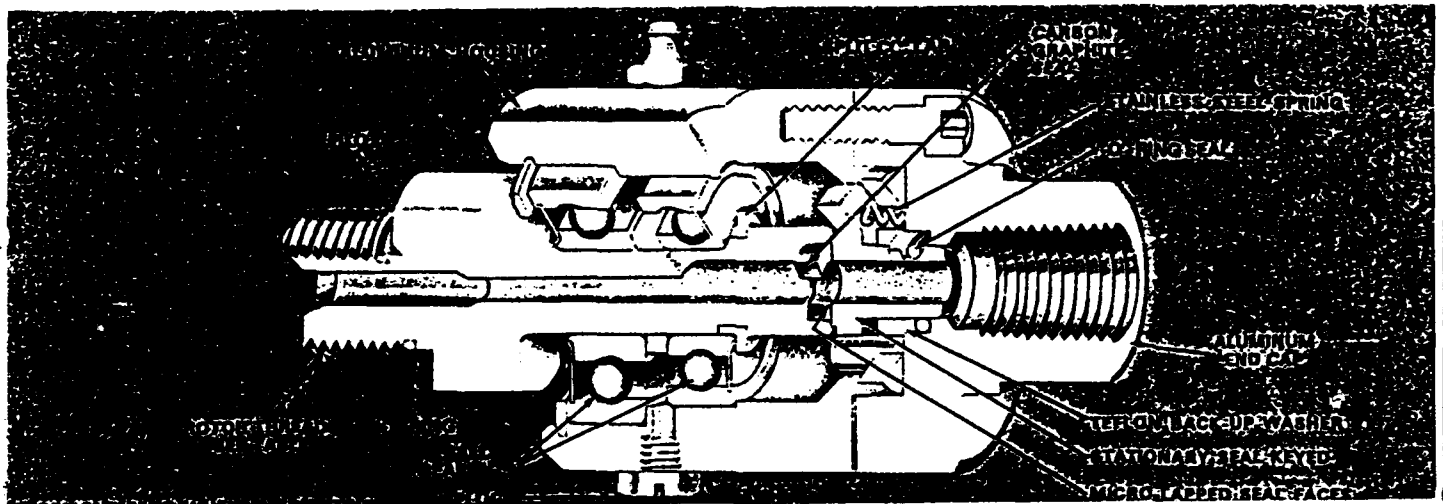


FIGURE 3.8

### 3.4 Mounting Platform.

The mounting platform consists of a stable optical breadboard table top similar to one used for experimental optical and mechanical precision assemblies. It is a honeycomb panel with 4.6 mm thick stainless steel skins bonded to an aluminum honeycomb core. The inherent advantage of a honeycomb panel over simple solid or ribbed plates is its structural efficiency of the design and highest possible rigidity-to-weight ratio.

The drawing with the dimensions of the selected design is illustrated in Fig. 3.9. It is a standard model manufactured by Newport Corporation of Fountain Valley, CA, modified by the addition of a clearance hole for the drive spindle body.

Overall dimensions are 122 cm x 91.4 cm x 11 cm (48 inch x 36 inch x 4.3 inch). The top skin contains an array of mounting holes at one inch center-to-center spacing with 1/4-20 threads. This feature facilitates the attachment of brackets, pedestals and all other components of the friction tester. Furthermore, the availability of the multitude of already threaded attachment points affords a convenient flexibility for checkout and dry-runs.

### 3.5 Portable Stand.

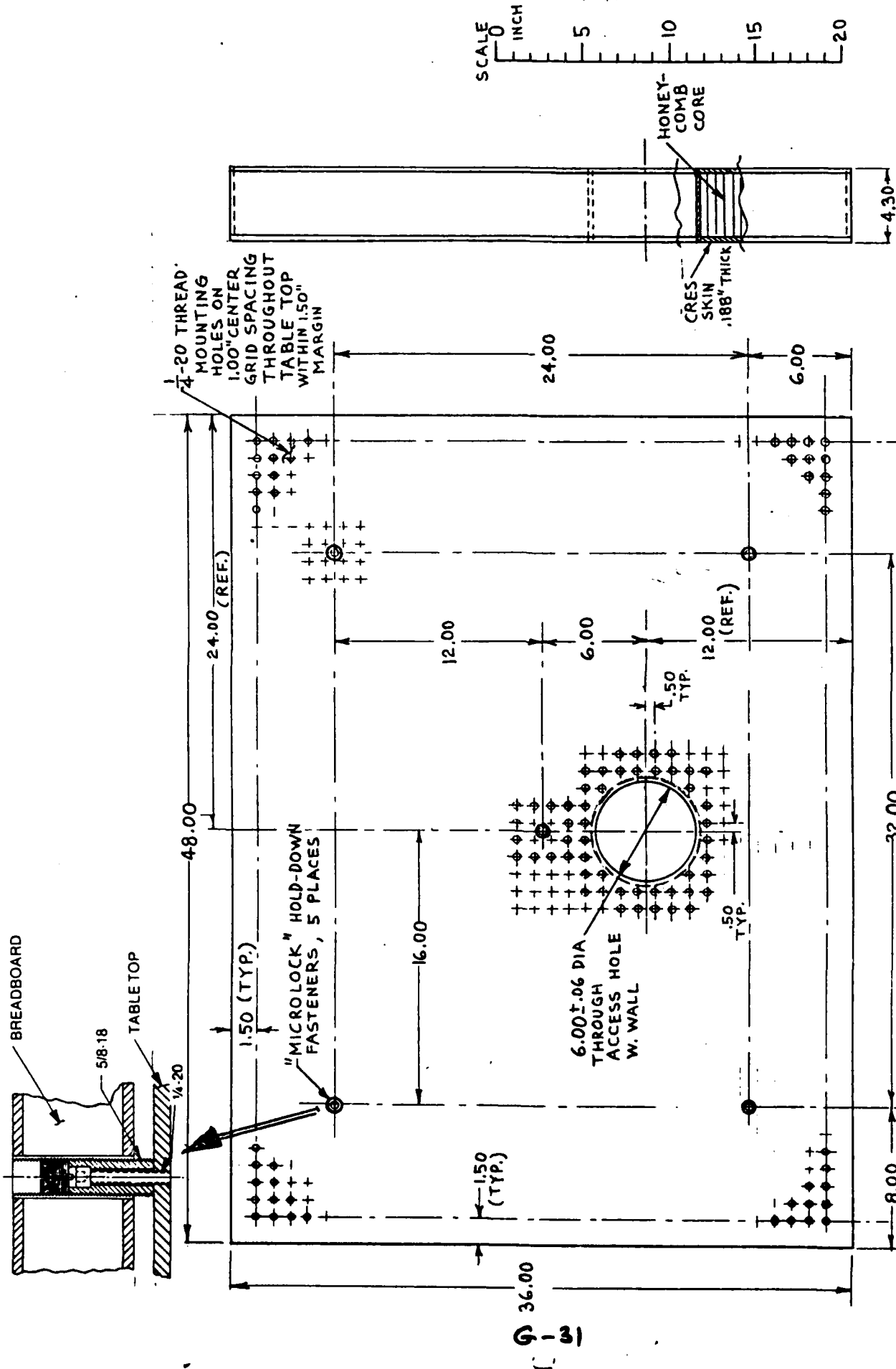
The Tribotester, including all the associated transducers, controllers and power supplies, is mounted on a movable equipment stand. This stand is constructed of a heavy duty equipment cart, modified by cutting a clearance hole for the drive spindle housing in the top shelf of the cart, as illustrated in Fig. 3.10. The available working area on the top shelf measures 91 cm x 152 cm approximately (36 x 60 inch).

Most of the top shelf area is occupied by the precision mounting platform described above and the load cell readout displays. The platform is fastened to the top shelf with the aid of the "Microlock" fastening devices.

The space below the platform is used for the mounting of the spindle drive motor, speed control, power supplies, coolant controls, and other controls and indicators. The attachment and mounting of these items to the cart is accomplished by a combination of angle posts, foot plates, heavy duty shelves and shelf clips, such as the ones illustrated in Fig. 3.11. The vertical posts that connect the top and bottom shelf of the cart, are also re-inforced by sway braces for added rigidity.

This arrangement permits maximum flexibility for the installation of the components under the mounting platform to suit the convenience of the operator. It also facilitates change-overs and relocation of items if such changes are considered desirable during the start-up and checkout of the Tribotester. At the same time, this arrangement allows convenient access for calibration and adjustment to all the transducers and measurement devices.



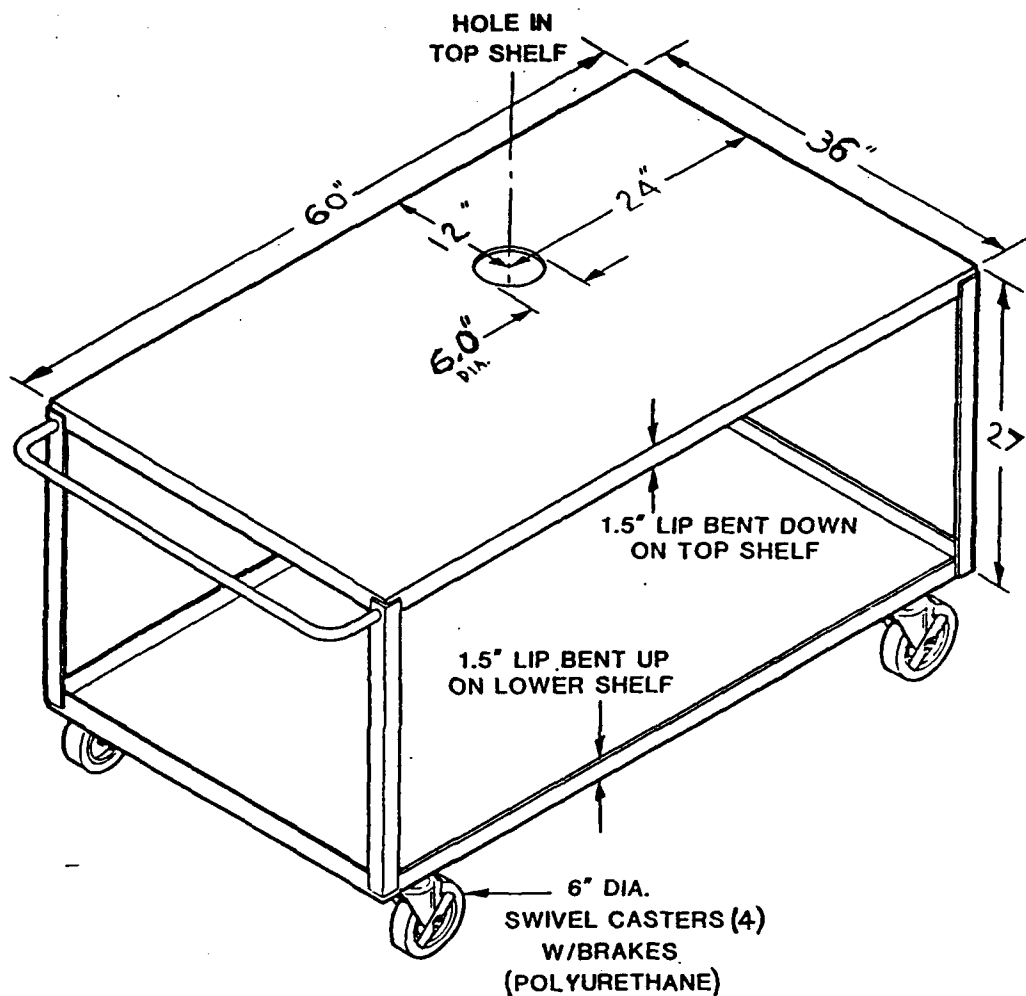


|                                           |         |                                                                |  |
|-------------------------------------------|---------|----------------------------------------------------------------|--|
| SPECIFICATION DWG.,<br>OPTICAL BREADBOARD |         | CONTRACT:<br>HUGHES AIRCRAFT COMPANY<br>EL SEGUNDO, CALIFORNIA |  |
| SIZE                                      | FSCM NO | DWG NO                                                         |  |
| A                                         | 82577   | SK-860813-01-LF                                                |  |
| DR: LEO FIDERER, AUG 13, 86               |         | SCALE: NOTED                                                   |  |
| TEL: (213) 616-4826                       |         | SHEET                                                          |  |

SUGGESTED SOURCE:  
NEWPORT CORP.  
FOUNTAIN VALLEY, CA  
PART NO. XS-34-4.3-SP

FIGURE 3.9

SP 519151



ALL WELDED CONSTRUCTION

SHELVES MADE OF #13 GAUGE STEEL

FINISHED IN GRAY

|                          |      |                        |            |                           |                            |                            |            |
|--------------------------|------|------------------------|------------|---------------------------|----------------------------|----------------------------|------------|
| PURPOSE                  |      |                        |            | TITLE<br>CART, HEAVY DUTY |                            |                            |            |
| MATL & SPEC<br>NOTED     |      |                        |            | SCALE<br>NONE             | TOLERANCES<br>ANGULAR<br>± | LINEAR<br>±                | SKETCH PAD |
| ORIGINATOR<br>L. FIDERER | APPR | DATE<br>SEP 22<br>1966 | BLOG<br>EI | ROOM (M/S)<br>D145        | PHONE<br>(213)<br>616-4026 | HUGHES AIRCRAFT<br>COMPANY | SP 519151  |

137 CS APR 85

FIGURE 3.10  
G-32

# STORAGE EQUIPMENT SPECIFICATIONS

## Outstanding Application Versatility

**Clip Shelving** units offer the versatility of interchangeable components for all open and closed shelving units, the option of assembling shelves with bolts and nuts (instead of clips), and a choice of front posts. Of course, "Starter" and "Adder" models are offered in most sizes.

### Specifications

- Heights to 15 ft. without splicing
- Widths to 48"
- Depths to 36"
- Standard heights 7'1" (85"), 8'1" (97")
- Vertical shelf adjustments in 1½" increments

**Post Designs**—all three post designs are roll formed of heavy gauge steel and are applicable to all storage unit arrangements except as noted. Shelving posts are also adaptable to mezzanine applications.

**Angle Posts**—the most economical design



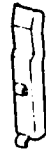
offering the greatest flexibility because of the stiffening offset rib. Angle posts are formed of heavy gauge steel, and are always used as rear posts when other posts are used. Four angle posts make up each unit, reducing shelf accessibility by 2 inches.

**Delta Posts**—offer versatility as front shelving



posts or common posts between multiple units, since they are designed for shelf adjustments on both sides. Formed of 14 gauge steel, they are engineered for unobstructed shelf access.

**Shelf Clips**—designed for easy installation and shelf repositioning. Clips are formed of heavy gauge steel for maximum weight bearing capability.



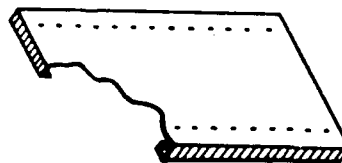
### SHELF CONSTRUCTION

Shelves are 18 gauge, except Class 0, which are 20 gauge, and all are flanged twice on each side and triple flanged front and rear. Top surface of shelves punched on 2" centers for adjustment of dividers. Also punched for label holders, angle sway braces, reinforcing bars and angles on both front and rear faces.

Standard Widths – 30", 36", 42", 48"

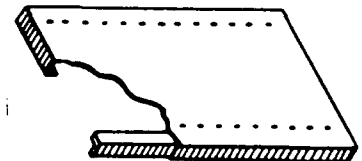
Standard Depths – 12", 15", 18", 24", 30", 36"

### SHELF CLASSIFICATION AND LOAD CAPACITIES

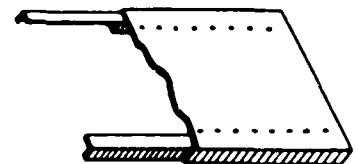


**Class 0 - 20 gauge:** for light loads, no reinforcements

**Class 1 - 18 gauge:** for normal loads, no reinforcements



**Class 1A - 18 gauge:**  
1" x 1" x 1/8" angle in front flange for medium loads



**Class 2A - 18 gauge:**  
1" x 1" x 1/8" angles in front and rear flanges for heavy loads

FIGURE 3.11

#### 4. INSTRUMENTATION.

The principal measuring instrumentation consists of the latest state-of-the art components with proven reliability and extremely low risk factors. Following are the descriptions and excerpts from vendors' catalog information bulletins for these devices.

##### 4.1 Force Measurements.

The force measurements are accomplished with the aid of a multi-axis load cell manufactured by Advanced Mechanical Technology, Inc., of Newton, Mass. This load cell combines the functions of the x-axis and y-axis load cells illustrated in Fig. 2.3, and is also capable of providing additional load indications in the z-axis, plus the moments about the three mutually perpendicular axes.

A brief description of the capabilities of such load cells and a diagram of the six output parameters is shown in the excerpt from the User's Manual reproduced in Fig. 4.1.

Each load cell can be fabricated for six separate output channels, as indicated in the diagram: Force output channels  $F(x)$ ,  $F(y)$ , and  $F(z)$ , and moment output channels  $M(x)$ ,  $M(y)$ , and  $M(z)$ . The signal from each channel is fed through a common cable to the six-channel amplifier.

In the tribotester application, only three channels are utilized in each load cell:  $F(x)$ ,  $F(y)$ , and  $M(y)$ . The moment reading about the Y-axis will be utilized to check the balance about the pivot point, which ideally should also be the center of gravity of the moment arm configuration. The counter weight shown in Fig. 3.2 can be shifted in the X-direction. At the start of each test series, the position of the counter weight will be adjusted until the reading for  $M(y)$  is close to zero.

Since only three channels are utilized in each load cell, one six-channel amplifier can be used for both of them.

During the hardware design phase, breadboard tests with a load cell model similar to the purchased model have been conducted. It was found that the single load cell can indicate simultaneously the X-axis and Y-axis force vectors with close correlation to the outputs of single axis load cells in the steady-state mode. For the dynamic component, a calibration factor has to be applied to indicate the total load value.

##### 4.2 Wear Measurements.

The measurement of the depth of the combined wear scar as a function of time is accomplished with the aid of a non-contact type probes that generate an electric signal produced by eddy-currents as a function of the width of the gap between two parallel metallic surfaces.

The probes selected for this application are manufactured by Bently Nevada of Minden, Nev. Copies of the pertinent catalog sheets with performance specifications are reproduced in Fig. 4.2a and 4.2b.

# GENERAL

The SRMC3 series of dynamometers are multicomponent platform-type dynamometers that are available in several capacities and with from one to six channels of output. Any or all of the three orthogonal forces and moments may be specified. The instrument model number SRMC3-X-XXXX reflects the capacity in the last series of digits and the number of channels in the second digit. For instances, Model SRMC3-6-500 has a capacity of 500 lbf and has six channels of output, i.e.,  $F_x$ ,  $F_y$ , and  $F_z$  and  $M_x$ ,  $M_y$ ,  $M_z$ . The coordinate system axes are shown on the calibration page.

The working surface of this instrument is 3 inches square and has four 1/4-20 threaded hold-down inserts on 2 inch centers. The mounting base is provided with four 1/4 inch bolt holes on the same centers. The dynamometer should be mounted on a flat surface.

## OPERATION

This instrument uses strain gages to perform the force and moment measurements. A elastic member sealed inside the dynamometer is gaged such that the three forces and three moments applied to the dynamometer may be isolated with minimum crosstalk. The gages are configured in four-arm bridges to provide high thermal stability.

In general, the dynamometer sensitivities are on the order of microvolts/volt unit load (in-lbf for moment and lbf for force). Amplification is therefore necessary to provide high level output signals. To determine the required amplifier gain use the following method:

$$G = \frac{V_o}{V_e \times S \times FSL}$$

where G is gain,  $V_o$  is desired full-scale output voltage,  $V_e$  is the bridge excitation voltage, S is the dynamometer sensitivity, and FSL is the expected full-scale load. It is often desirable to use different gains for different channels depending on the expected full-scale loads for those axes.

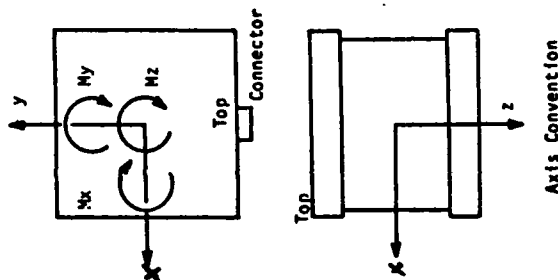


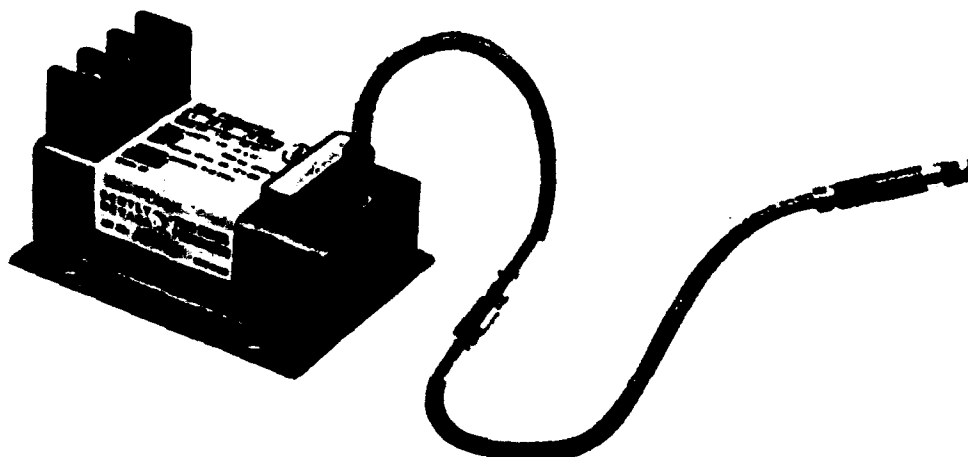
FIGURE 4.1

## SRMC3 SERIES DYNAMOMETER SPECIFICATIONS

| SPECIFICATION              | SRMC3-X-100 | SRMC3-X-250 | UNIT        |
|----------------------------|-------------|-------------|-------------|
| Capacity                   |             |             |             |
| $F_x, F_y, F_z$            | 100         | 250         | lbf         |
| $M_x, M_y, M_z$            | 100         | 250         | in-lbf      |
| Sensitivity                |             |             |             |
| $F_x, F_y$                 | 30.00       | 12.00       | microvolts  |
| $F_z$                      | 7.50        | 3.00        | volt-lbf    |
| $M_x, M_y$                 | 150.00      | 60.00       | microvolts  |
| $M_z$                      | 30.00       | 12.00       | volt-in-lbf |
| Stiffness (at top surface) |             |             |             |
| $F_x, F_y$                 | 12,000      | 30,000      | lbf/in      |
| $F_z$                      | 170,000     | 450,000     | lbf/in      |
| $M_y$                      | 20,000      | 50,000      | in-lbf/rad  |
| Lowest Resonant Frequency  | 300         | 500         | Hertz       |
| $M_x, M_y$                 |             |             |             |
| Non-Linearity (Max.)       | ----        | .20         | $\pm$ % FSO |
| $F_x, F_y, F_z$            |             |             |             |
| Hysteresis                 | ----        | .20         | % FSO       |
| $F_x, F_y, F_z$            |             |             |             |
| Excitation, Max.           | ----        |             |             |
| Recommended                | ----        | 10          | Volts       |
| Temperature Range          | ----        | 00 to 1250  | of          |
| Weight                     | ----        | 1.7         | lbm         |
| Working Surface            | ----        | 3x3         | Inches      |
| Dimensions                 | ----        | 3x3x2.75    | Inches      |

**ADVANCED MECHANICAL TECHNOLOGY, INC.**  
141 CALIFORNIA STREET • NEWTON, MASSACHUSETTS 02188

# 7200 Series 5mm and 8mm Proximity Transducer Systems



Bently Nevada's 7200 5mm Proximity Transducer System measures static and dynamic distances between a probe and the observed target.

The 5mm and 8mm Proximity Transducer Systems are non-contacting, gap-to-voltage transducer systems that measure static as well as dynamic distances between a probe and the observed target. They are designed for use with a variety of rotating machinery, such as gas and steam turbines, compressors, and generators. They offer 80 mils of linear measuring range and are compatible with API 670 type installations.

The systems consist of a probe with probe lead, extension cable, and Proximitor®. They are compatible with the 7200, 9000 Series, and the Smart Monitor® systems.

Eleven probe configurations are available to accommodate English and metric requirements. Standard 5mm and 8mm probes are constructed of fiberglass. The 8mm probes are optionally available in Rytan®, which provides additional environmental and mechanical protection for harsh environments.

For both probes, the actual diameter of the probe coil is 5mm with the same electrical properties for all configurations.

Four extension cables are available with or without armor and are designed to achieve a system length of either 5.0 or 9.0 meters.

The Proximitor produces a radio frequency signal, which is radiated through the probe tip into the observed surface. Eddy currents are generated in the surface, and the loss of strength in the return signal is detected by the Proximitor, which conditions the signal for linear display on a monitor.

The Proximitor signal output and power source input are transmitted to the Proximitor through a 3-conductor signal cable. The Proximitor can be placed up to 1,000 feet from standard Bently Nevada monitors without degradation of performance.

\*Rytan is a registered trademark of Phillips Chemical Company.

**BENTLY  
NEVADA**

P.O. BOX 157 • MINDEN, NEVADA USA 89423 • (702) 783-3611 • TELEX: 354437

**FIGURE 4.2 a**  
**G-36**

# System Specifications

Specifications were determined with - 24 Vdc power supply, 10,000 ohm load, and an AISI 4140 steel target at 22°C (72°F).

## INPUT

Power: - 18 Vdc to - 24 Vdc at 13 mA maximum.

## OUTPUT

Calibrated Range: 80 mils (2.0mm). Begins at approximately 10 mils (0.25mm) from probe face.

Scale Factor: 200 mV/mil,  $\pm 4\%$ , over 80 mil range, if calibrated as a system. Within  $\pm 9.5\%$  when interchangeability errors are included.

Linearity: Within 0.8 mils (0.02mm) of 200 mV/mil straight line if Proximator is calibrated for specific probe and cable. Within 2.3 mils (0.06mm) of 200 mV/mil straight line with interchangeability errors included.

Frequency Response: 0 to 600,000 rpm; - 5% at 600,000 rpm.

Temperature Sensitivity: Typically - 3% change in scale factor at 65°C (150°F) at 50 mils (1.27mm).

## ENVIRONMENTAL

### Temperature

#### Range:

Operating: Proximator options - 03 and - 04: - 51°C to + 100°C (- 60°F to + 212°F).

Probe and Cable: - 34°C to + 177°C (- 30°F to + 350°F).

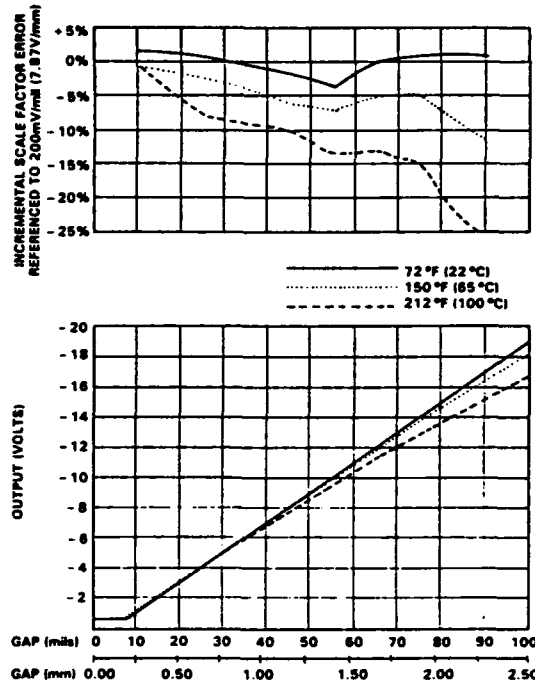
Note: 5mm Base Resistant probes and Ryton probes, catalog numbers 43081R and 43084R, are rated to 121°C maximum (250°F).

Relative Humidity: To 95% noncondensing.

Corrosion Resistance\*: Probe function is not affected by direct contact to the following:

Air, water, lube oil, ammonium hydroxide, sulfuric acid (10%), Dimethylethylketone, and Dimethylformamide.

## 7200 5mm SYSTEM (PROBE, PROXIMATOR, AND 9 METERS OF CABLE) AT TEMPERATURE



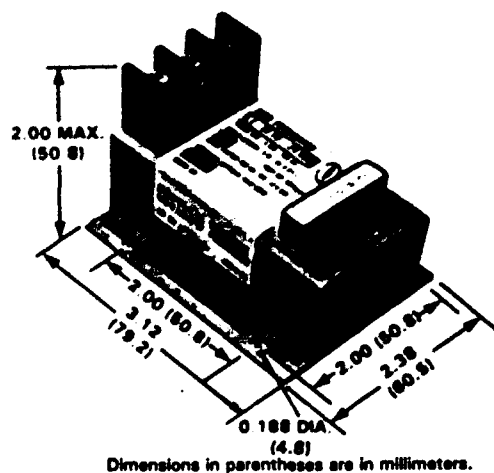
System Weight: 1.2 lbs. (.54 kg).

Dimensions: See pages 2, 3 and 4.

\*For Ryton probes only.

## 5mm Proximator

### Dimensions



Dimensions in parentheses are in millimeters.

### Ordering Information Proximator

18745-□□

□□ Option Description

03 For combined probe and extension cable electrical length of 5 meters (16.4 feet)

04 For combined probe and extension cable electrical length of 9 meters (29.5 feet)

The 7200 5mm and 8mm transducer system must use only 5mm and 8mm components — probe, Proximator, and extension cable.

FIGURE 4.2 b

The application of such probes is illustrated in Fig. 3.2, showing two proximity probes mounted at right angles to each other next to the specimen holding device. These two probes are not operated at the same time, actually performing to distinct functions.

One probe, the one mounted parallel to the tangential load in the x-direction, is used during the warm-up stage to compensate for thermal expansion of the moment arm while the specimen is heated to the maximum test temperature.

The reading for the width of the gap between the specimen clamp and the probe is taken at the beginning, before heating the specimen. As the moment arm expands during warm-up, the gap narrows, resulting in a changed reading. The tangential adjustment is then performed as described in Section 3.1, until the same reading as the one obtained at the beginning is achieved.

After thermal stabilization has been achieved, the amplifier is switched from the tangential probe to the one in line with the normal load in the Y-axis. Because of the danger of cross-talk and erroneous readings, the two probes cannot be operated simultaneously.

As the test proceeds and wear scars are created in both the rotating and the stationary specimen, the constant spring pressure pushes the specimen clamp toward the rod, thus widening the gap. The change in the gap width corresponds to the depth of the combined wear scars and can be determined from the signal generated by the probe.

#### 4.3 Speed Measurement.

The rotary speed of the drive spindle is measured with the aid of a photo-diode connected to simple circuitry, as described below.

The photo-diode is positioned near the rotating surface at the bottom of the spindle, which has a stripe with sharp contrast in brightness compared to the rest of the surface. The photo-diode detects the contrast in the reflecting surface once every revolution.

The established threshold of brightness activates a Schmidt-Trigger inverter which generates a cleaner wave form approximating a square wave. This square wave is channeled to a frequency counter which reads the output directly as Hertz or, with a suitable multiplying factor, as RPM.

The above described circuitry is already a well known state-of-the-art technology which can be implemented with inexpensive components. Therefore it is not necessary to elaborate here in further details.

#### 4.4 Temperature Measurements.

Temperature measurements are twofold: For the stationary pad specimen with the aid of thermocouples, and for the rotating rod specimen surface with the aid of a non-contacting I.R. pyrometer.



The method of placing the thermocouple probes into the stationary pad cavity is illustrated in Fig. 3.4 described in the earlier Section 3.1. The cavities are carefully drilled into the pads as close as possible to the contact surface as shown in the pictures in Fig. 2.6. Thus, the temperatures indicated by the thermocouple probes placed at the bottom of these cavities will come close to the ones at the contact point.

Infrared Radiation Pyrometers are widely used in industry for non-contact type temperature measurements at extremely high temperatures, such as required in steel mills or glass blowing facilities.

An I.R. temperature sensor is a precision electro-optical instrument that senses infrared radiation energy from a target surface at a distance and converts it into a continuous electrical signal proportional to the target temperature. The signal is coupled through the signal cable to a signal processor, where it can be converted into digital or analog form as input to a recorder/indicator, to a computer or to a process controller.

Proper application and installation of the I.R. sensor is extremely important. Even the best instrument may give inaccurate information if not used correctly, or if the principles of infrared temperature measurement are not taken into consideration.

One important consideration is the emissivity of the target surface. The targets we deal with in practice are usually non-blackbodies with surface emissivity values of less than 1.0. Therefore, the emissivity control factor on the instrument has to be adjusted to compensate for the difference between the target and an ideal blackbody radiator. This can be accomplished by calibration with ceramic samples at known controlled temperatures.

Another significant factor that could contribute to erroneous readings is stray background radiation. The sensor is sensitive to radiation in an area indicated by the I.R. Optics cone, also called "Cone of Vision" (see Fig. 4.3). It measures the temperature of objects inside but not outside the cone. The diameter of the cone at any point determines the area of measurement (spot size) at any point.

Since the radiant energy being measured should be from the target only, no foreign objects should interfere with the path of the cone. Furthermore, the cone should be centered on the target to make sure that the spot size at the target surface is smaller than the minimum width of the target, preferably  $1/2$  or less. Otherwise, the sensor would see around the target into the background. Therefore, the diameter of the cone of vision at the passage through the aperture plate (see Fig. 3.2) should be smaller than the opening in the plate.

From the above discussion, it is obvious that selection of the pyrometer model and its placement requires utmost care. Five well known manufacturers of I.R. temperature sensors have been investigated and a leading expert in the field of I.R. pyrometry has been consulted. The basic requirements for the pyrometer manufacturer and model were first established as follows:

TRIBOLOGICAL FUNDAMENTALS OF SOLID LUBRICATED CERAMICS

# TRIBOTESTER 2A I.R. SENSOR OPTICS

**HUGHES**

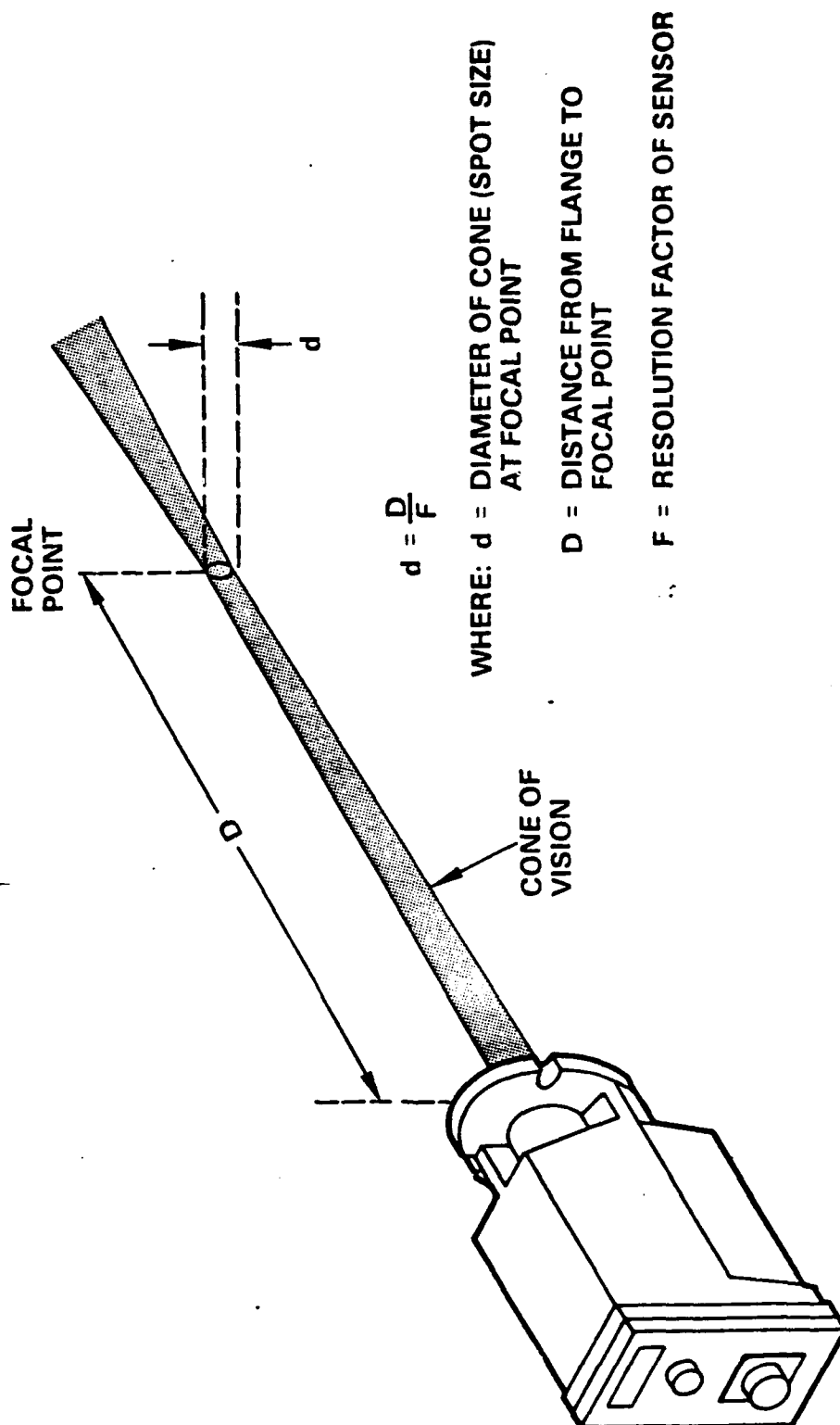


FIGURE 4.3

**Target Material:** Ceramic test rods, 0.375 inch diameter in a variety of materials with an estimated emissivity range from 0.6 to 0.95.

**Expected Measurement Range:** 260 to 870 deg. C (500 to 1600 deg. F)

**Accuracy Required:** + or - 1.0% of reading.

**Repeatability:** + or - 0.5% of reading.

**Spot Size and Working Distance:** The target is viewed through an aperture of 4.5 mm diameter. Considering aiming inaccuracies and the field-of-view spread of most commercial instruments, the selection of a 1.2 mm target spot size is appropriate. The working distance should be from 100 mm to 200 mm for convenience (4 to 8 inches).

**Response Time:** 0.1 seconds or faster.

**Pyrometer Sensing Head Requirements:** The sensor should be as small as possible for versatility. Aiming is critical and should be as reliable and convenient as possible.

**Spectral Region of Operation:** The instrument should operate far enough into the infrared region so that measurements are not affected by visible light and by energy from the line heater that is used to heat the tested rod specimen. The heater radiance is peaked at 0.85 microns and 1.1 microns. A reasonable safe selection for the pyrometer is an operating region of 3.5 microns or larger.

The five manufacturers, whose proposals were solicited for the application, are the following:

Ircon, Inc., of Niles, Illinois,

Land Instruments, of Tullytown, Pennsylvania,

Vanzetti Systems, of Stoughton, Massachusetts,

Williamson, of Concord, Massachusetts

Wahl Instruments, of Culver City, California.

All of the above manufacturers have a high reputation in the field and are known to produce quality instruments.

After a careful consideration of all the proposals submitted and review of the above requirements, the Consultant, Honeyhill Technical Co. of Norwalk, Connecticut, recommended a model produced by Vanzetti Systems, though not the model No. originally recommended by the company's representative. The illustration in Fig. 4.4 shows a picture of the sensing head of the recommended model. It has a target spot size of 1.25 mm at a target distance of 100 mm, it operates in the 4.5 micron region, has a convenient aiming method and, coincidentally, is also very reasonably priced.



## 5. SUMMARY AND CONCLUSIONS.

The description of the friction tester, designated TRIBOTESTER 2A, gives an insight to the detailed design and construction of the apparatus and its functions.

It has been shown that by using reliable state-of-the-art components and combining them in a novel fashion, it is possible to construct an apparatus that is capable of performing a variety of functions that up to now required several more cumbersome pieces of equipment.

This feat has been achieved by a cautious approach with attention to details, by performing essential analysis and breadboard tests, and by a series of design reviews, taking advantage of the experience of mechanical engineers and tribology experts.

The device is capable of performing the functions originally assigned to it. It also has the capability of performing at higher limits of speeds, actuating frequencies and temperatures, when the initial test series has been completed and a gradual venture into higher limits is indicated by the test results.

## 6. REFERENCES.

- 1) Smith, J. O. et al, "Stresses due to Tangential and Normal Loads on an Elastic Solid with Application to some Contact Stress Problems", Journal of Applied Mechanics, v. 20, p.157 (1953)
- 2) Mervin, J. E., and Johnson, K. L. "Analysis of Plastic Deformation in Rolling Contact", Proceedings of Institute of Mechanical Engineers, Applied Mechanics Group Paper, P25/63, (1963)
- 3) Johns, T. G. et al, " Engineering Analysis of Stresses in Railroad Rails, Phase I", Battelle Columbus Laboratories, FRA Contract DoT-TSC-1038, (June 1977)
- 4) Kannel, J.W., and Tevaarwerk, J. L., "Subsurface Stress Evaluations Under Rolling/Sliding Contacts", ASME/ASLE Joint Lubrication Conference Paper, ASME Paper 83-Lub-18, Hartford, Conn. (1983)
- 5) Gardos, M. N. "Determination of Tribological Fundamentals Governing Friction and Wear of Solid Lubricated Ceramics in Extreme Environments", First Semi-annual Report, Contract No. F33615-85-C-5087, Hughes Aircraft Co. EDSG, (May 1986)
- 6) Mc Laughlin, J. J., "Alternate Ceramic Materials for Roller Bearings - Final Report", Contract No. N00019-81-C-0824, Teledyne CAE, Toledo, OH (March 1984)
- 7) Dill, Dr. J. F. et al, "Rolling Contact Fatigue Evaluation of Hard Coated Bearing Steels", ASLE Proceedings, 3rd Int. Conf. on Solid Lubrication, Denver, CO, ASLE SP-14, pp.230-241 (Aug. 1984)
- 8) Glover, D. "A Ball-Rod Rolling Contact Fatigue Tester", ASTM Special Tech. Pub. 771, (1982)

## 7. ACKNOWLEDGEMENTS.

Special thanks are expressed to the following engineers at Hughes Aircraft Co., EDSG, whose contribution made the work on the friction tester and the completion of this report possible.

MICHAEL N. GARDOS, Senior Scientist, for his contribution to the theoretical basis and historical background of this report.

JOHN P. HARRELL, Section Head, for the mechanical and structural analysis of the loading mechanism.

RICK WILLIAMS, Member of Technical Staff, for the thermal analysis.

NATE ITKIN, Member of Technical Staff, for computer assisted test data reduction, mechanical analysis and valuable suggestions.

LARRY CHICKOLA, Member of Technical Staff, for diligence in performing the breadboard tests and helpful recommendations.

## APPENDIX H

J.P. Harrel, "Tribotester Structural analysis," Hughes Interdepartmental  
Correspondence No. 867282.20/930, 29 October 1986

## INTERDEPARTMENTAL CORRESPONDENCE

**HUGHES**

**TO: Leo Fiderer**  
**ORG: 72-82-22**

**SUBJECT: Tribotestor Structural  
Analysis**

**CC:**

**DATE: 29 Oct 86**  
**REF: 867282.20/930**

**FROM: J.P Harrell**  
**ORG: 72-82-21**

**BLDG: E1 MAIL STA: D145**  
**LOC: E0 PHONE: 64551**

---

A finite element structural analysis was performed on the Tribotestor loading mechanism to determine the frequencies and mode shapes of primary structural resonances, in particular those that might interfere with the proper functioning of the device. The analysis was performed using the MSC/PAL computer program for the IBM PC which uses finite element techniques to predict the normal modes of the structure based on the mechanical parameters and the geometry specified by the operator. The program recognizes beam and plate elements, lumped stiffnesses and masses, and rigid connections.

A counterweight is required to statically balance the loading mechanism about the load cell Z axis since imbalance could result in load measurement errors under dynamic conditions. Therefore, a GEOMOD model was made to determine the loading mechanism mass properties and center of mass location. Plots of this model are shown in Figures 1 and 2. A brass counterweight 3.00 x 1.00 x 0.75 inches was selected which when located as shown will balance the assembly. The total weight of the



components on the duplex pair bearings will be approximately 6.4 pounds. This counterweight information was used in conjunction with the structural analysis.

The undeformed geometry of the MSC/PAL model is shown in Figures 3 and 4 with node numbers. Thin dashed lines represent rigid interconnections. Nodes 4, 7, and 15 are virtually coincident and therefore the label for node 15 obscures the other two. Nodes 5 and 6 are also virtually coincident and therefore the label for node 6 obscures the other. Nodes 5 and 6 are interconnected by a lumped stiffness element representing the ball bearing stiffness parameters. Nodes 7 and 15 are interconnected by a lumped stiffness element representing the load cell stiffness parameters.

The shape of the first structural mode (61 Hz) is shown in Figure 5. This deformation pattern is primarily rotation of the assembly about the X axis of the ball bearings. Since there is no driving function for this mode in the operation of the Tribotestor, this resonant frequency should not present any detrimental effects.

The second structural mode shape (139 Hz) is shown in Figure 6. This mode has substantial bending deformation in the X-Y plane which can be excited by the sinusoidally varying input force of the electromagnetic actuator. Therefore, actuator input frequencies near this resonance should be avoided to ensure data integrity in the experiment. But this mode should not prevent the operation of the device up to 50 Hz.

A simple test was also performed on a breadboard Tribotestor in which an electromagnetic actuator was driven by a signal generator and power amplifier and scanned from 0 Hz to 200 Hz to find structural

resonances which are excited by this forcing function. The purpose of this IDC is not to report on that breadboard test but the results did confirm the presence of a resonance between 140 Hz and 145 Hz, and no resonances below this frequency were found. This test supports the conclusions of the analysis.

Copies of the load cell parameters, bearing stiffness values, and ceramic material specifications are attached for reference along with the MSC/PAL program input and output data.

SDRC I-DEAS 3.0Pre: System Assembly 14-MAY-86 18:04:01 UNITS = IN  
 DATABASE: TRIBOTESTER TRI-AXIS LOAD CELL DISPLAY: No stored OPTION  
 VIEWING: stored VIEW Bin: 1-MAIN  
 Task: SYSTEM Component: 5-CAP  
 System: 6-SYSTEM6 (modified)

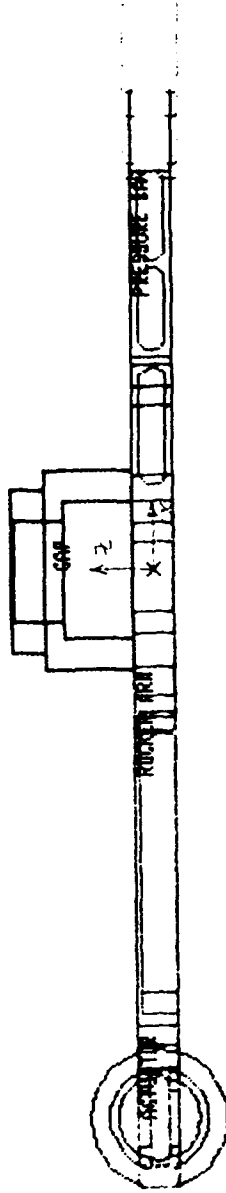


Figure 1. GEOMOD model side view

SDRC I-DEAS 3.0Pre: System Assembly 14-MAY-86 18:01:11  
 DATABASE: TRIBOTESTER TRI-AXIS LOAD CELL UNITS = IN  
 VIEWING STORED VIEW DISPLAYING STORED OPTION  
 Task: SYSTEM Dia: 1-MIN  
 System: 6-SYSTEMS (modified) Comments: 5-CAP

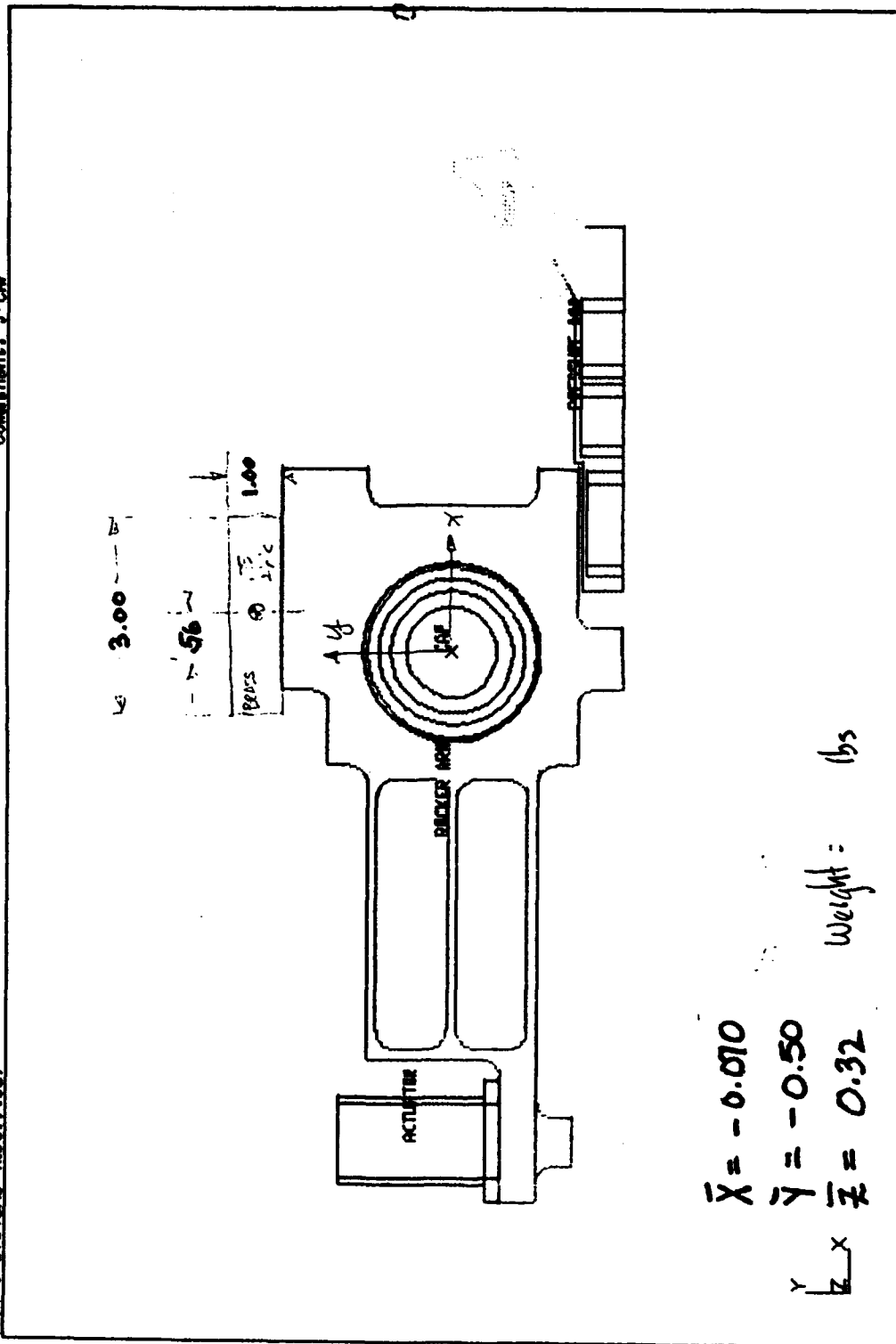


Figure 2. GEOMOD model top view

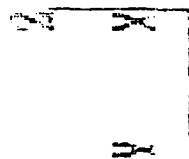
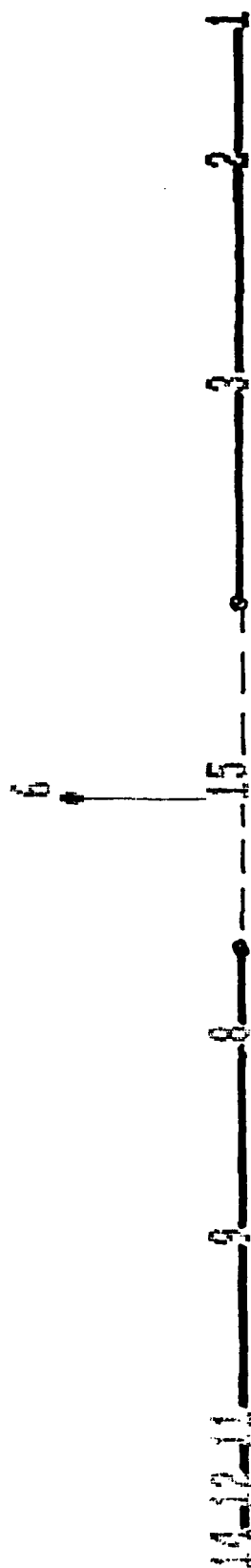


FIGURE 3. UNDEFORMED GEOMETRY Y-Z PLANE VIEW

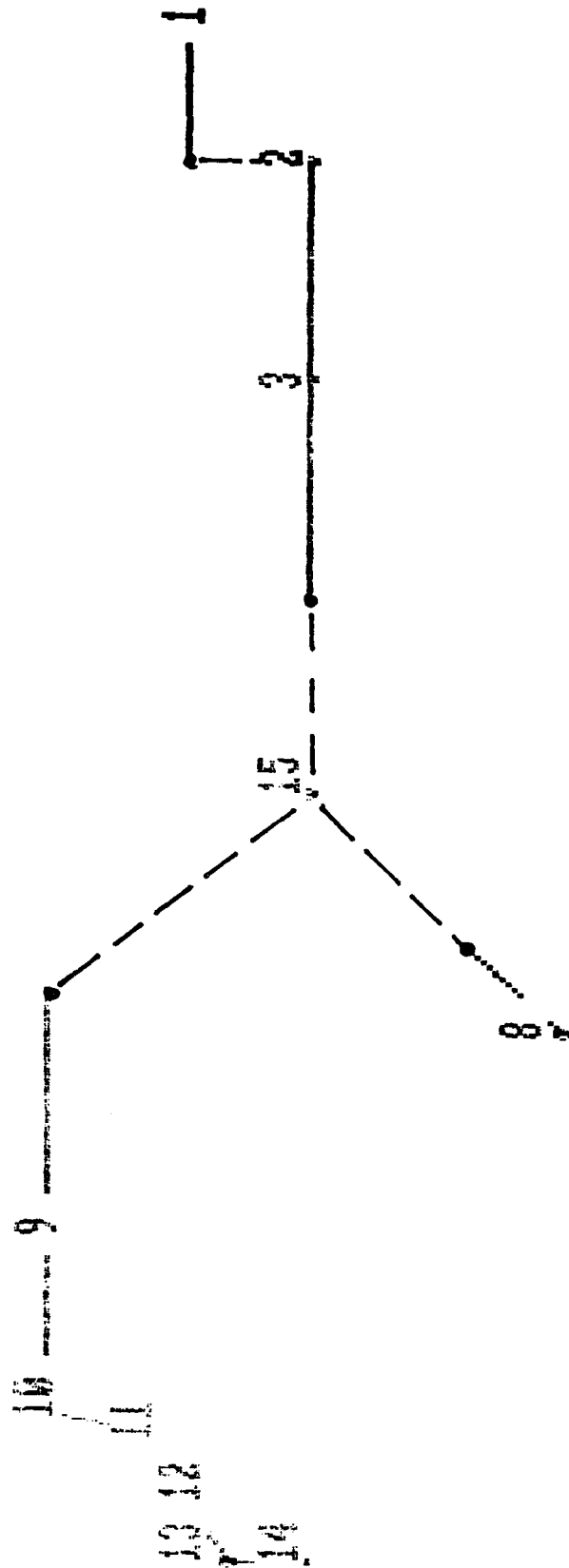


FIGURE 4. UNDEFORMED GEOMETRY X-Y PLANE VIEW

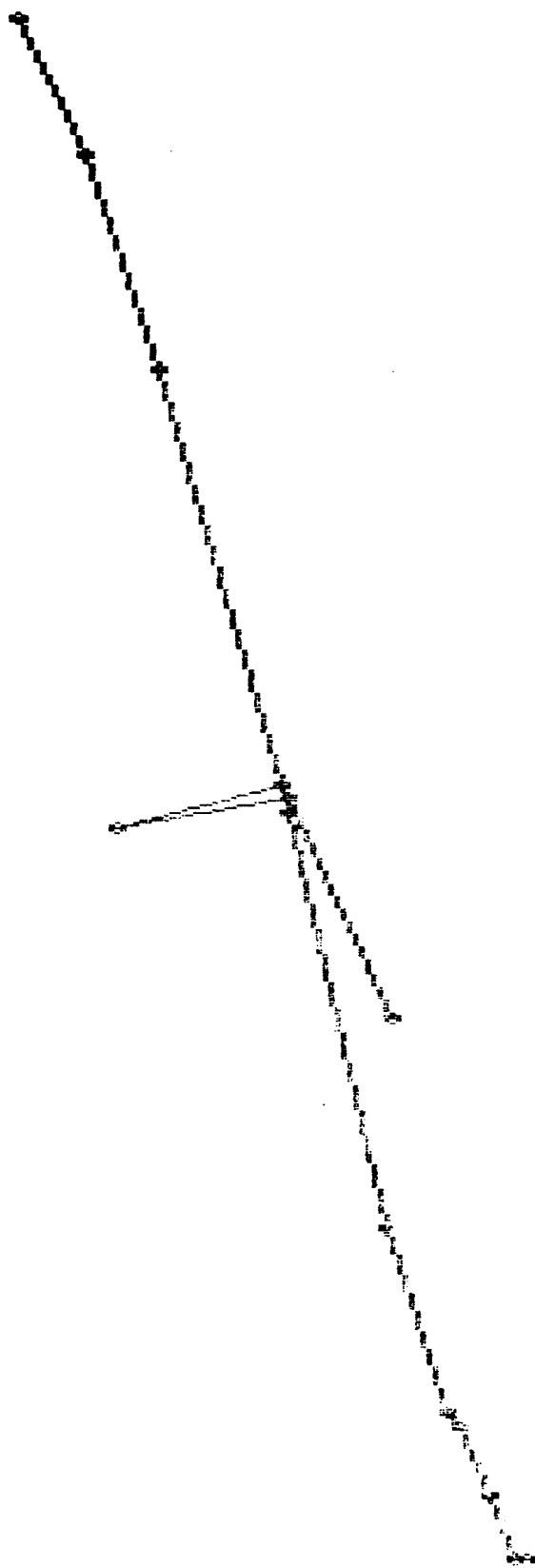


FIGURE 5. RIGHT DEFORMED GEOMETRY Y-Z PLANE VIEW

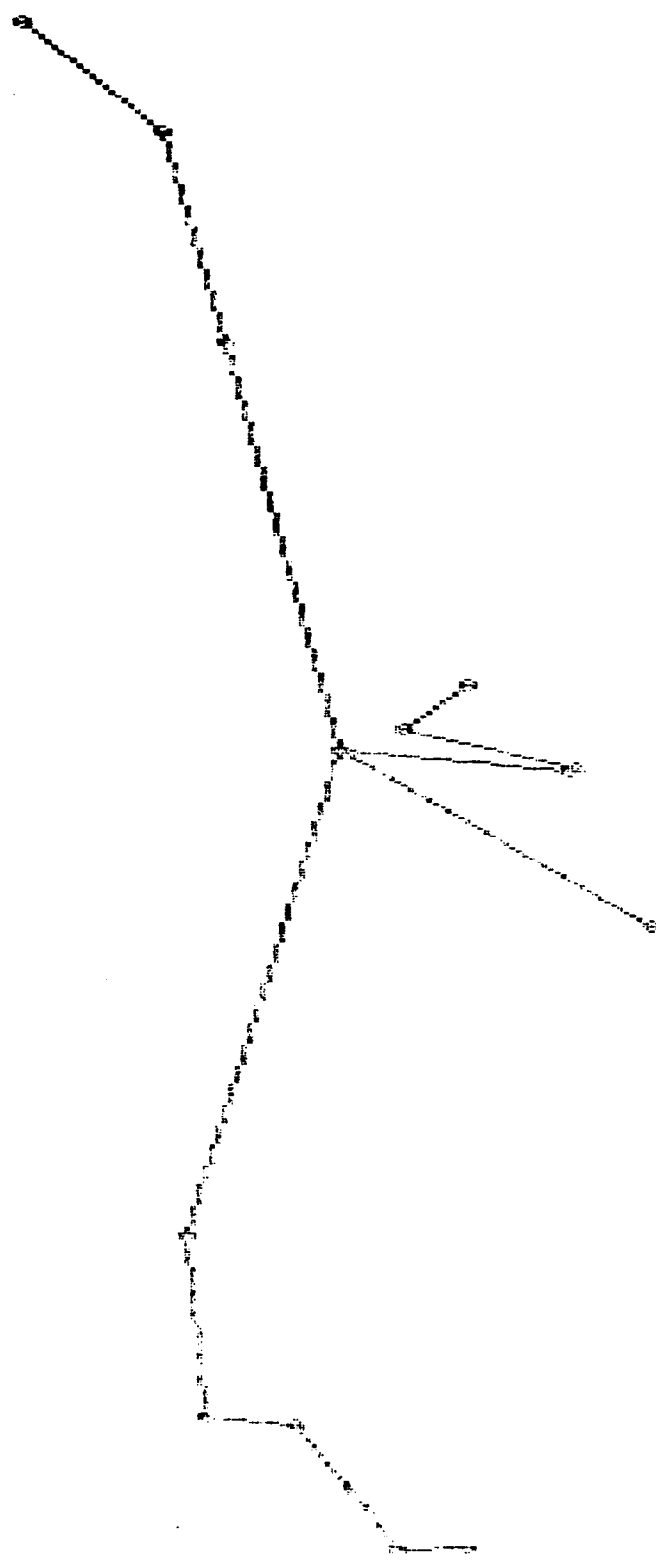


FIGURE 6. MAIN & DEFORMED GEOMETRY: X-Y PLANE VIEW



# TITLE - TRIBOTESTER #2A

## NOD POI LOC

|    |       |       |       |
|----|-------|-------|-------|
| 1  | 1.40  | -10.0 | 0.00  |
| 2  | 0.00  | -8.20 | 0.00  |
| 3  | 0.00  | -5.38 | 0.00  |
| 4  | 0.00  | 0.00  | 0.00  |
| 5  | 0.00  | 0.00  | 2.00  |
| 6  | 0.00  | 0.00  | 2.03  |
| 7  | 0.00  | 0.00  | -0.03 |
| 8  | -3.10 | 3.10  | 0.00  |
| 9  | 3.10  | 5.70  | 0.00  |
| 10 | 3.10  | 8.10  | 0.00  |
| 11 | 2.00  | 8.30  | 0.00  |
| 12 | 1.40  | 9.20  | 0.00  |
| 13 | 0.90  | 10.00 | 0.00  |
| 14 | 0.00  | 10.00 | 0.00  |
| 15 | 0.00  | 0.00  | -0.06 |

MAT 10.0E6 4.3E6 2.6E-4

BEAM TYP 2 0.75 0.75 0.75 0.75

ATTACH AT 1.40 -10.00 0.00 AND 1.40 -8.20 0.00

CONNECT 1 TO 2

BEAM TYP 1 0.69 0.18 0.06 1.13

CONNECT 2 TO 3

ATTACH AT 0.00 -5.38 0.00 AND 0.00 -2.50 0.00

CONNECT 3 TO 4

BEAM TYP 3 5.63 4.50

CONNECT 4 TO 5

BEAM TYP 2 3.00 0.75 1.50 0.75

ATTACH AT -1.95 1.95 0.00 AND -3.10 3.10 0.00

CONNECT 4 TO 8

MAT 3.0E7 0 0.73E-3 0.3

BEAM TYP 2 1.00 0.75 1.00 0.75

ATTACH AT 3.10 2.60 0.00 AND 3.10 5.70 0.00

CONNECT 4 TO 9

CONNECT 9 TO 10

CONNECT 10 TO 11

MATERIAL 9.3E6 0 -2.4E-4 0.25

BEAM TYP 2 1.00 1.00 1.00 1.00

CONNECT 11 TO 12

CONNECT 12 TO 13

BEAM TYP 2 1.00 1.00 0.30 1.00

CONNECT 13 TO 14

MATERIAL 10.0E8 0 1.0E-6 0.3

BEAM TYP 3 5.0 4.75

CONNECT 6 TO 7

STIFF ELE 2.3E5 8.1E5 8.1E5 1.0 2.4E5 2.4E5

CONNECT 5 TO 6

STIFF ELE 4.5E5 3.0E4 3.0E4 5.0E4 5.0E4 5.0E4

CONNECT 7 TO 15

MASS 1 0.0013 0.001 0.001 0.001 -1.0 -10.0 0.00

MASS 2 0.0001 0.0001 0.0001 0.0001

ZERO

ALL OF 15

X TRANS OF 14

ELIMINATE

Z ROT OF ALL

END DEF

- TRIBOTESTER #3A

MODE NO. 1 AT 6.11788E+01 CPS ( 3.84398E+02 RAD/SEC)

| NODE | X TRANS     | Y TRANS     | Z TRANS     | X ROT       | Y ROT       | Z ROT       |
|------|-------------|-------------|-------------|-------------|-------------|-------------|
| 1    | 6.4103E-02  | -4.3237E-02 | 4.2585E-01  | -4.1282E-02 | -2.1863E-02 | 2.4487E-02  |
| 2    | 3.8671E-02  | -4.8189E-02 | 3.1968E-01  | -4.1462E-02 | -2.2347E-02 | 3.7426E-03  |
| 3    | 2.8737E-02  | -4.7904E-02 | 2.0528E-01  | -3.9606E-02 | -2.0063E-02 | 3.3085E-03  |
| 4    | 1.2800E-02  | -4.7572E-02 | -1.6702E-03 | -3.8071E-02 | -1.7310E-02 | 2.8408E-03  |
| 5    | -2.1827E-02 | 2.8607E-02  | -1.6666E-03 | -3.8058E-02 | -1.7305E-02 | 2.8423E-03  |
| 6    | -2.2429E-02 | 3.0311E-02  | -9.7103E-04 | -2.6335E-02 | -1.3542E-02 | 1.6947E-03  |
| 7    | 5.4669E-03  | -2.3936E-02 | -9.7073E-04 | -2.6334E-02 | -1.3542E-02 | 1.6947E-03  |
| 8    | 3.9919E-03  | -5.6381E-02 | -1.7336E-01 | -3.8077E-02 | -1.7311E-02 | 2.8469E-03  |
| 9    | 6.7472E-05  | -3.8776E-02 | -1.6711E-01 | -3.9250E-02 | -1.7577E-02 | 8.0196E-04  |
| 10   | -8.0678E-04 | -3.8785E-02 | -2.6175E-01 | -3.9542E-02 | -1.7782E-02 | 4.9725E-05  |
| 11   | -7.8442E-04 | -3.8733E-02 | -2.8925E-01 | -3.9588E-02 | -1.7830E-02 | -1.4943E-04 |
| 12   | -4.6758E-04 | -3.8544E-02 | -3.3560E-01 | -3.9615E-02 | -1.7855E-02 | -4.8448E-04 |
| 13   | -3.8431E-05 | -3.8293E-02 | -3.7623E-01 | -3.9620E-02 | -1.7865E-02 | -5.4571E-04 |
| 14   | .0000E+00   | -3.7821E-02 | -3.9231E-01 | -3.9623E-02 | -1.7867E-02 | -5.1307E-04 |
| 15   | .0000E+00   | .0000E+00   | .0000E+00   | .0000E+00   | .0000E+00   | .0000E+00   |

MODE NO. 2 AT 1.38834E+02 CPS ( 8.72318E+02 RAD/SEC)

| NODE | X TRANS     | Y TRANS    | Z TRANS     | X ROT       | Y ROT       | Z ROT      |
|------|-------------|------------|-------------|-------------|-------------|------------|
| 1    | 3.0716E-01  | 9.2432E-02 | 3.4017E-01  | -2.7723E-02 | -9.0347E-02 | 1.1513E-02 |
| 2    | 2.7820E-01  | 6.4345E-02 | 1.4668E-01  | -2.7434E-02 | -1.0221E-01 | 1.9946E-02 |
| 3    | 2.2208E-01  | 6.4051E-02 | 7.6454E-02  | -2.1371E-02 | -1.0414E-01 | 1.9752E-02 |
| 4    | 1.1936E-01  | 6.3821E-02 | 7.4668E-03  | -9.2873E-03 | -1.0642E-01 | 1.8824E-02 |
| 5    | -9.3558E-02 | 8.2332E-02 | 7.4408E-03  | -9.2936E-03 | -1.0638E-01 | 1.8827E-02 |
| 6    | -9.8058E-02 | 8.1326E-02 | 2.3270E-03  | -1.7675E-02 | -7.6102E-02 | 2.1640E-03 |
| 7    | 5.8704E-02  | 4.4910E-02 | 2.3257E-03  | -1.7676E-02 | -7.6100E-02 | 2.1640E-03 |
| 8    | 6.1007E-02  | 5.4655E-03 | -3.5131E-01 | -9.3328E-03 | -1.0648E-01 | 1.8821E-02 |
| 9    | 2.6952E-02  | 1.2222E-01 | 2.9304E-01  | -4.6631E-03 | -1.0615E-01 | 1.0001E-02 |
| 10   | 7.8617E-03  | 1.2224E-01 | 2.8303E-01  | -3.9300E-03 | -1.0590E-01 | 6.3675E-03 |
| 11   | 6.7286E-03  | 1.1577E-01 | 1.6579E-01  | -3.8917E-03 | -1.0586E-01 | 5.3968E-03 |
| 12   | 2.6816E-03  | 1.1300E-01 | 9.8784E-02  | -3.8719E-03 | -1.0586E-01 | 3.8471E-03 |
| 13   | -1.4478E-04 | 1.1118E-01 | 4.2756E-02  | -3.8703E-03 | -1.0587E-01 | 3.4250E-03 |
| 14   | .0000E+00   | 1.0810E-01 | -5.2524E-02 | -3.8715E-03 | -1.0587E-01 | 3.4198E-03 |
| 15   | .0000E+00   | .0000E+00  | .0000E+00   | .0000E+00   | .0000E+00   | .0000E+00  |

MODE NO. 3 AT 1.77994E+02 CPS ( 1.11837E+03 RAD/SEC)

| NODE | X TRANS     | Y TRANS     | Z TRANS     | X ROT       | Y ROT       | Z ROT       |
|------|-------------|-------------|-------------|-------------|-------------|-------------|
| 1    | -2.1905E-01 | -1.9514E-01 | 1.4831E-01  | -3.1585E-02 | 1.0942E-02  | -4.0711E-03 |
| 2    | -2.0122E-01 | -1.7394E-01 | 5.8906E-02  | -2.5349E-02 | -2.6197E-02 | -1.4922E-02 |
| 3    | -1.5935E-01 | -1.7351E-01 | 2.5252E-03  | -1.3231E-02 | -3.5420E-02 | -1.4718E-02 |
| 4    | -8.2211E-02 | -1.7300E-01 | 1.1152E-02  | 7.5456E-03  | -4.4907E-02 | -1.4181E-02 |
| 5    | -1.7193E-01 | -1.8791E-01 | 1.1115E-02  | 7.5637E-03  | -4.4909E-02 | -1.4183E-02 |
| 6    | -1.7102E-01 | -1.8451E-01 | 3.6914E-03  | 3.1485E-02  | -5.1298E-02 | 6.3093E-04  |
| 7    | -6.5343E-02 | -1.1964E-01 | 3.6896E-03  | 3.1486E-02  | -5.1298E-02 | 6.3090E-04  |
| 8    | -3.8253E-02 | -1.2904E-01 | -1.0472E-01 | 7.5282E-03  | -4.4945E-02 | -1.4172E-02 |

|    |             |             |            |            |             |             |
|----|-------------|-------------|------------|------------|-------------|-------------|
| 9  | -1.3983E-02 | -2.1709E-01 | 2.0794E-01 | 1.5575E-02 | -4.3663E-02 | -6.6607E-03 |
| 10 | -2.4573E-03 | -2.1715E-01 | 2.4792E-01 | 1.7270E-02 | -4.2670E-02 | -3.2926E-03 |
| 11 | -1.9235E-03 | -2.1405E-01 | 2.0461E-01 | 1.7488E-02 | -4.2446E-02 | -2.3746E-03 |
| 12 | -4.8002E-04 | -2.1306E-01 | 1.9498E-01 | 1.7618E-02 | -4.2348E-02 | -1.0219E-03 |
| 13 | 1.1135E-04  | -2.1265E-01 | 1.8793E-01 | 1.7638E-02 | -4.2313E-02 | -6.2035E-04 |
| 14 | .0000E+00   | -2.1213E-01 | 1.4985E-01 | 1.7640E-02 | -4.2307E-02 | -5.6278E-04 |
| 15 | .0000E+00   | .0000E+00   | .0000E+00  | .0000E+00  | .0000E+00   | .0000E+00   |

MODE NO. 4 AT 1.97501E+02 CPS ( 1.24094E+03 RAD/SEC)

| NODE | X TRANS     | Y TRANS     | Z TRANS     | X ROT       | Y ROT      | Z ROT      |
|------|-------------|-------------|-------------|-------------|------------|------------|
| 1    | 4.1294E-01  | -1.2693E-01 | -1.3521E-01 | -1.0378E-03 | 3.6109E-02 | 4.4766E-02 |
| 2    | 3.4925E-01  | -1.5037E-01 | -8.6821E-02 | 2.9429E-03  | 3.3864E-02 | 2.4106E-02 |
| 3    | 2.8250E-01  | -1.5989E-01 | -7.1157E-02 | 8.5148E-03  | 3.5065E-02 | 2.3134E-02 |
| 4    | 1.6377E-01  | -1.5938E-01 | 2.3019E-03  | 1.5577E-02  | 3.6338E-02 | 2.1641E-02 |
| 5    | 2.3629E-01  | -1.9038E-01 | 2.2966E-03  | 1.5593E-02  | 3.6351E-02 | 2.1643E-02 |
| 6    | 2.3355E-01  | -1.8745E-01 | 1.2411E-03  | 3.6728E-02  | 5.5596E-02 | 2.1365E-04 |
| 7    | 1.1901E-01  | -1.1178E-01 | 1.2407E-03  | 3.6728E-02  | 5.5596E-02 | 2.1367E-04 |
| 8    | 9.6695E-02  | -2.2648E-01 | 1.6333E-01  | 1.5625E-02  | 3.6404E-02 | 2.1637E-02 |
| 9    | 5.2470E-02  | -9.2372E-02 | -1.7636E-02 | 1.7919E-02  | 3.7351E-02 | 1.4670E-02 |
| 10   | 2.0578E-02  | -9.2410E-02 | 2.6564E-02  | 1.8756E-02  | 3.8104E-02 | 1.2315E-02 |
| 11   | 1.8208E-02  | -1.0566E-01 | 7.2366E-02  | 1.8939E-02  | 3.8291E-02 | 1.1736E-02 |
| 12   | 8.2252E-03  | -1.1239E-01 | 1.1248E-01  | 1.9052E-02  | 3.8407E-02 | 1.0649E-02 |
| 13   | -1.1984E-04 | -1.1765E-01 | 1.4695E-01  | 1.9069E-02  | 3.8454E-02 | 1.0381E-02 |
| 14   | .0000E+00   | -1.2700E-01 | 1.8157E-01  | 1.9073E-02  | 3.8462E-02 | 1.0395E-02 |
| 15   | .0000E+00   | .0000E+00   | .0000E+00   | .0000E+00   | .0000E+00  | .0000E+00  |

MODE NO. 5 AT 3.35449E+02 CPS ( 2.10769E+03 RAD/SEC)

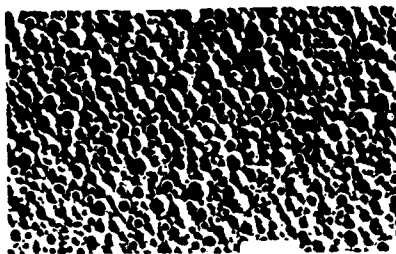
| NODE | X TRANS     | Y TRANS     | Z TRANS     | X ROT       | Y ROT       | Z ROT       |
|------|-------------|-------------|-------------|-------------|-------------|-------------|
| 1    | -2.1503E-03 | -7.1035E-02 | -2.0951E-01 | 7.6494E-02  | -7.3684E-02 | -4.8537E-02 |
| 2    | 4.2064E-02  | -7.0827E-02 | -1.4704E-01 | 6.4477E-02  | -4.8467E-02 | -5.8516E-04 |
| 3    | 4.2281E-02  | -7.1506E-02 | -1.1020E-03 | 3.4664E-02  | -5.3391E-02 | 3.8111E-04  |
| 4    | 3.8912E-02  | -7.2088E-02 | -3.2660E-02 | -2.2330E-02 | -5.9106E-02 | 7.9070E-04  |
| 5    | -7.9357E-02 | -2.7375E-02 | -3.2754E-02 | -2.2322E-02 | -5.9104E-02 | 7.9063E-04  |
| 6    | -5.1277E-02 | -2.5375E-02 | -1.0537E-02 | -9.6629E-03 | -4.5954E-02 | 4.0169E-04  |
| 7    | 1.3385E-02  | -4.5275E-02 | -1.0532E-02 | -9.6622E-03 | -4.5953E-02 | 4.0164E-04  |
| 8    | 3.6748E-02  | -7.4268E-02 | -2.8580E-01 | -2.2587E-02 | -5.9421E-02 | 1.9593E-04  |
| 9    | 2.8866E-02  | -7.0065E-02 | -2.4236E-02 | -4.9753E-02 | -5.8160E-02 | 1.7029E-04  |
| 10   | 1.5251E-02  | -7.0127E-02 | -1.5584E-01 | -5.9154E-02 | -7.5004E-02 | 6.3704E-07  |
| 11   | 1.3929E-02  | -7.7854E-02 | -2.5121E-01 | -5.9820E-02 | -7.6881E-02 | 7.7109E-07  |
| 12   | 6.7754E-03  | -8.2544E-02 | -3.5194E-01 | -6.0952E-02 | -7.7675E-02 | 8.0168E-07  |
| 13   | 7.2709E-03  | -8.6715E-02 | -4.3967E-01 | -6.1020E-02 | -7.8070E-02 | 8.1521E-07  |
| 14   | .0000E+00   | -9.4320E-02 | -5.0998E-01 | -6.1044E-02 | -7.8138E-02 | 8.1597E-07  |
| 15   | .0000E+00   | .0000E+00   | .0000E+00   | .0000E+00   | .0000E+00   | .0000E+00   |

--USE SCREEN PROGRAM TO PLOT--

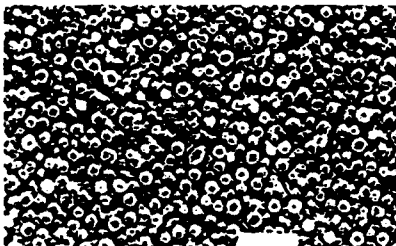
# SRMC3 SERIES DYNAMOMETER SPECIFICATIONS

| SPECIFICATION              | SRMC3-X-100 | SRMC3-X-250 | SRMC3-X-500 | UNIT              |
|----------------------------|-------------|-------------|-------------|-------------------|
| Capacity                   |             |             |             |                   |
| $F_x, F_y, F_z$            | 100         | 250         | 500         | lbf               |
| $M_x, M_y, M_z$            | 100         | 250         | 500         | in-lbf            |
| Sensitivity                |             |             |             |                   |
| $F_x, F_y$                 | 30.00       | 12.00       | 6.00        | <u>microvolts</u> |
| $F_z$                      | 7.50        | 3.00        | 1.50        | volt-lbf          |
| $M_x, M_y$                 | 150.00      | 60.00       | 30.00       | <u>microvolts</u> |
| $M_z$                      | 30.00       | 12.00       | 6.00        | volt-in-lbf       |
| Stiffness (at top surface) |             |             |             |                   |
| $F_x, F_y$                 | 12,000      | 30,000      | 60,000      | lbf/in            |
| $F_z$                      | 170,000     | 450,000     | 900,000     | lbf/in            |
| $M_y$                      | 20,000      | 50,000      | 100,000     | in-lbf/rad        |
| Lowest Resonant Frequency  |             |             |             |                   |
| $M_x, M_y$                 | 300         | 500         | 700         | Hertz             |
| Non-Linearity (Max.)       |             |             |             |                   |
| $F_x, F_y, F_z$            | ----        | .20         | ----        | $\pm$ % FSO       |
| Hysteresis                 |             |             |             |                   |
| $F_x, F_y, F_z$            | ----        | .20         | ----        | % FSO             |
| Excitation, Max.           |             |             |             |                   |
| Recommended                | ----        | 10          | ----        | Volts             |
| Temperature Range          | ----        | 0° to 125°  |             | °F                |
| Weight                     | ----        | 1.7         | ----        | lbm               |
| Working Surface            | ----        | 3x3         | ----        | Inches            |
| Dimensions                 | ----        | 3x3x2.75    | ----        | Inches            |

## Machining a machinable glass-ceramic



1. Droplet-imbedded parent-glass material before heat treatment



2. First intermediate crystal phase seen after heating to 750C



3. Second intermediate crystal phase seen after heating to 825C



4. Beginning of mica-crystal formation seen after heating to 850C



5. Fully crystallized Macor glass-ceramic seen after heating to 950C

### 6. Physical and mechanical properties of Macor

|                                    |                                                    |
|------------------------------------|----------------------------------------------------|
| Density                            | 157 lb/ft <sup>3</sup>                             |
| Porosity                           | 0                                                  |
| Thermal-expansion coeff. (20-800C) | $123 \times 10^{-7} \text{ }^{\circ}\text{C}^{-1}$ |
| Thermal conductivity               | 11.68 BTU-in./ft <sup>2</sup> -hr-°F               |
| Maximum use temperature            | 1000C (1832F)                                      |
| Compressive strength               | 50,000 psi                                         |
| Modulus of rupture                 | 15,000 psi                                         |
| Modulus of elasticity              | $9.3 \times 10^4$ psi                              |
| Shear modulus                      | $3.7 \times 10^4$ psi                              |
| Poisson's ratio                    | 0.26                                               |
| Knoop hardness (100-gm load)       | 250                                                |

is filled with the glass matrix. Macor has zero porosity. The plate-like crystals average 20  $\mu\text{m}$  in both width and breadth.

Some of the physical and mechanical properties of Macor are listed in Fig 6.

#### What makes Macor machinable?

The highly interlocked microstructure is the key to Macor's machinability. During machining, as the tool tears its way through the glass-ceramic stock, the interlocking intersections of the randomly oriented crystals stop the microscopic fractures that, in mass, make up the actual cut from propagating throughout the matrix outside the localized cutting area. The microscopic fractures are repeatedly deflected, branched, and blunted—in effect, turned around and arrested.

Since the fractures are localized, Macor glass-ceramic does not sacrifice strength or hardness for the sake of its machinability.

Macor's machining characteristics can be compared with those of many common metals. It is, however, not a metal, and there are special considerations that should be kept in mind when it is subjected to the bite of a tool.

#### Use coolant generously

In spite of the fact that Macor glass-ceramic is a refractory material, best machining results are obtained when both material and tool are kept cool. Water-soluble coolants, especially those formulated specifically for use in cutting or grinding glass or ceramics, are recommended for that purpose, and several, including Supercut S67 (Supercut Inc, Chicago) and Quaker 103 (Quaker Chemical Corp, Conshohocken, Pa), have been used successfully.

In addition to cooling the workpiece and tool, the fluids improve the cutting action and also trap and wash away the loose powder produced during machining. The Macor stock removed by a tool characteristically comes off in the form of fine chips or powder, composed of both mica crystals and dislodged gran-

ules of matrix glass, that can cause problems if not controlled; however, a generous flow of water-based cutting fluid applied at the cut provides an adequate solution. If the fluid is to be recirculated, use of a settling pot is strongly advised.

The powder generated by machining is somewhat abrasive, but the potential hazard to the machinery can be dealt with by increased equipment maintenance. Cleanliness is important.

If Macor must be machined dry, a useful technique is to drip Freon onto the tool and to use a vacuum system to remove the powder.

During any machining, operators should take care not to breathe in any of the fine powder.

Macor glass-ceramic is not resilient, and so, when small or delicate workpieces are clamped or chucked, the load should be evenly distributed by the use of fixtures like pie jaws. The material should be supported well. Usually, no special precautions are necessary when large workpieces are chucked or clamped.

**Turning.** For most machining operations involving Macor glass-ceramic, the key operating factor is the use of low cutting speeds. In turning, a cutting speed about one-half that used for cast iron is appropriate. The slower spindle speed helps keep the workpiece cool, thus helping prevent the formation of macroscopic surface cracks that could weaken the part. The use of low cutting speeds (such as 30-50 sfm with high-speed-steel tooling) does not mean that overall lathe time is increased excessively, because the allowable depths of cut that can be taken in Macor are greater than those allowed in turning steels. Depths of cut up to 0.250 in. are possible on a 12-in. lathe.

For steels, overall machinability is usually evaluated in terms of tool wear, since this assessment largely establishes production economics. With Macor, tool life is not the overall limiting factor in machining. Instead, surface-finish requirements set constraints on speeds and feedrates. Recommended feedrates are

DO YOU WANT (0) TO RERUN THE PRELOAD CALC'S  
DO YOU WANT (3) TO RUN LOAD TABLES  
OR (4) DO A LOAD CASE .WHAT NEXT: ? 0

DO YOU WANT (1) TO DETERMINE THE PRELOAD ?  
OR IS (2) THE PRELOAD KNOWN ? WHICH ? 2

ENTER PRELOAD (LBS): 18  
THE NORMAL APPROACH (MICRO INCH)= 74.38  
THE PRELOAD AXIAL DEFL.(MICRO INCH)= 234.87  
THE CONTACT ANGLE (DGR) = 18.92  
THE MAX.MEAN STRESS (KSI) = 100.8

DO YOU WANT (0) TO RERUN THE PRELOAD CALC'S  
DO YOU WANT (3) TO RUN LOAD TABLES  
OR (4) DO A LOAD CASE .WHAT NEXT: ? 3

WHAT IS THE MAX. ALLOWABLE STRESS (KSI) : ? 250  
THE PRELOAD STRESS (KSI) = 100.8

\*\*\*\*\* PROGRAM: TRIBO-3 LOAD TABLES:

| TABLE 1 RADIAL STIFFNESS. |               |                           |                            |
|---------------------------|---------------|---------------------------|----------------------------|
| DEFL.<br>(MICRO")         | LOAD<br>(LBS) | STIFFNESS<br>(LBS/MICRO") | MAX. MEAN STRESS<br>(KSI.) |
| 0                         | -0.00         | 1.0017                    | 100.8                      |
| 20                        | 20.00         | 0.9940                    | 123.0                      |
| 40                        | 30.74         | 0.9721                    | 134.0                      |
| 60                        | 50.00         | 0.9285                    | 145.8                      |
| 80                        | 76.82         | 0.8113                    | 156.0                      |
| 100                       | 92.67         | 0.7843                    | 165.5                      |
| 120                       | 100.33        | 0.7920                    | 174.5                      |
| 140                       | 124.38        | 0.8195                    | 183.1                      |
| 160                       | 140.92        | 0.8396                    | 191.3                      |
| 180                       | 157.05        | 0.8711                    | 199.2                      |
| 200                       | 175.61        | 0.9016                    | 206.7                      |
| 220                       | 193.86        | 0.9309                    | 214.0                      |
| 240                       | 212.60        | 0.9593                    | 221.1                      |
| 260                       | 232.00        | 0.9867                    | 228.0                      |
| 280                       | 252.02        | 1.0130                    | 234.6                      |
| 300                       | 272.47        | 1.0376                    | 241.1                      |
| 320                       | 293.41        | 1.0631                    | 247.4                      |
| 340                       | 314.86        | 1.0887                    | 253.5                      |

| TABLE 2 AXIAL STIFFNESS. |               |                           |                            |
|--------------------------|---------------|---------------------------|----------------------------|
| DEFL.<br>(MICRO")        | LOAD<br>(LBS) | STIFFNESS<br>(LBS/MICRO") | MAX. MEAN STRESS<br>(KSI.) |
| 0                        | 0.00          | 0.2426                    | 100.8                      |
| 60                       | 14.54         | 0.2417                    | 123.4                      |
| 120                      | 28.06         | 0.2383                    | 135.8                      |
| 180                      | 43.08         | 0.2302                    | 147.2                      |
| 240                      | 56.21         | 0.1972                    | 158.0                      |
| 300                      | 68.55         | 0.2150                    | 168.2                      |
| 360                      | 82.01         | 0.2345                    | 177.0                      |
| 420                      | 96.60         | 0.2533                    | 187.1                      |
| 480                      | 112.32        | 0.2724                    | 196.1                      |
| 540                      | 129.20        | 0.2917                    | 204.7                      |
| 600                      | 147.24        | 0.3113                    | 213.1                      |
| 660                      | 166.46        | 0.3312                    | 221.2                      |
| 720                      | 186.88        | 0.3513                    | 229.2                      |

## **APPENDIX I**

**R. Williams, "Thermal Analysis of the Tribotester Test Fixture," Hughes  
Interdepartmental Correspondence No. 7735.10/234, 09 September 1986**

**INTERDEPARTMENTAL CORRESPONDENCE****HUGHES**

TO: Mike Gardos  
ORG: 76-21

CC: L. Fiderer  
S. Gassel  
J. Hulstyn  
S. Russo  
I. Shuldiner

SUBJECT: THERMAL ANALYSIS OF THE TRIBOTESTER  
TEST FIXTURE

DATE: 9/9/86  
REF: 7735.10/234

FROM: Rick Williams *AK*  
ORG: 77-35-12

BLDG. E55  
LOC. EO

MAIL STA. G232  
PHONE 77472

---

**INTRODUCTION**

A steady state thermal analysis utilizing a CINDA model, was performed on the Tribotester Test Fixture to determine:

1. The heat input required to raise the temperature of a ceramic test specimen from room temperature to 1500°F at a specific location on the ceramic rod.
2. The steady state temperatures throughout the test fixture.

Determining the amount of heat required would address two concerns: concept feasibility and the number of quartz heating elements required. That is, can the ceramic rod be heated sufficiently to achieve the 1500°F and is the use of one quartz heater to accomplish this, versus the two initially proposed, adequate. If only one quartz heater is required this would greatly effect the tribotesters thermal design (simpler and less costly).

Determining the steady state temperatures throughout the test fixture would yield insight into:

- The change in temperature (Delta T) across the spindle bearings (upper & lower) with a large Delta T possibly having a deleterious effect on bearing performance.
- The existence of any "hot spots" which could pose safety and/or fixture performance problems.

A transient analysis was also performed to determine the circumferential temperature changes which might occur along the periphery of the rod during system operation (i.e. rod rotating).

The analyses showed that:

1. The concept is feasible, that is, the ceramic rod could be heated to the required 1500°F.
2. The heat required (approximately 150 watts) can be supplied by one quartz heater (rated @ 254 watts/linear inch), versus the two originally thought to be required.
3. The heat supplied via the quartz heater is augmented by the frictional heat generated during system operation.



4. The Delta T's across the upper and lower bearings are negligible. However, the actual bearing housings outside surface is well over 200<sup>0</sup>F.
5. The inclusion of a macor insert between the rod specimen and the spindle decreases the amount of heat transferred to the spindle from the rod. As a result, the rods temperature increases and that of the spindle assembly decreases, compared to the case without the macor insert.
6. The stationary pad mounts warm up to approximately 240<sup>0</sup>F while the pressure bar assemblies and load cell mounts reach 150<sup>0</sup>F.
7. The radial temperature gradients within the rod specimen are negligible.
8. The transient analysis revealed that the circumferential temperature variations are negligible, relative to the order of magnitude of the temperatures being considered at the contact area. These variations were actually less than the percent accuracy of the sensor. Hence, only one temperature sensor (pyrometer) is required for monitoring.

#### Test Fixture

The tribotester test fixture analyzed was as depicted in Figures I and II. Also, shown in these figures is the nodal layout. Drawings, materials, dimensions, heater configuration/specifications and other pertinent information was supplied by Leo Fiderer, the task REA.

In the actual test fixture the ceramic rod specimen will be rotated at over 3000 rpm. Two quartz lamps would supply the radiant energy for heating along a .75 inch length of the rod- at essentially midspan. These lamps have a "delivered" power rating of 254 watts/linear inch each. Contacting the rod at the same axial location as the incident energy but at different circumferential positions are the two stationary rod specimens. These stationary pads are fixed on two macor mounts to help minimize heat being conducted from the pads through the pressure bars to other components of the test fixture. Infrared pyrometers were to be positioned at this axial location but once

again at different circumferential positions. These pyrometers would provide input for any temperature controls.

The upper portion of the rod (above the spindle/collet assembly, the stationary pads/mounts and the quartz heaters) will have a cover placed over it. This cover would help minimize heat losses (essentially creating an ovenlike enclosure). It would also function as a safety shield in preventing operator exposure to "hot" spots and dust possibly generated during the test.

The rod specimen would be held by a collet which is connected to the spindle assembly. In an effort to reduce the amount of heat being conducted from the assembly, macor inserts were installed. It was thought that these inserts would perform two important functions:

1. Lower the amount of heat input required by reducing losses via conduction
2. Insulate the spindle bearing from the possible ill effects of too high a temperature gradient across them.

#### Assumptions

1. The thermal properties of the various materials used were considered constant over the operating temperature range.
2. Radiant exchange occurred only between a component and the ambient air. Any exchange amongst the various components was neglected.
3. One dimensional heat flow in the ceramic rod specimen
4. Contact conductances at various interfaces were based on minimum and maximum values of 100 and 1000 BTU/Hr-FT<sup>2</sup>-°F respectively when no other information/data was available.
5. Heat inputs from the quartz lamps can be expressed as impressed heat on the two nodes representing the portion of the rod which "sees" the lamps.
6. The quartz lamps delivered their full rated power (254 watts/linear inch each) to the specified length of rod (.75 inches)

7. Heat inputs due to the friction between the stationary pads and the rotating rod were based on a normal force of 10 lbs each, a kinetic coefficient of friction ( $\mu_k$ ) of .40 and an angular speed of 3000 rpm.
8. Frictional heat can be represented as impressed heat augmenting the heat supplied by the quartz lamps.
9. Convective heat transfer coefficients were based on free convection as a result of computations made using typical operating parameters.
10. The emissivity of the ceramic rod specimen was held constant at .85.
11. Radiant interchange factors between the rod, pad holders and enclosure air, as well as that between the various other components and ambient (outside) air were considered to be unity (1).
12. The cylindrical elements used for clamping the rod (collet and ceramic inserts) were considered as continuous parts not split.
13. The initial temperature of the test fixture components was 80°F.
14. Any dimensional instabilities caused by dissimilar thermal expansion of the components was not considered.

#### Thermal Models

The CINDA thermal analyzer computer program was utilized in the development of the steady state thermal model. The final model consists of 43 nodes and 85 connectors.

Initially computer runs were made based on the actual energy supplied by the quartz lamps. Each had a power rating of 254 watts/linear inch which translated to a total of approximately 380 watts delivered to the rod specimen. Then computer runs were made which included the power augmentation supplied by the frictional heating occurring at the rotating rod/stationary pad

interfaces. A value of approximately 50 watts total was computed as a representative value. During both of these sets of runs the spindle bearing housing was considered as a boundary condition being held at a constant temperature of 80°F. Also, the insert placed between the collet and spindle was fabricated from aluminum oxide as recommended by the manufacturer.

The refined steady state thermal model and subsequent runs differed from the aforementioned in several significant respects:

1. A macor insert was placed between the collet and spindle versus the aluminum oxide.
2. Modification of the conductive/convective heat transfer paths through the spindle, bearing housing and the rest of the lower assembly components to reflect possible design changes (influenced by the initial analysis).
3. The bearing housing was free to exchange heat with the surrounding air versus being held at a constant 80°F.
4. Instead of specifying the amount of heat impressed on specific nodes with the program computing resultant temperatures, the temperatures of these nodes were fixed at certain values. The program then computed the heat required to achieve these temperatures as well as the steady state temperatures at the various other nodes. The areas represented by these fixed temperature nodes, along with the temperature values are:
  - Section of rod being heated - 1500°F
  - Stationary pads - 1500°F
  - Ambient air - 80°F
  - Enclosure air - 150°F

The concern about any possible circumferential temperature differences from the rod/pad interface to the point at which the rods surface temperature is monitored (by an optical pyrometer) prompted formulation of a simple transient analysis. This analysis was performed utilizing transient "short-time" charts available in the heat transfer literature (Heisler Charts). For this analysis the following assumptions were made:

1. The rod specimen was silicon nitride with a constant thermal conductivity.
2. Surrounding air temperature was held at 100°F
3. An "effective" heat transfer coefficient combining convective and radiative effects can be computed.
4. The node representing the section of the rod being heated can be considered as a "lumped thermal mass".
5. The surface temperature of this cylindrical "lumped thermal mass" was initially 1500°F.
6. The angular speed of the rod was 3000 rpm.
7. The solution to the transient behavior of a heated cylinder of finite length (our "lumped thermal mass") can be represented as the product of the solutions of the infinite cylinder and an infinite plate - both of which have existing graphs.

#### Results

The initial analysis showed:

1. The incident energy supplied by the two quartz lamps raised the temperature of the desired section of rod well above the required 1500°F (~ 2200°F).
2. The heat augmentation supplied via friction had a significant influence on the temperature of the pertinent section of the rod (~ 2400°F).
3. The change in temperature across the upper spindle bearings could have a deleterious effect on bearing performance (~ 108°F @ heat augmented condition).

4. The macor stationary pad mounts reached an average temperature of approximately  $220^{\circ}\text{F}$  while the pressure bar and load cell assemblies reached  $136^{\circ}\text{F}$  - both of these occurring for the heat augmented case.
5. The aluminum oxide insert between the collet and spindle is an inadequate thermal insulator.

As a consequence of these findings the model was modified as mentioned previously with the following results:

1. To achieve the required  $1500^{\circ}\text{F}$  for both the rod and pads at the rod/pad interface, approximately 150 watts of power must be delivered to the rod. Since each quartz lamp supplies 191 watts, one lamp even at an efficiency of approximately .8 should be sufficient to meet the requirements. The adequacy of one lamp becomes even more evident when frictional heat augmentation is considered (50 watts).
2. The inclusion of a macor vs. an aluminum oxide insert between the collet and spindle significantly reduces the temperature at the upper spindle bearing housing and collet. This temperature reduction was typically on the order of  $70^{\circ}\text{F}$ . An additional advantage of having this macor insert is that the increased resistance to heat flow reduces the heat losses via conduction from the rod hence reducing power required to raise its temperature.
3. The Delta T across the upper and lower spindle bearing is minimal ( $1 \rightarrow 8^{\circ}\text{F}$ ).
4. The macor stationary pad mounts reached an average temperature of  $240^{\circ}\text{F}$  while the pressure bar and load cell assemblies reached an average temperature of  $150^{\circ}\text{F}$ .

It should be noted that while the Delta T's across the spindle bearing have been greatly reduced in the modified model - primarily as a result of including the effects of convective and radiative heat transfer between the hot spindle bearing housing

and ambient air (i.e. allowing the housing to get warmer) versus keeping the housing at 80°F - the maximum temperatures of the housing surface and the collet reach 200°F and 249°F respectively. One might consider active cooling via forced convection - blowing ambient air across the collet to reduce its temperature as well as the heat transferred to the spindle bearing housing - if either of these temperatures is considered unacceptable (safety or bearing performance considerations). The transient analysis showed that when a point on the surface of the rod, initially at 1500°F, is subjected to representative heat losses (via convection and radiation) in the time required to complete one revolution - completely disregarding frictional heating- the temperature decreases by 6°F. This represents a .4% change from the original 1500°F and is actually well below the percent accuracy of typical optical pyrometers. Hence, for monitoring temperatures on the surface of the rod during testing only one temperature sensing device is required.

Concurrence:



Irv. Shuldiner  
Thermal Analysis Section  
Thermo Mechanical Sciences Dept.

### Material Properties

| <u>Material</u> | <u>Conductivity</u> ( <sup>BTU</sup> /Hr-Ft-°F) |
|-----------------|-------------------------------------------------|
| Silicon Nitride | 16.5                                            |
| Macor           | .973                                            |
| Stainless Steel | 9.4                                             |
| Aluminum Oxide  | 4.6                                             |

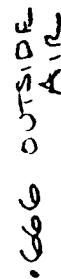


Table I: Node Temperatures ( $^{\circ}\text{F}$ )

| NODE                              | *LOW<br>G | HIGH | LOW G | NO MACOR |
|-----------------------------------|-----------|------|-------|----------|
| 10                                | 736       | 736  |       | 788      |
| 20                                | 787       | 788  |       | 788      |
| 30                                | 913       | 913  |       | 913      |
| 40                                | 1133      | 1133 |       | 1133     |
| 70                                | 1312      | 1248 |       | 1164     |
| 80                                | 1124      | 996  |       | 829      |
| 90                                | 936       | 745  |       | 494      |
| 100                               | 936       | 745  |       | 494      |
| 909                               | 490       | 367  |       | -        |
| 910                               | 269       | 332  |       | 402      |
| 920                               | 211       | 254  |       | 306      |
| 940                               | 230       | 280  |       | 358      |
| 950                               | 197       | 346  |       | 283      |
| 960                               | 200       | 239  |       | 293      |
| 970                               | 192       | 229  |       | 276      |
| 980                               | 193       | 230  |       | 280      |
| 990                               | 186       | 221  |       | 265      |
| 810                               | 173       | 202  |       | 242      |
| 811                               | 171       | 200  |       | 237      |
| 812                               | 172       | 201  |       | 238      |
| 813                               | 135       | 152  |       | 174      |
| 814                               | 132       | 147  |       | 167      |
| 815                               | 132       | 147  |       | 167      |
| 816                               | 98        | 103  |       | 110      |
| 817                               | 115       | 126  |       | 139      |
| 818                               | 104       | 111  |       | 120      |
| 819                               | 100       | 108  |       | 112      |
| 820                               | 102       | 109  |       | 117      |
| 821                               | 107       | 115  |       | 124      |
| 822                               | 101       | 107  |       | 114      |
| 32                                | 242       | 242  |       | 242      |
| 33                                | 150       | 150  |       | 150      |
| 34                                | 150       | 150  |       | 150      |
| 42                                | 241       | 242  |       | 242      |
| 43                                | 150       | 150  |       | 150      |
| 44                                | 150       | 150  |       | 150      |
| Boundary Conditions Held Constant |           |      |       |          |
| 50                                | 1500      |      |       |          |
| 60                                | 1500      |      |       |          |
| 31                                | 1500      |      |       |          |
| 41                                | 1500      |      |       |          |
| 555                               | 150       |      |       |          |
| 666                               | 80        |      |       |          |

\* "Low G" denotes computations made with the lower interface conductance values while "high G" are those made at the higher values.





# TRIBOTESTER SPINDLE ASSEMBLY

## APPENDIX J

B.L. Soriano, "Room Temperature Friction and Wear Testing for Bare Ceramic Contacts," Hughes Interdepartmental Correspondence No. 7621.12/121.87, 02 November 1987

# INTERDEPARTMENTAL CORRESPONDENCE



TO M.N. Gardos  
ORG 76/21.01

C

DATE 11/02/87  
REF 7621.12/121.87

SUBJECT: Room Temperature Friction and Wear Testing  
For Bare Ceramic Contacts

FROM: B.L. Soriano  
ORG: 76/21.12

BLDG E1 MAIL STA F150  
LOC PHONE 70692

## Abstract

A unique apparatus has been developed to evaluate ceramic on ceramic sliding contact configurations in both bare and solid lubricated modes. This tester, designed as "Tester 2A", evaluates the friction and wear characteristics of various high temperature ceramic material combinations in a range of load, sliding speed, and temperature conditions in both line and area contact geometries. To date, friction and wear data has been generated with Tester 2A on one of the four material combinations under consideration, Electro-schmelzwerk-Kempton Ekasic  $\alpha$ SiC sintered + post HIP-ed (ESK post HIP-ed). Initial tests were performed at room temperature using a flat rubshoe/cylinder contact geometry (i.e., line contact); each test was performed using a unique set of load and speed conditions. Complete steady state coefficient of friction traces for each of the two tests were calculated, as well as traces for the combined rod/rubshoe wear. Also, the effect of variations in the applied normal load and sliding speed on the coefficient of friction and wear was investigated. In addition, comparison of maximum runout levels with the dynamic variations in the normal load, tangential load and the coefficient of friction were made. Theoretical Hertzian stress analysis was performed the four different material combinations to calculate the initial stress levels, prior to wear scar formation (prior to dynamic operation).

## Foreword

This report is the first in a series of papers reporting the friction and wear behavior of solid lubricated or bare unlubricated ceramic-ceramic interfaces.

This series will relate the progress of ceramic materials evaluated on Tester 2A in support of the DARPA program entitled "Determination of Tribological Fundamentals". The topics addressed will include experimental equipment, test procedures and results for tests performed both at room temperature and 850°C. This paper will report specifically on an experimental test procedure developed for room temperature testing and the initial friction and wear results for one of the four baseline material combinations chosen for this investigation.

## 1.0 INTRODUCTION

The friction and wear behavior of ceramic tribocontacts between bare surfaces is of fundamental importance in establishing baseline values for the material combinations chosen for evaluation. A "worst case" baseline will provide a relative scale in which to evaluate the contribution of surface treatments to minimize friction and wear. The surface conditions may be altered by the formation of glassy oxide layers or the application of solid lubricants. The four baseline materials are shown in table 1. These materials will be evaluated at the lowest normal load and sliding speed values which are practical for this tester. Tests will be conducted at room temperature and up to 850°C with the rods and rubshoes pretreated under a matrix of different heat treatments. Preheat treatments will include baking the rod and rubshoes at a variety of time durations at 850°C to produce oxide layers of varied thicknesses. Theoretical contact stresses were calculated for the four materials in the initial Hertzian contact condition which predicts the state of stress before the formation of a wear scar. Experimental friction and wear behavior for the Elektroschmelzwerk-Kempton Ekasic sintered + post HIP-ed  $\alpha$ -SiC will be presented in addition to an established room temperature test procedure. The data recording, sampling rates and logging will be discussed briefly.

## 2.0 STRESS ANALYSIS

The maximum contact stress and contact width resulting from line contact between a cylindrical RCF rod and a planar rubshoe, both made of an

isotropically elastic material, can be determined by the application of the elastic contact solution (Hertz contact problem) (1). This solution yields values for the maximum contact stress ( $q_0$ ) at the center of the line contact ( $L$ ) in addition to the half contact width ( $b$ ). Each of these solutions are a function of the following variables:

1. Contact length ( $L$ )
2. Cylinder radius ( $R$ )
3. Applied load ( $P$ )
4. Material properties
  - a. Poisson's ratio
  - b. Modulus

This solution predicts the stress levels prior to dynamic operation (wear scar formation). Hertzian stress calculations were performed for those material combinations listed in table 1. The calculations for both the ESK HIP-ed and post HIP-ed materials were combined since the vendor supplied mechanical properties did not differentiate between the two. Since the rubshoes can be tested in two different orientations, the calculations were performed using two contact lengths (0.375 in, 0.297 in). Maximum stress levels as a function of applied load were calculated for the load range of interest for this investigation. These figures, in addition to sample calculations, material properties and rubshoe orientations are contained in Appendix I.

### 3.0 TESTING

This section outlines the general procedures for surface characterization, sample preparation, test hardware set-up, testing conditions and testing procedures. Also, the data recording and sampling rates will be outlined as they pertain to the reliability and resolution of the recorded data.

#### 3.1 Surface Characterization

Investigation of the available literature has shown that under pure sliding, the peak stresses occur primarily on the surface of the contact faces (2). Surface roughness, and SEM photomicrography analysis were performed on the flat rubshoes and surface analysis and runout measurements were

performed on the RCF rods to carefully characterize the pretest surface conditions. Each rubshoe was measured both in the direction of contact and in the direction of sliding. The surface finish of the rod was measured circumferentially at one-half inch from each end and also longitudinally, using a trace length of approximately two and one-half inches. SEM Photomicrographs of one of the rubshoes were taken in addition to EDAX analysis. The ESK post HIP-ed  $\alpha$ -SiC was sufficiently conductive for SEM imaging without a conductive coating which would alter the frictional behavior of the surface.

### 3.2 Sample Preparation And Test Set-Up

Prior to testing, both the rod and the rubshoes were ultrasonically cleaned in a mixture of isopropyl alcohol and trichlorotrifluoroethylene (Freon TF) and vapor degreased in Freon TF to remove any oils or polishing residues. After cleaning, the rod was inserted into the stainless steel collet and the height adjusted to guarantee four test positions per rod. Because these tests were performed at room temperature, the ceramic collet, designed to act as a thermal barrier between the heated rod and the spindle bearings, was not necessary. The two rubshoes were then inserted into the stainless steel holders and the "J" type thermocouples (T.C.) carefully inserted into the T.C. holes drilled in the back face of each rubshoe. Although the rubshoes were designed to be installed in a primary orientation (see Figure II, Appendix I), they were rotated 90 degrees which resulted in a longer contact length. The longer contact length reduced the lowest available stress levels for this tester.

The next two set-up procedures were, and will continue to be, critical to the relative success of each test and therefore, merit full explanation here.

These two procedures are as follows:

1. Mitigation of the combined runout of the rod and collet.
2. Alignment of the rubshoe contact area with respect to the rod.



Since this tester is equipped to measure the change in position of the rubshoes as they are loaded against the rod, it is ideally suited to measure the in-situ runout of the rod/collet combination. The total runout is a function of the combined alignment of the rod and the spindle and also the roundness of the rod. Mitigation of the runout was achieved by replacing the collet and then rotating the rod with respect to the collet. This tended to decrease the additive runout by cancelling the misalignments for the individual components. Since the runout values were larger than the anticipated wear values, this information was necessary to establish the true wear rates in comparison to the observed wear rates. Also, analysis has shown that large runout values contribute to dynamic loading, a test variable which is difficult to quantify (3). The significance of this information lies in predicting the magnitude of the shaft-runout induced cyclic loading of the rod (shaft)/runout interface. These superimposed dynamic loads are small for low speed and runout conditions, but are significant at higher speeds and can only be accounted for by actual measurements of dynamic runout. It is strongly recommended that a runout trace be made prior to and also after completion of each test since the magnitude of the runout will vary from test to test.

Alignment of the rubshoes with respect to the RCF rod is essential to ensure complete contact along the entire contact line. Alignment or misalignment was established by using the quartz heat lamp at a low intensity and visually determining if light could be seen along the contact length. By adjusting the angle of the rubshoe holder with respect to the horizontal, the alignment was refined until no light could be seen. The rod was then rotated by hand to ensure proper alignment for full rotation. This process was then repeated for the second rubshoe. Care was taken to minimize misalignments resulting from complete tightening of each rubshoe holder. Although this method insures mating along the contact length, it does not insure an even distribution of stress. The effect of uneven stress distribution was evident in the varying wear scar depths observed along the contact length upon test completion (see figures 9-12). Note that this method is only applicable for the rubshoes with a planar contact surface. When testing begins with the spherical and convex/concave rubshoes, this method will require modification to provide alignment of the more complex surfaces.

### 3.3 Data Recording

The quality, reliability and resolution of the data was dependent on the measurement techniques and sampling rates. Data recording and logging was performed by an open loop analog to digital computer system described in (4). The sampling rates for this measurement system were limited by the constraints of the real time display software. Because of these constraints, the critical measurements, load, wear and rod and rubshoe temperatures, were sampled more frequently than the secondary monitors, heater and bearing temperatures and power sources. The sampling rates for each measurement device are shown in table 2. In future tests, these sampling rates will be adjusted as the critical measurements are defined through experimentation. When testing at room temperature, the temperature values did not increase enough to merit faster sampling rates, but when testing at higher temperatures, the temperature values will be measured more frequently.

The resolution of each measurement device is a function of its full scale output and the resolution of the analog to digital (DAC) board (12 bit resolution). The individual resolution values were calculated by dividing the full scale input of the DAC ( $\pm 5$  V) by the total number of digital levels which are generated by the DAC:  $2^{12}-1$  for a twelve bit board. This value is the smallest voltage unit which can be distinguished by the computer. Multiplication of this basic voltage unit by the output conversion for the sensors, (lbs per volt for the load cells or inch per volt for the proximeters), yields the following resolution values:

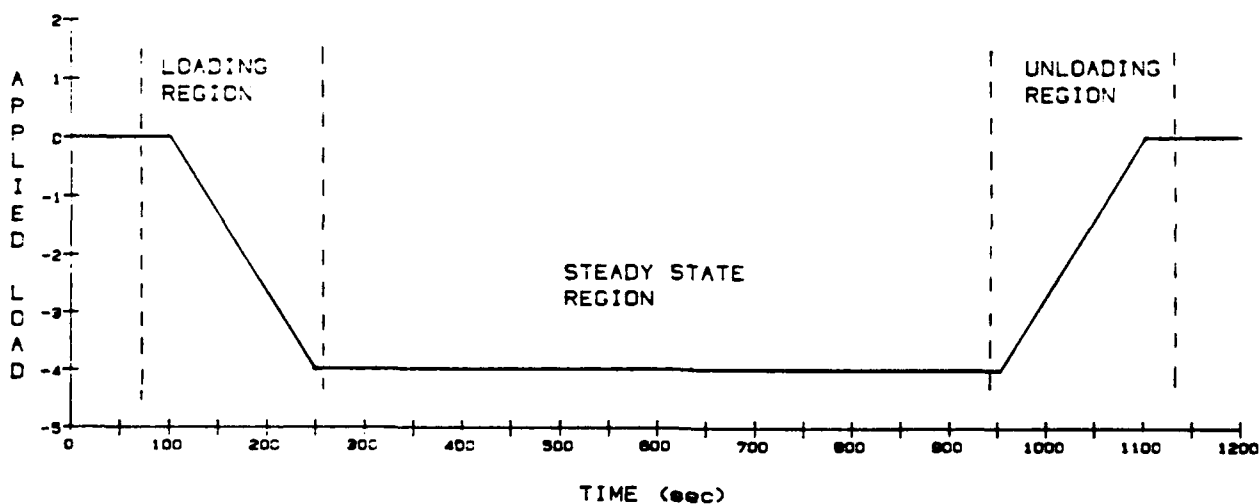
Proximeters....2.54  $\mu$ m = 0.0001 in  
Load Cells.....0.35 N = 0.079 lbs.

### 3.4 Experimental Apparatus and Techniques

Friction and wear measurements were performed using Tester 2A, a continuum mechanical sliding contact tester which is capable of a rotational speed range of 500-4600 rpms, steady state load to 200 N (45 lbs) and heating the test rod to an upper limit of 850°C. The specific details of this tester are described elsewhere (2).

The room temperature test procedure consisted of applying a pre-determined steady state spring load and then removing the spring load with the linear actuators, while still maintaining contact between the rod and rubshoes. This ensures that there was no impact loading upon start-up: use of the actuators to reapply the load allows a ramp loading of the rubshoes against the rod. The rod was then rotated at a fraction of the steady state speed while the steady state load was reapplied by decreasing the offsetting actuator load component. The actuator voltage source and power supply were then turned off. The actuator drive system, because of the switching amplifier, was a varified electronic noise source. Therefore, the quality of the recorded data was more reliable with this system disengaged. Since the test plan called for a constant applied load, the actuators were not necessary during the steady-state portion. Upon disengaging the actuators, the rotational speed was then increased to a pre-determined steady state value and maintained for a 20 minute test duration. At test completion, the actuators were reengaged to provide ramp unloading, the rod was unloaded and the rotation was stopped.

LOAD PROFILE  
FIGURE 1



LOAD SIGN INDICATES RADIAL DIRECTION  
(-) COMPRESSION, (+) TENSION

Figure 1 graphically represents the load profile as a function of time.

For the work reported here, the first set of test conditions consisted of a steady state load of 13.3 N (3.0 lbs) with a rotational speed of 1000 RPM. The second test was operated with a steady state load of 10.0 N (2.5 lbs) and a rotational speed of 700 rpms. Throughout the duration of the test, the spindle and test region were purged with a slow flow rate of dry, filtered air. In both tests, the test duration was 20 minutes at steady state. Initial loading and motor actuation required approximately 200 seconds. Upon test completion, the rubshoes were removed, photomicrographs were taken and profilometer traces were made to determine the wear scar dimensions and surface roughness within the scar depth.

#### 4.0 RESULTS AND DISCUSSION

The objectives of the individual experiments were multifold:

1. The first objective was to perform a general check-out of the test hardware and the recording system. Although a large number of shake-down tests had been performed, none had been performed with this type of "worst case" unlubricated ceramic on ceramic contact condition.
2. The second objective was to establish a practical and repeatable test procedure and to experimentally define the low end speed and load limits.
3. The third objective was to investigate the friction and wear behavior of one of the four material combinations: ESK post HIP-ed  $\Delta$ Sic.

Because we did not have prior practical test experience with these "worst case" conditions, the goal of the first two experiments was to experimentally determine the load and speed conditions which coincided with the objectives of this investigation and, more importantly, were in line with the practical low end limitations of this tester. The test parameters are outlined in table 2. After thorough analysis of the test data and the behavior of the tester, specifically the loading system, a combination of the two test conditions have been chosen to complete this baseline study.

Experimental assessment of the Tester 2A operation and dynamic behavior indicate the following:

1. The lowest speed that the motor will operate and maintain is 700 RPM  $\pm 5$  (1.14 ft/sec, 0.346 m/sec).
2. The spring tensioning rod must have lock nuts on the inner surface and the outer surface to prevent against tension relaxation during the test. Care must be taken when adjusting the spring load to prevent spring rotation. The spring rotation increases the initial load but allows load relaxation as the spring rotates back to its equilibrium position as a result of vibration.
3. Runout values should be kept below 2/10,000 of an inch. For the best results, runout should be theoretically zero. If the runout values are on the order of the combined wear, then the measured wear rates are meaningless.
4. The lowest maintainable steady-state spring load is 13.3 N (3.0 lbs). Because the loading system was designed for much higher loads (maximum of 200 N), spring loads lower than 13.3N are highly susceptible to load variations resulting from spring rotations.
5. Operation of Tester 2A requires two operators. One must handle and monitor the recording system while the other manually controls the motor, actuators, and heater. Since many different measurements are being performed simultaneously, it is the responsibility of both operators to continuously monitor the recording system and the test hardware to insure that each component is working correctly.

#### 4.1 Test Results

The data generated in each of the two experiments consisted of a pre-test runout trace, and compilation of the applied loads, frictional loads, coefficient of friction and the observed wear. The surface temperature of the shaft and the bulk temperatures of the rubshoes were recorded but are not included since at room temperature, the values did not increase significantly (5°C maximum). Upon completion of each test, photomicrographs were taken of the contact surface and surface profile measurements of the wear scar were made at three locations to determine the final depth of wear.

##### 4.1.1 Runout

Figures 2 & 5 represent the runout profile of each rod prior to testing for test one and two respectively. Note that the absolute value of the amplitude of the runout trace was much larger in the first experiment ( $\approx 0.0007$ in.), compared to that of the second test ( $\approx 0.0002$ in.). Initially

we attempted to use the Macor ceramic collet in order to test with fairly equal runout values at both room and high temperatures. We found that the lowest attainable runout values using the ceramic collet was approximately 0.0007 in. which was not acceptable. The effect of this high runout was evident in the dynamic behavior of the normal applied load.

#### 4.1.2 Applied Load and Coefficient of Friction (COF)

Figures 3, 6 and 7 are a compilation of the normal (applied) loads, the frictional loads and the calculated coefficients of friction for the first test, arm 1, and second test, arms 1 and 2, respectively. Although Tester 2A operates with two loading arms, an electrical malfunction in the recording system in arm #2 resulted in erroneous readings in the frictional load values in the first experiment. The malfunction was isolated and corrected prior to the second test. The ratio of the frictional load (FX) divided by the normal applied load (FY) is the calculated coefficient of friction (COF). Note that only the steady state region of each test was plotted since the values fluctuate widely in the loading and unloading regions.

For analysis, each of the load curves were broken down into two components: the mean level and the superimposed oscillatory value. Preliminary observation indicates that the mean level is a function of the frictional behavior of the contacting materials. The oscillatory component is a function of the frictional behavior combined with speed and runout dependent variables.

Observe that the mean value of the coefficient of friction is constant (0.5) for the two different experiments, while the peak amplitude of the alternating component is different. The amplitude of the alternating portion measured in the first test, which had larger shaft runout and was tested at a higher speed, was much larger than that of the second test. But the magnitude of the alternating portion of the frictional load for each test was approximately equal. The most interesting observation is that the range of COF values in each test was notably much smaller than that of the frictional force. This result substantiates the conclusion that the alternating components of the applied load and the frictional force are in phase to some degree. Because these dynamic effects were not observed in prior shake-down tests using much softer and higher

wearing materials. initial analysis concludes that they are not a result of dynamic resonance effects but of a combination of material characteristics and large shaft runout values.

#### 4.1.3 Combined Wear

The effects of runout can also be seen in the wear curves. The wear traces were plotted for each load arm in figures 4 and 8 for the first and second test respectively. The variation in the wear curves are in the range of the displacement resulting from shaft runout. An apparent wear rate can be observed from the graph. However, because the magnitude of the shaft runout was so large (compared to the true wear scar depth), these curves can be misleading. When wear depths are small, as they were in these tests, the true wear scar depth can only be determined by a profilometer trace upon test completion. Also for these specific load, speed and material conditions, the wear scar depths were on the order of the resolution values calculated for the proximeter probes. Although not an absolute measure, the curves can be used to determine trends in the wear rate. One important factor was observed when comparing the the wear rate in arm #2 in the second experiment, with the magnitude of the normal load (figures 6 and 8). Investigation shows a proportional increase in the wear rate in the region where the normal load was increased. Although this is not a complete investigation, this observation shows a general relationship between the wear rate and applied load.

The final set of figures (9-12) show the wear scar profile and depth at three locations along the line of contact in addition to the photomicrographs of the wear scar. As noted previously, the wear depths vary as a result of uneven stress distribution. In each of the figures, the sliding direction (S.D.) is from right to left.

#### 5.0 CONCLUSIONS

The results of the experiments above indicate that:

- 1) The lowest operational speed and load values are 700 RPM and 3.0 lbs (13.3N) respectively.

- 2) Large shaft runout values result in large dynamic variation in both the applied normal load and wear traces.
- 3) Dynamic variations in the applied load appear to be dependent on the rotational speed.
- 4) The mean coefficient of friction value for the ESK  $\alpha$ SiC post HIP-ed material sliding against itself is  $\approx 0.5$  and has a superimposed oscillating component that ranges from 0.0 to about 1.0.
- 5) Maximum wear of the ESK post Hip-ed  $\alpha$ SiC flat rubshoes after a test duration of 20 min ( $\approx 14,000$  cycles) was approximately 90 micro inches.
- 6) As a result of uneven load distribution along the contact length of the rubshoe, the depth of the wear scar varied.

#### 6.0 RECOMMENDATIONS

Assessment of the test hardware behavior, the test procedure, and the experimental results reveal the need for some modifications and/or evaluation of Tester 2A operation. The following additional effort is recommended:

- 1) Evaluate the frequency response of the loading arm system to experimentally define the first order resonant frequency. The ratio of operating speed and resonant speed will determine if a resonant frequency response is contributing to the oscillatory behavior that was observed in the experimental results (5).
- 2) Conduct further runout testing to find a ceramic collet insert which has an acceptable level of combined runout (less than 0.0002 in). The typical runout values for the two ceramic collets available for use are on the order of 0.0007 in.
- 3) Perform additional balancing of the two load actuators prior to any testing with a sinusoidally varying applied load. This is necessary since, currently, use of the actuators result in an erroneous frictional load component even when there is no contact between the rod and rubshoes. Whether this error is proportional to the applied load is unknown at this point.

#### FUTURE WORK

The goal of these first tests was to lay the groundwork necessary to successfully complete the scheduled baseline testing. Initially, baseline testing will include four materials tested under four different temperature



and heat treat conditions using only the cylinder of flat contact geometry. Once baseline tests are completed, the matrix of test variables will expand to include a wide range of contact geometries, surface treatments and material combinations.

B. L. Soriano  
B. L. Soriano

Approved by:

Ronald E. Hoover  
R. E. Hoover, Head  
Advanced Materials Section

Table 1. Material combinations for the initial Tester 2A experiments.

| Rod and Rubshoes Material                                                     | Main Grain Boundary Phase(s)                                        | Purchase Requisition No. for Traceability |
|-------------------------------------------------------------------------------|---------------------------------------------------------------------|-------------------------------------------|
| Norton NBD-100 $\text{Si}_3\text{N}_4$<br>(Sinter + HIP-ed)                   | $\text{MgO} \cdot \text{SiO}_2$<br>$2\text{MgO} \cdot \text{SiO}_2$ | 324632                                    |
| Sohio Engineered Materials<br>Hexoloy 80T-SA $\alpha$ -SiC<br>(Sintered only) | $\text{B}_2\text{O}_3 \cdot \text{SiO}_2$                           | 324631                                    |
| Elektrgschmelzwerk-Kempton<br>Ekasic $\alpha$ -SiC<br>(Sinter + HIP-ed)       | $\text{Al}_2\text{O}_3 \cdot \text{SiO}_2$                          | 324627                                    |
| Elektrgschmelzwerk-Kempton<br>Ekasic $\alpha$ -SiC<br>(fully can-HIP-ed)      | $\text{Al}_2\text{O}_3 \cdot \text{SiO}_2$                          | 324627                                    |

TABLE 2

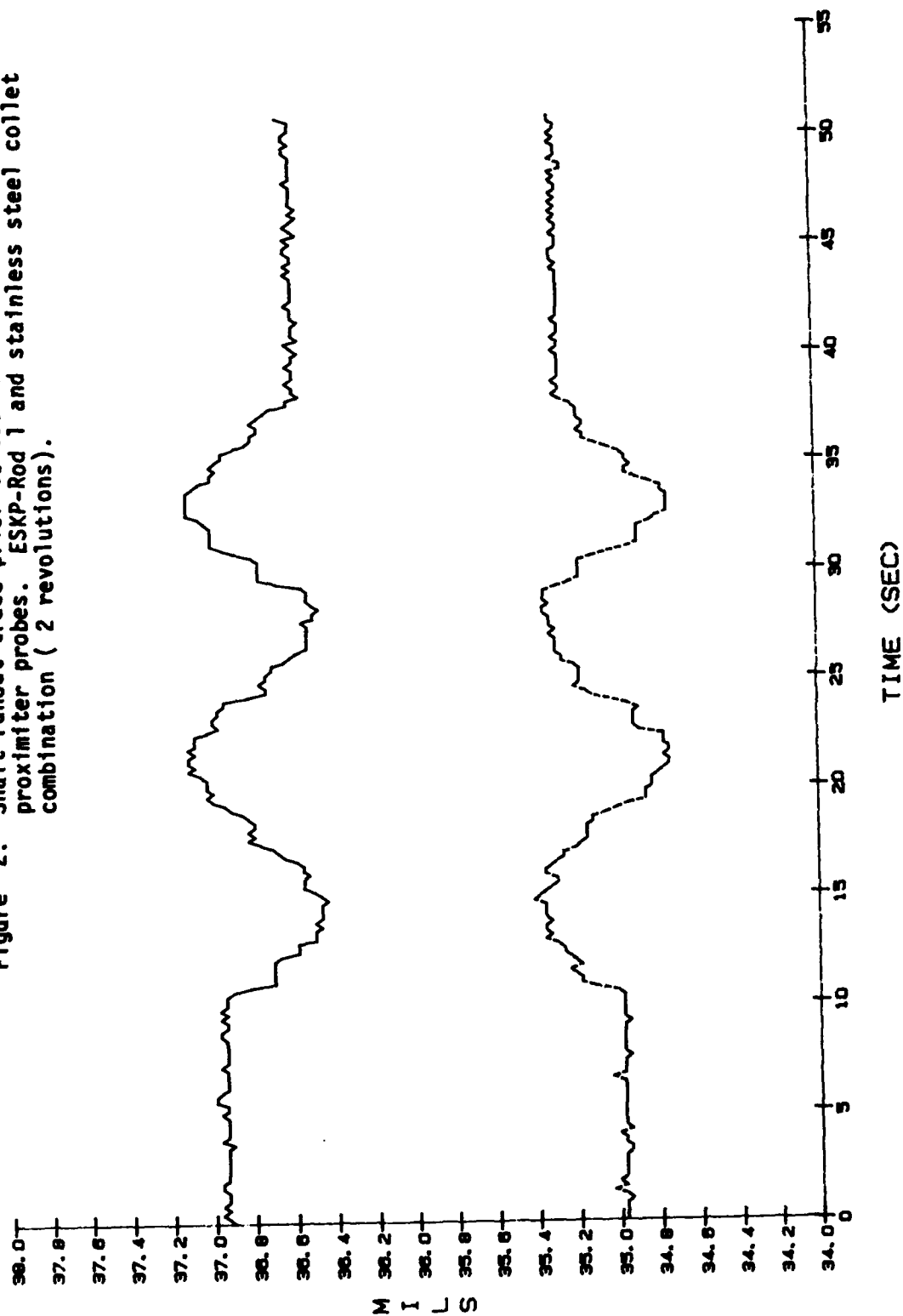
Test conditions for the initial Tester 2A experiments and projected test condition for completion of baseline investigation

| Test Parameter                 | TEST #1                             | TEST #2                             | Projected Test Conditions                                                                   |
|--------------------------------|-------------------------------------|-------------------------------------|---------------------------------------------------------------------------------------------|
| Sample Material                | ESK EKASIC SiC<br>Post HIP-ed       | ESK EKASIC SiC<br>Post HIP-ed       | SEE TABLE                                                                                   |
| Surface Finish                 |                                     |                                     |                                                                                             |
| Arithmetic Average (u in)      |                                     |                                     |                                                                                             |
| ° Rod                          | ESKP-Rod 1 1-3*                     | ESKP-Rod 1 1-3                      | -----                                                                                       |
| ° Rubshoe Arm #1               | ESKF-P1 1-2                         | ESKF-P3 1-2                         |                                                                                             |
| ° Rubshoe Arm #2               | ESKF-P2 1-2                         | ESKF-P4 1-2                         |                                                                                             |
| Applied                        |                                     |                                     |                                                                                             |
| Arm #1                         | 13.3 N (3.0 lbs)                    | 2.5-4.0 N (11-17.8 lbs)             | 13.3 N (3.0 lbs) Test                                                                       |
| Arm #2                         | 13.3 N (3.0 lbs)                    | 2.5 N (11.0 lbs)                    | 13.3 N (3.0 lbs) 1,2,3                                                                      |
| Normal Load                    |                                     |                                     | Test #4 TBD                                                                                 |
| Speed:                         |                                     |                                     |                                                                                             |
| ° during loading               | 400 RPM = 0.2 m/s (0.66 ft/sec)     | 400 RPM = 0.2 m/s (0.66 ft/sec)     | 400 RPM                                                                                     |
| ° steady-state                 | 1000 RPM = 0.5 m/s (1.64 ft/sec)    | 700 RPM = 0.3 m/s (1.14 ft/sec)     | 700 RPM                                                                                     |
| Duration:                      |                                     |                                     |                                                                                             |
| ° time                         | 27 minutes                          | 27 minutes                          | 25-30 minutes                                                                               |
| ° sliding distance             | 810 m (2656 ft)                     | 810 m (2656 ft)                     |                                                                                             |
| Data Sampling Rates:           |                                     |                                     |                                                                                             |
| ° Wear (Proximeter Probes)     | 5Hz                                 | 5Hz                                 | 1Hz                                                                                         |
| ° Load                         | 5Hz                                 | 5Hz                                 | 1Hz                                                                                         |
| ° Friction Force               | 5Hz                                 | 5Hz                                 | 1Hz                                                                                         |
| ° Rubshoe Temperature          | 1Hz                                 | 1Hz                                 | 1Hz                                                                                         |
| ° Pyrometer Temperature Output | 5Hz                                 | 5Hz                                 | 1Hz                                                                                         |
| ° Heater Temperature           | 1Hz                                 | 1Hz                                 | 0.5Hz                                                                                       |
| ° Bearing Temperature          | 1Hz                                 | 1Hz                                 | 0.5Hz                                                                                       |
| ° Proximity Probes Power       | 1Hz                                 | 1Hz                                 | 0.5Hz                                                                                       |
| ° L.C. Power                   | 1Hz                                 | 1Hz                                 | 0.5Hz                                                                                       |
| Test Atmosphere                | Dry, Filtered Air                   | Dry, Filtered Air                   | Dry, Filtered Air                                                                           |
| Test Temperatures              | Room Temperature<br>(No Heat Added) | Room Temperature<br>(No Heat Added) | 1) R.T.<br>2) 850°C No Pretreatment<br>3) 850°C Pretreat at<br>850°C Duration TBD<br>4) TBD |

\*Combined Range of Circumferential and Longitudinal Measurements (2 ea).

\*\*Combined Range of Length and Width Measurements (1 ea).

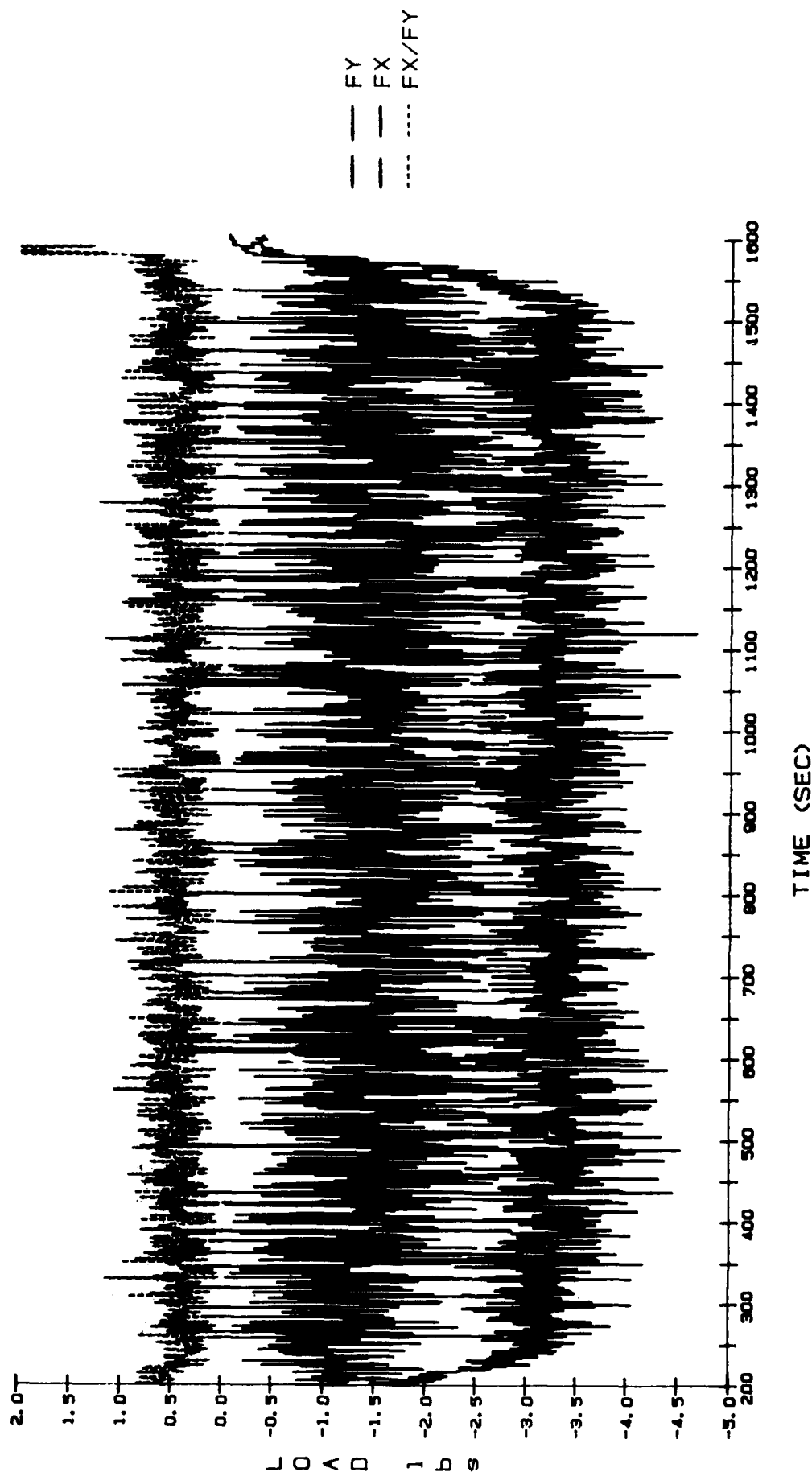
Figure 2. Shaft runout trace prior to test #1 as measured with proximiter probes. ESKP-Rod 1 and stainless steel collet combination ( 2 revolutions).



ESK EK661C 4S1C "POST HIP-ed" ROD/FLAT GEOMETRY  
RUNOUT TRACE PRIOR TO TEST ESKP1A

TEST #1  
13.3 N (3.0 lbe)  
1000 RPM

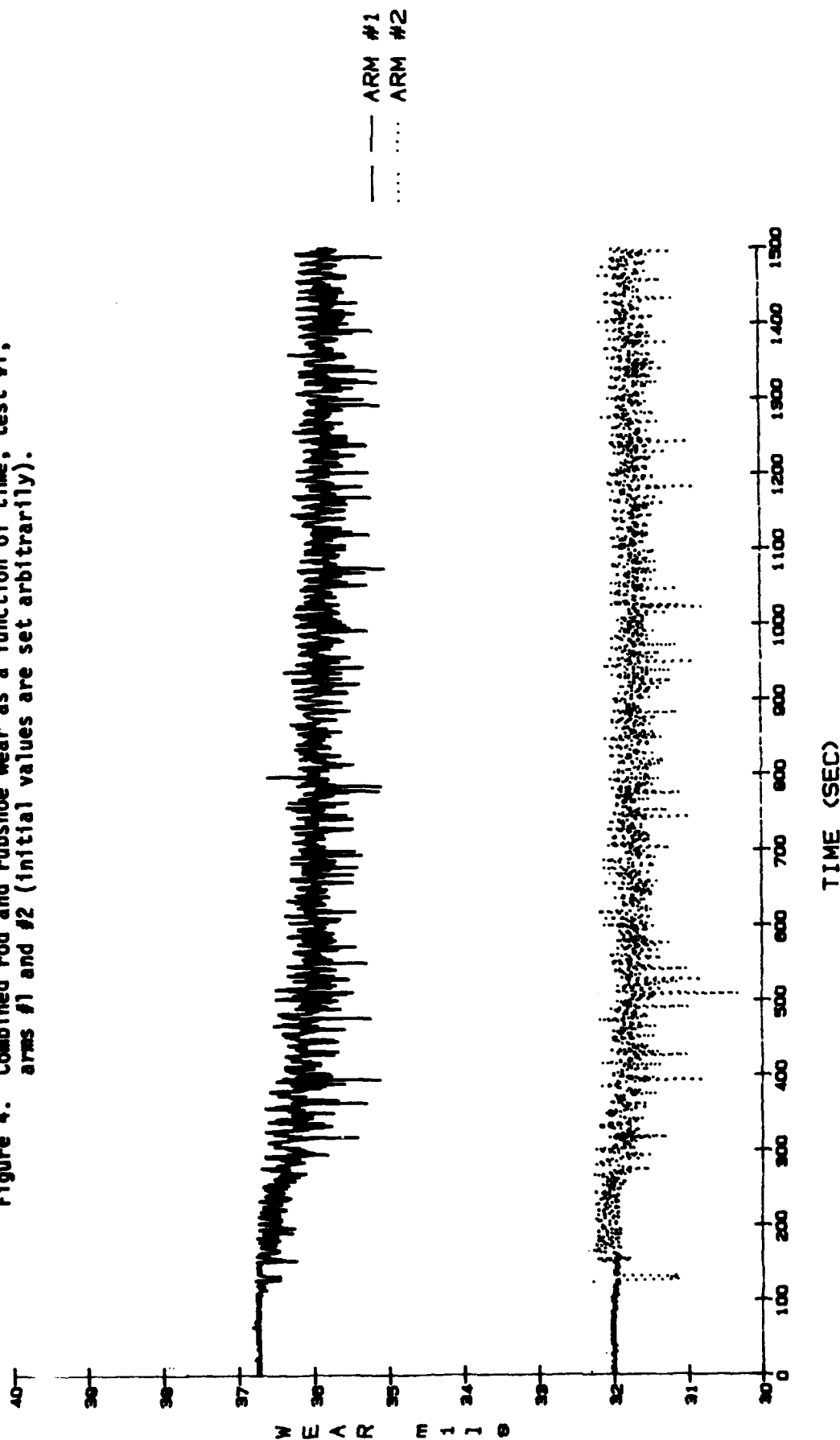
Figure 3. Normal applied load (Fy), frictional force (Fx), and calculated coefficient of friction (Fx/Fy) measured as a function of time, test #1, arm #1.



ESK EK61C & SIC "POST HIP-ed" ROD/FLAT GEOMETRY  
LOAD VALUES ARM #1

TEST #1  
13.3 N (3.0 lbf)  
1000 RPM

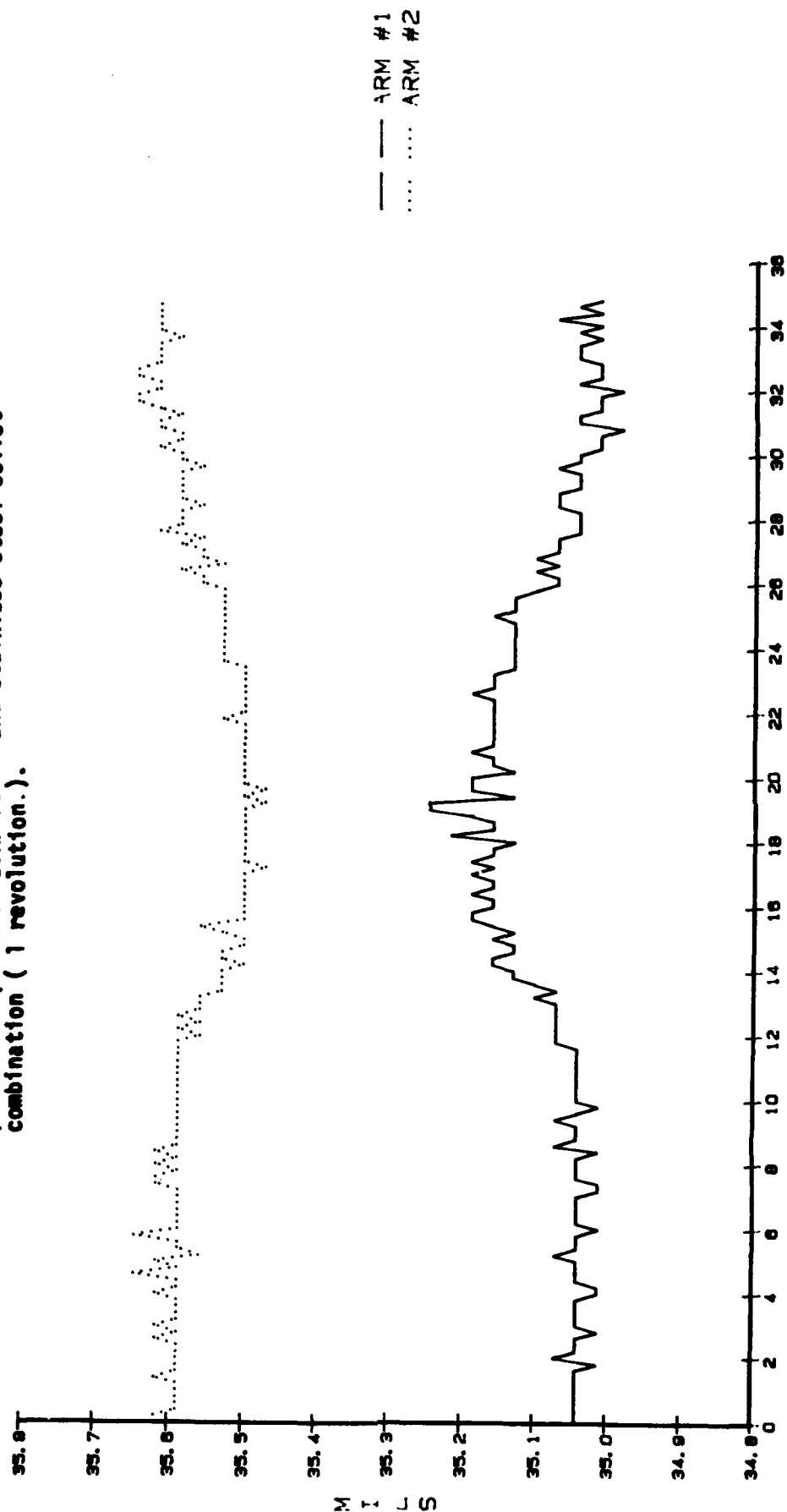
Figure 4. Combined rod and rubshoe wear as a function of time, test #1, arms #1 and #2 (initial values are set arbitrarily).



ESK EK610 (S1C "POST HIP-ed" ROD/FLAT GEOMETRY  
WEAR (mils) ARMS #1 AND #2

TEST #1  
13.3 N (3.0 lbs)  
1000 RPM

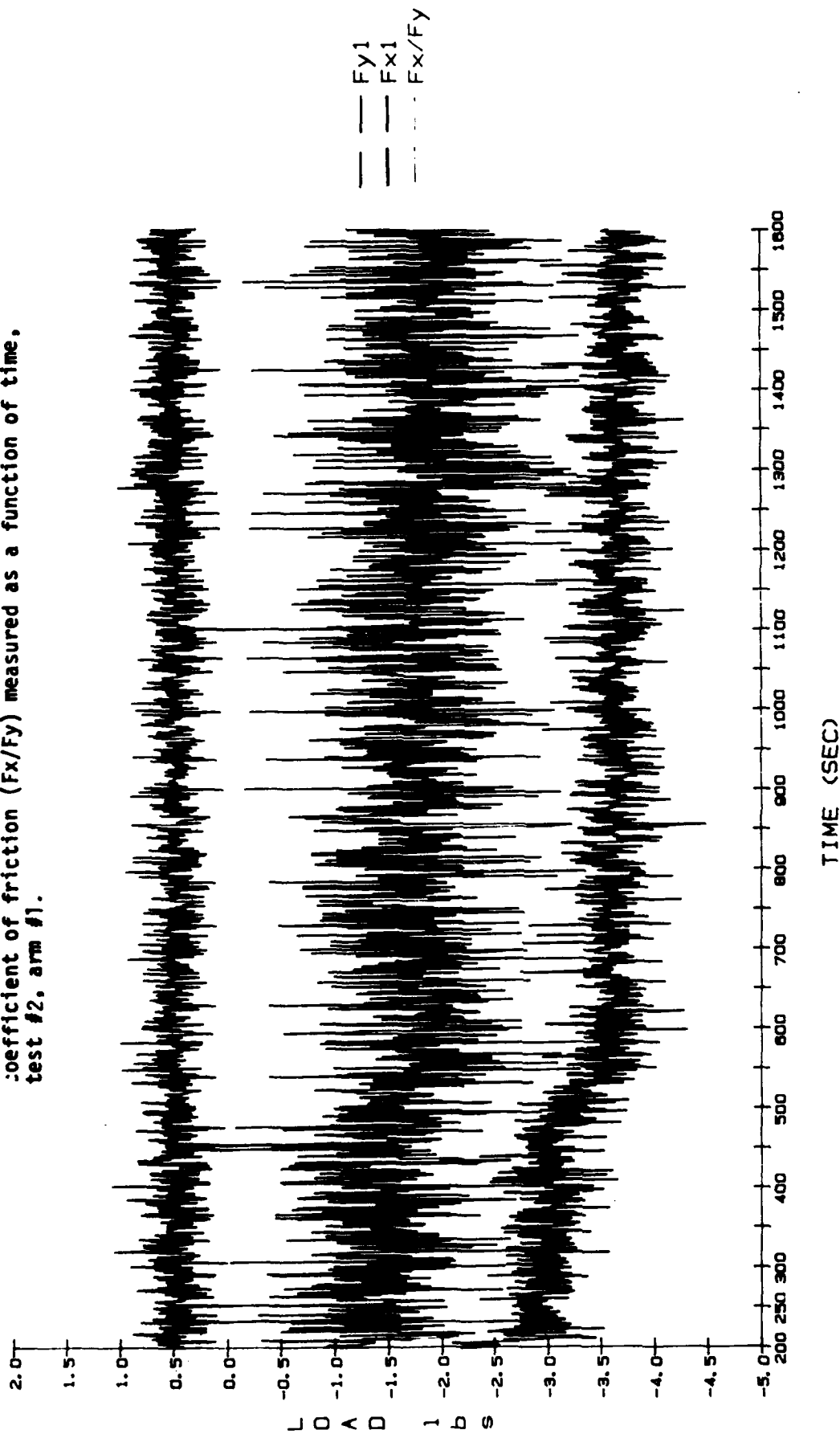
Figure 5. Shaft runout trace prior to test #2 as measured with proximiter probes. ESKP-Rod 1 and stainless steel collet combination (1 revolution.).



TEST #2  
11-17.7 N (2.5-4.0 lbs)  
700 RPM

ESK EK81C 4S1C "POST HIP-ed" ROD/FLAT GEOMETRY  
RUNOUT TRACE PRIOR TO TEST ESKP3

Figure 6. Normal applied load (Fy), frictional force (Fx), and calculated coefficient of friction (Fx/Fy) measured as a function of time, test #2, arm #1.

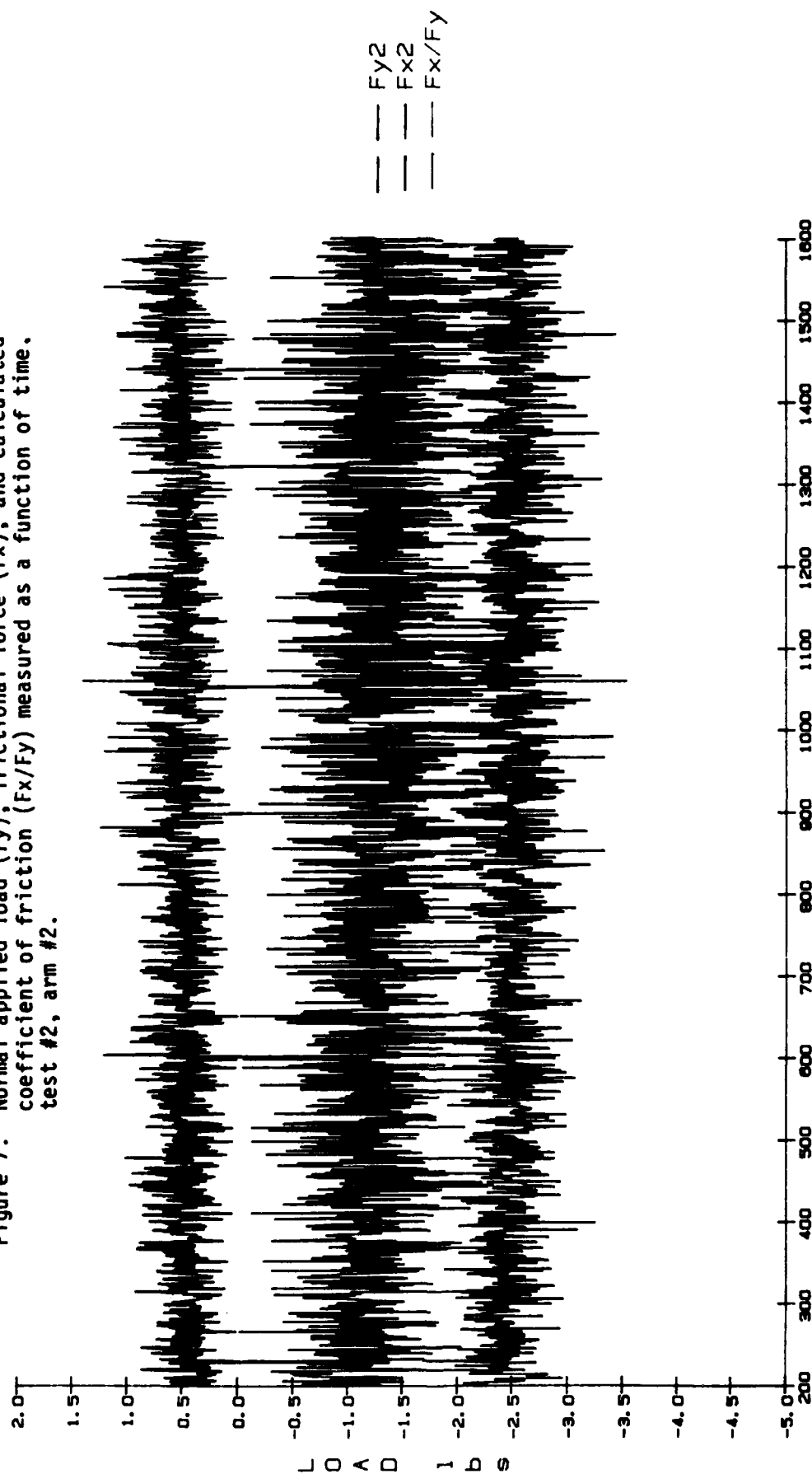


ESK EKasic 4SiC "POST HIP-ed" ROD/FLAT GEOMETRY  
LOAD VALUES ARM #1

TEST #2  
11-17.7 N (2.5-4.0 lbe)  
700 RPM



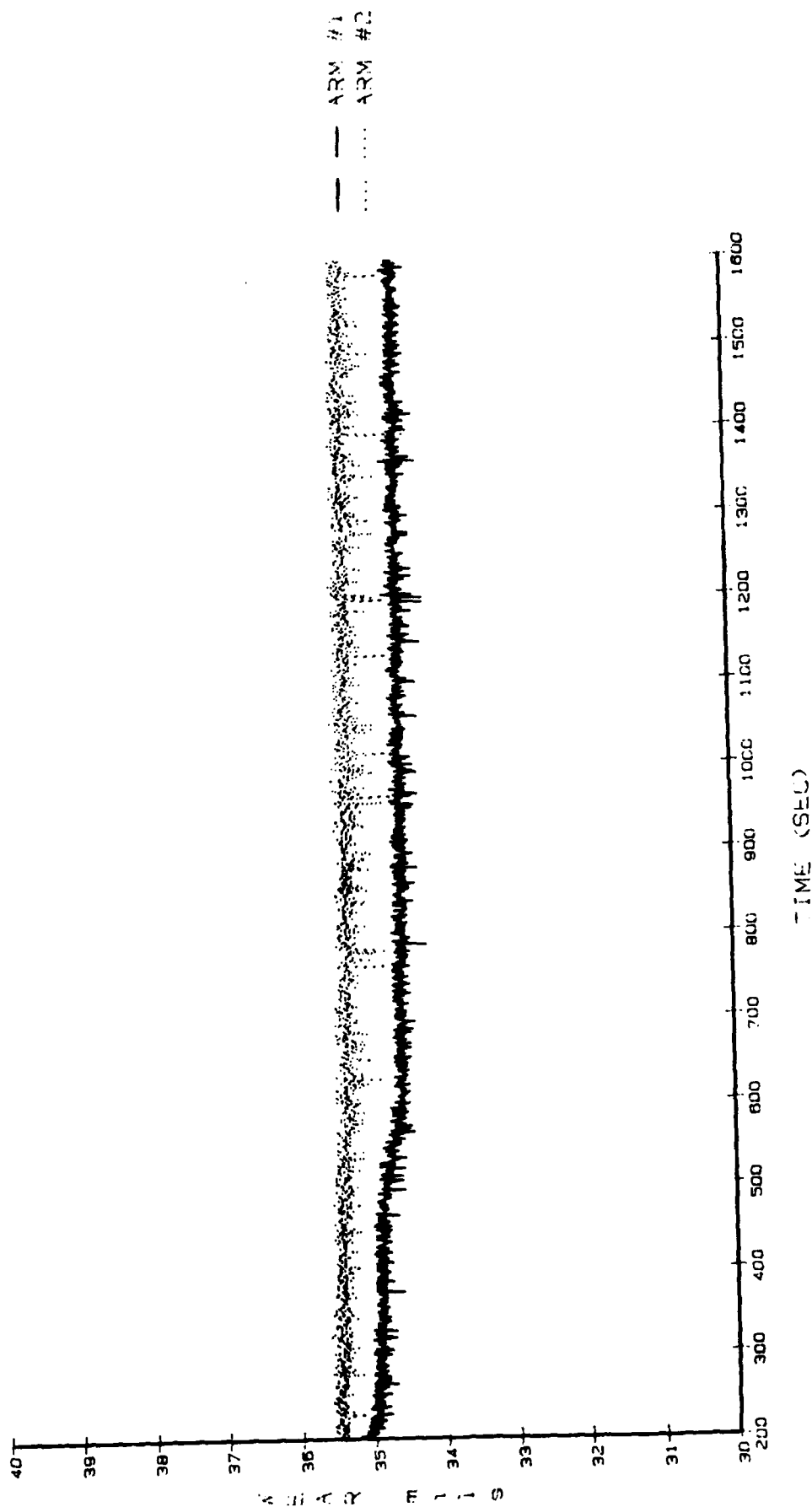
Figure 7. Normal applied load (Fy), frictional force (Fx), and calculated coefficient of friction (Fx/Fy) measured as a function of time. test #2, arm #2.



ESK EKasic "POST HIP-ed" ROD/FLAT GEOMETRY  
LOAD VALUES ARM #2

TEST #2  
11-17.7 N (2.5-4.0 lbf)  
700 RPM

Figure 8. Combined rod and rubshoe wear as a function of time, test #2, arms #1 and #2 (initial values are set arbitrarily).



TEST #2  
11-17.7 N (2.5-4.0 lbe)  
700 RPM

USK EK6510 Q51C "POST HIP-ED" ROD/FLAT GEOMETRY  
WEAR (mils) ARMS #1 AND #2

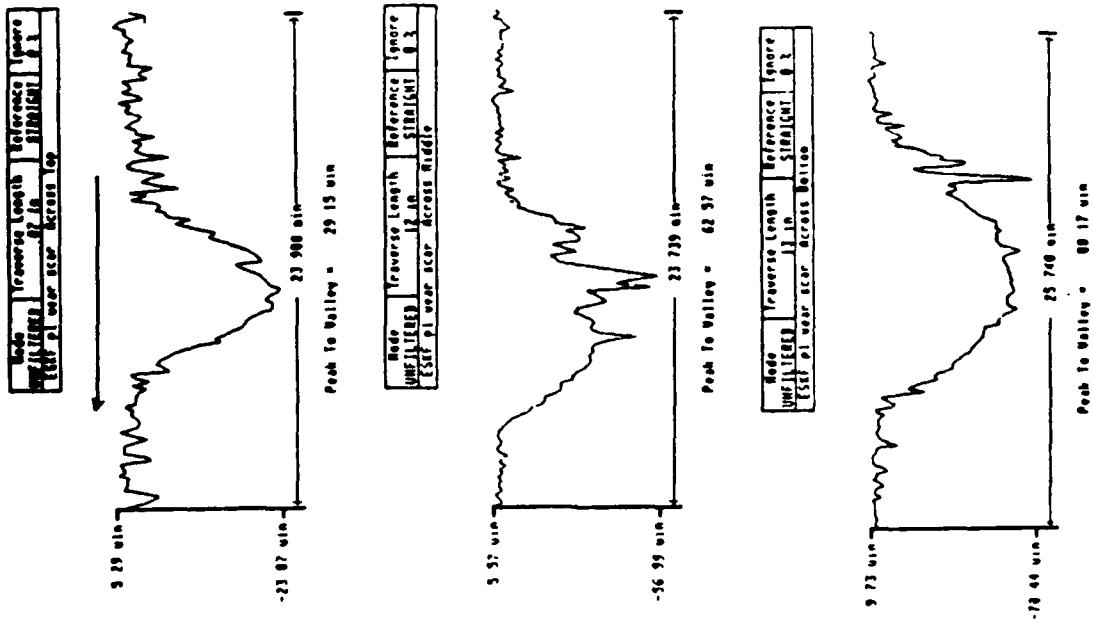


Figure 9a. Surface profile of rubshoe contact area (perpendicular to wear scar) showing wear depth

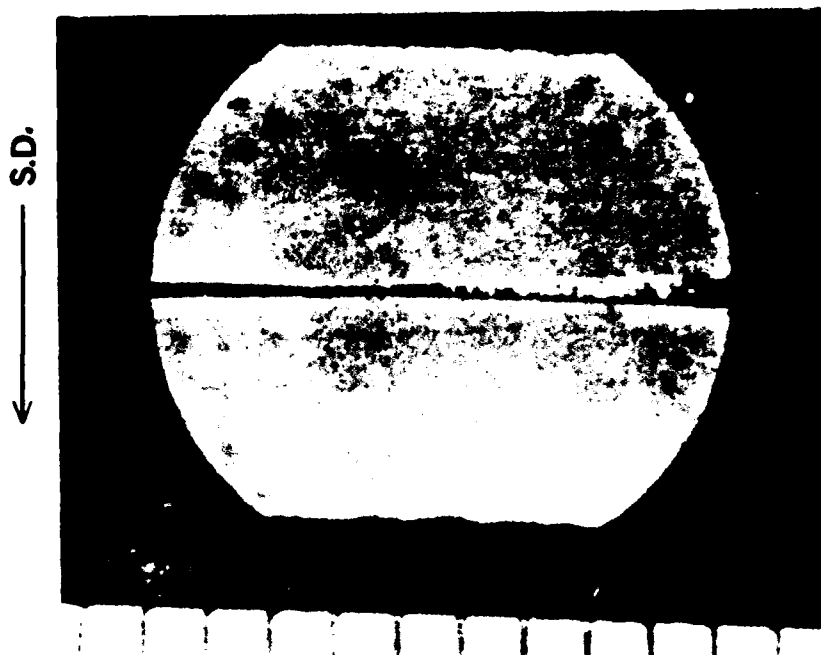
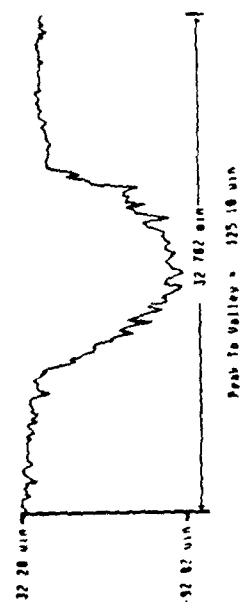
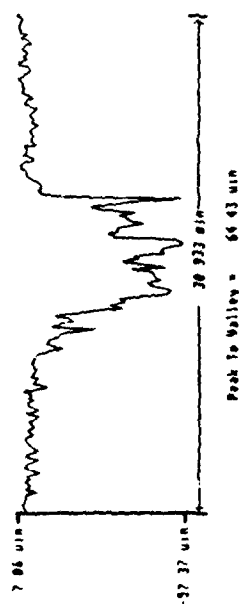


Figure 9b. Photomicrograph of rubshoe contact face  
Scale: 1 div = 1mm  
Test #1, arm #1  
Rubshoe ESKF\_P1

| Node                         | Transverse Length | Reference | Spade |
|------------------------------|-------------------|-----------|-------|
| 4001111111                   | 10 in             | SLIP(10)  | 0.1   |
| ESKF_P2 wear scar across top |                   |           |       |



| Node                            | Transverse Length | Reference | Spade |
|---------------------------------|-------------------|-----------|-------|
| 4001111111                      | 10 in             | SLIP(10)  | 0.1   |
| ESKF_P2 wear scar across middle |                   |           |       |



| Node                            | Transverse Length | Reference | Spade |
|---------------------------------|-------------------|-----------|-------|
| 4001111111                      | 10 in             | SLIP(10)  | 0.1   |
| ESKF_P2 wear scar across bottom |                   |           |       |

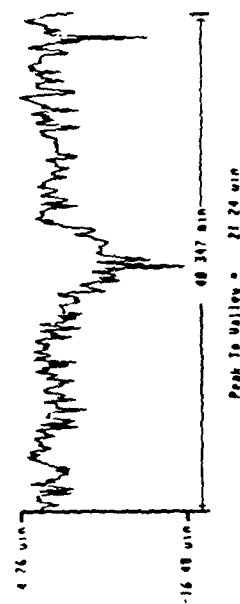


Figure 10a. Surface profile of rubshoe contact area (perpendicular to wear scar) showing wear depth

← S.D.

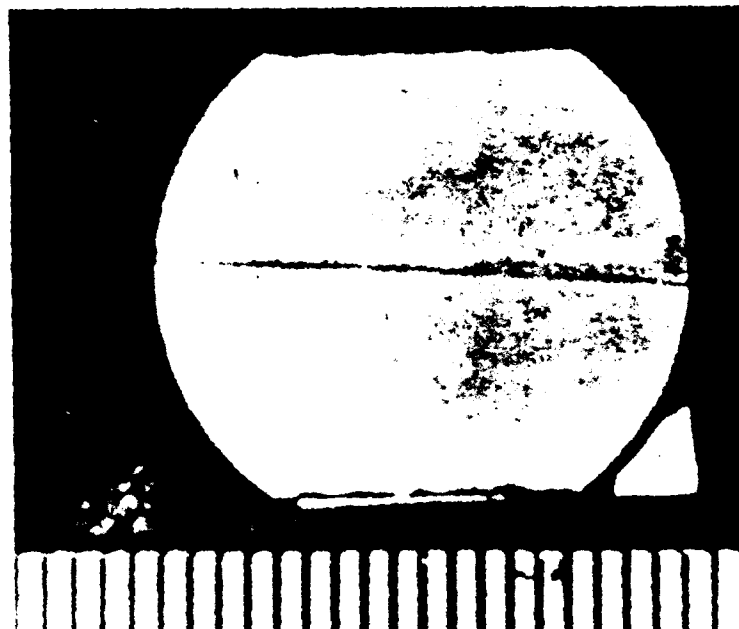
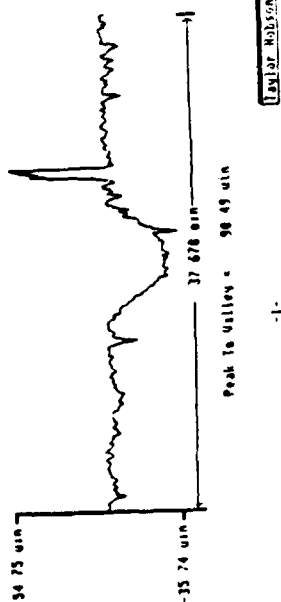
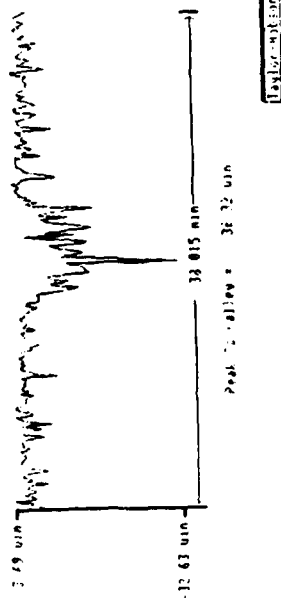


Figure 10b. Photomicrograph of rubshoe contact face  
Scale: 1 div = 1/2 mm  
Test #1, arm #2  
Rubshoe ESKF\_P2

| Mode                          | Transverse Length | Reference | Ignore |
|-------------------------------|-------------------|-----------|--------|
| UNFILTERED                    | 10 in             | SIGLIGHT  | 0      |
| Test #2, wear scar across top |                   |           |        |



| Mode                             | Transverse Length | Reference | Ignore |
|----------------------------------|-------------------|-----------|--------|
| UNFILTERED                       | 10 in             | SIGLIGHT  | 0      |
| Test #2, wear scar across middle |                   |           |        |



| Mode                             | Transverse Length | Reference | Ignore |
|----------------------------------|-------------------|-----------|--------|
| UNFILTERED                       | 9.5 in            | SIGLIGHT  | 0      |
| Test #2, wear scar across bottom |                   |           |        |

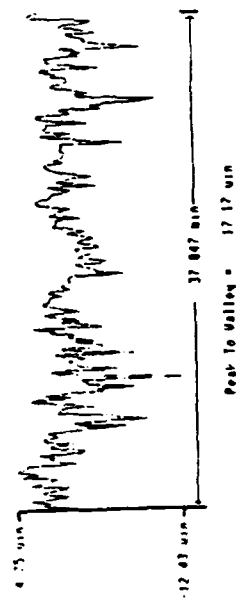


Figure 11a. Surface profile of rubshoe contact area (perpendicular to wear scar) showing wear depth

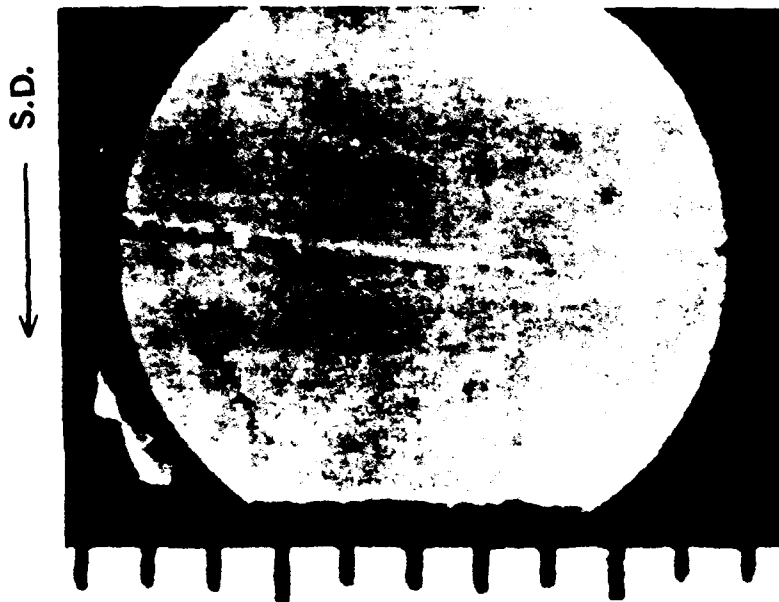
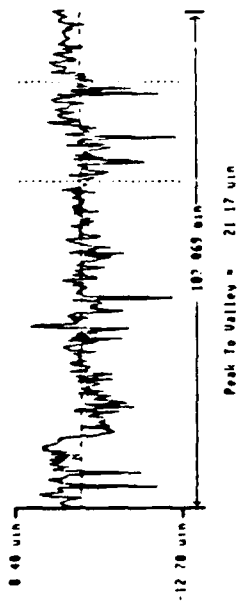
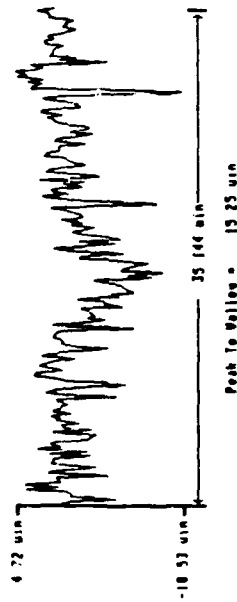


Figure 11b. Photomicrograph of rubshoe contact face  
Scale: 1 div = 1mm  
Test #2, arm #1  
Rubshoe ESKE\_P3

| Mode       | Traverse Length | Reference  | Ignore |
|------------|-----------------|------------|--------|
| UNFILTERED | 10 in           | SIRALCH    | 0.3    |
| ESKF       | Pe wear scar    | Across Top |        |



| Mode       | Traverse Length | Reference     | Ignore |
|------------|-----------------|---------------|--------|
| UNFILTERED | 10 in           | SIRALCH       | 0.3    |
| ESKF       | Pe wear scar    | Across Middle |        |



| Mode       | Traverse Length | Reference     | Ignore |
|------------|-----------------|---------------|--------|
| UNFILTERED | 10 in           | SIRALCH       | 0.3    |
| ESKF       | Pe wear scar    | Across Bottom |        |

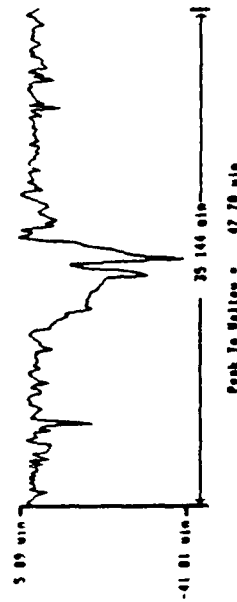


Figure 12a. Surface profile of rubshoe contact area (perpendicular to wear scar) showing wear depth

← S.D.

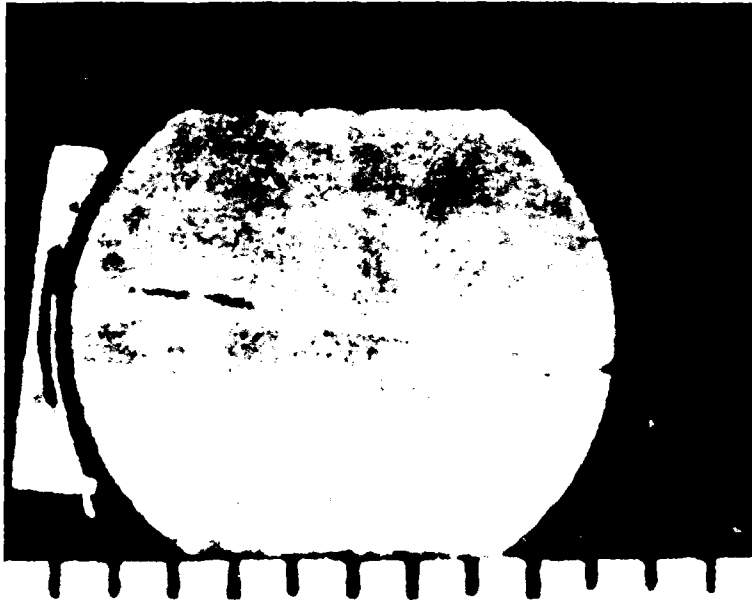


Figure 12b. Photomicrograph of rubshoe contact face  
Scale: 1 div = 1mm  
Test #2, arm #2  
Rubshoe ESKF\_p4

## REFERENCES

1. Carroll J. G., "Contact Stresses in Lubricant Testers", Lub. Eng. Vol. 24, No. 8, 359-365, August 1986
2. Fiderer, L., "Unique Friction and Wear Tester for Fundamental Tribology Research", Hughes Technical Internal Correspondence Report No. 86-7282.00/920, September 1986.
3. Heshmat, H., "Analytical Model of Loader Arm of Tribotester 2A, Appendix VII in "Determination of Tribological Fundamentals of Solid Lubricated Ceramics", Monthly Report, Written by M.N. Gardos, Contract F33615-85-C-5087, July, 1987.
4. Magallanes, P. G., "Data Logging and Analysis for Friction and Wear Testing of Solid Lubricated Ceramics", Hughes Internal Correspondence Report No. 7621.11/88, November 1986.
5. Fiderer, L., "Tribotester Structural Analysis", Hughes Internal Correspondence Report No. 867282.20/930, October 1986.

# APPENDIX I

**HUGHES**

ANALYSIS

MODEL

REPORT NO

PAGE I/1

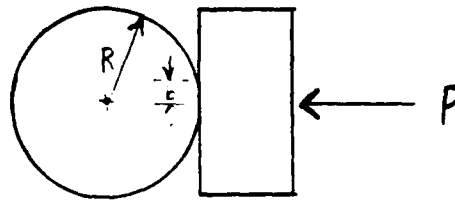
PREPARED BY E. L. SQUAD

10/3/44

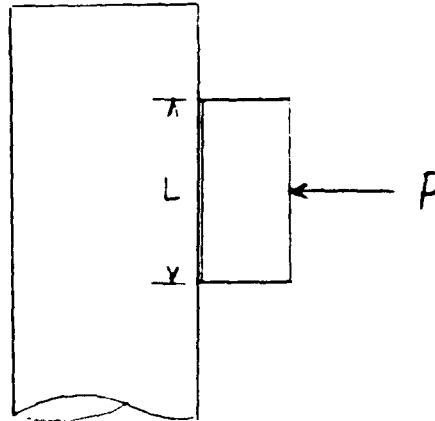
FIGURE 1

CHECKED BY

## HERTZIAN STRESS CALCULATIONS:



TOP VIEW



SIDE VIEW

$b$  = half width of linear contact

$P'$  = load per unit length

$P$  = applied load

FIGURE 1



ANALYSIS

MODEL

REPORT NO.

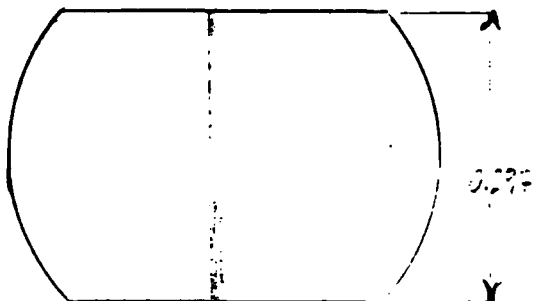
PAGE

PREPARED BY

B.L. SERIANO

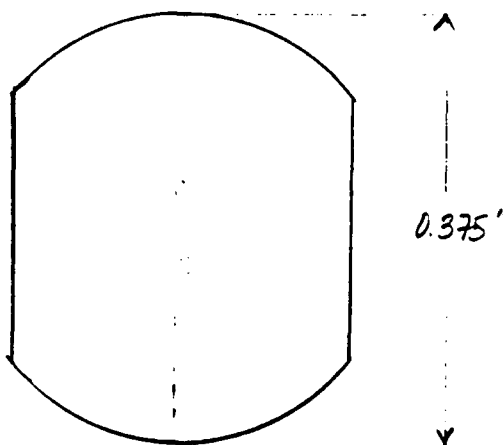
CHECKED BY

Rubshoe Contact Length

FLAT RUBSHOE ORIENTATION  
FIGURE 2.

CONTACT LENGTH = 0.297"

PRIMARY ORIENTATION



CONTACT LENGTH = 0.375"

SECONDARY ORIENTATION

ANALYSIS

MODEL

REPORT NO.

PAGE 1

PREPARED BY B.L. Soriano

CHECKED BY

## HERTZIAN STRESS ANAL.

HERTZIAN STRESS ANALYSIS

Two cylinders in contact

$$b = \left( \frac{4P' (K_1 + K_2) R_1 R_2}{R_1 + R_2} \right)^{1/2}$$

IN CASE OF ONE cylinder and FLX =

$$R_2 = \infty$$

$$F_2 \approx R_2 + R_1$$

$$L = \left( \frac{4P' (K_1 + K_2) R_1 R_2}{R_2} \right)^{1/2}$$

$$b = \left( 4P' (K_1 + K_2) R_1 \right)^{1/2}$$

where  $b$  = one half-width of linear contact $P'$  = Load/unit length

$$P' = \frac{P}{L} \quad (2)$$

$$K_1, K_2 = \frac{1 - \nu^2}{\pi E} \quad (3)$$

ANALYSIS

MODEL

REPORT NO.

PAGE

PREPARED BY BIL Soriano

CHECKED BY

Hertzian Stress. Final

$$\text{Rod RADIOS} = \frac{.375}{2} \Rightarrow 4.76 \times 10^{-3} \text{ m}$$

$$\text{CONTACT length A) } .375 \Rightarrow 9.53 \times 10^{-3} \text{ m}$$

$$\text{B) } .297 \Rightarrow 7.54 \times 10^{-3} \text{ m}$$

$$\text{Applied LOAD } 2 \text{ lbs} \rightarrow 4 \text{ lbs}$$

$$1 \text{ lb} = 4.44 \text{ N}$$

$$8.88 \text{ N} \rightarrow 17.76 \text{ N}$$

$$C = \left( \frac{4}{\pi} (K_1 + K_2) R_1 \right)^{1/2} (P')^{1/2}$$

For example (NEI-30)

$$K_1 = K_2 = \frac{1 - \nu^2}{\pi E} = \frac{1 - .26^2}{\pi \cdot 310 \text{ GPa}} = 9.57 \times 10^{-11} \text{ m}^2/\text{N}$$

For 3.b, .375 in contact,

$$C = \left( \frac{4 \cdot 2 \cdot \left( \frac{9.57 \times 10^{-11} \text{ m}^2/\text{N}}{1 \times 10^9} \right) \cdot 4.76 \times 10^{-3} \text{ m}}{9.53 \times 10^{-3} \text{ m}} \right)^{1/2}$$

$$b = \bar{r} = 8 \times 10^{-3} \text{ m}$$

For Computer

$$b = (1.955 \times 10^{-3} \text{ F})^{1/2} \text{ meter}$$

ANALYSIS \_\_\_\_\_

MODEL \_\_\_\_\_

REPORT NO. \_\_\_\_\_

PAGE 1/6

PREPARED BY \_\_\_\_\_

CHECKED BY \_\_\_\_\_

Hertzian stress and

$$b = 7.14 \times 10^{-6} \text{ m}$$

$$q_0 = \frac{2P'}{\pi b} = \frac{2 \cdot 316 \cdot 4.44 \text{ N/lb}}{\pi (7.14 \times 10^{-6} \text{ m}) (9.53 \times 10^{-3} \text{ m})}$$

$$q_0 = 1.246 \times 10^8 \text{ Pa} \cdot \frac{14.7 \text{ PSI}}{10^5 \text{ Pa}} = 18323 \text{ PSI}$$

$$\sigma_{10} = 124.6 \text{ MPa} = 18.32 \text{ KSI}$$

For Graphing  $b = 1.956 \times 10^{-6} F^{1/2}$

$$q_0 = \frac{2 F / 9.53 \times 10^{-3} \text{ m}}{\pi 1.956 \times 10^{-6} F^{1/2}}$$

$$q_0 = 34.16 \times 10^6 \sqrt{F} \text{ Pa} = 34.16 \sqrt{F} \text{ MPa}$$

CONVERSION  $14.7 \text{ PSI} = 1.01 \times 10^5 \text{ Pa}$

HERTZIAN CONTACT STRESS  
CYLINDER/FLAT  
ZERO WEAR CONDITION

| MATERIAL<br>COMBINATION | poison's<br>ratio | ELASTIC<br>MOD (GPa) | $K=1-\frac{2}{\pi E}$<br>GPa <sup>-1</sup> | HALF CONTACT<br>WIDTH (m) | MAX STRESS<br>MPa |
|-------------------------|-------------------|----------------------|--------------------------------------------|---------------------------|-------------------|
| 1 NBD-100               | 0.260             | 310                  | 0.000957                                   | 7.140000e-06              | 124.607280        |
| 2 Hexoloy               | 0.142             | 410                  | 0.000761                                   | 6.368583e-06              | 139.790911        |
| 3 Ekasic                | 0.160             | 440                  | 0.000705                                   | 6.130563e-06              | 145.218318        |

MATERIAL  
COMBINATION

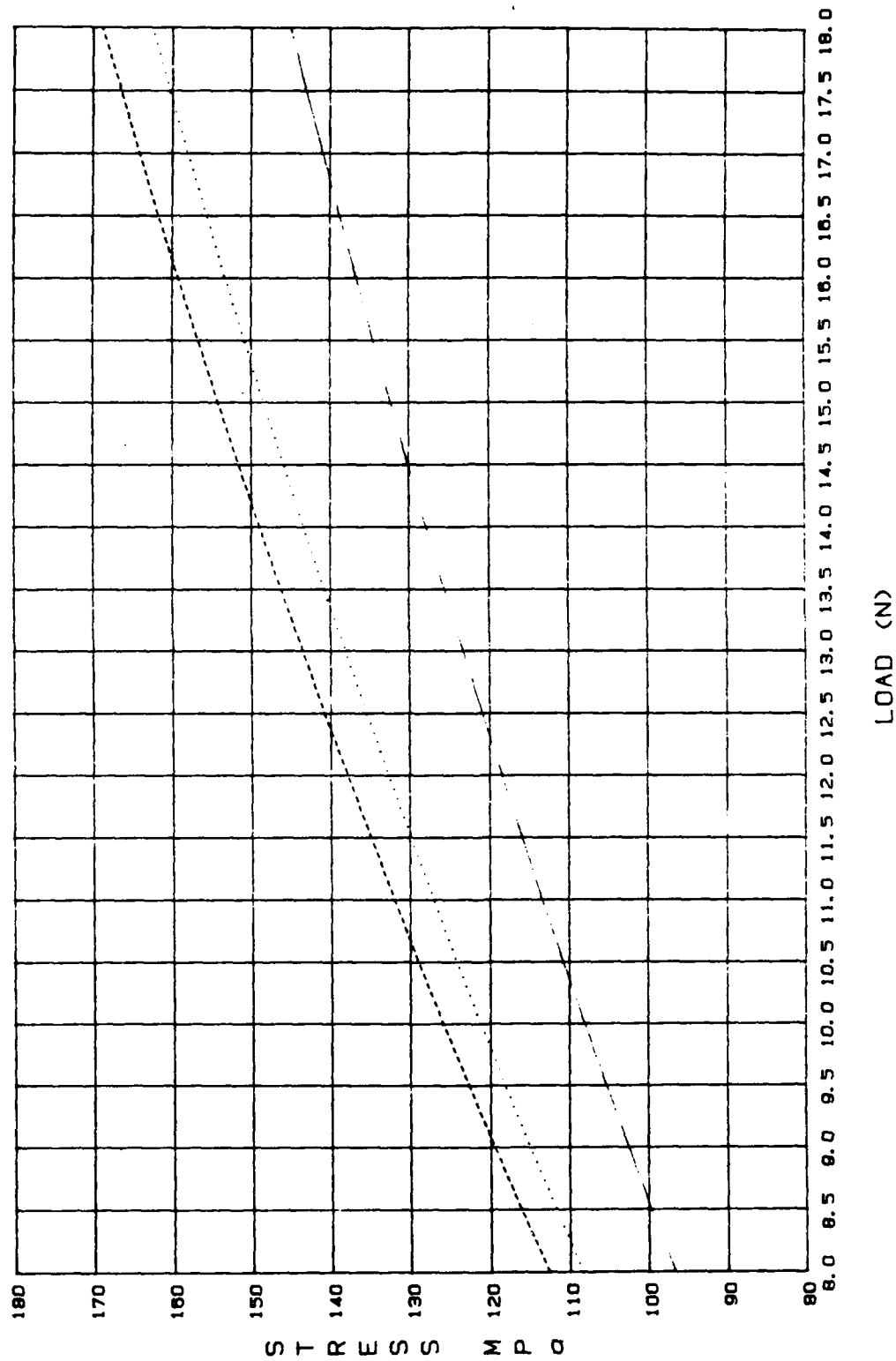
MAX STRESS  
(ksi)

|           |              |
|-----------|--------------|
| 1 NBD-100 | 1.831727e+01 |
| 2 Hexoloy | 2.054926e+01 |
| 3 Ekasic  | 2.134709e+01 |

Norton NBD-100 Si<sub>3</sub>N<sub>4</sub> Sinter + HIP-ed  
Hexoloy 80T-SA Sohio Engineered Materials  
Ekasic 4 SiC ESK Sintered + HIP-ed & Fully can HIP-ed  
Sample calculations for 3 lb (13.3 N) load, contact width = 0.375 in.

TABLE 1  
I/7

Figure 3  
MAX HERTZIAN STRESS VS. LOAD

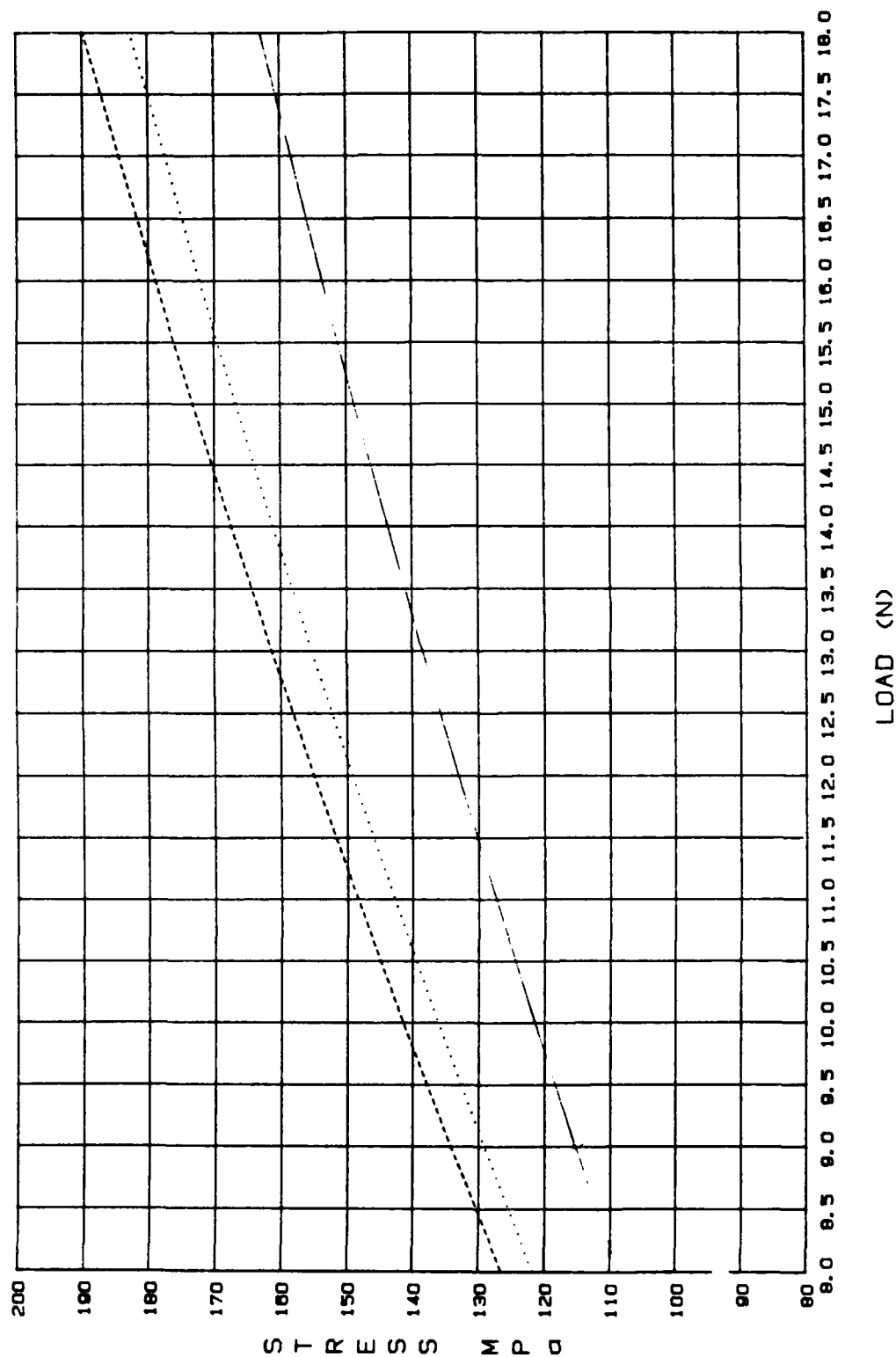


--- NBD-100  
... HEXOLOY  
-.- EKASIC

CONTACT WIDTH = 0.375 IN  
 NBD-100 F(x)=34.16 X\*\*.5  
 HEXOLOY SA F(x)=38.30 X\*\*.5  
 EKASIC F(x)=39.79 X\*\*.5

X=LOAD

Figure 4  
MAX HERTZIAN STRESS VS. LOAD



CONTACT WIDTH = 0.279 IN  
 NBD-100 F(x) = 38.41 X\*\*.5  
 HEXOLOLY SA F(x) = 43.07 X\*\*.5  
 EKASIC F(x) = 44.75 X\*\*.5

## **APPENDIX K**

**H. Kaplan, "Summary Report on Infrared Pyrometer Selection," Honeyhill  
Technical Co., Norwalk, CT, 01 August 1986, Hughes P.O. S9-245763-Z6X**



# **HT** Honeyhill Technical Co.

193 East Avenue, Norwalk, CT 06855

Telephone: (203) 838-8600

August 1, 1986

Hughes Aircraft Company  
Tactical Engineering Division  
P.O. Box 902, Building E-1  
El Segundo, CA 90245

ATTENTION: Mr. Leo Fiderer, MS D145

SUBJECT: Summary Report on Infrared Pyrometer Selection, your P.R.# 324612

Gentlemen:

The subject summary report with recommendations is enclosed herein. The report restates the measurement task, comments on each of the candidate instruments and recommends a selection as follows:

The purpose of this investigation is to evaluate five infrared pyrometers intended for use on the Tribotester 2A thermal breadboard tests and to recommend a selection from among these five candidates based on optimum suitability to the requirements. The measurement task is illustrated on HAC 82577 Figure 2, a copy of which is attached, and defined as follows:

Target material: Ceramic test rods, 0.375" in diameter and 3.5" long  
in a variety of materials with an estimated emissivity range of  
from 0.6 to 0.95.

Expected measurement range: 500 to 1500<sup>o</sup>F.

Accuracy: + or - 1.0% of reading

Repeatability: + or - 0.5% of reading.

Spot size and working distance: The target is viewed through a 0.156"  
aperture as shown. Considering aiming inaccuracies and the field-  
of-view spread of most commercial instruments, the selection of a  
0.050" spot size is appropriate. The working distance is not critical  
but a convenient distance would be from 4" to 10".

Response time: 0.1 second or faster.

Pyrometer sensing head (sensor) requirements: The sensor should be as small  
as possible for versatility in future use. Aiming is critical and  
should be as convenient and reliable as possible.

Spectral region of operation: The instrument should operate far enough into  
the infrared so that measurements are unaffected by visible light  
and by energy from the infrared line heater that will be used to  
heat the test rods. The heater radiance is peaked at 0.85 um (microns)  
and 1.1 um. A reasonably safe selection for the pyrometer would be  
an operating region of 3.5um or longer.

Output requirements: Analog DC voltage to a chart recorder linear with  
target temperature. 1 millivolt/degree F. would be desirable but  
the scale factor is not critical. Also a digital display of target  
temperature is required.

Special environmental considerations: none

# **HT** Honeyhill Technical Co.

193 East Avenue, Norwalk, CT 06855  
Telephone: (203) 838-8600

Five candidate pyrometers have been proposed as follows:

1. Ircon Maxline Model MX-M402-M402-0-3/2-0-0 with optional XZ-Z lens.
2. Land Model GP311 with LM4 controller/readout unit and drop-in aiming sight.
3. Vanzetti Model TM2-A-1-C-00-3-P-E-51F-00-00 with OH15-45-75mm detector head and Model LS15-1 fiber optic aiming device.
4. Wahl Model HSM 674 with close focus option and Model 600-1 indicator.
5. Williamson Model 4515C-F-FOVS.

Each candidate instrument is reviewed as follows:

## 1. Ircon

The instrument offered is wrong for the application, principally because it has a minimum spot size of 0.19". The offer is also for two units rather than one. This offer no doubt predated your most recent thinking. I phoned Ircon and reviewed the requirement with Mr. Barry Durr. They make a model which is more suited to the application. The model is MX-M703-0000-1-0/0-0-0 with the following characteristics:

Temperature range: 500 to 2500°F.  
Spot size: 0.065" at 5" working distance  
Spectral range: 4.8 to 5.3µm  
Accuracy: + or - 0.5% or 3°F. whichever is greater  
Repeatability: + or - 0.1% + or - one digit or 2°F. whichever is greater  
Response time: 0.025 seconds  
Outputs: 0-10VDC linear with temperature, LED display.  
Sighting: Erect through-the-lens reticle.  
Sensor dimensions: Approx. 10" long including lens and sight, approx 7" dia.  
Price: \$8,040.00  
Delivery: 8-10 weeks.

## 2. Land

Since there was no formal proposal from Land, I phoned Land's Bob Elfstrom to discuss the requirement. The GP311 is their model most closely suited to requirement with the following characteristics:

Temperature range: 250 to 2750°F.  
Spot size: 0.118" at 5" working distance  
Spectral range: 8-11.5µm  
Accuracy: + or - 0.5% +2°F.  
Repeatability: + or - 0.2%  
Response time: 1 second  
Outputs: 1 millivolt DC/degree, LED display  
Sighting: Drop-in mirror accessory. (Sighting not possible during measurement)  
Sensor dimensions: Approximately 6" long x 2" dia.  
Price: \$4,365.00  
Delivery: 4-6 weeks

# **HT** Honeyhill Technical Co.

193 East Avenue, Norwalk, CT 06855

Telephone: (203) 838-8600

## 3. Vanzetti

The instrument offered is correct for the application but the model code included options that are not presently necessary, such as the peak sensor and the PID controller. Based on conversations with Vanzetti's John DeCicco and Jeff Davis, the appropriate model designation is TM2-A-1-F-3-0-E-00-00-00-OH15-4.5-75mm with the following characteristics:

Temperature range: 500-1500°F.

Spot size: 0.050" at 4" working distance

Spectral range: 4.5um

Accuracy: + or - 1.0% of reading

Repeatability: + or - 0.5% of reading

Response time: selectable up to 0.005 seconds

Outputs: 1 millivolt DC/degree linear with temperature, LED display

Sighting: Projected reticle light spot with cross hairs (Option model LS15-1)

Sensor dimensions: 2.7"H x 4.0"W x Approx. 10"L including lens)

Price: \$3,625.00

Delivery: 4-6 weeks

## 4. Wahl

No proposal was received from Wahl. According to the Wahl catalog, the Model HSM674 with close focus option and 600-1 indicator appears to be the one most closely suited to your application. It has the following characteristics:

Temperature range: 400-3000°F.

Spot size: 0.046" at 4" working distance

Spectral range: 3.5 to 4.1um

Accuracy: + or - 1.0% of reading

Repeatability: + or - 0.5% of reading

Response time: 0.1 seconds

Outputs: 1 millivolt DC/ degree and 4-20 milliamps, linear with temperature, LED display

Sighting: Through-the-lens reflective with reticle.

Sensor dimensions: 3.25"H x 7.875"W x 10.5" long

Price: \$4,060.00

Delivery: 4-6 weeks

## 5. Williamson

The instrument quoted is the Model 4515C-F-FOVS. (There appears to be a slight error- the 4515C has the wrong temperature range according to the Williamson catalog. The 4515D has the range quoted.) The characteristics of the Model 4515D-F-FOVS are as follows:

Temperature range: 500-1500°F.

Spot size: 0.1" at 18" working distance

Spectral range: 5.1um

Accuracy: + or - 1.0% of reading

Readability: + or - 0.5% of reading

Outputs: Three DC outputs including 1 millivolt/degree linear, LED display

Sighting: See through, non-parallax

Sensor dimensions: 6"H x 3.875"W x 15" long

Price: \$4,500.00

Delivery: 5-6 weeks

# H Honeyhill Technical Co.

193 East Avenue, Norwalk, CT 06855

Telephone: (203) 838-8600

My recommendation is the Vanzetti Model TM2-A-1-F-3-0-E-00-00-00-OH15-4.5-75mm (Price \$3,185.00) with a Model LS15-1 Backlighting Source and OH15-0005-2 fiber optic projector (Price-\$340.00) which will will provide an illuminated projected aiming spot. Please note that this instrument is a direct measuring instrument and is not fiber optic coupled. Fiber optics do not transmit adequately at the 4.5um spectral range.

In addition, I recommend you purchase the calibration reference source, Model 1550H (Price-\$1,750.00) which will allow you to check the instrument calibration periodically to assure the validity of your data.

Although price was not a major consideration, the Vanzetti system is the least expensive of the five candidates

In terms of your application, this instrument meets the range and repeatability requirements, as do all the candidates. The spot size of 0.050" at 4" is compatible with your 0.156" aperture. Please be aware that the spot size is generally understood to mean that 85 to 90% of the energy at the target within that spot reaches the instrument. In our phone conversation, Mr. Jeff Davis of Vanzetti assured me that at least 99% of the energy in a 0.100" spot at the target would reach the instrument, thus assuring you that the 0.156" would result in no detectable aiming error.

The compact sensing head is an advantage to you since some of your future work may limit the space in which you may work. The 4.5um spectral range is far enough into the infrared to assure no interference from the quartz heater or from visible sources such as the projected aiming spot.

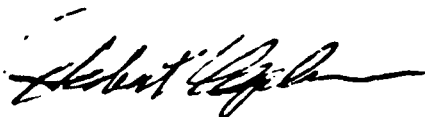
The deciding factor was the aiming system which no other candidate instrument offers. This projects a high intensity light beam with a darkened cross hair onto the target surface. This will allow you to aim and reaim without bending to sight through the instrument's optics, and will enable you to observe if, for any reason, the instrument becomes no longer aimed or focussed on the target.

The price of the recommended instrument comes to \$3,625.00 according to my calculations with an additional \$1,750.00 for the calibration source. I suggest you recheck model designation, price and delivery with the manufacturer prior to ordering.

Please don't hesitate to phone if you have any questions regarding this report.

Very truly yours,

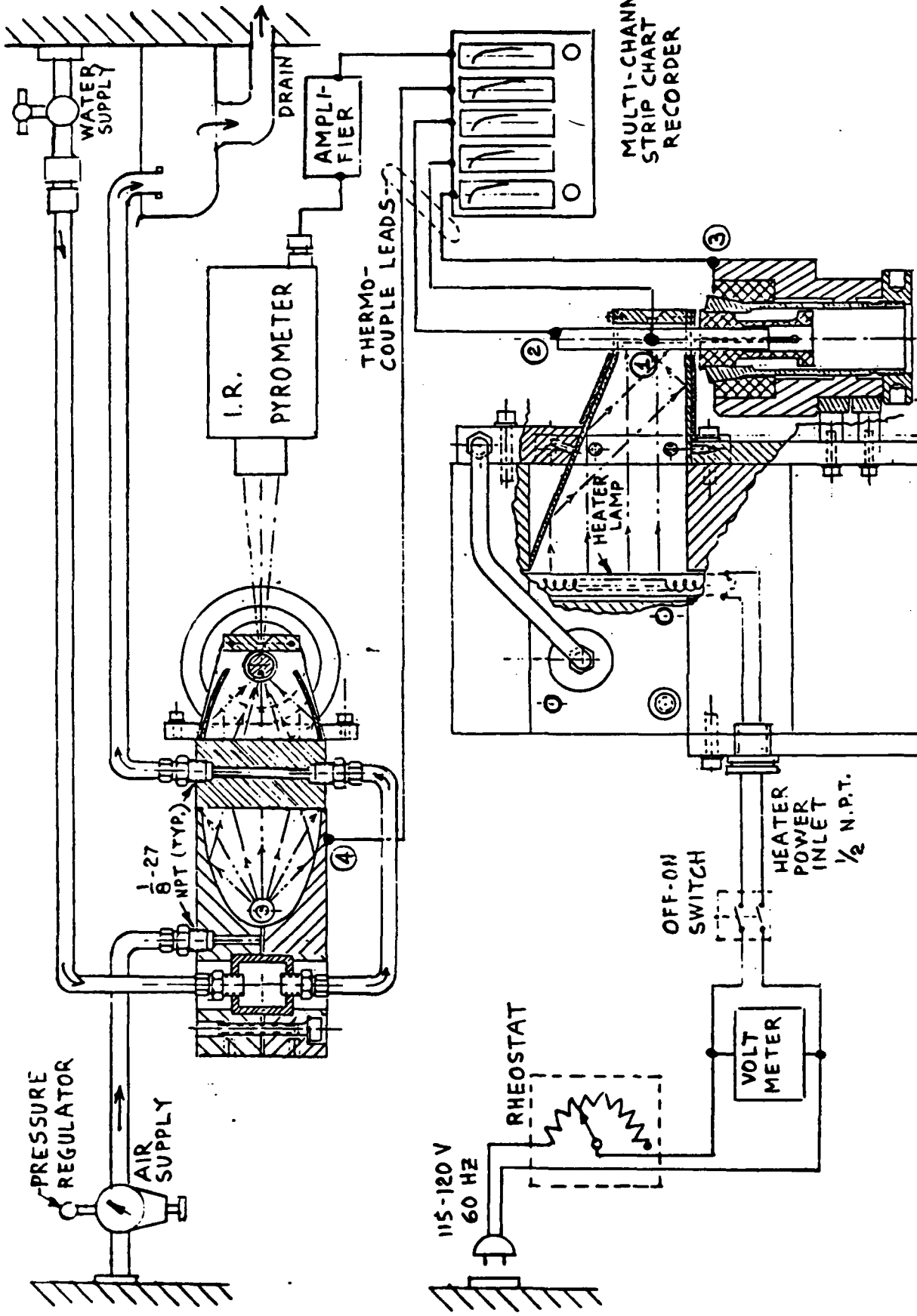
Honeyhill Technical Company



Herbert Kaplan, General Manager

enclosure

K-4



|                                                   |        |                                  |                 |
|---------------------------------------------------|--------|----------------------------------|-----------------|
| HUGHES AIRCRAFT COMPANY<br>EL SEGUNDO, CALIFORNIA |        | CONNECTION DIAGRAM, THERMAL TEST |                 |
| DR                                                | SIZE A | FSCM NO 82577                    | DWG NO FIGURE 2 |
| SCALE                                             |        | SHEET                            |                 |

K-5

## **APPENDIX L**

**PYROLASER Description and Specifications, Pyrometer Instrument Co.,  
Inc., Northvale, NJ, Tech. Bulletin**



THE PYROMETER INSTRUMENT CO., INC. • NORTHVALE, NEW JERSEY 07647

AREA CODE (201) 768-2000 • TWX (W.U.) 710-991-9611

**"PYRO-LASER" --- NEW PATENTED PYROMETER TECHNOLOGY**

The PYROLASER is an infrared radiation pyrometer which eliminates two major sources of error related to non-contact temperature measurements by introducing laser and micro-processor technology:

- The emissivity of radiating surfaces is precisely measured with a laser beam.
- Radiation from extraneous sources is measured and accounted for prior to use of Planck's equation calculations for True Temperature.

PYROLASER may be used as a portable instrument with internal data logger or on-line for computer process control.

Measured Parameters: Corrected Temperature, Uncorrected Temp., Emissivity & Distance

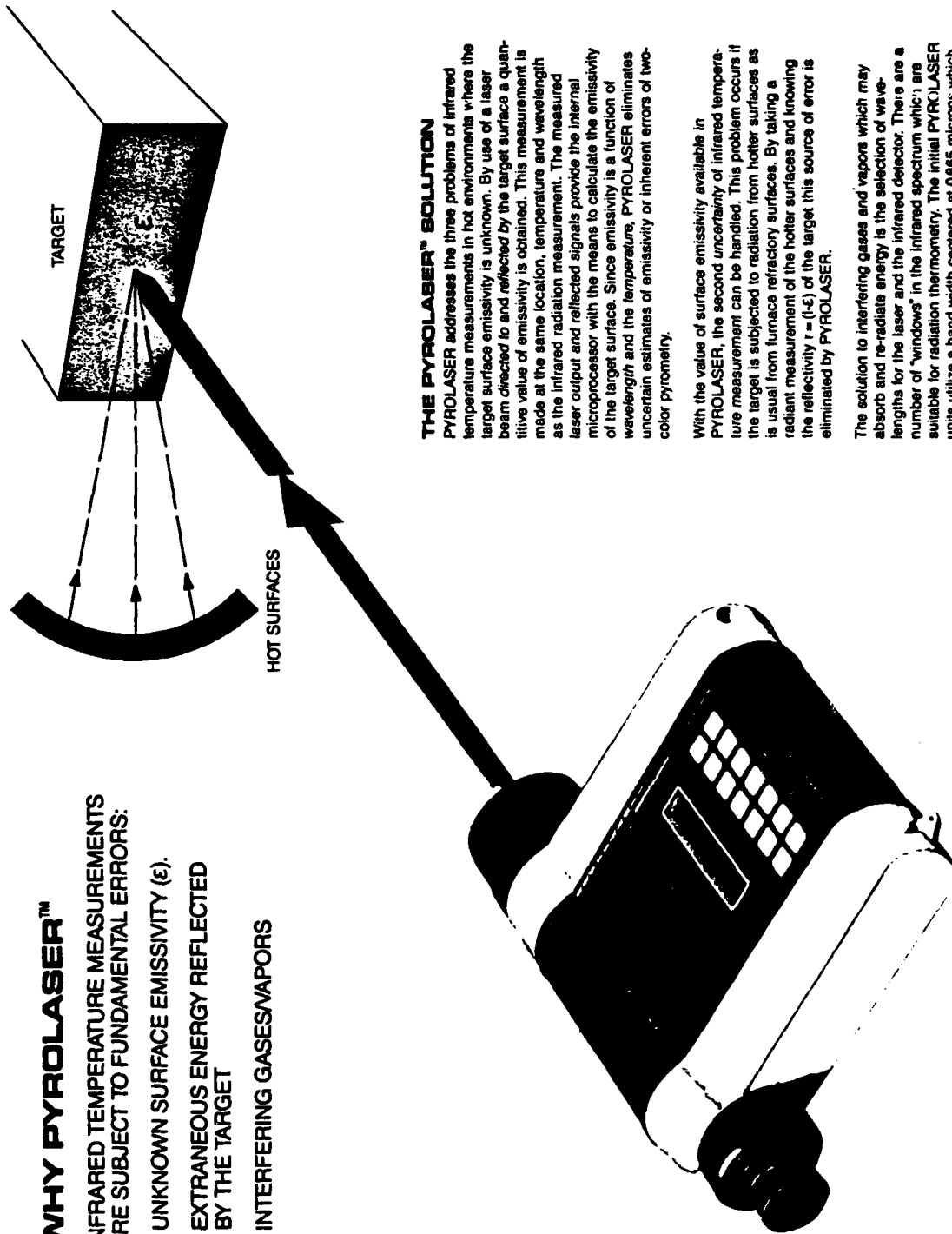
**LASER - PYROMETER - PRELIMINARY SPECS**

|                                              |                                                                                                                   |
|----------------------------------------------|-------------------------------------------------------------------------------------------------------------------|
| Temperature Range:                           | 600°C - 1500°C (1100 - 2730°F)                                                                                    |
| Resolution:                                  | 1°C (1°F)                                                                                                         |
| Accuracy:                                    | 3°C (5°F)                                                                                                         |
| Repeatability:                               | 1°C (1°F)                                                                                                         |
| Distance Range:                              | 2m - 10m (7 ft. - 33 ft.)                                                                                         |
| Emissivity Range:                            | 0.5 - 1.00                                                                                                        |
| LED Display in Viewfinder:                   | 4 digit LED corrected temperature                                                                                 |
| LCD Display:                                 | 40 character readout of: distance, emissivity, uncorrected temperature & corrected temperature                    |
| Operating Wavelength:                        | 0.865 microns $\pm$ 0.015                                                                                         |
| Visual Field of View:                        | 7°                                                                                                                |
| I.R. Measuring Field:                        | 1/3°                                                                                                              |
| Target Size:                                 | 1cm @ 2m (0.4" @ 7 ft.)                                                                                           |
| Acquisition Time:                            | 1s                                                                                                                |
| Samples/Measurement:                         | 900                                                                                                               |
| Storage Capacity:                            | 600 sets of measurements (time, location, distance, emissivity, uncorrected temperature, & corrected temperature) |
| Output:                                      | RS 232, baud rate selectable                                                                                      |
| Power Supply:                                | 2 x 9V rechargeable NiCd batteries                                                                                |
| Operating Time with Fully Charged Batteries: | 2h or 400 measurements                                                                                            |
| Operating Ambient Temperature:               | 0 to +50°C (32°F - 125°F)                                                                                         |
| Storage Temperature:                         | -20°C to +70°C (0 - 160°F)                                                                                        |
| Dimensions:                                  | 318 x 211 x 74mm (12 1/2 x 8 x 3")                                                                                |
| Weight with Batteries:                       | 3kg (6 lbs.)                                                                                                      |

## WHY PYROLASER™

INFRARED TEMPERATURE MEASUREMENTS ARE SUBJECT TO FUNDAMENTAL ERRORS:

- UNKNOWN SURFACE EMISSIVITY ( $\epsilon$ ).
- EXTRANEOUS ENERGY REFLECTED BY THE TARGET
- INTERFERING GASES/VAPORS



### THE PYROLASER™ SOLUTION

PYROLASER addresses the three problems of infrared temperature measurements in hot environments where the target surface emissivity is unknown. By use of a laser beam directed to and reflected by the target surface a quantitative value of emissivity is obtained. This measurement is made at the same location, temperature and wavelength as the infrared radiation measurement. The measured laser output and reflected signals provide the internal microprocessor with the means to calculate the emissivity of the target surface. Since emissivity is a function of wavelength and the temperature, PYROLASER eliminates uncertain estimates of emissivity or inherent errors of two-color pyrometry.

With the value of surface emissivity available in PYROLASER, the second uncertainty of infrared temperature measurement can be handled. This problem occurs if the target is subjected to radiation from hotter surfaces as is usual from furnace refractory surfaces. By taking a radiant measurement of the hotter surfaces and knowing the reflectivity  $r = (1-\epsilon)$  of the target this source of error is eliminated by PYROLASER.

The solution to interfering gases and vapors which may absorb and re-radiate energy is the selection of wavelengths for the laser and the infrared detector. There are a number of "windows" in the infrared spectrum which are suitable for radiation thermometry. The initial PYROLASER units utilize a band width centered at 0.865 microns which has been found effective in industrial applications.

### PYROLASER™ FEATURES

PYROLASER is designed for portable and On-Line infrared temperature measurement. The PYROLASER features of importance are—

**In View Display**—The operator will see the target and the target temperature.

**Data Notebook**—PYROLASER contains a microprocessor system which provides complete storage for up to 400 sets of radiation measurements. This eliminates the need for hand written or voice recorded data which is difficult to obtain in industrial applications and which requires subsequent rewriting. The information in the PYROLASER Notebook can be recalled via the keypad display or transmitted to (PC) or other computers with RS 232 compatibility. This includes date/time, location and all thermal data.

**Keypad Display**—The operator can see current as well as *all prior* information via the 'Recall' feature.

**Statistics**—The built-in microprocessor and the integral keyboard provide statistical evaluation of captured/stored data. For example, average emissivity over a surface. Peak, average, median & low temperature, etc.

**Process Control**—PYROLASER provides 0-5 volt output for use in process control systems. Continuous and/or self initiated data transmission plus alarm setting & triggering.

**Lightweight**—6.6 lbs. 3.0 kg

**Battery Life**—Two 9 volt rechargeable batteries providing 2.5 hrs. of continuous use. Battery condition and remaining usable battery time is displayed.

TRADEMARK OF PROMETTER INSTRUMENT CO., MANUFACTURED IN THE UNITED STATES  
DESIGNED AND DEVELOPED BY PROMETTER INSTRUMENT CO. RESEARCH AND ENGINEERING DEPARTMENT  
NEW JERSEY 07041





### THE LEADER IN NON-CONTACT TEMPERATURE MEASUREMENT

- **ThermaTrace®**—Provides visual and photo record of target temperature profile. Widely used for electrical and machinery inspection.
- **Instatherm®**—Portable analog or digital instrument for field/plant non-contact temperatures. Audio-output. Low cost.
- **PRT-5**—Precision I.R. system for environmental atmospheric/oceanic applications including aircraft surveying, forest fire and fish locating.
- **Optitherm II®**—On-line unit widely used in metals/plastics/ceramics/food/glass industries. Output 4-20 mA and 1 millivolt.
- **Photo II®**—Precision automatic optical Pyrometer. (760-10,000C)
- **Temp-Shooter I/II®**—Portable, digital and analog instruments covering (–40 to 3200F) ranges.
- **Micro-Optical**—Precision laboratory instrument (700-10,000C) ranges.



**PYROMETER INSTRUMENT CO., INC.**  
 234 Industrial Parkway, P.O. Box 174  
 Northvale, New Jersey 07647  
 (201) 768-2000(800) HOT PYRO  
 (800) 792- PYRO (NJ)  
 TWX (WU) 710-991-9611  
 FACS 201-768-2570

### PYROLASER™ SPECIFICATIONS

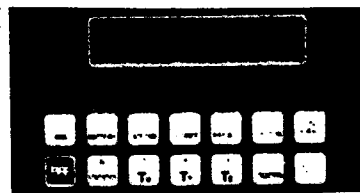
|                                                      |                                                        |
|------------------------------------------------------|--------------------------------------------------------|
| Temperature Range:<br>600°C-1500°C<br>(1100-2730°F)  | Emissivity Range:<br>0.45-1.0                          |
| Accuracy:<br>3°C (5°F)                               | Repeatability:<br>1°C (1°F)                            |
| Distance Range:<br>2m-10m (7 ft.-33 ft.)             | Target Size:<br>1 cm @ 2m<br>(0.4" @ 7 ft.)            |
| Operating Wavelength:<br>0.865 microns ±0.015        | Output:<br>RS 232, baud<br>rate selectable<br>0-5 VOLT |
| Acquisition Time:<br>1 second                        |                                                        |
| Power Supply:<br>2 x 9V rechar.<br>NiCd batteries    | Weight with batteries:<br>3 kg (6.6 lbs.)              |
| Dimensions:<br>318 x 211 x 74mm<br>(12 1/2 x 8 x 3") |                                                        |

#### Keypad Display

- Distance
- Emissivity
- Apparent Temperature
- True Temperature
- Target Identification

#### Int View Display

- Field of View (7°)
- Target fills inner reticle (1/5°)
- Temperature °F or °C



#### Operator Keypad

- Target Identification
- Numeric Data Entry
- Focus and Fire
- Set Values
- Select Mode(s)
- Data Recall
- Operation Functions
- Computer Functions: erase, baud rate, units selected, alarm limits set
- Statistics

## APPENDIX M

W.O. Winer, "Tester 2A," technical letter to M.N. Gardos (Hughes) from the Georgia Institute of Technology, 13 April 1987



GEORGIA TECH 1885-1985

DESIGNING TOMORROW TODAY

THE GEORGE W. WOODRUFF SCHOOL OF  
MECHANICAL ENGINEERING

April 13, 1987

Mr. Michael N. Gardos  
Program Manager  
Technology Support Division  
Hughes Aircraft Company  
P.O. 902 - Bldg. E1  
Mail Stop F 150  
El Segundo, California 90245

Dear Mike:

Re: Hughes Tester 2A

I enjoyed the meeting last week and was pleased we were able to be of assistance to Leo. There are two aspects of the Tester 2A which I would like to further comment on. These are (a) the friction measurement and (b) the IR surface temperature measurement.

- (a) The friction measurement: Leo understood our criticism that as wear takes place the measured forces are no longer what you think they are. However, if I understood Leo's talk correctly, I don't agree with his solution. He seemed to imply that he knew where the real contact point is in the apparent contact as wear proceeds, and therefore could, through straightforward vector analysis relate the real normal and friction forces to the two measured forces. I disagree with the assumption that you know where the real point of contact is. It is our experience that the real area of contact jumps unpredictably around in the apparent area of contact. If you don't know where the contact point is the analysis can only predict the bound on a range of values; e.g., when the real area of contact is at one extreme position or the other. You have no way of knowing where it is in that range and therefore no way of knowing the relationship of the measured forces to the real contact normal and friction forces, and therefore no way of knowing the actual coefficient of friction.

M-1

Georgia Institute of Technology  
Atlanta, Georgia 30332-0405

I have attached two sheets showing the analysis and a plot of the relationship of the band of "measured coefficient of friction" as a function of real coefficient of friction and wear depth. I predict what you will observe in an experiment as wear progresses is first a well-behaved friction coefficient and then as wear depth increases you will get an even widening band of fluctuation of "measured coefficient of friction" as a result of the real location of contact jumping around in the apparent area of contact (e.g., wear groove). The only solution I can see at this time is to restrict your friction measurements to periods where the wear is less than some small value, say  $10^{-3}$  inches.

Incidentally the flexibility of your load cells aggravates the problem but stiffer load cells probably would not eliminate it.

I have attached a couple of our reprints on hotspots only to document and remind you of how unpredictable they are.

- (b) IR Surface Temperature Measurement: After seeing your rig and hearing you and Leo discussing it my suggestion is simply to abandon this measurement. If you get the new sensor and make all the corrections necessary to your satisfaction (which I doubt you can) you will at best be measuring the cylinder bulk temperature. The route you are taking involves uncertainties and aggravation totally out of proportion with the best possible outcome.

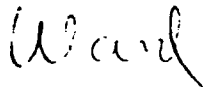
We have done a lot of analysis and experimental work with hotspots and surface temperature. Source reprints to support my comments are attached. Both experiment and analysis indicate that when you get 3 to 4 hotspot diameters away from the hotspot itself the surface temperature is essentially that of the bulk specimen. Typical hotspot diameters are 50 to 100 micrometers so by the time the surface passes out of the apparent area where you can see the surface, the temperature is essentially the bulk temperature. In addition your detector spot size is much bigger than any hotspot is expected to be and you have the background radiation problem from your heaters. If in the long run the best you can expect to do is measure the bulk specimen temperature, don't fight it, don't buy more detectors,

abandon this method for an easier one to measure the bulk temperature.

I recommend fabricating a cap to slip over the exposed end of the RCF rod. The cap should be thermally insulated and result in a black body cavity at the end of the rod. Put a hole in the cap at the axis of rotation and either use your current IR detector to measure the radiation out of the hole (note the emissivity will be one and the temperature the bulk RCF specimen temperature) or put a non-rotating thermocouple or thermistor in the hole to measure the cavity temperature. This is much simpler and more reliable. There will be a time lag associated with thermal transients but it can be calculated. I don't believe this lag would be a problem in any of the work I have heard you propose.

If you would like to discuss these comments further, give me a call.

Sincerely yours,



Ward O. Winer  
Regents' Professor

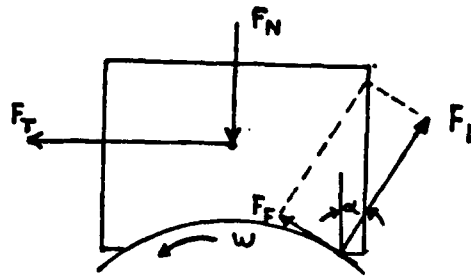
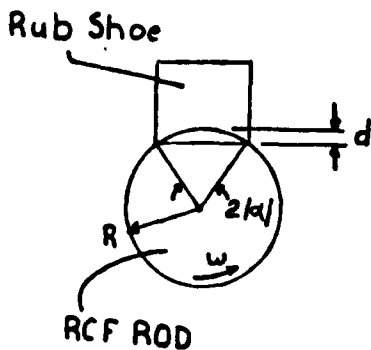
WOW/kf

Attachments

xc: without attachments  
Leo Fiderer

April 10, 1987  
P 1/2

# Hughes Rig Friction Measurement, Tester 2A



$$\cos \alpha = \frac{R-d}{R}$$

$$1 - \frac{d^2}{2R^2} \approx 1 - \frac{d}{R}$$

$$\alpha \approx \left(\frac{2d}{R}\right)^{1/2}$$

$$R = .188'' \text{ for } d = .005''$$

$$-.23 < \alpha < .23 \text{ rad}$$

$F_N, F_T$  are measured forces

$F_L$  actual contact normal force

$F_F$  actual contact friction force

$C_{FM} = \frac{F_T}{F_N}$  measured coefficient of friction

$C_{FA} = \frac{F_F}{F_L}$  actual coefficient of friction

$d$  wear depth

$$F_N = F_L \cos \alpha + F_F \sin \alpha$$

1a

$$F_T = F_F \cos \alpha - F_L \sin \alpha$$

1b

for small  $\alpha$ , a first order approximation is used

$$F_N = F_L + C_{FA} F_L \alpha = F_L (1 + C_{FA} \alpha)$$

2a

$$F_T = C_{FM} F_N = C_{FA} F_L - F_L \alpha = F_L (C_{FA} - \alpha)$$

2b

Therefore, from 2a and 2b,

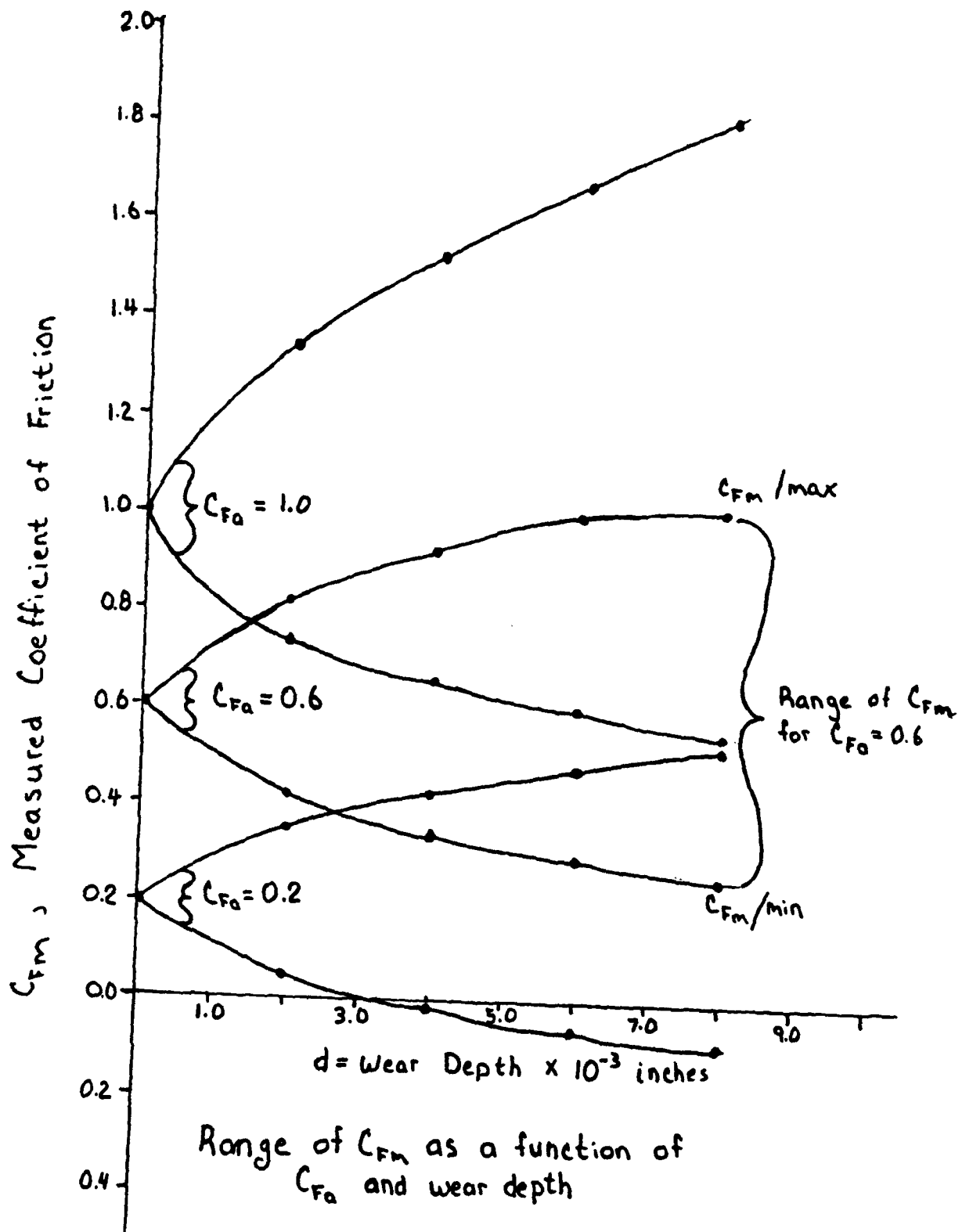
$$C_{FM} (1 + C_{FA} \alpha) = C_{FA} - \alpha$$

$$C_{FM} + C_{FM} C_{FA} \alpha = C_{FA} - \alpha$$

$$C_{FA} (1 - C_{FM} \alpha) = C_{FM} + \alpha$$

$$C_{FA} = \frac{C_{FM} + \alpha}{1 - C_{FM} \alpha}$$

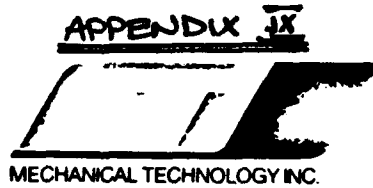
$$\text{Similarly } C_{FM} = \frac{C_{FA} - \alpha}{1 + \alpha C_{FA}}$$



## **APPENDIX N**

**H. Heshmat, "rotor and Structural Dynamic Analysis and Assessment of Hughes Tribotester 2A," Technical Report, Mechanical Technology, Inc., Latham, NY, Hughes P.O. S9-266415-S7H**





July 27, 1987

Mr. Michael N. Gardos  
Program Manager  
Hughes Aircraft Company  
Bldg. E1, M.S. F150  
P.O. Box 902  
2000 East El Segundo Blvd.  
El Segundo, CA 90245

Subject: Technical Report on Assessment of the Hughes Tribotester 2A

Reference: 1) Task 3, Req. No. 324633; 18 Feb. 7  
2) Hughes Drawings No. SP 51952 (3 sheets)

Dear Mike:

Pursuant to the reporting requirements of the subject matter, attached is the letter type report covering work performed under the program. I hope this report meets your needs. If I can be of further assistance, or if you need any further information, please let me know.

Very truly yours,



Hooshang Heshmat  
Sr. Project Engineer

cc: J. Dill

Enclosures  
/am

N-1

## ROTOR AND STRUCTURAL DYNAMIC ANALYSIS AND ASSESSMENT OF HUGHES TRIBOTESTER 2A

Based on an overall review of the assembly drawing (Reference 2), critical components were identified which might have an effect on the operation of the test rig. It appeared that there are three major items that must be given focused attention:

1. Dynamic force due to runout of the rotating rod specimen
2. Load and coefficient of friction measurements and their interlocking relationship with Item No. 1.
3. Wear measurements, their accuracy and interlocking relationship with Item No. 1

### APPROACH

The loader arm was decoupled from the spindle in order to conduct a first order analysis (see Figure 1 of Attachment 1). A small (0.1 mill) eccentric orbital motion due to runout of the rotating rod specimen was assigned to the contact end of the arm. If it is assumed that the rotating rod is very rigid and does not undergo any displacement or deflection due to static or dynamic loading of the arm (see details in Attachment 1) results of this analysis indicate that a dynamic load in addition to the applied load exists and is a function of the moment of inertia of the arm, the level of out of roundness of the rotating specimen and is proportional to the square of rotational speed. Since the dynamic load  $f_d$  is cyclic, each arm introduces  $f_d$  to the rotating specimen. Calculation of the rotor angular stiffness based on the simple spindle model shown in Figure 2 indicates that the rotor undergoes an additional displacement at the contact point of the same order of magnitude as the mechanical runout assigned to the loader arm. This displacement exaggerates the dynamic loading on the test specimens.

Therefore, it was decided to utilize three level finite element analytical tools for rotordynamic analysis. Figure 3 shows a schematic drawing of the Hughes tribotester 2A model. As seen in the model, loader arms are coupled with rotating specimens via Hertzian contact stiffnesses  $K$ . In other words, loader arms can be assumed as a lumped mass at the end of the spindle rotor. Proper stiffnesses were assigned to the rotor bearings and to the pivot bearings of the arm as well as loader springs (details of the model are given in Attachment 2). The range of contact stiffness  $K$  was evaluated based on pin and rotating specimen geometries and physical properties of specimens. The results of evaluations of twenty combinations of spherical and flat surfaces in contact with cylindrical specimen under various static loads are given in Table 1. Detailed input and output to the MTI EHD computer program is given in Attachment 3. The average  $K$ 's from Table 1 were used in the dynamic model.

The result of dynamic analysis indicated that the first natural frequency of the system appeared to be occurring at 14710. rpm dominated by rotor motion and two others at 24460, 30131 rpm and so on. The second natural frequency of the system 24460 rpm was dominated by the loader arm motion. The loader arm up to the second natural frequency of the system was following closely the rotating specimen (in-phase). However, beyond this speed the motion of the loader arm was not in phase with the motion of the rotor. Figure 4 shows rotor and structural dynamic mode shape at the first critical speed. As seen in this figure, rotor displacement mode dominates the system mode. Where as in Figure 5 (plots of mode shape at the second critical speed) the loader arm dominates the systems dynamic motion.

A parametric study was conducted based on the described finite element model of the system to identify dynamic loads on the test specimen at various operating conditions for various eccentricity levels. It should be mentioned that a very conservative runout condition was assumed here (i.e., perfect circular eccentric motion). For instance, if the shape of the rotating specimen was assumed to be elliptical at the contact region, then the assigned frequency  $\omega$  would be doubled for a given operating rotational frequency, thus, resulting dynamic forces would increase by a factor of  $\omega^2$ . Also, system response as well as mode shape could be totally different than that presented here.

Since the analytical prediction indicated that the first critical speed occurs at 14710 rpm, dynamic forces as a function of rotor speed analysis was limited to 12000 rpm, and rotor eccentricity values of 0.1 mil up to 1.0 mill was considered. Corresponding maximum dynamic load versus speed are given in Table 2 and Figure 6. From the plots of Figure 6 it can be concluded that the test load variation is insignificant at very low speeds for small runouts. However, dynamic load increased exponentially, as rotor speed increased. To explore the effect of dynamic load furthermore Figure 7 is given with related analytical derivations. In Figure 7,  $R_y$  and  $R_x$  is the force vectors that the test instruments will be recording at the pivot bearing locations of the loading arm. Since dynamic load is superimposed (see sketch of Table 2) over static load (applied test load), therefore, coefficient of friction of particular test specimens of interest seem to be a complex function of static and dynamic loads. Although, it is assumed that the dynamic coefficient of friction is equal to the static coefficient of friction, in these derivations. In order to minimize drastic variation of coefficient of friction for any given test run it is recommended to maintain rotating test specimen runout to its lowest value as much as possible and also test speed should be limited to 3000 rpm. It should be noted that, the test speed based on this analysis is not limited by the natural frequency of the leader arms but however, it should be limited based on excessive dynamic forces.

#### WEAR MEASUREMENTS WITH BENTLEY NEVADA PROBE

As shown in the dynamic analysis, distant probes output if indicates same dynamic components, they should not be filtered out as a parasite noise. Instead, they should be thoroughly evaluated in connection with dynamic loads if there exists such loads during test operations. In addition to wear depth and dynamic motion of loader arms, it should be kept in mind that thermal expansion of the components is function of test period and will effect the accuracy of the probe readings. It is strongly recommended to install a thermocouple closer to the tip of the probes in order to correct probe output versus ambient temperature, because, these probe outputs are sensitive to the ambient temperature. Good calibration of the probe versus ambient temperature would be extremely helpful to this project endeavor.

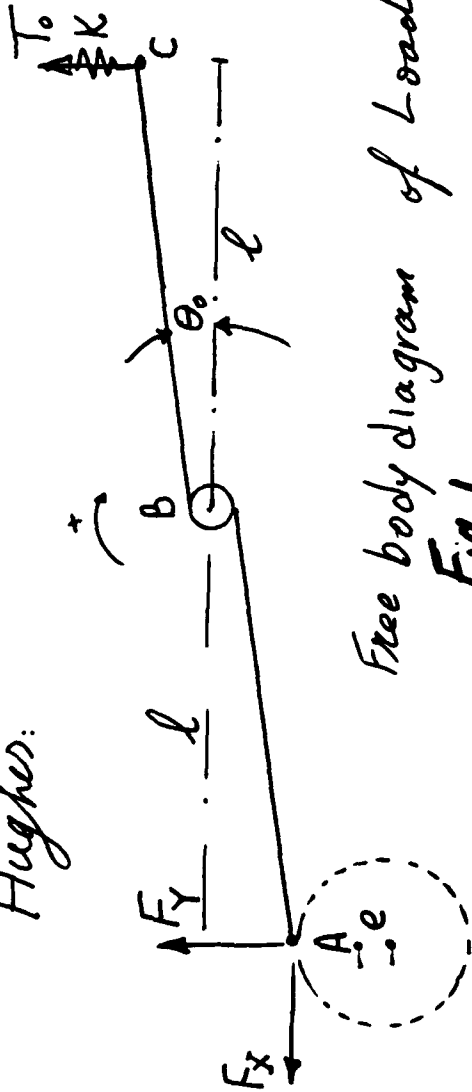
ATTACHMENT 1

ANALYTICAL MODEL OF LOADER ARM OF HUGHES TRIBOTESTER 2A

N-5

# Analytical Model of Loader Arm of Trikotester 2A

Hughes:



Free body diagram of Loader Arm.  
Fig. 1.

2-6

$$\text{Mom. @ B} = I_B \ddot{\theta}$$

$$\sum M @ B = -(F_y + f_y \sin \omega t) l -$$

$$\mu (F_y + f_y \sin \omega t) \theta_0 l +$$

$$(T_0 + K l \theta_0 \sin \omega t) l = I_B \ddot{\theta}$$

MECHANICAL TECHNOLOGY INCORPORATED  
7-12

$$F_y = F_y + f_y \sin \omega t$$

$$F_x = (F_y + f_y \sin \omega t) \mu$$

$$T_0 = \text{Preload}$$

$$W_{rad} = 6.4 \text{ lbs}$$

$$K \approx 10. \text{ lb/in}$$

$$I_B = 0.501 \text{ lb-in}^2$$

$$L = l \theta_0$$

$$\text{Spring Force} = T$$

$$T = T_0 + K e$$

# Analytical Model ... Continued

•  $I_B \ddot{\theta} = I_B \omega^2 \theta_0 \sin \omega t$  for assumed  $\theta_0 \sin \omega t$  motion.

Subs. & solve for dynamic force.  $f_y$

$$[-\mu (F_y + f_y \sin \omega t) \theta_0 l] - l f_y \sin \omega t = -K l^2 \theta_0 \sin \omega t - I_B \omega^2 \theta_0 \sin \omega t$$

$[I]$

Let  $[I]$  by virtue of order of magnitude to be zero.

$$f_y = \frac{I_B \omega^2 e}{l^2} + K e$$

eq 1



showing:

$$f_y (1 - e) = \left( \frac{I_B \omega^2}{l^2} + K + \frac{\mu F_y}{S_{in wt}} \right) l \quad \text{eq. 2}$$

limit  $l \rightarrow 0$  faster than  $S_{in wt} \rightarrow 0$ .

$S_{in wt} \rightarrow 1$  where  $l \rightarrow 0$

2-1-80

Subs. num. values.  $\omega = 12000 \text{ rpm}$ ,  $e = 0.1 \text{ MIL}$

$f_y$  from eq. Dia 0.79 lbs & from eq 2 yields 0.79 lbf



# Hughes Tester 2A Spindal Model

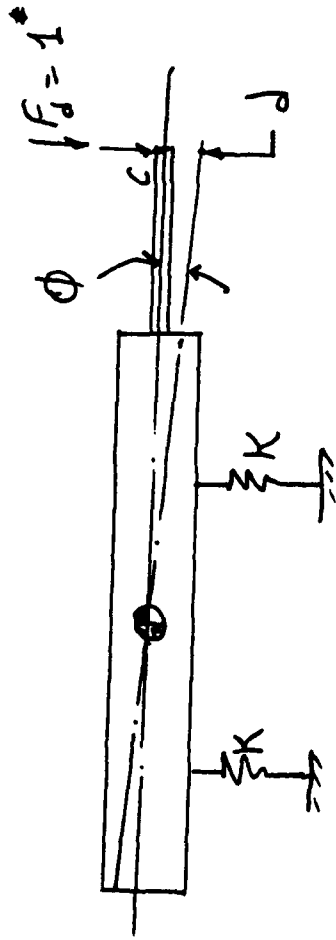


Fig. 2

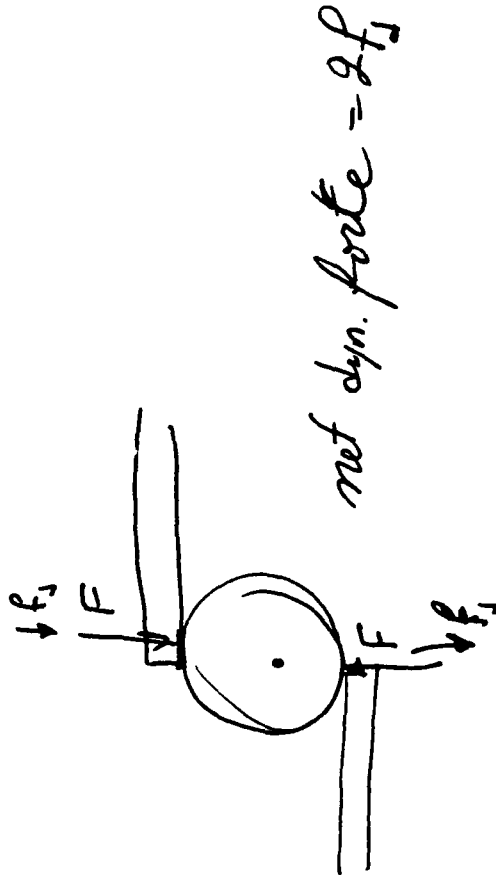
$$d \approx 20\phi = 25 \times 10^{-6} \text{ in/b}_5$$

Corresponds to 1 # of  $F_2$

1# force on the shaft at point of contact introduces 25  $\mu\text{in}$  displacement  
 Since there is two arms 2# each will be net load of 4 #

and  $4 \times 25 \mu\text{in} = 100 \mu\text{in}$

Since arm must follow the shaft  
 Do C can be considered  $2 \times 100$



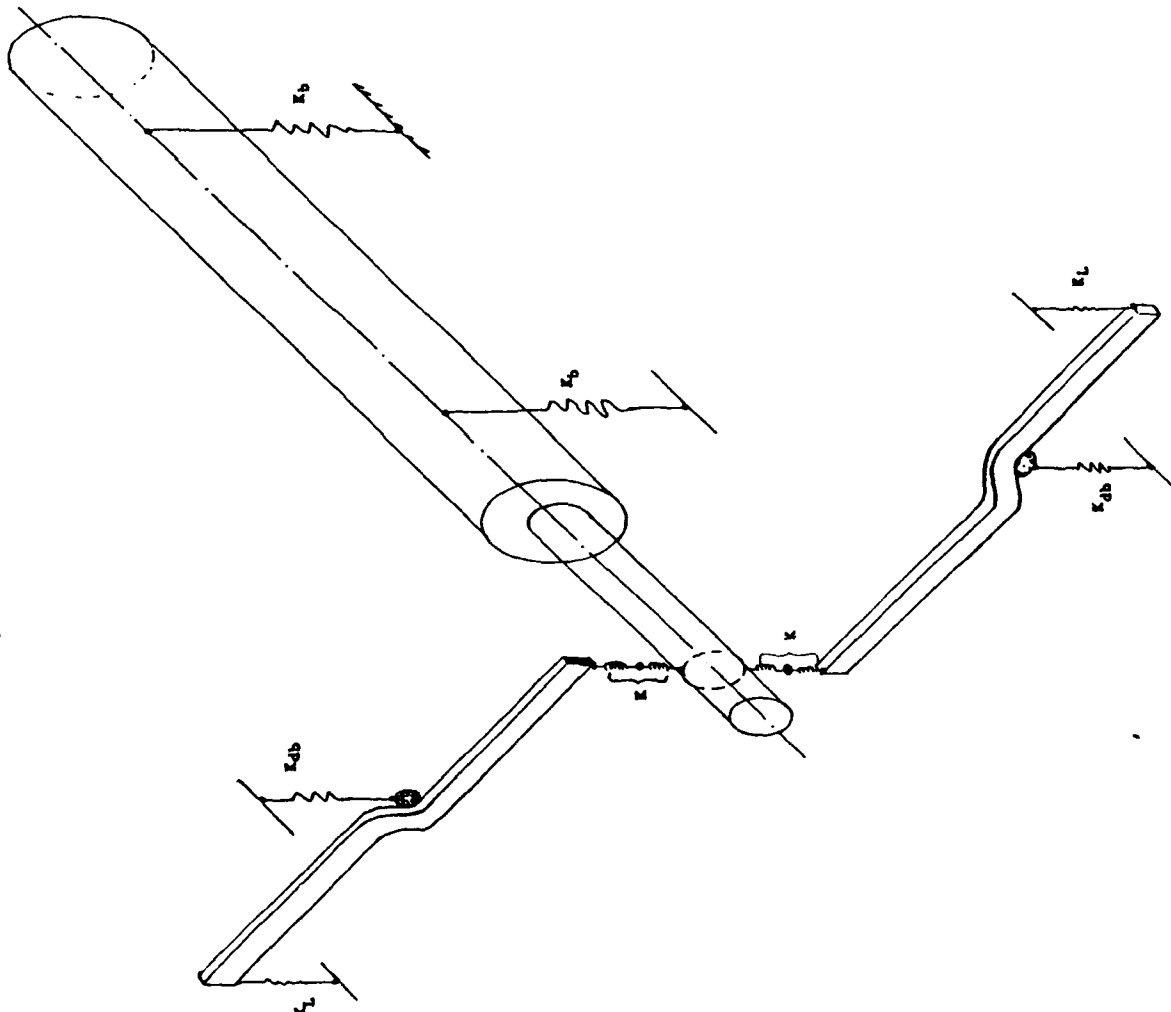


Fig. 3

HUGHES TRIBOTESTER ROTOR AND STRUCTURAL DYNAMIC MODEL

$k_b$  = rotor bearings stiffness (300K)

$k$  = contact hertz stiffness

$k_{db}$  = loading arm bearing stiffness

$k_L$  = loader spring stiffness

TABLE 1 Evaluation of Spherical "S" and Flat "F" Contact  
Surface With Cylindrical "C" Specimen and Static Load

| Case # | $\frac{E_1}{E_2}$<br>(PSI) $\times 10^6$ | $\frac{R_1}{R_2}$      | $\frac{CR_1}{CR_2}$     | Contact <sup>(1)</sup><br>Config. | *P | $\frac{D}{d}$<br>(Mil) | HPmax<br>(PSI) $\times 10^3$ | ( $\mu$ in) | K**<br>(lb <sub>in</sub> or lb <sub>in</sub> <sup>2</sup> ) $\times 10^6$ |
|--------|------------------------------------------|------------------------|-------------------------|-----------------------------------|----|------------------------|------------------------------|-------------|---------------------------------------------------------------------------|
| 1      | $\frac{40}{40}$                          | $\frac{0.375}{0.25}$   | $\frac{\infty}{0.25}$   | $\frac{C}{S}$                     | 4  | $\frac{3.5}{2.5}$      | 215                          | 46          | 0.13                                                                      |
| 2      | $\frac{40}{40}$                          | $\frac{0.375}{0.25}$   | $\frac{\infty}{0.25}$   | $\frac{C}{S}$                     | 5  | $\frac{3.8}{2.7}$      | 231                          | 54          | 0.14                                                                      |
| 3      | $\frac{40}{40}$                          | $\frac{0.375}{0.25}$   | $\frac{\infty}{0.25}$   | $\frac{C}{S}$                     | 6  | $\frac{4.1}{2.9}$      | 246                          | 61          | 0.15                                                                      |
| 4      | $\frac{50}{50}$                          | $\frac{0.375}{0.25}$   | $\frac{\infty}{0.25}$   | $\frac{C}{S}$                     | 3  | $\frac{3.0}{2.1}$      | 226                          | 32          | 0.14                                                                      |
| 5      | $\frac{50}{50}$                          | $\frac{0.375}{0.25}$   | $\frac{\infty}{0.25}$   | $\frac{C}{S}$                     | 4  | $\frac{3.3}{2.3}$      | 249                          | 40          | 0.15                                                                      |
| 6      | $\frac{50}{50}$                          | $\frac{0.375}{0.25}$   | $\frac{\infty}{0.25}$   | $\frac{C}{S}$                     | 5  | $\frac{3.5}{2.5}$      | 268                          | 46          | 0.16                                                                      |
| 7      | $\frac{60}{60}$                          | $\frac{0.375}{0.25}$   | $\frac{\infty}{0.25}$   | $\frac{C}{S}$                     | 5  | $\frac{3.3}{2.4}$      | 303                          | 41          | 0.18                                                                      |
| 8      | $\frac{60}{60}$                          | $\frac{0.375}{0.25}$   | $\frac{\infty}{0.25}$   | $\frac{C}{S}$                     | 4  | $\frac{3.1}{2.2}$      | 281                          | 35          | 0.17                                                                      |
| 9      | $\frac{60}{60}$                          | $\frac{0.375}{0.25}$   | $\frac{\infty}{0.25}$   | $\frac{C}{S}$                     | 3  | $\frac{2.8}{2.0}$      | 255                          | 29          | 0.15                                                                      |
| 10     | $\frac{80}{60}$                          | $\frac{0.375}{0.25}$   | $\frac{\infty}{0.25}$   | $\frac{C}{S}$                     | 3  | $\frac{2.7}{1.9}$      | 279                          | 26          | 0.17 +                                                                    |
| 11     | $\frac{80}{60}$                          | $\frac{0.375}{\infty}$ | $\frac{\infty}{\infty}$ | $\frac{C}{F}$                     | 8  | $\frac{-}{0.32}$       | 15.9                         | 0.7         | 13.5/5.1                                                                  |
| 12     | $\frac{40}{40}$                          | $\frac{0.375}{\infty}$ | $\frac{\infty}{\infty}$ | $\frac{C}{F}$                     | 8  | $\frac{-}{0.42}$       | 12.1                         | 1.1         | 7.9/2.96                                                                  |
| 13     | $\frac{40}{40}$                          | $\frac{0.375}{\infty}$ | $\frac{\infty}{\infty}$ | $\frac{C}{F}$                     | 11 | $\frac{-}{0.49}$       | 14.2                         | 1.5         | 8.2/3.1                                                                   |
| 14     | $\frac{40}{40}$                          | $\frac{0.375}{\infty}$ | $\frac{\infty}{\infty}$ | $\frac{C}{F}$                     | 13 | $\frac{-}{.53}$        | 15.4                         | 1.7         | 8.4/3.2                                                                   |
| 15     | $\frac{50}{50}$                          | $\frac{0.375}{\infty}$ | $\frac{\infty}{\infty}$ | $\frac{C}{F}$                     | 13 | $\frac{-}{.48}$        | 17.3                         | 1.4         | 10.2/3.83                                                                 |
| 16     | $\frac{50}{50}$                          | $\frac{0.375}{\infty}$ | $\frac{\infty}{\infty}$ | $\frac{C}{F}$                     | 11 | $\frac{-}{.44}$        | 15.9                         | 1.2         | 10/3.75                                                                   |
| 17     | $\frac{50}{50}$                          | $\frac{0.375}{\infty}$ | $\frac{\infty}{\infty}$ | $\frac{C}{F}$                     | 8  | $\frac{-}{.38}$        | 13.6                         | 0.9         | 9.6/3.6                                                                   |
| 18     | $\frac{60}{60}$                          | $\frac{0.375}{\infty}$ | $\frac{\infty}{\infty}$ | $\frac{C}{F}$                     | 8  | $\frac{-}{.34}$        | 14.9                         | 0.8         | 11.3/4.24                                                                 |
| 19     | $\frac{60}{60}$                          | $\frac{0.375}{\infty}$ | $\frac{\infty}{\infty}$ | $\frac{C}{F}$                     | 11 | $\frac{-}{0.4}$        | 17.4                         | 1.0         | 11.8/4.43                                                                 |
| 20     | $\frac{60}{60}$                          | $\frac{0.375}{\infty}$ | $\frac{\infty}{\infty}$ | $\frac{C}{F}$                     | 13 | $\frac{-}{0.44}$       | 18.9                         | 1.2         | 12.0/4.5 ++                                                               |

\* -  $P = \frac{W}{L} = \frac{3}{.375} = 8 \text{ lb/in contact}$

\* -  $P = W \dots \text{in} \dots \text{lb} \dots \text{point contact}$

\*\* - line contact —  $K(\text{psi}) \times L = \text{lb/in}$ ,  $L = .375 \text{ in}$ .

+ -  $K_{\text{avg}}$  for point contact =  $155 \times 10^3 \text{ lb/in}$

++ -  $K_{\text{avg}}$  for line contact =  $4191 \times 10^3 \text{ lb/in}$

(1) F = Flat

S = Spherical

C = Cylindrical

N-11

FIG. 4 HUGHES TRIBOTESTER — MODE SHAPE OF THE FIRST CRITICAL SPEED

|              |              |            |       |       |             |
|--------------|--------------|------------|-------|-------|-------------|
| SYSTEM COND. | 1            | SPIN SPEED | LEVEL | LEVEL | DRIVE-SHAFT |
| MODE NUMBER  | 1            | RATIO      | 1     | 2     | BEAM ONE    |
| NATURAL FREQ | 14710.00 RPM |            | 2     | 3     | BEAM TWO    |
|              |              |            | 3     |       |             |

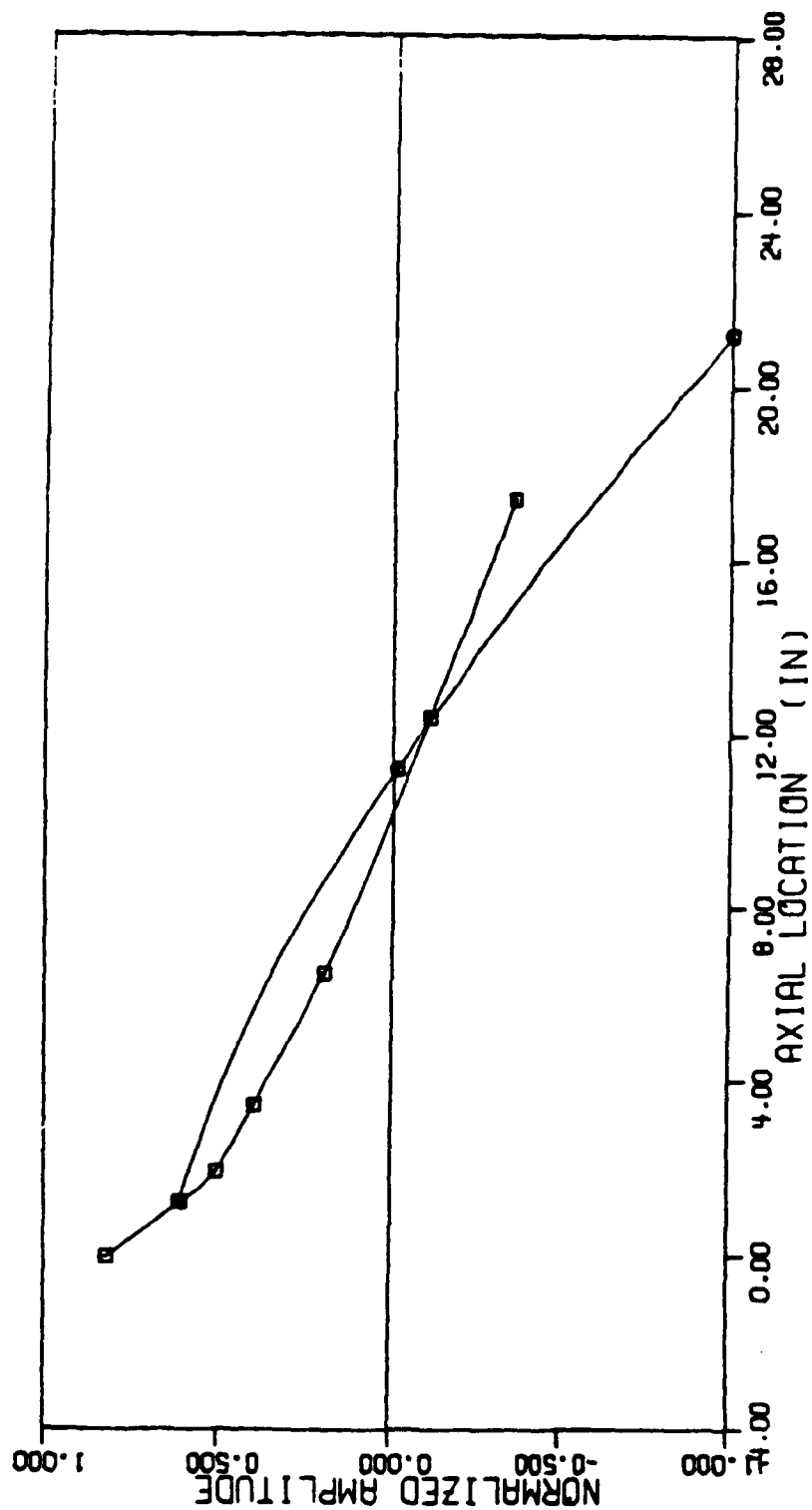


FIG. 5 HUGHES TRIBOTESTER - MODE SHAPE AT SECOND CRITICAL SPEED

|              |              |             |       |       |   |             |   |
|--------------|--------------|-------------|-------|-------|---|-------------|---|
| SYSTEM COND. | 1            | MSPIN SPEED |       | LEVEL | 1 | DRIVE-SHAFT | □ |
| MODE NUMBER  | 2            | LEVEL       | RATIO | 2     | 2 | BEAM ONE    | ○ |
| NATURAL FREQ | 24460.00 RPM | 3           | 0.00  | 3     | 3 | BEAM TWO    | △ |

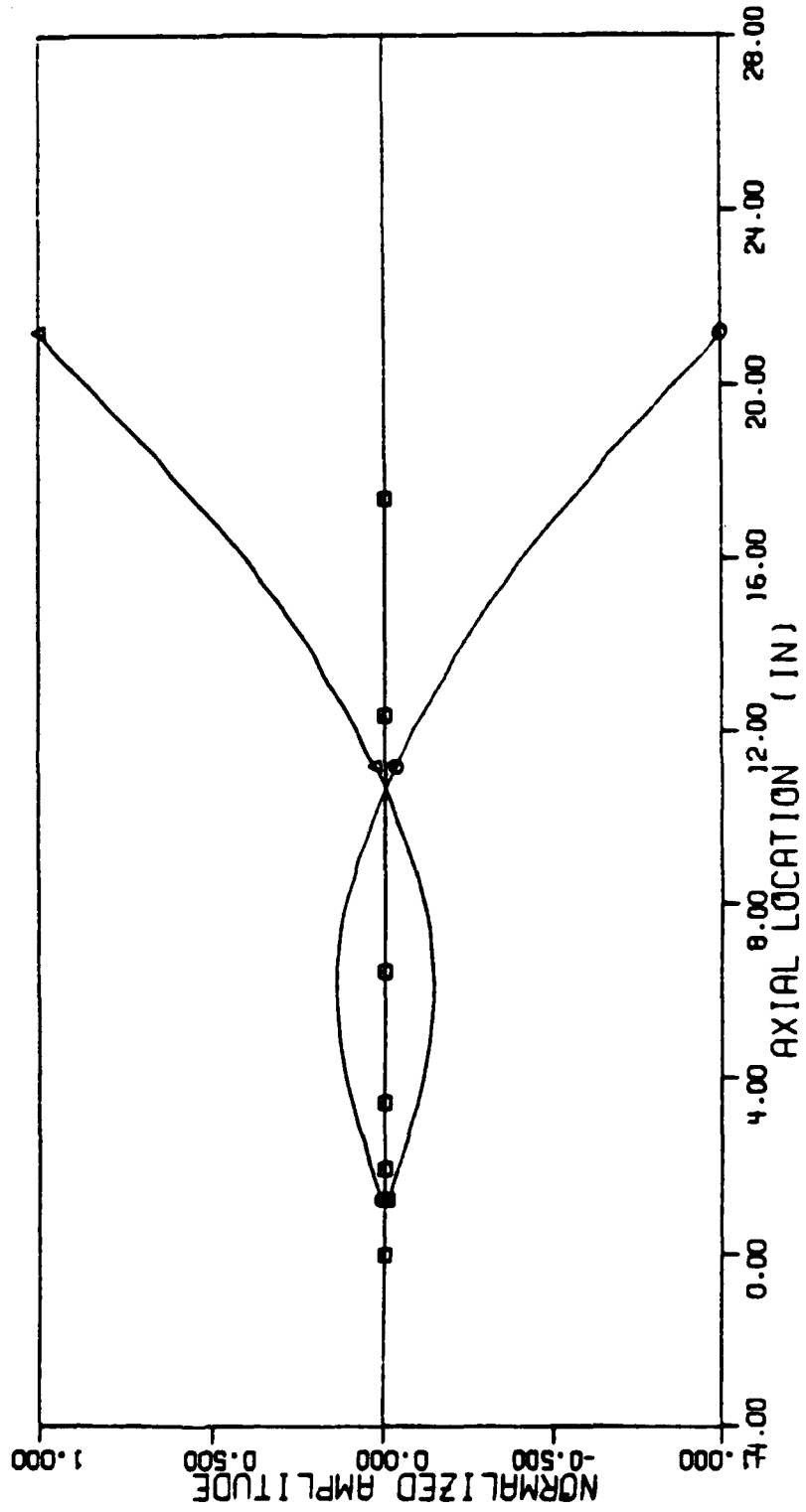


TABLE 2

HUGHES TRIBOTESTER  
 ROTOR AND STRUCTURAL DYNAMIC ANALYSIS

RESPONSE TO ECCENTRIC ORBITAL MOTION (RUNOUT)  
 OF ROTATING ROD SPECIMEN

| ROTOR<br>SPIN SPEED<br>(RPM) | 0.1 MIL                    | 0.2 MIL                    | 0.5 MIL                    | 1.0 MIL                    |
|------------------------------|----------------------------|----------------------------|----------------------------|----------------------------|
|                              | FORCE <sup>*</sup><br>(LB) | FORCE <sup>*</sup><br>(LB) | FORCE <sup>*</sup><br>(LB) | FORCE <sup>*</sup><br>(LB) |
| 4000.                        | 0.094                      | 0.186                      | 0.470                      | 0.940                      |
| 8000.                        | 0.462                      | 0.924                      | 2.300 <sup>††</sup>        | 4.620                      |
| 12000.                       | 1.942                      | 3.880                      | 9.710                      | 19.420                     |

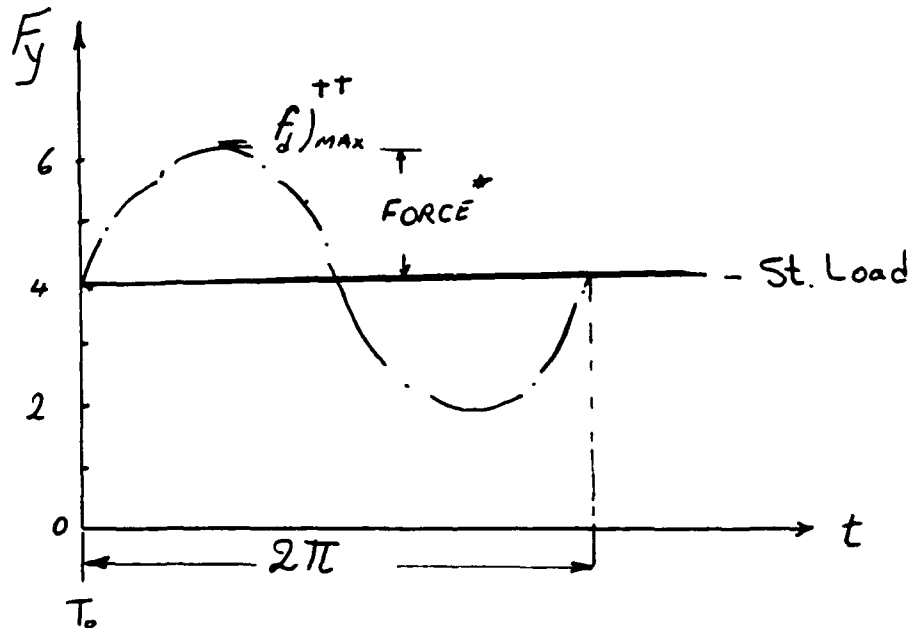


Fig 6

$F_d^{\max}$  as a function of  $(\delta \sin \omega t)$  orbital motion of shaft on Test Specimen

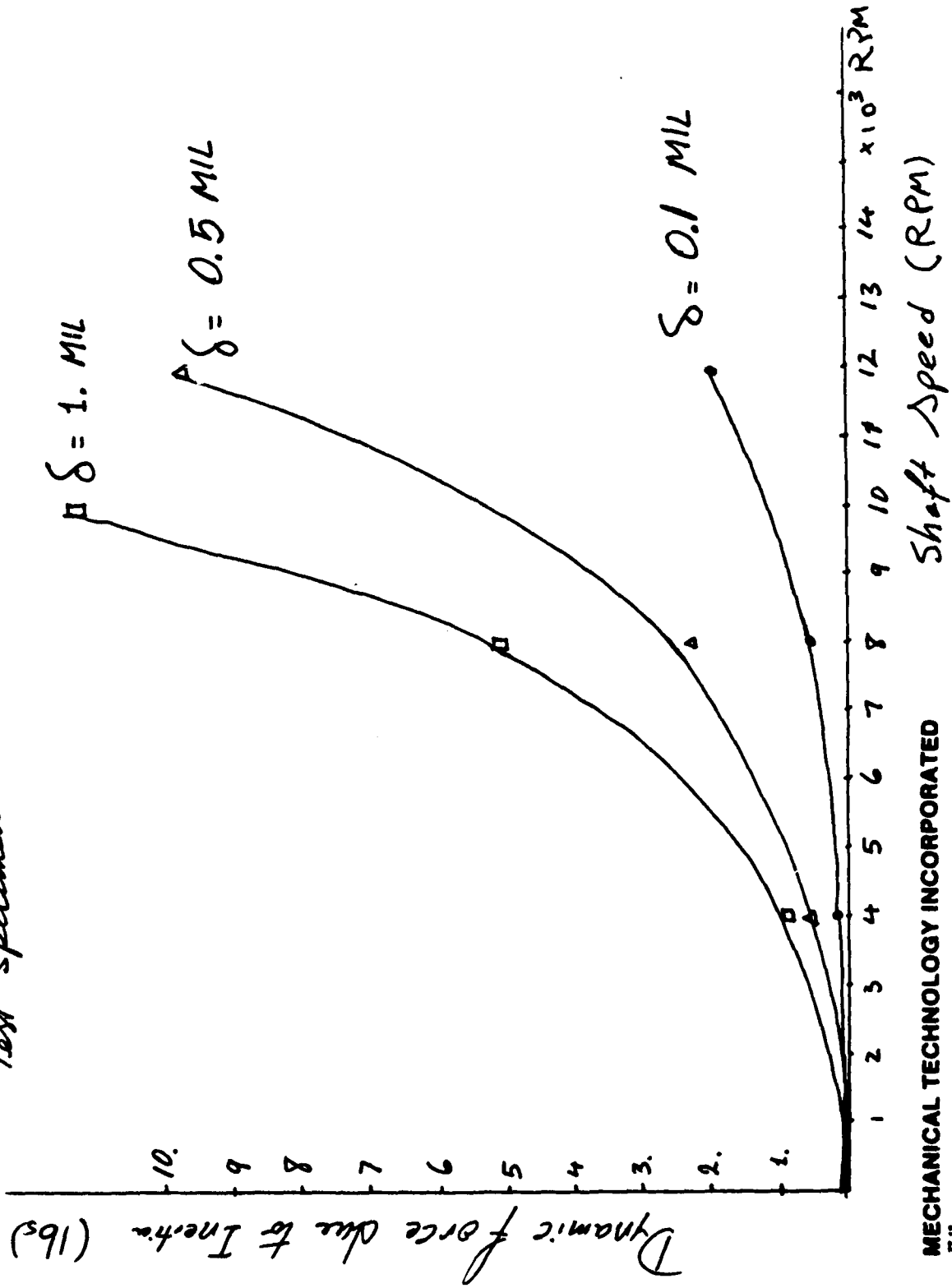
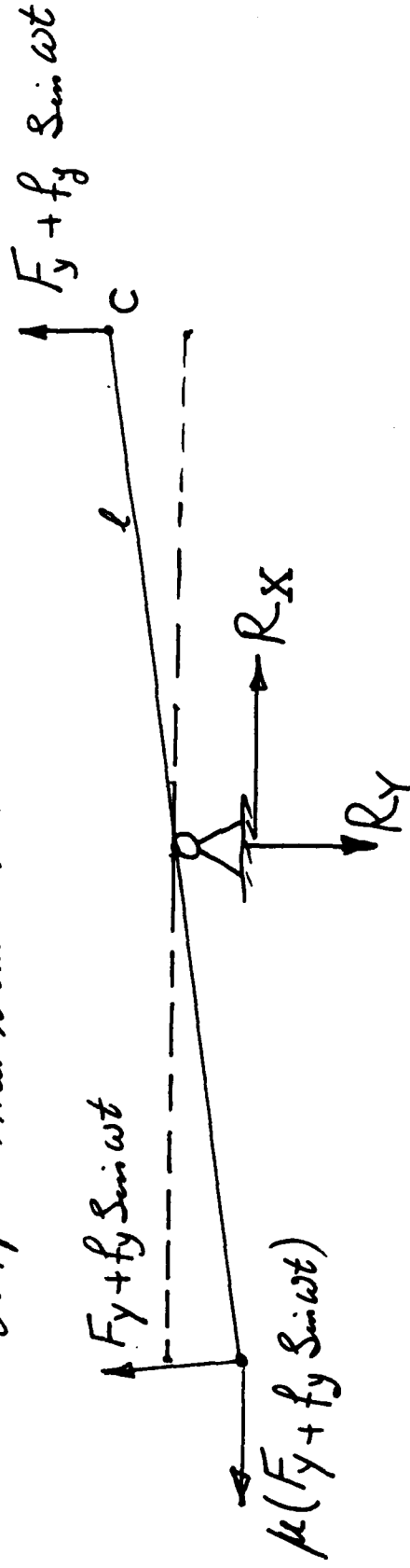


Fig. 7

 Hughes Trikotester

H. Heshmat

output measurements.



$$\sum \vec{M}_C = (F_y + f_y \sin \omega t) 2l + \mu \theta_0 l (F_y + f_y \sin \omega t) - R_y l =$$

$$I_c \omega^2 \theta_0 \sin \omega t$$

assume output has the form:

$$R_x = (R_x + R_x \sin \omega t) ; R_y = (R_y + R_y \sin \omega t)$$

$$\mu = \frac{I_c \omega^2 \theta_0 \sin \omega t + (R_y + R_y \sin \omega t) l - 2l (F_y + f_y \sin \omega t)}{\theta_0 l (F_y + f_y \sin \omega t)}$$

MECHANICAL TECHNOLOGY INCORPORATED  
17-12

$$\sum F_x = 0 ; \mu = \frac{R_x + R_x \sin \omega t}{F_y + f_y \sin \omega t}$$



**ATTACHMENT 2**

**ROTOR & STRUCTURAL DYNAMIC ANALYSIS OF HUGHES TRIBOTESTER**

DATE: 07/23/87  
TIME: 14:53:16

```
*****  
* PROGRAM PN1023B *  
* ALIAS FEATURE *  
* *  
* FINITE ELEMENT BASED ROTOR DYNAMIC ANALYSIS *  
* *  
* DATE WRITTEN.....07/01/86 *  
* DATE LAST REVISED.....07/01/86 *  
*****
```

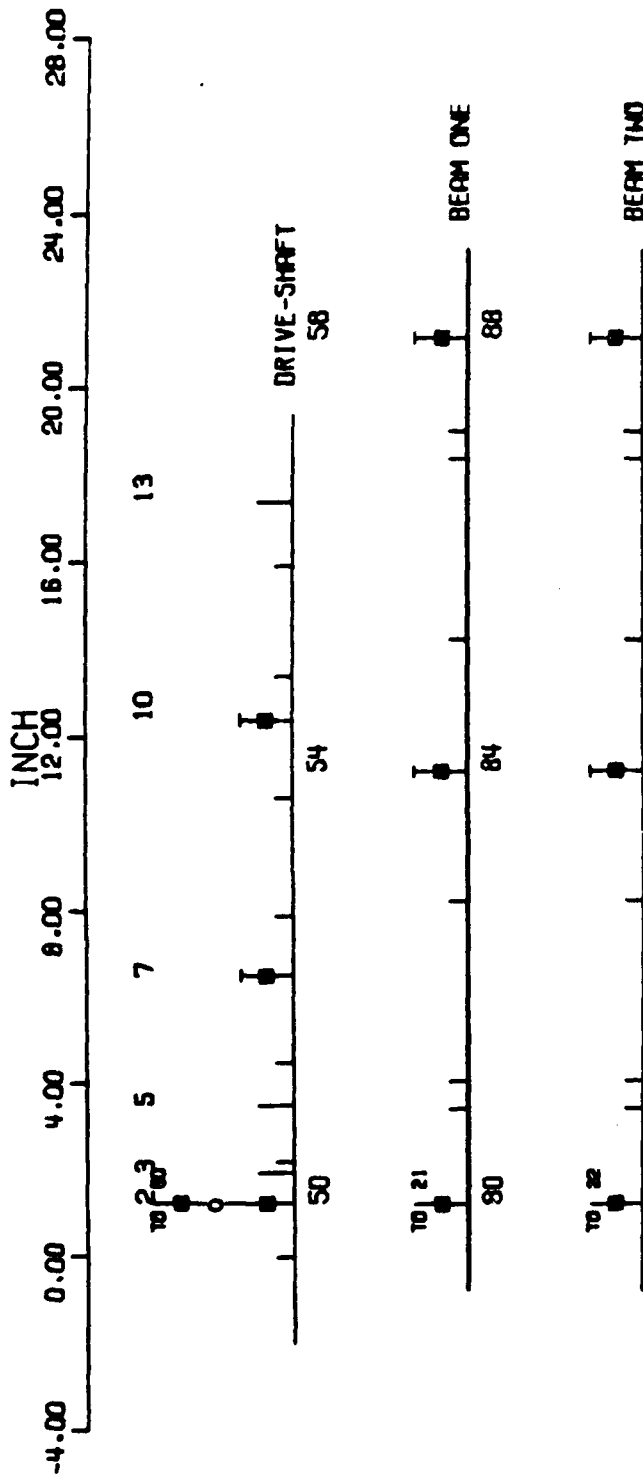
MECHANICAL TECHNOLOGY INCORPORATED

968 ALBANY SHAKER ROAD  
LATHAM, NEW YORK 12110

HUGHES TURBOTESTER - ROTOR AND STRUCTURAL DYNAMIC MODEL



# HUGHES TURBOTESTER - ROTOR AND STRUCTURAL DYNAMIC MODEL



\*\*\*\*\*  
 \* SYSTEM SUMMARY - SYSTEM CONDITION 1 \*  
 \*\*\*\*\*

| 1. TOTAL MASS, IP AND CENTER OF GRAVITY |             |           |                     | ( CALCULATED ) |                         |
|-----------------------------------------|-------------|-----------|---------------------|----------------|-------------------------|
| LEVEL                                   | SUB TITLE   | MASS (LB) | TOTAL IP (LB-IN**2) | C. G. (IN)     | IT W.R.T C.G (LB-IN**2) |
| 1                                       | DRIVE-SHAFT | 14.95     | 9.147               | 9.077          | 310.5                   |
| 2                                       | BEAM ONE    | 6.604     | 0.0000E+00          | 11.11          | 194.6                   |
| 3                                       | BEAM TWO    | 6.604     | 0.0000E+00          | 11.11          | 194.6                   |
| TOTAL                                   |             | 28.15     | 9.147               | 10.03          | 728.8                   |

| 2. APPLIED FORCES AND MOMENTS |                      |                       |                         | LOCATION                    |             |
|-------------------------------|----------------------|-----------------------|-------------------------|-----------------------------|-------------|
| STATION NUMBER                | ROTATING SPEED (RPM) | PULSATING SPEED (RPM) | MAGNITUDE OF FORCE (LB) | MAGNITUDE OF MOMENT (IN-LB) | ANGLE (DEG) |
| 2.                            | 0.0000E+00           | 0.1200E+05            | -1800.                  | 0.0000E+00                  | 0.0000E+00  |
| 21.                           | 0.0000E+00           | 0.1200E+05            | 900.0                   | 0.0000E+00                  | 0.0000E+00  |
| 22.                           | 0.0000E+00           | 0.1200E+05            | 900.0                   | 0.0000E+00                  | 0.0000E+00  |

### 3. DYNAMICAL SUPPORT COEFFICIENTS

#### LATERAL COEFFICIENTS (TRANSLATIONAL)

| STATION   | SPEED | KXX<br>(LB/IN) | KXY<br>(LB/IN) | KYX<br>(LB/IN) | KVY<br>(LB/IN) | CXX<br>(LB-S/IN) | CKY<br>(LB-S/IN) | CVX<br>(LB-S/IN) | CVY<br>(LB-S/IN) |
|-----------|-------|----------------|----------------|----------------|----------------|------------------|------------------|------------------|------------------|
| 2 AND 21  | - -   | 0.3000E+07     | 0.0000E+00     | 0.0000E+00     | 0.3000E+07     | 0.0000E+00       | 0.0000E+00       | 0.0000E+00       | 0.0000E+00       |
| 2 AND 22  | - -   | 0.3000E+07     | 0.0000E+00     | 0.0000E+00     | 0.3000E+07     | 0.0000E+00       | 0.0000E+00       | 0.0000E+00       | 0.0000E+00       |
| 50 AND 21 | - -   | 0.3000E+07     | 0.0000E+00     | 0.0000E+00     | 0.3000E+07     | 0.0000E+00       | 0.0000E+00       | 0.0000E+00       | 0.0000E+00       |
| 80 AND 22 | - -   | 0.3000E+07     | 0.0000E+00     | 0.0000E+00     | 0.3000E+07     | 0.0000E+00       | 0.0000E+00       | 0.0000E+00       | 0.0000E+00       |
| 7 AND 0   | - -   | 0.3000E+06     | 0.0000E+00     | 0.0000E+00     | 0.3000E+06     | 0.0000E+00       | 0.0000E+00       | 0.0000E+00       | 0.0000E+00       |
| 10 AND 0  | - -   | 0.3000E+06     | 0.0000E+00     | 0.0000E+00     | 0.3000E+06     | 0.0000E+00       | 0.0000E+00       | 0.0000E+00       | 0.0000E+00       |
| 14 AND 0  | - -   | 0.1000E+07     | 0.0000E+00     | 0.0000E+00     | 0.1000E+07     | 0.0000E+00       | 0.0000E+00       | 0.0000E+00       | 0.0000E+00       |
| 58 AND 0  | - -   | 10.00          | 0.0000E+00     | 0.0000E+00     | 10.00          | 0.0000E+00       | 0.0000E+00       | 0.0000E+00       | 0.0000E+00       |
| 84 AND 0  | - -   | 0.1000E+07     | 0.0000E+00     | 0.0000E+00     | 0.1000E+07     | 0.0000E+00       | 0.0000E+00       | 0.0000E+00       | 0.0000E+00       |
| 88 AND 0  | - -   | 10.00          | 0.0000E+00     | 0.0000E+00     | 10.00          | 0.0000E+00       | 0.0000E+00       | 0.0000E+00       | 0.0000E+00       |

NO ANGULAR COEFFICIENT SPECIFIED

READ -EXEC- FROM INPUT ...START TO EXECUTE

DIMENSION OF 17623 IS REQUIRED FOR MATRIX GC

READ -SYST- FROM INPUT ...START TO READ SYSTEM PROPERTIES  
 READ CARD GROUP 4 --ECHO OF INPUT

|         |            |            |            |            |            |            |            |            |            |
|---------|------------|------------|------------|------------|------------|------------|------------|------------|------------|
| ASYN    | 3.         | 0.         | 12000.     |            |            |            |            |            |            |
| FORCE   | 2.000      | -1800.     | 0.0000E+00 | 0.0000E+00 | 0.0000E+00 | 0.0000E+00 | 0.0000E+00 | 0.0000E+00 | 0.0000E+00 |
|         | 21.00      | 900.0      | 0.0000E+00 | 0.0000E+00 | 0.0000E+00 | 0.0000E+00 | 0.0000E+00 | 0.0000E+00 | 0.0000E+00 |
|         | 22.00      | 900.0      | 0.0000E+00 | 0.0000E+00 | 0.0000E+00 | 0.0000E+00 | 0.0000E+00 | 0.0000E+00 | 0.0000E+00 |
| COEFF1  |            |            |            |            |            |            |            |            |            |
| BEARING | 2.         | 21.        | 1.         | 0.         | 0.0000E+00 | 0.0000E+00 | 0.0000E+00 | 0.0000E+00 | 0.0000E+00 |
|         | 0.0000E+00 | 0.3000E+07 | 0.0000E+00 | 0.0000E+00 | 0.0000E+00 | 0.0000E+00 | 0.0000E+00 | 0.0000E+00 | 0.0000E+00 |
| BEARING | 2.         | 22.        | 1.         | 0.         | 0.0000E+00 | 0.0000E+00 | 0.0000E+00 | 0.0000E+00 | 0.0000E+00 |
|         | 0.0000E+00 | 0.3000E+07 | 0.0000E+00 | 0.0000E+00 | 0.0000E+00 | 0.0000E+00 | 0.0000E+00 | 0.0000E+00 | 0.0000E+00 |
| BEARING | 50.        | 21.        | 1.         | 0.         | 0.0000E+00 | 0.0000E+00 | 0.0000E+00 | 0.0000E+00 | 0.0000E+00 |
|         | 0.0000E+00 | 0.3000E+07 | 0.0000E+00 | 0.0000E+00 | 0.0000E+00 | 0.0000E+00 | 0.0000E+00 | 0.0000E+00 | 0.0000E+00 |
| BEARING | 80.        | 22.        | 1.         | 0.         | 0.0000E+00 | 0.0000E+00 | 0.0000E+00 | 0.0000E+00 | 0.0000E+00 |
|         | 0.0000E+00 | 0.3000E+07 | 0.0000E+00 | 0.0000E+00 | 0.0000E+00 | 0.0000E+00 | 0.0000E+00 | 0.0000E+00 | 0.0000E+00 |
| BEARING | 7.         | 0.         | 1.         | 0.         | 0.0000E+00 | 0.0000E+00 | 0.0000E+00 | 0.0000E+00 | 0.0000E+00 |
|         | 0.0000E+00 | 0.3000E+06 | 0.0000E+00 | 0.0000E+00 | 0.0000E+00 | 0.0000E+00 | 0.0000E+00 | 0.0000E+00 | 0.0000E+00 |
| BEARING | 10.        | 0.         | 1.         | 0.         | 0.0000E+00 | 0.0000E+00 | 0.0000E+00 | 0.0000E+00 | 0.0000E+00 |
|         | 0.0000E+00 | 0.3000E+06 | 0.0000E+00 | 0.0000E+00 | 0.0000E+00 | 0.0000E+00 | 0.0000E+00 | 0.0000E+00 | 0.0000E+00 |
| BEARING | 54.        | 0.         | 1.         | 0.         | 0.0000E+00 | 0.0000E+00 | 0.0000E+00 | 0.0000E+00 | 0.0000E+00 |
|         | 0.0000E+00 | 0.1000E+07 | 0.0000E+00 | 0.0000E+00 | 0.0000E+00 | 0.0000E+00 | 0.0000E+00 | 0.0000E+00 | 0.0000E+00 |
| BEARING | 58.        | 0.         | 1.         | 0.         | 0.0000E+00 | 0.0000E+00 | 0.0000E+00 | 0.0000E+00 | 0.0000E+00 |
|         | 0.0000E+00 | 10.00      | 0.0000E+00 | 0.0000E+00 | 0.0000E+00 | 0.0000E+00 | 0.0000E+00 | 0.0000E+00 | 0.0000E+00 |
| BEARING | 84.        | 0.         | 1.         | 0.         | 0.0000E+00 | 0.0000E+00 | 0.0000E+00 | 0.0000E+00 | 0.0000E+00 |
|         | 0.0000E+00 | 0.1000E+07 | 0.0000E+00 | 0.0000E+00 | 0.0000E+00 | 0.0000E+00 | 0.0000E+00 | 0.0000E+00 | 0.0000E+00 |
| BEARING | 88.        | 0.         | 1.         | 0.         | 0.0000E+00 | 0.0000E+00 | 0.0000E+00 | 0.0000E+00 | 0.0000E+00 |
|         | 0.0000E+00 | 10.00      | 0.0000E+00 | 0.0000E+00 | 0.0000E+00 | 0.0000E+00 | 0.0000E+00 | 0.0000E+00 | 0.0000E+00 |
| SPEED   | -4.        | 0.         |            |            | 0.0000E+00 | 0.0000E+00 | 0.0000E+00 | 0.0000E+00 | 0.0000E+00 |
|         | 4000.      | 8000.      | 0.1000E+05 | 0.1200E+05 |            |            |            |            |            |

## HUGHES TURBOTESTER - ROTOR AND STRUCTURAL DYNAMIC MODEL

\*\*\*\*\*  
\* MATERIAL SUMMARY \*  
\*\*\*\*\*

| MATERIAL<br>NUMBER | MODULUS OF<br>ELASTICITY<br>(LB/IN*2) | DENSITY<br>(LB/IN*3) | SHEAR<br>MODULUS<br>(LB/IN*2) | POISSON'S<br>RATIO |
|--------------------|---------------------------------------|----------------------|-------------------------------|--------------------|
| 1                  | 0.3000E+08                            | 0.2830               | 0.1100E+08                    | 0.3000             |
| 2                  | 0.1000E+08                            | 0.1000               | 0.3200E+07                    | 0.3000             |
| 4                  | 0.5000E+08                            | 0.1700               | 0.2000E+08                    | 0.2500             |

POISSON'S RATIO WILL BE CALCULATED BY THE PROGRAM IF NOT SPECIFIED

```

*****
* SUMMARY OF STATIC CONDENSATION *
*****
ACTIVE STATIONS SELECTED ON LEVEL - 1
NO. OF ACTIVE STATIONS - 7
NO. OF ACTIVE PEDESTAL STATIONS - 2
*****

```

| SYSTEM BEFORE STATIC CONDENSATION |         | SYSTEM AFTER STATIC CONDENSATION |      |
|-----------------------------------|---------|----------------------------------|------|
| NUMBER OF STATIONS                | - - - - | NUMBER OF ACTIVE STATIONS        | -    |
| NUMBER OF DEGREES OF FREEDOM      | -       | NUMBER OF D-O-F (FIXED FRAME)    | - 56 |
|                                   |         | NUMBER OF D-O-F (WHIRL FRAME)    | - 28 |

| ACTIVE STA. # | DOF | FIXED FRAME DOF # | WHIRL FRAME DOF # |
|---------------|-----|-------------------|-------------------|
| 1             | 4   | 1                 | 1                 |
| 2             | 4   | 5                 | 3                 |
| 3             | 4   | 9                 | 5                 |
| 5             | 4   | 13                | 7                 |
| 7             | 4   | 17                | 9                 |
| 10            | 4   | 21                | 11                |
| 13            | 4   | 25                | 13                |
| 21            | 2   | 29                | 15                |
| 22            | 2   | 31                | 16                |
| 50            | 4   | 33                | 17                |
| 54            | 4   | 37                | 19                |
| 58            | 4   | 41                | 21                |
| 80            | 4   | 45                | 23                |
| 84            | 4   | 49                | 25                |
| 88            | 4   | 53                | 27                |



# ECHU PRINT OF INPUT FILE

HUGHES TURBOTESTER - ROTOR AND STRUCTURAL DYNAMIC MODEL  
 POST  
 RESPONSE 1. 0. 0.  
 DEBUG 1. 0. 0.  
 MOIAGRAM  
 CRIT 0. 0. 100000.  
 TABILITY 4. /  
 HORT  
 LOCK  
 TATIC  
 FILE  
 END1

CARD GROUPS 2 & 3 WILL BE READ FROM A DISK FILE

!!SYSTEM MATRICES ARE NOT AVAILABLE.  
 ALL MATRICES WILL BE FORMULATED

| MATERIAL   | 1.         | 4.000      | 0.5000E+08 | 0.1700 | 0.2000E+08 | 0.0000E+00 | DRIVE-SHAFT |
|------------|------------|------------|------------|--------|------------|------------|-------------|
| GEOMETRY   | 12.        | 1.         | 1.         | 0.     |            |            |             |
| 0.0000E+00 | 0.0000E+00 | 0.0000E+00 | 0.0000E+00 | 1.250  | 0.3750     | 0.3750     | 4.000       |
| 0.0000E+00 | 0.0000E+00 | 0.0000E+00 | 0.0000E+00 | 0.7000 | 0.3750     | 0.0000E+00 | 4.000       |
| 0.5000E-02 | 0.0000E+00 | 0.0000E+00 | 0.0000E+00 | 0.2500 | 1.250      | 0.3750     | 1.000       |
| 0.2500E-01 | 0.0000E+00 | 0.0000E+00 | 0.0000E+00 | 1.300  | 2.500      | 0.3750     | 1.000       |
| 0.0000E+00 | 0.0000E+00 | 0.0000E+00 | 0.0000E+00 | 1.000  | 2.500      | 0.0000E+00 | 1.000       |
| 0.0000E+00 | 0.0000E+00 | 0.0000E+00 | 0.0000E+00 | 2.000  | 2.125      | 0.0000E+00 | 1.000       |
| 0.0000E+00 | 0.0000E+00 | 0.0000E+00 | 0.0000E+00 | 1.375  | 2.125      | 0.0000E+00 | 1.000       |
| 0.0000E+00 | 0.0000E+00 | 0.0000E+00 | 0.0000E+00 | 2.750  | 2.125      | 0.7500     | 1.000       |
| 0.0000E+00 | 0.0000E+00 | 0.0000E+00 | 0.0000E+00 | 1.750  | 2.125      | 0.7500     | 1.000       |
| 0.0000E+00 | 0.0000E+00 | 0.0000E+00 | 0.0000E+00 | 1.000  | 2.125      | 0.7500     | 1.000       |
| 0.0000E+00 | 0.0000E+00 | 0.0000E+00 | 0.0000E+00 | 2.500  | 2.000      | 0.0000E+00 | 1.000       |
| 0.0000E+00 | 0.0000E+00 | 0.0000E+00 | 0.0000E+00 | 1.500  | 1.900      | 0.0000E+00 | 1.000       |

PEDESTAL 2. 21.  
 2.000 2.000 0.1000E-01 0.0000E+00  
 2.000 2.000 0.1000E-01 0.0000E+00

ACTIVE 8.  
 2. 3. 5. 7 10. 13. 21. 22.  
 LEVEL 0. 50. 1.25  
 GEOMETRY 8.

| GEOMETRY   | 8.    | 0.2860 | 0.3230 | 0.3650 | 1.328 | 2.000 | 1.328 | 0.3650 | 0.6090 |
|------------|-------|--------|--------|--------|-------|-------|-------|--------|--------|
| 0.0000E+00 | 2.741 | 2.175  | 2.175  | 2.175  | 2.354 | 1.493 | 1.844 | 1.493  | 2.354  |
| 0.0000E+00 | 3.029 | 0.6250 | 0.6250 | 0.6250 | 1.493 | 1.844 | 1.493 | 1.844  | 1.493  |
| 0.0000E+00 | 2.935 | 4.188  | 4.188  | 4.188  | 1.844 | 1.493 | 1.844 | 1.493  | 1.844  |
| 0.0000E+00 | 9.237 | 2.969  | 2.969  | 2.969  | 2.421 | 2.421 | 2.421 | 2.421  | 2.421  |
| 0.0000E+00 | 13.18 | 2.969  | 2.969  | 2.969  | 2.421 | 2.421 | 2.421 | 2.421  | 2.421  |
| 0.0000E+00 | 9.237 | 4.188  | 4.188  | 4.188  | 1.844 | 1.493 | 1.844 | 1.493  | 1.844  |
| 0.0000E+00 | 2.935 | 0.6250 | 0.6250 | 0.6250 | 1.493 | 1.844 | 1.493 | 1.844  | 1.493  |
| 0.0000E+00 | 5.760 | 2.175  | 2.175  | 2.175  | 2.354 | 1.493 | 1.844 | 1.493  | 2.354  |

ACTIVE 3.  
 50. 54. 58.  
 LEVEL 0. 80. 1.25  
 GEOMETRY 8.

| GEOMETRY   | 8.    | 0.2860 | 0.3230 | 0.3650 | 1.328 | 2.000 | 1.328 | 0.3650 | 0.6090 |
|------------|-------|--------|--------|--------|-------|-------|-------|--------|--------|
| 0.0000E+00 | 2.741 | 2.175  | 2.175  | 2.175  | 2.354 | 1.493 | 1.844 | 1.493  | 2.354  |
| 0.0000E+00 | 3.029 | 0.6250 | 0.6250 | 0.6250 | 1.493 | 1.844 | 1.493 | 1.844  | 1.493  |
| 0.0000E+00 | 2.935 | 4.188  | 4.188  | 4.188  | 1.844 | 1.493 | 1.844 | 1.493  | 1.844  |
| 0.0000E+00 | 9.237 | 2.969  | 2.969  | 2.969  | 2.421 | 2.421 | 2.421 | 2.421  | 2.421  |
| 0.0000E+00 | 13.18 | 2.969  | 2.969  | 2.969  | 2.421 | 2.421 | 2.421 | 2.421  | 2.421  |
| 0.0000E+00 | 9.237 | 4.188  | 4.188  | 4.188  | 1.844 | 1.493 | 1.844 | 1.493  | 1.844  |
| 0.0000E+00 | 2.935 | 0.6250 | 0.6250 | 0.6250 | 1.493 | 1.844 | 1.493 | 1.844  | 1.493  |
| 0.0000E+00 | 5.760 | 2.175  | 2.175  | 2.175  | 2.354 | 1.493 | 1.844 | 1.493  | 2.354  |

ACTIVE 3.  
 80. 84. 88.  
 SYSTEM

```

*****
STATUS..... (VERSION 2.0 10-10-85)
*****
NUMBER OF LEVELS - - - - 3      DEBUG OPTIONS
NUMBER OF STATIONS - - - - 33    NBUG1 = 1 BASIC DEBUG
NUMBER OF BEARINGS - - - - 10    NBUG2 = 0 ELEMENT FORMULATION
NO. OF USER INPUT MATERIALS - 1  NBUG3 = 0 BLOCK-STODOLA ITERATION
NO. OF DEGREES-OF-FREEDOM - -128 NBUG4 = 0 MATH ROUTINES
*****

```

```

*****
OPTIONS IN EFFECT
*****
* CRIT - CRITICAL SPEEDS CALCULATION
* UNIT - AMERICAN
* POST - SPECIAL OUTPUT FILE FOR POST PLOT WILL BE
*       GENERATED
* TIMO - TIMOSHENKO BEAM
*****

```

```

*****
DIMENSION REQUIRED FOR THE 3 GLOBAL ARRAYS
*****
*
* PROBLEM FORMULATION      IG      GR      GC
* AVAILABLE - - - - 2000  10000  5441  200000
*
*****

```

\*\*\*\*\*  
 \* SUMMARY OF LEVEL NO. 1 \* DRIVE-SHAFT \*  
 \*\*\*\*\*

\*TYPE OF ELEMENT - BEAM \*NUMBER OF ROTOR SEGMENTS - 12 \*SPEED RATIO - 1.00 \*STARTING AXIAL LOCATION - 0.000

1. SHAFT GEOMETRY

| ROTOR SEGMENT<br>BTWN. STATIONS | SEGMENT<br>LENGTH<br>(IN) | STIFFNESS<br>DIAMETER<br>(IN) | MASS<br>DIAMETER<br>(IN) | INNER<br>DIAMETER<br>(IN) | MATERIAL<br>NUMBER |
|---------------------------------|---------------------------|-------------------------------|--------------------------|---------------------------|--------------------|
| 1 AND 2                         | 1.2500                    | 0.3750                        | 0.3750                   | 0.0000                    | 4.                 |
| 2 AND 3                         | 0.7000                    | 0.3750                        | 0.3750                   | 0.0000                    | 4.                 |
| 3 AND 4                         | 0.2500                    | 1.2500                        | 1.2500                   | 0.3750                    | 1.                 |
| 4 AND 5                         | 1.3000                    | 2.5000                        | 2.5000                   | 0.3750                    | 1.                 |
| 5 AND 6                         | 1.0000                    | 2.5000                        | 2.5000                   | 0.0000                    | 1.                 |
| 6 AND 7                         | 2.0000                    | 2.1250                        | 2.1250                   | 0.0000                    | 1.                 |
| 7 AND 8                         | 1.3750                    | 2.1250                        | 2.1250                   | 0.0000                    | 1.                 |
| 8 AND 9                         | 2.7500                    | 2.1250                        | 2.1250                   | 0.7500                    | 1.                 |
| 9 AND 10                        | 1.7500                    | 2.1250                        | 2.1250                   | 0.7500                    | 1.                 |
| 10 AND 11                       | 1.0000                    | 2.1250                        | 2.1250                   | 0.7500                    | 1.                 |
| 11 AND 12                       | 2.5000                    | 2.0000                        | 2.0000                   | 0.0000                    | 1.                 |
| 12 AND 13                       | 1.5000                    | 1.9000                        | 1.9000                   | 0.0000                    | 1.                 |
| TOTAL                           | 17.3750                   |                               |                          |                           |                    |

2. LUMPED MASS DATA

| STATION | MASS<br>(LB) | IT<br>(LB-IN**2) | IP<br>(LB-IN**2) | ECC<br>(IN) | ANGLE<br>(DEG) |
|---------|--------------|------------------|------------------|-------------|----------------|
| 3       | 0.5000E-02   | 0.0000E+00       | 0.0000E+00       | 0.0000E+00  | 0.0000E+00     |
| 4       | 0.2500E-01   | 0.0000E+00       | 0.0000E+00       | 0.0000E+00  | 0.0000E+00     |

11NO SHAFT ECCENTRICITY SPECIFIED IN CARD GROUP 3

3. PEDESTAL MASS AND INERTIA

| DEG OF FREEDOM | STATION NO. | MASS       | IT         | CONNECTED TO STATION NO. |
|----------------|-------------|------------|------------|--------------------------|
| 2              | 21          | 0.1000E-01 | 0.0000E+00 | 2                        |
| 2              | 22          | 0.1000E-01 | 0.0000E+00 | 2                        |

HUGHES TURBOTESTER - ROTOR AND STRUCTURAL DYNAMIC MODEL

\*\*\*\*\*  
 \* SUMMARY OF LEVEL NO. 2 \* BEAM ONE  
 \*\*\*\*\*

\*TYPE OF ELEMENT - BEAM \*NUMBER OF ROTOR SEGMENTS - 8 \*SPEED RATIO - 0.00 \*STARTING AXIAL LOCATION - 1.250

1. SHAFT GEOMETRY

| ROTOR SEGMENT<br>BTWN. STATIONS | SEGMENT<br>LENGTH<br>(IN) | STIFFNESS<br>DIAMETER<br>(IN) | MASS<br>DIAMETER<br>(IN) | INNER<br>DIAMETER<br>(IN) | MATERIAL<br>NUMBER |
|---------------------------------|---------------------------|-------------------------------|--------------------------|---------------------------|--------------------|
| 50 AND 51                       | 2.1750                    | 2.3540                        | 0.0000                   | 0.0000                    | 2.                 |
| 51 AND 52                       | 0.6250                    | 1.4930                        | 0.0000                   | 0.0000                    | 2.                 |
| 52 AND 53                       | 4.1880                    | 1.8440                        | 0.0000                   | 0.0000                    | 2.                 |
| 53 AND 54                       | 2.9690                    | 2.4210                        | 0.0000                   | 0.0000                    | 2.                 |
| 54 AND 55                       | 2.9690                    | 2.4210                        | 0.0000                   | 0.0000                    | 2.                 |
| 55 AND 56                       | 4.1880                    | 1.8440                        | 0.0000                   | 0.0000                    | 2.                 |
| 56 AND 57                       | 0.6250                    | 1.4930                        | 0.0000                   | 0.0000                    | 2.                 |
| 57 AND 58                       | 2.1750                    | 2.3540                        | 0.0000                   | 0.0000                    | 2.                 |

TOTAL 19.9140

2. LUMPED MASS DATA

| STATION | MASS<br>(LB) | IT<br>(LB-IN**2) | IP<br>(LB-IN**2) | ECC<br>(IN) | ANGLE<br>(DEG) |
|---------|--------------|------------------|------------------|-------------|----------------|
| 50      | 0.2860       | 2.741            | 0.0000E+00       | 0.0000E+00  | 0.0000E+00     |
| 51      | 0.3230       | 3.029            | 0.0000E+00       | 0.0000E+00  | 0.0000E+00     |
| 52      | 0.3650       | 2.835            | 0.0000E+00       | 0.0000E+00  | 0.0000E+00     |
| 53      | 1.328        | 9.237            | 0.0000E+00       | 0.0000E+00  | 0.0000E+00     |
| 54      | 2.000        | 13.18            | 0.0000E+00       | 0.0000E+00  | 0.0000E+00     |
| 55      | 1.328        | 9.237            | 0.0000E+00       | 0.0000E+00  | 0.0000E+00     |
| 56      | 0.3650       | 2.835            | 0.0000E+00       | 0.0000E+00  | 0.0000E+00     |
| 57      | 0.6090       | 5.760            | 0.0000E+00       | 0.0000E+00  | 0.0000E+00     |

NO SHAFT ECCENTRICITY SPECIFIED IN CARD GROUP 3

\*\*\*\*\*  
 \* SUMMARY OF LEVEL NO. 3 \* BEAM TWO  
 \*\*\*\*\*

\*TYPE OF ELEMENT - BEAM \*NUMBER OF ROTOR SEGMENTS - 8 \*SPEED RATIO - 0.00 \*STARTING AXIAL LOCATION - 1.250

1. SHAFT GEOMETRY

| ROTOR SEGMENT<br>BTWN. STATIONS | SEGMENT<br>LENGTH<br>(IN) | STIFFNESS<br>DIAMETER<br>(IN) | MASS<br>DIAMETER<br>(IN) | INNER<br>DIAMETER<br>(IN) | MATERIAL<br>NUMBER |
|---------------------------------|---------------------------|-------------------------------|--------------------------|---------------------------|--------------------|
| 80 AND 81                       | 2.1750                    | 2.3540                        | 0.0000                   | 0.0000                    | 2.                 |
| 81 AND 82                       | 0.6250                    | 1.4930                        | 0.0000                   | 0.0000                    | 2.                 |
| 82 AND 83                       | 4.1880                    | 1.8440                        | 0.0000                   | 0.0000                    | 2.                 |
| 83 AND 84                       | 2.9690                    | 2.4210                        | 0.0000                   | 0.0000                    | 2.                 |
| 84 AND 85                       | 2.9690                    | 2.4210                        | 0.0000                   | 0.0000                    | 2.                 |
| 85 AND 86                       | 4.1880                    | 1.8440                        | 0.0000                   | 0.0000                    | 2.                 |
| 86 AND 87                       | 0.6250                    | 1.4930                        | 0.0000                   | 0.0000                    | 2.                 |
| 87 AND 88                       | 2.1750                    | 2.3540                        | 0.0000                   | 0.0000                    | 2.                 |

TOTAL 19.9140

2. LUMPED MASS DATA

| STATION | MASS<br>(LB) | IT<br>(LB-IN**2) | IP<br>(LB-IN**2) | ECC<br>(IN) | ANGLE<br>(DEG) |
|---------|--------------|------------------|------------------|-------------|----------------|
| 80      | 0.2860       | 2.741            | 0.0000E+00       | 0.0000E+00  | 0.0000E+00     |
| 81      | 0.3230       | 3.029            | 0.0000E+00       | 0.0000E+00  | 0.0000E+00     |
| 82      | 0.3650       | 2.935            | 0.0000E+00       | 0.0000E+00  | 0.0000E+00     |
| 83      | 1.328        | 9.237            | 0.0000E+00       | 0.0000E+00  | 0.0000E+00     |
| 84      | 2.000        | 13.18            | 0.0000E+00       | 0.0000E+00  | 0.0000E+00     |
| 85      | 1.328        | 9.237            | 0.0000E+00       | 0.0000E+00  | 0.0000E+00     |
| 86      | 0.3650       | 2.935            | 0.0000E+00       | 0.0000E+00  | 0.0000E+00     |
| 87      | 0.6090       | 5.760            | 0.0000E+00       | 0.0000E+00  | 0.0000E+00     |

!!NO SHAFT ECCENTRICITY SPECIFIED IN CARD GROUP 3

ELEMENT MATRICES WERE STORED ON LOGICAL UNIT 2

HUGHES TURBOTESTER - ROTOR AND STRUCTURAL DYNAMIC MODEL

| *****                                  |         |           |           |           |           |        |  |  |  | .....CALCULATED OUTPUT |  |  |
|----------------------------------------|---------|-----------|-----------|-----------|-----------|--------|--|--|--|------------------------|--|--|
| * SUMMARY OF LEVEL NO. 1 * DRIVE-SHAFT |         |           |           |           |           |        |  |  |  | *****                  |  |  |
| *****                                  |         |           |           |           |           |        |  |  |  |                        |  |  |
| ROTOR SEGMENT                          | ACC LEN | EI        | MASS      | IT        | IP        | SHAPE  |  |  |  |                        |  |  |
| BTWN. STATIONS                         | (IN)    | LB-IN**2  | (LB)      | LB-IN**2  | LB-IN**2  | FACTOR |  |  |  |                        |  |  |
| 1 AND 2                                | 1.2500  | 0.485E+05 | 0.235E-01 | 0.326E-02 | 0.413E-03 | 0.882  |  |  |  |                        |  |  |
| 2 AND 3                                | 1.9500  | 0.485E+05 | 0.131E-01 | 0.652E-03 | 0.231E-03 | 0.882  |  |  |  |                        |  |  |
| 3 AND 4                                | 2.2000  | 0.357E+07 | 0.790E-01 | 0.882E-02 | 0.168E-01 | 0.737  |  |  |  |                        |  |  |
| 4 AND 5                                | 3.5000  | 0.575E+08 | 1.77      | 0.954     | 1.41      | 0.838  |  |  |  |                        |  |  |
| 5 AND 6                                | 4.5000  | 0.575E+08 | 1.39      | 0.658     | 1.09      | 0.886  |  |  |  |                        |  |  |
| 6 AND 7                                | 6.5000  | 0.300E+08 | 2.01      | 1.24      | 1.13      | 0.886  |  |  |  |                        |  |  |
| 7 AND 8                                | 7.8750  | 0.300E+08 | 1.38      | 0.607     | 0.779     | 0.886  |  |  |  |                        |  |  |
| 8 AND 9                                | 10.6250 | 0.296E+08 | 2.42      | 2.29      | 1.53      | 0.701  |  |  |  |                        |  |  |
| 9 AND 10                               | 12.3750 | 0.296E+08 | 1.54      | 0.880     | 0.976     | 0.701  |  |  |  |                        |  |  |
| 10 AND 11                              | 13.3750 | 0.296E+08 | 0.879     | 0.352     | 0.558     | 0.701  |  |  |  |                        |  |  |
| 11 AND 12                              | 15.8750 | 0.236E+08 | 2.22      | 1.71      | 1.11      | 0.886  |  |  |  |                        |  |  |
| 12 AND 13                              | 17.3750 | 0.192E+08 | 1.20      | 0.497     | 0.543     | 0.886  |  |  |  |                        |  |  |

```

*****
* SUMMARY OF LEVEL NO. 2 * BEAM ONE
*****
*.....CALCULATED OUTPUT
*****
  ROTOR SEGMENT  ACC LEN  EI  MASS  IT  IP  SHAPE
  BTWN. STATIONS  (IN)  LB-IN**2  (LB)  LB-IN**2  LB-IN**2  FACTOR

50 AND 51      3.4250  0.151E+08  0.000E+00  0.000E+00  0.000E+00  0.886
51 AND 52      4.0500  0.244E+07  0.000E+00  0.000E+00  0.000E+00  0.886
52 AND 53      8.2380  0.568E+07  0.000E+00  0.000E+00  0.000E+00  0.886
53 AND 54     11.2070  0.169E+08  0.000E+00  0.000E+00  0.000E+00  0.886

54 AND 55     14.1760  0.169E+08  0.000E+00  0.000E+00  0.000E+00  0.886
55 AND 56     18.3640  0.568E+07  0.000E+00  0.000E+00  0.000E+00  0.886
56 AND 57     18.9890  0.244E+07  0.000E+00  0.000E+00  0.000E+00  0.886
57 AND 58     21.1640  0.151E+08  0.000E+00  0.000E+00  0.000E+00  0.886
  
```

HUGHES TURBOTESTER - ROTOR AND STRUCTURAL DYNAMIC MODEL

| *****CALCULATED OUTPUT*****           |         |           |           |           |           |        |  |  |  |
|---------------------------------------|---------|-----------|-----------|-----------|-----------|--------|--|--|--|
| * SUMMARY OF LEVEL NO. 3 * BEAM TWO * |         |           |           |           |           |        |  |  |  |
| *****                                 |         |           |           |           |           |        |  |  |  |
| ROTOR SEGMENT                         | ACC LEN | EI        | MASS      | IT        | IP        | SHAPE  |  |  |  |
| BTWN. STATIONS                        | (IN)    | LB-IN**2  | (LB)      | LB-IN**2  | LB-IN**2  | FACTOR |  |  |  |
| 80 AND 81                             | 3.4250  | 0.151E+08 | 0.000E+00 | 0.000E+00 | 0.000E+00 | 0.886  |  |  |  |
| 81 AND 82                             | 4.0500  | 0.244E+07 | 0.000E+00 | 0.000E+00 | 0.000E+00 | 0.886  |  |  |  |
| 82 AND 83                             | 8.2380  | 0.568E+07 | 0.000E+00 | 0.000E+00 | 0.000E+00 | 0.886  |  |  |  |
| 83 AND 84                             | 11.2070 | 0.169E+08 | 0.000E+00 | 0.000E+00 | 0.000E+00 | 0.886  |  |  |  |
| 84 AND 85                             | 14.1760 | 0.169E+08 | 0.000E+00 | 0.000E+00 | 0.000E+00 | 0.886  |  |  |  |
| 85 AND 86                             | 18.3640 | 0.568E+07 | 0.000E+00 | 0.000E+00 | 0.000E+00 | 0.886  |  |  |  |
| 86 AND 87                             | 18.9890 | 0.244E+07 | 0.000E+00 | 0.000E+00 | 0.000E+00 | 0.886  |  |  |  |
| 87 AND 88                             | 21.1640 | 0.151E+08 | 0.000E+00 | 0.000E+00 | 0.000E+00 | 0.886  |  |  |  |



\*\*\*\*\*  
 \* MATERIAL SUMMARY \*  
 \*\*\*\*\*

| MATERIAL<br>NUMBER | MODULUS OF<br>ELASTICITY<br>(LB/IN**2) | DENSITY<br>(LB/IN**3) | SHEAR<br>MODULUS<br>(LB/IN**2) | POISSON'S<br>RATIO |
|--------------------|----------------------------------------|-----------------------|--------------------------------|--------------------|
| 1                  | 0.3000E+08                             | 0.2830                | 0.1100E+08                     | 0.3000             |
| 2                  | 0.1000E+08                             | 0.1000                | 0.3200E+07                     | 0.3000             |
| 4                  | 0.5000E+08                             | 0.1700                | 0.2000E+08                     | 0.2500             |

POISSON'S RATIO WILL BE CALCULATED BY THE PROGRAM IF NOT SPECIFIED

\*\*\*\*\*  
 \* SUMMARY OF STATIC CONDENSATION \*  
 \*\*\*\*\*  
 ACTIVE STATIONS SELECTED ON LEVEL - 1 2 3  
 NO. OF ACTIVE STATIONS - 7 3 3  
 NO. OF ACTIVE PEDESTAL STATIONS- 2 0 0  
 SYSTEM BEFORE STATIC CONDENSATION  
 NUMBER OF STATIONS - - - - - 33  
 NUMBER OF DEGREES OF FREEDOM - 128

SYSTEM AFTER STATIC CONDENSATION  
 NUMBER OF ACTIVE STATIONS - 15  
 NUMBER OF D-O-F (FIXED FRAME) - 56  
 NUMBER OF D-O-F (WHIRL FRAME) - 28

| ACTIVE<br>STA. # | DOF | FIXED FRAME<br>DOF# | WHIRL FRAME<br>DOF# |
|------------------|-----|---------------------|---------------------|
| 1                | 4   | 1                   | 1                   |
| 2                | 4   | 5                   | 3                   |
| 3                | 4   | 9                   | 5                   |
| 5                | 4   | 13                  | 7                   |
| 7                | 4   | 17                  | 9                   |
| 10               | 4   | 21                  | 11                  |
| 13               | 4   | 25                  | 13                  |
| 21               | 2   | 29                  | 15                  |
| 22               | 2   | 31                  | 16                  |
| 50               | 4   | 33                  | 17                  |
| 54               | 4   | 37                  | 19                  |
| 58               | 4   | 41                  | 21                  |
| 80               | 4   | 45                  | 23                  |
| 84               | 4   | 49                  | 25                  |
| 88               | 4   | 53                  | 27                  |

## HUGHES TURBOTESTER - ROTOR AND STRUCTURAL DYNAMIC MODEL

READ -SYST- FROM INPUT ...START TO READ SYSTEM PROPERTIES  
READ CARD GROUP 4 --ECHO OF INPUT

[illegible]

HUGHES TURBOTESTER - ROTOR AND STRUCTURAL DYNAMIC MODEL

\*\*\*\*\*  
 \* SYSTEM SUMMARY - SYSTEM CONDITION 1 \*  
 \*\*\*\*\*

| 1. TOTAL MASS, IP AND CENTER OF GRAVITY |             |       | ( CALCULATED ) | C. G. | IT W.R.T C.G |
|-----------------------------------------|-------------|-------|----------------|-------|--------------|
| LEVEL                                   | SUB TITLE   | MASS  | TOTAL IP       | (IN)  | (LB-IN**2)   |
|                                         |             | (LB)  | (LB-IN**2)     |       |              |
| 1                                       | DRIVE-SHAFT | 14.95 | 9.147          | 9.077 | 310.5        |
| 2                                       | BEAM ONE    | 6.604 | 0.0000E+00     | 11.11 | 194.6        |
| 3                                       | BEAM TWO    | 6.604 | 0.0000E+00     | 11.11 | 194.6        |
| TOTAL                                   |             | 28.15 | 9.147          | 10.03 | 728.8        |

READ - 0- FROM INPUT ...IGNORED

HUGHES TURBOTESTER - ROTOR AND STRUCTURAL DYNAMIC MODEL

2. DYNAMICAL SUPPORT COEFFICIENTS

LATERAL COEFFICIENTS (TRANSLATIONAL)

| STATION   | SPEED | KXX<br>(LB/IN) | KXY<br>(LB/IN) | KVX<br>(LB/IN) | KVY<br>(LB/IN) | CXX<br>(LB-S/IN) | CXY<br>(LB-S/IN) | CVX<br>(LB-S/IN) | C/Y<br>(LB-S/IN) |
|-----------|-------|----------------|----------------|----------------|----------------|------------------|------------------|------------------|------------------|
| 2 AND 21  | - -   | 0.3000E+07     | 0.0000E+00     | 0.0000E+00     | 0.3000E+07     | 0.0000E+00       | 0.0000E+00       | 0.0000E+00       | 0.0000E+00       |
| 2 AND 22  | - -   | 0.3000E+07     | 0.0000E+00     | 0.0000E+00     | 0.3000E+07     | 0.0000E+00       | 0.0000E+00       | 0.0000E+00       | 0.0000E+00       |
| 50 AND 21 | - -   | 0.3000E+07     | 0.0000E+00     | 0.0000E+00     | 0.3000E+07     | 0.0000E+00       | 0.0000E+00       | 0.0000E+00       | 0.0000E+00       |
| 80 AND 22 | - -   | 0.3000E+07     | 0.0000E+00     | 0.0000E+00     | 0.3000E+07     | 0.0000E+00       | 0.0000E+00       | 0.0000E+00       | 0.0000E+00       |
| 7 AND 0   | - -   | 0.3000E+06     | 0.0000E+00     | 0.0000E+00     | 0.3000E+06     | 0.0000E+00       | 0.0000E+00       | 0.0000E+00       | 0.0000E+00       |
| 10 AND 0  | - -   | 0.3000E+06     | 0.0000E+00     | 0.0000E+00     | 0.3000E+06     | 0.0000E+00       | 0.0000E+00       | 0.0000E+00       | 0.0000E+00       |
| 54 AND 0  | - -   | 0.1000E+07     | 0.0000E+00     | 0.0000E+00     | 0.1000E+07     | 0.0000E+00       | 0.0000E+00       | 0.0000E+00       | 0.0000E+00       |
| 58 AND 0  | - -   | 10.00          | 0.0000E+00     | 0.0000E+00     | 10.00          | 0.0000E+00       | 0.0000E+00       | 0.0000E+00       | 0.0000E+00       |
| 84 AND 0  | - -   | 0.1000E+07     | 0.0000E+00     | 0.0000E+00     | 0.1000E+07     | 0.0000E+00       | 0.0000E+00       | 0.0000E+00       | 0.0000E+00       |
| 88 AND 0  | - -   | 10.00          | 0.0000E+00     | 0.0000E+00     | 10.00          | 0.0000E+00       | 0.0000E+00       | 0.0000E+00       | 0.0000E+00       |

NO ANGULAR COEFFICIENT SPECIFIED

READ -EXEC- FROM INPUT ...START TO EXECUTE

!! DIMENSION OF 8437 IS REQUIRED FOR MATRIX GC

\*\*\*\*\*  
 \* CRITICAL SPEEDS ANALYSIS \*  
 \*\*\*\*\*

\*\*\*\*\*  
 \* SYSTEM CONDITION 1 \*\*\*\*\*  
 \*\*\*\*\*

FREQUENCY RANGE REQUESTED  
 LOWER BOUND (RPM) = 0.00000E+00  
 UPPER BOUND (RPM) = 0.10000E+06

\*\*\*SYSTEM WHIRL SPEED RATIO = 0.000E+00\*\*\*

- SPIN SPEED RATIO -  
 LEVEL 1 0.00  
 LEVEL 2 0.00  
 LEVEL 3 0.00

- - - - -SYSTEM SPIN-SPEED-DEPENDENT SUPPORT COEFFICIENTS - - - - -

| STA. | NO.     | --LATERAL COEFFICIENTS AT ROTATIONAL SPEED |            |            | KXX (LB/IN) |            |            | KXY (LB/IN) |            |            | KVX (LB/IN) |            |            | KVY (LB/IN) |            |            | CXK (LB-S/IN) |            |            | CVX (LB-S/IN) |            |            | CVY (LB-S/IN) |            |            |
|------|---------|--------------------------------------------|------------|------------|-------------|------------|------------|-------------|------------|------------|-------------|------------|------------|-------------|------------|------------|---------------|------------|------------|---------------|------------|------------|---------------|------------|------------|
| 2.   | AND 21. | 0.3000E+07                                 | 0.0000E+00 | 0.0000E+00 | 0.0000E+00  | 0.0000E+00 | 0.0000E+00 | 0.0000E+00  | 0.0000E+00 | 0.0000E+00 | 0.0000E+00  | 0.0000E+00 | 0.0000E+00 | 0.0000E+00  | 0.0000E+00 | 0.0000E+00 | 0.0000E+00    | 0.0000E+00 | 0.0000E+00 | 0.0000E+00    | 0.0000E+00 | 0.0000E+00 | 0.0000E+00    | 0.0000E+00 | 0.0000E+00 |
| 2.   | AND 22. | 0.3000E+07                                 | 0.0000E+00 | 0.0000E+00 | 0.0000E+00  | 0.0000E+00 | 0.0000E+00 | 0.0000E+00  | 0.0000E+00 | 0.0000E+00 | 0.0000E+00  | 0.0000E+00 | 0.0000E+00 | 0.0000E+00  | 0.0000E+00 | 0.0000E+00 | 0.0000E+00    | 0.0000E+00 | 0.0000E+00 | 0.0000E+00    | 0.0000E+00 | 0.0000E+00 | 0.0000E+00    | 0.0000E+00 | 0.0000E+00 |
| 50.  | AND 21. | 0.3000E+07                                 | 0.0000E+00 | 0.0000E+00 | 0.0000E+00  | 0.0000E+00 | 0.0000E+00 | 0.0000E+00  | 0.0000E+00 | 0.0000E+00 | 0.0000E+00  | 0.0000E+00 | 0.0000E+00 | 0.0000E+00  | 0.0000E+00 | 0.0000E+00 | 0.0000E+00    | 0.0000E+00 | 0.0000E+00 | 0.0000E+00    | 0.0000E+00 | 0.0000E+00 | 0.0000E+00    | 0.0000E+00 | 0.0000E+00 |
| 80.  | AND 22. | 0.3000E+07                                 | 0.0000E+00 | 0.0000E+00 | 0.0000E+00  | 0.0000E+00 | 0.0000E+00 | 0.0000E+00  | 0.0000E+00 | 0.0000E+00 | 0.0000E+00  | 0.0000E+00 | 0.0000E+00 | 0.0000E+00  | 0.0000E+00 | 0.0000E+00 | 0.0000E+00    | 0.0000E+00 | 0.0000E+00 | 0.0000E+00    | 0.0000E+00 | 0.0000E+00 | 0.0000E+00    | 0.0000E+00 | 0.0000E+00 |
| 7.   | AND 0.  | 0.3000E+06                                 | 0.0000E+00 | 0.0000E+00 | 0.0000E+00  | 0.0000E+00 | 0.0000E+00 | 0.0000E+00  | 0.0000E+00 | 0.0000E+00 | 0.0000E+00  | 0.0000E+00 | 0.0000E+00 | 0.0000E+00  | 0.0000E+00 | 0.0000E+00 | 0.0000E+00    | 0.0000E+00 | 0.0000E+00 | 0.0000E+00    | 0.0000E+00 | 0.0000E+00 | 0.0000E+00    | 0.0000E+00 | 0.0000E+00 |
| 10.  | AND 0.  | 0.3000E+06                                 | 0.0000E+00 | 0.0000E+00 | 0.0000E+00  | 0.0000E+00 | 0.0000E+00 | 0.0000E+00  | 0.0000E+00 | 0.0000E+00 | 0.0000E+00  | 0.0000E+00 | 0.0000E+00 | 0.0000E+00  | 0.0000E+00 | 0.0000E+00 | 0.0000E+00    | 0.0000E+00 | 0.0000E+00 | 0.0000E+00    | 0.0000E+00 | 0.0000E+00 | 0.0000E+00    | 0.0000E+00 | 0.0000E+00 |
| 54.  | AND 0.  | 0.1000E+07                                 | 0.0000E+00 | 0.0000E+00 | 0.0000E+00  | 0.0000E+00 | 0.0000E+00 | 0.0000E+00  | 0.0000E+00 | 0.0000E+00 | 0.0000E+00  | 0.0000E+00 | 0.0000E+00 | 0.0000E+00  | 0.0000E+00 | 0.0000E+00 | 0.0000E+00    | 0.0000E+00 | 0.0000E+00 | 0.0000E+00    | 0.0000E+00 | 0.0000E+00 | 0.0000E+00    | 0.0000E+00 | 0.0000E+00 |
| 58.  | AND 0.  | 10.00                                      | 0.0000E+00 | 0.0000E+00 | 0.0000E+00  | 0.0000E+00 | 0.0000E+00 | 0.0000E+00  | 0.0000E+00 | 0.0000E+00 | 0.0000E+00  | 0.0000E+00 | 0.0000E+00 | 0.0000E+00  | 0.0000E+00 | 0.0000E+00 | 0.0000E+00    | 0.0000E+00 | 0.0000E+00 | 0.0000E+00    | 0.0000E+00 | 0.0000E+00 | 0.0000E+00    | 0.0000E+00 | 0.0000E+00 |
| 84.  | AND 0.  | 0.1000E+07                                 | 0.0000E+00 | 0.0000E+00 | 0.0000E+00  | 0.0000E+00 | 0.0000E+00 | 0.0000E+00  | 0.0000E+00 | 0.0000E+00 | 0.0000E+00  | 0.0000E+00 | 0.0000E+00 | 0.0000E+00  | 0.0000E+00 | 0.0000E+00 | 0.0000E+00    | 0.0000E+00 | 0.0000E+00 | 0.0000E+00    | 0.0000E+00 | 0.0000E+00 | 0.0000E+00    | 0.0000E+00 | 0.0000E+00 |
| 88.  | AND 0.  | 10.00                                      | 0.0000E+00 | 0.0000E+00 | 0.0000E+00  | 0.0000E+00 | 0.0000E+00 | 0.0000E+00  | 0.0000E+00 | 0.0000E+00 | 0.0000E+00  | 0.0000E+00 | 0.0000E+00 | 0.0000E+00  | 0.0000E+00 | 0.0000E+00 | 0.0000E+00    | 0.0000E+00 | 0.0000E+00 | 0.0000E+00    | 0.0000E+00 | 0.0000E+00 | 0.0000E+00    | 0.0000E+00 | 0.0000E+00 |

--NO ANGULAR COEFFICIENT SPECIFIED

HUGHES TURBOTESTER - ROTOR AND STRUCTURAL DYNAMIC MODEL

\*\*\*\*\*  
 \* SYSTEM CRITICAL SPEED SUMMARY \*  
 \*\*\*\*\*

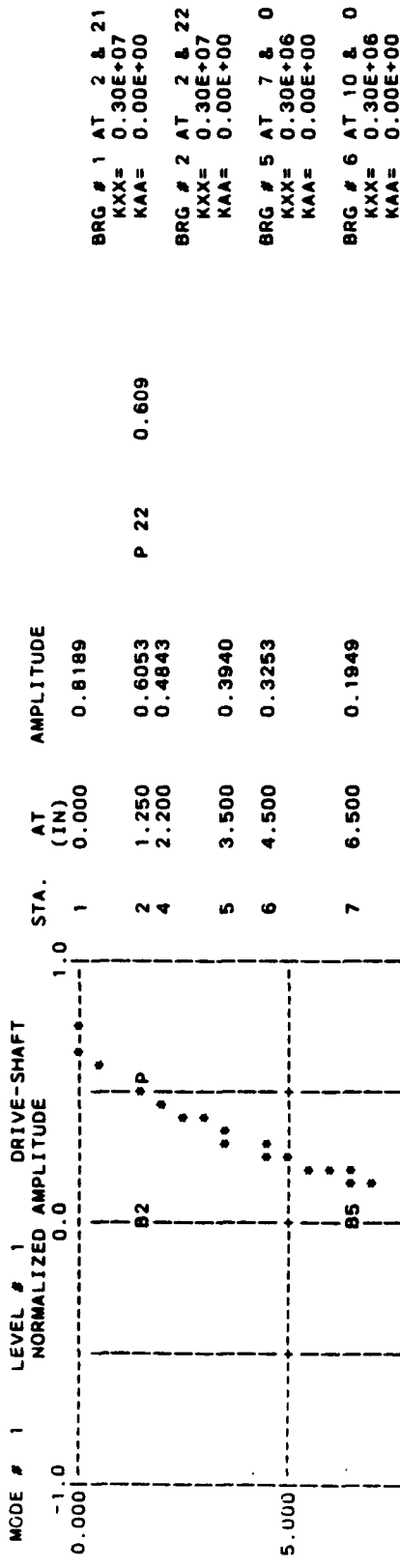
|   | ( RPM ) | ( RPS ) | ( RAD/S ) |
|---|---------|---------|-----------|
| 1 | 14707.  | 245.11  | 1540.1    |
| 2 | 24460.  | 407.66  | 2561.4    |
| 3 | 30131.  | 502.19  | 3155.3    |
| 4 | 36487.  | 608.12  | 3820.9    |
| 5 | 69322.  | 1155.4  | 7259.4    |
| 6 | 72829.  | 1213.8  | 7626.6    |

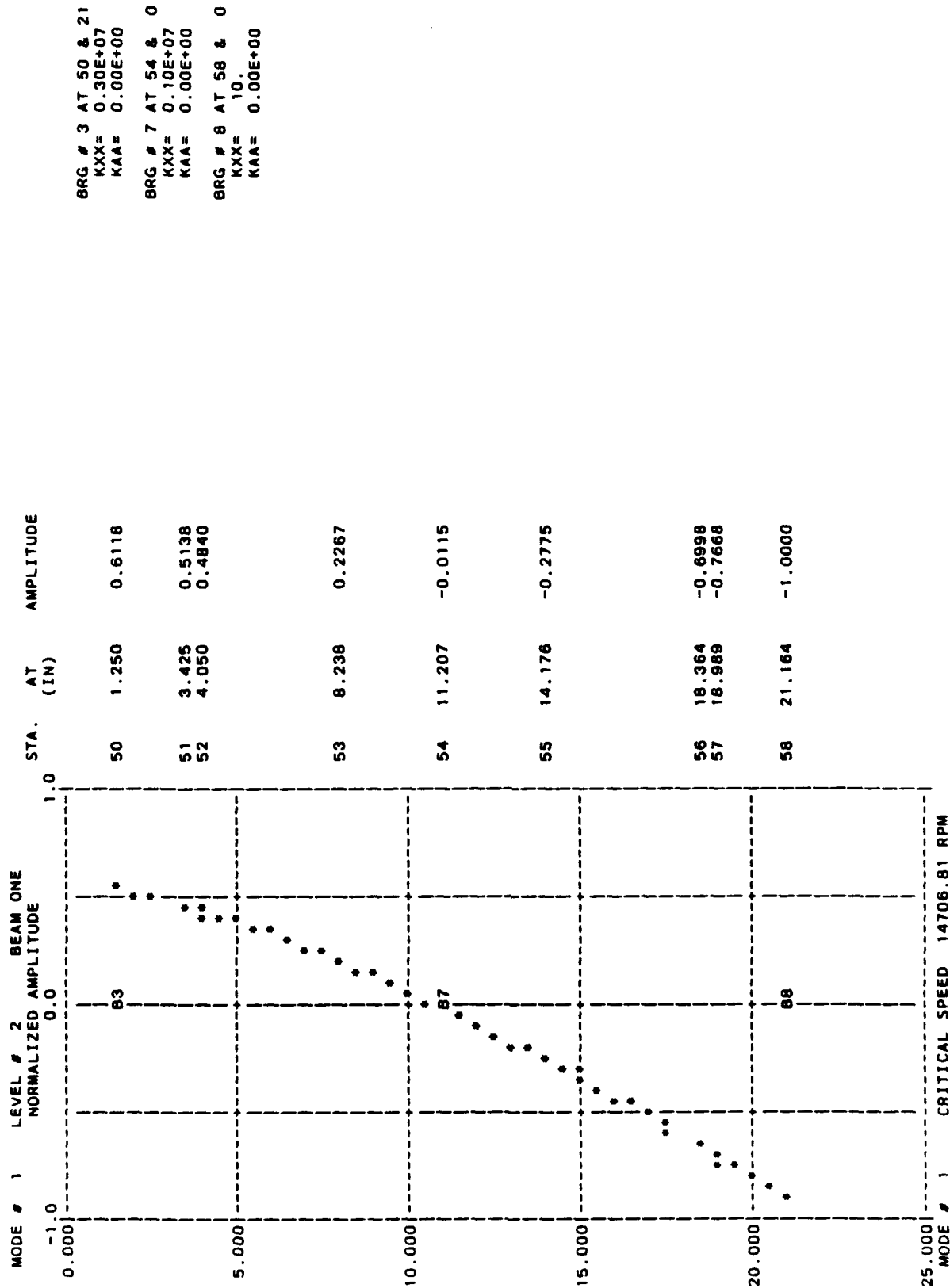
THE FOLLOWING NATURAL FREQUENCIES ARE FOR REFERENCE USE ONLY

|   |        |        |        |
|---|--------|--------|--------|
| 7 | 82924. | 1382.1 | 8683.8 |
| 8 | 83085. | 1384.8 | 8700.7 |
| 9 | 83548. | 1392.5 | 8749.1 |

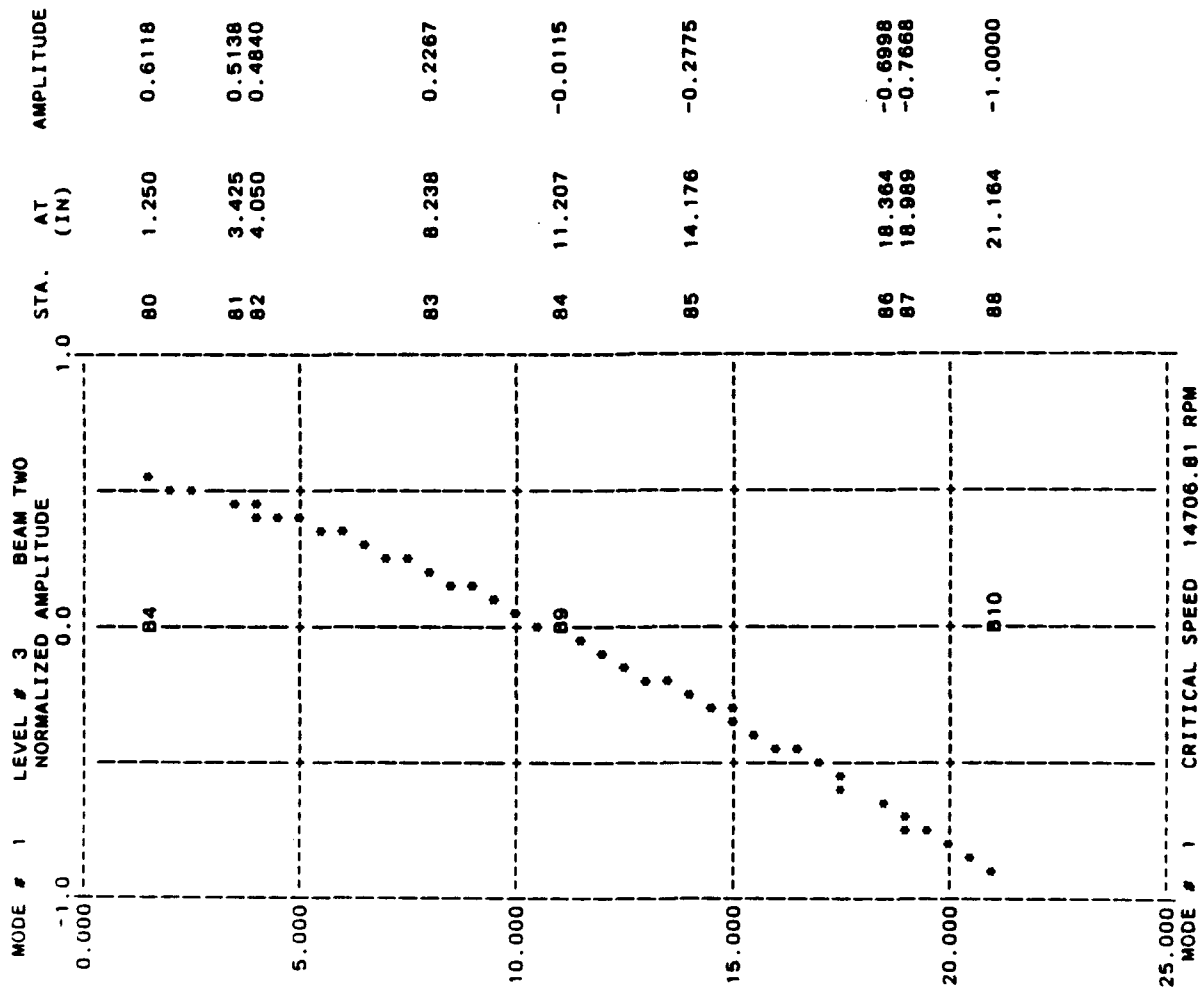
9 NATURAL FREQUENCIES WITHIN THE RANGE SPECIFIED

HUGHES TURBOTESTER - ROTOR AND STRUCTURAL DYNAMIC MODEL



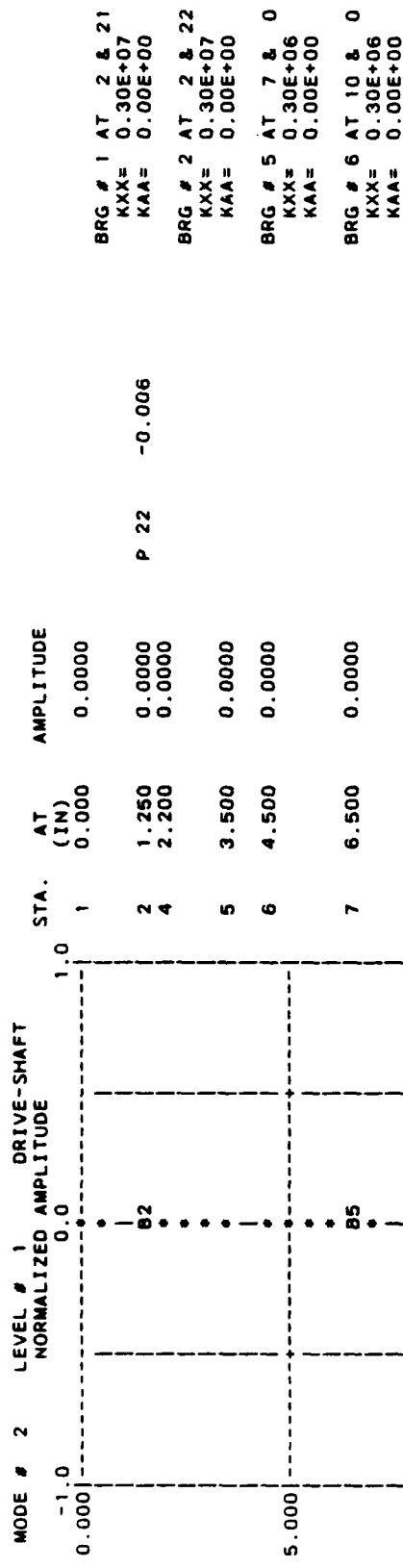


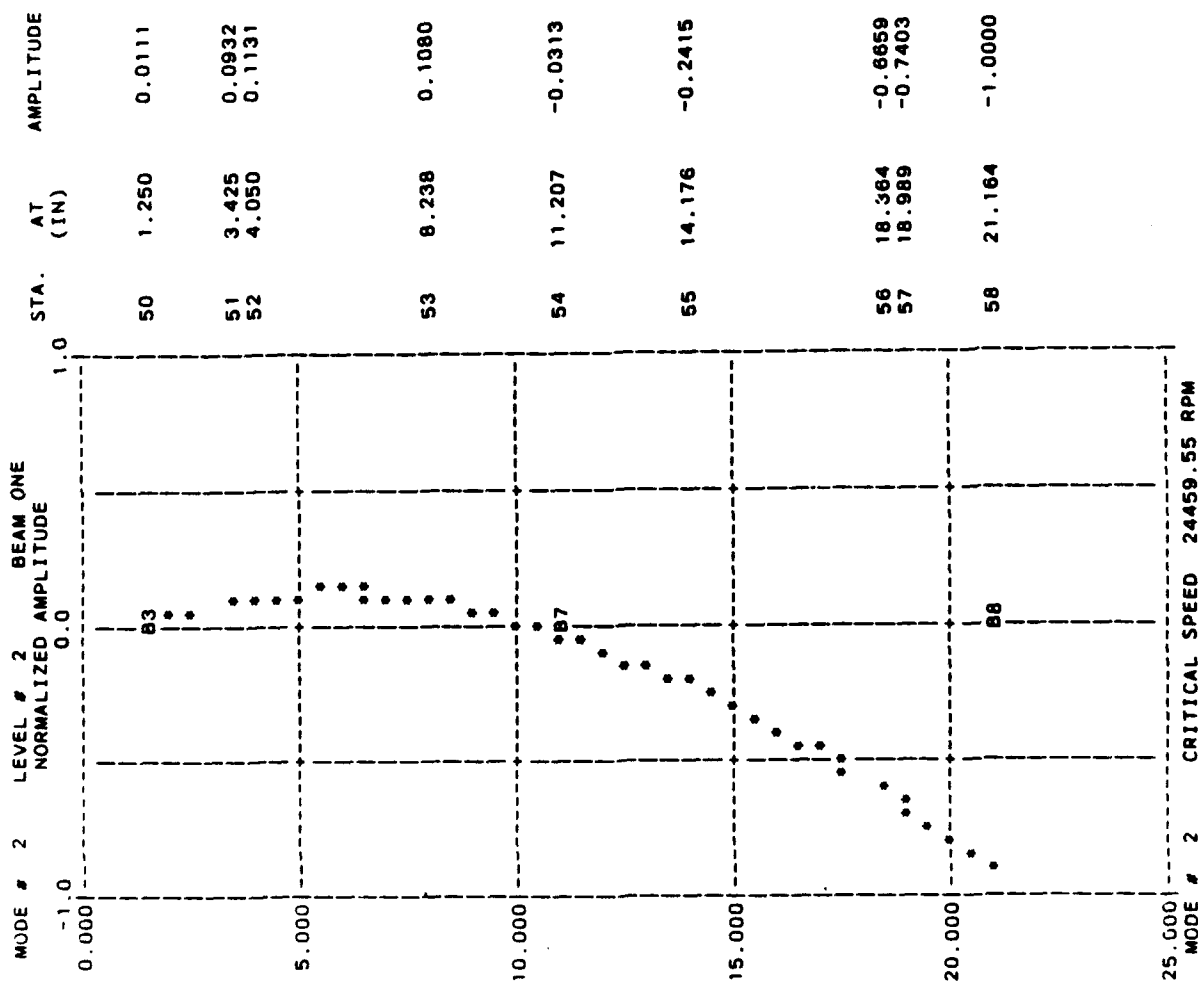




BRG # 4 AT 80 & 22  
 KXX= 0.30E+07  
 KAA= 0.00E+00  
 BRG # 9 AT 84 & 0  
 KXX= 0.10E+07  
 KAA= 0.00E+00  
 BRG #10 AT 88 & 0  
 KXX= 10.  
 KAA= 0.00E+00

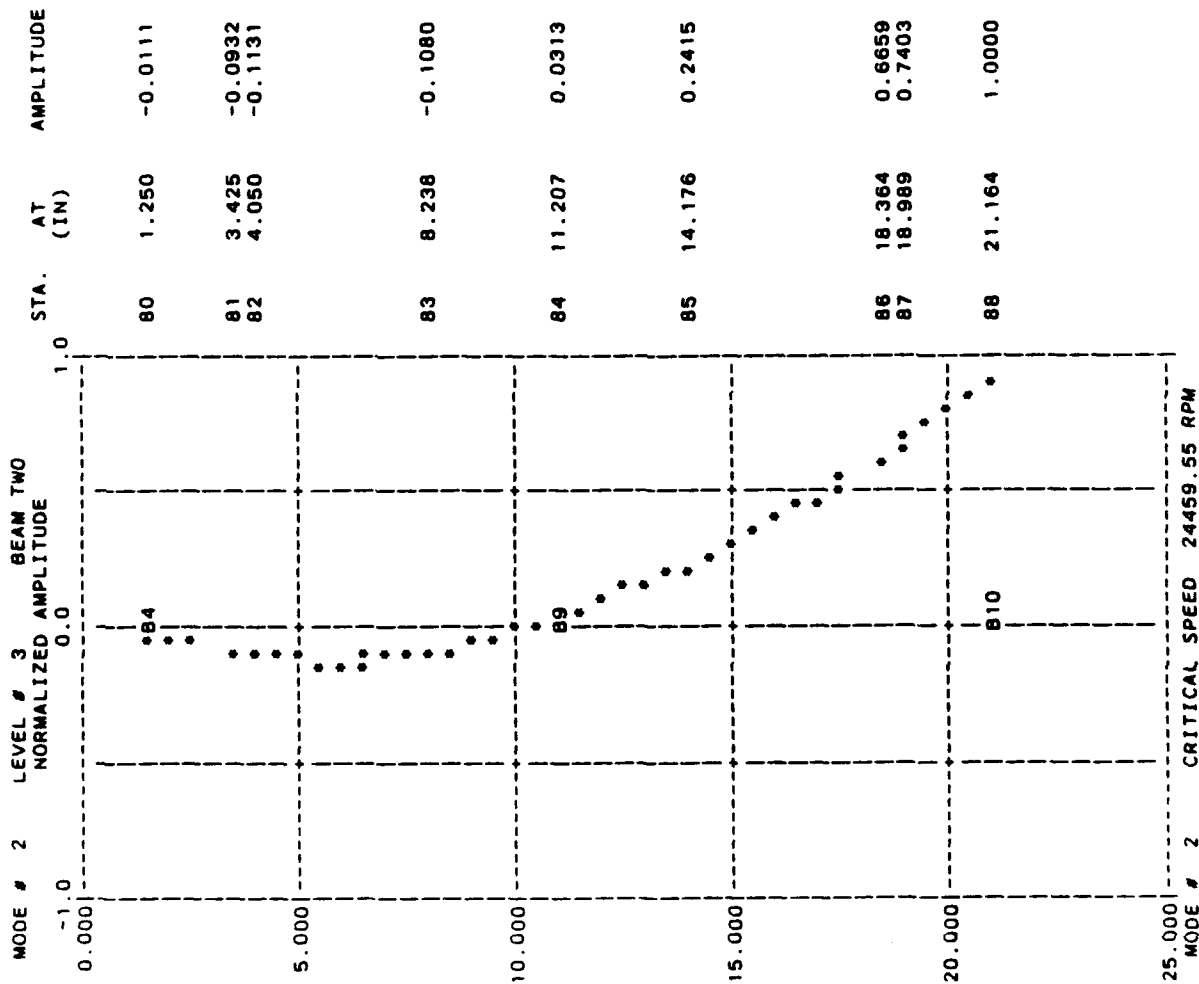
HUGHES TURBOTESTER - ROTOR AND STRUCTURAL DYNAMIC MODEL





BRG # 3 AT 50 & 21  
 KXX= 0.30E+07  
 KAA= 0.00E+00  
 BRG # 7 AT 54 & 0  
 KXX= 0.10E+07  
 KAA= 0.00E+00  
 BRG # 8 AT 58 & 0  
 KXX= 10.  
 KAA= 0.00E+00

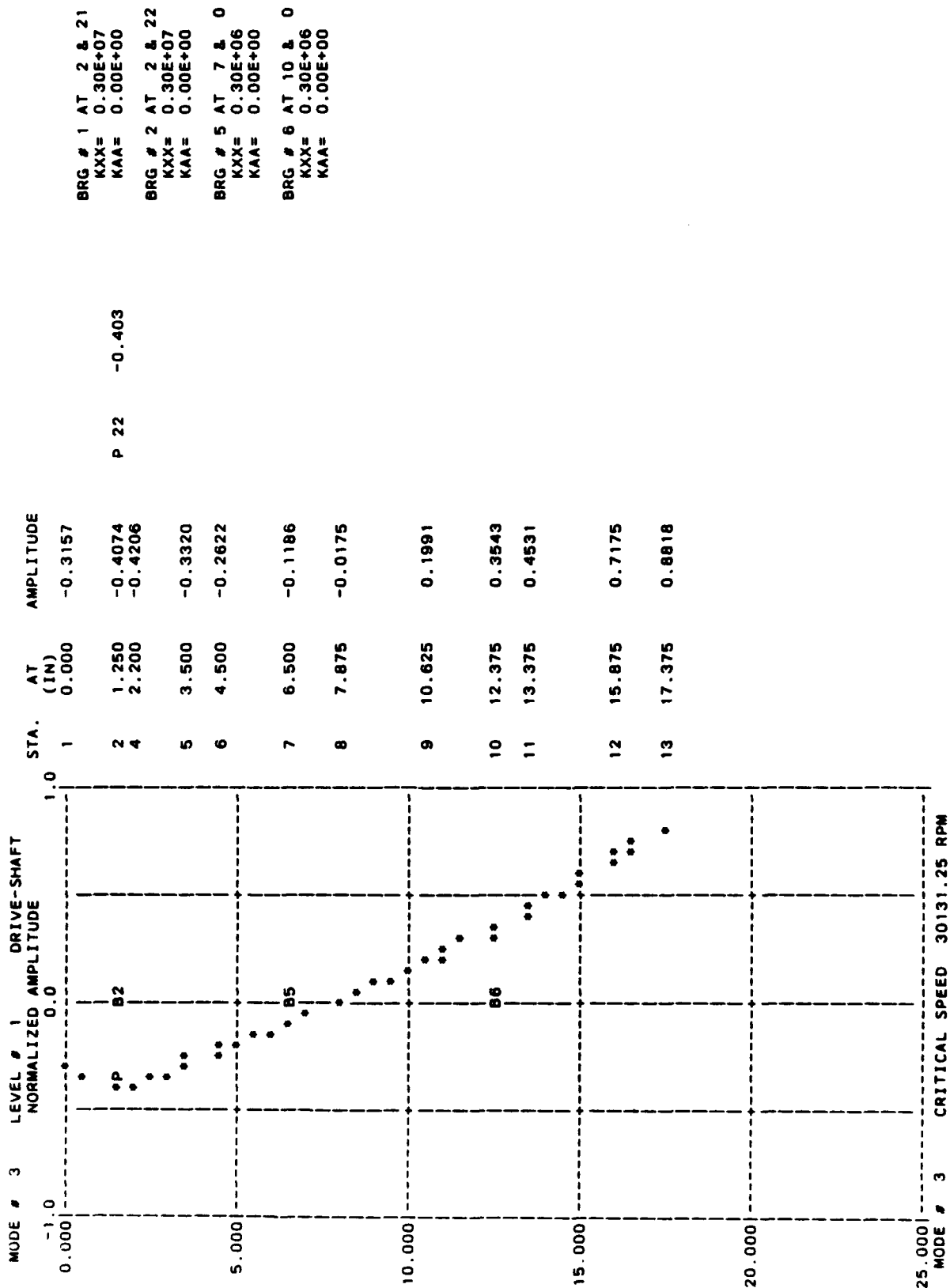
HUGHES TURBOTESTER - ROTOR AND STRUCTURAL DYNAMIC MODEL

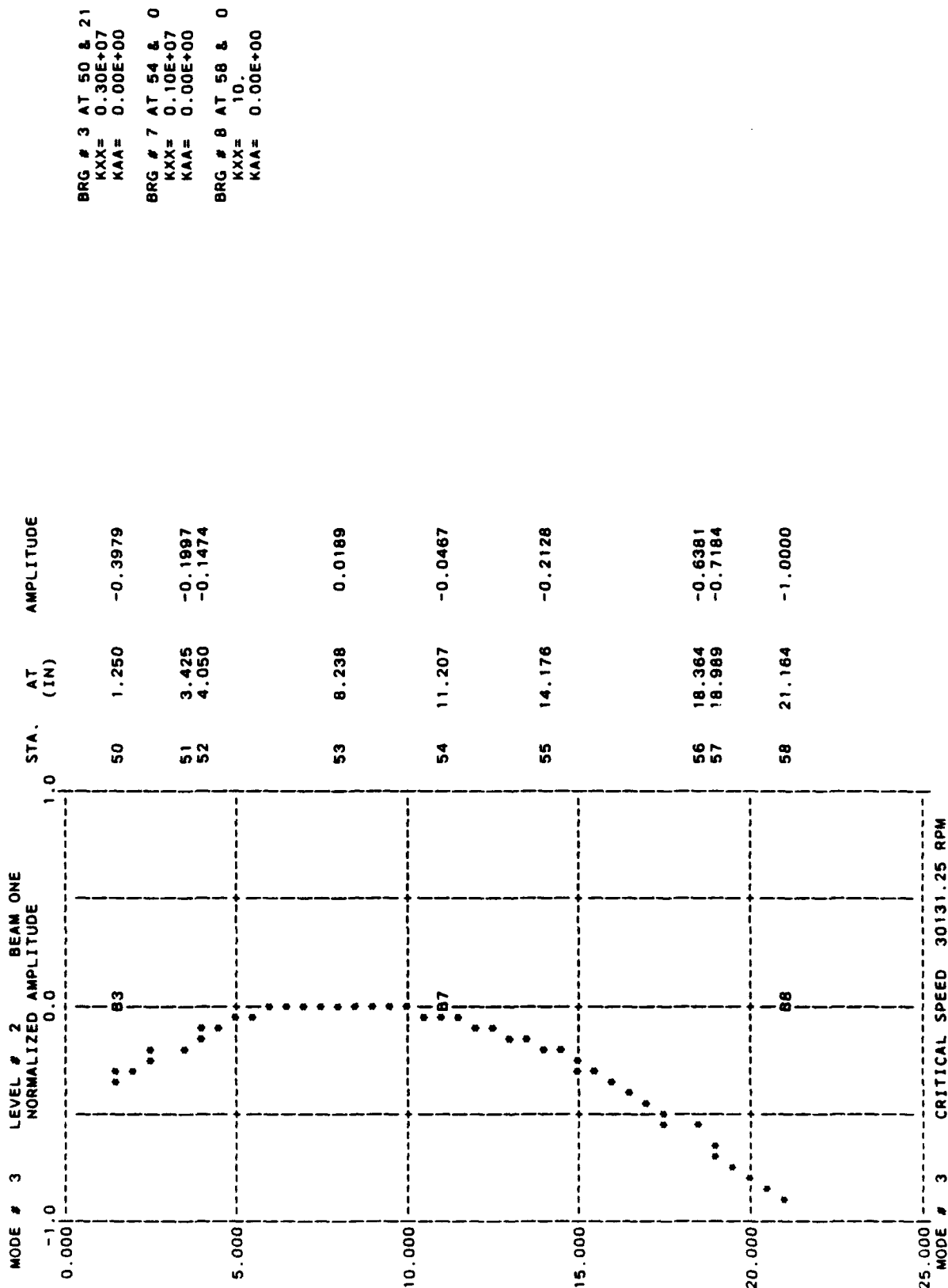


BRG # 4 AT 80 & 22  
KXX= 0.30E+07  
KAA= 0.00E+00

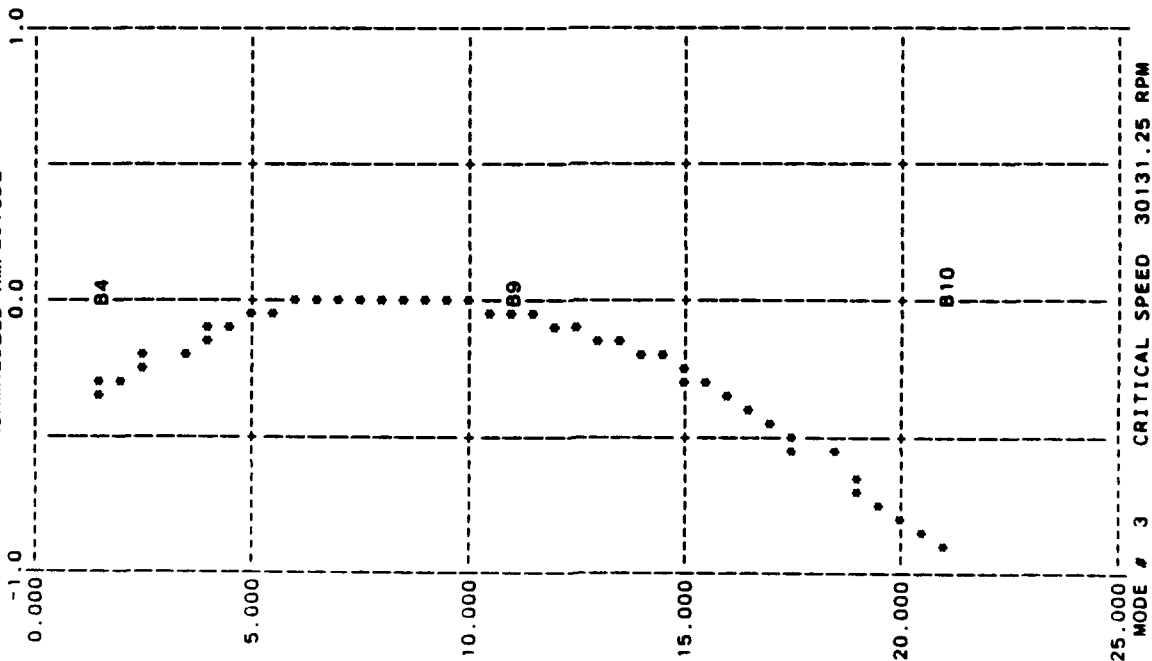
BRG # 9 AT 84 & 0  
KXX= 0.10E+07  
KAA= 0.00E+00

BRG #10 AT 88 & 0  
KXX= 10.  
KAA= 0.00E+00





MODE # 3 LEVEL # 3 BEAM TWO  
 NORMALIZED AMPLITUDE



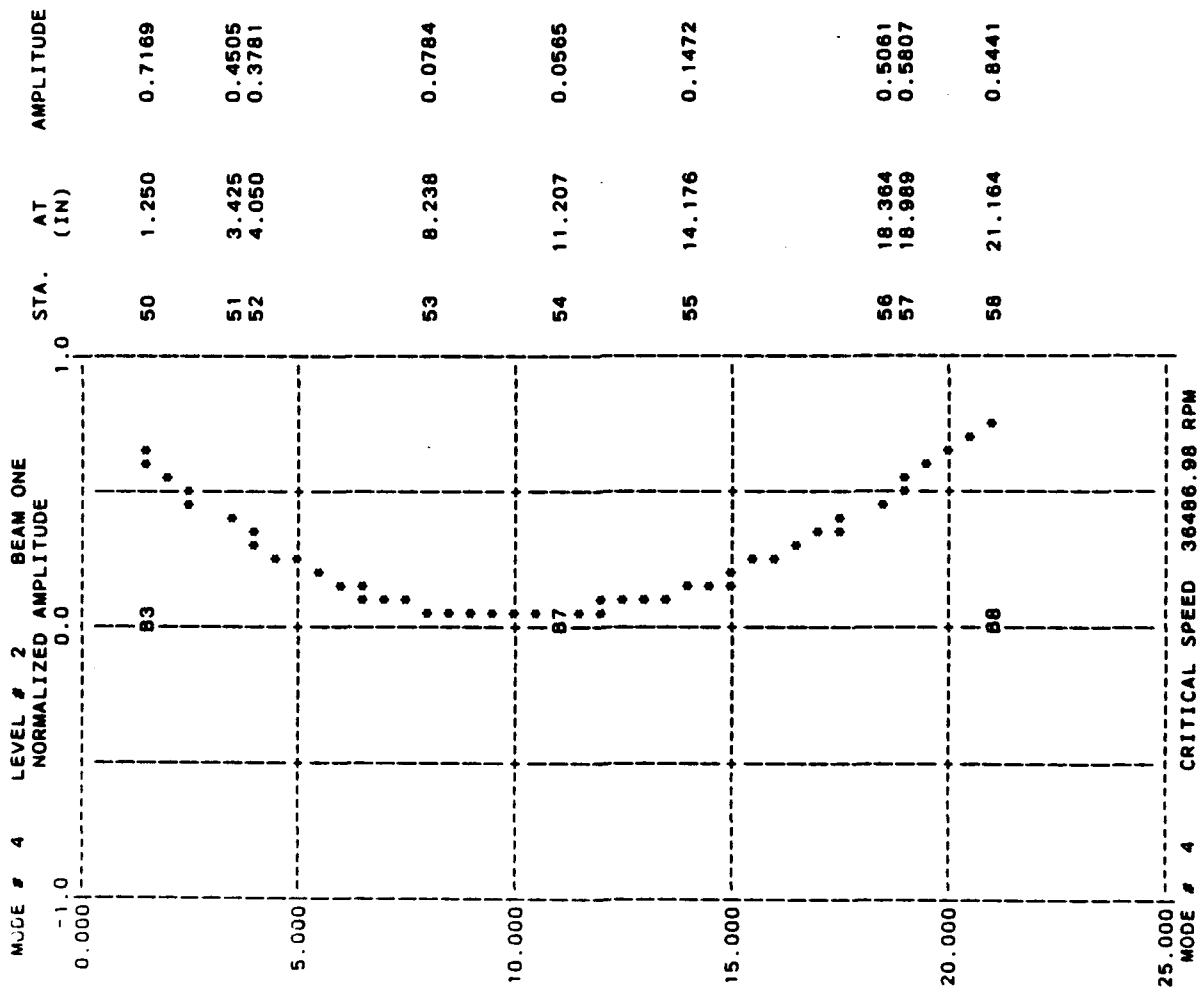
BRG # 4 AT 80 & 22  
 KXX= 0.30E+07  
 KAA= 0.00E+00

BRG # 9 AT 84 & 0  
 KXX= 0.10E+07  
 KAA= 0.00E+00

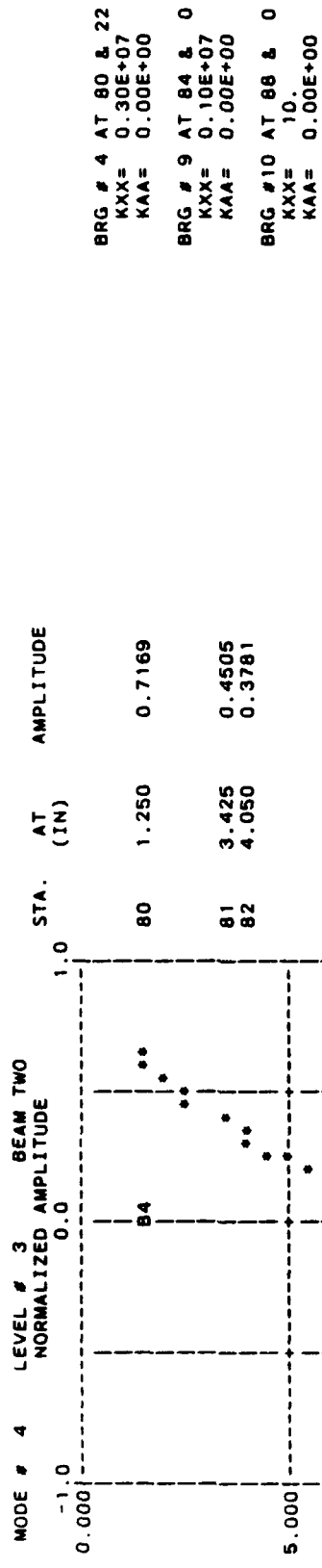
BRG #10 AT 88 & 0  
 KXX= 10.  
 KAA= 0.00E+00

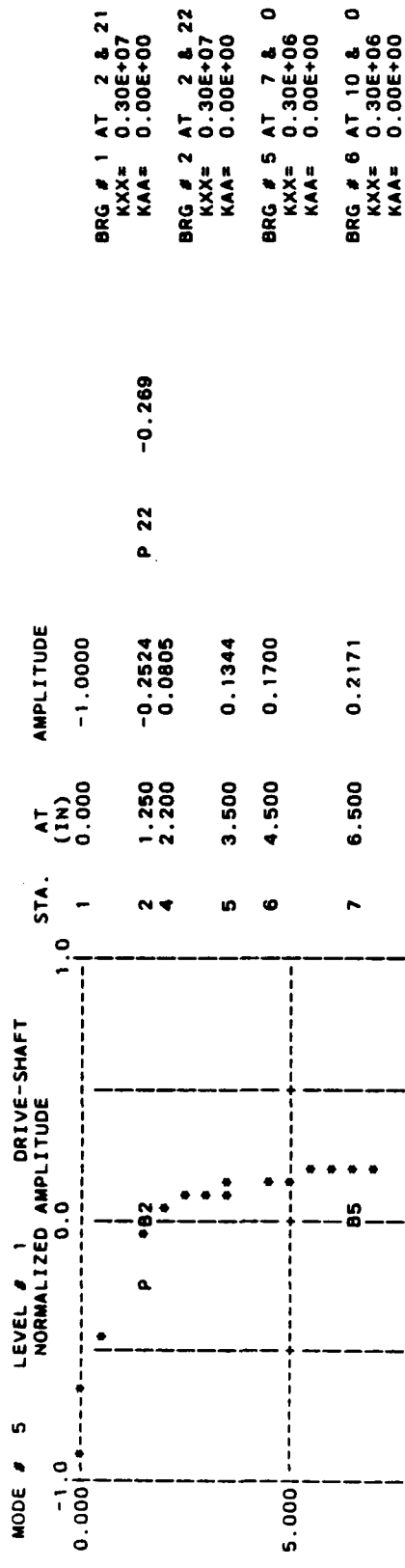






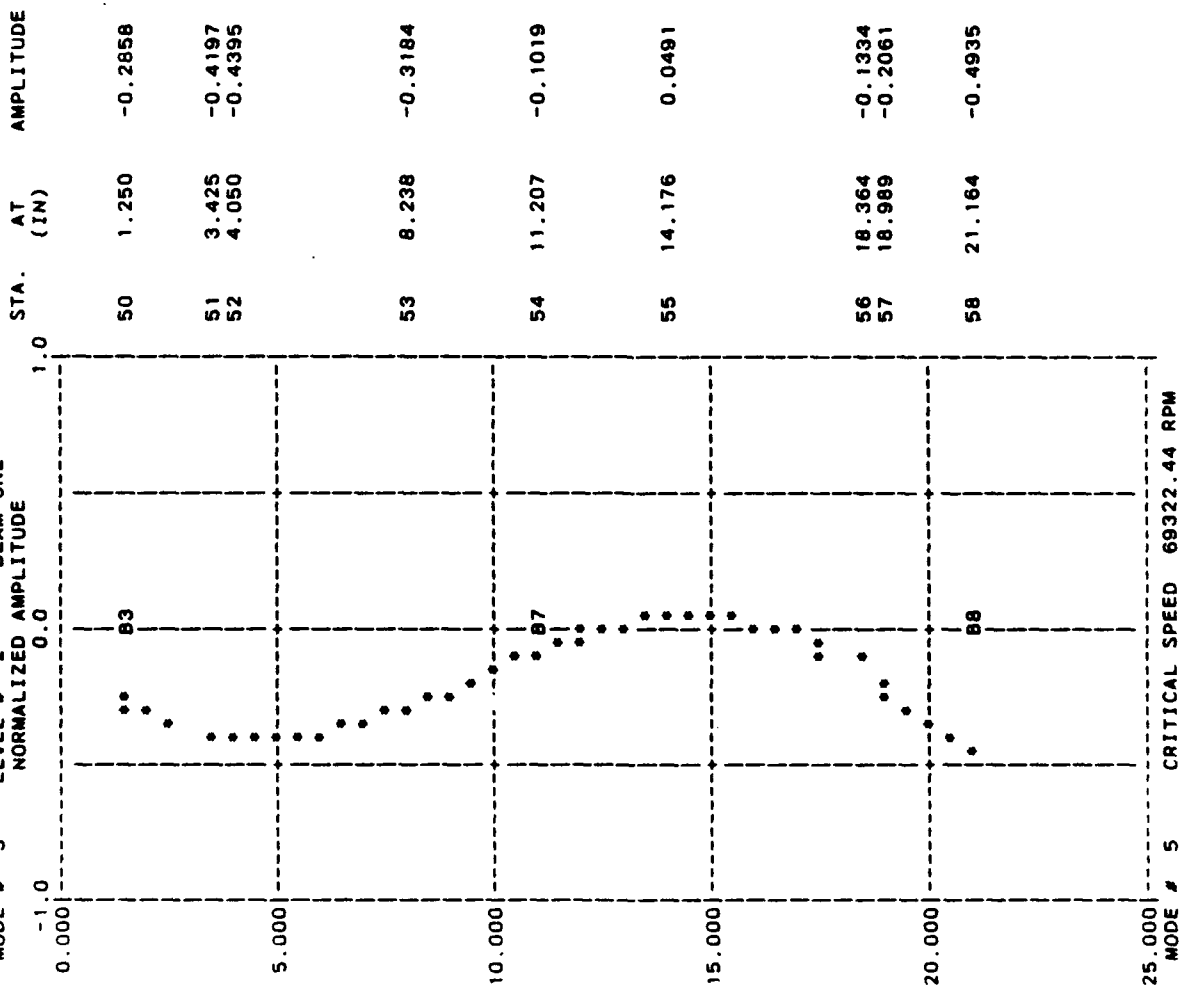
BRG # 3 AT 50 & 21  
 KXX= 0.30E+07  
 KAA= 0.00E+00  
 BRG # 7 AT 54 & 0  
 KXX= 0.10E+07  
 KAA= 0.00E+00  
 BRG # 8 AT 58 & 0  
 KXX= 10.  
 KAA= 0.00E+00





HUGHES TURBOTESTER - ROTOR AND STRUCTURAL DYNAMIC MODEL

MODE # 5 LEVEL # 2 BEAM ONE

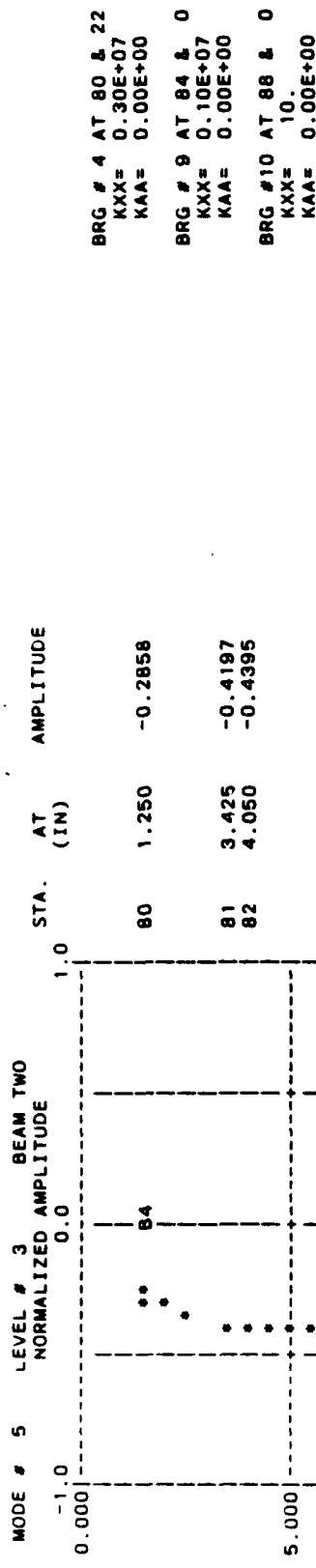


BRG # 3 AT 50 & 21  
KXX= 0.30E+07  
KAA= 0.00E+00

BRG # 7 AT 54 & 0  
KXX= 0.10E+07  
KAA= 0.00E+00

BRG # 8 AT 58 & 0  
KXX= 10.  
KAA= 0.00E+00

HUGHES TURBOTESTER - ROTOR AND STRUCTURAL DYNAMIC MODEL



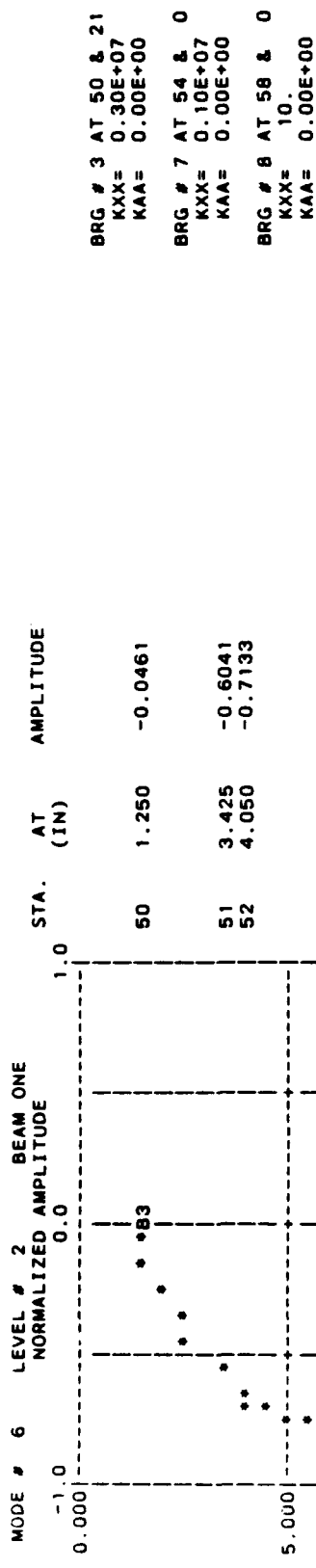
HUGHES TURBOTESTER - ROTOR AND STRUCTURAL DYNAMIC MODEL

| MODE # | 6 | LEVEL # | 1 | DRIVE-SHAFT<br>NORMALIZED AMPLITUDE | STA. | AT<br>(IN) | AMPLITUDE |                                                     |
|--------|---|---------|---|-------------------------------------|------|------------|-----------|-----------------------------------------------------|
|        |   |         |   | 0.0                                 | 1    | 0.000      | 0.0000    |                                                     |
|        |   |         |   | 0.2                                 | 2    | 1.250      | 0.0000    | BRG # 1 AT 2 & 21<br>KXX= 0.30E+07<br>KAA= 0.00E+00 |
|        |   |         |   | 0.4                                 | 4    | 2.200      | -0.0000   |                                                     |
|        |   |         |   | 0.6                                 | 5    | 3.500      | -0.0000   | BRG # 2 AT 2 & 22<br>KXX= 0.30E+07<br>KAA= 0.00E+00 |
|        |   |         |   | 0.8                                 | 6    | 4.500      | -0.0000   | BRG # 5 AT 7 & 0<br>KXX= 0.30E+06<br>KAA= 0.00E+00  |
|        |   |         |   | 1.0                                 | 7    | 6.500      | -0.0000   | BRG # 6 AT 10 & 0<br>KXX= 0.30E+06<br>KAA= 0.00E+00 |
|        |   |         |   | 1.2                                 | 8    | 7.875      | -0.0000   |                                                     |
|        |   |         |   | 1.4                                 | 9    | 10.625     | -0.0000   |                                                     |
|        |   |         |   | 1.6                                 | 10   | 12.375     | -0.0000   |                                                     |
|        |   |         |   | 1.8                                 | 11   | 13.375     | -0.0000   |                                                     |
|        |   |         |   | 2.0                                 | 12   | 15.875     | 0.0000    |                                                     |
|        |   |         |   | 2.2                                 | 13   | 17.375     | 0.0000    |                                                     |

N-54

25.000|-----  
 MODE # 6 CRITICAL SPEED 72828.62 RPM

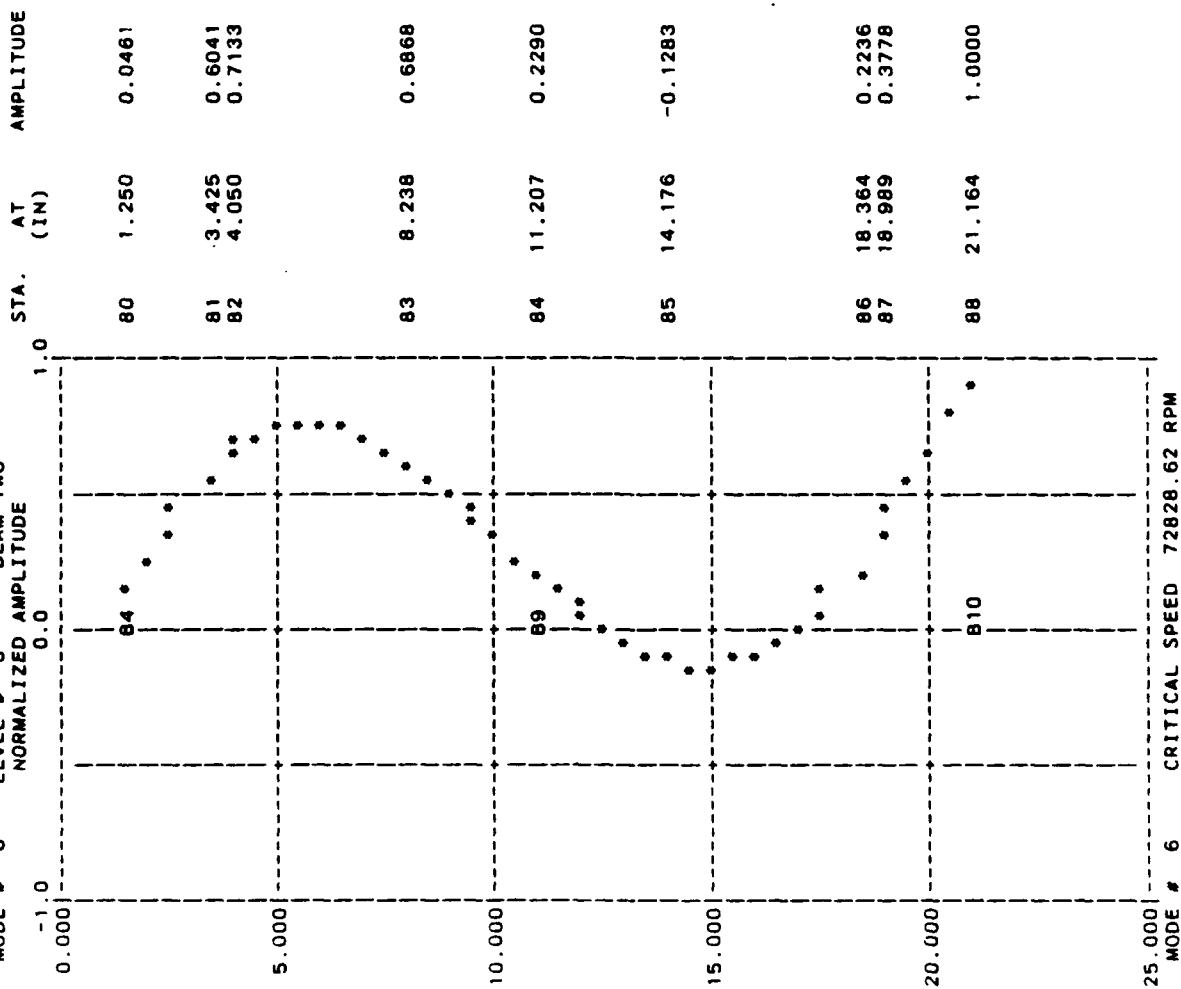
HUGHES TURBOTESTER - ROTOR AND STRUCTURAL DYNAMIC MODEL



N-55

HUGHES TURBOTESTER - ROTOR AND STRUCTURAL DYNAMIC MODEL

MODE # 6 LEVEL # 3 BEAM TWO



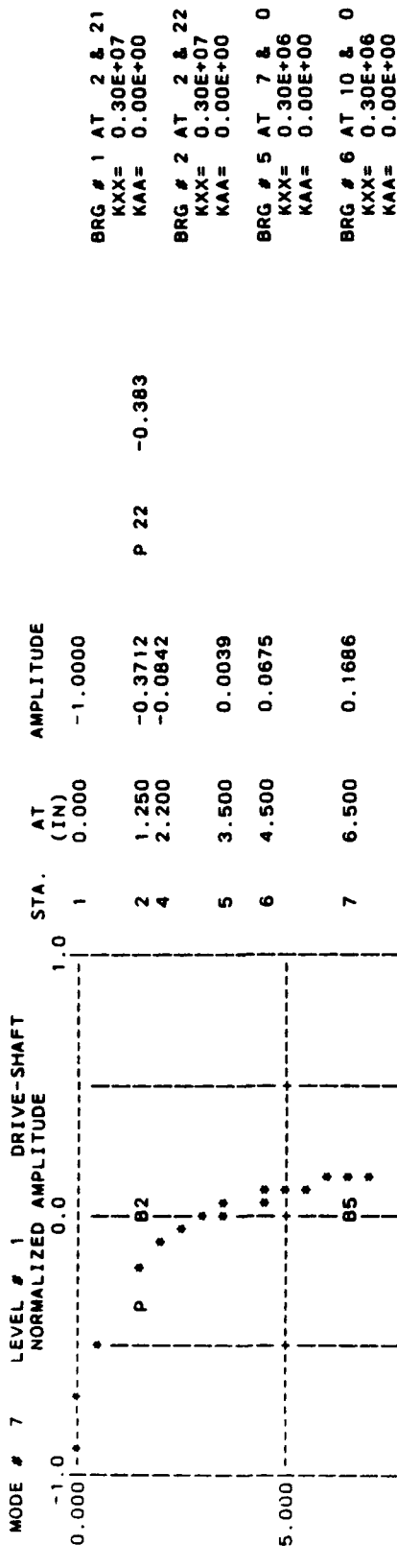
BRG # 4 AT 80 & 22  
 KXX= 0.30E+07  
 KAA= 0.00E+00

BRG # 9 AT 84 & 0  
 KXX= 0.10E+07  
 KAA= 0.00E+00

BRG #10 AT 88 & 0  
 KXX= 10.  
 KAA= 0.00E+00



HUGHES TURBOTESTER - ROTOR AND STRUCTURAL DYNAMIC MODEL



N-57

AMPLITUDE

STA. AT (IN)

MODE # 7

LEVEL # 1

DRIVE-SHAFT

NORMALIZED AMPLITUDE

BRG # 1 AT 2 & 21  
 KXX= 0.30E+07  
 KAA= 0.00E+00  
 BRG # 2 AT 2 & 22  
 KXX= 0.30E+07  
 KAA= 0.00E+00  
 BRG # 5 AT 7 & 0  
 KXX= 0.30E+06  
 KAA= 0.00E+00  
 BRG # 6 AT 10 & 0  
 KXX= 0.30E+06  
 KAA= 0.00E+00

P 22 -0.383

-1.0000

1 0.000

2 1.250

4 2.200

5 3.500

6 4.500

-0.3712

0.0039

0.0675

0.1686

0.2007

0.1711

0.0924

0.0283

-0.1643

-0.2917

10 12.375

11 13.375

12 15.875

13 17.375

10.000

15.000

20.000

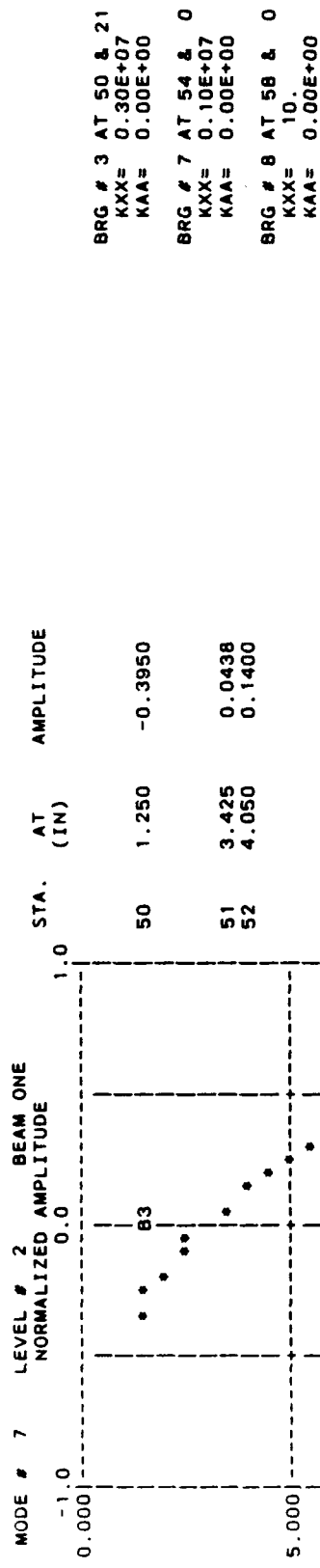
25.000

CRITICAL SPEED

82923.81 RPM

MODE # 7

HUGHES TURBOTESTER - ROTOR AND STRUCTURAL DYNAMIC MODEL



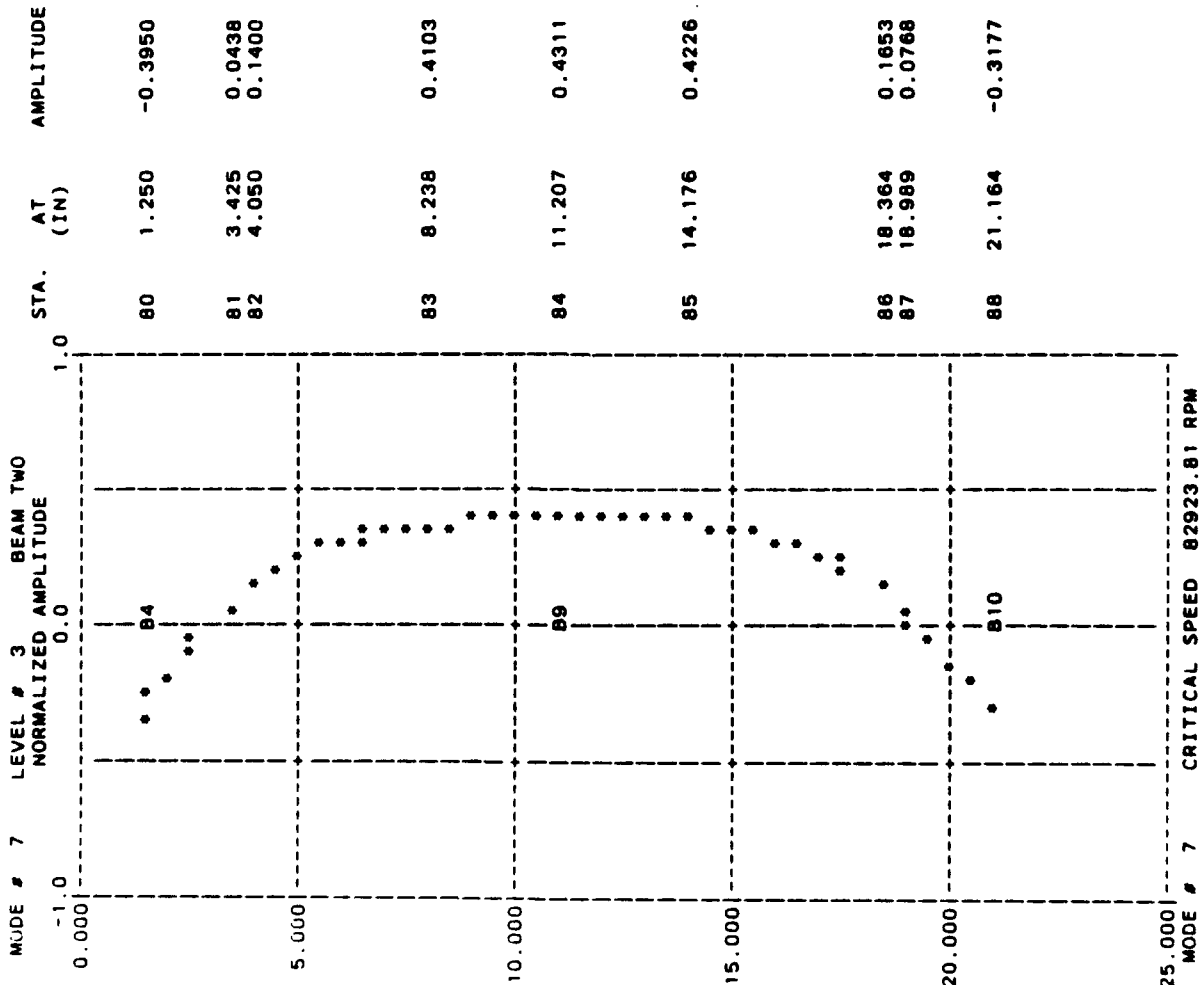
N-58

MODE # 7 LEVEL # 3 BEAM TWO  
 NORMALIZED AMPLITUDE

BRG # 4 AT 80 & 22  
 KXX= 0.30E+07  
 KAA= 0.00E+00

BRG # 9 AT 84 & 0  
 KXX= 0.10E+07  
 KAA= 0.00E+00

BRG #10 AT 88 & 0  
 KXX= 10.  
 KAA= 0.00E+00



HUGHES TURBOTESTER - ROTOR AND STRUCTURAL DYNAMIC MODEL

| MODE # | 8 | LEVEL # | 1 | DRIVE-SHAFT<br>NORMALIZED AMPLITUDE | STA. | AT<br>(IN) | AMPLITUDE |
|--------|---|---------|---|-------------------------------------|------|------------|-----------|
|        |   |         |   | 0.0                                 | 1    | 0.000      | -0.0000   |
|        |   |         |   | 0.0                                 | 2    | 1.250      | -0.0000   |
|        |   |         |   | 0.0                                 | 4    | 2.200      | -0.0000   |
|        |   |         |   | 0.0                                 | 5    | 3.500      | -0.0000   |
|        |   |         |   | 0.0                                 | 6    | 4.500      | 0.0000    |
|        |   |         |   | 0.0                                 | 7    | 6.500      | 0.0000    |
|        |   |         |   | 0.0                                 | 8    | 7.875      | 0.0000    |
|        |   |         |   | 0.0                                 | 9    | 10.625     | 0.0000    |
|        |   |         |   | 0.0                                 | 10   | 12.375     | 0.0000    |
|        |   |         |   | 0.0                                 | 11   | 13.375     | 0.0000    |
|        |   |         |   | 0.0                                 | 12   | 15.875     | -0.0000   |
|        |   |         |   | 0.0                                 | 13   | 17.375     | -0.0000   |

BRG # 1 AT 2 & 21  
 KXX= 0.30E+07  
 KAA= 0.00E+00

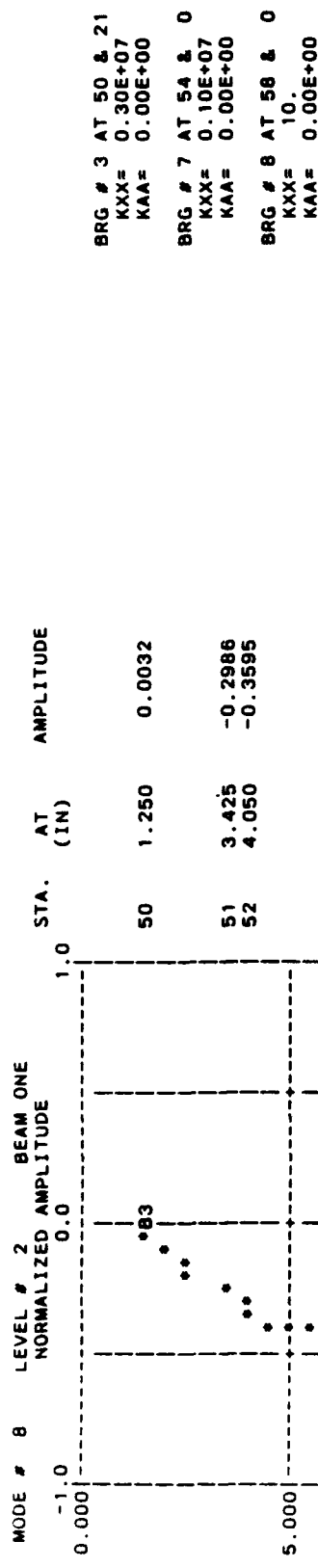
BRG # 2 AT 2 & 22  
 KXX= 0.30E+07  
 KAA= 0.00E+00

BRG # 5 AT 7 & 0  
 KXX= 0.30E+06  
 KAA= 0.00E+00

BRG # 6 AT 10 & 0  
 KXX= 0.30E+06  
 KAA= 0.00E+00

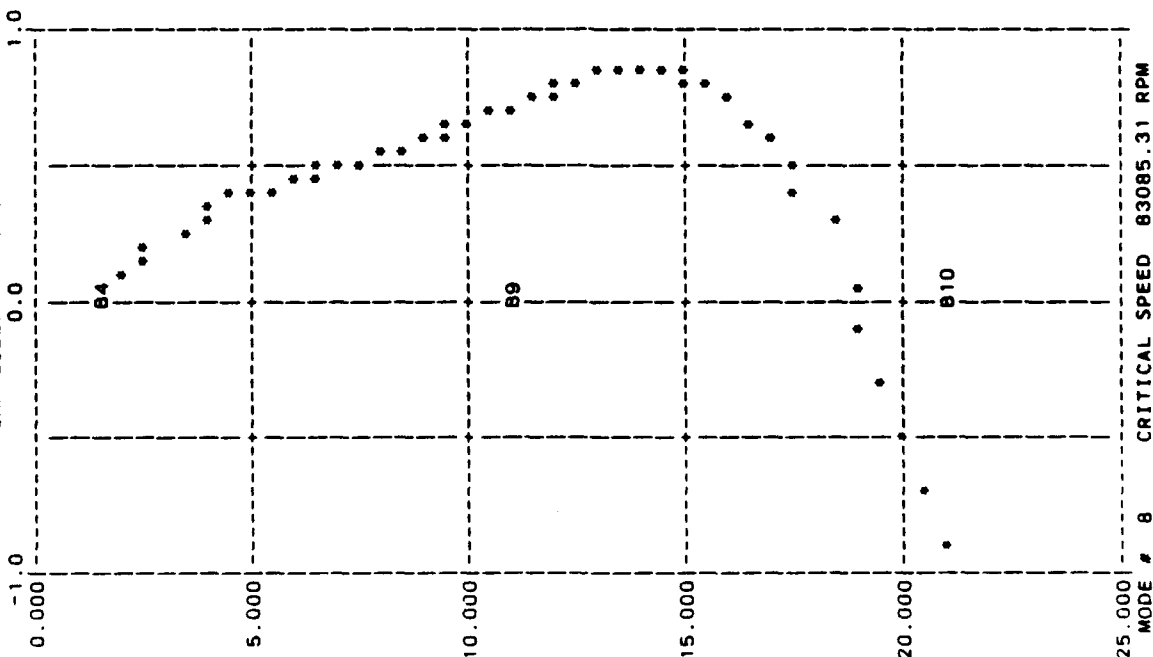
25.000  
 MODE # 8 CRITICAL SPEED 83085.31 RPM

HUGHES TURBOTESTER - ROTOR AND STRUCTURAL DYNAMIC MODEL



HUGHES TURBOTESTER - ROTOR AND STRUCTURAL DYNAMIC MODEL

MODE # 8 LEVEL # 3 BEAM TWO  
NORMALIZED AMPLITUDE

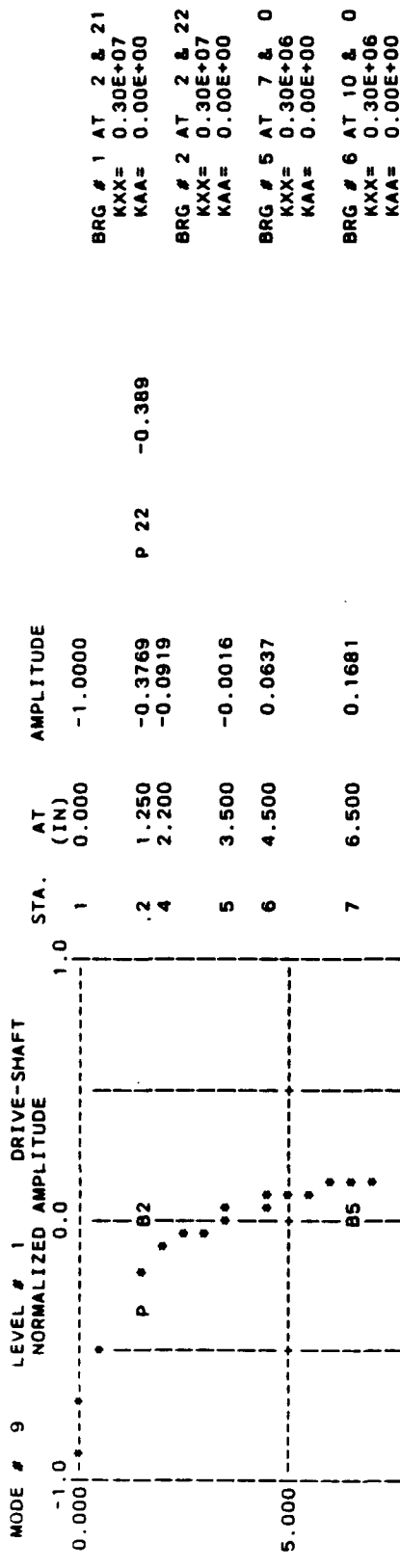


BRG # 4 AT 80 & 22  
KXX= 0.30E+07  
KAA= 0.00E+00

BRG # 9 AT 84 & 0  
KXX= 0.10E+07  
KAA= 0.00E+00

BRG #10 AT 88 & 0  
KXX= 10.  
KAA= 0.00E+00

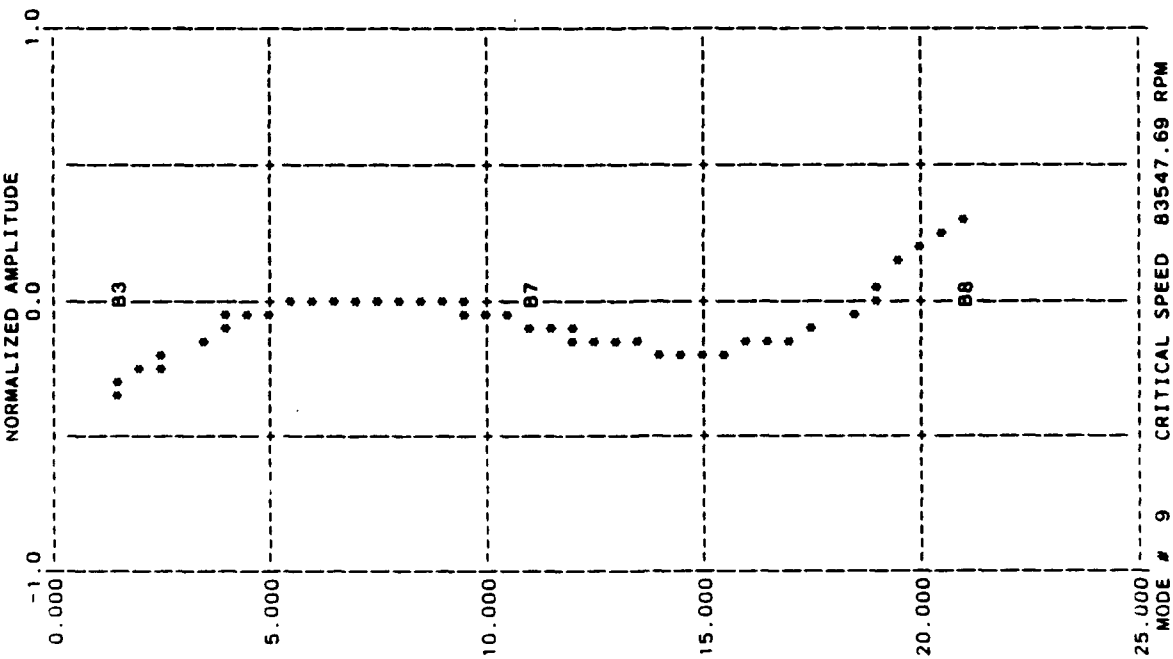
HUGHES TURBOTESTER - ROTOR AND STRUCTURAL DYNAMIC MODEL



N-63

HUGHES TURBOTESTER - ROTOR AND STRUCTURAL DYNAMIC MODEL

MODE # 9 LEVEL # 2 BEAM ONE



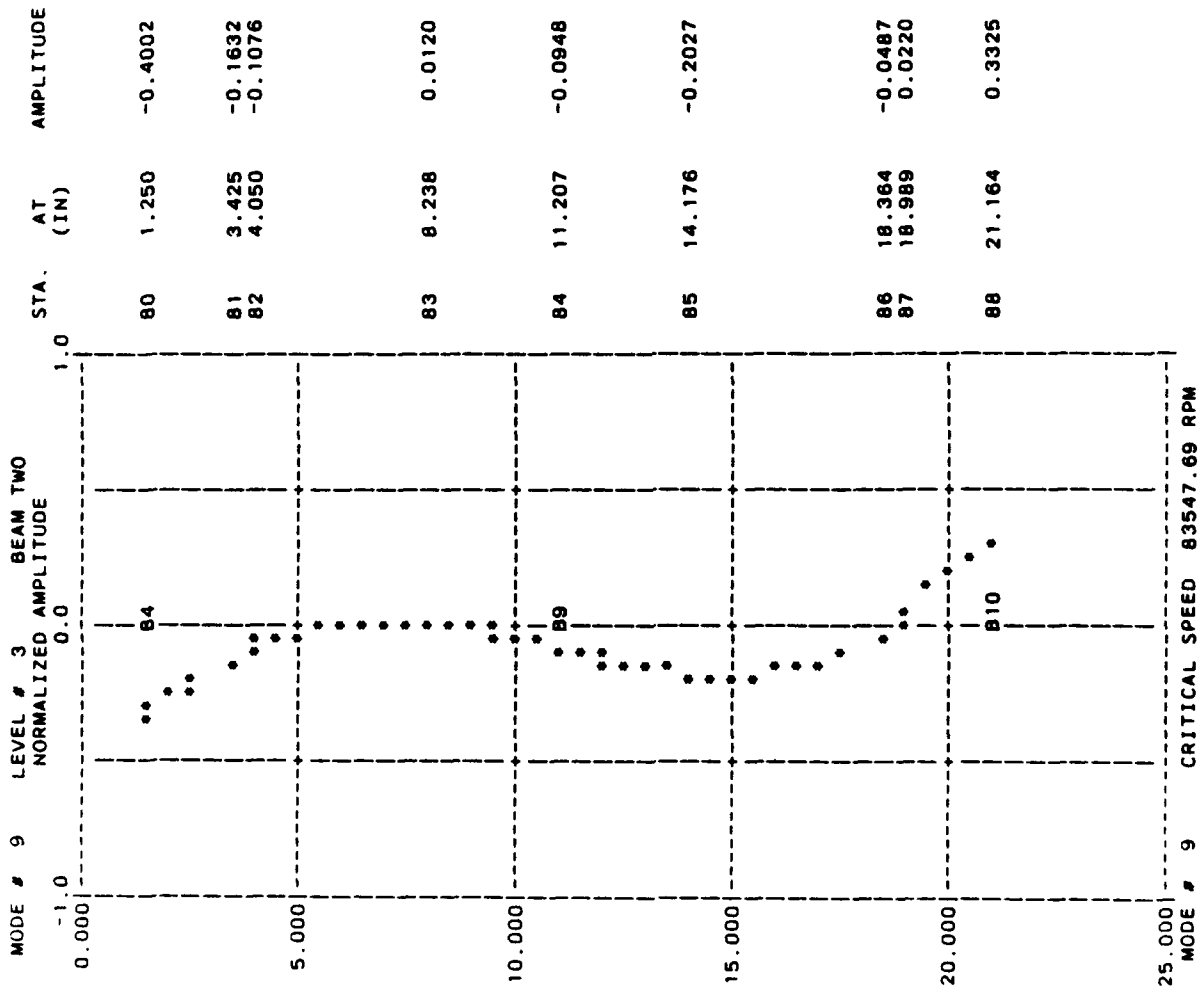
BRG # 3 AT 50 & 21  
KXX= 0.30E+07  
KAA= 0.00E+00

BRG # 7 AT 54 & 0  
KXX= 0.10E+07  
KAA= 0.00E+00

BRG # 8 AT 58 & 0  
KXX= 10.  
KAA= 0.00E+00



HUGHES TURBOTESTER - ROTOR AND STRUCTURAL DYNAMIC MODEL



BRG # 4 AT 80 & 22  
 KXX= 0.30E+07  
 KAA= 0.00E+00

BRG # 9 AT 84 & 0  
 KXX= 0.10E+07  
 KAA= 0.00E+00

BRG #10 AT 88 & 0  
 KXX= 10.  
 KAA= 0.00E+00

READ -PLOT- FROM INPUT ...IGNORED  
 READ -MAVL- FROM INPUT ...IGNORED  
 READ -MPL- FROM INPUT ...IGNORED  
 READ -MPL- FROM INPUT ...IGNORED

READ - AVL- FROM INPUT ...IGNORED  
READ - MPL- FROM INPUT ...IGNORED  
READ - MPL- FROM INPUT ...IGNORED  
READ - MPL- FROM INPUT ...IGNORED  
TOTAL EXECUTION TIME 22.5 SEC

N-66

DO 100

111

N-67

ATTACHMENT 3

SOLID CONTACT LOAD & DEFLECTION ANALYSIS  
OF HUGHES TRIBOTESTER 2A SPECIMENS

N-68

|            |                                                           |
|------------|-----------------------------------------------------------|
| $E_1$      | ELASTIC MODULUS OF BODY 1 (PSI)                           |
| $E_2$      | ELASTIC MODULUS OF BODY 2 (PSI)                           |
| $\nu_1$    | POISSONS RATIO FOR BODY 1                                 |
| $\nu_2$    | POISSONS RATIO FOR BODY 2                                 |
| $R_1$      | RADIUS OF BODY 1 (IN)                                     |
| $R_2$      | RADIUS OF BODY 2 (IN)                                     |
| $CR_1$     | CROWN RADIUS OF BODY 1 (IN)                               |
| $CR_2$     | CROWN RADIUS OF BODY 2 (IN)                               |
| $F$        | LOAD (LB FOR POINT CONTACT; LB/IN FOR LINE CONTACT)       |
| $d_1$      | EFF. THICKNESS OF BODY 1 FOR LINE CONTACT DEFLECTION (IN) |
| $d_2$      | EFF. THICKNESS OF BODY 2 FOR LINE CONTACT DEFLECTION (IN) |
| $U$        | EFFECTIVE SPEED, $(U_1+U_2)/2$ (IN/SEC)                   |
| $\mu$      | VISCOSITY (REYNS)                                         |
| $\alpha$   | VISCOSITY-PRESSURE COEFFICIENT (IN/LB)                    |
| $HW_1$     | MAJOR HALF WIDTH (IN)                                     |
| $HW_2$     | MINOR HALF WIDTH (IN)                                     |
| $HP_{max}$ | HERTZ MAXIMUM PRESSURE (PSI)                              |
| $\delta$   | DEFLECTION (IN)                                           |
| $K$        | STIFFNESS (LB/IN FOR POINT CONTACT; PSI FOR LINE CONTACT) |
| $h_{END}$  | EHD FILM THICKNESS (IN)                                   |
| $L$        | Length of Flat body                                       |
| $W$        | Applied Normal Load (lb)                                  |

|               |                                                           |
|---------------|-----------------------------------------------------------|
| 40000000.0    | ELASTIC MODULUS OF BODY 1 (PSI)                           |
| 40000000.0    | ELASTIC MODULUS OF BODY 2 (PSI)                           |
| 0.28          | POISSONS RATIO FOR BODY 1                                 |
| 0.27          | POISSONS RATIO FOR BODY 2                                 |
| 0.375         | RADIUS OF BODY 1 (IN)                                     |
| 0.25          | RADIUS OF BODY 2 (IN)                                     |
| 0.1000000E+13 | CROWN RADIUS OF BODY 1 (IN)                               |
| 0.25          | CROWN RADIUS OF BODY 2 (IN)                               |
| 4.0           | LOAD (LB FOR POINT CONTACT; LB/IN FOR LINE CONTACT)       |
| 0.0           | EFF. THICKNESS OF BODY 1 FOR LINE CONTACT DEFLECTION (IN) |
| 0.0           | EFF. THICKNESS OF BODY 2 FOR LINE CONTACT DEFLECTION (IN) |
| 0.0           | EFFECTIVE SPEED, (U1+U2)/2 (IN/SEC)                       |
| 0.0           | VISCOSITY (REYNS)                                         |
| 0.0           | VISCOSITY-PRESSURE COEFFICIENT (IN/LB)                    |
| 0.3536820E-02 | MAJOR HALF WIDTH (IN)                                     |
| 0.2517040E-02 | MINOR HALF WIDTH (IN)                                     |
| 214535.0      | HERTZ MAXIMUM PRESSURE (PSI)                              |
| 0.4613640E-04 | DEFLECTION (IN)                                           |
| 130049.0      | STIFFNESS (LB/IN FOR POINT CONTACT; PSI FOR LINE CONTACT) |
| 0.0           | EHD FILM THICKNESS (IN)                                   |

|               |                                                           |
|---------------|-----------------------------------------------------------|
| 40000000.0    | ELASTIC MODULUS OF BODY 1 (PSI)                           |
| 40000000.0    | ELASTIC MODULUS OF BODY 2 (PSI)                           |
| 0.28          | POISSONS RATIO FOR BODY 1                                 |
| 0.27          | POISSONS RATIO FOR BODY 2                                 |
| 0.375         | RADIUS OF BODY 1 (IN)                                     |
| 0.25          | RADIUS OF BODY 2 (IN)                                     |
| 0.1000000E+13 | CROWN RADIUS OF BODY 1 (IN)                               |
| 0.25          | CROWN RADIUS OF BODY 2 (IN)                               |
| 5.0           | LOAD (LB FOR POINT CONTACT; LB/IN FOR LINE CONTACT)       |
| 0.0           | EFF. THICKNESS OF BODY 1 FOR LINE CONTACT DEFLECTION (IN) |
| 0.0           | EFF. THICKNESS OF BODY 2 FOR LINE CONTACT DEFLECTION (IN) |
| 0.0           | EFFECTIVE SPEED, (U1+U2)/2 (IN/SEC)                       |
| 0.0           | VISCOSITY (REYNS)                                         |
| 0.0           | VISCOSITY-PRESSURE COEFFICIENT (IN/LB)                    |
| 0.3809930E-02 | MAJOR HALF WIDTH (IN)                                     |
| 0.2711400E-02 | MINOR HALF WIDTH (IN)                                     |
| 231100.0      | HERTZ MAXIMUM PRESSURE (PSI)                              |
| 0.5353660E-04 | DEFLECTION (IN)                                           |
| 140091.0      | STIFFNESS (LB/IN FOR POINT CONTACT; PSI FOR LINE CONTACT) |
| 0.0           | EHD FILM THICKNESS (IN)                                   |

|               |                                                           |
|---------------|-----------------------------------------------------------|
| 40000000.0    | ELASTIC MODULUS OF BODY 1 (PSI)                           |
| 40000000.0    | ELASTIC MODULUS OF BODY 2 (PSI)                           |
| 0.28          | POISSONS RATIO FOR BODY 1                                 |
| 0.27          | POISSONS RATIO FOR BODY 2                                 |
| 0.375         | RADIUS OF BODY 1 (IN)                                     |
| 0.25          | RADIUS OF BODY 2 (IN)                                     |
| 0.1000000E+13 | CROWN RADIUS OF BODY 1 (IN)                               |
| 0.25          | CROWN RADIUS OF BODY 2 (IN)                               |
| 6.0           | LOAD (LB FOR POINT CONTACT; LB/IN FOR LINE CONTACT)       |
| 0.0           | EFF. THICKNESS OF BODY 1 FOR LINE CONTACT DEFLECTION (IN) |
| 0.0           | EFF. THICKNESS OF BODY 2 FOR LINE CONTACT DEFLECTION (IN) |
| 0.0           | EFFECTIVE SPEED, (U1+U2)/2 (IN/SEC)                       |

|               |                                                           |
|---------------|-----------------------------------------------------------|
| 0.0           | VISCOSITY (REYNS)                                         |
| 0.0           | VISCOSITY-PRESSURE COEFFICIENT (IN/LB)                    |
| 0.4048660E-02 | MAJOR HALF WIDTH (IN)                                     |
| 0.2881300E-02 | MINOR HALF WIDTH (IN)                                     |
| 245580.0      | HERTZ MAXIMUM PRESSURE (PSI)                              |
| 0.6045570E-04 | DEFLECTION (IN)                                           |
| 148869.0      | STIFFNESS (LB/IN FOR POINT CONTACT; PSI FOR LINE CONTACT) |
| 0.0           | EHD FILM THICKNESS (IN)                                   |
|               |                                                           |
| 50000000.0    | ELASTIC MODULUS OF BODY 1 (PSI)                           |
| 50000000.0    | ELASTIC MODULUS OF BODY 2 (PSI)                           |
| 0.28          | POISSONS RATIO FOR BODY 1                                 |
| 0.27          | POISSONS RATIO FOR BODY 2                                 |
| 0.375         | RADIUS OF BODY 1 (IN)                                     |
| 0.25          | RADIUS OF BODY 2 (IN)                                     |
| 0.1000000E+13 | CROWN RADIUS OF BODY 1 (IN)                               |
| 0.25          | CROWN RADIUS OF BODY 2 (IN)                               |
| 3.0           | LOAD (LB FOR POINT CONTACT; LB/IN FOR LINE CONTACT)       |
| 0.0           | EFF. THICKNESS OF BODY 1 FOR LINE CONTACT DEFLECTION (IN) |
| 0.0           | EFF. THICKNESS OF BODY 2 FOR LINE CONTACT DEFLECTION (IN) |
| 0.0           | EFFECTIVE SPEED, $(U1+U2)/2$ (IN/SEC)                     |
| 0.0           | VISCOSITY (REYNS)                                         |
| 0.0           | VISCOSITY-PRESSURE COEFFICIENT (IN/LB)                    |
| 0.2983080E-02 | MAJOR HALF WIDTH (IN)                                     |
| 0.2122960E-02 | MINOR HALF WIDTH (IN)                                     |
| 226181.0      | HERTZ MAXIMUM PRESSURE (PSI)                              |
| 0.3282040E-04 | DEFLECTION (IN)                                           |
| 137110.0      | STIFFNESS (LB/IN FOR POINT CONTACT; PSI FOR LINE CONTACT) |
| 0.0           | EHD FILM THICKNESS (IN)                                   |
|               |                                                           |
| 50000000.0    | ELASTIC MODULUS OF BODY 1 (PSI)                           |
| 50000000.0    | ELASTIC MODULUS OF BODY 2 (PSI)                           |
| 0.28          | POISSONS RATIO FOR BODY 1                                 |
| 0.27          | POISSONS RATIO FOR BODY 2                                 |
| 0.375         | RADIUS OF BODY 1 (IN)                                     |
| 0.25          | RADIUS OF BODY 2 (IN)                                     |
| 0.1000000E+13 | CROWN RADIUS OF BODY 1 (IN)                               |
| 0.25          | CROWN RADIUS OF BODY 2 (IN)                               |
| 4.0           | LOAD (LB FOR POINT CONTACT; LB/IN FOR LINE CONTACT)       |
| 0.0           | EFF. THICKNESS OF BODY 1 FOR LINE CONTACT DEFLECTION (IN) |
| 0.0           | EFF. THICKNESS OF BODY 2 FOR LINE CONTACT DEFLECTION (IN) |
| 0.0           | EFFECTIVE SPEED, $(U1+U2)/2$ (IN/SEC)                     |
| 0.0           | VISCOSITY (REYNS)                                         |
| 0.0           | VISCOSITY-PRESSURE COEFFICIENT (IN/LB)                    |
| 0.3283290E-02 | MAJOR HALF WIDTH (IN)                                     |
| 0.2336620E-02 | MINOR HALF WIDTH (IN)                                     |
| 248945.0      | HERTZ MAXIMUM PRESSURE (PSI)                              |
| 0.3975920E-04 | DEFLECTION (IN)                                           |
| 150909.0      | STIFFNESS (LB/IN FOR POINT CONTACT; PSI FOR LINE CONTACT) |
| 0.0           | EHD FILM THICKNESS (IN)                                   |
|               |                                                           |
| 50000000.0    | ELASTIC MODULUS OF BODY 1 (PSI)                           |
| 50000000.0    | ELASTIC MODULUS OF BODY 2 (PSI)                           |
| 0.28          | POISSONS RATIO FOR BODY 1                                 |
| 0.27          | POISSONS RATIO FOR BODY 2                                 |

|               |                                                           |
|---------------|-----------------------------------------------------------|
| 0.375         | RADIUS OF BODY 1 (IN)                                     |
| 0.25          | RADIUS OF BODY 2 (IN)                                     |
| 0.1000000E+13 | CROWN RADIUS OF BODY 1 (IN)                               |
| 0.25          | CROWN RADIUS OF BODY 2 (IN)                               |
| 5.0           | LOAD (LB FOR POINT CONTACT; LB/IN FOR LINE CONTACT)       |
| 0.0           | EFF. THICKNESS OF BODY 1 FOR LINE CONTACT DEFLECTION (IN) |
| 0.0           | EFF. THICKNESS OF BODY 2 FOR LINE CONTACT DEFLECTION (IN) |
| 0.0           | EFFECTIVE SPEED, $(U1+U2)/2$ (IN/SEC)                     |
| 0.0           | VISCOSITY (REYNS)                                         |
| 0.0           | VISCOSITY-PRESSURE COEFFICIENT (IN/LB)                    |
| 0.3536820E-02 | MAJOR HALF WIDTH (IN)                                     |
| 0.2517040E-02 | MINOR HALF WIDTH (IN)                                     |
| 268168.0      | HERTZ MAXIMUM PRESSURE (PSI)                              |
| 0.4613640E-04 | DEFLECTION (IN)                                           |
| 162561.0      | STIFFNESS (LB/IN FOR POINT CONTACT; PSI FOR LINE CONTACT) |
| 0.0           | EHD FILM THICKNESS (IN)                                   |
| 60000000.0    | ELASTIC MODULUS OF BODY 1 (PSI)                           |
| 60000000.0    | ELASTIC MODULUS OF BODY 2 (PSI)                           |
| 0.28          | POISSONS RATIO FOR BODY 1                                 |
| 0.27          | POISSONS RATIO FOR BODY 2                                 |
| 0.375         | RADIUS OF BODY 1 (IN)                                     |
| 0.25          | RADIUS OF BODY 2 (IN)                                     |
| 0.1000000E+13 | CROWN RADIUS OF BODY 1 (IN)                               |
| 0.25          | CROWN RADIUS OF BODY 2 (IN)                               |
| 5.0           | LOAD (LB FOR POINT CONTACT; LB/IN FOR LINE CONTACT)       |
| 0.0           | EFF. THICKNESS OF BODY 1 FOR LINE CONTACT DEFLECTION (IN) |
| 0.0           | EFF. THICKNESS OF BODY 2 FOR LINE CONTACT DEFLECTION (IN) |
| 0.0           | EFFECTIVE SPEED, $(U1+U2)/2$ (IN/SEC)                     |
| 0.0           | VISCOSITY (REYNS)                                         |
| 0.0           | VISCOSITY-PRESSURE COEFFICIENT (IN/LB)                    |
| 0.3328290E-02 | MAJOR HALF WIDTH (IN)                                     |
| 0.2368640E-02 | MINOR HALF WIDTH (IN)                                     |
| 302825.0      | HERTZ MAXIMUM PRESSURE (PSI)                              |
| 0.4085590E-04 | DEFLECTION (IN)                                           |
| 183572.0      | STIFFNESS (LB/IN FOR POINT CONTACT; PSI FOR LINE CONTACT) |
| 0.0           | EHD FILM THICKNESS (IN)                                   |
| 60000000.0    | ELASTIC MODULUS OF BODY 1 (PSI)                           |
| 60000000.0    | ELASTIC MODULUS OF BODY 2 (PSI)                           |
| 0.28          | POISSONS RATIO FOR BODY 1                                 |
| 0.27          | POISSONS RATIO FOR BODY 2                                 |
| 0.375         | RADIUS OF BODY 1 (IN)                                     |
| 0.25          | RADIUS OF BODY 2 (IN)                                     |
| 0.1000000E+13 | CROWN RADIUS OF BODY 1 (IN)                               |
| 0.25          | CROWN RADIUS OF BODY 2 (IN)                               |
| 4.0           | LOAD (LB FOR POINT CONTACT; LB/IN FOR LINE CONTACT)       |
| 0.0           | EFF. THICKNESS OF BODY 1 FOR LINE CONTACT DEFLECTION (IN) |
| 0.0           | EFF. THICKNESS OF BODY 2 FOR LINE CONTACT DEFLECTION (IN) |
| 0.0           | EFFECTIVE SPEED, $(U1+U2)/2$ (IN/SEC)                     |
| 0.0           | VISCOSITY (REYNS)                                         |
| 0.0           | VISCOSITY-PRESSURE COEFFICIENT (IN/LB)                    |
| 0.3089710E-02 | MAJOR HALF WIDTH (IN)                                     |
| 0.2198850E-02 | MINOR HALF WIDTH (IN)                                     |
| 281118.0      | HERTZ MAXIMUM PRESSURE (PSI)                              |



|               |                                                           |
|---------------|-----------------------------------------------------------|
| 0.3520860E-04 | DEFLECTION (IN)                                           |
| 170413.0      | STIFFNESS (LB/IN FOR POINT CONTACT; PSI FOR LINE CONTACT) |
| 0.0           | EHD FILM THICKNESS (IN)                                   |
| 60000000.0    | ELASTIC MODULUS OF BODY 1 (PSI)                           |
| 60000000.0    | ELASTIC MODULUS OF BODY 2 (PSI)                           |
| 0.28          | POISSONS RATIO FOR BODY 1                                 |
| 0.27          | POISSONS RATIO FOR BODY 2                                 |
| 0.375         | RADIUS OF BODY 1 (IN)                                     |
| 0.25          | RADIUS OF BODY 2 (IN)                                     |
| 0.1000000E+13 | CROWN RADIUS OF BODY 1 (IN)                               |
| 0.25          | CROWN RADIUS OF BODY 2 (IN)                               |
| 3.0           | LOAD (LB FOR POINT CONTACT; LB/IN FOR LINE CONTACT)       |
| 0.0           | EFF. THICKNESS OF BODY 1 FOR LINE CONTACT DEFLECTION (IN) |
| 0.0           | EFF. THICKNESS OF BODY 2 FOR LINE CONTACT DEFLECTION (IN) |
| 0.0           | EFFECTIVE SPEED, $(U_1+U_2)/2$ (IN/SEC)                   |
| 0.0           | VISCOSITY (REYNS)                                         |
| 0.0           | VISCOSITY-PRESSURE COEFFICIENT (IN/LB)                    |
| 0.2807180E-02 | MAJOR HALF WIDTH (IN)                                     |
| 0.1997780E-02 | MINOR HALF WIDTH (IN)                                     |
| 255414.0      | HERTZ MAXIMUM PRESSURE (PSI)                              |
| 0.2906410E-04 | DEFLECTION (IN)                                           |
| 154830.0      | STIFFNESS (LB/IN FOR POINT CONTACT; PSI FOR LINE CONTACT) |
| 0.0           | EHD FILM THICKNESS (IN)                                   |
| 80000000.0    | ELASTIC MODULUS OF BODY 1 (PSI)                           |
| 60000000.0    | ELASTIC MODULUS OF BODY 2 (PSI)                           |
| 0.28          | POISSONS RATIO FOR BODY 1                                 |
| 0.27          | POISSONS RATIO FOR BODY 2                                 |
| 0.375         | RADIUS OF BODY 1 (IN)                                     |
| 0.25          | RADIUS OF BODY 2 (IN)                                     |
| 0.1000000E+13 | CROWN RADIUS OF BODY 1 (IN)                               |
| 0.25          | CROWN RADIUS OF BODY 2 (IN)                               |
| 3.0           | LOAD (LB FOR POINT CONTACT; LB/IN FOR LINE CONTACT)       |
| 0.0           | EFF. THICKNESS OF BODY 1 FOR LINE CONTACT DEFLECTION (IN) |
| 0.0           | EFF. THICKNESS OF BODY 2 FOR LINE CONTACT DEFLECTION (IN) |
| 0.0           | EFFECTIVE SPEED, $(U_1+U_2)/2$ (IN/SEC)                   |
| 0.0           | VISCOSITY (REYNS)                                         |
| 0.0           | VISCOSITY-PRESSURE COEFFICIENT (IN/LB)                    |
| 0.2685350E-02 | MAJOR HALF WIDTH (IN)                                     |
| 0.1911080E-02 | MINOR HALF WIDTH (IN)                                     |
| 279114.0      | HERTZ MAXIMUM PRESSURE (PSI)                              |
| 0.2659610E-04 | DEFLECTION (IN)                                           |
| 169198.0      | STIFFNESS (LB/IN FOR POINT CONTACT; PSI FOR LINE CONTACT) |
| 0.0           | EHD FILM THICKNESS (IN)                                   |
| 80000000.0    | ELASTIC MODULUS OF BODY 1 (PSI)                           |
| 60000000.0    | ELASTIC MODULUS OF BODY 2 (PSI)                           |
| 0.28          | POISSONS RATIO FOR BODY 1                                 |
| 0.27          | POISSONS RATIO FOR BODY 2                                 |
| 0.375         | RADIUS OF BODY 1 (IN)                                     |
| 0.1000000E+13 | RADIUS OF BODY 2 (IN)                                     |
| 0.1000000E+13 | CROWN RADIUS OF BODY 1 (IN)                               |
| 0.1000000E+13 | CROWN RADIUS OF BODY 2 (IN)                               |
| 8.0           | LOAD (LB FOR POINT CONTACT; LB/IN FOR LINE CONTACT)       |

|               |                                                           |
|---------------|-----------------------------------------------------------|
| .18           | EFF. THICKNESS OF BODY 1 FOR LINE CONTACT DEFLECTION (IN) |
| .375          | EFF. THICKNESS OF BODY 2 FOR LINE CONTACT DEFLECTION (IN) |
| 0.0           | EFFECTIVE SPEED, $(U1+U2)/2$ (IN/SEC)                     |
| 0.0           | VISCOSITY (REYNS)                                         |
| 0.0           | VISCOSITY-PRESSURE COEFFICIENT (IN/LB)                    |
| 1000000.0     | MAJOR HALF WIDTH (IN)                                     |
| 0.3209740E-03 | MINOR HALF WIDTH (IN)                                     |
| 15867.2       | HERTZ MAXIMUM PRESSURE (PSI)                              |
| 0.9964470E-06 | DEFLECTION (IN)                                           |
| 8622880.0     | STIFFNESS (LB/IN FOR POINT CONTACT; PSI FOR LINE CONTACT) |
| 0.0           | EHD FILM THICKNESS (IN)                                   |
|               |                                                           |
| 40000000.0    | ELASTIC MODULUS OF BODY 1 (PSI)                           |
| 40000000.0    | ELASTIC MODULUS OF BODY 2 (PSI)                           |
| 0.28          | POISSONS RATIO FOR BODY 1                                 |
| 0.27          | POISSONS RATIO FOR BODY 2                                 |
| 0.375         | RADIUS OF BODY 1 (IN)                                     |
| 0.1000000e+13 | RADIUS OF BODY 2 (IN)                                     |
| 0.1000000e+13 | CROWN RADIUS OF BODY 1 (IN)                               |
| 0.1000000e+13 | CROWN RADIUS OF BODY 2 (IN)                               |
| 8.0           | LOAD (LB FOR POINT CONTACT; LB/IN FOR LINE CONTACT)       |
| .18           | EFF. THICKNESS OF BODY 1 FOR LINE CONTACT DEFLECTION (IN) |
| .375          | EFF. THICKNESS OF BODY 2 FOR LINE CONTACT DEFLECTION (IN) |
| 0.0           | EFFECTIVE SPEED, $(U1+U2)/2$ (IN/SEC)                     |
| 0.0           | VISCOSITY (REYNS)                                         |
| 0.0           | VISCOSITY-PRESSURE COEFFICIENT (IN/LB)                    |
| 1000000.0     | MAJOR HALF WIDTH (IN)                                     |
| 0.4201640E-03 | MINOR HALF WIDTH (IN)                                     |
| 12121.4       | HERTZ MAXIMUM PRESSURE (PSI)                              |
| 0.1631590E-05 | DEFLECTION (IN)                                           |
| 5284380.0     | STIFFNESS (LB/IN FOR POINT CONTACT; PSI FOR LINE CONTACT) |
| 0.0           | EHD FILM THICKNESS (IN)                                   |
|               |                                                           |
| 40000000.0    | ELASTIC MODULUS OF BODY 1 (PSI)                           |
| 40000000.0    | ELASTIC MODULUS OF BODY 2 (PSI)                           |
| 0.28          | POISSONS RATIO FOR BODY 1                                 |
| 0.27          | POISSONS RATIO FOR BODY 2                                 |
| 0.375         | RADIUS OF BODY 1 (IN)                                     |
| 0.1000000e+13 | RADIUS OF BODY 2 (IN)                                     |
| 0.1000000e+13 | CROWN RADIUS OF BODY 1 (IN)                               |
| 0.1000000e+13 | CROWN RADIUS OF BODY 2 (IN)                               |
| 11.           | LOAD (LB FOR POINT CONTACT; LB/IN FOR LINE CONTACT)       |
| .18           | EFF. THICKNESS OF BODY 1 FOR LINE CONTACT DEFLECTION (IN) |
| .375          | EFF. THICKNESS OF BODY 2 FOR LINE CONTACT DEFLECTION (IN) |
| 0.0           | EFFECTIVE SPEED, $(U1+U2)/2$ (IN/SEC)                     |
| 0.0           | VISCOSITY (REYNS)                                         |
| 0.0           | VISCOSITY-PRESSURE COEFFICIENT (IN/LB)                    |
| 1000000.0     | MAJOR HALF WIDTH (IN)                                     |
| 0.4926860E-03 | MINOR HALF WIDTH (IN)                                     |
| 14213.5       | HERTZ MAXIMUM PRESSURE (PSI)                              |
| 0.2191900E-05 | DEFLECTION (IN)                                           |
| 5418520.0     | STIFFNESS (LB/IN FOR POINT CONTACT; PSI FOR LINE CONTACT) |
| 0.0           | EHD FILM THICKNESS (IN)                                   |
|               |                                                           |
| 40000000.0    | ELASTIC MODULUS OF BODY 1 (PSI)                           |

|               |                                                           |
|---------------|-----------------------------------------------------------|
| 40000000.0    | ELASTIC MODULUS OF BODY 2 (PSI)                           |
| 0.28          | POISSONS RATIO FOR BODY 1                                 |
| 0.27          | POISSONS RATIO FOR BODY 2                                 |
| 0.375         | RADIUS OF BODY 1 (IN)                                     |
| 0.1000000e+13 | RADIUS OF BODY 2 (IN)                                     |
| 0.1000000E+13 | CROWN RADIUS OF BODY 1 (IN)                               |
| 0.1000000e+13 | CROWN RADIUS OF BODY 2 (IN)                               |
| 13.           | LOAD (LB FOR POINT CONTACT; LB/IN FOR LINE CONTACT)       |
| .18           | EFF. THICKNESS OF BODY 1 FOR LINE CONTACT DEFLECTION (IN) |
| .375          | EFF. THICKNESS OF BODY 2 FOR LINE CONTACT DEFLECTION (IN) |
| 0.0           | EFFECTIVE SPEED, $(U1+U2)/2$ (IN/SEC)                     |
| 0.0           | VISCOSITY (REYNS)                                         |
| 0.0           | VISCOSITY-PRESSURE COEFFICIENT (IN/LB)                    |
| 1000000.0     | MAJOR HALF WIDTH (IN)                                     |
| 0.5356060E-03 | MINOR HALF WIDTH (IN)                                     |
| 15451.8       | HERTZ MAXIMUM PRESSURE (PSI)                              |
| 0.2558480E-05 | DEFLECTION (IN)                                           |
| 5491650.0     | STIFFNESS (LB/IN FOR POINT CONTACT; PSI FOR LINE CONTACT) |
| 0.0           | EHD FILM THICKNESS (IN)                                   |
|               |                                                           |
| 50000000.0    | ELASTIC MODULUS OF BODY 1 (PSI)                           |
| 50000000.0    | ELASTIC MODULUS OF BODY 2 (PSI)                           |
| 0.28          | POISSONS RATIO FOR BODY 1                                 |
| 0.27          | POISSONS RATIO FOR BODY 2                                 |
| 0.375         | RADIUS OF BODY 1 (IN)                                     |
| 0.1000000e+13 | RADIUS OF BODY 2 (IN)                                     |
| 0.1000000E+13 | CROWN RADIUS OF BODY 1 (IN)                               |
| 0.1000000e+13 | CROWN RADIUS OF BODY 2 (IN)                               |
| 13.           | LOAD (LB FOR POINT CONTACT; LB/IN FOR LINE CONTACT)       |
| .18           | EFF. THICKNESS OF BODY 1 FOR LINE CONTACT DEFLECTION (IN) |
| .375          | EFF. THICKNESS OF BODY 2 FOR LINE CONTACT DEFLECTION (IN) |
| 0.0           | EFFECTIVE SPEED, $(U1+U2)/2$ (IN/SEC)                     |
| 0.0           | VISCOSITY (REYNS)                                         |
| 0.0           | VISCOSITY-PRESSURE COEFFICIENT (IN/LB)                    |
| 1000000.0     | MAJOR HALF WIDTH (IN)                                     |
| 0.4790600E-03 | MINOR HALF WIDTH (IN)                                     |
| 17275.6       | HERTZ MAXIMUM PRESSURE (PSI)                              |
| 0.2080920E-05 | DEFLECTION (IN)                                           |
| 6743000.0     | STIFFNESS (LB/IN FOR POINT CONTACT; PSI FOR LINE CONTACT) |
| 0.0           | EHD FILM THICKNESS (IN)                                   |
|               |                                                           |
| 50000000.0    | ELASTIC MODULUS OF BODY 1 (PSI)                           |
| 50000000.0    | ELASTIC MODULUS OF BODY 2 (PSI)                           |
| 0.28          | POISSONS RATIO FOR BODY 1                                 |
| 0.27          | POISSONS RATIO FOR BODY 2                                 |
| 0.375         | RADIUS OF BODY 1 (IN)                                     |
| 0.1000000e+13 | RADIUS OF BODY 2 (IN)                                     |
| 0.1000000E+13 | CROWN RADIUS OF BODY 1 (IN)                               |
| 0.1000000e+13 | CROWN RADIUS OF BODY 2 (IN)                               |
| 11.           | LOAD (LB FOR POINT CONTACT; LB/IN FOR LINE CONTACT)       |
| .18           | EFF. THICKNESS OF BODY 1 FOR LINE CONTACT DEFLECTION (IN) |
| .375          | EFF. THICKNESS OF BODY 2 FOR LINE CONTACT DEFLECTION (IN) |
| 0.0           | EFFECTIVE SPEED, $(U1+U2)/2$ (IN/SEC)                     |
| 0.0           | VISCOSITY (REYNS)                                         |
| 0.0           | VISCOSITY-PRESSURE COEFFICIENT (IN/LB)                    |

|               |                                                           |
|---------------|-----------------------------------------------------------|
| 1000000.0     | MAJOR HALF WIDTH (IN)                                     |
| 0.4406720E-03 | MINOR HALF WIDTH (IN)                                     |
| 15891.2       | HERTZ MAXIMUM PRESSURE (PSI)                              |
| 0.1782410E-05 | DEFLECTION (IN)                                           |
| 6654770.0     | STIFFNESS (LB/IN FOR POINT CONTACT; PSI FOR LINE CONTACT) |
| 0.0           | EHD FILM THICKNESS (IN)                                   |
|               |                                                           |
| 50000000.0    | ELASTIC MODULUS OF BODY 1 (PSI)                           |
| 50000000.0    | ELASTIC MODULUS OF BODY 2 (PSI)                           |
| 0.28          | POISSONS RATIO FOR BODY 1                                 |
| 0.27          | POISSONS RATIO FOR BODY 2                                 |
| 0.375         | RADIUS OF BODY 1 (IN)                                     |
| 0.1000000e+13 | RADIUS OF BODY 2 (IN)                                     |
| 0.1000000E+13 | CROWN RADIUS OF BODY 1 (IN)                               |
| 0.1000000e+13 | CROWN RADIUS OF BODY 2 (IN)                               |
| 8.            | LOAD (LB FOR POINT CONTACT; LB/IN FOR LINE CONTACT)       |
| .18           | EFF. THICKNESS OF BODY 1 FOR LINE CONTACT DEFLECTION (IN) |
| .375          | EFF. THICKNESS OF BODY 2 FOR LINE CONTACT DEFLECTION (IN) |
| 0.0           | EFFECTIVE SPEED, $(U_1+U_2)/2$ (IN/SEC)                   |
| 0.0           | VISCOSITY (REYNS)                                         |
| 0.0           | VISCOSITY-PRESSURE COEFFICIENT (IN/LB)                    |
| 1000000.0     | MAJOR HALF WIDTH (IN)                                     |
| 0.3758060E-03 | MINOR HALF WIDTH (IN)                                     |
| 13552.1       | HERTZ MAXIMUM PRESSURE (PSI)                              |
| 0.1326280E-05 | DEFLECTION (IN)                                           |
| 6492830.0     | STIFFNESS (LB/IN FOR POINT CONTACT; PSI FOR LINE CONTACT) |
| 0.0           | EHD FILM THICKNESS (IN)                                   |
|               |                                                           |
| 60000000.0    | ELASTIC MODULUS OF BODY 1 (PSI)                           |
| 60000000.0    | ELASTIC MODULUS OF BODY 2 (PSI)                           |
| 0.28          | POISSONS RATIO FOR BODY 1                                 |
| 0.27          | POISSONS RATIO FOR BODY 2                                 |
| 0.375         | RADIUS OF BODY 1 (IN)                                     |
| 0.1000000e+13 | RADIUS OF BODY 2 (IN)                                     |
| 0.1000000E+13 | CROWN RADIUS OF BODY 1 (IN)                               |
| 0.1000000e+13 | CROWN RADIUS OF BODY 2 (IN)                               |
| 8.            | LOAD (LB FOR POINT CONTACT; LB/IN FOR LINE CONTACT)       |
| .18           | EFF. THICKNESS OF BODY 1 FOR LINE CONTACT DEFLECTION (IN) |
| .375          | EFF. THICKNESS OF BODY 2 FOR LINE CONTACT DEFLECTION (IN) |
| 0.0           | EFFECTIVE SPEED, $(U_1+U_2)/2$ (IN/SEC)                   |
| 0.0           | VISCOSITY (REYNS)                                         |
| 0.0           | VISCOSITY-PRESSURE COEFFICIENT (IN/LB)                    |
| 1000000.0     | MAJOR HALF WIDTH (IN)                                     |
| 0.3430620E-03 | MINOR HALF WIDTH (IN)                                     |
| 14845.6       | HERTZ MAXIMUM PRESSURE (PSI)                              |
| 0.1119540E-05 | DEFLECTION (IN)                                           |
| 7684350.0     | STIFFNESS (LB/IN FOR POINT CONTACT; PSI FOR LINE CONTACT) |
| 0.0           | EHD FILM THICKNESS (IN)                                   |
|               |                                                           |
| 60000000.0    | ELASTIC MODULUS OF BODY 1 (PSI)                           |
| 60000000.0    | ELASTIC MODULUS OF BODY 2 (PSI)                           |
| 0.28          | POISSONS RATIO FOR BODY 1                                 |
| 0.27          | POISSONS RATIO FOR BODY 2                                 |
| 0.375         | RADIUS OF BODY 1 (IN)                                     |
| 0.1000000e+13 | RADIUS OF BODY 2 (IN)                                     |

|               |                                                           |
|---------------|-----------------------------------------------------------|
| 0.1000000E+13 | CROWN RADIUS OF BODY 1 (IN)                               |
| 0.1000000E+13 | CROWN RADIUS OF BODY 2 (IN)                               |
| 11.           | LOAD (LB FOR POINT CONTACT; LB/IN FOR LINE CONTACT)       |
| .18           | EFF. THICKNESS OF BODY 1 FOR LINE CONTACT DEFLECTION (IN) |
| .375          | EFF. THICKNESS OF BODY 2 FOR LINE CONTACT DEFLECTION (IN) |
| 0.0           | EFFECTIVE SPEED, $(U1+U2)/2$ (IN/SEC)                     |
| 0.0           | VISCOSITY (REYNS)                                         |
| 0.0           | VISCOSITY-PRESSURE COEFFICIENT (IN/LB)                    |
| 1000000.0     | MAJOR HALF WIDTH (IN)                                     |
| 0.4022760E-03 | MINOR HALF WIDTH (IN)                                     |
| 17408.0       | HERTZ MAXIMUM PRESSURE (PSI)                              |
| 0.1505010E-05 | DEFLECTION (IN)                                           |
| 7873310.0     | STIFFNESS (LB/IN FOR POINT CONTACT; PSI FOR LINE CONTACT) |
| 0.0           | EHD FILM THICKNESS (IN)                                   |
|               |                                                           |
| 60000000.0    | ELASTIC MODULUS OF BODY 1 (PSI)                           |
| 60000000.0    | ELASTIC MODULUS OF BODY 2 (PSI)                           |
| 0.28          | POISSONS RATIO FOR BODY 1                                 |
| 0.27          | POISSONS RATIO FOR BODY 2                                 |
| 0.375         | RADIUS OF BODY 1 (IN)                                     |
| 0.1000000E+13 | RADIUS OF BODY 2 (IN)                                     |
| 0.1000000E+13 | CROWN RADIUS OF BODY 1 (IN)                               |
| 0.1000000E+13 | CROWN RADIUS OF BODY 2 (IN)                               |
| 13.           | LOAD (LB FOR POINT CONTACT; LB/IN FOR LINE CONTACT)       |
| .18           | EFF. THICKNESS OF BODY 1 FOR LINE CONTACT DEFLECTION (IN) |
| .375          | EFF. THICKNESS OF BODY 2 FOR LINE CONTACT DEFLECTION (IN) |
| 0.0           | EFFECTIVE SPEED, $(U1+U2)/2$ (IN/SEC)                     |
| 0.0           | VISCOSITY (REYNS)                                         |
| 0.0           | VISCOSITY-PRESSURE COEFFICIENT (IN/LB)                    |
| 1000000.0     | MAJOR HALF WIDTH (IN)                                     |
| 0.4373200E-03 | MINOR HALF WIDTH (IN)                                     |
| 18924.5       | HERTZ MAXIMUM PRESSURE (PSI)                              |
| 0.1757350E-05 | DEFLECTION (IN)                                           |
| 7976200.0     | STIFFNESS (LB/IN FOR POINT CONTACT; PSI FOR LINE CONTACT) |
| 0.0           | EHD FILM THICKNESS (IN)                                   |

LATHAM

HESHMAT

7/20/87

15:42:17 G.M.T. WAS THE ORIGIN\*\*\*\*\*

*Sensitivity analysis respect to Eff. thickness*

N-78

|               |                                                           |
|---------------|-----------------------------------------------------------|
| 40000000.0    | ELASTIC MODULUS OF BODY 1 (PSI)                           |
| 40000000.0    | ELASTIC MODULUS OF BODY 2 (PSI)                           |
| 0.25          | POISSONS RATIO FOR BODY 1                                 |
| 0.25          | POISSONS RATIO FOR BODY 2                                 |
| 0.375         | RADIUS OF BODY 1 (IN)                                     |
| 0.1000000e+13 | RADIUS OF BODY 2 (IN)                                     |
| 0.1000000E+13 | CROWN RADIUS OF BODY 1 (IN)                               |
| 0.1000000e+13 | CROWN RADIUS OF BODY 2 (IN)                               |
| 8.0           | LOAD (LB FOR POINT CONTACT; LB/IN FOR LINE CONTACT)       |
| 0.375         | EFF. THICKNESS OF BODY 1 FOR LINE CONTACT DEFLECTION (IN) |
| 0.2           | EFF. THICKNESS OF BODY 2 FOR LINE CONTACT DEFLECTION (IN) |
| 0.0           | EFFECTIVE SPEED, $(U1+U2)/2$ (IN/SEC)                     |
| 0.0           | VISCOSITY (REYNS)                                         |
| 0.0           | VISCOSITY-PRESSURE COEFFICIENT (IN/LB)                    |
| 1000000.0     | MAJOR HALF WIDTH (IN)                                     |
| 0.4231420E-03 | MINOR HALF WIDTH (IN)                                     |
| 12036.0       | HERTZ MAXIMUM PRESSURE (PSI)                              |
| 0.1670920E-05 | DEFLECTION (IN)                                           |
| 5156110.0     | STIFFNESS (LB/IN FOR POINT CONTACT; PSI FOR LINE CONTACT) |
| 0.0           | EHD FILM THICKNESS (IN)                                   |
|               |                                                           |
| 40000000.0    | ELASTIC MODULUS OF BODY 1 (PSI)                           |
| 40000000.0    | ELASTIC MODULUS OF BODY 2 (PSI)                           |
| 0.25          | POISSONS RATIO FOR BODY 1                                 |
| 0.25          | POISSONS RATIO FOR BODY 2                                 |
| 0.375         | RADIUS OF BODY 1 (IN)                                     |
| 0.1000000e+13 | RADIUS OF BODY 2 (IN)                                     |
| 0.1000000E+13 | CROWN RADIUS OF BODY 1 (IN)                               |
| 0.1000000e+13 | CROWN RADIUS OF BODY 2 (IN)                               |
| 8.0           | LOAD (LB FOR POINT CONTACT; LB/IN FOR LINE CONTACT)       |
| 0.1           | EFF. THICKNESS OF BODY 1 FOR LINE CONTACT DEFLECTION (IN) |
| 0.1           | EFF. THICKNESS OF BODY 2 FOR LINE CONTACT DEFLECTION (IN) |
| 0.0           | EFFECTIVE SPEED, $(U1+U2)/2$ (IN/SEC)                     |
| 0.0           | VISCOSITY (REYNS)                                         |
| 0.0           | VISCOSITY-PRESSURE COEFFICIENT (IN/LB)                    |
| 1000000.0     | MAJOR HALF WIDTH (IN)                                     |
| 0.4231420E-03 | MINOR HALF WIDTH (IN)                                     |
| 12036.0       | HERTZ MAXIMUM PRESSURE (PSI)                              |
| 0.1430410E-05 | DEFLECTION (IN)                                           |
| 6102000.0     | STIFFNESS (LB/IN FOR POINT CONTACT; PSI FOR LINE CONTACT) |
| 0.0           | EHD FILM THICKNESS (IN)                                   |
|               |                                                           |
| 40000000.0    | ELASTIC MODULUS OF BODY 1 (PSI)                           |
| 40000000.0    | ELASTIC MODULUS OF BODY 2 (PSI)                           |
| 0.25          | POISSONS RATIO FOR BODY 1                                 |
| 0.25          | POISSONS RATIO FOR BODY 2                                 |
| 0.375         | RADIUS OF BODY 1 (IN)                                     |
| 0.1000000E+13 | RADIUS OF BODY 2 (IN)                                     |
| 0.1000000E+13 | CROWN RADIUS OF BODY 1 (IN)                               |
| 0.1000000E+13 | CROWN RADIUS OF BODY 2 (IN)                               |
| 8.0           | LOAD (LB FOR POINT CONTACT; LB/IN FOR LINE CONTACT)       |
| 0.2           | EFF. THICKNESS OF BODY 1 FOR LINE CONTACT DEFLECTION (IN) |
| 0.2           | EFF. THICKNESS OF BODY 2 FOR LINE CONTACT DEFLECTION (IN) |
| 0.0           | EFFECTIVE SPEED, $(U1+U2)/2$ (IN/SEC)                     |

|               |                                                           |
|---------------|-----------------------------------------------------------|
| 0.0           | VISCOSITY (REYNS)                                         |
| 0.0           | VISCOSITY-PRESSURE COEFFICIENT (IN/LB)                    |
| 1000000.0     | MAJOR HALF WIDTH (IN)                                     |
| 0.4231420E-03 | MINOR HALF WIDTH (IN)                                     |
| 12036.0       | HERTZ MAXIMUM PRESSURE (PSI)                              |
| 0.1595890E-05 | DEFLECTION (IN)                                           |
| 5418140.0     | STIFFNESS (LB/IN FOR POINT CONTACT; PSI FOR LINE CONTACT) |
| 0.0           | EHD FILM THICKNESS (IN)                                   |
|               |                                                           |
| 40000000.0    | ELASTIC MODULUS OF BODY 1 (PSI)                           |
| 40000000.0    | ELASTIC MODULUS OF BODY 2 (PSI)                           |
| 0.25          | POISSONS RATIO FOR BODY 1                                 |
| 0.25          | POISSONS RATIO FOR BODY 2                                 |
| 0.375         | RADIUS OF BODY 1 (IN)                                     |
| 0.1000000E+13 | RADIUS OF BODY 2 (IN)                                     |
| 0.1000000E+13 | CROWN RADIUS OF BODY 1 (IN)                               |
| 0.1000000E+13 | CROWN RADIUS OF BODY 2 (IN)                               |
| 8.0           | LOAD (LB FOR POINT CONTACT; LB/IN FOR LINE CONTACT)       |
| 0.4           | EFF. THICKNESS OF BODY 1 FOR LINE CONTACT DEFLECTION (IN) |
| 0.4           | EFF. THICKNESS OF BODY 2 FOR LINE CONTACT DEFLECTION (IN) |
| 0.0           | EFFECTIVE SPEED, $(U_1+U_2)/2$ (IN/SEC)                   |
| 0.0           | VISCOSITY (REYNS)                                         |
| 0.0           | VISCOSITY-PRESSURE COEFFICIENT (IN/LB)                    |
| 1000000.0     | MAJOR HALF WIDTH (IN)                                     |
| 0.4231420E-03 | MINOR HALF WIDTH (IN)                                     |
| 12036.0       | HERTZ MAXIMUM PRESSURE (PSI)                              |
| 0.1761360E-05 | DEFLECTION (IN)                                           |
| 4872110.0     | STIFFNESS (LB/IN FOR POINT CONTACT; PSI FOR LINE CONTACT) |
| 0.0           | EHD FILM THICKNESS (IN)                                   |
|               |                                                           |
| 40000000.0    | ELASTIC MODULUS OF BODY 1 (PSI)                           |
| 40000000.0    | ELASTIC MODULUS OF BODY 2 (PSI)                           |
| 0.25          | POISSONS RATIO FOR BODY 1                                 |
| 0.25          | POISSONS RATIO FOR BODY 2                                 |
| 0.375         | RADIUS OF BODY 1 (IN)                                     |
| 0.1000000E+13 | RADIUS OF BODY 2 (IN)                                     |
| 0.1000000E+13 | CROWN RADIUS OF BODY 1 (IN)                               |
| 0.1000000E+13 | CROWN RADIUS OF BODY 2 (IN)                               |
| 8.0           | LOAD (LB FOR POINT CONTACT; LB/IN FOR LINE CONTACT)       |
| 0.4           | EFF. THICKNESS OF BODY 1 FOR LINE CONTACT DEFLECTION (IN) |
| 0.4           | EFF. THICKNESS OF BODY 2 FOR LINE CONTACT DEFLECTION (IN) |
| 0.0           | EFFECTIVE SPEED, $(U_1+U_2)/2$ (IN/SEC)                   |
| 0.0           | VISCOSITY (REYNS)                                         |
| 0.0           | VISCOSITY-PRESSURE COEFFICIENT (IN/LB)                    |
| 1000000.0     | MAJOR HALF WIDTH (IN)                                     |
| 0.4231420E-03 | MINOR HALF WIDTH (IN)                                     |
| 12036.0       | HERTZ MAXIMUM PRESSURE (PSI)                              |
| 0.1761360E-05 | DEFLECTION (IN)                                           |
| 4872110.0     | STIFFNESS (LB/IN FOR POINT CONTACT; PSI FOR LINE CONTACT) |
| 0.0           | EHD FILM THICKNESS (IN)                                   |
|               |                                                           |
| 40000000.0    | ELASTIC MODULUS OF BODY 1 (PSI)                           |
| 40000000.0    | ELASTIC MODULUS OF BODY 2 (PSI)                           |
| 0.25          | POISSONS RATIO FOR BODY 1                                 |
| 0.25          | POISSONS RATIO FOR BODY 2                                 |



|               |                                                           |
|---------------|-----------------------------------------------------------|
| 0.375         | RADIUS OF BODY 1 (IN)                                     |
| 0.1000000E+13 | RADIUS OF BODY 2 (IN)                                     |
| 0.1000000E+13 | CROWN RADIUS OF BODY 1 (IN)                               |
| 0.1000000E+13 | CROWN RADIUS OF BODY 2 (IN)                               |
| 8.0           | LOAD (LB FOR POINT CONTACT; LB/IN FOR LINE CONTACT)       |
| 234e+13       | EFF. THICKNESS OF BODY 1 FOR LINE CONTACT DEFLECTION (IN) |
| 234e+13       | EFF. THICKNESS OF BODY 2 FOR LINE CONTACT DEFLECTION (IN) |
| 0.0           | EFFECTIVE SPEED, $(U1+U2)/2$ (IN/SEC)                     |
| 0.0           | VISCOSITY (REYNS)                                         |
| 0.0           | VISCOSITY-PRESSURE COEFFICIENT (IN/LB)                    |
| 1000000.0     | MAJOR HALF WIDTH (IN)                                     |
| 0.4231420E-03 | MINOR HALF WIDTH (IN)                                     |
| 12036.0       | HERTZ MAXIMUM PRESSURE (PSI)                              |
| 0.1042860E-04 | DEFLECTION (IN)                                           |
| 776005.0      | STIFFNESS (LB/IN FOR POINT CONTACT; PSI FOR LINE CONTACT) |
| 0.0           | EHD FILM THICKNESS (IN)                                   |
|               |                                                           |
| 40000000.0    | ELASTIC MODULUS OF BODY 1 (PSI)                           |
| 40000000.0    | ELASTIC MODULUS OF BODY 2 (PSI)                           |
| 0.25          | POISSONS RATIO FOR BODY 1                                 |
| 0.25          | POISSONS RATIO FOR BODY 2                                 |
| 0.375         | RADIUS OF BODY 1 (IN)                                     |
| 0.1000000E+13 | RADIUS OF BODY 2 (IN)                                     |
| 0.1000000E+13 | CROWN RADIUS OF BODY 1 (IN)                               |
| 0.1000000E+13 | CROWN RADIUS OF BODY 2 (IN)                               |
| 8.0           | LOAD (LB FOR POINT CONTACT; LB/IN FOR LINE CONTACT)       |
| 534e-6        | EFF. THICKNESS OF BODY 1 FOR LINE CONTACT DEFLECTION (IN) |
| 534e-6        | EFF. THICKNESS OF BODY 2 FOR LINE CONTACT DEFLECTION (IN) |
| 0.0           | EFFECTIVE SPEED, $(U1+U2)/2$ (IN/SEC)                     |
| 0.0           | VISCOSITY (REYNS)                                         |
| 0.0           | VISCOSITY-PRESSURE COEFFICIENT (IN/LB)                    |
| 1000000.0     | MAJOR HALF WIDTH (IN)                                     |
| 0.4231420E-03 | MINOR HALF WIDTH (IN)                                     |
| 12036.0       | HERTZ MAXIMUM PRESSURE (PSI)                              |
| 0.1812380E-06 | DEFLECTION (IN)                                           |
| 0.1293000E+09 | STIFFNESS (LB/IN FOR POINT CONTACT; PSI FOR LINE CONTACT) |
| 0.0           | EHD FILM THICKNESS (IN)                                   |
|               |                                                           |
| 40000000.0    | ELASTIC MODULUS OF BODY 1 (PSI)                           |
| 40000000.0    | ELASTIC MODULUS OF BODY 2 (PSI)                           |
| 0.25          | POISSONS RATIO FOR BODY 1                                 |
| 0.25          | POISSONS RATIO FOR BODY 2                                 |
| 0.375         | RADIUS OF BODY 1 (IN)                                     |
| 0.1000000E+13 | RADIUS OF BODY 2 (IN)                                     |
| 0.1000000E+13 | CROWN RADIUS OF BODY 1 (IN)                               |
| 0.1000000E+13 | CROWN RADIUS OF BODY 2 (IN)                               |
| 8.0           | LOAD (LB FOR POINT CONTACT; LB/IN FOR LINE CONTACT)       |
| 534e-6        | EFF. THICKNESS OF BODY 1 FOR LINE CONTACT DEFLECTION (IN) |
| 534e-6        | EFF. THICKNESS OF BODY 2 FOR LINE CONTACT DEFLECTION (IN) |
| 0.0           | EFFECTIVE SPEED, $(U1+U2)/2$ (IN/SEC)                     |
| 0.0           | VISCOSITY (REYNS)                                         |
| 0.0           | VISCOSITY-PRESSURE COEFFICIENT (IN/LB)                    |
| 1000000.0     | MAJOR HALF WIDTH (IN)                                     |
| 0.4231420E-03 | MINOR HALF WIDTH (IN)                                     |
| 12036.0       | HERTZ MAXIMUM PRESSURE (PSI)                              |

0.1812380E-06  
0.1293000E+09  
0.0

DEFLECTION (IN)  
STIFFNESS (LB/IN FOR POINT CONTACT; PSI FOR LINE CONTACT)  
EHD FILM THICKNESS (IN)

Case # 11'-20'

In these run Eff. thickness of body <sup>1</sup> & body 2 is corrected

$d_1 = R_{\text{cylinder}}$  &  $d_2 = 20 \times \text{half width from case \# } \underline{11-20}$

|               |                                                           |
|---------------|-----------------------------------------------------------|
| 80000000.0    | ELASTIC MODULUS OF BODY 1 (PSI)                           |
| 60000000.0    | ELASTIC MODULUS OF BODY 2 (PSI)                           |
| 0.28          | POISSONS RATIO FOR BODY 1                                 |
| 0.27          | POISSONS RATIO FOR BODY 2                                 |
| 0.375         | RADIUS OF BODY 1 (IN)                                     |
| 0.1000000e+13 | RADIUS OF BODY 2 (IN)                                     |
| 0.1000000E+13 | CROWN RADIUS OF BODY 1 (IN)                               |
| 0.1000000E+13 | CROWN RADIUS OF BODY 2 (IN)                               |
| 8.0           | LOAD (LB FOR POINT CONTACT; LB/IN FOR LINE CONTACT)       |
| 0.19          | EFF. THICKNESS OF BODY 1 FOR LINE CONTACT DEFLECTION (IN) |
| 0.5e-2        | EFF. THICKNESS OF BODY 2 FOR LINE CONTACT DEFLECTION (IN) |
| 0.0           | EFFECTIVE SPEED, (U1+U2)/2 (IN/SEC)                       |
| 0.0           | VISCOSITY (REYNS)                                         |
| 0.0           | VISCOSITY-PRESSURE COEFFICIENT (IN/LB)                    |
| 1000000.0     | MAJOR HALF WIDTH (IN)                                     |
| 0.3209740E-03 | MINOR HALF WIDTH (IN)                                     |
| 15867.2       | HERTZ MAXIMUM PRESSURE (PSI)                              |
| 0.6598560E-06 | DEFLECTION (IN)                                           |
| 13532400.0    | STIFFNESS (LB/IN FOR POINT CONTACT; PSI FOR LINE CONTACT) |
| 0.0           | EHD FILM THICKNESS (IN)                                   |

11

|               |                                                           |
|---------------|-----------------------------------------------------------|
| 40000000.0    | ELASTIC MODULUS OF BODY 1 (PSI)                           |
| 40000000.0    | ELASTIC MODULUS OF BODY 2 (PSI)                           |
| 0.28          | POISSONS RATIO FOR BODY 1                                 |
| 0.27          | POISSONS RATIO FOR BODY 2                                 |
| 0.375         | RADIUS OF BODY 1 (IN)                                     |
| 0.1000000e+13 | RADIUS OF BODY 2 (IN)                                     |
| 0.1000000E+13 | CROWN RADIUS OF BODY 1 (IN)                               |
| 0.1000000E+13 | CROWN RADIUS OF BODY 2 (IN)                               |
| 8.0           | LOAD (LB FOR POINT CONTACT; LB/IN FOR LINE CONTACT)       |
| 0.19          | EFF. THICKNESS OF BODY 1 FOR LINE CONTACT DEFLECTION (IN) |
| 0.5e-2        | EFF. THICKNESS OF BODY 2 FOR LINE CONTACT DEFLECTION (IN) |
| 0.0           | EFFECTIVE SPEED, (U1+U2)/2 (IN/SEC)                       |
| 0.0           | VISCOSITY (REYNS)                                         |
| 0.0           | VISCOSITY-PRESSURE COEFFICIENT (IN/LB)                    |
| 1000000.0     | MAJOR HALF WIDTH (IN)                                     |
| 0.4201640E-03 | MINOR HALF WIDTH (IN)                                     |
| 12121.4       | HERTZ MAXIMUM PRESSURE (PSI)                              |
| 0.1128290E-05 | DEFLECTION (IN)                                           |
| 7916120.0     | STIFFNESS (LB/IN FOR POINT CONTACT; PSI FOR LINE CONTACT) |
| 0.0           | EHD FILM THICKNESS (IN)                                   |

12

|               |                                                           |
|---------------|-----------------------------------------------------------|
| 40000000.0    | ELASTIC MODULUS OF BODY 1 (PSI)                           |
| 40000000.0    | ELASTIC MODULUS OF BODY 2 (PSI)                           |
| 0.28          | POISSONS RATIO FOR BODY 1                                 |
| 0.27          | POISSONS RATIO FOR BODY 2                                 |
| 0.375         | RADIUS OF BODY 1 (IN)                                     |
| 0.1000000e+13 | RADIUS OF BODY 2 (IN)                                     |
| 0.1000000E+13 | CROWN RADIUS OF BODY 1 (IN)                               |
| 0.1000000E+13 | CROWN RADIUS OF BODY 2 (IN)                               |
| 11.           | LOAD (LB FOR POINT CONTACT; LB/IN FOR LINE CONTACT)       |
| 0.19          | EFF. THICKNESS OF BODY 1 FOR LINE CONTACT DEFLECTION (IN) |
| 0.5e-2        | EFF. THICKNESS OF BODY 2 FOR LINE CONTACT DEFLECTION (IN) |
| 0.0           | EFFECTIVE SPEED, (U1+U2)/2 (IN/SEC)                       |

0.0 VISCOSITY (REYNS)  
 0.0 VISCOSITY-PRESSURE COEFFICIENT (IN/LB)  
 1000000.0 MAJOR HALF WIDTH (IN)  
 0.4926860E-03 MINOR HALF WIDTH (IN)  
 14213.5 HERTZ MAXIMUM PRESSURE (PSI)  
 0.1499860E-05 DEFLECTION (IN)  
 8221010.0 STIFFNESS (LB/IN FOR POINT CONTACT; PSI FOR LINE CONTACT)  
 0.0 EHD FILM THICKNESS (IN)

13

40000000.0 ELASTIC MODULUS OF BODY 1 (PSI)  
 40000000.0 ELASTIC MODULUS OF BODY 2 (PSI)  
 0.28 POISSONS RATIO FOR BODY 1  
 0.27 POISSONS RATIO FOR BODY 2  
 0.375 RADIUS OF BODY 1 (IN)  
 0.1000000E+13 RADIUS OF BODY 2 (IN)  
 0.1000000E+13 CROWN RADIUS OF BODY 1 (IN)  
 0.1000000E+13 CROWN RADIUS OF BODY 2 (IN)  
 13. LOAD (LB FOR POINT CONTACT; LB/IN FOR LINE CONTACT)  
 0.19 EFF. THICKNESS OF BODY 1 FOR LINE CONTACT DEFLECTION (IN)  
 0.5e-2 EFF. THICKNESS OF BODY 2 FOR LINE CONTACT DEFLECTION (IN)  
 0.0 EFFECTIVE SPEED, (U1+U2)/2 (IN/SEC)  
 0.0 VISCOSITY (REYNS)  
 0.0 VISCOSITY-PRESSURE COEFFICIENT (IN/LB)  
 1000000.0 MAJOR HALF WIDTH (IN)  
 0.5356060E-03 MINOR HALF WIDTH (IN)  
 15451.8 HERTZ MAXIMUM PRESSURE (PSI)  
 0.1740620E-05 DEFLECTION (IN)  
 8390530.0 STIFFNESS (LB/IN FOR POINT CONTACT; PSI FOR LINE CONTACT)  
 0.0 EHD FILM THICKNESS (IN)

14

50000000.0 ELASTIC MODULUS OF BODY 1 (PSI)  
 50000000.0 ELASTIC MODULUS OF BODY 2 (PSI)  
 0.28 POISSONS RATIO FOR BODY 1  
 0.27 POISSONS RATIO FOR BODY 2  
 0.375 RADIUS OF BODY 1 (IN)  
 0.1000000E+13 RADIUS OF BODY 2 (IN)  
 0.1000000E+13 CROWN RADIUS OF BODY 1 (IN)  
 0.1000000E+13 CROWN RADIUS OF BODY 2 (IN)  
 13. LOAD (LB FOR POINT CONTACT; LB/IN FOR LINE CONTACT)  
 0.19 EFF. THICKNESS OF BODY 1 FOR LINE CONTACT DEFLECTION (IN)  
 0.5e-2 EFF. THICKNESS OF BODY 2 FOR LINE CONTACT DEFLECTION (IN)  
 0.0 EFFECTIVE SPEED, (U1+U2)/2 (IN/SEC)  
 0.0 VISCOSITY (REYNS)  
 0.0 VISCOSITY-PRESSURE COEFFICIENT (IN/LB)  
 1000000.0 MAJOR HALF WIDTH (IN)  
 0.4790600E-03 MINOR HALF WIDTH (IN)  
 17275.6 HERTZ MAXIMUM PRESSURE (PSI)  
 0.1426630E-05 DEFLECTION (IN)  
 10207000.0 STIFFNESS (LB/IN FOR POINT CONTACT; PSI FOR LINE CONTACT)  
 0.0 EHD FILM THICKNESS (IN)

15

50000000.0 ELASTIC MODULUS OF BODY 1 (PSI)  
 50000000.0 ELASTIC MODULUS OF BODY 2 (PSI)  
 0.28 POISSONS RATIO FOR BODY 1  
 0.27 POISSONS RATIO FOR BODY 2

0.375 RADIUS OF BODY 1 (IN)  
 0.1000000e+13 RADIUS OF BODY 2 (IN)  
 0.1000000E+13 CROWN RADIUS OF BODY 1 (IN)  
 0.1000000E+13 CROWN RADIUS OF BODY 2 (IN)  
 11. LOAD (LB FOR POINT CONTACT; LB/IN FOR LINE CONTACT)  
 0.19 EFF. THICKNESS OF BODY 1 FOR LINE CONTACT DEFLECTION (IN)  
 0.5e-2 EFF. THICKNESS OF BODY 2 FOR LINE CONTACT DEFLECTION (IN)  
 0.0 EFFECTIVE SPEED, (U1+U2)/2 (IN/SEC)  
 0.0 VISCOSITY (REYNS)  
 0.0 VISCOSITY-PRESSURE COEFFICIENT (IN/LB)  
 1000000.0 MAJOR HALF WIDTH (IN)  
 0.4406720E-03 MINOR HALF WIDTH (IN)  
 15891.2 HERTZ MAXIMUM PRESSURE (PSI)  
 0.1228780E-05 DEFLECTION (IN)  
 10006200.0 STIFFNESS (LB/IN FOR POINT CONTACT; PSI FOR LINE CONTACT)  
 0.0 EHD FILM THICKNESS (IN)

16'

50000000.0 ELASTIC MODULUS OF BODY 1 (PSI)  
 50000000.0 ELASTIC MODULUS OF BODY 2 (PSI)  
 0.28 POISSONS RATIO FOR BODY 1  
 0.27 POISSONS RATIO FOR BODY 2  
 0.375 RADIUS OF BODY 1 (IN)  
 0.1000000e+13 RADIUS OF BODY 2 (IN)  
 0.1000000E+13 CROWN RADIUS OF BODY 1 (IN)  
 0.1000000E+13 CROWN RADIUS OF BODY 2 (IN)  
 8. LOAD (LB FOR POINT CONTACT; LB/IN FOR LINE CONTACT)  
 0.19 EFF. THICKNESS OF BODY 1 FOR LINE CONTACT DEFLECTION (IN)  
 0.5e-2 EFF. THICKNESS OF BODY 2 FOR LINE CONTACT DEFLECTION (IN)  
 0.0 EFFECTIVE SPEED, (U1+U2)/2 (IN/SEC)  
 0.0 VISCOSITY (REYNS)  
 0.0 VISCOSITY-PRESSURE COEFFICIENT (IN/LB)  
 1000000.0 MAJOR HALF WIDTH (IN)  
 0.3758060E-03 MINOR HALF WIDTH (IN)  
 13552.1 HERTZ MAXIMUM PRESSURE (PSI)  
 0.9236410E-06 DEFLECTION (IN)  
 9644510.0 STIFFNESS (LB/IN FOR POINT CONTACT; PSI FOR LINE CONTACT)  
 0.0 EHD FILM THICKNESS (IN)

17'

60000000.0 ELASTIC MODULUS OF BODY 1 (PSI)  
 60000000.0 ELASTIC MODULUS OF BODY 2 (PSI)  
 0.28 POISSONS RATIO FOR BODY 1  
 0.27 POISSONS RATIO FOR BODY 2  
 0.375 RADIUS OF BODY 1 (IN)  
 0.1000000e+13 RADIUS OF BODY 2 (IN)  
 0.1000000E+13 CROWN RADIUS OF BODY 1 (IN)  
 0.1000000E+13 CROWN RADIUS OF BODY 2 (IN)  
 8. LOAD (LB FOR POINT CONTACT; LB/IN FOR LINE CONTACT)  
 0.19 EFF. THICKNESS OF BODY 1 FOR LINE CONTACT DEFLECTION (IN)  
 0.5e-2 EFF. THICKNESS OF BODY 2 FOR LINE CONTACT DEFLECTION (IN)  
 0.0 EFFECTIVE SPEED, (U1+U2)/2 (IN/SEC)  
 0.0 VISCOSITY (REYNS)  
 0.0 VISCOSITY-PRESSURE COEFFICIENT (IN/LB)  
 1000000.0 MAJOR HALF WIDTH (IN)  
 0.3430620E-03 MINOR HALF WIDTH (IN)  
 14845.6 HERTZ MAXIMUM PRESSURE (PSI)

0.7840060E-06 DEFLECTION (IN)  
11338800.0 STIFFNESS (LB/IN FOR POINT CONTACT; PSI FOR LINE CONTACT)  
0.0 EHD FILM THICKNESS (IN)

60000000.0 ELASTIC MODULUS OF BODY 1 (PSI)  
60000000.0 ELASTIC MODULUS OF BODY 2 (PSI)  
0.28 POISSONS RATIO FOR BODY 1  
0.27 POISSONS RATIO FOR BODY 2  
0.375 RADIUS OF BODY 1 (IN)  
0.1000000E+13 RADIUS OF BODY 2 (IN)  
0.1000000E+13 CROWN RADIUS OF BODY 1 (IN)  
0.1000000E+13 CROWN RADIUS OF BODY 2 (IN)  
11. LOAD (LB FOR POINT CONTACT; LB/IN FOR LINE CONTACT)  
0.19 EFF. THICKNESS OF BODY 1 FOR LINE CONTACT DEFLECTION (IN)  
0.5e-2 EFF. THICKNESS OF BODY 2 FOR LINE CONTACT DEFLECTION (IN)  
0.0 EFFECTIVE SPEED, (U1+U2)/2 (IN/SEC)  
0.0 VISCOSITY (REYNS)  
0.0 VISCOSITY-PRESSURE COEFFICIENT (IN/LB)  
1000000.0 MAJOR HALF WIDTH (IN)  
0.4022760E-03 MINOR HALF WIDTH (IN)  
17408.0 HERTZ MAXIMUM PRESSURE (PSI)  
0.1043650E-05 DEFLECTION (IN)  
11755100.0 STIFFNESS (LB/IN FOR POINT CONTACT; PSI FOR LINE CONTACT)  
0.0 EHD FILM THICKNESS (IN)

60000000.0 ELASTIC MODULUS OF BODY 1 (PSI)  
60000000.0 ELASTIC MODULUS OF BODY 2 (PSI)  
0.28 POISSONS RATIO FOR BODY 1  
0.27 POISSONS RATIO FOR BODY 2  
0.375 RADIUS OF BODY 1 (IN)  
0.1000000E+13 RADIUS OF BODY 2 (IN)  
0.1000000E+13 CROWN RADIUS OF BODY 1 (IN)  
0.1000000E+13 CROWN RADIUS OF BODY 2 (IN)  
13. LOAD (LB FOR POINT CONTACT; LB/IN FOR LINE CONTACT)  
0.19 EFF. THICKNESS OF BODY 1 FOR LINE CONTACT DEFLECTION (IN)  
0.5e-2 EFF. THICKNESS OF BODY 2 FOR LINE CONTACT DEFLECTION (IN)  
0.0 EFFECTIVE SPEED, (U1+U2)/2 (IN/SEC)  
0.0 VISCOSITY (REYNS)  
0.0 VISCOSITY-PRESSURE COEFFICIENT (IN/LB)  
1000000.0 MAJOR HALF WIDTH (IN)  
0.4373200E-03 MINOR HALF WIDTH (IN)  
18924.5 HERTZ MAXIMUM PRESSURE (PSI)  
0.1212110E-05 DEFLECTION (IN)  
11985900.0 STIFFNESS (LB/IN FOR POINT CONTACT; PSI FOR LINE CONTACT)  
0.0 EHD FILM THICKNESS (IN)

## **APPENDIX O**

**H. Heshmat, P. Albrecht, and J.F. Dill, "Friction and Wear Testing of Ceramic Materials," Final Report, MTI Report No. 90TR1, Mechanical Technology, Inc., Latham, NY, Hughes P.O. S9-316055-SAC**



MTI 90TR1

Final Report

---

# FRICTION AND WEAR TESTING OF CERAMIC MATERIALS

---

Prepared for:

Hughes Aircraft Company  
P.O. Box 902  
2000 East El Segundo Boulevard  
El Segundo, California 90245

Prepared under:

Contract No. S-9-316055 SAC

Prepared by:

Hooshang Heshmat, Peter Albrecht, James Dill  
Mechanical Technology Incorporated  
968 Albany-Shaker Road  
Latham, New York 12110

29 January 1990

# EXECUTIVE SUMMARY

---

This program, Contract No. S-9-316055 SAC, was sponsored by Hughes Aircraft Co. It was a continuation of an earlier program that investigated the effect of friction and loads on predicting shaft runout caused by cyclic loading of the rubshoe-rod interface. Work on this program was split into two phases. Phase I testing used a disk-on-disk tribometer to investigate the influence of powder lubricants on the traction coefficient between two ceramic materials - Kyocera silicon nitride ( $\text{Si}_3\text{N}_4$ ) hot pressed, and ESK alpha silicon carbide ( $\alpha$  SiC) post hipped\*. Powder lubricants used included titanium dioxide ( $\text{TiO}_2$ ), boron nitride (BN), and molybdenum disulfide ( $\text{MoS}_2$ ). Phase II testing investigated the sliding wear characteristics of ( $\alpha$  SiC),  $\text{Si}_3\text{N}_4$ , and an  $\text{Si}_3\text{N}_4$  matrix containing varying amounts of BN. The samples were studied on a pin-on-disk tribometer using speed and temperature as variables.

The most notable results of the Phase I investigation were:

- Similarity of characteristic curves for the traction force versus slide/roll ratio using dry powder to characteristic curves using liquid lubricants
- Some dry powder lubricants had substantially lower traction coefficients and wear
- Measured tractions decreased moderately with slip speed and load and were found to be related to the type of powder-lubricant used. Collected data show little sensitivity to temperature.

Results of the Phase II testing showed dramatic wear of the elevated-temperature, 40% BN pin sample compared to the same sample at ambient temperatures. The elevated-temperature sample showed total wear over 1,000 times (100,000%) greater than the sample tested at ambient temperatures. In contrast,  $\alpha$  SiC pins showed a slight decrease in wear at higher temperatures when an  $\text{Si}_3\text{N}_4$  disk with 0% BN was used. When the 3.5% BN disk was used, the  $\alpha$  SiC pin showed an increase in wear of only 38.9% at elevated temperatures compared to ambient temperatures.

The coefficient of friction was significantly lower for tests using  $\text{Si}_3\text{N}_4$  samples compared to the same tests using  $\alpha$  SiC samples. Wear, however, tended to be greater for the  $\text{Si}_3\text{N}_4$  samples. The addition of BN to the  $\text{Si}_3\text{N}_4$  samples tended to increase both the wear and the coefficient of friction regardless of whether BN existed in the disk, the pin, or both.

---

\*Hot isostatically pressed.

## **ACKNOWLEDGMENTS**

---

This program was performed for the Hughes Aircraft Company with Mr. Michael N. Gardos, who has supported the evaluation effort as Program Manager. Acknowledgement is due to Hughes Aircraft Company for its sponsorship of the present program and, in particular, to Mr. Gardos for his sustained interest and support of this work.

The authors gratefully acknowledge Mr. Bobby D. McConnell (AFWAL/MLBT), Project Engineer, for support, guidance, and supervision given at various stages of this effort; Mr. Ronald Dayton for his sustained interest and technical contribution to this research; and Mr. David Hosterman and Mr. Roy Howarth of MTI.

# TABLE OF CONTENTS

---

| SECTION                                                                                         | PAGE |
|-------------------------------------------------------------------------------------------------|------|
| EXECUTIVE SUMMARY .....                                                                         | iii  |
| ACKNOWLEDGMENTS .....                                                                           | v    |
| LIST OF FIGURES .....                                                                           | ix   |
| LIST OF TABLES .....                                                                            | xi   |
| <br><b>Phase I - Traction Characteristics of High-Temperature Powder-Lubricated Ceramics</b>    |      |
| 1.0 INTRODUCTION .....                                                                          | 1    |
| 2.0 TEST RIG DISCRIPTION .....                                                                  | 3    |
| 3.0 TEST RESULTS .....                                                                          | 5    |
| 3.1 System Checkout .....                                                                       | 5    |
| 3.2 Unlubricated Tests .....                                                                    | 5    |
| 3.3 Tests with $\text{TiO}_2$ .....                                                             | 5    |
| 3.4 Tests with BN .....                                                                         | 6    |
| 3.5 Tests with $\text{MoS}_2$ .....                                                             | 6    |
| 4.0 CONCLUSIONS .....                                                                           | 7    |
| <br><b>Phase II - Wear and Friction Properties of Silicon Nitride and Alpha Silicon Carbide</b> |      |
| 5.0 INTRODUCTION .....                                                                          | 47   |
| 6.0 TEST RIG DESCRIPTION .....                                                                  | 49   |
| 7.0 TEST PROCEDURE .....                                                                        | 51   |
| 7.1 Load .....                                                                                  | 52   |
| 7.2 Speed .....                                                                                 | 52   |
| 7.3 Temperature .....                                                                           | 52   |
| 8.0 RESULTS .....                                                                               | 53   |
| 8.1 Pin Wear .....                                                                              | 53   |
| 8.2 Disk Wear .....                                                                             | 55   |
| 8.3 Frictional Force .....                                                                      | 55   |
| 9.0 CONCLUSIONS .....                                                                           | 57   |

# LIST OF FIGURES

---

| NUMBER |                                                                                                                                       | PAGE |
|--------|---------------------------------------------------------------------------------------------------------------------------------------|------|
| 1      | Overall View of Disk-On-Disk Tribometer . . . . .                                                                                     | 8    |
| 2      | Schematic of Disk-On-Disk Tribometer. . . . .                                                                                         | 9    |
| 3      | Wear Track Identification Convention. . . . .                                                                                         | 10   |
| 4      | Contact Pressure vs. Applied Load . . . . .                                                                                           | 11   |
| 5      | Initial Spindle Alignment . . . . .                                                                                                   | 12   |
| 6      | Thermocouples Close to Disks . . . . .                                                                                                | 13   |
| 7      | Test Cell Installation . . . . .                                                                                                      | 14   |
| 8      | Control and Data Acquisition System . . . . .                                                                                         | 15   |
| 9      | Traction Coefficient Data for Oil . . . . .                                                                                           | 16   |
| 10     | Definition of Traction Curve Parameters. . . . .                                                                                      | 17   |
| 11     | Traction Data, Unlubricated, Room Temperature, Load = 4 lb . . . . .                                                                  | 18   |
| 12     | Traction Data, Unlubricated, Room Temperature, Load = 10 lb . . . . .                                                                 | 19   |
| 13     | Traction Data, Unlubricated, Temperature = 1200°F, Load = 5 lb . . . . .                                                              | 20   |
| 14     | Traction Data, Unlubricated, Temperature = 1200°F, Load = 10 lb . . . . .                                                             | 21   |
| 15     | Traction Data, TiO <sub>2</sub> , Room Temperature, Load = 4 lb . . . . .                                                             | 22   |
| 16     | Traction Data, TiO <sub>2</sub> , Room Temperature, Load = 10 lb . . . . .                                                            | 23   |
| 17     | Traction Data, TiO <sub>2</sub> , Temperature = 1200°F, Load = 5 lb . . . . .                                                         | 24   |
| 18     | Traction Data, TiO <sub>2</sub> , Temperature = 1200°F, Load = 10 lb . . . . .                                                        | 25   |
| 19     | Wear Track for TiO <sub>2</sub> , Room Temperature, Loads = 4 and 10 lb . . . . .                                                     | 26   |
| 20     | Wear Track for TiO <sub>2</sub> , Temperature = 1200°F, Loads 5 and 10 lb . . . . .                                                   | 27   |
| 21     | Traction Data for TiO <sub>2</sub> /Inconel 718 Stick Lube, Temperature = 1200°F, Load = 5 lb . . . . .                               | 28   |
| 22     | Traction Data for TiO <sub>2</sub> /Inconel 718 Stick Lube, Temperature = 1200°F, Load = 10 lb . . . . .                              | 29   |
| 23     | Wear Track for TiO <sub>2</sub> /Inconel 718 Stick Lube, Temperature = 1200°F,<br>Loads = 5 and 10 lb . . . . .                       | 30   |
| 24     | Traction Data, BN, Room Temperature, Load = 4 lb . . . . .                                                                            | 31   |
| 25     | Traction Data, BN, Room Temperature, Loads = 10 and 15 lb . . . . .                                                                   | 32   |
| 26     | Traction Data, BN, Temperature = 1200°F, Load = 5 lb . . . . .                                                                        | 33   |
| 27     | Traction Data, BN, Temperature = 1200°F, Load = 10 lb . . . . .                                                                       | 34   |
| 28     | Wear Track for BN, Room Temperature, Loads = 4, 10, and 15 lb . . . . .                                                               | 35   |
| 29     | Wear Track for BN, Temperature = 1200°F, Loads = 5 and 10 lb . . . . .                                                                | 36   |
| 30     | Wear Track on Crowned Disk with BN, Temperature = 1200°F, Loads = 5 and 10 lb . . . . .                                               | 37   |
| 31     | Higher Magnification of Wear Track on Crowned Disk with BN,<br>Temperature = 1200°F, Loads = 5 and 10 lb . . . . .                    | 38   |
| 32     | Traction Data, MoS <sub>2</sub> , Room Temperature, Loads = 4, 10, 15, 20, and 25 lb . . . . .                                        | 39   |
| 33     | Traction Data, MoS <sub>2</sub> , Temperature = 800°F, Loads = 5, 10, and 15 lb . . . . .                                             | 40   |
| 34     | Traction Data, MoS <sub>2</sub> , Temperature = 800°F, Loads = 15, 20, and 25 lb . . . . .                                            | 41   |
| 35     | Traction Data, MoS <sub>2</sub> , Temperature = 1200°F, Loads = 5, 10, and 15 lb . . . . .                                            | 42   |
| 36     | Traction Data, MoS <sub>2</sub> , Temperature = 1200°F, Loads = 15, 20, and 25 lb . . . . .                                           | 43   |
| 37     | Wear Track for MoS <sub>2</sub> , Room Temperature to 1200°F, Load = 4 to 25 lb . . . . .                                             | 44   |
| 38     | Wear Track on Crowned Disk with MoS <sub>2</sub> , Room Temperature to 1200°F,<br>Load = 4 to 25 lb . . . . .                         | 45   |
| 39     | Higher Magnification of Wear Track on Crowned Disk with MoS <sub>2</sub> , Room<br>Temperature to 1200°F, Load = 4 to 25 lb . . . . . | 46   |
| 40     | High-Speed, High-Temperature Test Rig (Tribometer). . . . .                                                                           | 58   |
| 41     | Strip Chart Recording for Test HU-17. . . . .                                                                                         | 59   |

# LIST OF FIGURES

---

| NUMBER |                                                                                 | PAGE |
|--------|---------------------------------------------------------------------------------|------|
| 42     | Strip Chart Recording for Test HU-18.....                                       | 60   |
| 43     | Strip Chart Recording for Test HU-19.....                                       | 61   |
| 44     | Strip Chart Recording for Test HU-20.....                                       | 62   |
| 45     | Pin Wear (SiN with 40% BN; Flay Lay on SiC Disk at Ambient Temperature).....    | 63   |
| 46     | Pin Wear (SiN with 3.5% BN; Edge Lay on SiC Disk at Ambient Temperature).....   | 63   |
| 47     | Pin Wear (SiN with 40% BN; Edge Lay on SiC Disk at Ambient Temperature).....    | 64   |
| 48     | Pin Wear (COMBAT BN on SiC Disk at Ambient Temperature).....                    | 64   |
| 49     | Pin Wear (SiN with 40% BN; Edge Lay at 1200°F).....                             | 65   |
| 50     | Pin Wear (SiN with 15% BN; Edge Lay on SiC Disk at Ambient Temperature).....    | 66   |
| 51     | Pin Wear (SiC, Post Hipped, on SiC Disk at Ambient Temperature).....            | 66   |
| 52     | Pin Wear (SiC, Hipped, on SiC Disk at Ambient Temperature).....                 | 67   |
| 53     | Pin Wear (SiN; Flay Lay on SiN Disk at Ambient Temperature).....                | 67   |
| 54     | Pin Wear (SiN; Flay Lay with 40% BN on SiN Disk at Ambient Temperature).....    | 68   |
| 55     | Pin Wear (SiC, Hipped, on SiN Disk at Ambient Temperature).....                 | 68   |
| 56     | Pin Wear (SiC, Hipped, on SiN Disk at 1200°F).....                              | 69   |
| 57     | Pin Wear (SiN on SiN Disk with 3.5% BN at Ambient Temperature).....             | 69   |
| 58     | Pin Wear (SiN with 40% BN on SiN Disk with 3.5% BN at Ambient Temperature)..... | 70   |
| 59     | Pin Wear (SiC, Hipped, on SiN Disk with 3.5% BN at Ambient Temperature).....    | 70   |
| 60     | Pin Wear (SiC, Hipped, on SiN Disk with 3.5% BN at 1200°F).....                 | 71   |
| 61     | SiC (Post Hipped) Disk Wear; Disk 1.....                                        | 72   |
| 62     | SiC (Post Hipped) Disk Wear; Disk 2.....                                        | 73   |
| 63     | SiC (Post Hipped) Disk Wear; Disk 3.....                                        | 74   |
| 64     | SiN (0% BN) Disk Wear; Disk 4.....                                              | 75   |
| 65     | SiN (3.5% BN) Disk Wear; Disk 5.....                                            | 76   |
| 66     | Photo of Disk 1 Wear.....                                                       | 77   |
| 67     | Photo of Disk 2 Wear.....                                                       | 78   |
| 68     | Photo of Disk 3 Wear.....                                                       | 79   |
| 69     | Photo of Disk 4 Wear.....                                                       | 80   |
| 70     | Photo of Disk 5 Wear.....                                                       | 81   |
| 71     | Frictional Force vs. Total Wear.....                                            | 82   |

# LIST OF TABLES

---

| NUMBER |                                                            | PAGE |
|--------|------------------------------------------------------------|------|
| 1      | Disk-On-Disk Test Conditions . . . . .                     | 1    |
| 2      | Pin-On-Disk Test Matrix and Test Results Summary . . . . . | 51   |
| 3      | Pin Volumetric Wear Factor . . . . .                       | 54   |
| 4      | Coefficients of Friction . . . . .                         | 55   |
| 5      | Normalized Contact Shear Stress ( $\tau$ ) . . . . .       | 56   |

**Phase I**  
**Traction Characteristics of**  
**High-Temperature Powder-Lubricated Ceramics**



# 1.0 INTRODUCTION

The objective of this phase of the program was to investigate the influence of powder lubricants on the traction coefficient between two ceramic materials. The ceramic materials used were Kyocera silicon nitride ( $\text{Si}_3\text{N}_4$ ), hot pressed; and ESK alpha silicon carbide ( $\alpha \text{ SiC}$ ), post hipped\*. The powder lubricants used were titanium dioxide ( $\text{TiO}_2$ ), rutile form; boron nitride (BN), hexagonal form; and molybdenum disulfide, ( $\text{MoS}_2$ ). The investigation was carried out using a disk-on-disk machine and measurements were made for a range of loads and ambient temperatures up to 1200°F. A matrix of the test conditions is provided in Table 1.

TABLE 1. Disk-On-Disk Test Conditions

| Lubricant           | Room Temperature |    |    |    |    | ≅ 800°F |    |    |    |    | ≅ 1200°F |    |    |    |    |
|---------------------|------------------|----|----|----|----|---------|----|----|----|----|----------|----|----|----|----|
|                     | Load (lb)        |    |    |    |    |         |    |    |    |    |          |    |    |    |    |
|                     | 4                | 10 | 15 | 20 | 25 | 5       | 10 | 15 | 20 | 25 | 5        | 10 | 15 | 20 | 25 |
| None                | 4*               | 4  | 3  |    |    |         |    |    |    |    | 4        | 2  |    |    |    |
| TiO <sub>2</sub> ** | 3                | 2  |    |    |    |         |    |    |    |    | 4        | 3  |    |    |    |
| BN                  | 6                | 3  | 4  |    |    |         |    |    |    |    | 8        | 5  |    |    |    |
| MoS <sub>2</sub>    | 6                | 1  | 2  | 1  | 1  | 1       | 1  | 4  | 1  | 4  | 2        | 1  | 4  | 2  | 2  |

\*Number of repeated tests.

\*\* $\text{TiO}_2$  - Rutile form,  $< 2 \mu\text{m}$

\*Hot isostatically pressed.

## 2.0 TEST RIG DESCRIPTION

---

A photograph of the disk-on-disk tribometer used for Phase I testing is presented in Figure 1\* and a schematic of the machine is given in Figure 2. The lower disk, mounted on spindle A, has a plain cylindrical form with a radius of 36 mm. The disk material for the tests was  $\alpha$  SiC. The upper, crowned disk on spindle B has a major radius of 36 mm and a crown radius of 14.4 mm. For the tests, the crowned disk was made from  $\text{Si}_3\text{N}_4$ . With this arrangement, it was possible to run up to three series of tests on each of the plain cylindrical disks by changing the relative axial positions of the disks to generate separate wear tracks. The design methodology and dynamic analysis of the test apparatus is given in Appendix A. The convention used to identify the different tracks is shown in Figure 3. For the chosen disk materials and geometries, the maximum Hertz stress as a function of normal load is given in Figure 4.

As shown in Figure 2, spindle A is rigidly mounted on the base and is driven by a variable-speed electric motor through a quill shaft. Spindle B is driven by an integral air turbine. The spindle unit is suspended on a soft spring, but is restrained by hydrostatic bearings. These bearings operate against a vertical member which is integral with the base. The hydrostatic bearings keep the axes of the two spindles parallel but present virtually no resistance to the vertical motion of spindle B. During the initial assembly, the spindle axes were set up parallel to each other and were aligned in a vertical plane. This ensured that the wear tracks generated on the plain cylindrical disk were parallel to the face of the disk, as shown in Figure 5. In operation, the disks are loaded by a pneumatic cylinder that pulls down on spindle B through a load cell. The traction force is measured by a tangential load cell, as shown in Figure 2. An insulated oven enclosure surrounds the two disks to control the environment for high-temperature testing. During the tests, temperatures were monitored by three thermocouples located close to the disks, as shown in Figure 6.

The system for delivering powder lubricants to the contact zone in these tests is based on a conventional air brush. A tube from the airbrush nozzle penetrates the oven wall and discharges the air/powder mixture approximately 1 in. from the contact zone. Dry air is supplied to the unit at 40 psi.

Prior to operation, the suspension spring for spindle B is adjusted so that the disks are separated from each other by a distance of 90 to 100  $\mu\text{m}$  with no pressure in the loading cylinder. Spindle A is then accelerated to a preselected speed that is maintained throughout the test. Spindle B is then accelerated to a speed higher than that of spindle A. The traction test is started by applying the load, which brings the disks into contact, and then shutting off the air to the drive turbine. Spindle B subsequently coasts down to a speed lower than that of spindle A. The sequence of events for each test is carried out automatically by a rig control and data acquisition system based on a PC/AT computer. The system automatically initiates and maintains the speed of spindle A, sets up the initial speed of spindle B, applies the load, and shuts off the air to the drive turbine. During coastdown, the speed and traction force are continuously monitored and data are stored for subsequent analysis. During a typical 5- to 6-sec coastdown, 1.5 to 2 megabytes of data are recorded and 250 to 300 data points are subsequently extracted from this raw data. During coastdown, speed and traction force are also recorded on a multichannel magnetic tape recorder.

Figure 7 is an overall view of the tribometer and test cell facilities. Figure 8 shows the control room with the control and data acquisition equipment. Each test was repeated up to eight times to verify repeatability of the traction data.

---

\*Figures for Phase I testing are appended to Section 4.0.

## 3.0 TEST RESULTS

---

### 3.1 System Checkout

To check out and validate the system, the first tests were carried out at room temperature using a traction fluid equivalent to 20 wt oil as lubricant. The results, presented in Figure 9, correlate well with other available data for the same oil\*.

Figure 9 includes some additional data that are valuable in comparing and classifying different traction curves. These quantities are:

- $\tau_0$  = Yield shear stress (threshold)
- $\tau_1$  = Limiting shear stress
- $\tau_T$  = Temperature limiting shear stress
- $\alpha_1$  = Slope at maximum traction
- $\alpha_2$  = Initial slope of stable portion of traction curve.

The parameters for a typical traction curve are defined in Figure 10.

### 3.2 Unlubricated Tests

To provide a baseline for assessing the advantages of powder lubricants, tests were carried out with no lubricant at room temperature and 1200°F. The results at room temperature are shown in Figures 11 and 12 for loads of 4 and 10 lb respectively. The different loads did not change the threshold shear stress. However, at the higher load the yield shear stress was slightly lower and occurred at a higher sliding velocity. With the 4-lb load, the traction coefficient approached a value of approximately 0.39 at high sliding velocities, but the traction coefficient had fallen to approximately 0.27 at 150% slip and was still decreasing.

At 1200°F with a 5-lb load, the traction coefficient peaked at approximately 0.45 and then decreased slowly as the slip increased, as shown in Figure 13. With a higher load of 10 lb, the traction coefficient increased to a value slightly in excess of 0.3 and then stayed essentially constant (see Figure 14). At the higher load, the threshold shear stress was significantly reduced.

### 3.3 Tests with TiO<sub>2</sub>

The traction coefficient data generated using TiO<sub>2</sub> as lubricant are presented in Figures 15 through 18. At room temperature, the threshold shear stresses were significantly lower than those with no lubricant, but the yield shear stresses were essentially the same. At 1200°F and 5-lb load (see Figure 17), there was virtually no change in the yield shear stress, but at 1200°F and 10 lb, the traction curve was still rising to its peak at the highest value of slip (4.00%).

The wear track generated on the plain disk during the room-temperature tests is shown in Figure 19. The photographs were taken on the same track at locations 180° apart. Photographs of the wear track produced in the high-temperature tests are given in Figure 20. In this case, the wear track is much more clearly defined. The dimension, Dm, marked on the photographs, is the apparent major Hertzian diameter.

During initial tests with TiO<sub>2</sub> at 1200°F, some material from an Inconel 718 thermocouple was inadvertently introduced into the contact zone. While this was not a planned test, the results have been included because the presence of the Inconel 718 did appear to have a significant effect. As shown in Figures 21 and 22, the yield shear stresses were much lower than those with just TiO<sub>2</sub> present. The wear track produced, shown in Figure 23, also had a distinctly different appearance.

---

\*Gupta, P.K., "Traction Modeling of Military Oils." Technical Report G-104-86-TR, prepared for AFAPL/AFWAL, January 1986.

### 3.4 Tests with BN

The traction data at room temperature using BN, shown in Figures 24 and 25, gave yield shear stresses that were much lower than those for the unlubricated tests. At 1200°F (see Figures 26 and 27), the yield shear stresses were more comparable to the unlubricated data.

At room temperature, damage to the surface of the plain disk was not excessive, as shown in Figure 28. At 1200°F, the wear track showed significant damage with particles of the BN powder embedded in the track (see Figure 29). The crowned disk suffered similar damage, as shown in Figures 30 and 31.

### 3.5 Tests with MoS<sub>2</sub>

The traction data using MoS<sub>2</sub> at room temperature is given in Figure 32. This shows a progressive decrease in the yield shear stress with increasing load. The same holds for the traction data at 800°F and 1200°F given in Figures 33 through 36. In all cases, the threshold shear stress was zero, which is what might be expected with a liquid lubricant. The yield shear stresses were also an order of magnitude less than those measured with no lubricant and with TiO<sub>2</sub> and BN. Overall, the traction curves with MoS<sub>2</sub> lubrication indicate that the powder performs in a manner very similar to liquid lubricants.

The wear tracks using MoS<sub>2</sub> on the plain disk and the crowned disk are shown in Figures 37 through 39.

## 4.0 CONCLUSIONS

---

- Tests with oil of known characteristics showed that the disk-on-disk tribometer, with its automated control and data acquisition system, produced accurate traction data.
- The  $\text{TiO}_2$  powder lubricant changed the shapes of the traction curves. Compared with the unlubricated data, the powder reduced the traction coefficients at low slip ratios but it did not have any significant effect on the yield shear stresses.
- When Iconel 718 was inadvertently mixed with  $\text{TiO}_2$  powder, the yield shear stress was lower than with  $\text{TiO}_2$  alone.
- At room temperature, BN powder gave lower traction coefficients than both the unlubricated case and when lubricated with  $\text{TiO}_2$ . At 1200°F, the BN powder gave traction coefficients similar to the unlubricated condition and there was heavy damage in the wear tracks.
- The traction characteristics of the  $\text{MoS}_2$  powder were quite different compared to the other two powders. The  $\text{MoS}_2$  powder gave zero threshold shear stress and low traction coefficients under all test conditions. Overall, the behavior of the powder and the magnitude of the traction coefficients were very similar to those seen with liquid lubricants.
- Due to the short duration of each test, the amount of wear that took place on the disks was too small to measure accurately. Therefore, the data reported should only be used to compare the traction characteristics of the powder lubricants with the chosen combination of disk materials.
- Changes in the composition and processing of ceramic materials can affect both traction and wear properties. Therefore the data generated in the program may not be valid for equivalent ceramic materials from other sources.

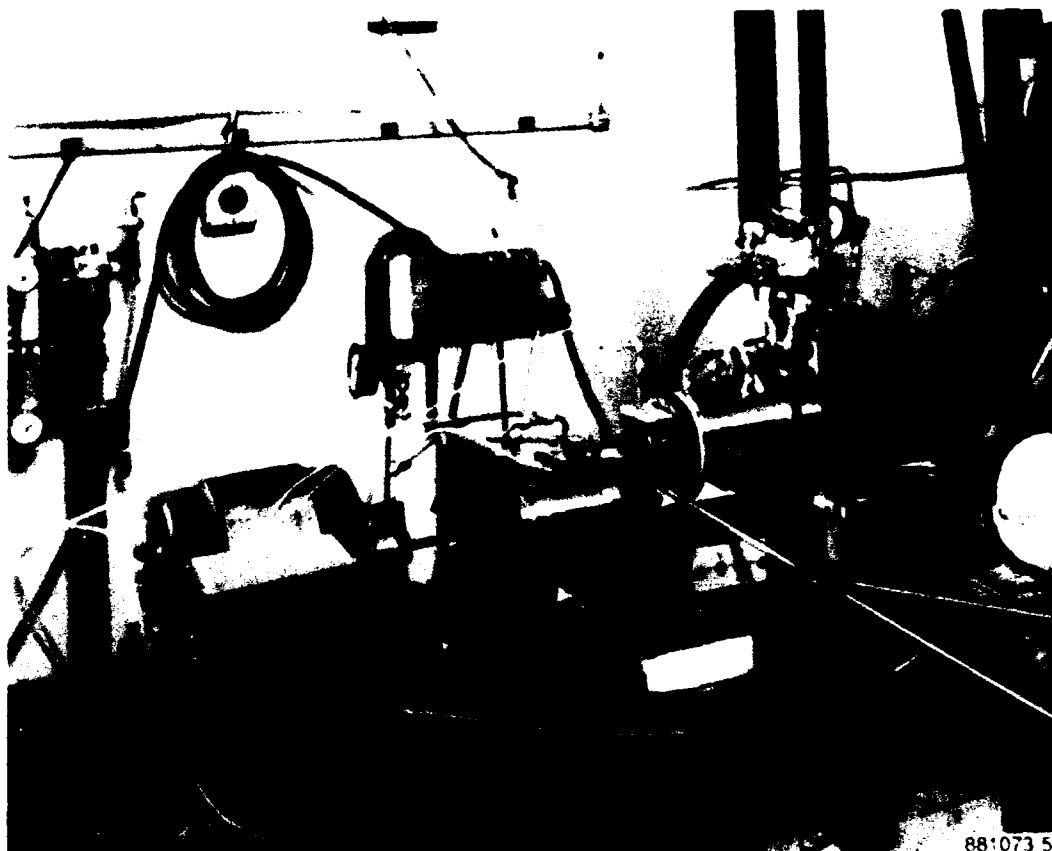
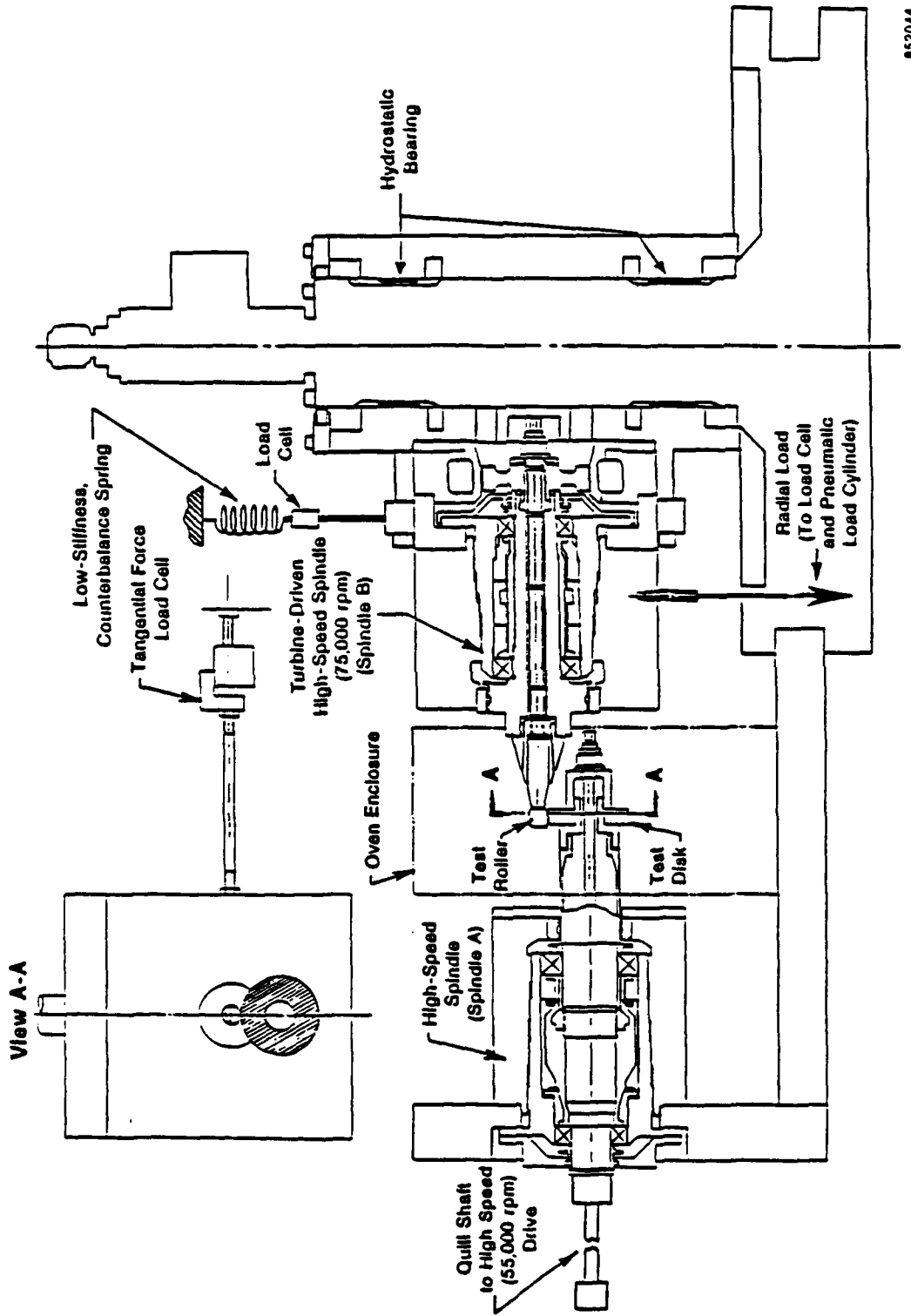
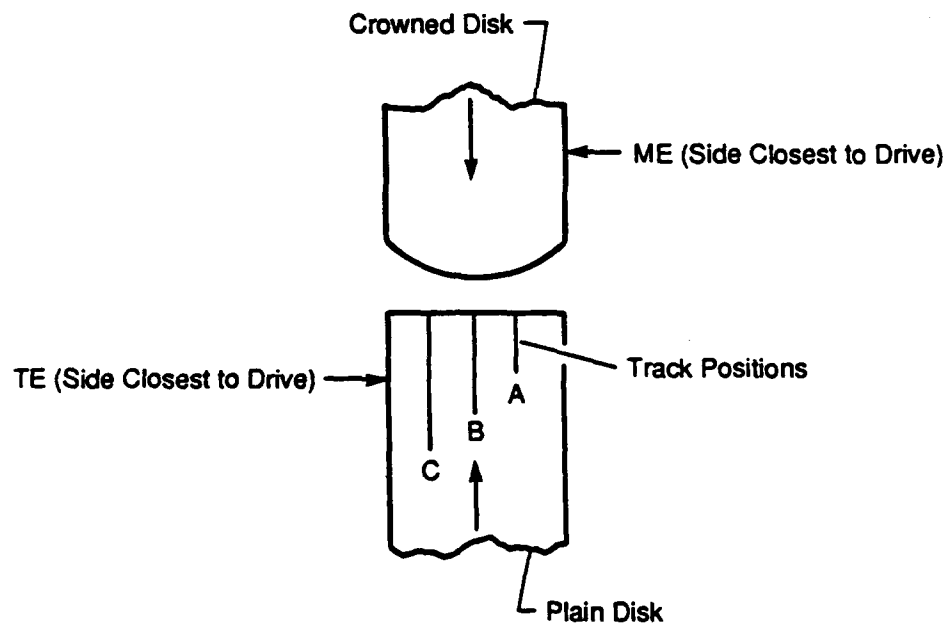


Figure 1. Overall View of Disk-On-Disk Tribometer



852044

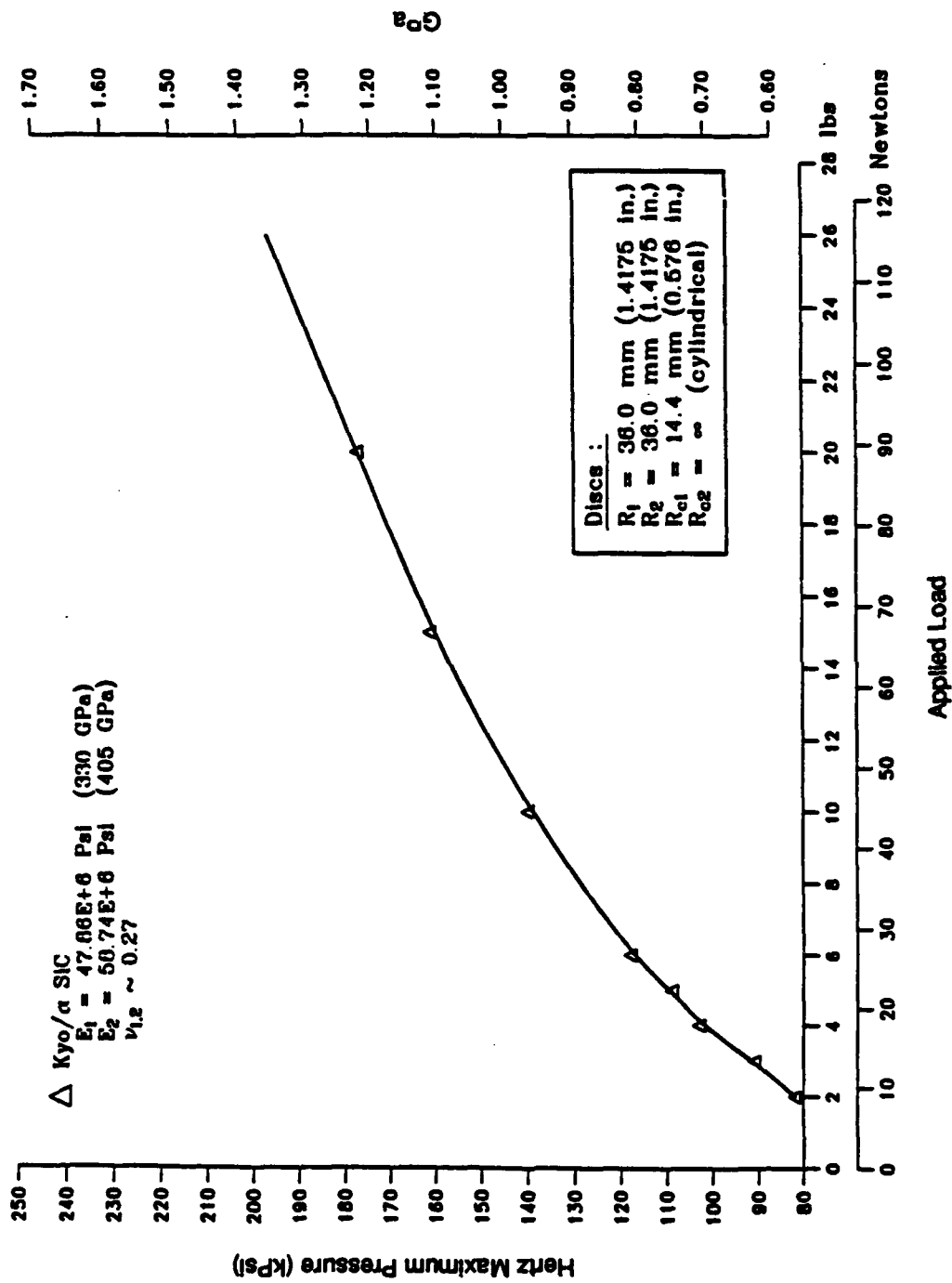
Figure 2. Schematic of Disk-On-Disk Tribometer



90097

Figure 3. Wear Track Identification Convention





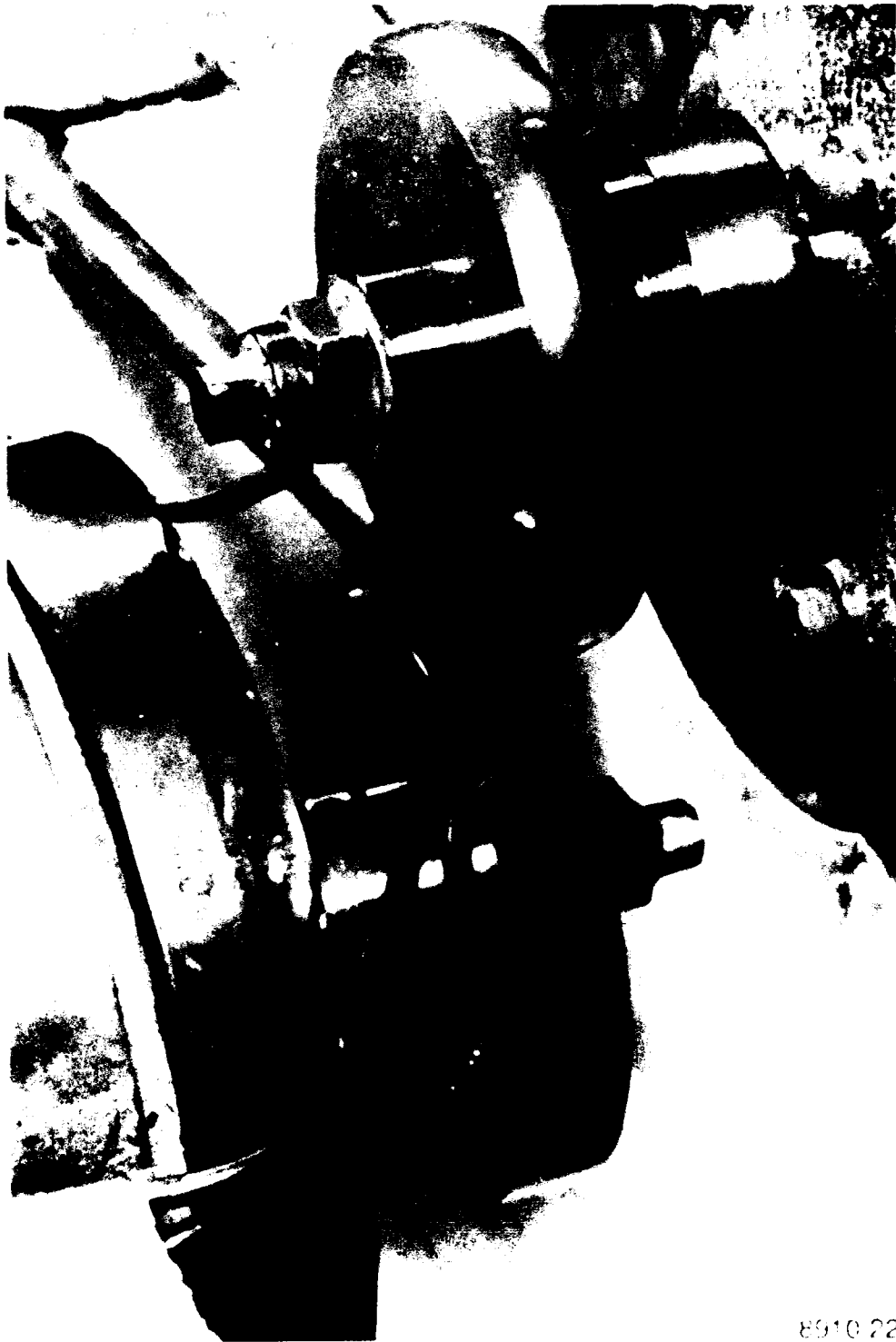
90074

Figure 4. Contact Pressure vs. Applied Load



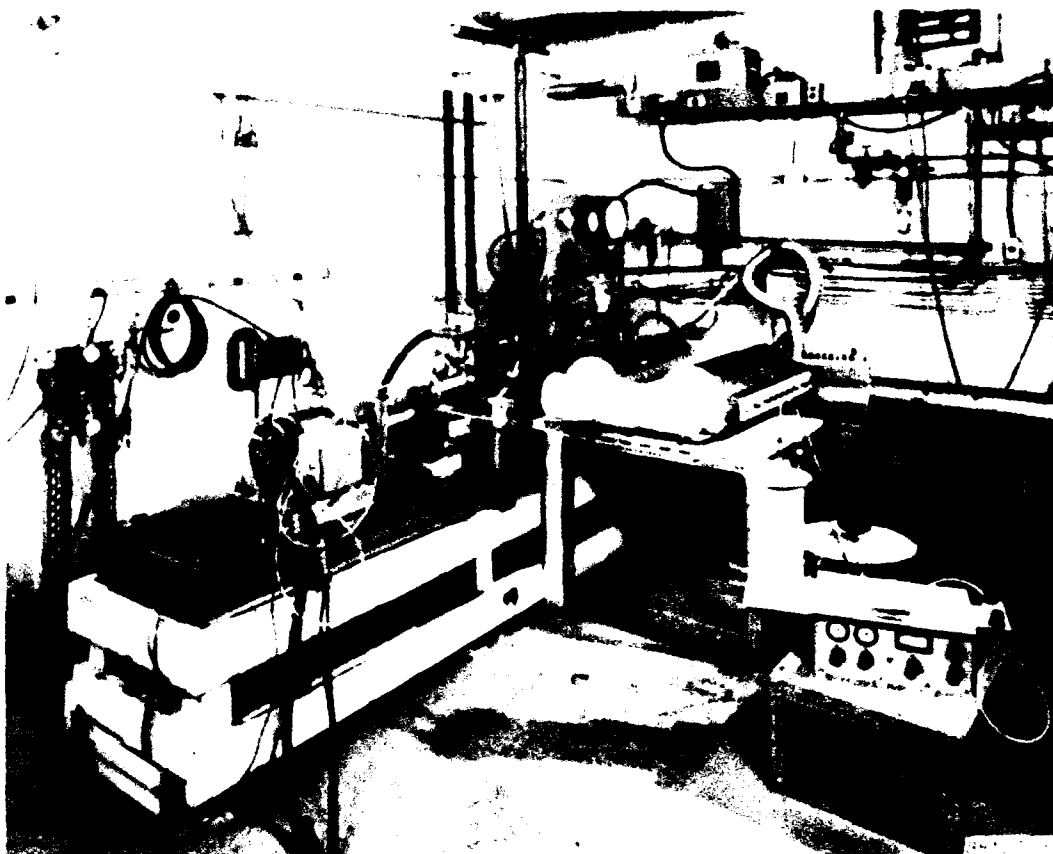
V9-201

Figure 5. Initial Spindle Alignment



8910 22  
V9-199

Figure 6. Thermocouples Close to Disks



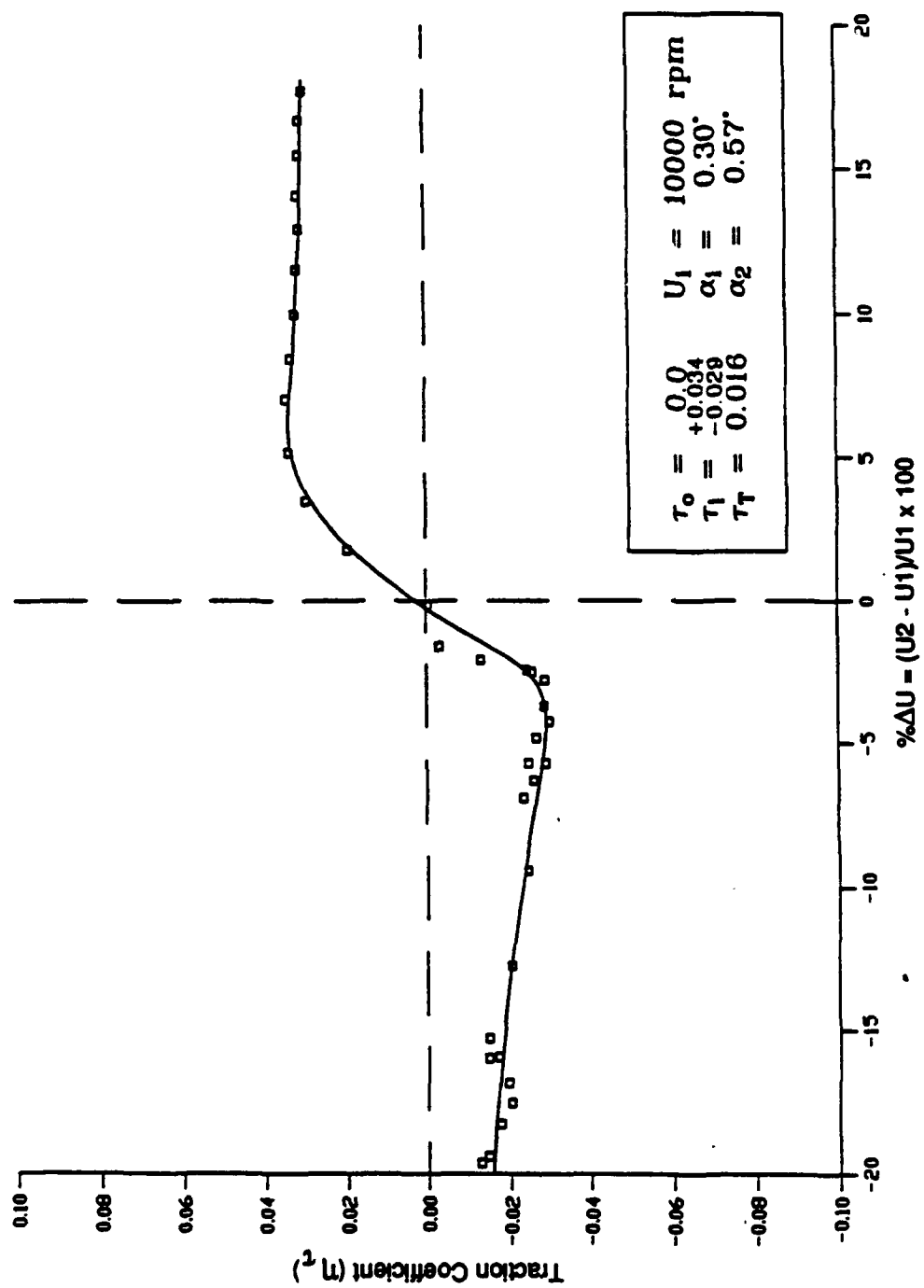
V9-203

Figure 7. Test Cell Installation



V9-200

Figure 8. Control and Data Acquisition System



90075

Figure 9. Traction Coefficient Data for Oil

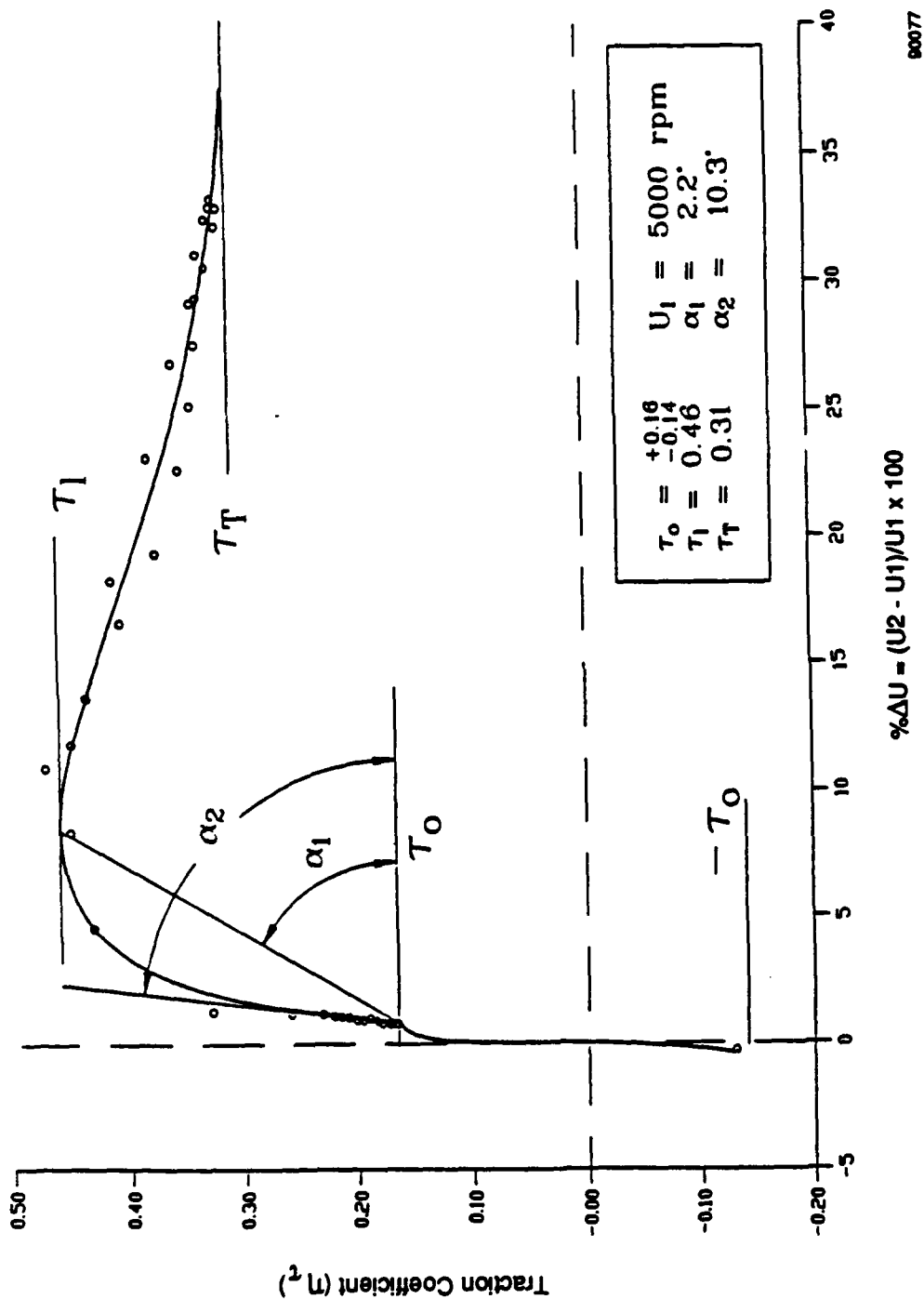


Figure 10. Definition of Traction Curve Parameters

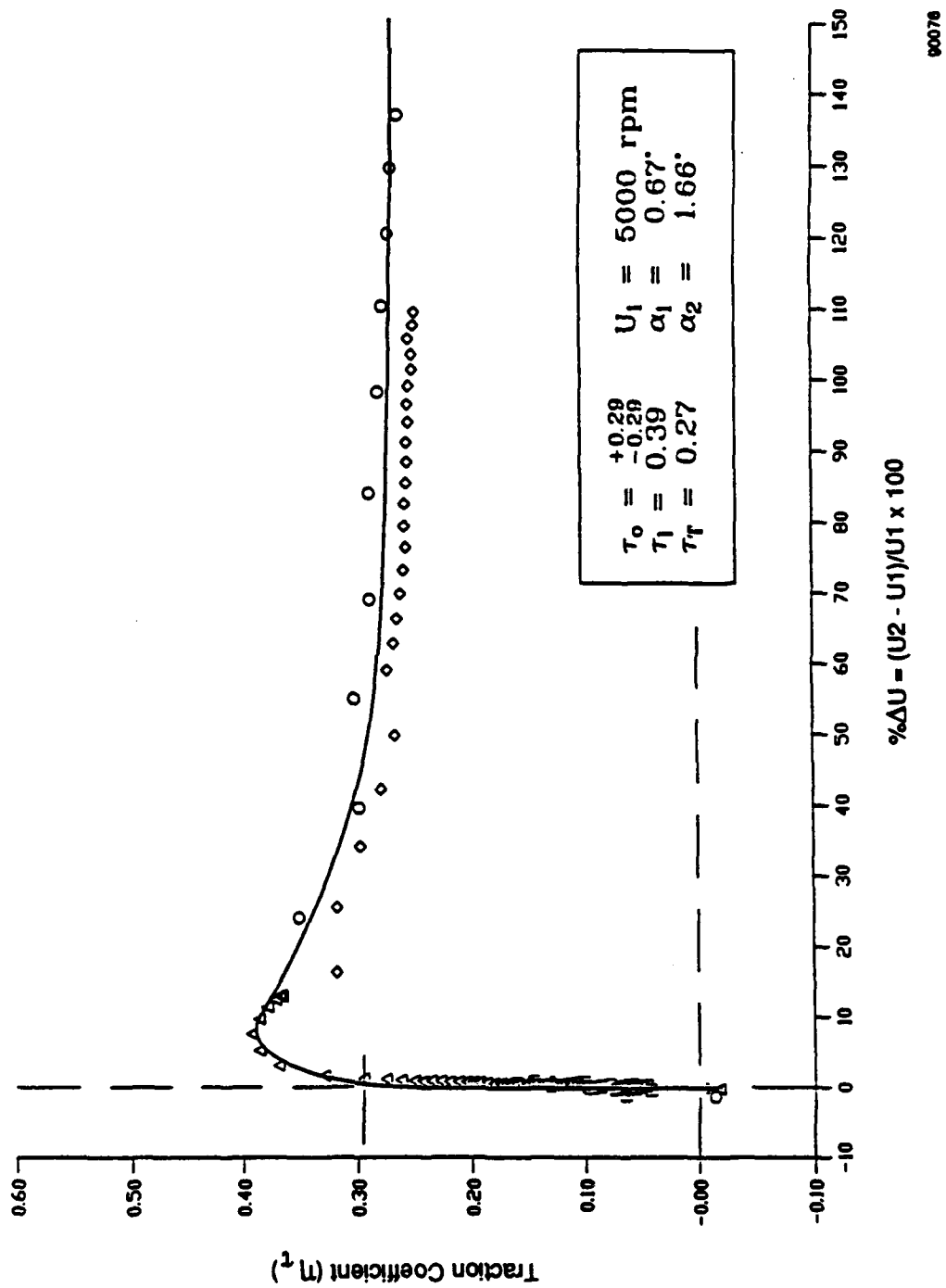


Figure 11. Traction Data, Unlubricated, Room Temperature, Load = 4 lb



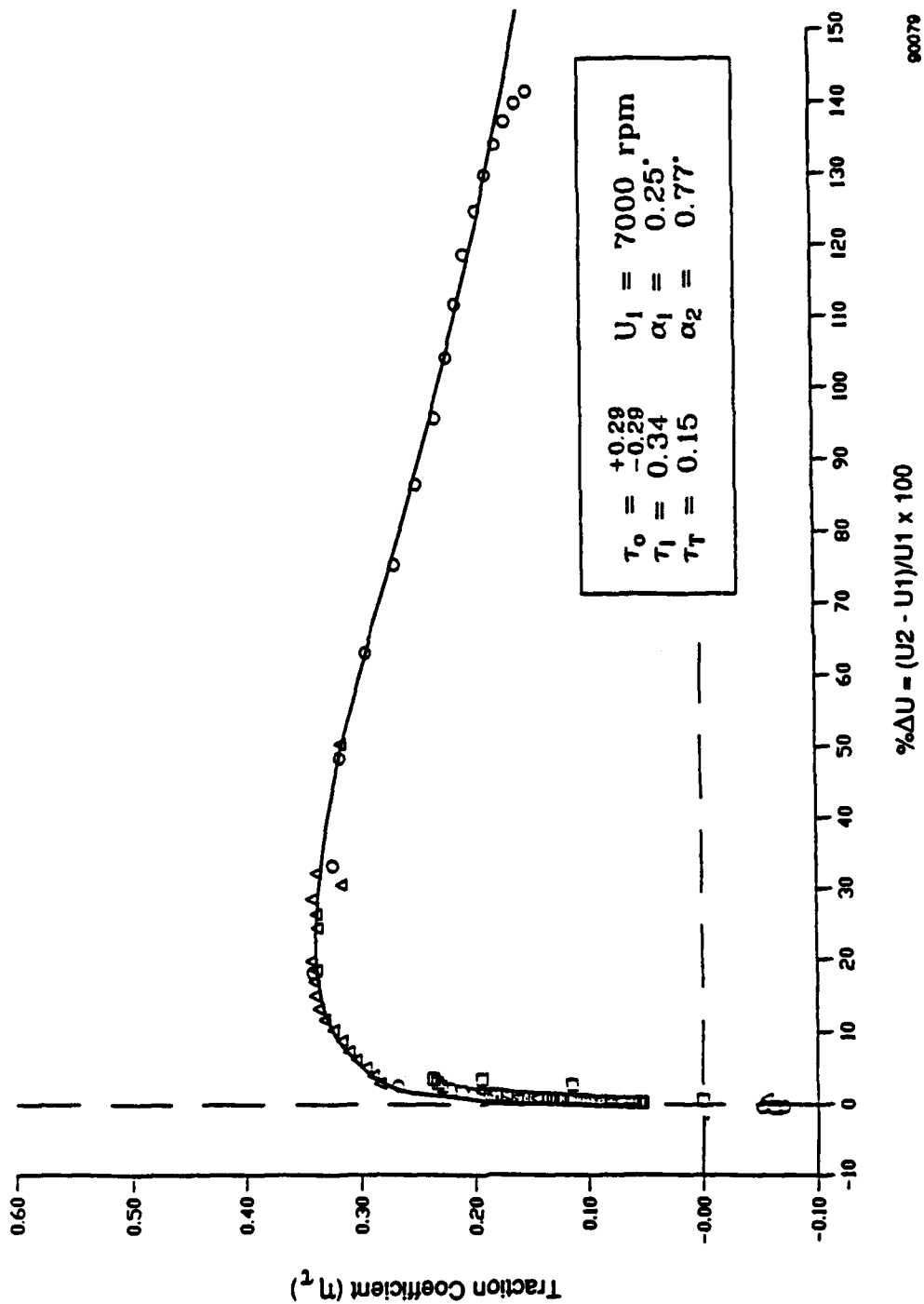


Figure 12. Traction Data, Unlubricated, Room Temperature, Load = 10 lb

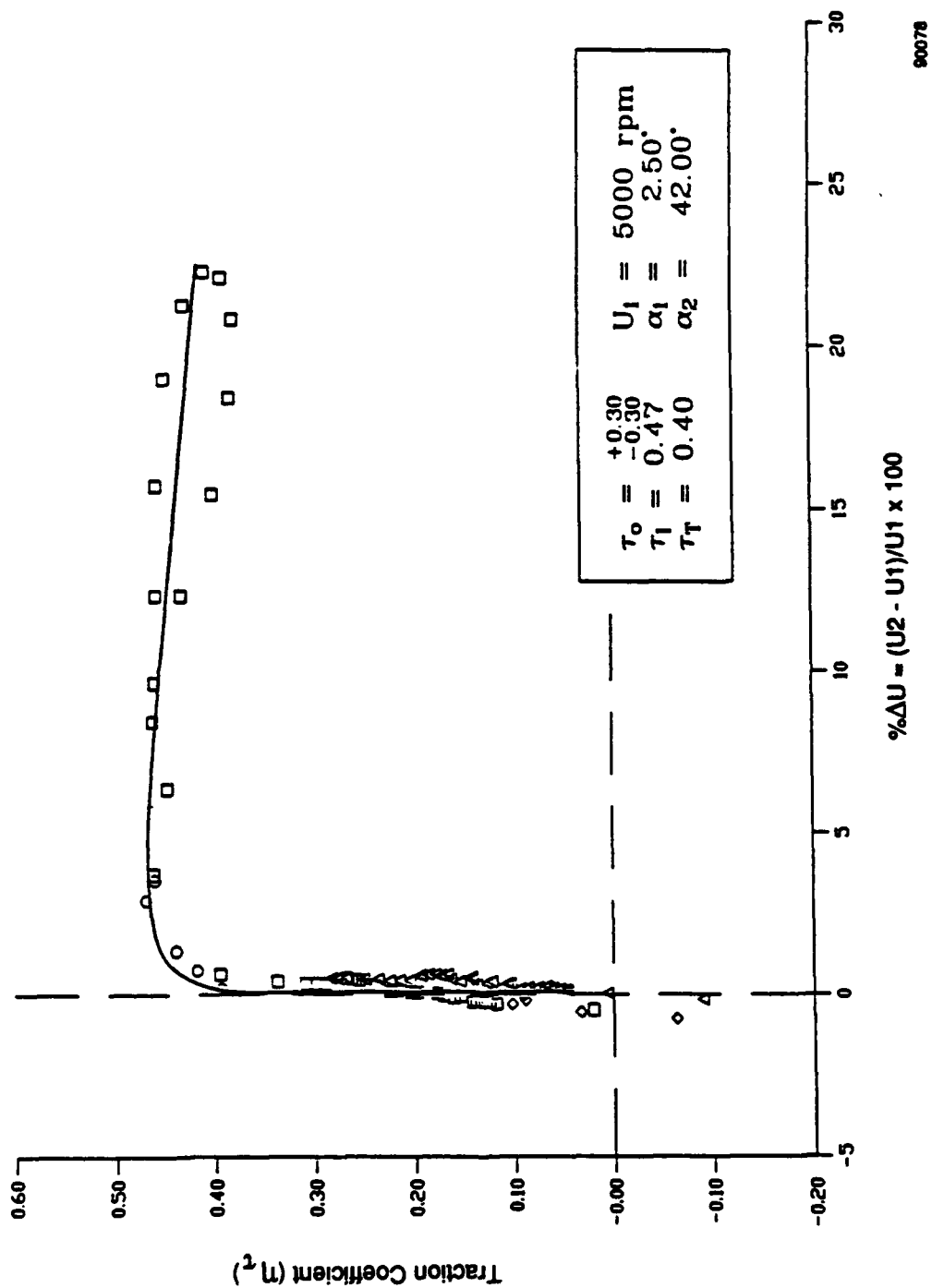


Figure 13. Traction Data, Unlubricated, Temperature = 1200°F, Load = 5 lb

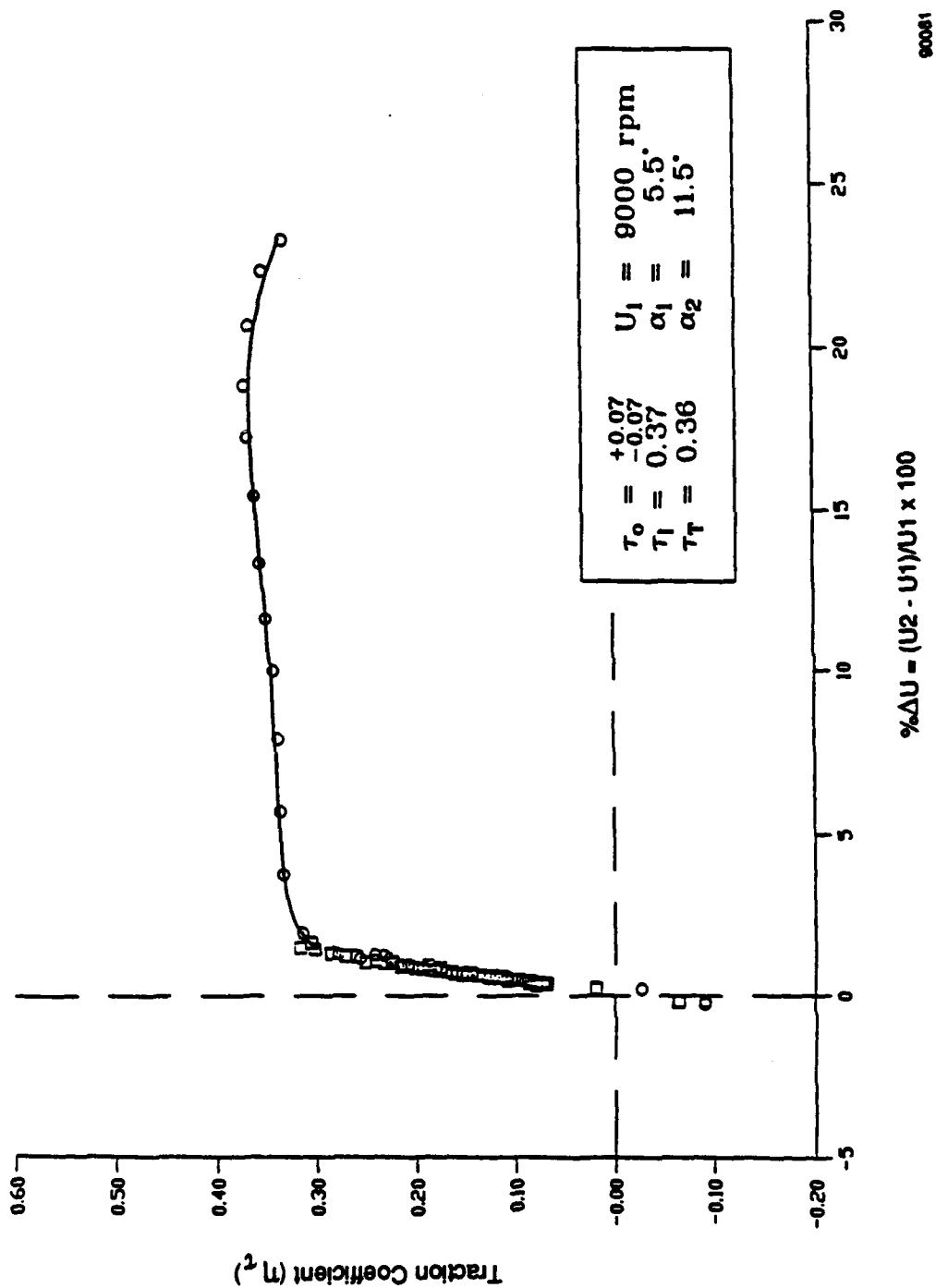


Figure 14. Traction Data, Unlubricated, Temperature = 1200°F, Load = 10 lb

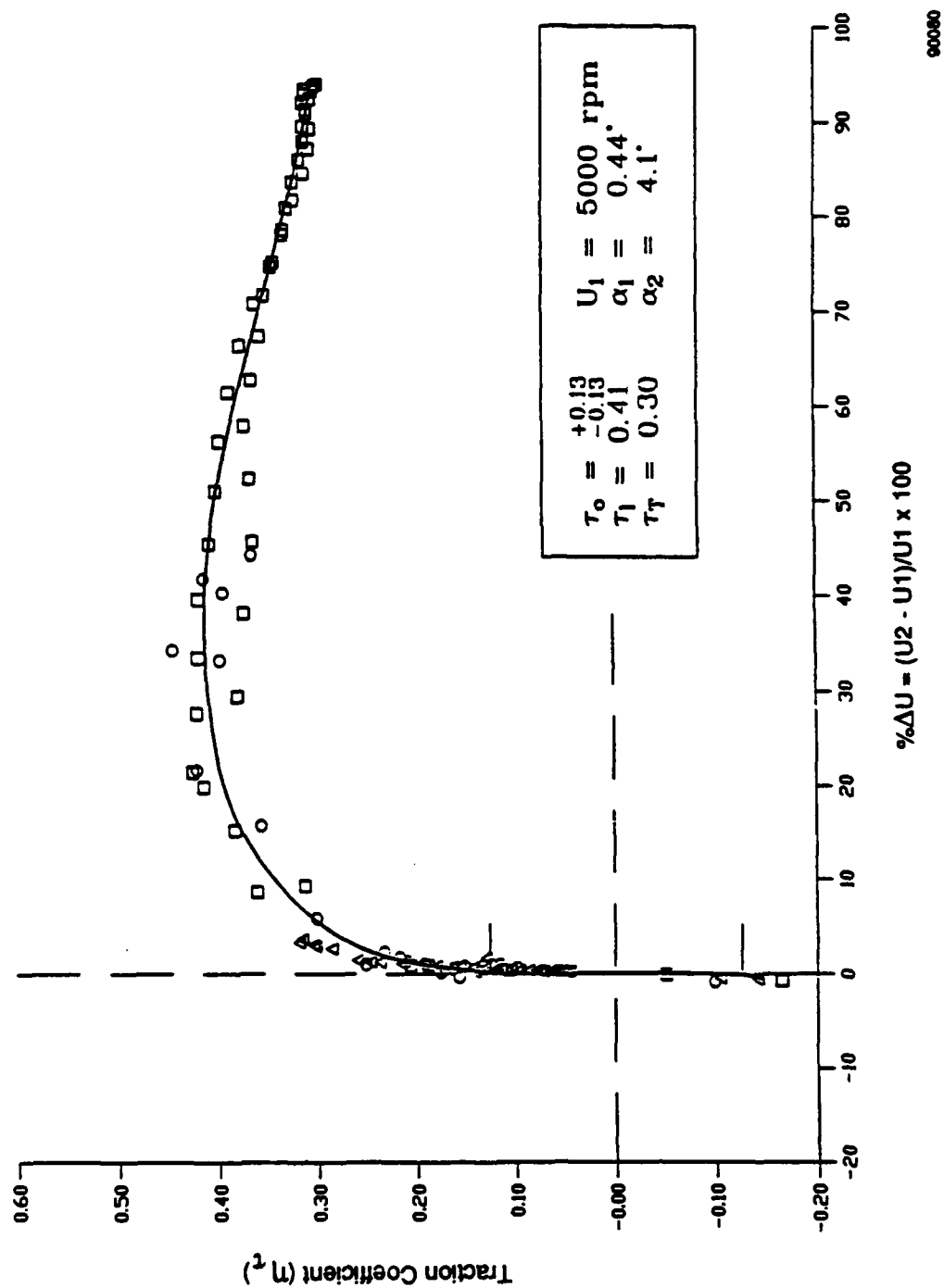


Figure 15. Traction Data,  $\text{TiO}_2$ , Room Temperature, Load = 4 lb

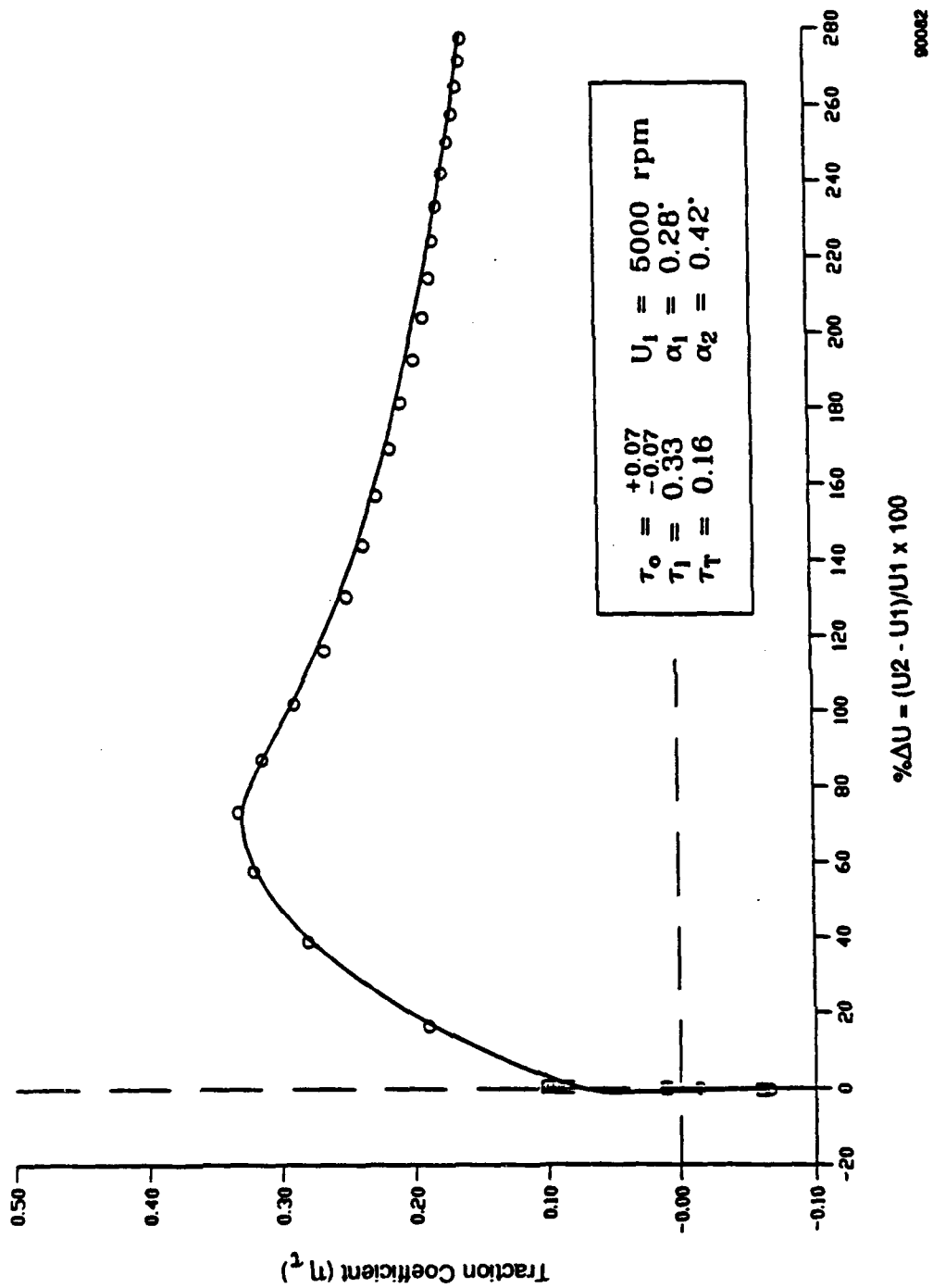


Figure 16. Traction Data,  $\text{TiO}_2$ , Room Temperature, Load = 10 lb

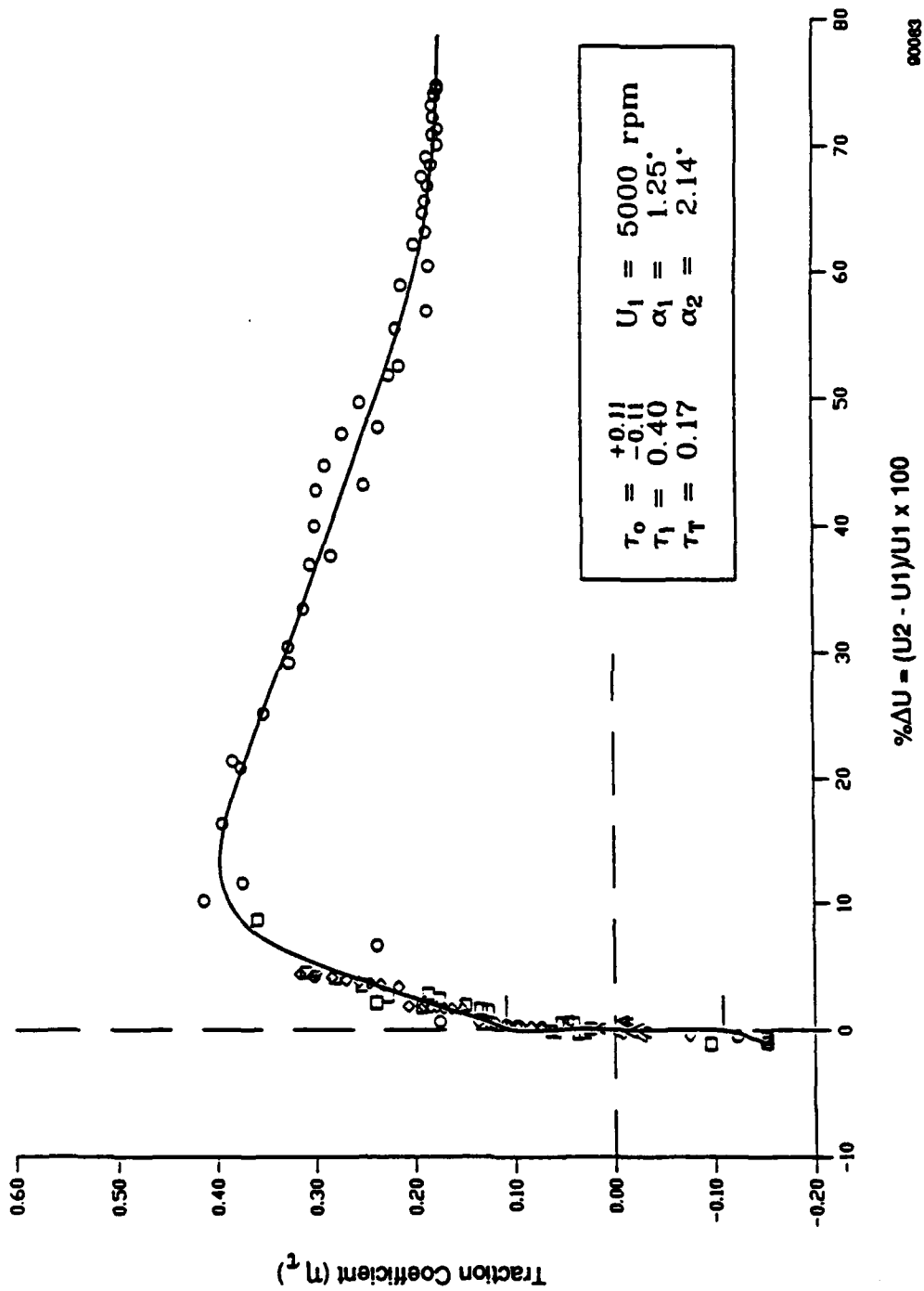


Figure 17. Traction Data,  $\text{TiO}_2$ , Temperature =  $1200^\circ\text{F}$ , Load = 5 lb

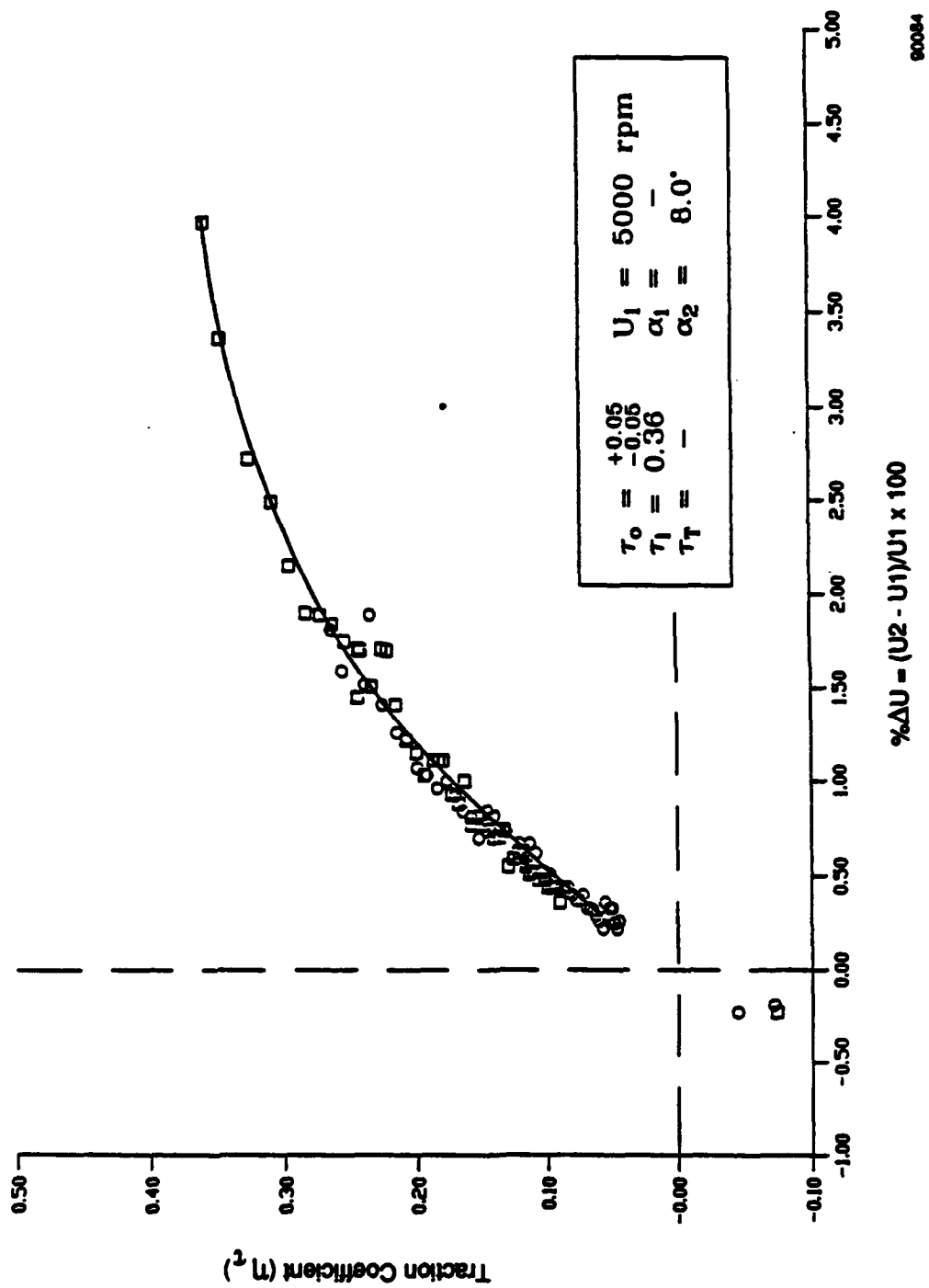
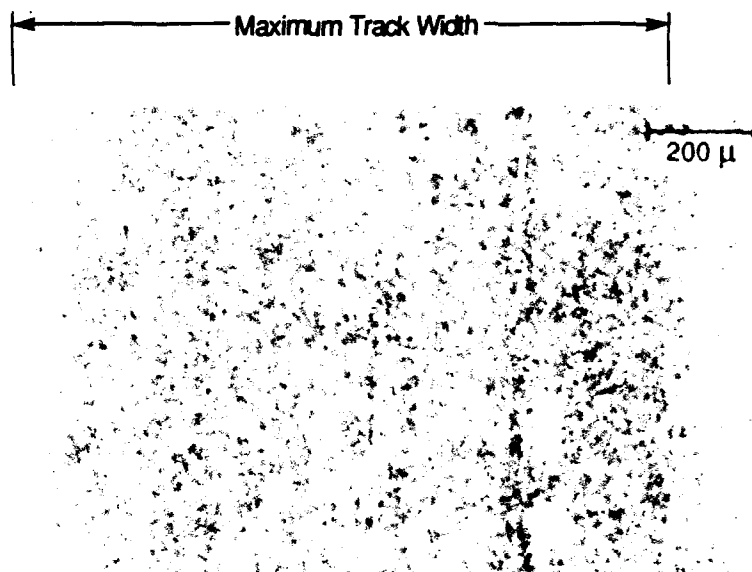


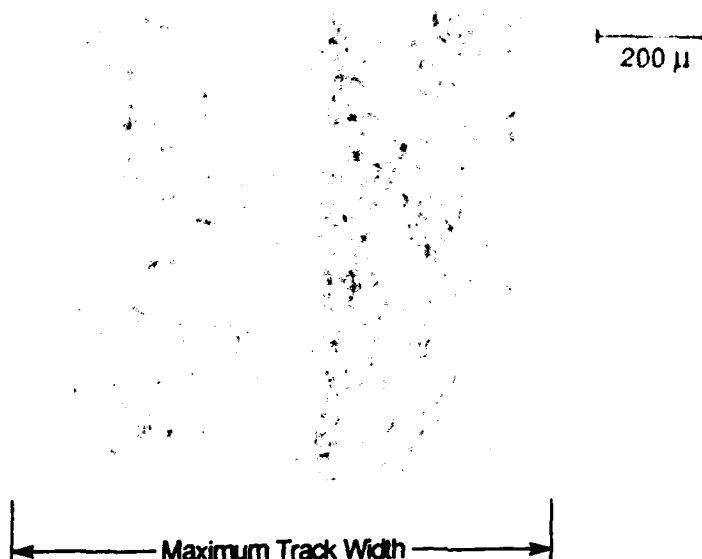
Figure 18. Traction Data,  $\text{TiO}_2$ , Temperature =  $1200^\circ\text{F}$ , Load = 10 lb



**Flat Disk: 22A**  
**Track A: 0°**

TE Side  
 ←

(L566-4)



**Flat Disk: 22A**  
**Track A: 180°**

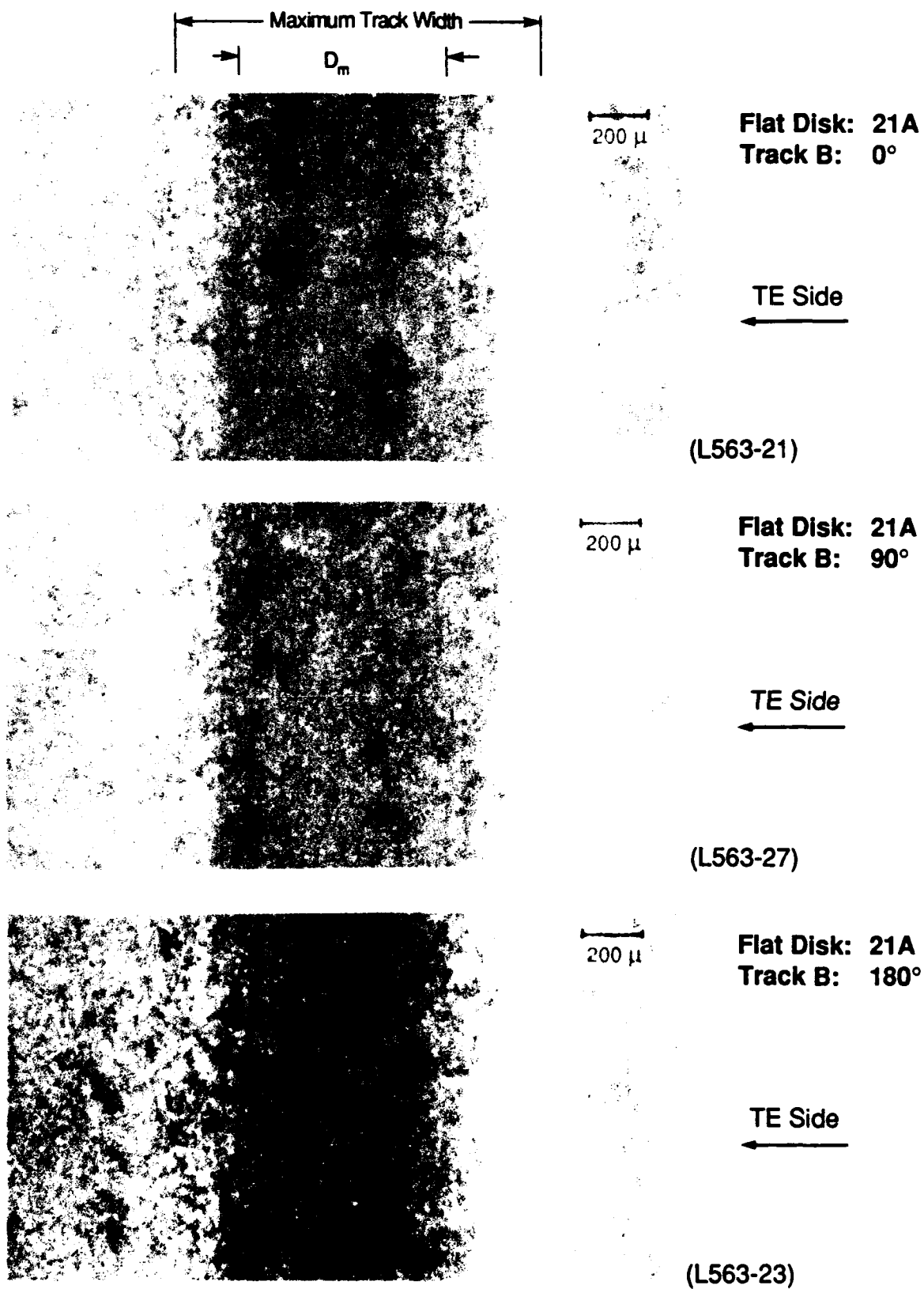
TE Side  
 ←

(L566-7)

V9-191

Figure 19. Wear Track for  $\text{TiO}_2$ , Room Temperature, Loads = 4 and 10 lb





V9-195

Figure 20. Wear Track for TiO<sub>2</sub>, Temperature = 1200°F, Loads 5 and 10 lb

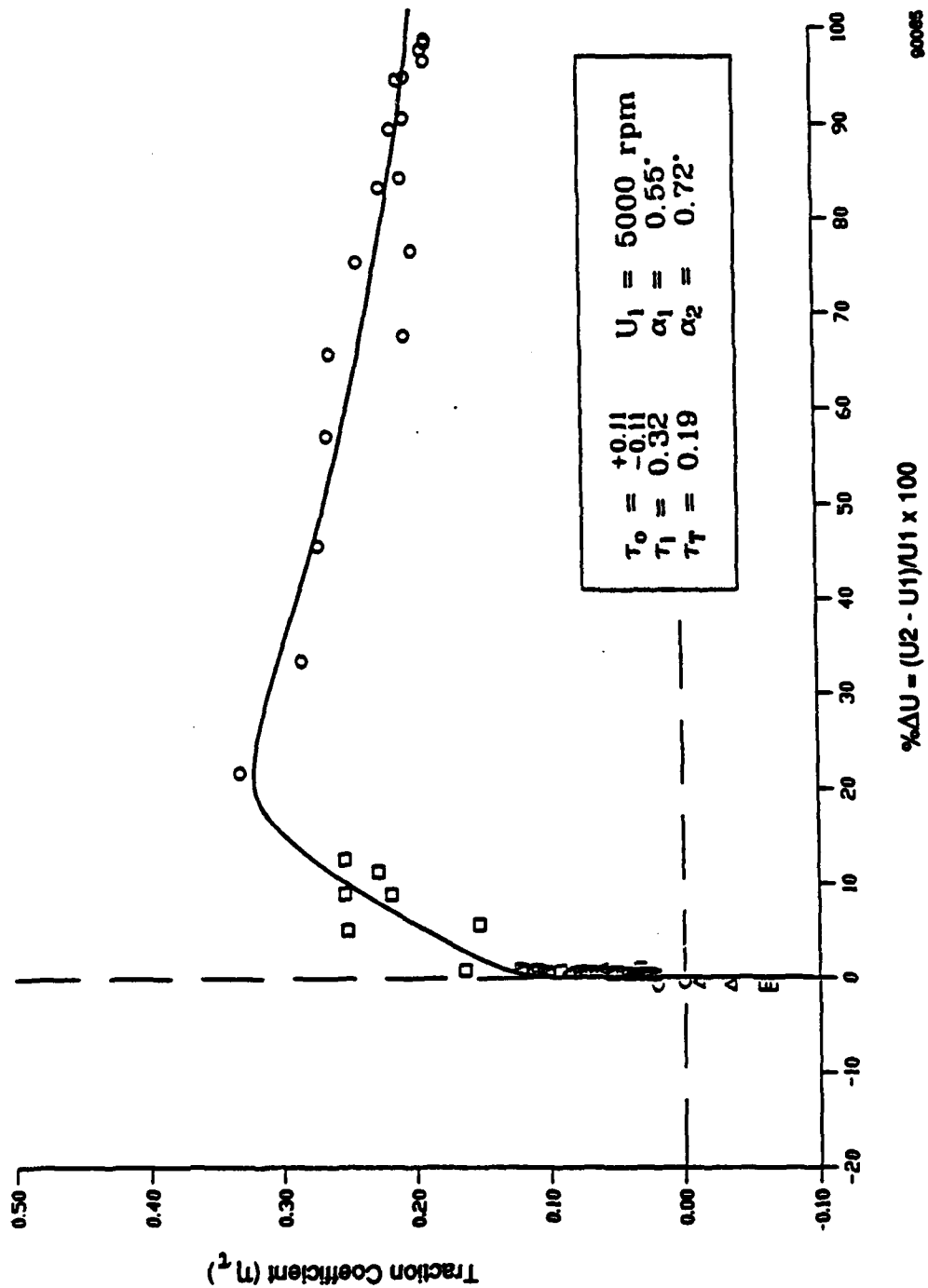


Figure 21. Traction Data for  $\text{TiO}_2/\text{Inconel 718}$  Slick Lube, Temperature =  $1200^\circ\text{F}$ , Load = 5 lb

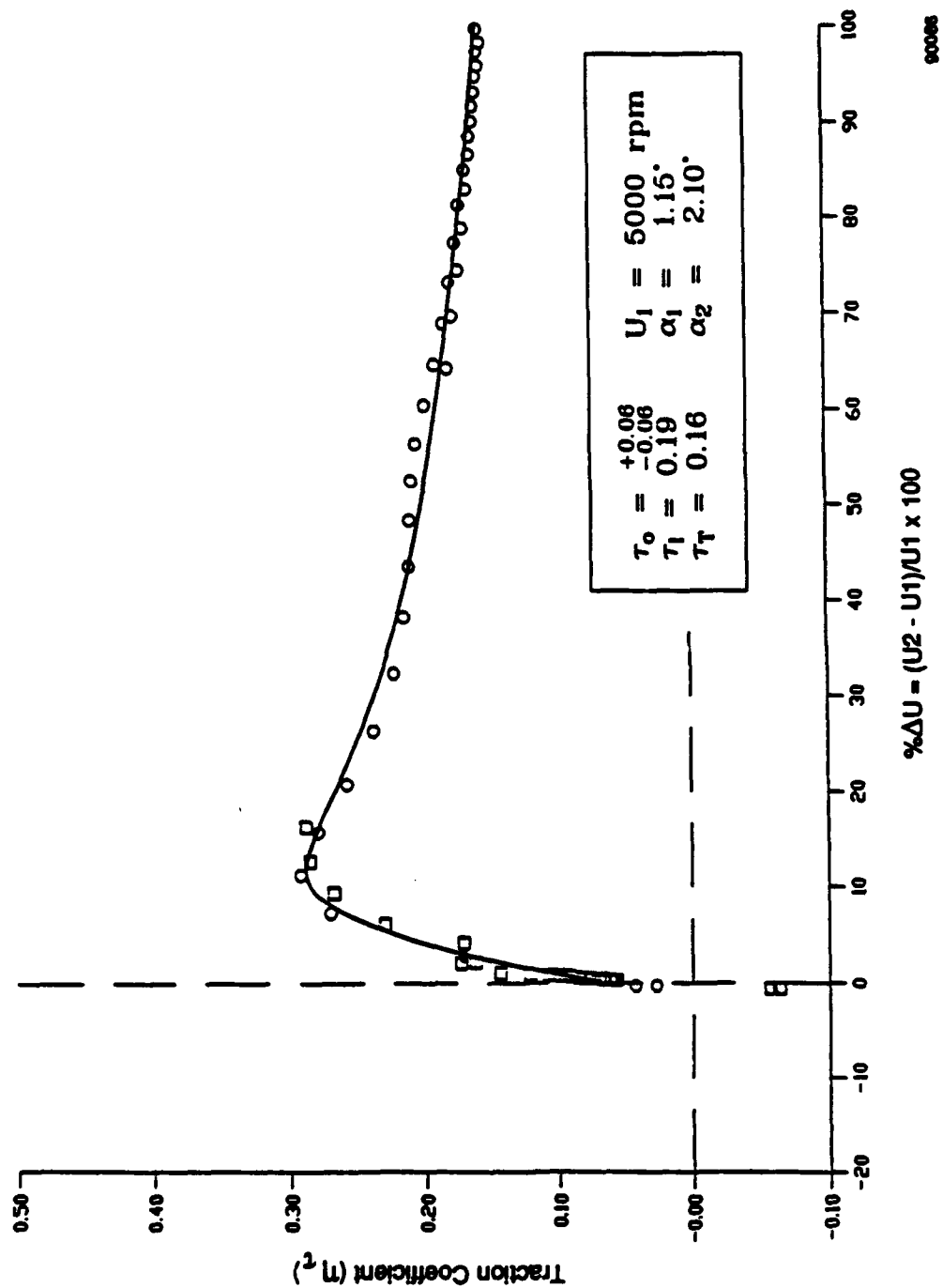
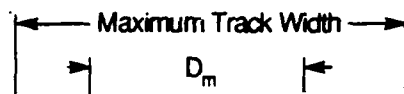


Figure 22. Traction Data for  $\text{TiO}_2$ /Inconel 718 Stick Lube, Temperature = 1200°F, Load = 10 lb



200  $\mu$

**Flat Disk: 21A**  
**Track A: 0°**

TE Side  
←

(L563-19)

200  $\mu$

**Flat Disk: 21A**  
**Track A: 90°**

TE Side  
←

(L563-26)

200  $\mu$

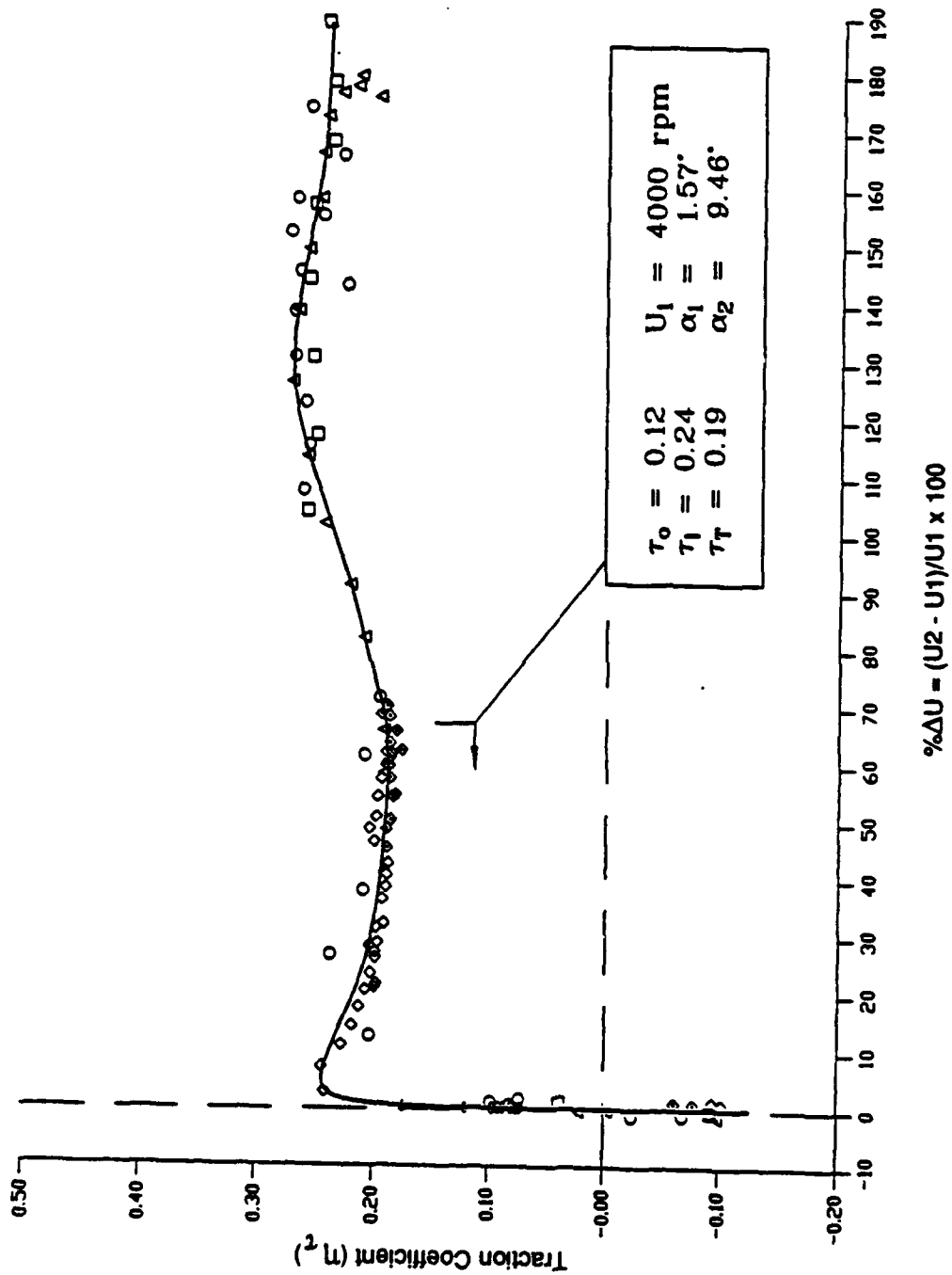
**Flat Disk: 21A**  
**Track A: 180°**

TE Side  
←

(L563-24)

V9-198

Figure 23. Wear Track for  $\text{TiO}_2$ /Inconel 718 Stick Lube, Temperature = 1200°F, Loads = 5 and 10 lb



90087

Figure 24. Traction Data, BN, Room Temperature, Load = 4 lb

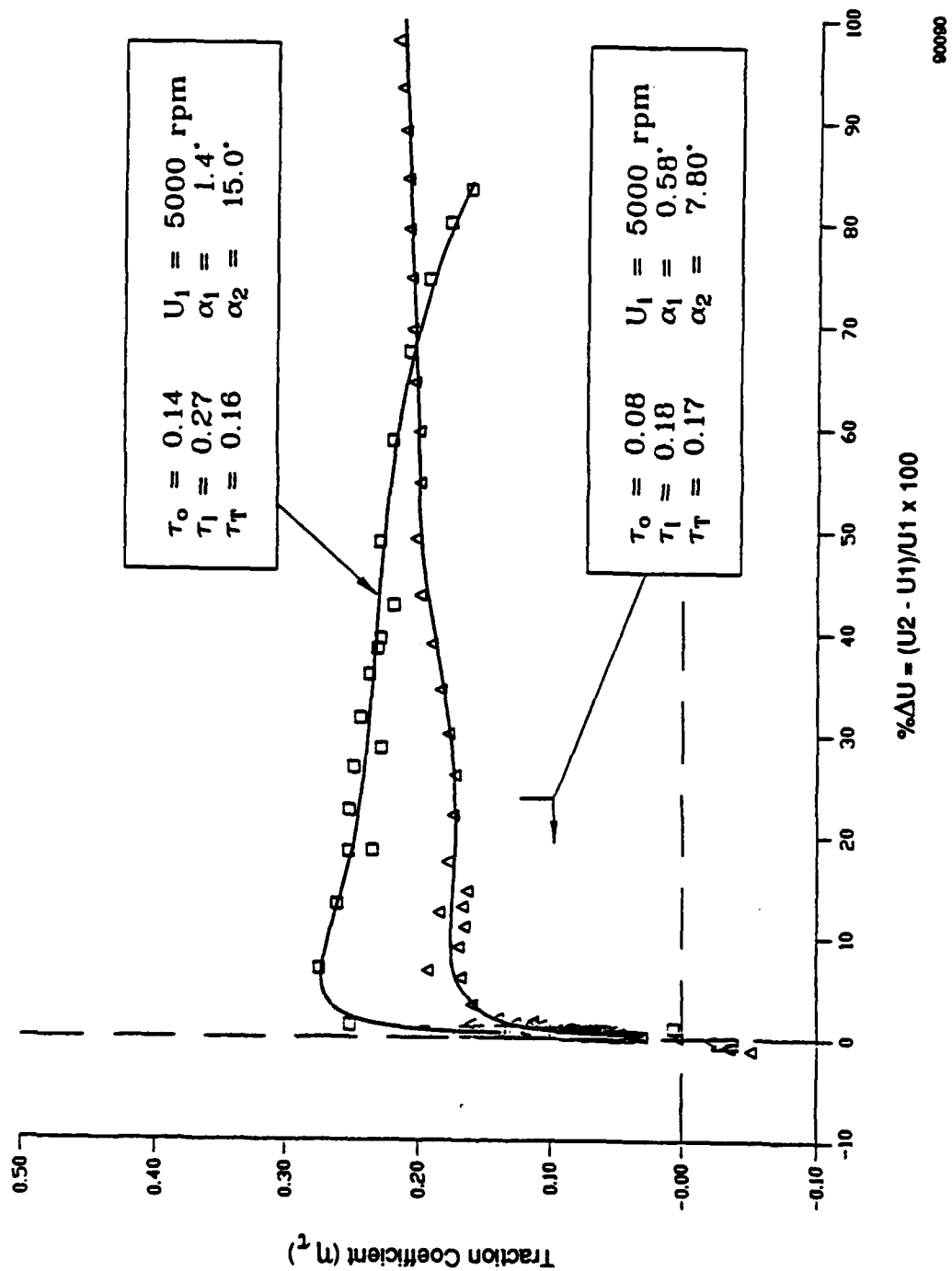


Figure 25. Traction Data, BN, Room Temperature, Loads = 10 and 15 lb

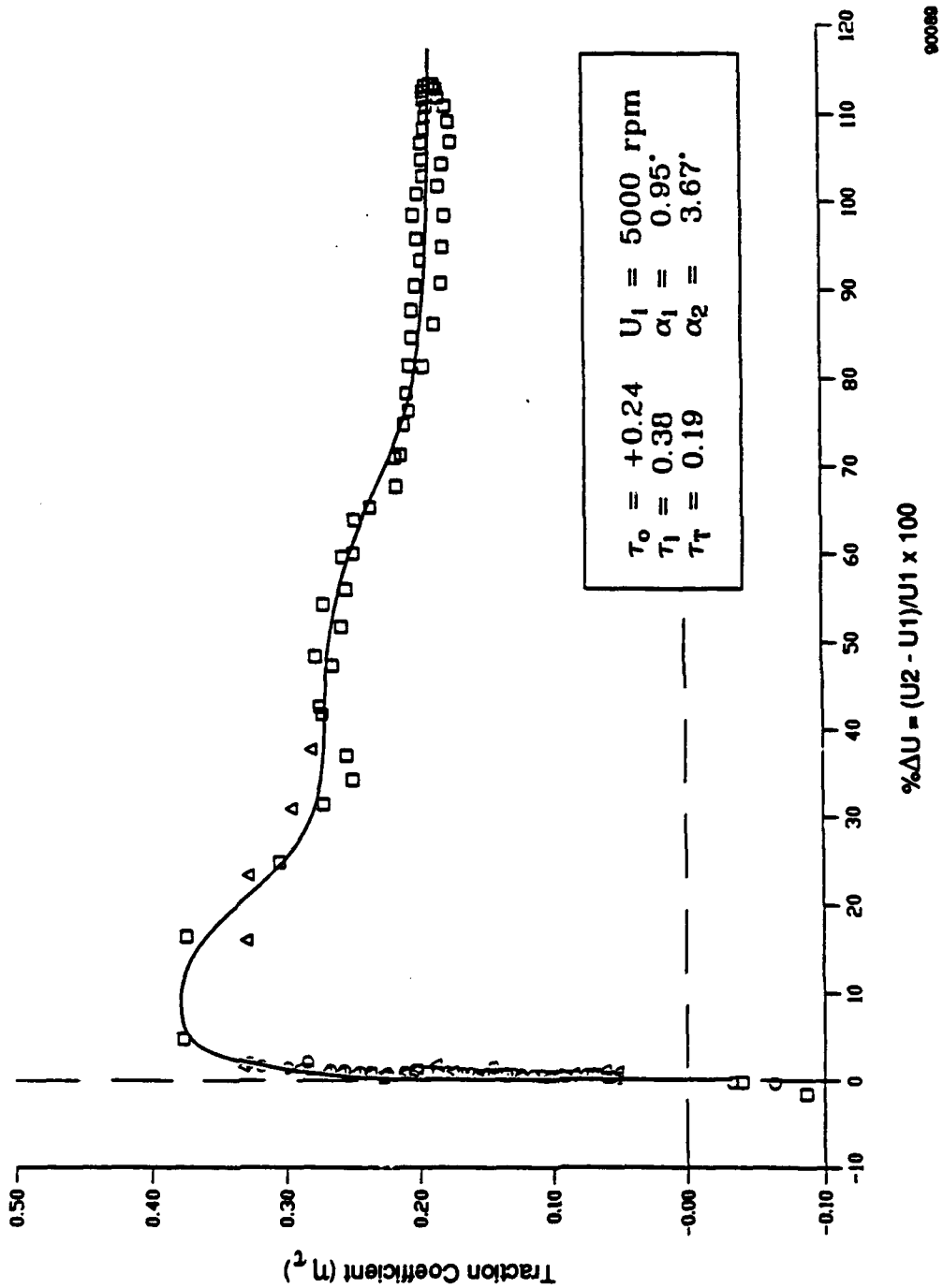


Figure 26. Traction Data, BN, Temperature = 1200°F, Load = 5 lb

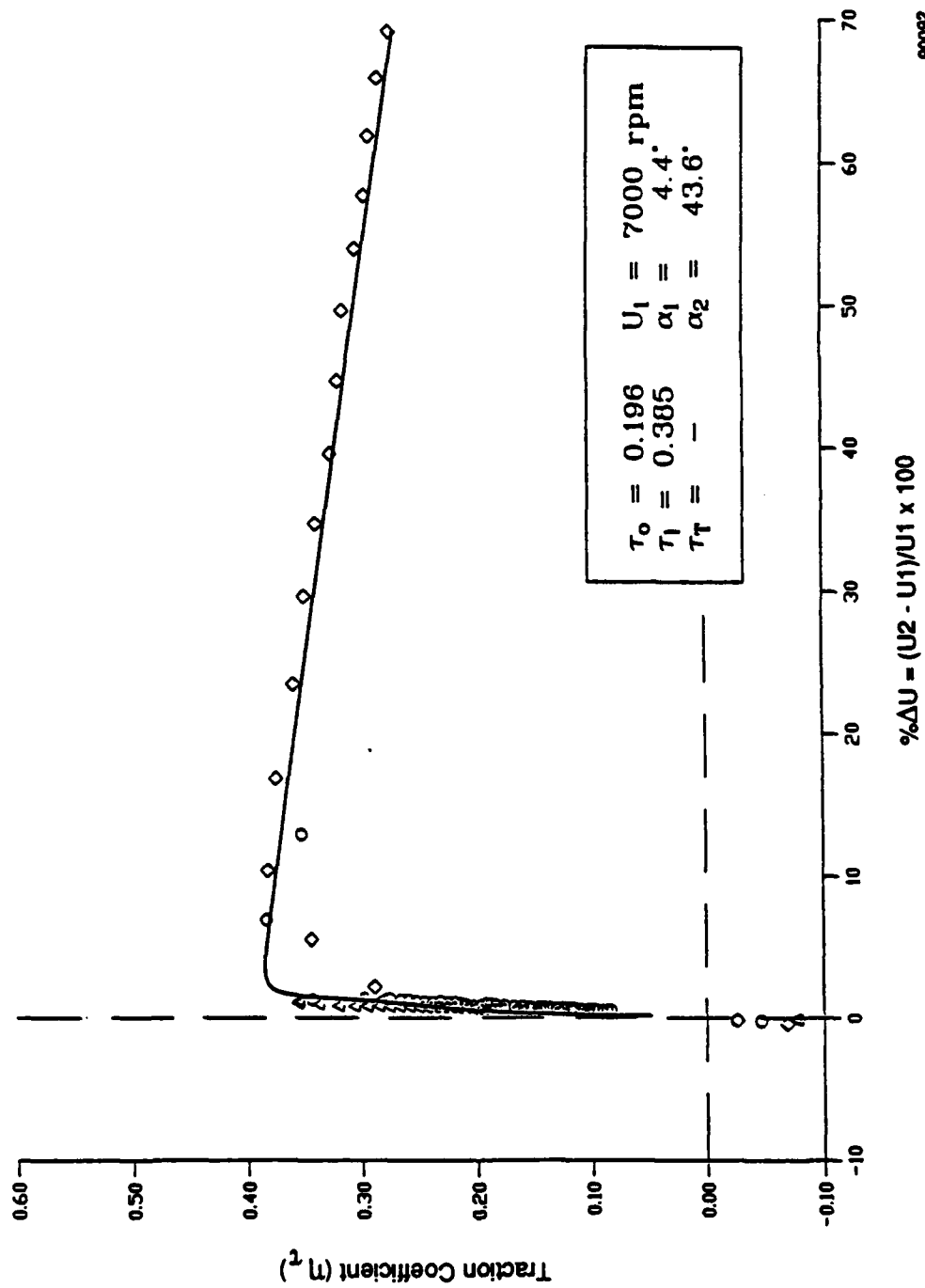
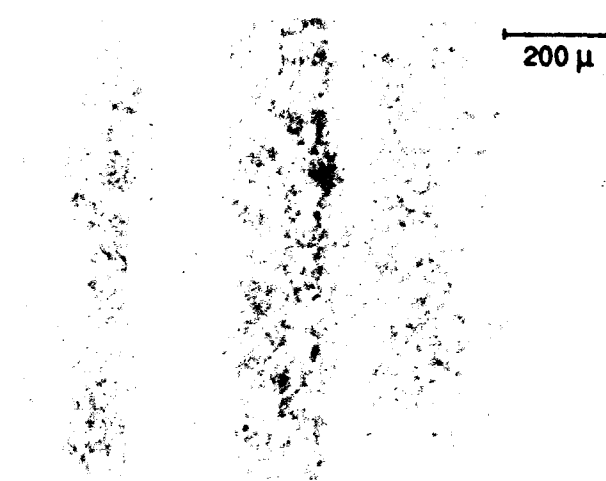


Figure 27. Traction Data, BN, Temperature = 1200°F, Load = 10 lb



Maximum Track Width

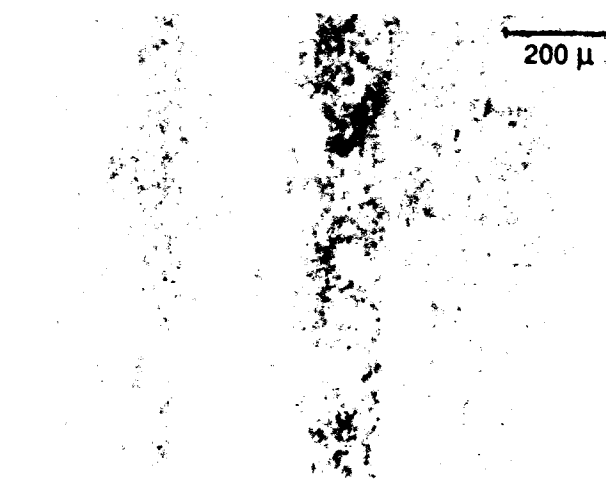


200 μ

Flat Disk: 22A  
Track B: 0°

TE Side  
←

(L566-3)



200 μ

Flat Disk: 22A  
Track B: 180°

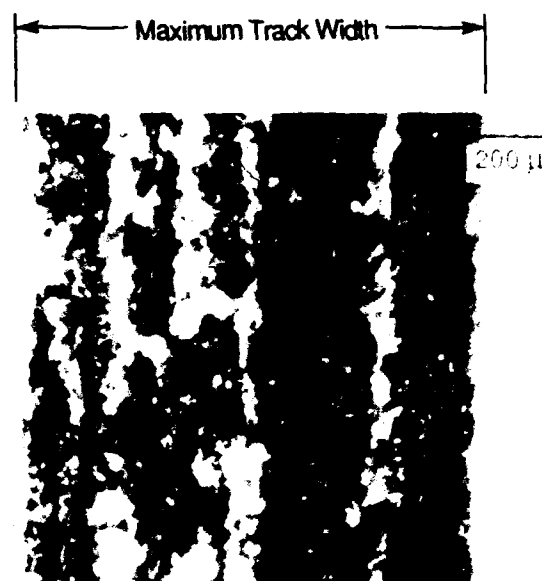
TE Side  
←

(L566-6)

Maximum Track Width

V9-190

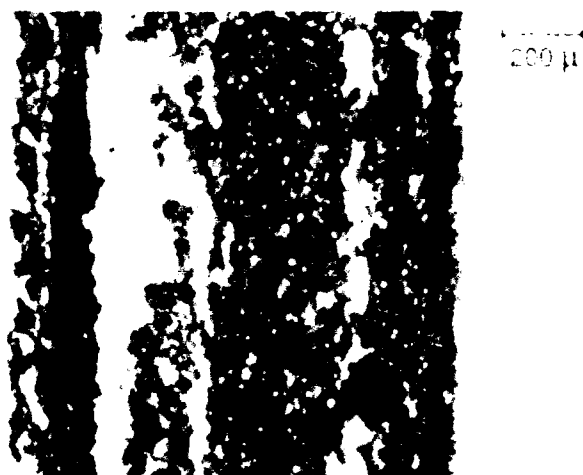
Figure 28. Wear Track for BN, Room Temperature, Loads = 4, 10, and 15 lb



**Flat Disk: 22A**  
**Track C: 0°**

**TE Side**  
 ←

(L566-1)



**Flat Disk: 22A**  
**Track C: 180°**

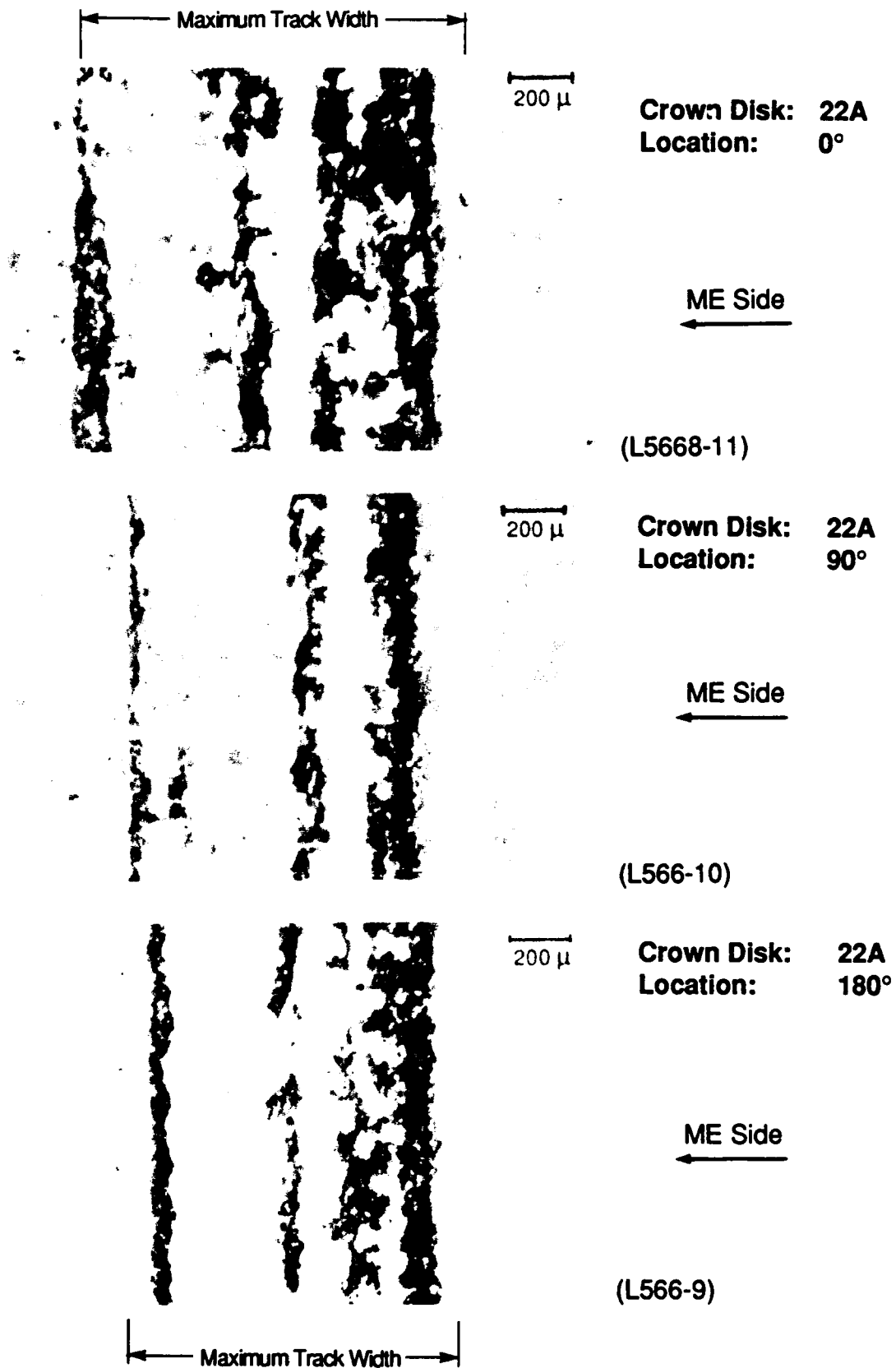
**TE Side**  
 ←

(L566-5)



V9-189

Figure 29. Wear Track for BN, Temperature = 1200°F, Loads = 5 and 10 lb



V9-192

Figure 30. Wear Track on Crowned Disk with BN, Temperature = 1200°F, Loads = 5 and 10 lb



Crown Disk: 22A  
(Higher Magnification)  
Location: 90°

ME Side  
←

(L566-12)

← Maximum Track Width →

V9-193

Figure 31. Higher Magnification of Wear Track on Crowned Disk with BN,  
Temperature = 1200°F, Loads = 5 and 10 lb

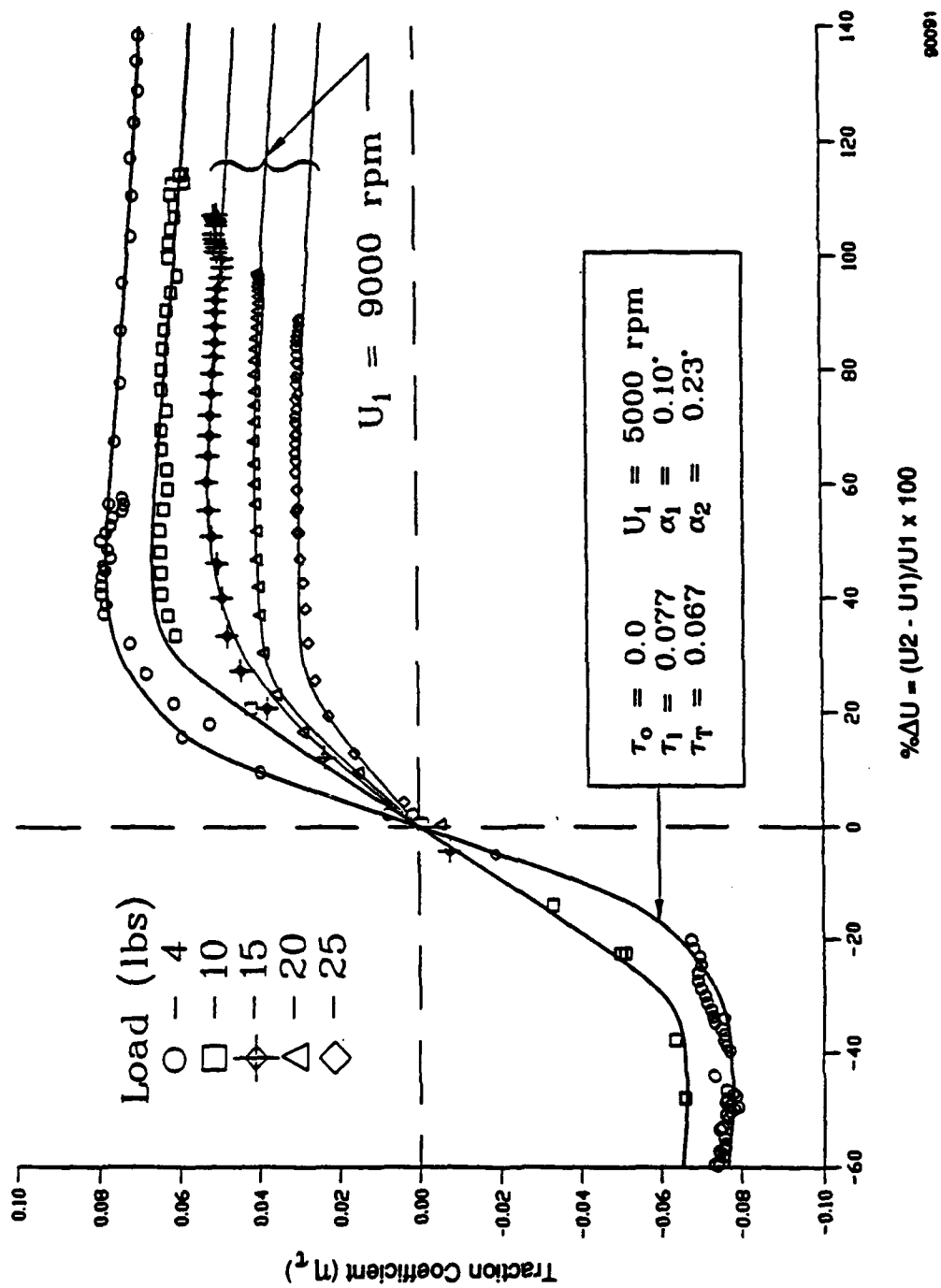


Figure 32. Traction Data, MoS<sub>2</sub>, Room Temperature, Loads = 4, 10, 15, 20, and 25 lb

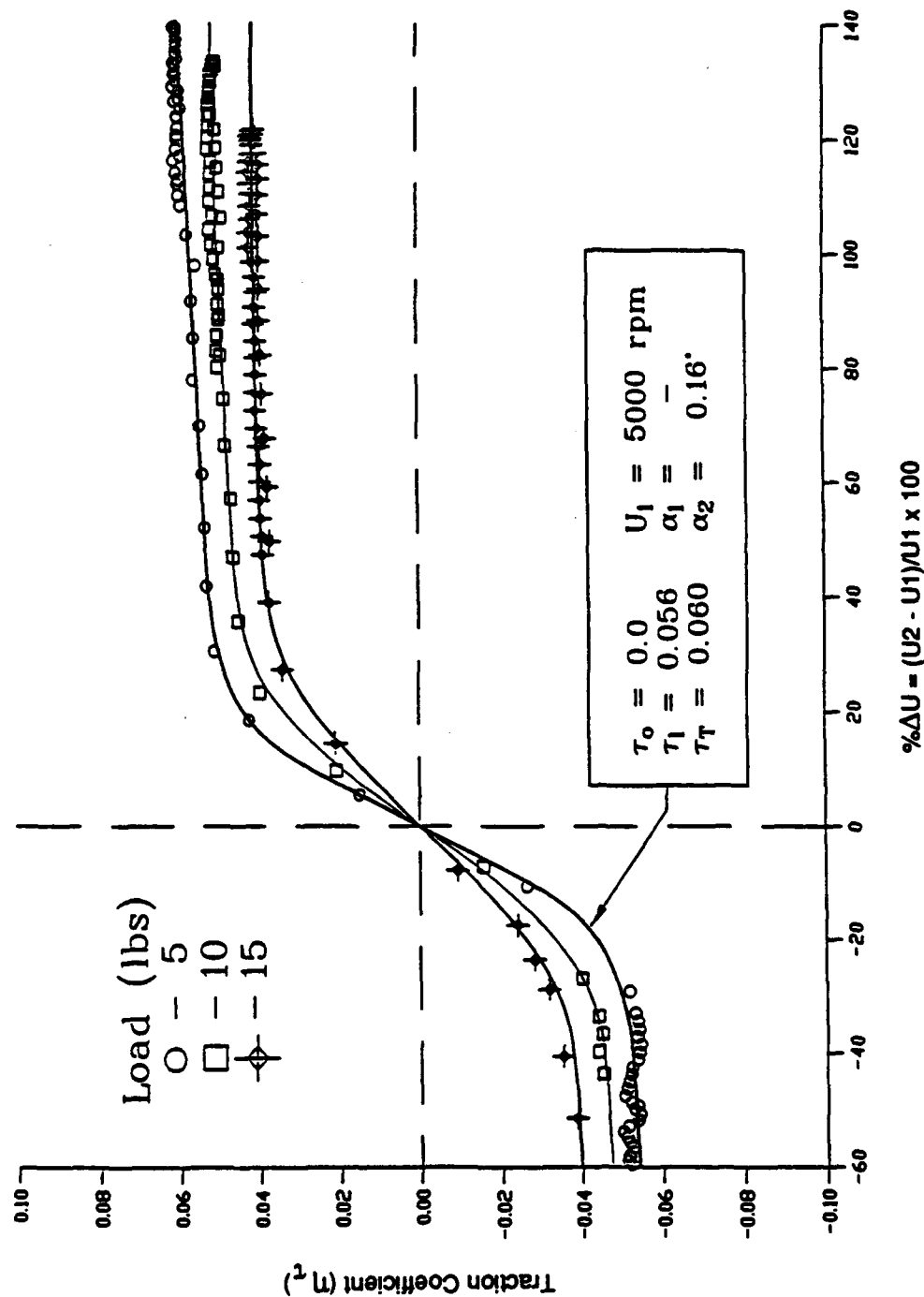
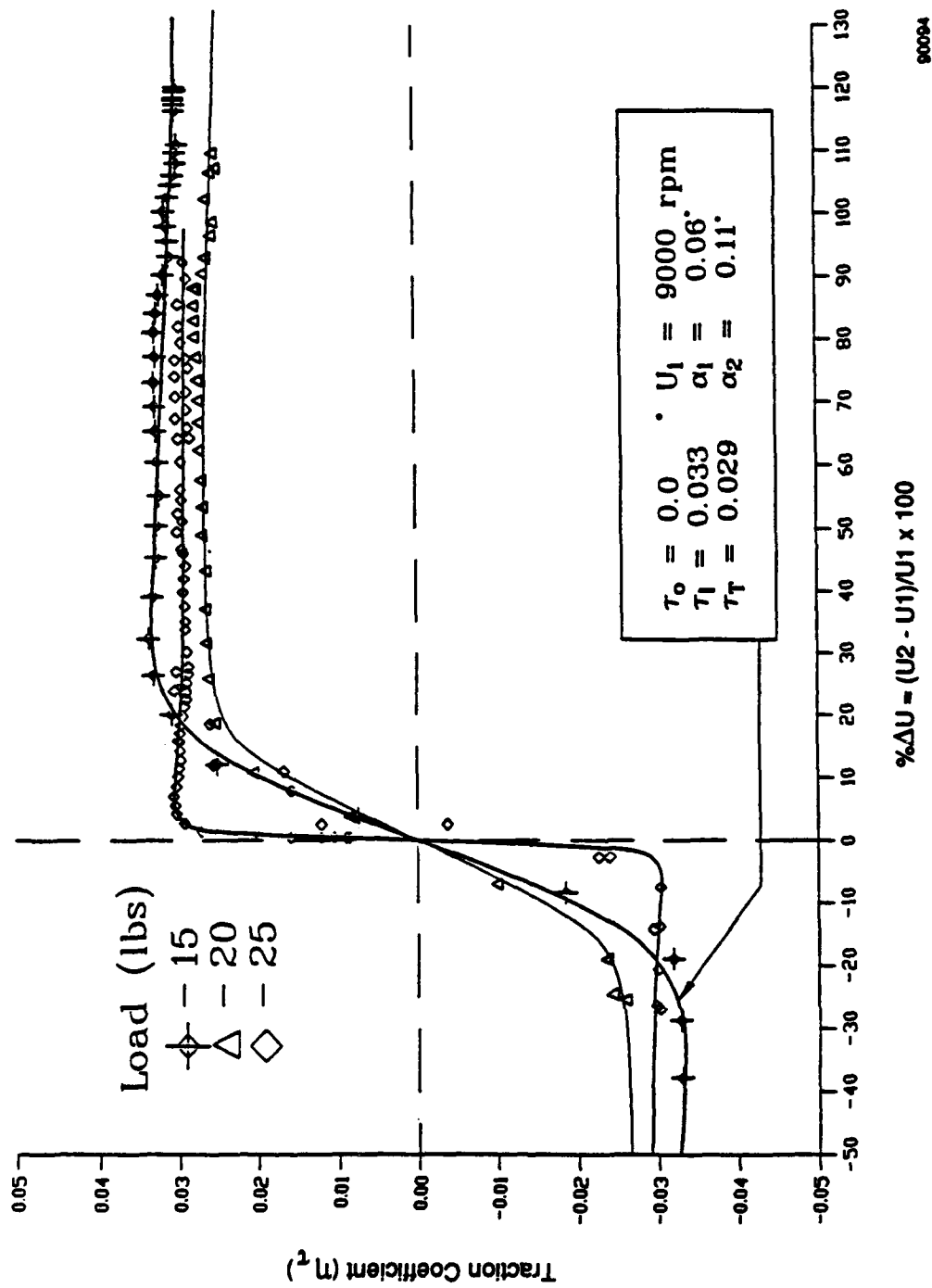


Figure 33. Traction Data, MoS<sub>2</sub>, Temperature = 800°F, Loads = 5, 10, and 15 lb



90094

Figure 34. Traction Data, MoS<sub>2</sub>, Temperature = 800°F, Loads = 15, 20, and 25 lb

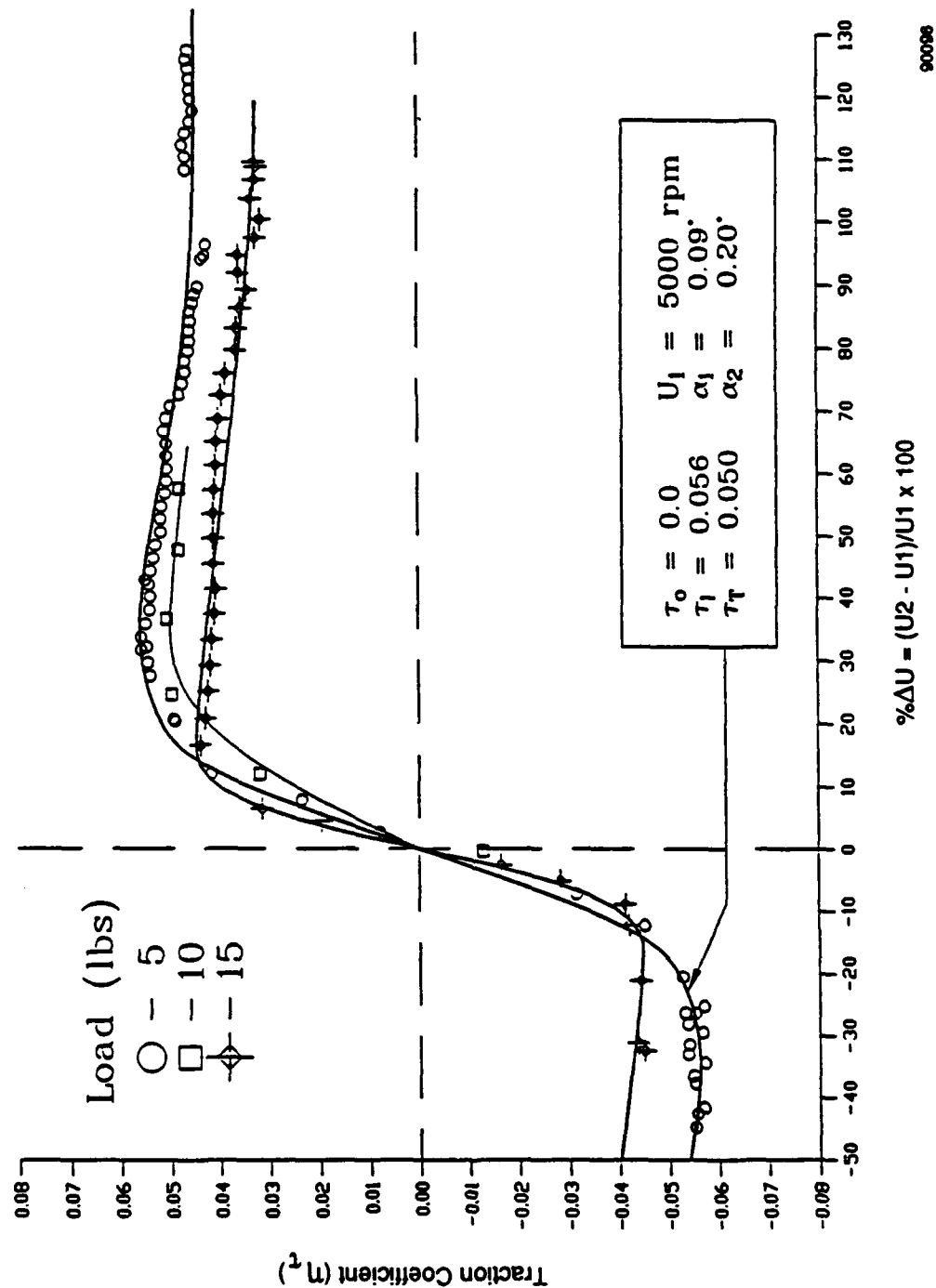


Figure 35. Traction Data, MoS<sub>2</sub>, Temperature = 1200°F, Loads = 5, 10, and 15 lb



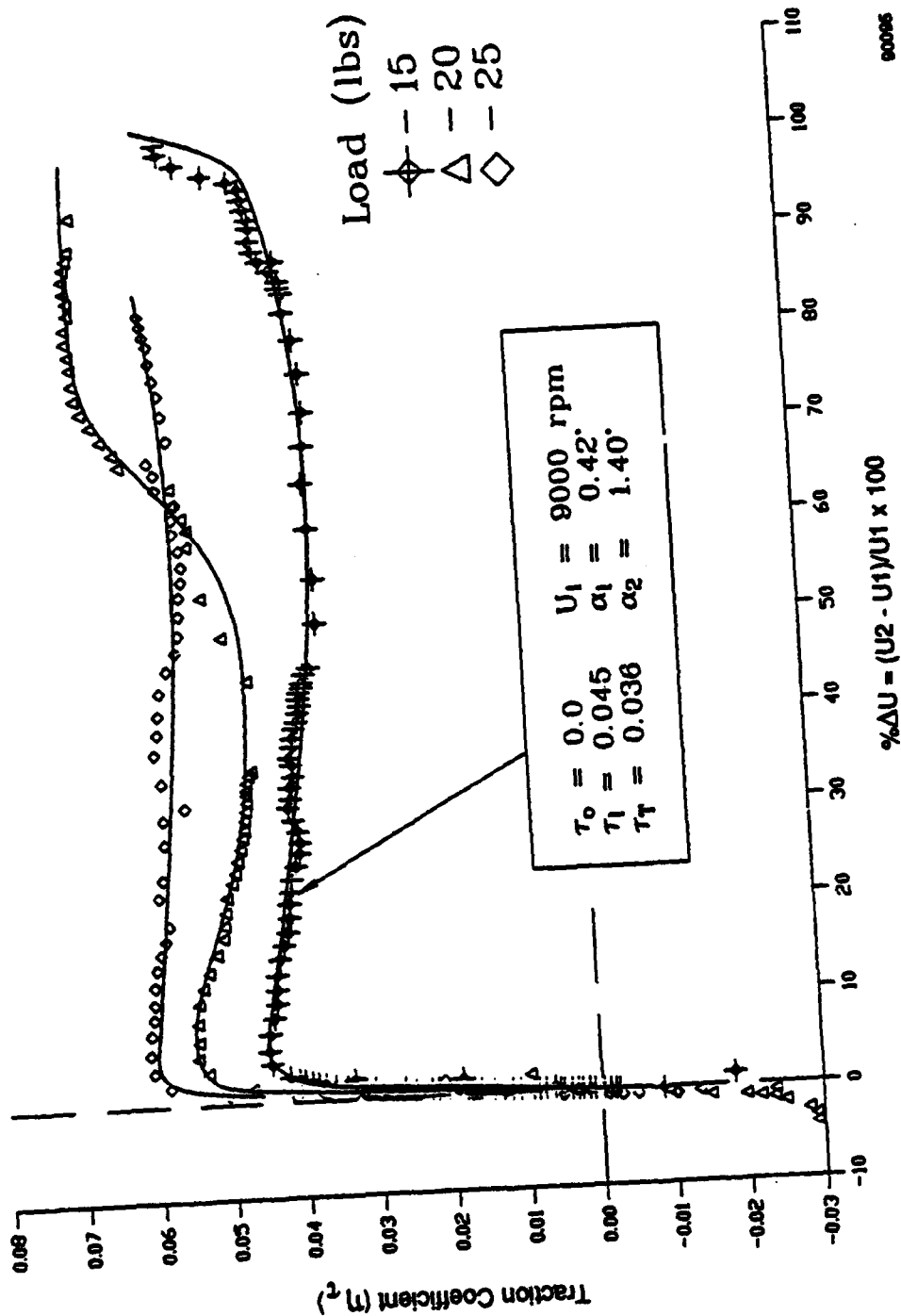
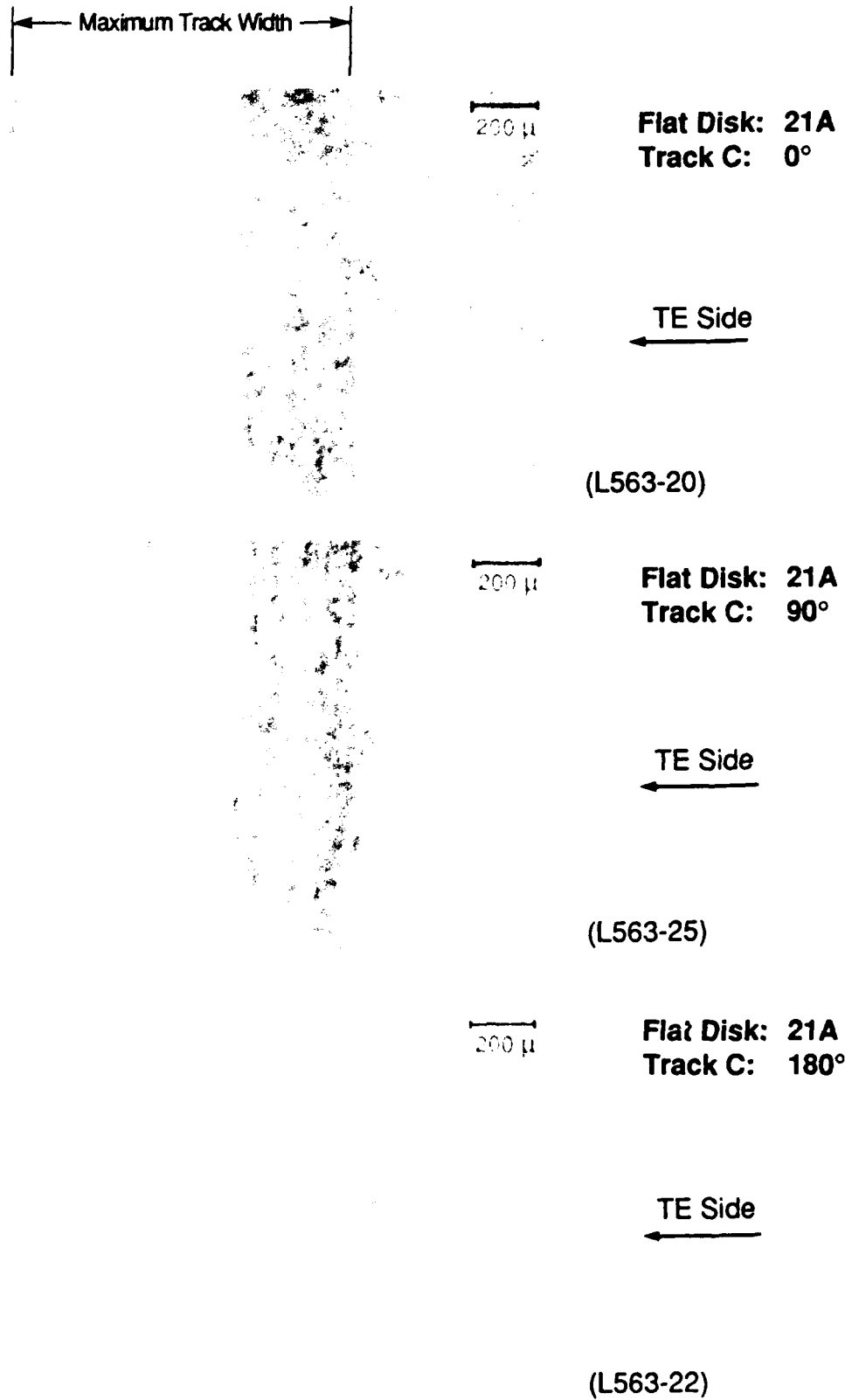
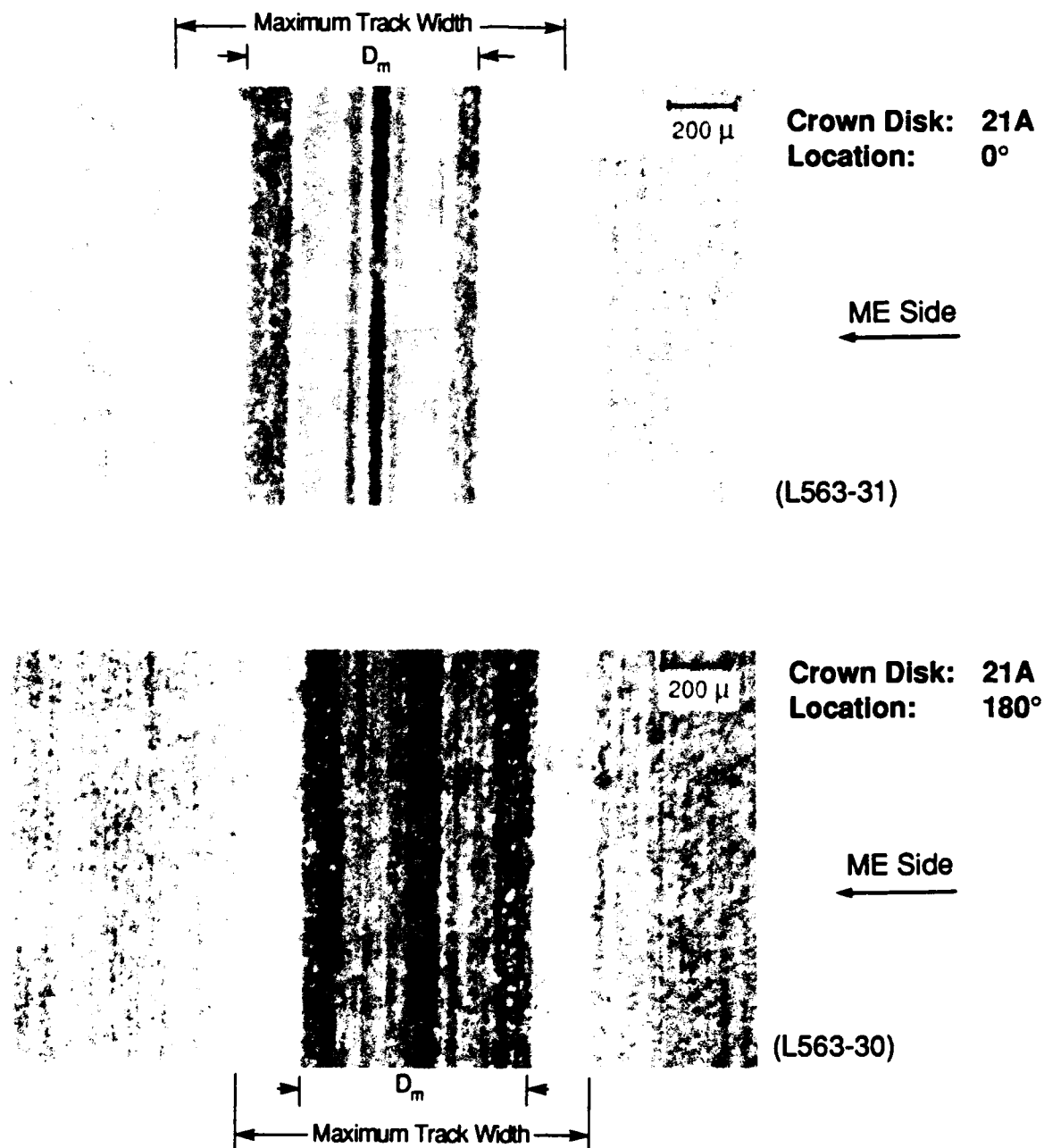


Figure 36. Traction Data, MoS<sub>2</sub>, Temperature = 1200°F, Loads = 15, 20, and 25 lb



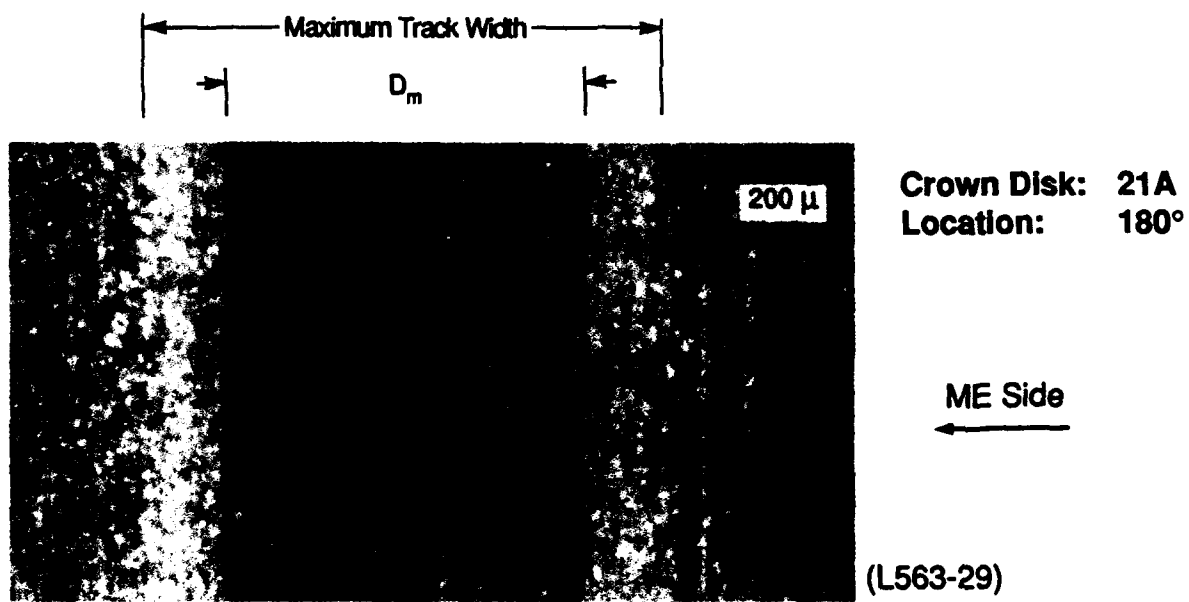
V9-194

Figure 37. Wear Track for MoS<sub>2</sub>, Room Temperature to 1200°F, Load = 4 to 25 lb



V9-198

Figure 38. Wear Track on Crowned Disk with MoS<sub>2</sub>, Room Temperature to 1200°F, Load = 4 to 25 lb



V9-197

Figure 39. Higher Magnification of Wear Track on Crowned Disk with  $\text{MoS}_2$ ,  
Room Temperature to 1200°F, Load = 4 to 25 lb

# **Phase II**

## **Wear and Friction Properties of Silicon Nitride and Alpha Silicon Carbide**

## 5.0 INTRODUCTION

---

The objective of this phase of the test program was to determine the most wear-resistant combination of the ceramic materials supplied by Hughes. In particular, the effects of adding BN to a  $\text{Si}_3\text{N}_4$  matrix were investigated. In addition, the friction coefficients for each combination of materials were explored.

## 6.0 TEST RIG DESCRIPTION

---

The sliding-wear tribometer shown in Figure 40\* has a water-cooled support spindle to minimize bearing temperatures and to allow the rotor to operate at speeds up to 50,000 rpm and 1500°F. Auxiliary cooling is used during high-temperature and high-speed conditions because a rotor long enough to provide thermal isolation cannot achieve acceptable dynamic behavior. Friction and wear studies have been conducted on the tester shown in Figure 40 at shaft speeds up to 30,000 rpm, or at an equivalent surface speed of 3,000 in./sec.

In addition to rotor dynamic and thermal isolation considerations, the testing design ensures that dynamic loads are minimized. When friction and wear tests are conducted on the tribometer shown in Figure 40, any runout in disk motion will produce an additional load due to the inertia of the static pin sample. Therefore, rotating sample runout must be kept to a minimum (usually within 0.0001 in.); this also holds for the weight of the static sample and the sample holder.

Although dynamic loads will always be present in high-speed testing, careful calculations permit the loads to be taken into account when data are interpreted. Similarly, friction-induced dynamic vibration of the static pin sample must be avoided if reliable friction and wear data are to be obtained.

---

\*Figures for Phase II testing are appended to Section 9.0.

## 7.0 TEST PROCEDURE

The materials tested during pin-on-disk wear tests were supplied by Hughes and consisted of:

- Three  $\alpha$  SiC disks
- One  $\text{Si}_3\text{N}_4$  disk containing 0.0% BN
- One  $\text{Si}_3\text{N}_4$  disk containing 3.5% BN
- $\text{Si}_3\text{N}_4$  pins containing 0.0% BN
- $\text{Si}_3\text{N}_4$  pins containing 3.5% BN
- $\text{Si}_3\text{N}_4$  pins containing 15.0% BN
- $\text{Si}_3\text{N}_4$  pins containing 40.0% BN
- $\alpha$  SiC pins hipped
- $\alpha$  SiC pins post hipped.

A total of 20 tests were attempted on the 5 disks supplied by designating 4 separate test areas on each disk. Table 2 contains the test matrix developed to maximize the number of variations of material combinations that could be tested within the time constraints. These tests were intended only as a screening, with further testing necessary to verify the results.

TABLE 2. Pin-On-Disk Test Matrix and Test Results Summary

|                           |                                 | Test No. | Track | Material            | Process     | Temperature | Comments                                |
|---------------------------|---------------------------------|----------|-------|---------------------|-------------|-------------|-----------------------------------------|
| SiC <sup>1</sup><br>Disks | Disk 1<br>$\alpha$ SiC (Hipped) | HU-1     | 1     | 40% BN <sup>3</sup> | Flat        | Ambient     | 7000 rpm Maximum Speed                  |
|                           |                                 | HU-2     | 2     | 40% BN              | Flat        | 1200°F      | Destroyed                               |
|                           |                                 | HU-3     | 3     | 40% BN              | Edge        | Ambient     | Destroyed                               |
|                           |                                 | HU-4     | 4     | 40% BN              | Edge        | 1200°F      | Destroyed                               |
|                           | Disk 2<br>$\alpha$ SiC (Hipped) | HU-5     | 1     | 3.5% BN             | Edge        | Ambient     | Completed                               |
|                           |                                 | HU-6     | 2     | 40% BN              | Edge        | Ambient     | Completed                               |
|                           |                                 | HU-7     | 3     | COMBAT              | Edge        | Ambient     | Completed                               |
|                           |                                 | HU-8     | 4     | 40% BN              | Edge        | 1200°F      | 1000 rpm Maximum Speed;<br>Pin Wore Out |
|                           | Disk 3<br>$\alpha$ SiC (Hipped) | HU-9     | 1     | SiC                 | Hipped      | Ambient     | Inconclusive                            |
|                           |                                 | HU-10    | 2     | 15% BN              | Edge        | Ambient     | Completed                               |
|                           |                                 | HU-11    | 3     | SiC                 | Post Hipped | Ambient     | 5000 rpm Maximum Speed                  |
|                           |                                 | HU-12    | 4     | SiC                 | Hipped      | Ambient     | 7000 rpm Maximum Speed                  |
| SiN <sup>2</sup><br>Disks | Disk 4<br>0% BN in Disk         | HU-13    | 1     | 0% BN               | Flat        | Ambient     | Completed                               |
|                           |                                 | HU-14    | 2     | 40% BN              | Flat        | Ambient     | Completed                               |
|                           |                                 | HU-15    | 3     | $\alpha$ SiC        | Hipped      | Ambient     | 7000 rpm Maximum Speed                  |
|                           |                                 | HU-16    | 4     | $\alpha$ SiC        | Hipped      | 1200°F      | Completed                               |
|                           | Disk 5<br>3.5% BN in Disk       | HU-17    | 1     | 0% BN               | Flat        | Ambient     | 7000 rpm Maximum Speed                  |
|                           |                                 | HU-18    | 2     | 40% BN              | Flat        | Ambient     | Completed                               |
|                           |                                 | HU-19    | 3     | $\alpha$ SiC        | Hipped      | Ambient     | Completed                               |
|                           |                                 | HU-20    | 4     | $\alpha$ SiC        | Hipped      | 1200°F      | Completed                               |

<sup>1</sup>Silicon Carbide

<sup>2</sup>Silicon Nitride

<sup>3</sup>Boron Nitride



### **7.1 Load**

A Hertzian contact stress of between  $1.29 \times 10^5$  and  $1.61 \times 10^5$  psi, depending on the materials, was developed in the initial contact area at the start of each test. This stress decreases as wear occurs on the test specimens.

### **7.2 Speed**

There were five distinct speeds used for this testing:

- 3.990 m/sec (1000 rpm, 157.08 in./sec)
- 11.969 m/sec (3000 rpm, 471.24 in./sec)
- 19.949 m/sec (5000 rpm, 785.40 in./sec)
- 27.929 m/sec (7000 rpm, 1099.56 in./sec)
- 35.908 m/sec (9000 rpm, 1413.72 in./sec).

During each test, the test pin was lifted from the surface of the disk and speed was increased from 0 to 1000 rpm. The test pin was then lowered to the surface of the disk and the speed was maintained for 3 min. After that time, the speed was slowly increased to the next speed range (3000 rpm) and held for 3 min. This sequence was repeated until the specimen ran for 3 min at 9000 rpm. At that time, the pin was lifted and the spindle was shut down.

### **7.3 Temperature**

Two temperatures were used during this testing — ambient, and approximately 1200°F. The majority of the screening was done at ambient temperatures, with the final testing of the lowest wear sample of each variation conducted at 1200°F.

## 8.0 RESULTS

---

In general, compared to the  $\alpha$  SiC pins, the  $\text{Si}_3\text{N}_4$  pins — with and without the BN additive — had a significantly lower frictional force when running against either  $\text{Si}_3\text{N}_4$  or  $\alpha$  SiC disks. The wear on the  $\text{Si}_3\text{N}_4$  pins, however, was significantly greater than the  $\alpha$  SiC pins, especially at elevated temperatures. In fact, at elevated temperatures (1200°F), the volumetric wear on the  $\text{Si}_3\text{N}_4$  pins was almost 200 times greater than the equivalent wear on a SiC pins.

### 8.1 Pin Wear

Pin wear was evaluated using three different measurement methods. The first, and most direct method, used a capacitance probe to directly measure the linear wear of the pin during the test and record the measurements on a strip-chart recorder. There are two inherent problems with these measurements. First, a linear measurement is a poor representation of actual wear. Since the pin has a spherical nose, the actual wear is a cubic function of the measured wear. Second, due to the test rig design it was impossible to measure linear wear during high-temperature tests. Figures 41 through 44 show strip-chart recordings describing the linear wear of the pin for one disk. The results of tests HU-17 through HU-20 are typical of the measurements for each disk.

The second assessment of pin wear was made by microscopically measuring the wear-scar diameter on the pin after testing. The advantage of this measurement is that it can be used on all tests regardless of temperatures. The disadvantage is that it can only be used after the test is completed. Thus, wear measurements as a function of speed were impossible to obtain and the measurements were still linear. Figures 45 through 60 are photographs of magnified ( $\times 30$ ) wear scars on the pins.

Certain tests were suspended for various reasons. Tests HU-2, 3, and 4 were never run due to extensive damage to the disk. Test HU-8 was aborted after less than a minute because excessive wear was detected by the force sensor. During Test HU-9, the pin support arm of the test rig contacted the wear probe, which removed the load from the pin. This caused an inconclusive test. Tests HU-11, 12, 15, and 17 were stopped at various stages because the wear on the pin exceeded the allowable range of wear measurement.

The third technique for evaluating pin wear was to weigh the pins before and after testing. This technique eliminated linear measurements, but the very small differences in weight before and after testing left some question as to the reliability of this technique. These errors in weight measurement were mainly due to the inability of the scale to measure the pins with enough accuracy to enable two relatively large numbers to be subtracted to yield a small result (e.g., Test HU-16 yielded  $0.5988 - 0.5970 = 0.0018$  g). It should be noted that the 0.1% full-scale accuracy balance used would be expected to have an error of up to  $\pm 0.0010$  g per reading for the settings used. Thus, in the example from Test HU-16, the result would be  $0.0018 \text{ g} \pm 0.0020 \text{ g}$ , which leaves the results questionable.

Because of the various rubbing distances of disk-pin contact during each test and the different measured parameters available for the hot and cold testing, a Volumetric Wear Factor (VWF) was devised to enable all the tests to be compared equally. The VWF was determined by calculating the volume of the pin worn away per thousand surface meters of rubbing contact. The volume worn away was determined by calculations based on the total measured linear wear, where available, and the average wear scar diameter for a given pin. These two calculations were compared and found to be in reasonable agreement. The volume of material removed, calculated using the average wear scar diameter (available for all tests), was then divided by the number of thousand surface meters of rubbing contact to yield the VWF:

$$\text{VWF} = \frac{M_1}{Nt \times M_2} \times 10^{-13}$$














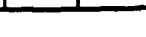
where:

$M_1$  = quantity of material removed (cubic meters)  
 $M_2$  = sliding distance (meters)  
 $Nt$  = load at pin/disk interface (Newtons)

Table 3 summarizes these results and compares the wear capabilities of the various material combinations.

As Table 3 shows, a  $Si_3N_4$  pin with 40% BN demonstrated remarkably long wear at ambient temperatures, but had extraordinarily high wear (over 1000 times higher) at elevated temperatures. Table 3 also shows the lower wear of the on-edge orientation as opposed to the flat orientation of the  $Si_3N_4$  crystals (see differences in Tests HU-1 and HU-6). In addition, the relatively high wear of COMBAT BN as compared to the  $Si_3N_4$  is seen in the results of test HU-7.

TABLE 3. Pin Volumetric Wear Factor

| Test Number | Disk/Pin                                          | Volumetric Wear Factor (In.)                                                         |    |    |    |    |    | Temperature (°F) |
|-------------|---------------------------------------------------|--------------------------------------------------------------------------------------|----|----|----|----|----|------------------|
|             |                                                   | 5                                                                                    | 10 | 15 | 20 | 25 | 30 |                  |
| HU-1        | $\alpha SiC^1/SiN^2$ , 40% BN <sup>3</sup> (Flat) |    |    |    |    |    |    | Ambient          |
| HU-5        | $\alpha SiC/SiN$ , 3.5% BN (Edge)                 |     |    |    |    |    |    | Ambient          |
| HU-6        | $\alpha SiC/SiN$ , 40% BN (Edge)                  |     |    |    |    |    |    | Ambient          |
| HU-7        | COMBAT                                            | Pin Volumetric Wear Factor = 49.02                                                   |    |    |    |    |    | Ambient          |
| HU-8        | $\alpha SiC/SiN$ , 40% BN (Edge)                  | Pin Volumetric Wear Factor = 3093.3                                                  |    |    |    |    |    | 1200             |
| HU-10       | $\alpha SiC/SiN$ , 15% BN (Edge)                  |   |    |    |    |    |    | Ambient          |
| HU-11       | $\alpha SiC/SiC$ (Post Hipped)                    |  |    |    |    |    |    | Ambient          |
| HU-12       | $\alpha SiC/SiC$ (Hipped)                         |   |    |    |    |    |    | Ambient          |
| HU-13       | $SiN/SiN$ , 0% BN (Flat)                          |   |    |    |    |    |    | Ambient          |
| HU-14       | $SiN/SiN$ , 40% BN (Flat)                         |  |    |    |    |    |    | Ambient          |
| HU-15       | $SiN/SiC$ (Hipped)                                |  |    |    |    |    |    | Ambient          |
| HU-16       | $SiN/SiC$ (Hipped)                                |   |    |    |    |    |    | 1200             |
| HU-17       | $SiN$ , 3.5% BN/ $SiN$ , 0% BN (Flat)             |   |    |    |    |    |    | Ambient          |
| HU-18       | $SiN$ , 3.5% BN/ $SiN$ , 40% BN (Flat)            |  |    |    |    |    |    | Ambient          |
| HU-19       | $SiN$ , 3.5% BN/ $SiC$ (Hipped)                   |   |    |    |    |    |    | Ambient          |
| HU-20       | $SiN$ , 3.5% BN/ $SiC$ (Hipped)                   |   |    |    |    |    |    | 1200             |

<sup>1</sup>Silicon Carbide  
<sup>2</sup>Silicon Nitride  
<sup>3</sup>Boron Nitride

All values expressed in  $([M^3]/[Nt \cdot M]) \times 10^{-13}$   
 where M = Meters and Nt = Newtons

## 8.2 Disk Wear

Wear tracks were examined optically and measured using a standard profilometer. The profilometer results in Figures 61 through 65 show the average track worn in each disk to be in the order of 0.20 in. wide. No definite conclusions can be drawn regarding material. Wear track depths of about 60  $\mu$ in. were typically experienced regardless of the disk material or test conditions. Figures 66 through 70 show photographs ( $\times 10$ ) of each of the five disks.

## 8.3 Frictional Force

Frictional loads were measured during the testing and were recorded using a data acquisition system and using a strip-chart recorder. Figures 41 through 44 are copies of the strip-chart recordings for Tests HU-17 through HU-20. These figures are typical of all the results and show a high initial force corresponding to the high initial wear rate, rapidly reducing to a lower force with a very low slope. The high forces and wear rates also correspond to the 1000-rpm test speed. Whether this is coincidental or symptomatic is unknown since both the higher wear rate and load could also be caused by the high Hertzian stresses of the initial contact. Figure 71 is a plot of frictional force versus linear wear of the pin for Tests HU-17 through HU-19 and is typical of all the tests.

The results of Tests HU-17 through HU-20 are of interest because they show that an  $\alpha$  SiC pin (HU-19) pin has a lower frictional force than an  $\text{Si}_3\text{N}_4$  pin (HU-17) until at least 50% of the total wear on the pin has occurred (HU-17). When BN is present, the frictional force for a given amount of wear is always lower. This is true even though the coefficient of friction, shown in Table 4, is higher for  $\alpha$  SiC. Generally, the wear experienced by the  $\alpha$  SiC pins was enough lower than that of the  $\text{Si}_3\text{N}_4$  pins to offset any advantages of lower friction coefficient if wear is the primary evaluation criteria.

TABLE 4. Coefficients of Friction

| Test Number | Disk/Pin                                                       | Speed (rpm) |       |       |       | Average | Average Standard Deviation |
|-------------|----------------------------------------------------------------|-------------|-------|-------|-------|---------|----------------------------|
|             |                                                                | 3000        | 5000  | 7000  | 9000  |         |                            |
| HU-1        | $\alpha\text{SiC}^1/\text{SiN}^2$ , 40% BN <sup>3</sup> (Flat) | 0.266       | 0.112 | 0.073 | N/A   | 0.150   | 0.086                      |
| HU-5        | $\alpha\text{SiC}/\text{SiN}$ , 3.5% BN (Edge)                 | 0.240       | 0.145 | 0.172 | 0.256 | 0.203   | 0.091                      |
| HU-6        | $\alpha\text{SiC}/\text{SiN}$ , 40% BN (Edge)                  | 0.134       | 0.099 | 0.088 | 0.117 | 0.110   | 0.086                      |
| HU-10       | $\alpha\text{SiC}/\text{SiN}$ , 15% BN (Edge)                  | 0.227       | 0.180 | 0.132 | 0.100 | 0.159   | 0.084                      |
| HU-11       | $\alpha\text{SiC}/\text{SiC}$ (Post Hipped)                    | 0.507       | 0.321 | 0.261 | N/A   | 0.363   | 0.081                      |
| HU-12       | $\alpha\text{SiC}/\text{SiC}$ (Hipped)                         | 0.481       | 0.310 | 0.238 | N/A   | 0.343   | 0.085                      |
| HU-13       | $\text{SiN}/\text{SiN}$ , 0% BN (Flat)                         | 0.070       | 0.057 | 0.036 | 0.023 | 0.046   | 0.079                      |
| HU-14       | $\text{SiN}/\text{SiN}$ , 40% BN (Flat)                        | 0.091       | 0.061 | 0.039 | 0.015 | 0.052   | 0.079                      |
| HU-15       | $\text{SiN}/\text{SiC}$ (Hipped)                               | 0.378       | 0.297 | 0.161 | N/A   | 0.249   | 0.086                      |
| HU-16       | $\text{SiN}/\text{SiC}$ (Hipped)                               | 0.477       | 0.394 | 0.416 | 0.418 | 0.426   | 0.092                      |
| HU-17       | $\text{SiN}$ , 3.5% BN/ $\text{SiN}$ , 0% BN (Flat)            | 0.078       | 0.060 | 0.050 | 0.073 | 0.062   | 0.081                      |
| HU-18       | $\text{SiN}$ , 3.5% BN/ $\text{SiN}$ , 40% BN (Flat)           | 0.115       | 0.049 | N/A   | N/A   | 0.082   | 0.075                      |
| HU-19       | $\text{SiN}$ , 3.5% BN/ $\alpha\text{SiC}$ (Hipped)            | 0.360       | 0.209 | 0.138 | 0.101 | 0.202   | 0.093                      |
| HU-20       | $\text{SiN}$ , 3.5% BN/ $\alpha\text{SiC}$ (Hipped)            | 0.537       | 0.477 | 0.496 | 0.507 | 0.504   | 0.088                      |

<sup>1</sup>Silicon Carbide

<sup>2</sup>Silicon Nitride

<sup>3</sup>Boron Nitride

Table 4 was generated from data collected by the automatic data collection system. This system collects and reduces speed and load cell output using a 100-kHz sampling rate and dumps all new data to hard disk every two seconds. A sample output of this system is shown in Appendix B.

A normalized contact shear stress ( $\tau$ ) was calculated by dividing the average frictional force by the final contact area. These values are given in Table 5 for the different material combinations studied.

TABLE 5. Normalized Contact Shear Stress ( $\tau$ )<sup>1</sup>

|                    | Pin Material        | Disk Material |      |              |
|--------------------|---------------------|---------------|------|--------------|
|                    |                     | SiC           | SiN  | SiN, 3.5% BN |
| Ambient Conditions | SiN, 40% BN (Flat)  | 13.1          | 13.8 | 23.4         |
|                    | SiN, 3.5% BN (Edge) | 36.5          |      |              |
|                    | SiN, 40% BN (Edge)  | 35.1          |      |              |
|                    | SiN, 15% BN         | 26.2          |      |              |
|                    | SiC (Hipped)        | 115.1         |      | 16.5         |
|                    | SiC (Post Hipped)   | 102.0         | 54.5 |              |
|                    | SiN, 0% BN          |               | 17.9 | 13.1         |
| 1200°F             | SiN, 40% BN (Edge)  |               |      |              |
|                    | SiC (Hipped)        |               | 93.1 |              |
|                    | SiC (Hipped)        |               |      | 144.1        |

<sup>1</sup>  $\tau$  = Frictional force ÷ contact area of wear scar.  
Expressed in Newtons per square meter.

## 9.0 CONCLUSIONS

---

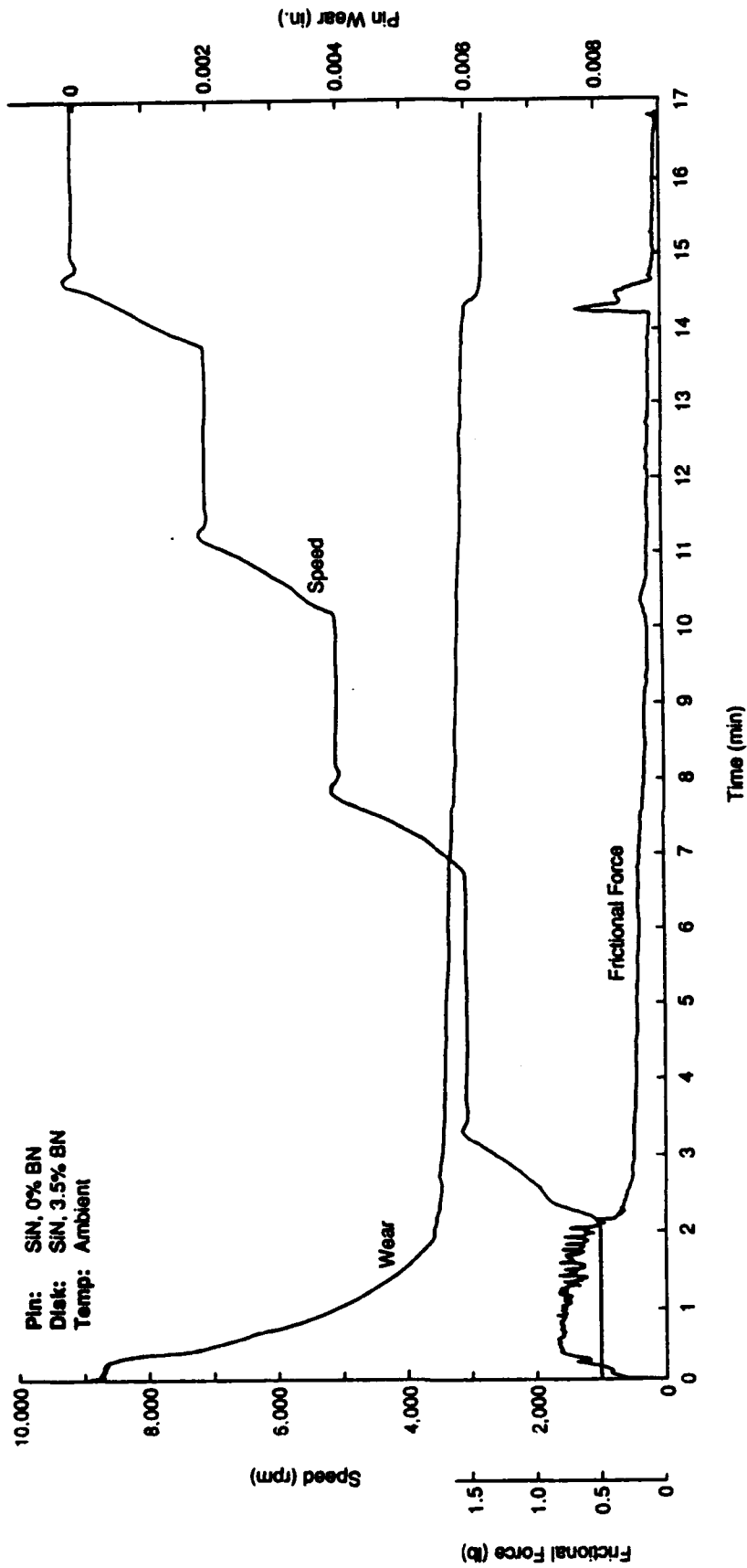
The results of this testing indicate that  $\alpha$  SiC wears less than  $\text{Si}_3\text{N}_4$ , especially at elevated temperatures. The addition of BN tends to exaggerate this difference in wear. However,  $\text{Si}_3\text{N}_4$  had a significantly lower coefficient of friction than  $\alpha$  SiC. The data scatter seems to overwhelm the effect of BN added to  $\text{Si}_3\text{N}_4$  on friction coefficient. Indications are, however, that BN tends to increase the friction coefficient slightly, at least at ambient temperatures. The combined effect of increased or comparable friction with BN addition to the  $\text{Si}_3\text{N}_4$ , coupled with increased wear, gives these materials an undesirable combination of properties. The hope that BN additions would be lubricious and reduce friction at the expense of added wear was not supported by the test data. In general, the edge-cut BN samples had lower wear than the flat-cut samples.

Because of the limited testing attempts and the number of variables of interest, additional testing should be undertaken to establish any type of statistical confidence in the results shown.



V90-66

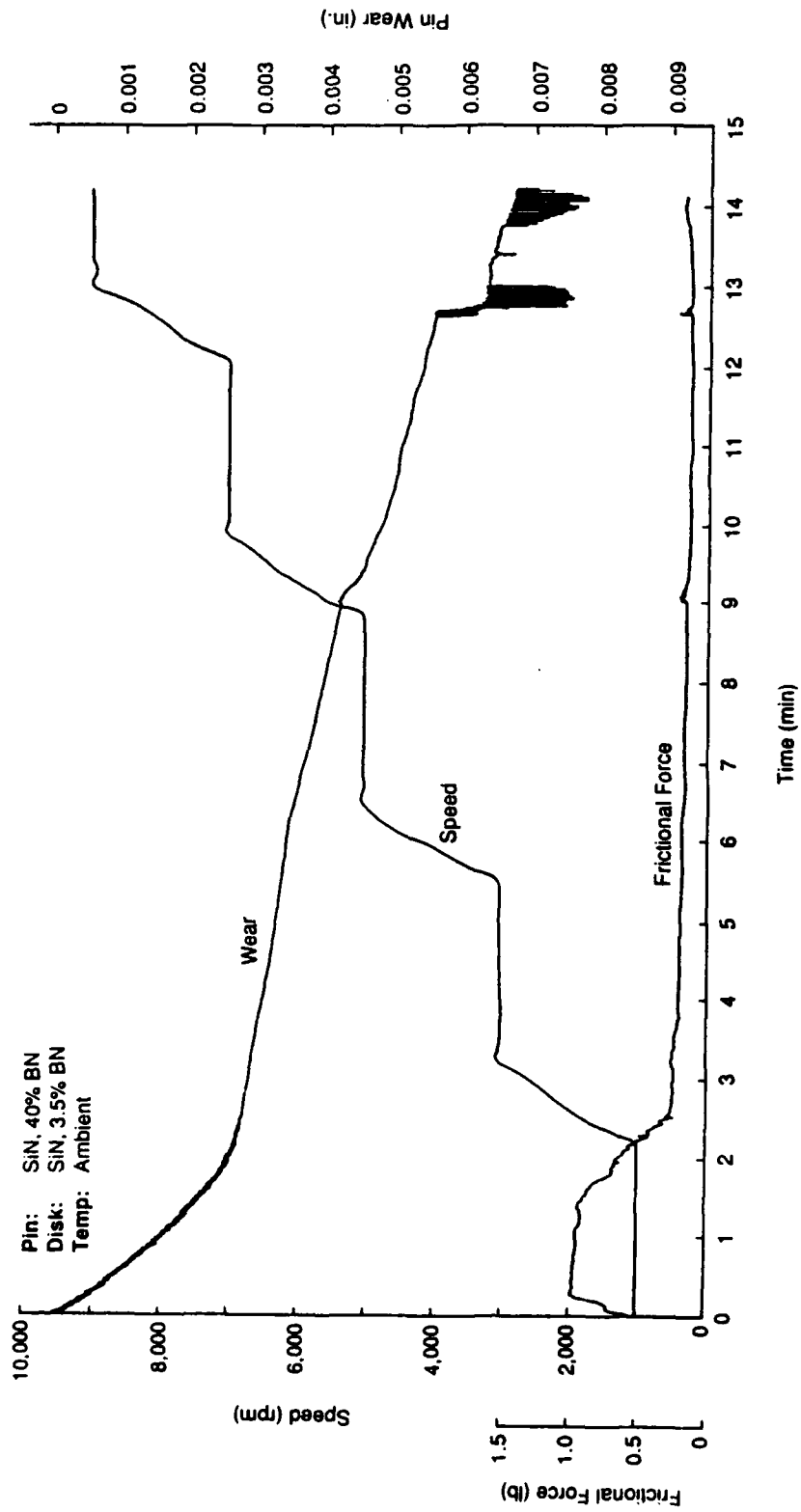
Figure 40. High-Speed, High-Temperature Test Rig (Tribometer)



90235

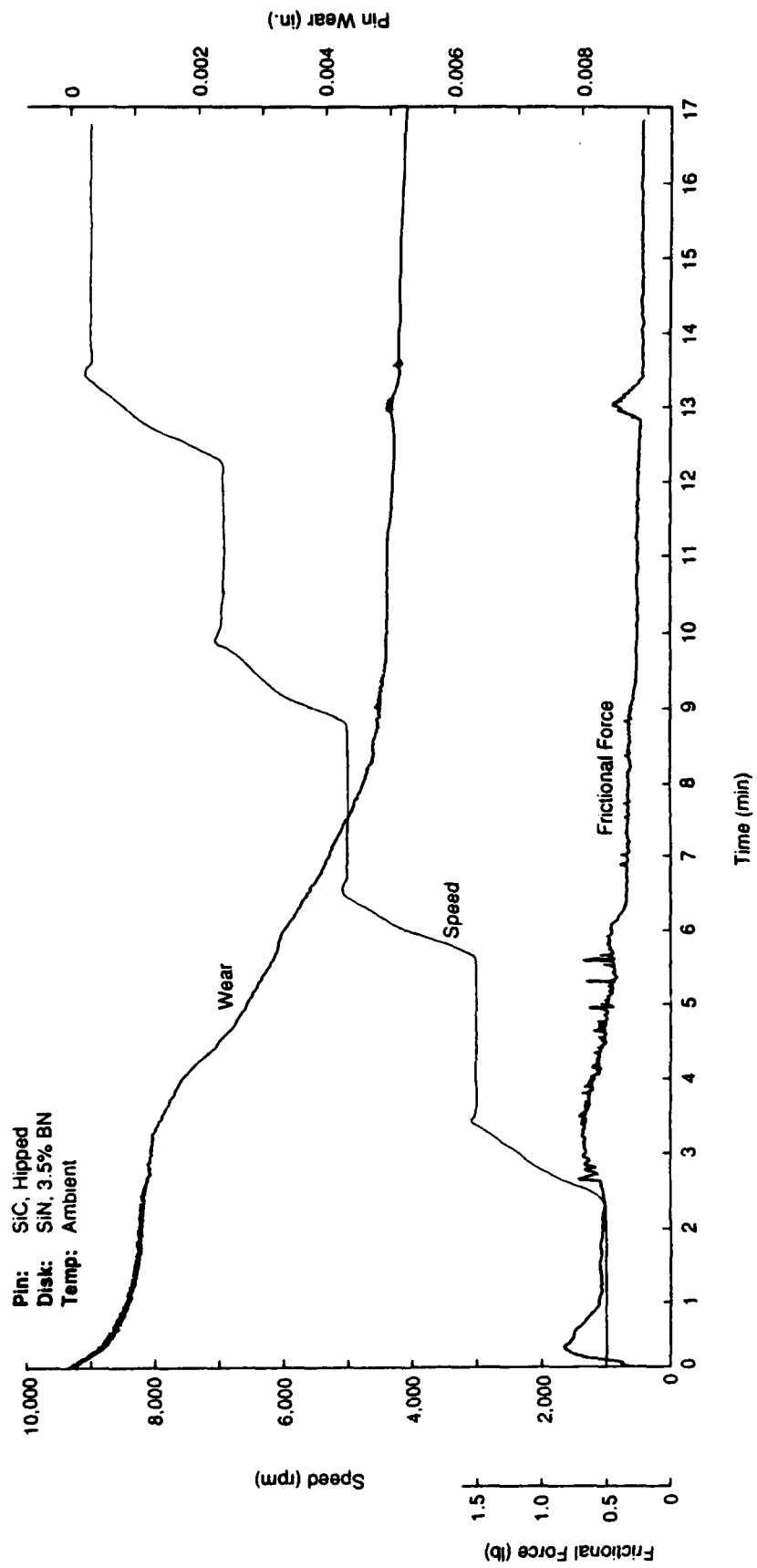
Figure 41. Strip Chart Recording for Test HU-17





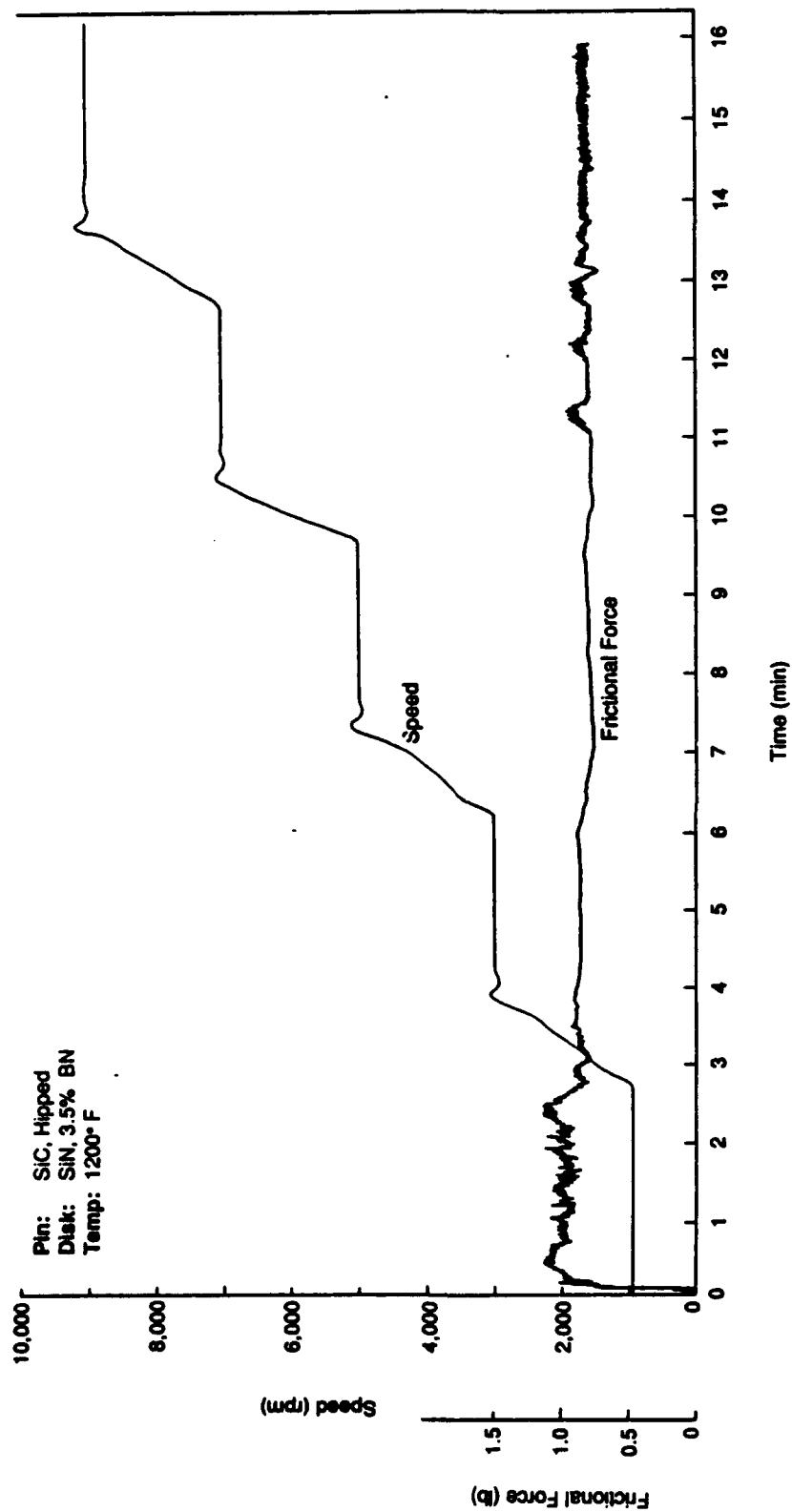
90282

Figure 42. Strip Chart Recording for Test HU-18



90284

Figure 43. Strip Chart Recording for Test HU-19



90283

Figure 44. Strip Chart Recording for Test HU-20

### Test HU-1



Figure 45. Pin Wear (SiN with 40% BN; Flay Lay on SiC Disk at Ambient Temperature)

### Test HU-5

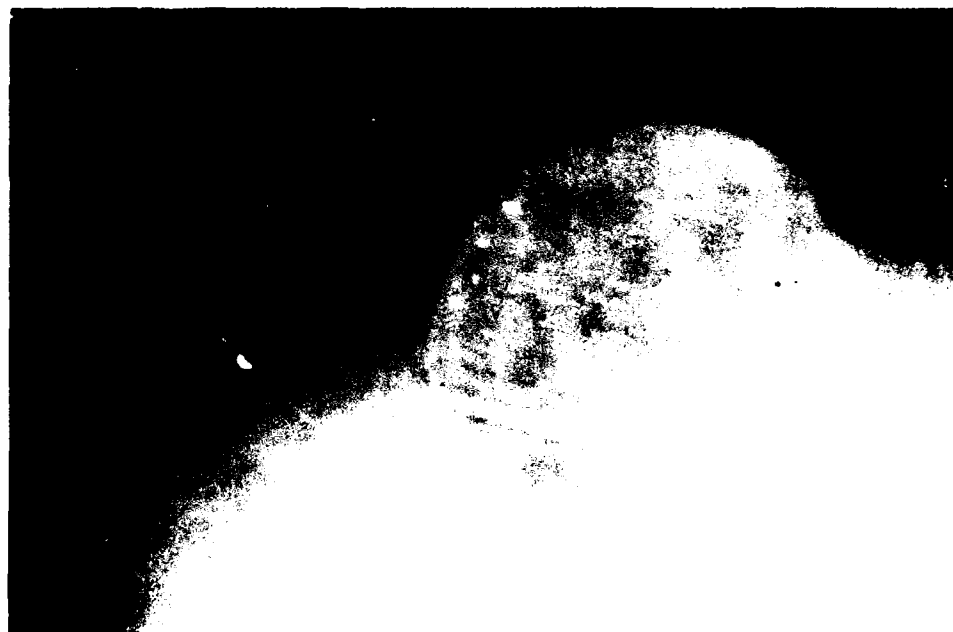


Figure 46. Pin Wear (SiN with 3.5% BN; Edge Lay on SiC Disk at Ambient Temperature)

### Test HU-6



Figure 47. Pin Wear (SiN with 40% BN; Edge Lay on SiC Disk at Ambient Temperature)

### Test HU-7

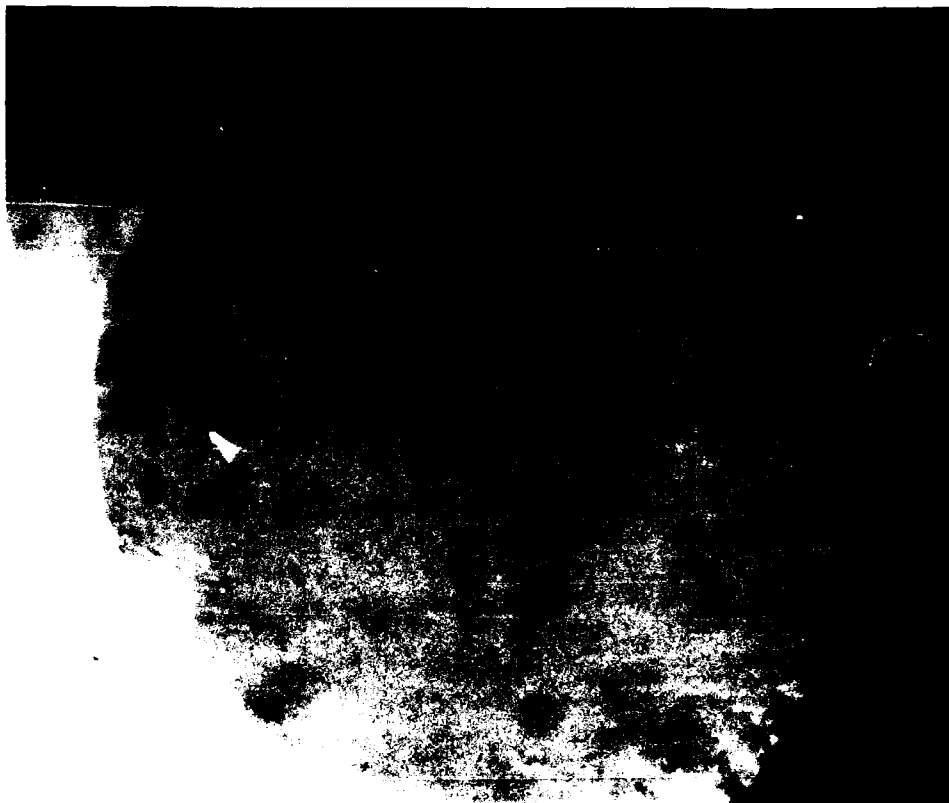


Figure 48. Pin Wear (COMBAT BN on SiC Disk at Ambient Temperature)

**Test HU-8**



V90-27

**Figure 49. Pin Wear (SiN with 40% BN; Edge Lay at 1200°F)**

### Test HU-10

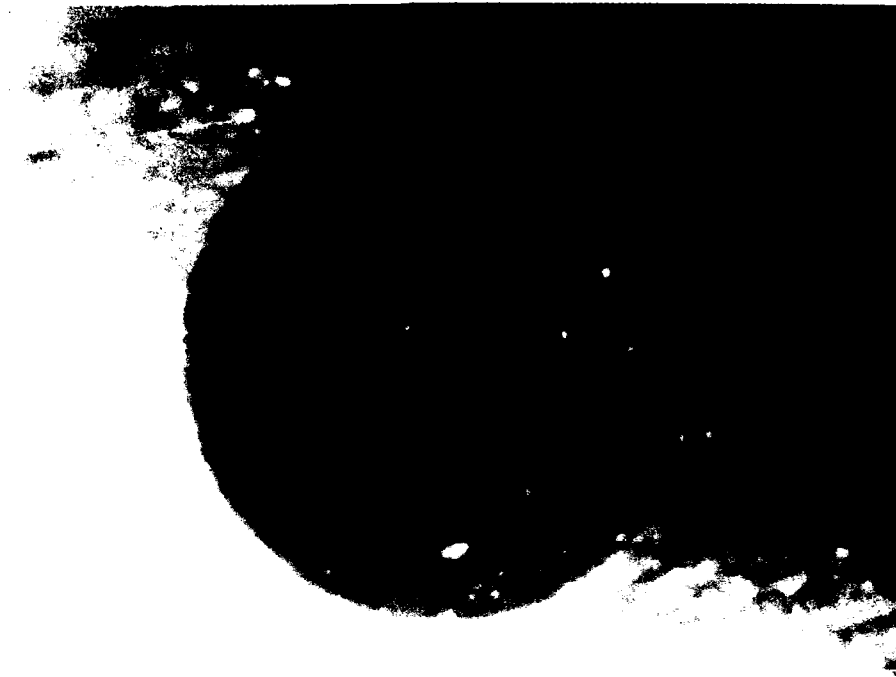


Figure 50. Pin Wear (SiN with 15% BN; Edge Lay on SiC Disk at Ambient Temperature)

### Test HU-11

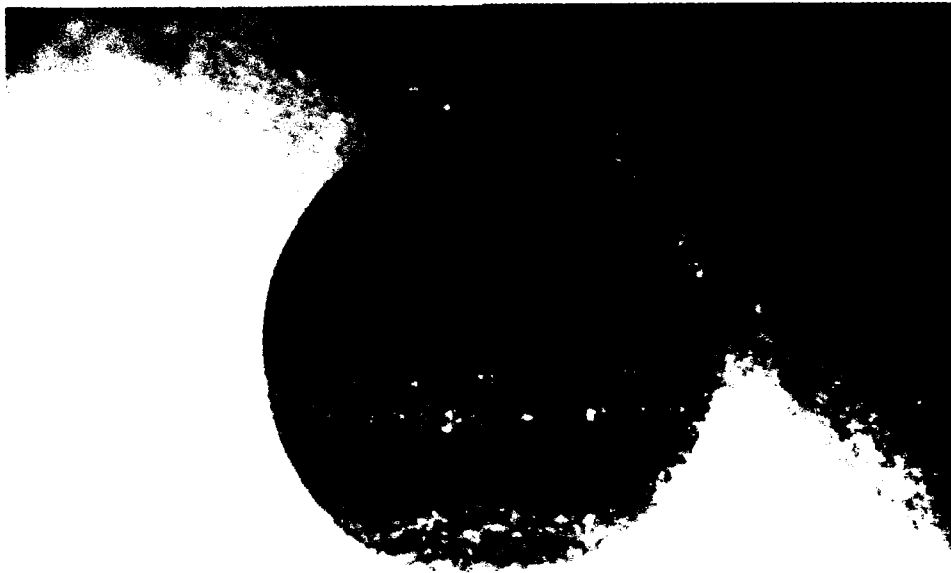


Figure 51. Pin Wear (SiC, Post Hipped, on SiC Disk at Ambient Temperature)

**Test HU-12**



Figure 52. Pin Wear (SiC, Hipped, on SiC Disk at Ambient Temperature)

**Test HU-13**

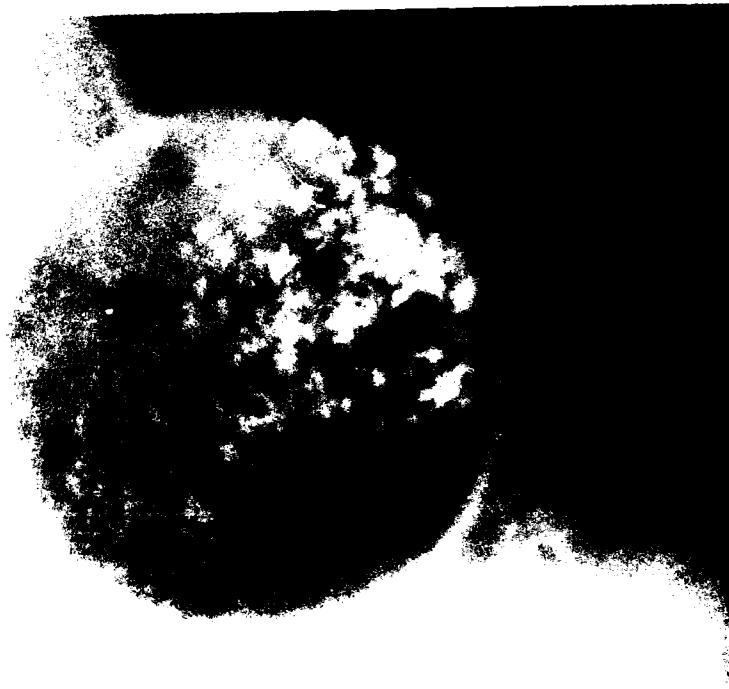
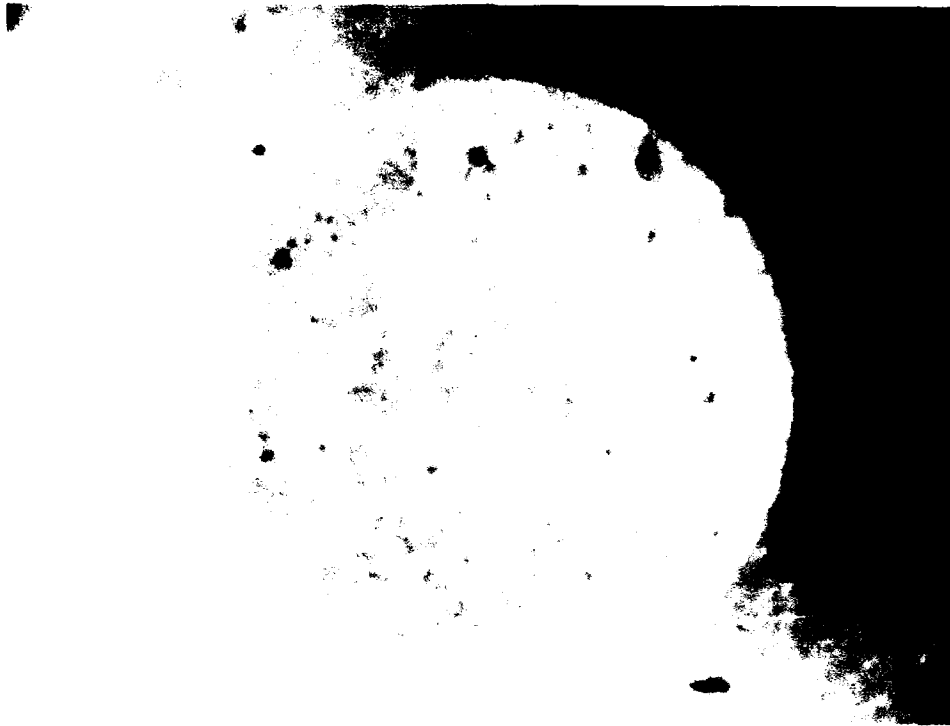


Figure 53. Pin Wear (SiN; Flay Lay on SiN Disk at Ambient Temperature)



**Test HU-14**



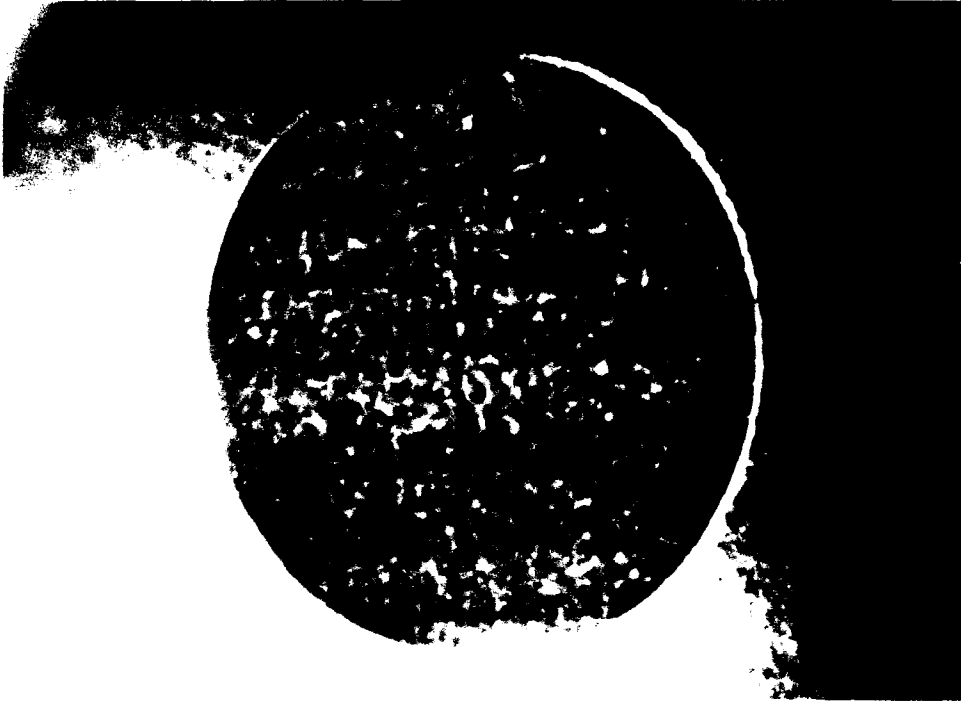
**Figure 54. Pin Wear (SiN; Flay Lay with 40% BN on SiN Disk at Ambient Temperature)**

**Test HU-15**



**Figure 55. Pin Wear (SiC, Hipped, on SiN Disk at Ambient Temperature)**

**Test HU-16**



**Figure 56. Pin Wear (SiC, Hipped, on SiN Disk at 1200°F)**

**Test HU-17**



**Figure 57. Pin Wear (SiN on SiN Disk with 3.5% BN at Ambient Temperature)**

**Test HU-18**



Figure 58. Pin Wear (SiN with 40% BN on SiN Disk with 3.5% BN at Ambient Temperature)

**Test HU-19**

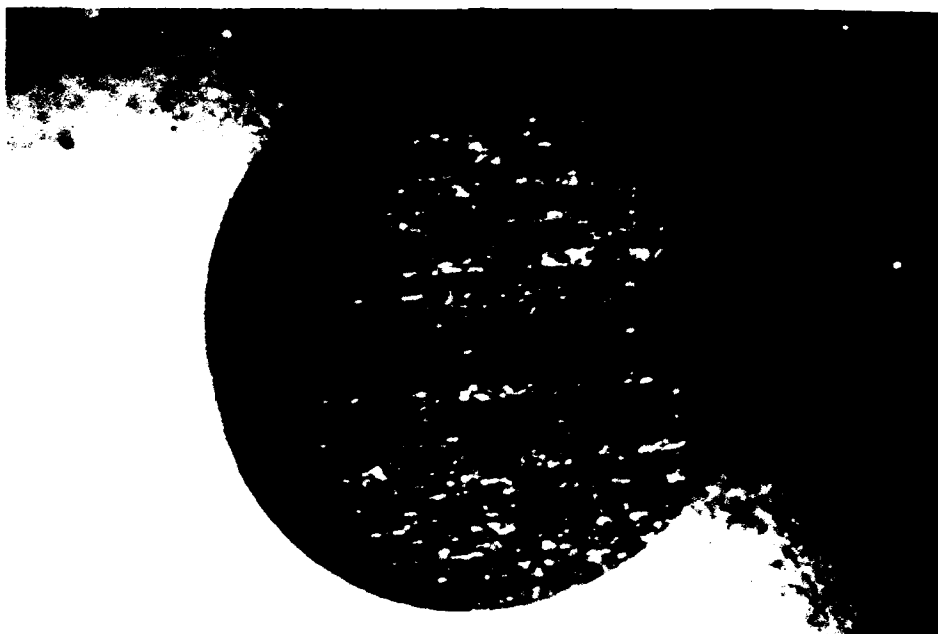
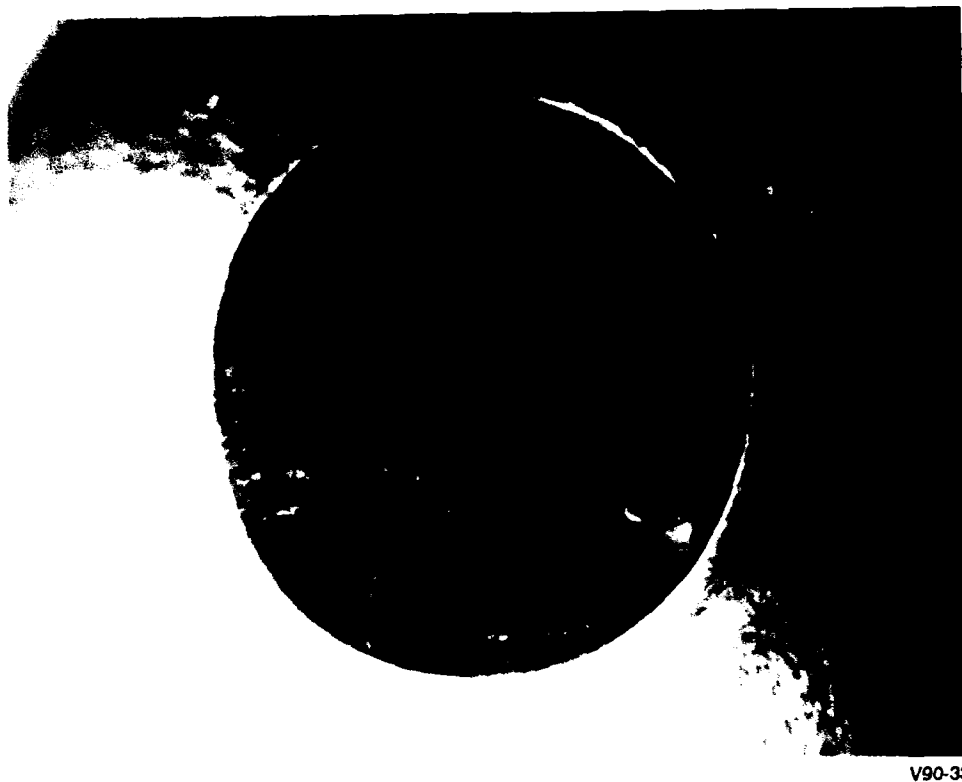


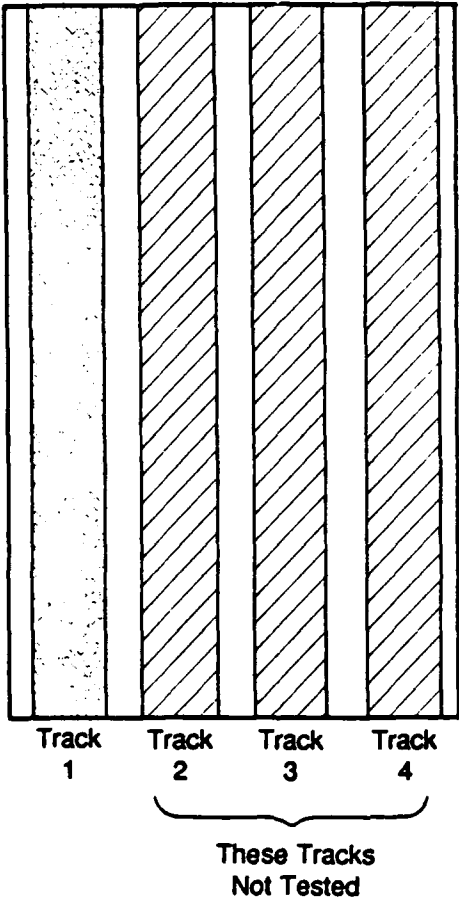
Figure 59. Pin Wear (SiC, Hipped, on SiN Disk with 3.5% BN at Ambient Temperature)

**Test HU-20**



**Figure 60. Pin Wear (SiC, Hipped, on SiN Disk with 3.5% BN at 1200°F)**

Disk No.: 1  
Disk Material:  $\alpha$ SiC Post Hipped  
Magnification: x10

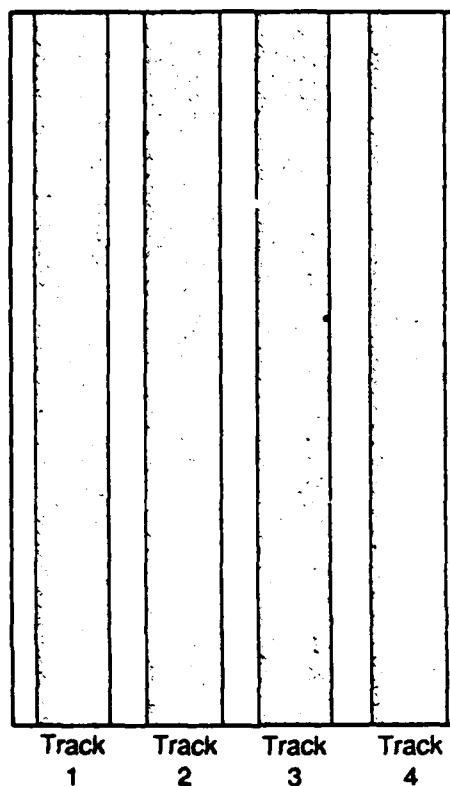


| Test No. | Description                     | Track No. | Wear (In.) |
|----------|---------------------------------|-----------|------------|
| HU-1     | $\alpha$ SiC/SiN, 40% BN (Flat) | 1         | 0.025      |

90281

Figure 61. SiC (Post Hipped) Disk Wear, Disk 1

**Disk No.:** 2  
**Disk Material:**  $\alpha$ SiC Post Hipped  
**Magnification:** x10

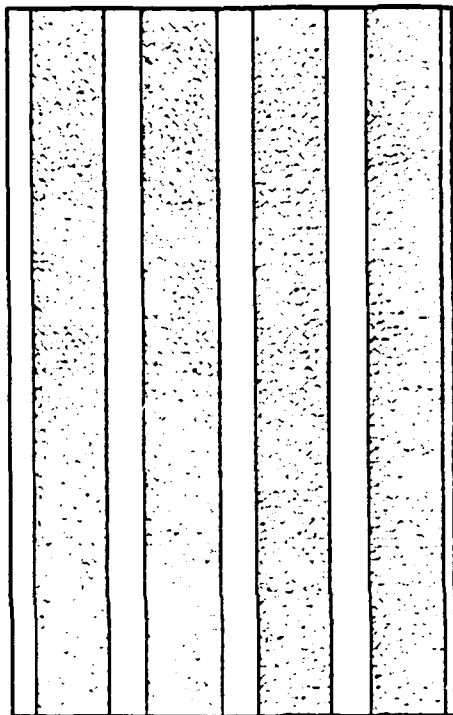


| Test No. | Description                      | Track No. | Wear (In.) |
|----------|----------------------------------|-----------|------------|
| HU-5     | $\alpha$ SiC/SiN, 3.5% BN (Edge) | 1         | 0.014      |
| HU-6     | $\alpha$ SiC/SiN, 40% BN (Edge)  | 2         | 0.017      |
| HU-7     | $\alpha$ SiC/SiN (COMBAT)        | 3         | 0.015      |
| HU-8     | $\alpha$ SiC/SiN, 40% BN (Edge)  | 4         | 0.036      |

90280

Figure 62. SiC (Post Hipped) Disk Wear; Disk 2

Disk No.: 3  
 Disk Material:  $\alpha$ SiC Post Hipped  
 Magnification: x10



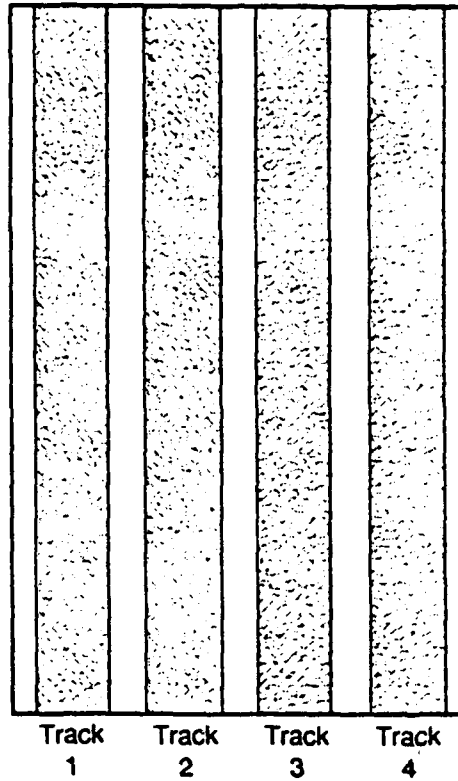
| Test No. | Description                     | Track No. | Wear (In.) |
|----------|---------------------------------|-----------|------------|
| HU-9     | $\alpha$ SiC/SiC (Hipped)       | 1         | 0.005*     |
| HU-10    | $\alpha$ SiC/SiN, 15% BN (Edge) | 2         | 0.023      |
| HU-11    | $\alpha$ SiC/SiC, (Post Hipped) | 3         | 0.020      |
| HU-12    | $\alpha$ SiC/SiC (Hipped)       | 4         | 0.018      |

\*Inconclusive

90279

Figure 63. SiC (Post Hipped) Disk Wear; Disk 3

**Disk No.:** 4  
**Disk Material:** 0% BN  
**Magnification:** x10



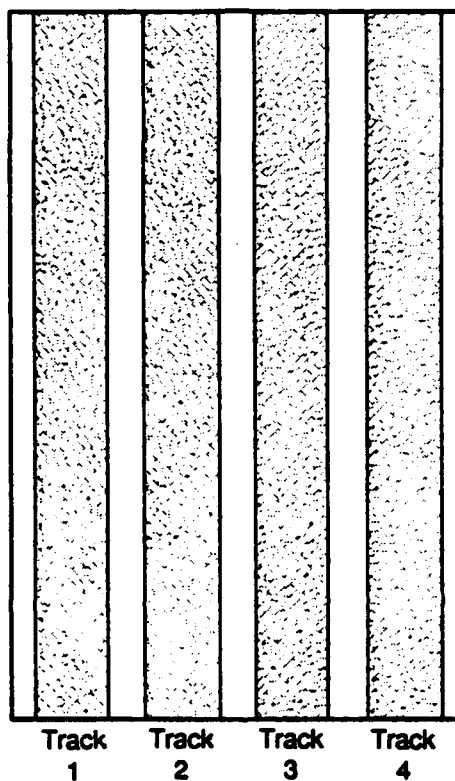
| Test No. | Description            | Track No. | Wear (In.) |
|----------|------------------------|-----------|------------|
| HU-13    | SiN/SiN, 0% BN (Flat)  | 1         | 0.016      |
| HU-14    | SiN/SiN, 40% BN (Flat) | 2         | 0.025      |
| HU-15    | SiN/SiC (Hipped)       | 3         | 0.024      |
| HU-16    | SiN/SiC (Hipped)       | 4         | 0.040      |

90277

Figure 64. SiN (0% BN) Disk Wear; Disk 4



**Disk No.:** 5  
**Disk Material:** SiN with 3.5% BN  
**Magnification:** x10



| Test No. | Description               | Track No. | Wear (In.) |
|----------|---------------------------|-----------|------------|
| HU-17    | SiN, 3.5% BN/SiN, 0% BN   | 1         | 0.0609     |
| HU-18    | SiN, 3.5% BN/SiN, 40% BN  | 2         | 0.0640     |
| HU-19    | SiN, 3.5% BN/SiC (Hipped) | 3         | 0.0593     |
| HU-20    | SiN, 3.5% BN/SiC (Hipped) | 4         | 0.0620     |

90278

Figure 65. SiN (3.5% BN) Disk Wear; Disk 5

Track  
1



| Test No. | Description                     | Track No. | Wear (In.) |
|----------|---------------------------------|-----------|------------|
| HU-1     | $\alpha$ SiC/SiN, 40% BN (Flat) | 1         | 0.025      |

Figure 66. Photo of Disk 1 Wear



| Test No. | Description                      | Track No. | Wear (In.) |
|----------|----------------------------------|-----------|------------|
| HU-5     | $\alpha$ SiC/SiN, 3.5% BN (Edge) | 1         | 0.014      |
| HU-6     | $\alpha$ SiC/SiN, 40% BN (Edge)  | 2         | 0.017      |
| HU-7     | $\alpha$ SiC/SiN (COMBAT)        | 3         | 0.015      |
| HU-8     | $\alpha$ SiC/SiN, 40% BN (Edge)  | 4         | 0.036      |

Figure 67. Photo of Disk 2 Wear



Track  
1

Track  
2

Track  
3

Track  
4

| Test No. | Description                     | Track No. | Wear (In.) |
|----------|---------------------------------|-----------|------------|
| HU-9     | $\alpha$ SiC/SiC (Hipped)       | 1         | 0.005*     |
| HU-10    | $\alpha$ SiC/SiN, 15% BN (Edge) | 2         | 0.023      |
| HU-11    | $\alpha$ SiC/SiC, (Post Hipped) | 3         | 0.020      |
| HU-12    | $\alpha$ SiC/SiC (Hipped)       | 4         | 0.018      |

\*Inconclusive

Figure 68. Photo of Disk 3 Wear



Track  
1

Track  
2

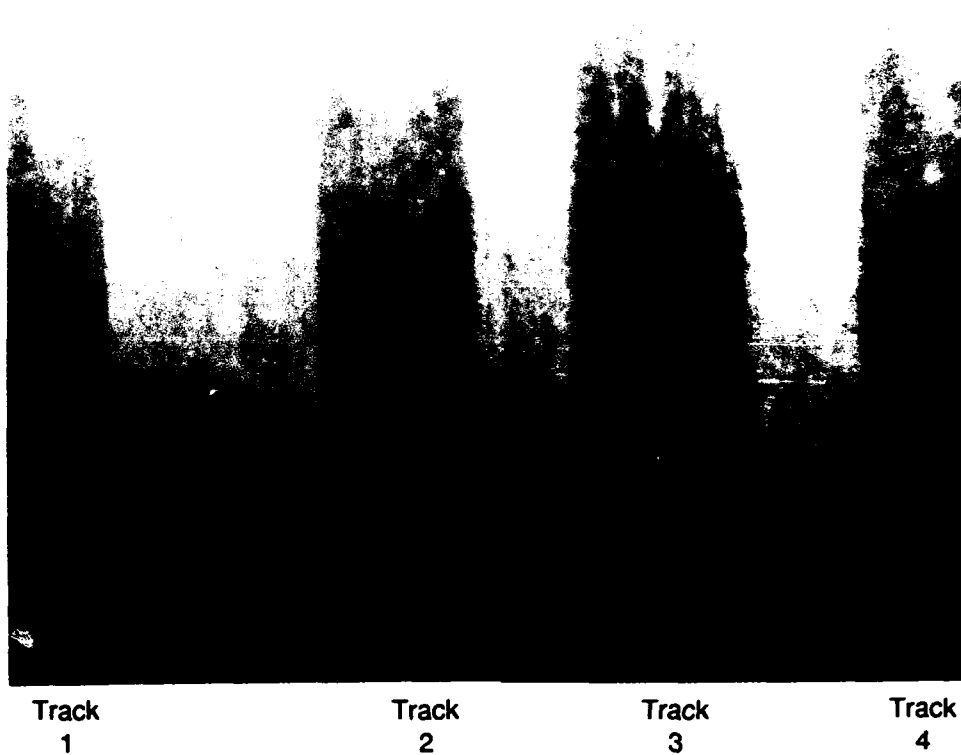
Track  
3

Track  
4

| Test No. | Description            | Track No. | Wear (In.) |
|----------|------------------------|-----------|------------|
| HU-13    | SiN/SiN, 0% BN (Flat)  | 1         | 0.016      |
| HU-14    | SiN/SiN, 40% BN (Flat) | 2         | 0.025      |
| HU-15    | SiN/SiC (Hipped)       | 3         | 0.024      |
| HU-16    | SiN/SiC (Hipped)       | 4         | 0.040      |

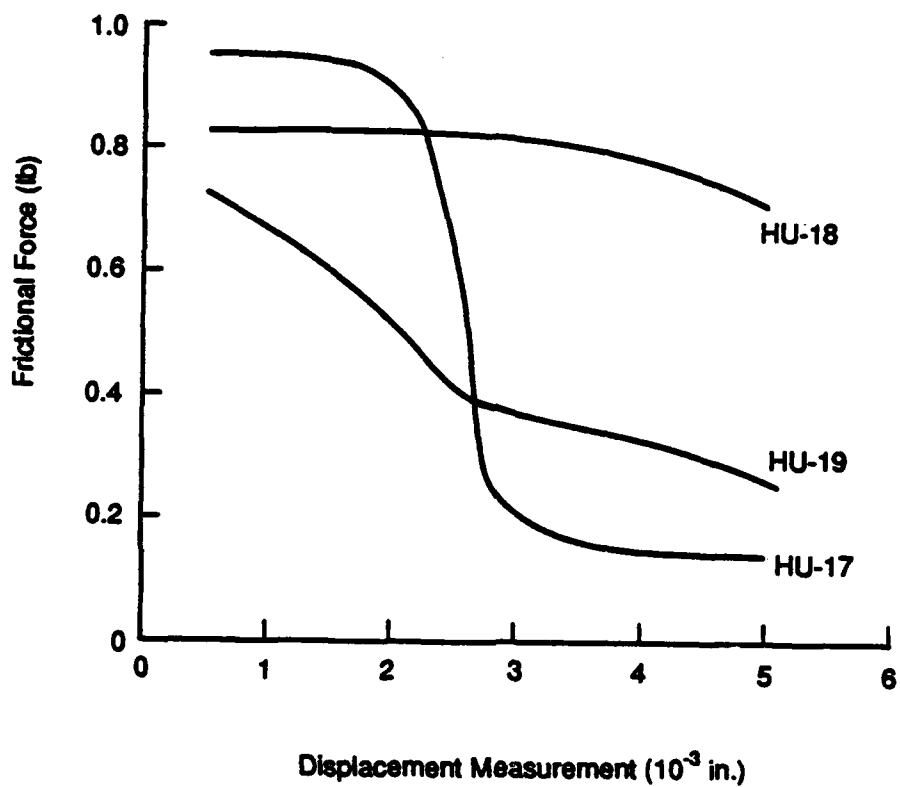
Figure 69. Photo of Disk 4 Wear

0-85



| Test No. | Description               | Track No. | Wear (in.) |
|----------|---------------------------|-----------|------------|
| HU-17    | SiN, 3.5% BN/SiN, 0% BN   | 1         | 0.0609     |
| HU-18    | SiN, 3.5% BN/SiN, 40% BN  | 2         | 0.0640     |
| HU-19    | SiN, 3.5% BN/SiC (Hipped) | 3         | 0.0593     |
| HU-20    | SiN, 3.5% BN/SiC (Hipped) | 4         | 0.0620     |

Figure 70. Photo of Disk 5 Wear



90446

Figure 71. Frictional Force vs. Total Wear